The Investigation of III-V Semiconductors Using SuperSTEM

Paul D. Robb

UNIVERSITY
of
GLASGOW

Presented as a thesis for the degree of Ph.D. at the

Department of Physics and Astronomy, University of Glasgow.

September 2007

ProQuest LLC.
789 East Eisenhower Parkway
P.O. Box 1346
Ann Arbor, MI 48106 – 1346

Abstract

In recent years, the performance of electron microscopes has been greatly improved through the implementation of practical aberration correction technology. This has allowed the creation of instruments that can form Å-scale electron probes at acceleration voltages of only 100kV. As an example, SuperSTEM 1 was the first UK based aberration-corrected 100kV field emission gun scanning transmission electron microscope (FEG-STEM) that was capable of achieving a spatial resolution of 1Å. Instruments, such as SuperSTEM 1, permit a wide range of nanostructures to be studied at scales that were not previously possible in commercial microscopes.

The introduction of aberration-corrected instruments has been an important development for the characterisation of state of the art semiconductor materials. For instance, some III-V semiconductor structures already incorporate layers that are only a single atom in width. However, due to the limitations of the techniques that have been previously used to characterise such materials, it remains unclear exactly how successful growth methods (such as MBE i.e. molecular beam epitaxy) actually are at producing sharp interfaces. Hence, the ability to study semiconductor materials at the atomic scale has become ever more crucial for technological and economic reasons.

In this project, SuperSTEM 1 was used to study several MBE grown III-V semiconductor nanostructures. These materials have applications in present, and possibly future, semiconductor devices. However, in order to improve the performance of such devices, a more in-depth appraisal of the associated growth techniques is necessary. Hence, the aim of this project was to provide atomic scale information on the composition and interfacial sharpness of the various layers that were present in the MBE grown III-V semiconductor nanostructures. This project also required a greater understanding of some aspects of probe scattering and the HAADF (high angle annular dark field) imaging technique due to the exceptional Å-scale spatial resolution of SuperSTEM 1.

Background information on the type of III-V materials that were studied in this project is given in Chapter 1. This information involves a description of superlattices and doped heterostructures. In addition, the molecular beam epitaxy growth technique is explained along with previous estimates of the sharpness of AlAs / GaAs and InAs / GaAs interfaces. At the end of Chapter 1, a small section is devoted to the background of the SuperSTEM project.

Chapter 2 is mainly concerned with the experimental apparatus and techniques that were employed to characterise the various materials. For instance, the chapter begins with a short introduction to the foundations of electron microscopy such as electron lenses and their associated aberrations. The CTEM (conventional transmission electron microscope) and STEM imaging techniques are also explained along with the principles of the HAADF STEM imaging process and EELS (electron energy loss spectroscopy). The two electron microscopes that were utilised in this project are also outlined. These instruments comprise a Tecnai F20 and SuperSTEM 1. In the case of SuperSTEM 1, the method of aberration correction is also outlined. It should be noted that the majority of the results in this project were obtained using SuperSTEM 1 and the HAADF imaging technique. Finally, a summary of the specimen preparation techniques are given at the end of Chapter 2.

In this project, all of the specimens were orientated along the <110> direction to give the familiar dumbbell configuration characteristic of zinc-blende crystals. In addition, the first material that was studied through the use of SuperSTEM 1 was a MBE grown III-V semiconductor heterostructure that formed part of a high frequency modulation doped field effect transistor (MODFET). The results from this investigation are presented in Chapter 3. In order to enhance the analysis of the SuperSTEM 1 data, HAADF images were converted into maps of the dumbbell column ratio. These maps gave an indication of the dumbbell composition of the various layers that were present in the heterostructure. HAADF images also revealed that several growth defects were present throughout the heterostructure.

Frozen phonon multislice computer simulations were also performed in order to gain a deeper understanding of the scattering behaviour of Å-scale electron probes in III-V semiconductor materials. Real space electron intensity distributions in crystals of GaAs [110], AlAs [110] and InAs [110] were calculated as a function of probe size, probe position and crystal thickness. It was found that the strong channelling depth was largest in atomic columns constructed from low Z number atoms such as Al. The extensive set of results from the simulations is discussed in Chapter 4.

In addition, the HAADF image contrast and the HAADF dumbbell column ratio of AlAs [110] and GaAs [110] were calculated as a function of thickness for the SuperSTEM 1 probe. These HAADF imaging attributes were compared against experimental values obtained using SuperSTEM 1. It was established that the simulated and experimental values of the dumbbell column ratio were in good agreement. However, there was a poor correspondence between simulation and experiment when the image contrast was

considered. The comparison between simulated and experimental values is shown in Chapter 5.

In the case of MBE grown AlAs / GaAs structures, interfacial sharpness was investigated as a function of specimen thickness. This is presented in Chapter 6. It was demonstrated that AlAs-on-GaAs interfaces were associated with large [110] surface step lengths and GaAs-on-AlAs interfaces were associated with elemental diffusion. These results were obtained from a single AlAs / GaAs interface and a wide layer 9ML AlAs / 9ML GaAs superlattice. Furthermore, the quality of a narrow layer 1ML AlAs / 2ML GaAs superlattice is reported in Chapter 6.

A study of InAs / GaAs superlattices is presented in Chapter 7. Despite the fact that In tends to spread over several monolayers, the results highlight that such multilayers are able to be grown using MBE. However, it is not clear whether such structures can be grown to a similar quality as MBE grown AlAs / GaAs structures. In addition, a study of Si δ-doped layers is detailed in Chapter 7. The results suggest that the detection of such a small concentration of Si in GaAs is at the limit of what can be achieved using SuperSTEM 1.

The final chapter (Chapter 8) contains a discussion of the experimental findings from this project. This chapter also considers some improvements that could be made to the experiments along with possible future work.

Acknowledgements

Firstly, I would like to thank my principal supervisor, Prof. Alan Craven, and my second supervisor, Dr Stephen McVitie, for continuous help and guidance over the past few years.

I am also grateful for the microscope training I received in the SSP Group from Dr. Sam McFadzean, Dr. Maureen MacKenzie and Mr. Colin How. I also appreciate the general assistance provided by Dr. Sam McFadzean, Dr. Maureen MacKenzie, Mr. Colin How, Mr. William Smith, Mr. Brian Miller and Dr. Jamie Scott throughout my time in the SSP Group. I am also very grateful to Mr. Brian Miller who taught me the black art of specimen preparation, provided valuable advice on specimen preparation and who was also kind enough to prepare most of the specimens I examined. I would also like to thank Mr. Michael Finnie for helping to investigate the problems with the simulated probe shape and for continuing the investigation into the level of specimen damage along with Mr. Brian Miller and Mr. William Smith.

This thesis would not have been possible without materials to investigate. Therefore, I am indebted to Dr. Martin Holland for growing the MBE wafers and also for feedback given on the results.

I am also grateful to the members of the SuperSTEM team. In particular, I would like to thank Dr. Andrew Bleloch and Dr. Uwe Falke for teaching me to operate SuperSTEM 1 and for advice in general. I would also like to thank Dr. Mhairi Gass for microscope assistance and Mr. Iain Godfrey for technical support whilst at SuperSTEM. Special thanks should also go to the other SuperSTEM students who made trips to SuperSTEM more enjoyable.

I would like to thank the other members of the SSP Group who provided an entertaining and 'intellectually' stimulating environment. The main culprits included Craig, Paolo, James, Michael, Catriona, Frances, Robin, Kerry, Brian, Jamie, Susan, Beverley, Gary and Michelle. Cheers folks. I would also like to acknowledge the (minimal) support of my family- Mo, Bo and the red one. They said: "The more you explain it, the more I don't understand it." Typical.

Declaration

This thesis is a record of the work carried out by myself in the Department of Physics and Astronomy at the University of Glasgow. The work described herein is my own, except for Figure 2.8, which was supplied by the SuperSTEM team, some of images shown in Chapter 3, which were acquired with the help of Dr. Uwe Falke, and most of the specimens were prepared by Mr. Brian Miller.

This thesis has not previously been submitted for a higher degree.

Contents

Abstract i

Acknowledgements iv

Declaration v

Chapter 1: Introduction 1

1.1 Background 1

1.2 Heterostructures 3

1.2.1 Introduction 3

1.2.2 Superlattices 4

1.2.3 Doped Heterostructures 5

1.3 Molecular Beam Epitaxy 7

1.4 MBE Interfacial Sharpness 10

1.5 The Background to the SuperSTEM Project 12

1.6 Outline of Thesis 14

References 15

Chapter 2: Instrumentation and Techniques 18

2.1 Introduction 18

2.2 Electron Microscopy Foundations 19

2.2.1 Wavelength of Electrons 19

2.2.2 Interaction with Matter 20

2.2.2.1 Introduction 20

2.2.2.2 Elastic Scattering 21

2.2.2.3 Inelastic Scattering 23

2.2.3 Electron Sources 25

2.2.3.1 Introduction 25

2.2.3.2 Thermionic Guns 26

2.2.3.3 Field Emission Guns 27

2.2.4 Electron Lenses and Aberrations 28

2.2.5 Electron Detectors 32

2.3 Basics of CTEM and STEM 34

2.3.1 CTEM Imaging Process 34

2.3.2 STEM Imaging Process 36

2.3.3 HAADF STEM Imaging 39

2.3.4 CTEM / STEM Instrument 41
2.4 Aberration-corrected STEM 43
2.4.1 Background 43
2.4.2 SuperSTEM 1 Instrument 45
2.4.3 Method of Aberration Correction in SuperSTEM 1 47
2.5 Electron Energy Loss Spectroscopy 50
2.6 Specimen Preparation 53
2.7 Summary 57
References 58
Chapter 3: The Investigation of a MODFET Heterostructure Using SuperSTEM 1 61
3.1 Introduction to the MODFET Heterostructure 61
3.2 Deep Superlattice 63
3.2.1 Background 63
3.2.2 Image Background Signal 64
3.2.3 Dumbbell Column Ratio Maps 68
3.2.4 Compositional Variation across the Deep Superlattice 74
3.3 Surface Region 78
3.3.1 Background 78
3.3.2 Growth Errors 80
3.3.3 Composition of the Surface Region 83
3.3.4 Conducting Channel 88
3.4 Discussion 92
3.4.1 Summary of Results from the MODFET Heterostructure 92
3.4.2 Averaged Column Ratios 93
References 96
Chapter 4: Computer Modelling: The Scattering of Å-scale Electron Probes in III-V Semiconductor Crystals 98
4.1 Introduction 98
4.2 Computer Modelling Background 100
4.2.1 Software Package 100
4.2.2 Simulation Interpretation 100
4.2.3 Frozen Phonon Method 104
4.2.4 Simulation Outline 105
4.3 24mrad Probe Results 110

4.3.1 24mrad Probe Characteristics 110
4.3.2 GaAs Results 114
4.3.2.1 Real Space Crystal Intensity Maps 114
4.3.2.2 Channelling, EELS and the HAADF STEM Signal 120
4.3.2.3 Beam Spreading in GaAs 129
4.3.3 AlAs 132
4.3.3.1 Real Space Crystal Intensity Maps 132
4.3.3.2 Channelling, EELS and the HAADF STEM Signal in the PPAl Case 136
4.3.4 InAs 140
4.3.4.1 Real Space Crystal Intensity Maps 140
4.3.4.2 Channelling, EELS and the HAADF STEM Signal in the PPIn Case 144
4.3.5 24mrad Probe: A Comparison of AlAs, GaAs and InAs 148
4.4 Comparison of the Results from the 3 Probes 153
4.4.1 Introduction 153
4.4.2 Probe Characteristics 153
4.4.2.1 50mrad Probe 153
4.4.2.2 12mrad Probe 155
4.4.3 Comparison of the Real Space Crystal Intensities 158
4.4.4 Comparison of the HAADF STEM Signals and Beam Spread 162
4.5 Summary 166
References 169
Chapter 5: Experimentally Derived HAADF STEM Image Contrast and Dumbbell Column Ratios 171
5.1 Introduction 171
5.2 Tecnai F20 HAADF Image Contrast 172
5.2.1 Method 172
5.2.2 Si [110] Results 176
5.2.3 GaAs [110] Results 177
5.3 SuperSTEM 1 HAADF Image Contrast 178
5.3.1 Method 178
5.3.2 GaAs [110] Results 183
5.3.3 AlAs [110] Results 184
5.3.4 Comparison to Simulations 185

5.4 Dumbbell Column Ratios 188
5.5 Conclusions 192
References 194
Chapter 6: The Characterisation of AlAs and GaAs Based Structures as a Function of Specimen Thickness 196
6.1 Introduction 196
6.2 Single Interfaces 199
6.2.1 Introduction 199
6.2.2 Beam Spreading Explanation of Non-sharpness 201
6.2.3 Stepping and Diffusion Explanations of Non-sharpness 205
6.2.4 Level of Sharpness as a Function of Thickness 206
6.2.4.1 Sharpness of the Interfacial Dumbbell Column Ratio 206
6.2.4.2 Sharpness of the Interfacial HAADF Background Signal 210
6.3 Wide Layer 9ML AlAs / 9ML GaAs Superlattice 214
6.3.1 Introduction 214
6.3.2 Sharpness of the Interfacial Transition Region 216
6.4 Narrow Layer Superlattice 219
6.5 Conclusion 223
References 225
Chapter 7: The Characterisation of Various MBE Grown Nanostructures using SuperSTEM 1 226
7.1 Introduction 226
7.2 InAs / GaAs Based Superlattices 227
7.2.1 Background 227
7.2.2 1ML InAs / 6ML GaAs Superlattice 229
7.2.3 1ML InAs / 3ML GaAs Superlattice 234
7.3 Si δ-doped Layers in GaAs 239
7.3.1 Background 239
7.3.2 Test Specimen 240
7.3.3 The Highest δ-doped Si Layer 241
7.4 Conclusion 247
References 250
Chapter 8: Conclusions and Further Work 251

8.1 Introduction 251
8.2 Conclusions 251
8.3 Improvements and Future Work 260
References 263
Appendix A: Diagrams from Computer Modelling Investigation 265
A.1 24mrad Probe Simulations 265
A.1.1 GaAs PPGa Condition 265
A.1.2 AlAs PPAs Condition 267
A.1.3 AlAs PPBD Condition 269
A.1.4 InAs PPAs Condition 270
A.1.5 InAs PPDB Condition 272
A.2 50mrad Probe Simulations 273
A.2.1 GaAs Real Space Intensity Maps 273
A.2.2 GaAs PPAs Condition 277
A.2.3 GaAs PPGa Condition 279
A.2.4 GaAs PPBD Condition 281
A.2.5 AlAs Real Space Intensity Maps 282
A.2.6 AlAs PPAs Condition 286
A.2.7 AlAs PPAl Condition 288
A.2.8 AlAs PPBD Condition 290
A.3 12mrad Probe Simulations 291
A.3.1 GaAs Real Space Intensity Maps 291
A.3.2 GaAs PPAs Condition 295
A.3.3 GaAs PPGa Condition 297
A.3.4 GaAs PPBD Condition 299
A.3.5 AlAs Real Space Intensity Maps 300
A.3.6 AlAs PPAs Condition 304
A.3.7 AlAs PPAl Condition 306
A.3.8 AlAs PPAl Condition 308
Appendix B: Transition Region Widths of AlAs / GaAs Structures 309

1 Introduction

1.1 Background

Solid state materials can be grouped into the 3 classes of insulators, semiconductors and conductors [1]. Semiconductors have conductivities that are intermediate between those of insulators and conductors. Furthermore, the conductivity of a semiconductor is typically sensitive to temperature, the presence of magnetic fields, illumination and small amounts of impurity atoms [1-3]. For these reasons, semiconductor devices are the foundation of the electronics industry.

The continuing trend of device miniaturisation not only reduces the cost of manufacture but also improves the intrinsic switching time of devices such as metal oxide semiconductor field effect transistors (MOSFETs) [1]. In addition, smaller devices also consume less power. However, the current Si based technology is rapidly approaching the point at which improvements in device performance can no longer be achieved through miniaturisation because device components are already fabricated on the scale of only a few atoms. For instance, the SiO_2 gate dielectric in state of the art CMOS (complementary metal oxide semiconductor) devices is only 1.4nm in width [4, 21]. Hence, other semiconductor materials are being actively investigated.

In recent years, compound semiconductors have been used to create various devices [1, 2, 5-7]. Many of the compound semiconductors have electrical and optical properties that are distinct from those of Si. Some of the most important compounds for high speed electronic and photonic applications are made from a combination of a Column III and Column V elements from the periodic table. Of these, GaAs has been the most widely studied [1, 2]. This material has the zinc-blende crystal structure and is an example of a direct energy band gap semiconductor [8, 10]. In addition, GaAs based nanostructures can be used to form devices that are similar to Si / SiO_2 based MOSFETs (see Section 1.2.3). However, the mobility of n-type carriers in GaAs based devices is typically much higher than their Si based equivalents. For instance, in GaAs, the electron mobility is $9200cm^2V^{-1}s^{-1}$ compared to only $1450cm^2V^{-1}s^{-1}$ in Si [1].

It is evident that low dimensional GaAs based systems have improved the performance of, for example, optoelectronic devices [22]. However, the small scale of the systems has created the need for extremely precise growth techniques. This can be appreciated by

considering that in some heterostructures (see Section 1.2) the composition should ideally change abruptly over a single atomic plane. Several different growth methods have been developed over the years that attempt to confine the individual elements on an atomic scale [9]. For example, all of the results that are presented in later chapters were from materials that were grown by molecular beam epitaxy (MBE). This technique is explained in Section 1.3.

A number of techniques can be used to characterise the sharpness of the interfaces that are grown by MBE. These methods include electron microscopy, photoluminescence, capacitance methods and scanning tunnelling microscopy [9]. Previous estimates of the sharpness of different types of MBE grown interfaces are given in Section 1.4. Nevertheless, it remains unclear exactly how successful MBE actually is at growing abrupt heterojunctions. This is due to the limitations of the techniques that are exploited in order to characterise the resulting semiconductor materials. For example, the spatial resolution that was attainable from pre-aberration-corrected electron microscopes (at an accelerating voltage of 100kV) was about 2Å [11-17]. Therefore, the ability of typical electron microscopes in providing information on the required scale was restricted since the atomic plane spacing in GaAs <110> is 1.4Å [8, 10]. In addition, it should also be noted that as device sizes become smaller, deviations from the ideal growth structure become increasingly important and there is, therefore, a greater need to investigate the materials in more detail.

Electron microscopes are now able to attain a spatial resolution of 1Å [16, 18]. Hence, the accuracy of the semiconductor growth methods can now be ascertained on the necessary atomic scale. The SuperSTEM project established the first UK based 100kV scanning transmission electron microscope (STEM) that was capable of achieving such a resolution. The aim of the continuing project is to provide a centre of excellence through which the highest resolution analytical microscopy research can be pursued. The background to this project is given in Section 1.5.

The first SuperSTEM instrument (termed SuperSTEM 1) was utilised in order to study the quality and the composition of a GaAs based nanostructure that formed part of a high speed device. The results are presented in Chapter 3. The analysis of this structure gave an indication of the precision of the MBE growth method and also led to various follow up investigations that concerned the sensitivity of SuperSTEM 1 in the detection of different III-V materials. In addition, the investigations were also a way of assessing the performance of a new generation of aberration-corrected instruments.

The improved performance offered by SuperSTEM 1 also created new challenges in the interpretation of the acquired data. For instance, a lack of understanding of how the image signal is generated in instruments like SuperSTEM 1 required a computer simulation investigation to be performed of how a 1Å scale electron probe is scattered by various III-V semiconductors. This investigation was complemented by experimental investigations into particular features of SuperSTEM 1 images such as the image contrast. This improved the analysis of a number of important III-V nanostructures that were grown by MBE. These included AlAs / GaAs based structures (Chapter 6), InAs / GaAs based multilayers (Chapter 7) and Si δ-doping layers (Chapter 7).

1.2 Heterostructures

1.2.1 Introduction

Heterostructures are semiconductor materials in which the chemical composition of the structure changes with position along the growth direction [1, 2, 6]. The simplest heterostructure is composed of a single heterojunction, which is an interface between 2 different types of material such as between layers of GaAs and AlAs. However, most heterostructures contain many heterojunctions. In addition, heterostructures are important due to the fact that the motion and state of charge carriers within such materials can be controlled [2]. In fact, heterostructures also permit the control of other fundamental parameters of semiconductor crystals. These parameters include band gaps, the effective masses of charge carriers, refractive indices and the electronic band structure [2]. The control of these parameters is accomplished by varying the composition of the various layers that form the heterostructures.

A large variety of devices can be fabricated from heterostructures for both electronic and optical applications. For instance, their properties have been exploited to form low noise high electron mobility transistors that are commonly used in high frequency applications such as in satellite television, wireless local-area networks and in integrated photoreceivers [19, 20]. In this instance, the cut-off frequency refers to the frequency at which a device can no longer amplify the input signal and thus is considered to be a figure of merit for the speed and performance of a device [1].

The range of properties that are associated with heterostructures can be increased through the presence of alloys. For example, the alloy $Al_xGa_{1-x}As$ is widely used to construct wide

layer superlattices (see Section 1.2.2). Furthermore, it is possible (in principle) to perfectly connect 2 different materials together if they have the same crystal structure and possess nearly identical lattice constants in order that the resulting structure is not under strain. For that reason, it is possible to grow $Al_xGa_{1-x}As$ on top of GaAs without the introduction of significant stress since they have the same zinc-blende crystal structure and similar lattice parameters. For instance, the lattice parameter of GaAs and $Al_xGa_{1-x}As$ is 5.6533Å and (5.6533 + 0.0078x)Å, respectively [8, 10]. Moreover, the band gap energy in $Al_xGa_{1-x}As$ can be altered due to its dependence on the alloy composition.

Nevertheless, even in the case of lattice matched $Al_{0.3}Ga_{0.7}As$ / GaAs heterojunctions, it is impossible (in practice) to join different materials together in a seamless way. This has important consequences if it is considered that the active regions of heterostructures are close to the interfaces [2]. For example, the electrical characteristics of an interface can be affected by the existence of compositional variations along the interfaces. These imperfections can result in the creation of localised energy states that trap or scatter charge carriers [2]. The associated scattering mechanism of the charge carriers is termed surface roughness. This can limit the mobility of the carriers and, therefore, have a negative effect on the overall performance of a device that is constructed from a heterostructure [22]. This therefore imposes stringent demands on the processes that are employed to grow heterostructures (see Section 1.3). In addition, in a typical Si / SiO_2 based MOSFET, the charge carriers can also be scattered by the presence of charged defects in the oxide [2]. Due to the fact that an oxide layer is not used in III-V heterostructures, there should be no scattering from the presence of net charge along the interfaces. Hence, III-V heterostructures have an advantage over Si / SiO_2 based devices in terms of the scattering from charged defects.

1.2.2 Superlattices

As was stated above, the behaviour of electrons and holes can be manipulated through the variation of the precise composition of the different layers that are present in heterostructures. This is essentially because different materials have different energy band gap characteristics. For instance, GaAs has a narrower principal energy band gap than $Al_xGa_{1-x}As$. Hence, if a layer GaAs is grown between 2 layers of $Al_xGa_{1-x}As$, the GaAs acts like a quantum well in which electrons and holes are confined [6]. However, in practice, it is usually necessary to compute band-structure calculations in order to determine the exact alignment of the various conduction and valence energy bands that are associated with the 2 interfacial materials [2].

Heterostructures can also be grown to contain many alternating layers of quantum wells and barriers in which the electrons can tunnel from one well to another. These structures are called superlattices since a second level of periodicity is imposed on the first level, which is the crystalline nature of the semiconductors. Furthermore, a superlattice generates a periodic potential so that the motion of carriers along the direction of growth is governed by Bloch's theorem and band structure [6]. The ordered layer structure of a superlattice only affects the motion of the carriers along one direction.

The period of a superlattice is always longer than the period of the underlying crystal and, therefore, the periodic potential that is related to the superlattice is weaker than the crystal potential. Consequently, the energy bands of the superlattice appear on a much smaller scale of energies. In addition, the large number of wells and barriers eliminate the discrete bound levels within each of the wells. This produces a miniband energy structure [2]. The miniband structure that emerges in the superlattice can be finely tuned by changing the thickness and composition of the various layers. Hence, the properties of the superlattice can be adjusted for a particular application. For example, superlattices have been exploited in order to filter the energy of electrons in a heterostructure. Moreover, infrared radiation that falls on a superlattice can be detected through the absorption of the radiation by the minibands [2]. Furthermore, as the thickness of the barriers in a superlattice is increased, the width of the minibands decrease and the tunnelling of the carriers between wells has less effect on the overall properties of the structure [2].

1.2.3 Doped Heterostructures

Semiconductor devices require the introduction of dopant atoms in order to provide the electrons or holes for conduction. The areas that require the presence of carriers cannot be directly doped due to the fact that charged donors (or acceptors) are left behind when the electrons or holes are released. These ions scatter the carriers through Coulomb interactions [1]; this particular mechanism is termed ionised impurity scattering. Hence, the motion and the mobility of the carriers are adversely affected and the finely tuned energy levels of a heterostructure become blurred. To overcome this difficulty, modulation doping is utilised in which the dopant atoms are inserted in a region away from where the carriers are needed.

In high mobility GaAs based devices, Si δ-doping is usually employed in order to provide the charge carriers [2, 27, 28]. The background to Si δ-doping and the problems that are associated with it are discussed in greater detail in Chapters 3 and 7. However, it should be

noted that δ-doping is a technique that confines dopant atoms within a very narrow region during the epitaxial growth of the host material. This produces advantages such as increased free carrier concentration (in the conducting channel of the parent device) and increased carrier mobility [27, 28]. It may also allow a smaller gate to channel distance in devices. Nevertheless, there is direct evidence that (above a certain doping concentration) the Si doping efficiency drops off [27, 28]. Indirect evidence also suggests that this may be the result of silicon clustering which involves the spreading of silicon over more than the ideal single Ga plane [27, 28]. An investigation into δ-doping is given in Chapters 3 and 7.

A simple example of modulation doping concerns a heterojunction of n-doped $Al_xGa_{1-x}As$ and undoped GaAs. Some of the electrons that are released from the dopant atoms (in the $Al_xGa_{1-x}As$ region) cross into the GaAs region. Due to the difference in the energy band gaps of the two materials (ΔE), the electrons lose energy and become trapped in the GaAs well. Thus, this process has separated the negatively charged carriers from the positively charged donors [6]. However, the electrostatic field that is produced by the ionised donors attracts the electrons back towards the $Al_xGa_{1-x}As$. The electrons cannot travel back into the $Al_xGa_{1-x}As$ due to ΔE and, therefore, they are squeezed against the interface [5, 6]. Hence, the energy levels for motion along the growth direction are quantised but the electrons remain free to travel in the two perpendicular directions. This forms a two-dimensional electron gas (2DEG) that is formed at a heterojunction and is the most important low dimensional system for electronic transport [2].

A simple schematic of a semiconductor device that utilises modulation doping in a heterostructure is shown in Figure 1.1. In such a device, the density of the 2DEG is controlled through the formation of a capacitor between the 2DEG and a metallic gate. Furthermore, the addition of a source and drain creates a modulation doped field effect transistor (MODFET) [6]. The heterostructure in this case contains layers of n-doped $Al_xGa_{1-x}As$ and undoped GaAs. Hence, the electrons from the donors in the n-doped $Al_xGa_{1-x}As$ layer travel into the GaAs conducting channel where they become trapped by the difference in the energy band gaps between the 2 materials. The presence of the undoped $Al_xGa_{1-x}As$ spacer region further separates the carriers and the ionised donors thereby reducing the ionised impurity scattering. Moreover, the shape of the gate is designed to reduce its resistance whilst keeping its contact with the heterostructure small. On the other hand, the capping layer of GaAs prevents the oxidation of the $Al_xGa_{1-x}As$ underneath.

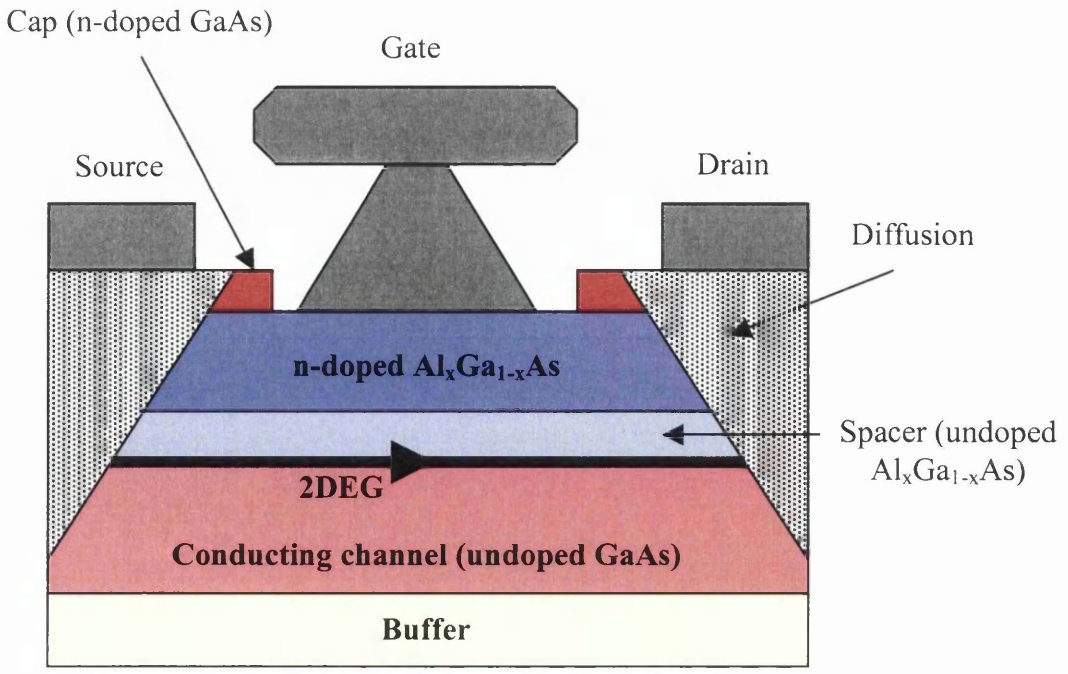

Figure 1.1: Schematic of a cross- section through a high frequency GaAs-$Al_xGa_{1-x}As$ modulation doped field effect transistor. Figure adapted from [7].

A key parameter for the operation of a MODFET is the threshold voltage (V_T) which is the gate bias at which the channel starts to form between the source and drain [1, 2, 5, 6]. When the gate voltage is larger than V_T, a 2DEG is induced by the gate voltage at the heterojunction interface inside the conducting channel that shown in Figure 1.1. Thus, the device acts like a capacitor with the charge density on one plate (the channel) controlled by the voltage on the metallic contacts [1, 2]. In fact, the output current (drain current) of a MODFET is controlled by varying the gate and drain voltages whereas V_T determines the on and off conditions at zero gate voltage [1]. For instance, a positive V_T results in an enhancement mode (normally off) device whereas a negative V_T results in a depletion mode (normally on) device. Furthermore, the output characteristics of FETs have a linear region (in a graph of output current versus drain voltage) at low drain biases [1]. As the drain bias increases, the output current eventually saturates. However, at a sufficiently high drain voltage, avalanche breakdown occurs at the drain and the output current goes to zero [1, 2].

1.3 Molecular Beam Epitaxy

As was explained in Section 1.2, high quality interfaces are desirable in heterostructures. For instance, the atomic structures of the 2 adjacent materials must match and the

heterojunctions must not contain any contaminants such as impurities or defects. Moreover, in order to fine tune the energy band structure for a certain application, the layers in a heterostructure may have to be very narrow in width [2]. Hence, during the growth process, the composition of successive layers must be changed very rapidly, preferably on a monolayer scale. A monolayer (ML) of a composite material (such as GaAs) is defined as containing 2 atomic planes each made from a different type of atoms. In the case of GaAs, the Ga and As <001> planes are separated by 0.14nm (i.e. the dumbbell spacing).

Growth methods, such as liquid phase epitaxy, have been used in the past to grow coarser heterostructures but more specialised processes are required for the desired sharpness of the interfaces [6, 7]. To this end, two methods are generally utilised. These methods are molecular beam epitaxy (MBE) and metal organic chemical vapour deposition (MOCVD) [1]. It should be noted that MOCVD does offer some advantages over MBE. For instance, structures can be grown over a shorter period of time and the technique has been successfully scaled up for commercial production [2]. On the other hand, MBE is an expensive and time consuming process. In addition, MOCVD also has a reputation for growing better optoelectronic devices than MBE [6]. Nonetheless, several million high electron mobility transistors and AlGaAs / GaAs semiconductor based lasers are actually produced each month by MBE [20]. Furthermore, MBE does in fact produce abrupt junctions between different materials and also provides good control of the thickness of each layer [2]. MOCVD also has some major disadvantages compared to MBE. These include carbon contamination and the practical problem that is associated with the highly toxic gases that are used in MOCVD [2]. Due to the fact that all of the materials that are shown in later chapters were grown solely by MBE, the technique of MOCVD is not considered here.

In MBE, the substrate (on top of which the heterostructure is to be grown), is positioned on a heated holder in a chamber that is held under ultra high vacuum (UHV) conditions. The vacuum is typically better than 5×10^{-11}mbar [20]. A simple schematic of a MBE machine is portrayed in Figure 1.2. The chemical elements, which are used to construct the heterostructure, are vaporised (at high temperature) in ovens that have openings directed towards the substrate [20]. The ovens are made of high melting point materials such as boron nitride. In addition, molybdenum or tantalum are widely used in the construction of the shutters [9]. The diagram in Figure 1.2 only shows 3 ovens but, in reality, many more can be present. For instance, a Si oven is usually present in order to introduce dopant atoms into the structure.

Under the low pressure conditions of the MBE chamber, the time to form a single monolayer made of the ambient background impurities on top of the substrate is very long [10]. In addition, the UHV conditions ensure that the mean free path of molecules between collisions is much larger than the geometrical size of the chamber. This is the Knudsen or molecular flow regime of a gas and the ovens are sometimes called Knudsen cells for this reason [6]. In this regime, molecules that emerge from the ovens do not diffuse as they would at high pressure but form a molecular beam that travels in a straight line towards the substrate [20]. The growth of the heterostructure begins when the shutter in front of a particular oven is opened. The operation time of a shutter (about 0.1sec) is normally much shorter than the time required to grow 1 monolayer of material (typically 1 to 5sec). The exact sequence of opening and closing the different shutters determines the composition and structure of the multilayer that is grown. Furthermore, the temperature of each oven controls the intensity of the flux of each element on the substrate [9].

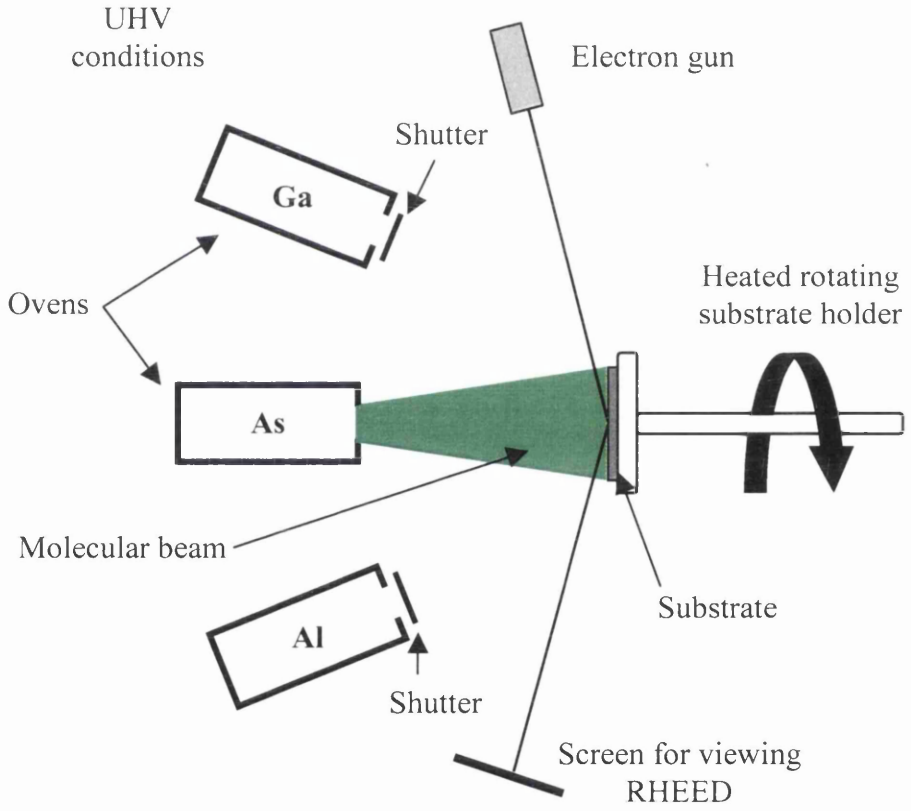

Figure 1.2: Simple schematic of a MBE machine with 3 ovens and a rotating substrate holder. RHEED is used for analysing the surface

If the elemental flux that emanates from each of the ovens is not uniform across the substrate a compositional variation will arise across the wafer [29]. However, this effect

can be reduced through the close control of the oven temperatures and also by the rotation of the wafer during the growth process. In addition, the temperature of the substrate is also important for the quality of the heterostructure. For instance, if the substrate temperature is too low then defects will not have had enough time to be removed by annealing [6]. In addition, the atoms on the growing surface tend to redistribute themselves to give a smoother surface due to the higher mobility of the atoms at high temperature. On the other hand, if the temperature is too high then unwanted diffusion may also occur which may result in compositional spreading across the layers. Hence, it is evident that the morphology of the wafer surface depends in a complicated way on temperature. Moreover, it is known that different materials are grown better through the use of different MBE conditions [6, 20].

Reflection high energy electron diffraction (RHEED) is a diagnostic technique that is often employed to monitor the growth process in MBE machines. This technique involves the generation of a diffraction pattern from the interaction of an electron beam with the wafer surface. The electron beam strikes the wafer at a glancing angle in order that the component of the incident electron momentum normal to the surface is very small. This ensures that it is only the uppermost few atomic layers that are probed by the beam [20]. The resulting diffraction pattern is formed on a fluorescent screen that is situated on the opposite side of the chamber (see Figure 1.2). Furthermore, the surface of the wafer varies in a periodic way as each atomic layer is grown and this can be observed in the structure and intensity of the RHEED pattern [9]. For instance, the intensity oscillation of the RHEED pattern exactly corresponds to the time needed to grow a single atomic plane of material. In addition, the difference between As and Ga stabilised surfaces (at the end of the growth of GaAs <001>) can be ascertained using the RHEED pattern [20]. Hence, the growth of each monolayer of material in the heterostructure can be distinguished, and controlled, precisely through the observation of the RHEED pattern [20].

1.4 MBE Interfacial Sharpness

The sharpness of semiconductor interfaces, grown by MBE, is an active area of interest since the quality of the interfaces directly affects the electronic and optical properties of the parent devices [6, 9]. For example, as was stated previously, surface roughness and the presence of charged defects can have an adverse effect on the mobility of the charge carriers in a device. In fact, the contribution of surface roughness to the observed sharpness of interfaces can be separated into the 2 categories of surface stepping and elemental

intermixing [26, 33]. The first category involves the collection of islands of one type of material on the other side of the ideal interface. This can lead to the existence of a stepped boundary between the 2 materials [22, 26]. The steps are typically associated with a characteristic step length. The second category is associated with the diffusion of the different elements across the boundary. Both categories of roughness are introduced during the growth process.

Many studies have been carried out on the sharpness of MBE grown AlAs and GaAs interfaces [22-25]. It is known that an interface made from GaAs grown on top of AlAs (GaAs-on-AlAs interface) has a different level of sharpness compared to that of the opposite configuration with AlAs grown on top of GaAs (AlAs-on-GaAs interface) [2]. It should be noted that AlAs / GaAs is used to refer to both types of interface. CTEM studies have investigated the difference between the 2 types of interface. For instance, such studies suggest that AlAs-on-GaAs interfaces are almost atomically abrupt at very small specimen thicknesses (~14nm) [22]. This is in contrast to GaAs-on-AlAs interfaces for which a sharpness of about 2MLs was found at the same small value of specimen thickness [22].

The reason for the abrupt nature of the AlAs-on-GaAs interface is due to the presence of large steps along the interface. For example, CTEM studies have revealed that (although step lengths have a range of values) the majority of steps along an AlAs-on-GaAs interface are above 55nm in length (along the [110] direction) [22]. Hence, at specimen thicknesses below 55nm, it is likely that the interface would appear as being atomically abrupt in a CTEM image since these images present a projection through the entire specimen thickness. In comparison, no consistent pattern of stepping was observed along the equivalent GaAs-on-AlAs interface [22]. The non-sharpness of this interface was likely the result of very small steps and elemental diffusion.

It should be noted that the surface steps along an AlAs-on-GaAs interface have different lengths along the [110] and [1-10] directions [22, 32]. For instance, it has been reported that whereas the majority of the [110] steps along an AlAs-on-GaAs interface are above 55nm in length, the majority of [1-10] steps along an AlAs-on-GaAs interface are below 15nm. In fact, the most probable [1-10] step length is about 5nm for AlAs-on-GaAs interfaces [22]. However, since all of the specimens that were studied for this project were always viewed along the [110] direction, the electron beam always projected through the longer steps of the [110] direction in AlAs-on-GaAs interfaces. Nevertheless, the perpendicular [1-10] direction can still be seen in the plane of [110] projected images and

this provides the possibility of observing the smaller steps in the [1-10] direction (see Chapter 6).

Another type of interface that is being actively studied is the interface between layers of In(Ga)As and (Al)GaAs [24]. It is known that in InGaAs / AlGaAs systems, the diffusion of the In atoms (during the MBE process) is recognized as a cause of severe degradation of the compositional abruptness of the heterointerfaces. For instance, an In diffusion length of 1.57nm (~5MLs) was measured across a MBE grown $In_{0.08}Ga_{0.92}As$ / GaAs interface [24]. In addition, CTEM studies have also showed that the In atoms from a single InAs monolayer spread over 4MLs into the surrounding GaAs [25]. An investigation into the sharpness of InAs / GaAs based superlattices is presented in Chapter 7.

Despite the fact that the results of the CTEM investigations are consistent with photoluminescence and scanning tunnelling microscopy (STM) results, the precise atomic structure of the interfaces have not determined [22]. This is due to the fact that the CTEM studies were conducted using pre-aberration-corrected microscopes. Hence, the limited spatial resolution of such instruments does not permit the study of such materials on an atomic scale. Inherent limitations of other characterisation techniques also do not allow the sharpness of the interfaces to be ascertained on an atomic scale [9]. For instance, only every other As or Ga plane along the [001] direction in GaAs can be observed in scanning tunnelling microscopy [23]. Hence, a qualitative characterisation of short range interfacial non-sharpness is difficult to achieve using this method. Consequently, the improved performance of the aberration-corrected SuperSTEM 1 was utilised in order to study MBE interfaces on a scale not previously possible.

1.5 The Background to the SuperSTEM Project

This section provides a brief overview of the SuperSTEM project. However, more details of aberration correction and its use in the SuperSTEM 1 instrument are given in Chapter 2. The main parameters that determine the spatial resolution of probe forming electron microscopes concern the size of the electron probe and the current it contains. Both of these attributes are ultimately set by the balance between the effects of electron diffraction and the existence of spherical aberration in the main probe forming lens [11-17]. In fact, all rotationally symmetric electromagnetic lenses that are used in electron microscopes suffer from a range of optical aberrations [16]. These have the effect of limiting the image resolution and, hence, impose a limit on the amount of information obtainable from a specimen [11-17]. Lens aberrations are discussed in greater detail in Section 2.2.4.

Over the last 50 years, the improvement in the performance of electron microscopes has been mainly achieved by focusing upon electronic and mechanical stability, electron source size and lens design [4, 16]. This resulted in spherical aberration becoming one of the dominant factors in the limitation of image resolution. Several methods have been proposed and built over the years in order to correct aberrations such as spherical aberration. For instance, 2 basic types of aberration correctors have been produced. These are based on octupole / quadrupole systems (pioneered by Scherzer, Deltrap and Krivanek) [16, 30] and hexapole systems (pioneered by Crewe, Rose and Haider) [16, 31]. Such systems rely upon computer software in order to correct the aberrations.

With the recent advent of practical corrector technology for STEMs (pioneered through the work of Professor Ondrej Krivanek at the University of Cambridge) the SuperSTEM project was established in 2002. This project is based on the construction and operation of two aberration corrected instruments (SuperSTEM 1 and 2) over an initial five-year period with the first one already operational. Four UK universities, Cambridge, Glasgow, Leeds and Liverpool, jointly manage the SuperSTEM project. However, a small onsite team that is based at a special facility at Daresbury undertakes the daily maintenance and operation of the microscope(s). This facility was needed in order to provide a stable working environment, free from mechanical and electrical vibration, to suit the high performance of the SuperSTEM instrument(s). A description of the SuperSTEM 1 instrument and the method of aberration correction are given in Section 2.4.

SuperSTEM 1 allows a quantitative picture of the electrical and bonding properties of a material to be ascertained on a scale not previously possible. The areas in which such an instrument can be applied are wide ranging. These include research into catalysts, alloys, bio-molecules and semiconductors. In addition, it was primarily this microscope that was used in order to study the interface sharpness of MBE nanostructures. These results are shown in later chapters.

1.6 Outline of Thesis

Chapter 2 deals with the background theory of electron microscopy and also provides a description of the experimental techniques that were employed. For instance, high angle annular dark field imaging and electron energy loss spectroscopy are explained. Furthermore, Chapter 2 includes an explanation of aberration correction and its exploitation in the SuperSTEM 1 instrument. The same chapter also outlines the instruments and techniques that were employed to prepare suitable specimens for use in the microscopes.

Chapter 3 presents the results from the first experimental investigation that utilised SuperSTEM 1 in this project. This investigation was concerned with a MBE grown III-V semiconductor heterostructure that was designed to form part of a high frequency modulation doped field effect transistor. On the other hand, Chapter 4 deals with a computer modelling investigation into how a 1Å scale electron probe is scattered by III-V semiconductor crystals. This study was undertaken on 3 different materials that are commonly used in structures such as the heterostructure shown in Chapter 3. In addition, Chapter 4 also compares some of the more important aspects of the scattering of a 1Å probe with the scattering that is associated with 0.7Å and 1.6Å probes.

Chapter 5 provides an investigation into the variation of the HAADF image contrast and the HAADF image dumbbell column ratio as a function of specimen thickness. These were obtained for different semiconductor materials and the results were compared to simulations.

In Chapter 6, a study into 3 different types of AlAs / GaAs based nanostructures is presented. Theses structures included a single AlAs-on-GaAs (and GaAs-on-AlAs) interface, a wide layer 9ML AlAs / 9ML GaAs superlattice and a narrow layer 1ML AlAs / 2ML GaAs superlattice. The study of 2 of these structures involved the measurement of interfacial sharpness as a function of specimen thickness for both types of AlAs / GaAs interface.

An investigation of MBE grown InAs / GaAs based superlattices and Si δ-doped layers embedded in GaAs is shown in Chapter 7. Finally, Chapter 8 gives a discussion of the results from the earlier chapters.

References

[1] S. M. Sze, Semiconductor devices: physics and technology, John Wiley & Sons, INC. (2002)

[2] J. H. Davies, The physics of low-dimensional semiconductors, Cambridge University Press (2005)

[3] J. R. Christman, Fundamentals of solid state physics, John Wiley & Sons (1988)

[4] A. J. Craven, Perspectives in nanoanalysis, EMAG (2003)

[5] R. Enderlein, N. J. M. Horing, Fundamentals of semiconductor physics and devices, World Scientific (1999)

[6] K. Eberl, P. M. Petroff, P. Demeester, Low dimensional structures prepared by epitaxial growth or regrowth on patterned substrates, Series E: Applied Sciences Vol. 298, Kluwer Academic Publishers (1995)

[7] E. F. Schubert, Doping in III-V semiconductors, Cambridge University Press (1993)

[8] J. S. Blakemore, Key papers in physics: gallium arsenide, The American Institute of Physics (1987)

[9] R. A. Stradling, P. C. Klipstein, Growth and characterisation of semiconductors, Aam Hilger (1991)

[10] S. Adachi, GaAs, AlAs and $Al_xGa_{1-x}As$: material parameters for use in research and device applications, Journal of Applied Physics 58, R1-R29 (1985)

[11] P. J. Goodhew, F. J. Humphreys, Electron microscopy and analysis 2nd edition, Taylor and Francis (1988)

[12] D. B. Williams, C. B. Carter, Transmission electron microscopy, Plenum Press (1996)

[13] M. H. Loretto, Electron beam analysis of materials, Chapman and Hall (1994)

[14] R. D. Heidenreich, Fundamentals of transmission electron microscopy Volume XIII, Interscience monographs and texts in physics and astronomy, John Wiley & Sons, Inc. (1964)

[15] J. A. Belk, Electron microscopy and microanalysis of crystalline materials, Applied Science Publishers LTD (1978)

[16] M. Valera, A. R. Lupini, K. van Benthem, A. Y. Borisevich, M. F. Chisholm, N. Shibata, E. Abe, S. J. Pennycook, Materials characterization in the aberration-corrected scanning transmission electron microscope, Annual Review of Materials Research, Vol. 35, 359-569 (2005)

[17] C. Hetherington, Aberration correction for TEM, Materials today (2004)

[18] U. Falke, A. Bleloch, M. Falke, Atomic structure of a (2×1) reconstructed $NiSi_2$ / Si(001) interface, Physics Review Letters (2003)

[19] P. Fay, W. Wohlmuth, C. Caneau, I. Adesida, 15GHz monolithic MODFET-MSM integrated photoreceiver operating at 1.55μm wavelength, Electronic Letters Vol. 31, no. 9 (1995)

[20] K. Y. Cheng, Molecular beam epitaxy technology of III-V compound semiconductors for optoelectronic applications, Proceedings of the IEEE, Vol. 85, No. 11 (1997)

[21] T. Kauerauf, B. Govoreanu, R. Degraeve, G. Groeseneken, H. Maes, Scaling CMOS: finding the gate stack with the lowest leakage current, Solid-State Electronics 49, 695-701 (2005)

[22] N. Ikarashi, K. Ishida, High-resolution transmission electron microscopy of AlAs-GaAs semiconductor superlattices, Journal of Materials Science: Materials in Electronics 7, 285-295 (1996)

[23] B. Z. Nosho, W. Barvosa-Carter; M. J. Yang, B. R. Bennett, L. J. Whitman, Interpreting interfacial structure in cross-sectional STM images of III-V semiconductor heterostructures, Surface Science 465, 361-371 (2000)

[24] T. Kitada, S. Shimomura, S. Hiyamizu, Surface segregation of indium atoms during molecular beam epitaxy of InGaAs / GaAs superlattices on (n11)A GaAs substrates, Journal of Crystal Growth 2006, doi:10.1016/j.jcrysgro.2006.11.170 (2006)

[25] V. V. Chaldyshev, Two-dimensional organization of As clusters in GaAs, Materials Science and Engineering B88, 195-204 (2002)

[26] B. R. Nag, Interface roughness scattering limited mobility in AlAs / GaAs, $Al_{0.3}Ga_{0.7}As$ / GaAs and $Ga_{0.5}InP$ / GaAs quantum wells, Semiconductor Science Technology 19, 162-166 (2004)

[27] G. Li, C. Jagadish, Confinement and concentration of electrons in Si δ-doped $Al_xGa_{1-x}As$ (x=0 and 0.35) grown by metalorganic vapour phase epitaxy, Journal of Crystal growth 167, 421-428 (1996)

[28] L. Hart, Si δ-doping in GaAs: investigation of the degree of confinement and the effects of post-growth annealing, Semiconductor Science Technology 10, 32-40 (1995)

[29] W. L. Sarney, S.P. Svensson, Characterization of compositional oscillations in InGaAs films induced by MBE cell configuration and substrate rotation, Sensors and Electron Devices Directorate, U.S. Army Research Laboratory, Adelphi, MD 20783 USA (2005)

[30] O. L. Krivanek, P. D. Nellist, N. Dellby, M. F. Murfitt, Z. Szilagyi, Towards sub-0.5Å electron beams, Ultramicroscopy 96, 229-237 (2003)

[31] M. Haider, H. Rose, S. Uhlemann, E. Schwan, B. Kabius, K. Urban, A spherical-aberration-corrected 200kV transmission electron microscope, Ultramicroscopy 75, 53-60 (1998)

[32] J. H. Neave, B. A. Joyce, Dynamic RHEED observations of the MBE growth of GaAs: substrate temperature and beam azimuth effects, Applied Physics A 34, 179-184 (1984)

[33] M. A. Herman, D. Bimberg, J. Christen, Heterointerfaces in quantum wells and epitaxial growth processes: Evaluation by luminescence techniques, Journal of Applied Physics, Vol. 70, No. 2 (1991)

2 Instrumentation and Techniques

2.1 Introduction

Electron microscopy is an invaluable tool for the characterisation of materials on a scale that is simply not possible using standard light based microscopes. Moreover, a wide range of information on the structure and chemical properties of a material can be obtained through a variety of different instrumentation setups. A description of the experimental apparatus that was utilised for the study of materials is presented in this chapter. This includes a description of the essentials of electron microscopy and a discussion on the aberrations that are present in electromagnetic lenses which are used in the different instruments.

A description of the most important components of a conventional transmission electron microscope (CTEM) and the associated CTEM imaging process is also presented. However, greater detail is provided on the scanning transmission electron microscope (STEM) as most of the experimental data was obtained using this type of instrument. This includes the high angle annular dark field imaging (HAADF) technique. The technique of aberration correction, which is utilised in SuperSTEM 1, is also explained. Furthermore, the analytical technique of Electron Energy Loss Spectroscopy (EELS) is also discussed.

The final section of this chapter centres on specimen preparation. This includes a description of the types of different specimens and the apparatus that was used to produce electron transparent specimens. In addition, the level of surface damage that is present in specimens is also discussed at the end of this chapter.

2.2 Electron Microscopy Foundations

2.2.1 Wavelength of Electrons

The whole of electron microscopy relies upon the properties of the imaging particle, the electron. These particles can be generated in a reproducible manner (see Section 2.2.3) and their trajectory can be controlled through the use of electromagnetic lenses due their possession of negative charge (see Section 2.2.4). However their most important quality, as far as their use in microscopy is concerned, centres upon the size of the electron's wavelength. In a working electron microscope, the electron wavelength is substantially smaller than that of visible light [1]. In addition, the value of the wavelength can be controlled through the variation of the microscope's accelerating voltage. This is highlighted by the relativistic electron wavelength (λ) expression:

$$\lambda = \frac{h}{\left[2m_o eV\left(1+\frac{eV}{2m_o c^2}\right)\right]^{1/2}}$$

In this expression, h is Planck's constant, m_o is the electron rest mass, e is the electric charge, V is accelerating voltage of the microscope and c is the speed of light [2].

Table 2.1 provides the wavelength and velocity of an electron at the 2 accelerating voltages that are used in the experimental instruments. It can be seen that, at 100kV, the wavelength of an electron (0.0037nm) is far shorter than that of visible light (400-700nm). Hence, in a fundamental way, much greater detail can be obtained from a sample material if it is irradiated with electrons as opposed to visible light [2].

Accelerating voltage (kV)	Relativistic wavelength (nm)	Velocity ($\times 10^8$m/s)
100	0.00370	1.644
200	0.00251	2.086

Table 2.1: Electron properties as a function of accelerating voltage.

2.2.2 Interaction with Matter

2.2.2.1 Introduction

In an electron microscope, a thin foil of specimen material is irradiated by electrons that have energies of the order of hundreds of kilo-electron volts. In the interior of the crystal, the electrons can be scattered by many different mechanisms that generate a range of secondary signals. Figure 2.1 provides a schematic of some of the signals that can be generated from the interaction of the specimen with a high energy electron beam. The collection of these signals can be used to give information about the specimen. If the specimen is thin enough, most of the incident electron intensity is transmitted through the specimen to give a direct beam. It can also be noted that the scattered electrons can be elastically or inelastically scattered due to the interaction with the specimen.

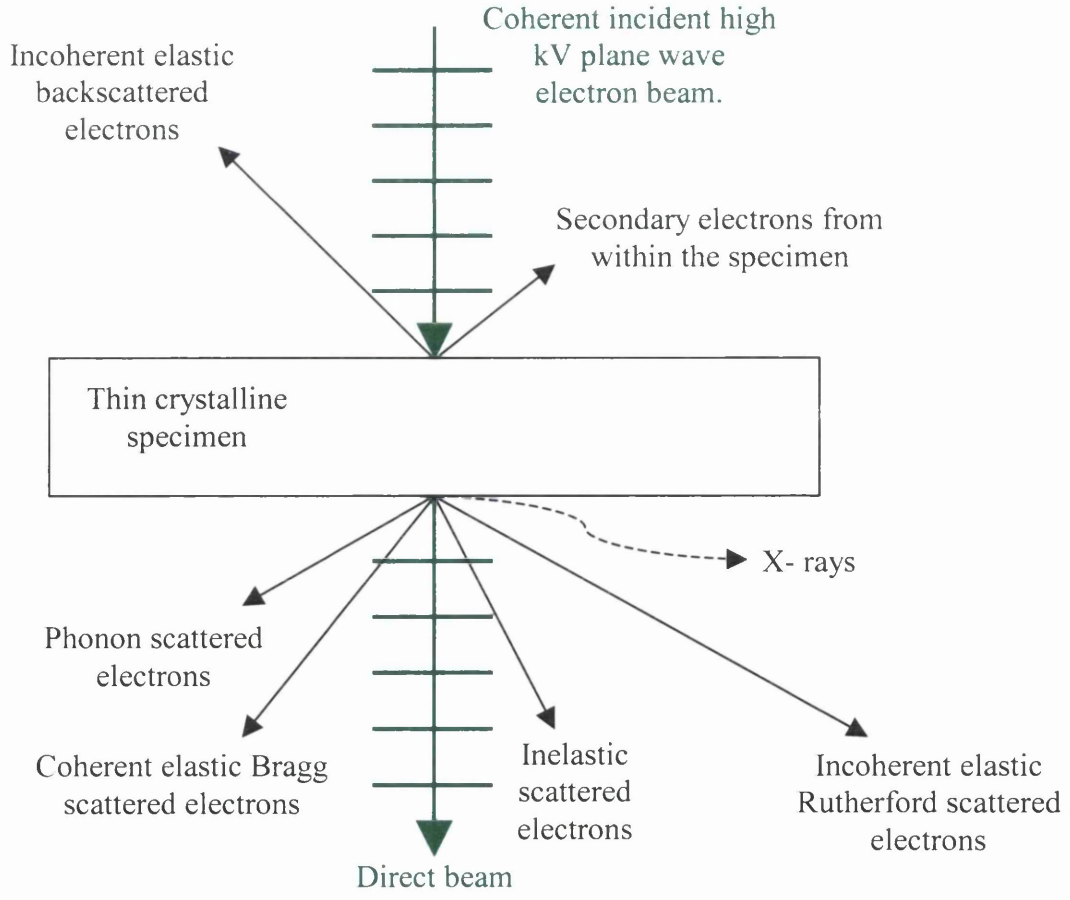

Figure 2.1: Simple schematic of the interaction of an electron beam with a thin foil. Scattered angles are not shown to scale. Adapted from [2].

2.2.2.2 Elastic Scattering

In the case of elastic scattering, the electrons mainly interact with the electrostatic potential of the atoms within the material. This potential can alter the trajectory of the electrons with a negligible energy loss. The relationship between the angle through which electrons are scattered by a single atom (θ) and the energy of the electrons is given by the atomic scattering amplitude, $f(\theta)$. It can be shown that $f(\theta) = (me^2 / 2h^2) \{\lambda / \sin\theta\}^2 (Z - f_x)$ where m is the relativistic electron mass, f_x is the atomic scattering factor for X-rays, Z is the atomic number of the atom and all other symbols have the same meaning as before [35].

The expression for $f(\theta)$ indicates that the scattering of electrons by a single specimen atom is associated with 2 separate mechanisms that are significant at different scattering angles. To be specific, the part of the expression that contains Z is associated with the scattering contribution from the nucleus (Rutherford like scattering) and f_x is associated with the scattering from the electron shells of the atom [3]. In addition, it can be noted that Rutherford like scattering is more important at large scattering angles whilst the scattering from the electron cloud is more important at low scattering angles.

It is clear that $f(\theta)$ is strongly influenced by the atomic (Z) number of the atom involved but it also decays very rapidly for large scattering angles [2]. Furthermore, the scattering factors for many elements have been calculated through the use of approximations that model the interaction of the incident electrons with the specimen atom [34]. However, it is known that the values of $f(\theta)$ for heavy atoms are likely to be the least accurate because the approximations do not simulate the interaction with high Z atoms sufficiently well [3].

The idea of the scattering amplitude for single atoms has to be modified in order to take into account the periodic nature of crystalline materials. This is due to the fact that the scattering from periodic arrays of atoms (rather than from an isolated atom) generates coherently diffracted waves. This particular process is governed by Bragg's Law and involves the diffraction of the electron waves out to characteristic angles through their reflection off crystallographic planes within the specimen. This leads to a structure factor, $F(\theta)$, which is a measure of the amplitude that is scattered by a unit cell of the specimen crystal [2]. $F(\theta)$ is defined by the sum of the individual atomic scattering factors of all of the atoms in a particular unit cell multiplied by a phase factor. The phase factor takes into consideration the difference in phase between waves that are scattered from different atomic planes within the unit cell.

It should be noted that electron diffraction is actually almost invariably dynamical in nature. This means that a Bragg diffracted electron beam can be re-diffracted by the crystal planes. This is in contrast to the kinematical approximation in which the diffracted beam is weak (compared to the direct beam) and it is not re-diffracted. The likelihood of dynamical diffraction increases as the specimen thickness is increased [4].

The angle at which Bragg scattering is generated is inversely proportional to the distance between the planes that diffract the electron waves [2]. However, Bragg diffraction is limited at large scattering angles due to the introduction of small displacements in the atomic positions by the thermal motion of the atoms. These displacements are enough to blur out the very closely spaced planes and they, therefore, cannot scatter in a coherent fashion [3]. Hence, the high angle diffraction information is smeared out by this mechanism. Furthermore, to take into account the effect of the thermal motion of the atoms, the intensities of Bragg diffracted beams are reduced through the multiplication with the Debye-Waller factor. This factor is given by $\exp(-16\pi^2u^2\{\sin^2\theta / \lambda^2\})$ where u^2 is the mean square of the atomic displacement that is perpendicular to the Bragg planes. It should also be noted that the magnitude of u increases with the temperature of the specimen [3].

Along with the use of structure factors, a crystalline material also necessitates the modification of the individual atomic scattering factors since the scattering is altered by the presence of bonding effects between atoms. For example, despite the fact that in semiconductors each atom still possesses localised core electron energy states, delocalised conduction and valence bands are also present. Since it is the energy of the outer electrons that are influenced by bonding effects, the change in the atomic scattering factors are more significant for low angle scattering. This effect is also present in ionically bonded solids such NaCl. In this case, $f(\theta)$ for both ions (at zero scattering angle) is about 20% greater than that of the neutral atoms [34].

On the other hand, high angle scattering can be described sufficiently well by considering only the scattering that is generated from the atomic nuclei and neglecting the scattering from the electron cloud. Hence, the scattering to large angles can be thought of as depending only on the nature of the atoms in the crystal and not on their relative positions as in diffraction from a set of crystal planes. Nevertheless, in Section 2.3.3 the channelling effect is discussed in which the scattered intensity to large angles is influenced by the periodic nature of the specimen. The amplitude of Rutherford scattering (at a particular

angle) is proportional to Z^2 / V^2 and is essentially an incoherent process as the various atoms do not scatter in phase [36].

It can be shown that the angle at which the scattering from the electron cloud in an atom can be neglected, θ_{nuc}, is given by $3.69Z^{1/3}V^{-1/2}$ [3]. For example, at an accelerating voltage of 100kV, the values of θ_{nuc} for Al, As and In are 27.4mrad, 37.4mrad and 43.0mrad, respectively. Hence, an electron microscope image can be produced solely from the scattering that originates from Rutherford like scattering from Al, As and In atoms if a suitable annular detector is utilised with an acceptance angle that is greater than 43mrad (θ_{nuc}). In fact, the inner and outer angles of the HAADF detector in SuperSTEM 1 are 70mrad and 210mrad, respectively. Hence, Rutherford like scattering from Al, As and In atoms will be picked up by SuperSTEM 1's HAADF detector. This is the basis of Z-contrast imaging (the image signal should vary approximately with Z^2), which is described in Section 2.3.3. However, the value of $f(\theta)$ is small at high scattering angles (>20mrad) and a high current electron probe is therefore required in order to produce a reasonable signal on the detector. On the other hand, the image contrast should be high.

2.2.2.3 Inelastic Scattering

Inelastic scattering involves the transfer of the energy of the incident electron beam to internal degrees of freedom in the atom or specimen [1]. This can occur in several ways. For instance, this transfer may result in the removal (from the attractive field of the nucleus) of one of the tightly bound inner-shell electrons. This allows chemical information to be obtained from the specimen through the analysis of the precise energy loss of the scattered electrons. This technique is explained in Section 2.5.

The transfer of energy from the imaging electron to the specimen material may also result in radiation damage to the specimen [2]. For instance, chemical bonds can be broken (radiolysis) and atoms can be directly displaced from the crystal lattice (knock-on damage). Due to the fact that knock-on damage increases with increasing beam energy, high voltage instruments are more likely to introduce this type of damage in low Z materials despite the improved resolution that they offer [2].

The valence electrons in solid state materials can interact with the imaging electrons through Coulomb interactions. This can result in a collective oscillation of the valence electrons that exist in a free electron gas (for example in a semiconductor). Such oscillations are called plasmons [1]. In addition, the energy of a plasmon is related to the

density of valence electrons and the associated scattering angle is inversely proportional to the energy of the incident electron beam. For instance, the scattered intensity per unit solid angle has an angular half-width equal to the energy of the plasmon divided by 2 times the incident beam energy [2]. Furthermore, the electrons in the specimen material that are ejected through the interaction of the incident electron beam are termed secondary electrons. For instance, the electrons that exist in the conduction or valence bands of the specimen are relatively easy to remove and are emitted with low energies (~20eV).

Specimen electrons can also be ejected if an ionised atom returns to the ground state. For example, the hole left by an ionised K-shell electron can be filled by a L_1-shell electron. The energy that is released by this process can be transferred to an electron in the $L_{2,3}$-shell which is then ejected. These ejected electrons are called Auger electrons and the probability of their emission is greatest for small Z atoms. They are emitted at characteristic energies that are given by the difference between the original excitation energy and the binding energy of the outer shell from which the electron was ejected [2]. Hence, Auger electrons are dependent upon the electronic structure of the ionised atom and can, therefore, be used to provide chemical information about the specimen. However, due to the fact that Auger electrons have low energies, only electrons near to the surface of the specimen can escape. This fact can be used to probe the chemistry of the specimen surface. Instead of Auger emission, specimen atoms can also return to the ground state by the emission of X-rays that also have characteristic energies [2]. X-rays and Auger electrons were not used to characterise any of the materials shown in later chapters.

As was stated in Section 2.2.2.2, atoms within a solid oscillate about their mean atomic position due to thermal vibrations. The collective oscillation of atoms in a crystal lattice is termed a phonon [2]. Phonon scattering can occur when an incident electron strikes the atomic bonds between atoms in the lattice structure. Hence, elastic scattering is reduced by the Debye-Waller factor and the lost intensity of the diffracted beams is redistributed as thermal diffuse background intensity that can be observed between diffraction spots in the diffraction pattern of the specimen [3]. The energy loss that is associated with phonon scattering (or thermal diffuse scattering) is of the order of k_BT where k_B is Boltzmann's constant and T is the temperature. Since thermal energy is transferred to the specimen, phonon scattering is equivalent to the heating of the specimen. At room temperature, the energy loss due to phonon scattering is very small (~0.025eV) but phonon scattering can blur the specimen diffraction pattern at high angles due to the strong scattering angle dependence of the Debye-Waller factor.

2.2.3 Electron Sources

2.2.3.1 Introduction

All electron microscopes require an electron source in order to illuminate the specimen material. Furthermore, the characteristics of a particular electron source are incredibly important in an electron microscope as these have a direct effect on the capability of the instrument as a whole. For instance, the brightness and the total current (for CTEM) from the source have a direct effect on the amount of detail that can be obtained from a particular specimen [5]. In addition, the electrons must also be accelerated in a controlled manner. This is accomplished through the incorporation of the source in an assembly called an electron gun.

One of the most important characteristics of electron guns concerns the source brightness, which is defined as the current density per unit solid angle [2]. It can be shown that the brightness increases linearly with accelerating voltage and also determines the total current which can be focused into a given spot size onto the specimen. Hence, it determines whether the current is sufficient in order to be used in probe forming instruments that require a large current in a small probe. The stability of the emission current with time is another important factor in the operation of electron guns. For instance, in scanned images, the presence of instabilities in the emission from the gun can produce image flicker that degrades the image quality. In addition, the energy spread of the source is also important as the chromatic aberration of the electromagnetic lenses (which are used in electron microscopes) can increase the size of the incident probe. The energy spread is caused by instabilities in the accelerating voltage supply and also by the inherent energy spread of the various emission processes. In fact, this will be a limiting factor in probe forming systems that have been corrected for spherical aberration.

There are two main types of electron guns that are commonly used in electron microscopes. The first type is called a thermionic gun in which the source material is heated in order to provide the conduction electrons with sufficient energy to overcome the material's work function [2]. On the other hand, this barrier is overcome through the application of an intense electric field in the second type of source which is called a field emission gun (FEG). The emission from a FEG may also be aided through the heating of the source material. This variation is termed a thermally assisted FEG (as opposed to a cold FEG in which no heating occurs). Furthermore, another FEG variation also exists in which the tip is both heated and coated with a material that lowers the work function (Schottky

FEG). In general, FEGs generate an electron beam with a far higher brightness, a reduced size and a smaller energy spread than is possible with thermionic guns.

2.2.3.2 Thermionic Guns

Electrons in any material can be given the required energy to overcome that material's particular work function and escape to the surroundings. However, most materials will simply melt or vaporise if given even a few eV of thermal energy. Hence, a high melting point material (like tungsten) or a material with a low work function (such as lanthanum hexaboride- LaB_6) is required to perform as a viable electron source material [2]. In the case of a tungsten source, a thin wire of tungsten is bent into a 'V' shape to form a hairpin filament in order that the emitted electrons originate from as small an area as possible. In contrast, LaB_6 sources are usually grown with a [100] crystal orientation to enhance the electron emission. However, due to the fact that LaB_6 is highly reactive, the gun vacuum must be 10-100 times better than in a tungsten thermionic source [2].

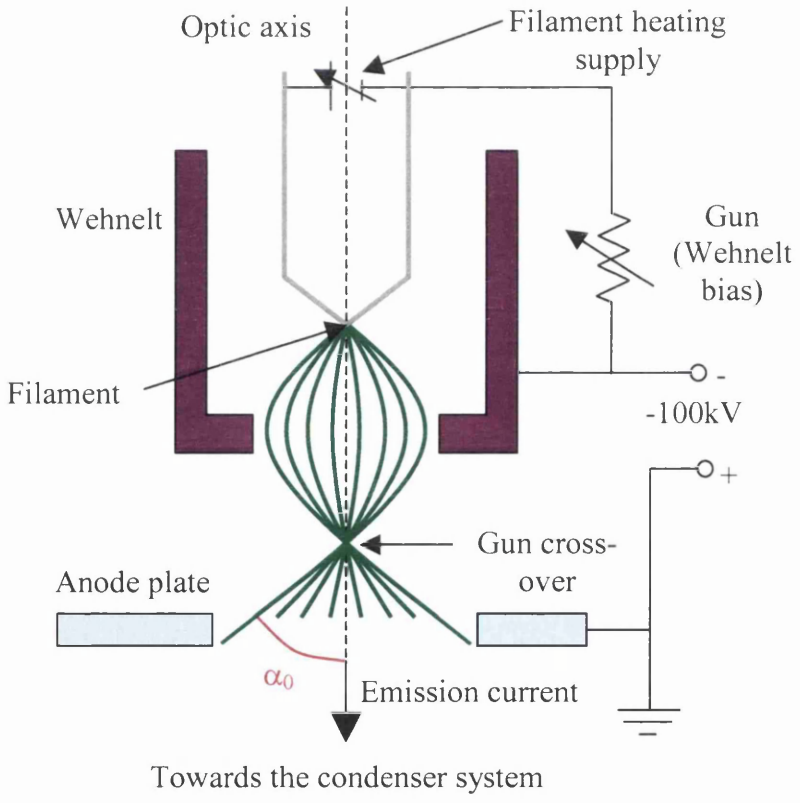

Figure 2.2: Schematic of a thermionic electron gun. Adapted from [2].

A schematic of a thermionic gun is shown in Figure 2.2. The assembly acts as a triode system in which the source material (tungsten or LaB_6) forms the cathode. The cathode is

heated (by the application of a current) up to the proper operating temperature at which thermionic emission occurs. The operating temperature in a standard tungsten based gun is usually about 2700°C [2].

The electrons that emanate from the filament are accelerated by the potential difference that exists between the cathode and anode (~100kV). In addition, in order to control the trajectory of the emitted electrons, a small negative bias is applied to the Wehnelt cylinder. This acts as a simple electrostatic lens. For that reason, the electron paths converge to form a cross-over point between the Wehnelt and anode [2]. The value of the Wehnelt bias is chosen in order to provide the optimum condition of a reasonably high current and a small enough source size (at the cross-over point). As an example, the source size that is obtained from a 100kV tungsten filament is typically about 10μm in diameter compared to about 1μm for a 100kV LaB_6 filament. Furthermore, the brightness of 100kV tungsten and 100kV LaB_6 filaments is about 3×10^6 and $10^7 Acm^{-2}sr^{-1}$, respectively [3]. These brightness values are not as high as the value that can be obtained from FEGs, which is about 10^7-$10^9 Acm^{-2}sr^{-1}$ for cold FEGs and about 5×10^8-$10^9 Acm^{-2}sr^{-1}$ for Schottky FEGs. Figure 2.2 also reveals that the electron paths diverge (at an angle of α_0 to the optic axis) after the gun cross-over point. α_0 defines the angle of the electron beam that enters the condenser system after the gun assembly.

2.2.3.3 Field Emission Guns

In contrast to thermionic emitters, electrons are emitted from FEGs by the application of an electric field. For instance, an anode close to the very fine filament tip (usually made of tungsten) is held at a few kV potential with respect to the tip. This extraction voltage generates an intense electric field that enables the electrons to tunnel out of the filament. The electric field around the tip is equal to the applied voltage divided by the radius of the tip. Furthermore, the electrons are accelerated by the potential difference that exists between the tip and a second anode (~100kV).

In some FEGs, the combined electric fields of the 2 anodes create a cross-over point in the trajectories of the electrons below the second anode. The source size at the cross-over point is typically less than 10nm in diameter for cold emission FEGs. Hence, a much smaller source demagnification is required in instruments that contain FEGs compared to ones that have thermionic guns. Moreover, the degree of source coherence in a FEG is much higher than in a thermionic gun due to the relatively small size of the FEG source [2].

The SuperSTEM 1 instrument (see Section 2.4.2) employs a 100kV cold FEG. This is operated with an extraction voltage below 4kV. The FWHM (full width half maximum) energy resolution of the gun is 0.3eV and has a gun brightness of $10^8 Acm^{-2}Sr^{-1}$. This gun produces a virtual source close to but behind the tip. In addition, this FEG also employs a magnetic lens in order to improve the control of the beam diameter and divergence angle that enters the condenser system. It should be noted that the gun does not need to be aligned at the start of each experimental session.

In comparison to thermionic guns, ultra-high-vacuum conditions are also necessary in FEGs in order to reduce the build up of contaminants on the surface of the tip. However, the tip must also be 'flashed' on a regular basis to remove the inevitable presence of surface contaminants. This involves either a reversal of the potential on the tip, which blows away the surface atoms, or the heating of the tip to about 2000-2800°C which vaporises the contaminants [2]. Moreover, the tip flash must be performed every ~30mins in SuperSTEM 1.

A Tecnai F20 microscope was also used to collect experimental data. This particular instrument is operated at an accelerating voltage of 200kV and is fitted with a Schottky field emission gun. The main component of the gun comprises a very fine tip made from a [100] orientated single crystal of tungsten. The tip is mounted on a tungsten hairpin that is used for heating the tip to about 1800K in order to enhance the emission of the electrons. A suppressor cap around the emitter is used to block electrons emitted by the heated hairpin. In addition, the presence of a thin layer of zirconia (ZrO_2) over the surface of tip lowers the work function of the material. An extraction anode (1.8-7kV) below the tip controls the electron emission and an electrostatic gun lens (positioned below the anode) is also used to control the beam that enters the condenser system. A beam cross-over is formed above the condenser system. Furthermore, a series of gun alignment files are loaded at the start of each session on the microscope. These control the gun excitation parameters for particular values of extraction voltage, spot size and gun lens excitation. Hence, the user is not required to align the gun at the start of each microscope session.

2.2.4 Electron Lenses and Aberrations

In an electron microscope, the trajectories of the electrons that are emitted from the gun are controlled through the use of electromagnetic lenses (except for an electrostatic gun lens that are employed in some electron guns). In this way, electron lenses are the magnetic equivalent of glass lenses that are used in light based microscopes.

Electromagnetic lenses are composed of a coil (usually made of copper) and a magnetic circuit which is made of a magnetic alloy (usually soft iron) with a specific shape [5]. The magnetic circuit has a hole, called the bore, drilled through it. If a current is passed through the coils, a magnetic field is generated within the magnetic circuit. However, the magnetic field also extends into a specially designed gap in the magnetic circuit. It is this magnetic field (in free space) that provides the focusing action on the paths of the electrons, which can be described by the calculation of the Lorentz force on the electrons [2]. For instance, an electron that is travelling along the axis of the lens, but not passing centrally though the lens, will interact with the radial component of the lens field. This interaction will cause the electron to experience a force directed towards the axis. In fact, the radial and axial components of the magnetic field of a lens results in a helical electron path through the axis of the lens. In addition, the strength of the magnetic field (and hence of the focusing action) depends upon the current that is passed through the coils. Furthermore, the magnification of an electromagnetic lens can be approximated by Newton's lens equation. Strictly speaking, Newton's equation is valid only for a thin lens and not for a thick one. In Newton's equation, the magnification is given by the distance from the lens to the image plane divided by the distance from the lens to the object plane. Hence, the magnification of a lens can be controlled by changing the lens focal length that is dependent upon the current that is applied to the lens [2].

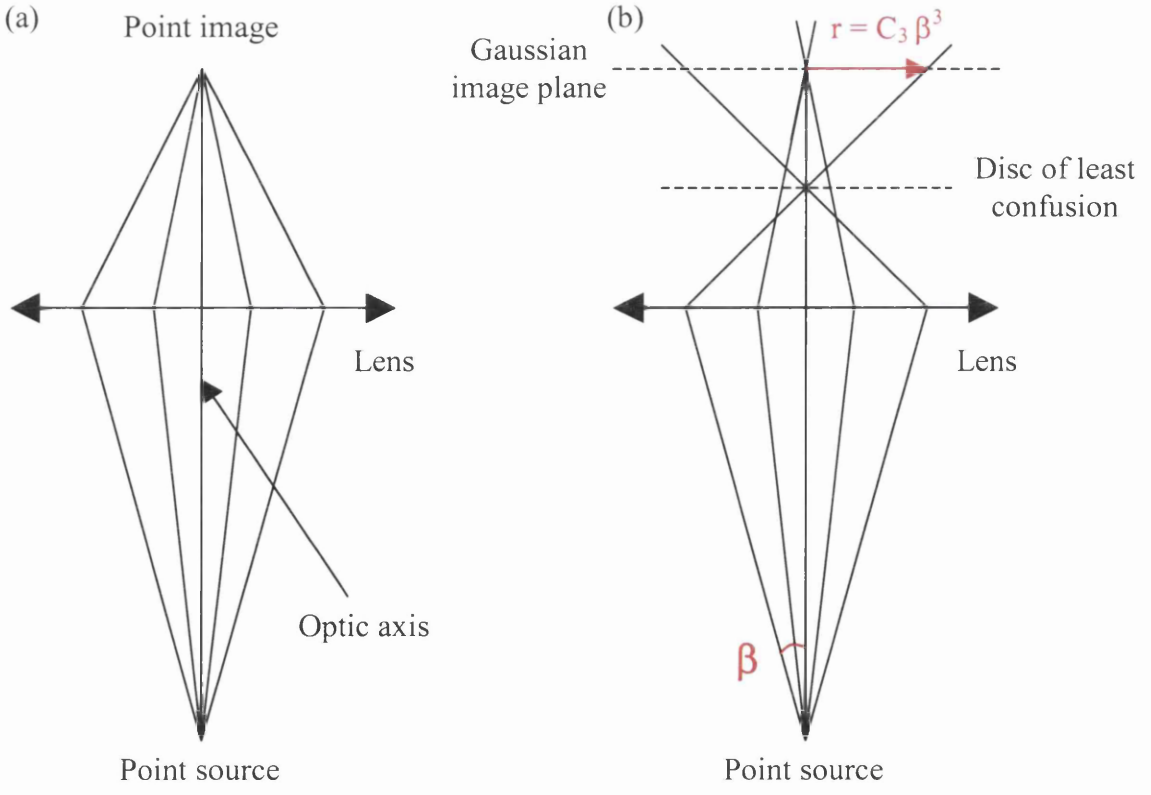

Figure 2.3(a): Ray diagram of a point source through a perfect lens. **(b)** is a ray diagram of a point source through a lens with spherical aberration.

Due to the inevitable presence of imperfections in the manufacture of magnetic lenses, lens aberrations are always present. In fact, spherical aberration and other 3rd order aberrations (see Table 2.2) are always present in ideal rotationally symmetric electromagnetic lenses [6]. In general, these aberrations cause degradation of the focused beam spot and severely restrict the amount of detail that can be obtained from an electron microscope. Furthermore, the reason for the significant disparity between the spatial resolution associated with electron microscopes and the wavelength of electrons is primarily due to aberrations of the magnetic lenses (particularly that of the objective lens) [2]. For instance, at an accelerating voltage of 100kV, the electron wavelength is 0.0037nm (see Table 2.1) but the resolution of non-aberration-corrected microscopes is only about 0.2nm at best.

In non-aberration-corrected microscopes, the main limiting lens aberration is termed spherical aberration of the objective lens [4]. A ray diagram of this particular aberration is shown in Figure 2.3(b). Figure 2.3(a) demonstrates that a point source of illumination will be focused into a point image by a perfect lens. The effect of the intrinsic lens aperture, which creates an image with an Airy disc pattern, is not considered in this case. On the other hand, a lens with spherical aberration (see Figure 2.3(b)) smears the point source into a disc. This is a result of the fact that a lens with spherical aberration more strongly focuses rays that travel at large angles with respect to the optic axis than rays that travel at small angles [2].

It is apparent that the basic limit to resolution is determined by the wavelength of the electrons and by the quality of the objective lens, which is related to the spherical aberration coefficient (C_3) [7]. Hence, a simple measure of the image spatial resolution in an electron microscope lens can be given as the combination (in quadrature) of the spherical aberration disk radius (proportional to $C_3\beta^3$ in which β is the maximum ray angle that is imaged by the objective lens) and the Airy disk radius (equal to $0.61\lambda/\beta$). In this case, the Rayleigh disk criterion is defined as the minimum distance between 2 object points that can be distinguished if they are imaged by a particular lens. It should be noted that each object point generates a separate Airy disc pattern due to the diffraction of the illumination from an object point by the intrinsic lens aperture. Furthermore, the combination of spherical aberration and the Rayleigh criterion leads to a practical measure of the resolution of a microscope called the point resolution limit, which is proportional to $\sim C_3^{1/4}\lambda^{3/4}$ [2].

In an optical system with spherical aberration, the incorrectly focused high angle beams can be removed by the use of a suitable aperture. However, the high angle rays carry

information about the smaller spacings in the illuminated object. Hence, spacings in the image can only be observed down to the point resolution limit [7].

In reality, many different types of lens aberration may be present in the optical system of a microscope. Therefore an aberration function, $\chi(\theta_x, \theta_y)$, can be exploited in order to fully describe the effect of all of the aberrations in a mathematical sense. $\chi(\theta_x, \theta_y)$ is defined as the phase shift that is imparted to a beam (by an aberrated optical system) that arrives on axis in the sample plane at an axial angle θ and an azimuthal angle φ. θ_x and θ_y are defined as being equal to $\theta\cos(\varphi)$ and $\theta\sin(\varphi)$, respectively [8]. However, the aberration function does not include the chromatic aberration that is associated with a lens. This particular type of aberration results in electrons with different energies being focused in different places. Nonetheless, the aberration function is a useful quantity and it can also be expanded as a polynomial as shown in the following equation:

$$\chi(\theta_x,\theta_y) = (2\pi/\lambda)\{C_1(\theta_x^{\,2}+\theta_y^{\,2})/2 + C_3(\theta_x^{\,2}+\theta_y^{\,2})^2/4 + C_5(\theta_x^{\,2}+\theta_y^{\,2})^4/6 + \ldots\}$$

In this equation, only aberrations up to fifth order that are rotationally symmetric about the azimuthal axis are shown. C_1, C_3 and C_5 are the aberration coefficients that are associated with defocus, spherical aberration and 5th order aberration, respectively. The coefficients have units of distance in each case.

Furthermore, a list of all of the aberration coefficients up to, and including, fifth order is shown in Table 2.2. All of the coefficients are denoted by C_{mn} where C denotes an axial aberration, m is the order of the aberrations and 2π / n denotes the smallest rotational angle that results in the same phase shift (for $n \geq 1$). Note that no n is used for cylindrically symmetric aberrations. Moreover, the suffixes a and b refer to 2 mutually orthogonal contributions to the same aberration that arise for all non-cylindrically symmetric aberrations [8]. It should be noted that C_0 (x and y shift) is used to move to the appropriate part of the specimen. In uncorrected microscopes, C_{12} and C_{23} (astigmatism and 3-fold astigmatism) can be corrected by using multipole lenses. Furthermore, C_{21} (coma) is made zero close to the axis by alignment. It should be noted that the method of aberration correction that is employed in SuperSTEM 1 is presented in Section 2.4.3.

Aberration coefficient	Name	Azimuthal symmetry
C_{01a}	x shift	1-fold
C_{01b}	y shift	1-fold
C_1	defocus	rotational
C_{12}	astigmatism	2-fold
C_{21}	coma	1-fold
C_{23}	3-fold astig	3-fold
C_3 or C_s	spherical	rotational
C_{32}	C_s 2-fold astig	2-fold
C_{34}	C_s 4-fold astig	4-fold
C_{41}	4^{th} order coma	1-fold
C_{43}	4^{th} order 3-fold astig	3-fold
C_{45}	5-fold astig	5-fold
C_5	5^{th} order	rotational
C_{52}	2-fold astig of C_5	2-fold
C_{54}	4-fold astig of C_5	4-fold
C_{56}	4-fold astig of C_5	6-fold

Table 2.2: Lens aberration coefficients up to fifth order. Taken from [8].

2.2.5 Electron Detectors

All electron microscopes must have the capability to detect the electrons that have been scattered by the specimen material. In fact, all electron detectors convert the variations in the scattered electron wavefunction into intensity variations that can be observed by the operator of the microscope in some way. In addition, several different types of detectors are commonly employed in CTEMs and STEMs. For instance, in CTEMs, a viewing screen is usually present at the bottom of the microscope [2]. This screen is coated with a scintillator (such as ZnS) that emits light in the visible part of the spectrum when electrons strike its surface [2]. The size of the scintillator grains must be small enough in order that the eye cannot distinguish the different particles. Furthermore, this particular type of detector generates an analogue image on the screen because the image cannot be manipulated in any way (for example, the contrast cannot be enhanced).

In comparison to the analogue nature of a viewing screen, digital detectors are also utilised in electron microscopes. These detectors allow the image to be digitised and electronically manipulated before being displayed on, for example, a CRT (cathode ray tube) screen as an analogue image. One of the most used types of digital detectors is the charge-coupled device (CCD). These are present in all of the specific experimental instruments that are described in later Sections. CCD arrays consist of many electrically isolated pixels that collect charge in proportion to the incident intensity of the electrons. The CCD array can be optically coupled to a suitable scintillator. In this way, the incident electrons do not directly interact with the CCD.

In order to generate an image, the CCD array must be read out which is accomplished through a change in the applied pixel potentials. This transfers the charge from each pixel along a line to an output amplifier. The output charge current is then fed through an analogue to digital converter to give the required number of grey levels. In this way, a digitally scanned image can be produced [2]. Furthermore, CCDs have very low noise, high quantum detection efficiency (defined by the division of the signal to noise ratio of the output signal by that of the input signal) as well as a large dynamic range [2]. However, CCDs are associated with dark currents such as thermal leakage currents as well as inherent electronic noise. These contributions to the output from CCD devices must be subtracted from the measured signal [9].

The SuperSTEM 1 instrument (see Section 2.4.2) also employs a scintillation-photomultiplier system which is another type of electron detector. This device is comprised of a scintillator material, such as Ce-doped yttrium-aluminium garnet (YAG), which is attached to a photomultiplier tube (PMT) via a light pipe. A different type of scintillator, compared to the viewing screen, is used in this system as the light emission decays more rapidly than it does in ZnS [2]. The energy conversion efficiency of the scintillator is rather low (as low as 2%) and only about 4000 photons are generated for each incident 100keV electron. The light (generated from the interaction of the imaging electrons with the scintillator) that impinges upon the top entrance of the PMT is converted back into electrons and these are multiplied by the electrodes in the PMT. This gain in the PM tube offsets the low energy conversion efficiency of the scintillator and ensures that every input electron gives an output pulse. At the end of the PMT, the electron signal is digitised and sent to a CRT screen for display. Scintillator-PMT systems typically have very high quantum detection efficiency and a low noise level. However, they are also susceptible to radiation damage [2].

2.3 Basics of CTEM and STEM

2.3.1 CTEM Imaging Process

The principal of imaging in a conventional transmission electron microscope is shown in the simple schematic of Figure 2.4. The electrons from a source material (see Section 2.2.3) are accelerated by the presence of a stable potential difference. This potential difference is usually 100-200kV (i.e. 100kV in SuperSTEM 1 and 200kV in the Tecnai F20). The electrons are then focused and attenuated by a series of condenser lenses and apertures. This creates a beam of electrons with a uniform intensity. The electron wavefunction, which is incident upon the top surface of the specimen, can be approximated by a plane wave of constant intensity that is given by $\psi_{inc}(\underline{r}) \sim 1$. The vector quantity $\underline{r}$ refers to the position in two-dimensional space.

If the specimen is thin enough, the incident electrons pass through the material with only small deviations in their trajectories due to the principal scattering mechanisms that were outlined in Section 2.2.2 [10]. If this is the case, then the effect of the specimen can be modelled as a simple transmission function, $t(\underline{r})$, through which a spatially varying phase shift is introduced into the electron wavefunction as it passes through the specimen [11]. It also can be shown that $t(\underline{r})$ is a function of the projected atomic potential of the specimen, which is the integration of the individual atom potentials along the direction of electron beam propagation (z). Moreover, the transmitted electron wavefunction (at the exit surface of the specimen) is denoted by $\psi_t(\underline{r}) = t(\underline{r})\psi_{inc}(\underline{r})$. In addition, the exact nature of the modification to the electron wave is a characteristic of the particular specimen material. This is because the projected potential is unique for each material and crystal orientation. Moreover, Section 4.2.2 provides a description of the multislice method that calculates the effect of dynamical scattering.

The objective lens, situated after the specimen, is manipulated in order to focus the transmitted electrons into a real image in the plane of the detector. In reality, a series of projector lenses are also used in order to magnify the final CTEM image. However, the effect of the magnification by the projector lenses can be ignored, in a mathematical sense, if the image coordinates are referred back to the dimensions of the specimen [10]. Furthermore, the imperfections in the objective lens distort the paths of the transmitted electrons in such a way as to degrade the detail in the final image. These lens aberrations were discussed in Section 2.2.4.

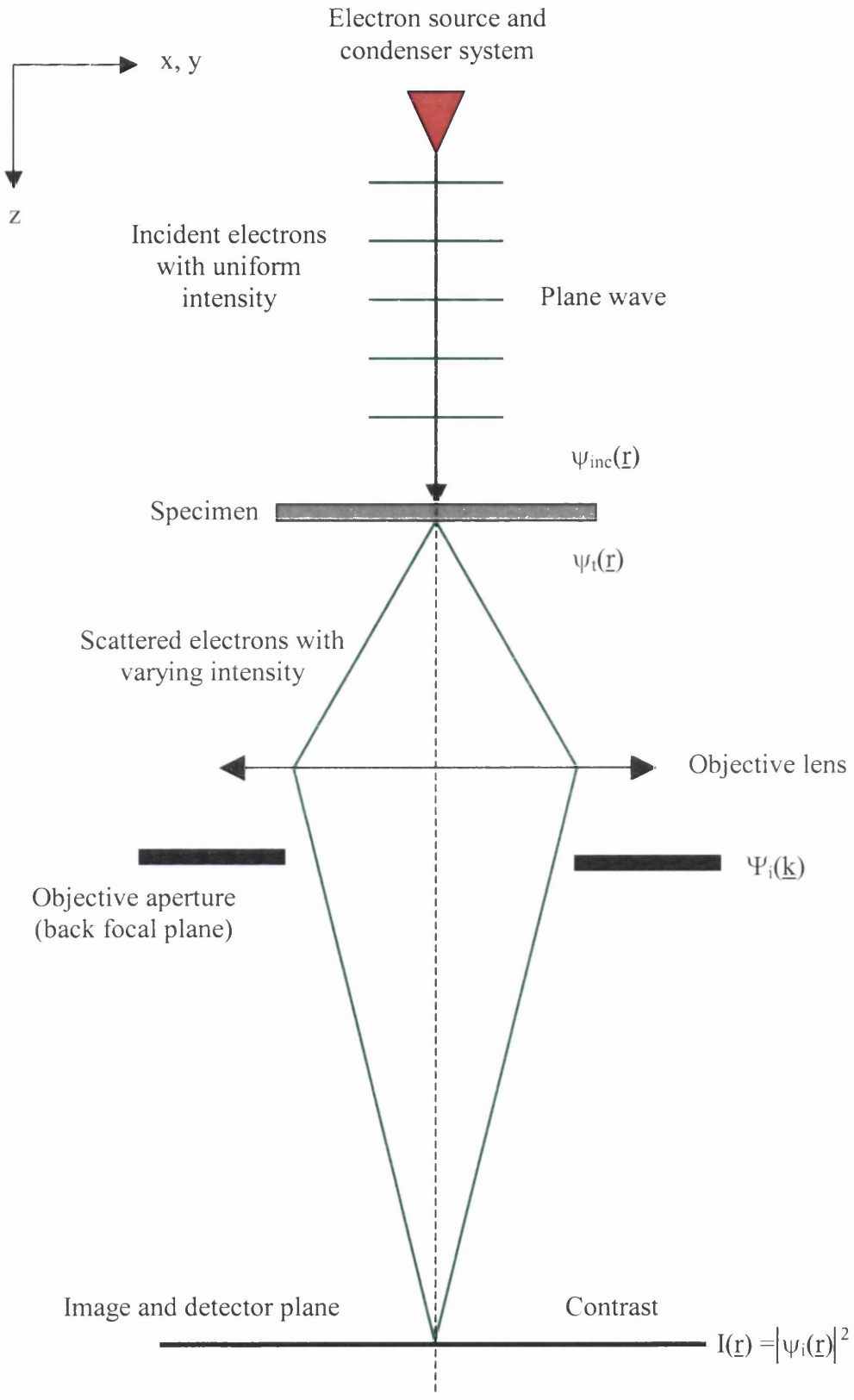

Figure 2.4: Simple schematic of the imaging process in a conventional transmission electron microscope.

In the back focal plane of the objective lens, the diffraction pattern of the specimen is also formed. It can be understood from simple optical theory that the electron wavefunction, in the back focal plane, is actually the Fourier transform of $\psi_t(\underline{r})$ [12]. Hence, the electron wavefunction is a function of wavevector ($\underline{k}$) and not of real space ($\underline{r}$). In this case, $|\underline{k}| = 1 / d$ where d is a spacing on the specimen. It should be noted that this definition of k does not include the 2π factor that is frequently used by solid state physicists. Furthermore, the aberrations of the objective lens alter the phase of each frequency component of the wavefunction by a different amount. This results in a diffraction image wavefunction, $\Psi_i(\underline{k}) = \exp(-i\chi(\underline{k}))\ FT[t(\underline{r})\psi_{inc}(\underline{r})]$ where $\chi(\underline{k})$ is the lens aberration function (this is given as a function of $\underline{k}$ where $\underline{k}$ is proportional to angle) and FT denotes a Fourier transform [10]. It should also be noted that an objective aperture can be employed to truncate the transmitted electrons in the back focal plane.

The wavefunction in the detector plane, $\psi_i(\underline{r})$, can be found by taking the inverse Fourier transform of $\Psi_i(\underline{k})$. A suitable detector, such as a scintillation material like ZnS (see Section 2.2.5), can be utilised in order to convert the electron wavefunction into a real image of the electron intensity distribution, $I(\underline{r})$ [2]. Hence, the modification of the electron wavefunction by the specimen material (and by the objective lens aberrations) can be seen as intensity variations in the final image. In addition, it is apparent that every part of the CTEM image is acquired at the same time and is therefore a parallel imaging process.

Coherent phase-contrast high resolution (HR-CTEM) imaging can be used to obtain lattice images of a crystalline specimen. The contrast that is observed in such images is related to the interference between the various diffracted beams that reach the detector [13]. For that reason, the contrast in a HR-CTEM image depends upon the relative phases of the diffracted beams. These phases depend sensitively on the lens aberrations, the defocus, the atomic number of the specimen material and also on the thickness of the specimen. HR-CTEM images therefore show complex contrast changes as a function of thickness and microscope operating conditions. In addition, information at specific values of $\underline{k}$ can also be missing from an image. Hence, image simulations or a through focal image series are usually required to properly interpret HR-CTEM images.

2.3.2 STEM Imaging Process

The order of the optical system in a STEM is reversed from that in a CTEM. For example, the objective lens is situated before the specimen [1]. A simple schematic of a STEM is

presented in Figure 2.5. It should be noted that the electron source is at the bottom of Figure 2.5 in order to reflect the position of the electron gun in real, dedicated STEMs.

The electrons from the gun, after passing through the condenser system, are focused into a fine probe by the objective lens. The probe that is generated is therefore the de-magnified image of the electron source (after passing through the condenser system). To ensure that an appropriate probe current is obtained after de-magnification, a high brightness FEG is typically used in STEMs (see Section 2.2.3).

The electrons that emanate from the objective lens are considered to be composed of many plane waves that travel at different angles to the optic axis [14]. Hence, these plane waves all have different wavevectors ($\underline{k}$). In addition, the probe wavefunction, which is incident on the top surface of the specimen, is a function of both space ($\underline{r}$) and probe position ($\underline{r}_p$). Moreover, the probe wavefunction is calculated through the integration of the plane waves over all of the present wavevectors. These range up to a value of k_{max}, which is equivalent to the maximum semi-angle subtended by the objective aperture ($\beta_{max} = \lambda k_{max}$). The plane waves are also influenced by the presence of the aberrations in the objective lens. Hence, the probe wavefunction is given by:

$$\psi_p(\underline{r},\underline{r}_p) = A\int_0^{kmax} \exp[-i\chi(\underline{k}) - 2\pi i\underline{k}(\underline{r}-\underline{r}_p)]d^2\underline{k}$$

In this case, A is a normalisation constant that is chosen in order that the integration of $\psi_p(\underline{r}, \underline{r}_p)$, over all space, generates the value of the total probe intensity (in suitable units). The expression of the probe wavefunction also assumes that the image of the electron source, after demagnification by the condenser system, has a negligible size [10]. Therefore, coherent illumination of the objective aperture is also assumed.

The probe interacts with the specimen through the transmission function, $t(\underline{r})$, as was the case with CTEM imaging in Section 2.3.1. This produces a transmitted wavefunction, $\psi_t(\underline{r}, \underline{r}_p) = t(\underline{r})\psi_p(\underline{r}, \underline{r}_p)$. This wavefunction is then diffracted onto the detector plane by taking its Fourier transform to generate $\Psi_t(\underline{k}, \underline{r}_p)$ [10]. The intensity of $\Psi_t(\underline{k}, \underline{r}_p)$ as a function of scattering angle ($\lambda\underline{k}$) is actually the convergent beam electron diffraction (CBED) pattern. The CBED pattern is then integrated over the suitable detector inner and outer angles to calculate the intensity for 1 image pixel only. The rest of the image is formed by scanning the probe across the desired section of the specimen through the use of the scan coils.

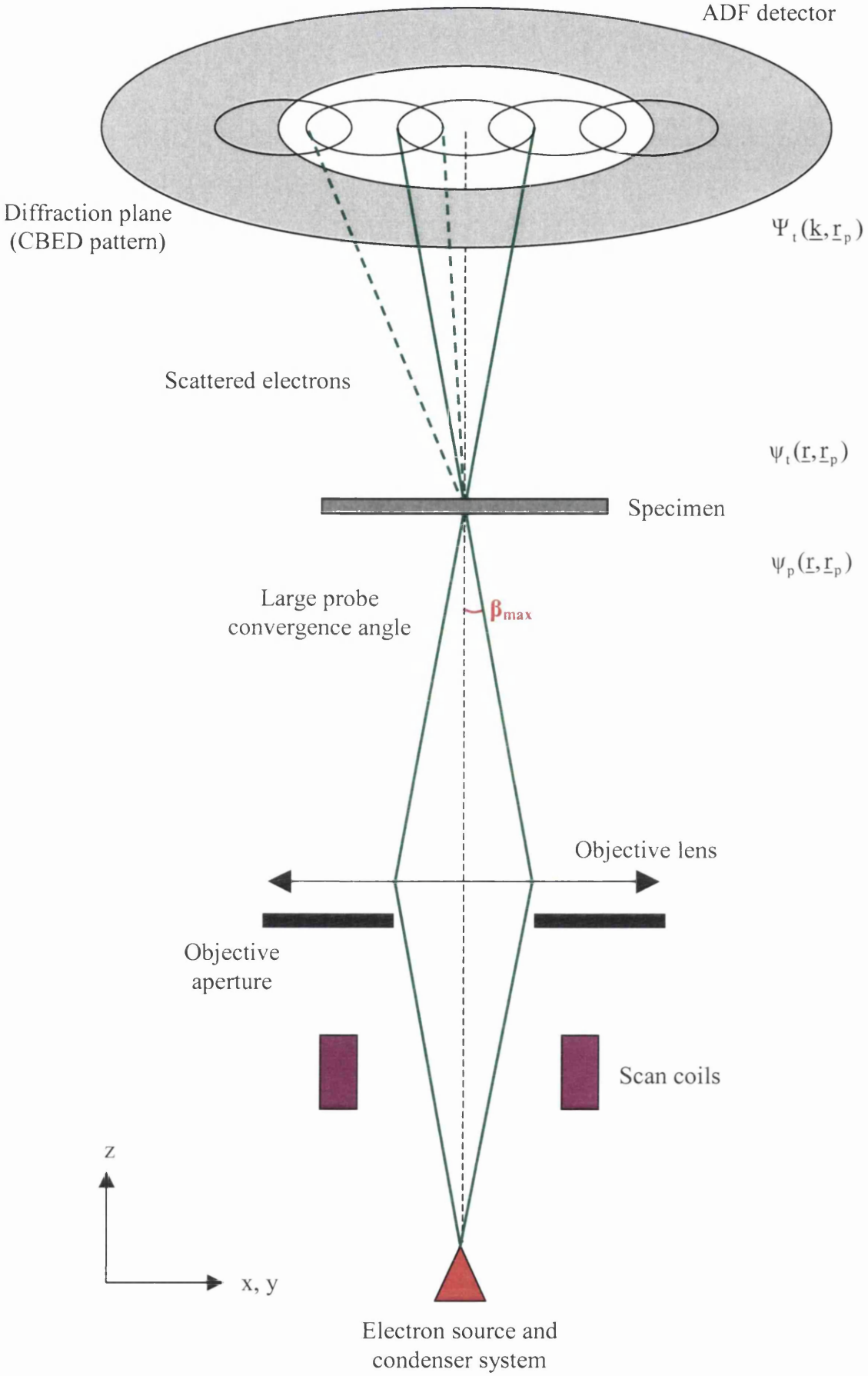

Figure 2.5: Simple schematic of the imaging process in a scanning transmission electron microscope.

2.3.3 HAADF STEM Imaging

The physical size and the position of the detector in a STEM have a great influence on the acquired image signal and, hence, on the information that can be obtained from a particular specimen. In recent years, high angle annular dark field (HAADF) detectors have become widely used in STEMs. Moreover, most of the results that are presented in the later chapters were obtained from the use of such a detector.

It is known, that the large inner angle of the HAADF detector (>50mrad) excludes most of the coherent elastic diffraction from the specimen [15]. It has also been widely reported that the imaging technique that is associated with the HAADF detector can provide atomic resolution structure images that are, in general, easier to interpret than conventional HR-CTEM images [14]. This is due to the fact that no contrast reversals are observed in HAADF images over a wide range of spatial frequencies. This enables the optimum focus to be established by simply adjusting the focus to obtain the sharpest image possible.

In addition, HAADF images are commonly referred to as atomic number (Z) contrast images since (at high angles) the scattered intensity varies approximately with Z^2 due to Rutherford like scattering [6]. The exact variation with Z depends upon the accelerating voltage, detector angles and the orientation and nature of the atomic columns of the specimen. Furthermore, as was stated in Section 2.2.2, most of the scattered intensity (at high angles) is termed thermal diffuse scattering (TDS) because it is generated by single atoms that are uncorrelated with each other due to the presence of thermal lattice vibrations within the specimen. Hence, the TDS tends to blur out the diffraction pattern at high angles [16].

As was stated above, the HAADF contrast transfer function has no reversal of sign. This is because HAADF imaging is essentially an incoherent imaging technique. There are different ways to understand the incoherent nature of this imaging process. First of all, the reciprocity theorem demonstrates that a large STEM detector is equivalent to a large incoherent source in CTEM [2]. Therefore, the large angles of the HAADF detector ensure incoherent imaging. A second reason behind the incoherent nature of HAADF imaging centres on the fact that it is primarily TDS that falls upon the detector. In addition, it has also been shown that for electron probe sizes that are smaller than the distances between the atomic columns in a specimen and for large HAADF detector angles, transverse interference effects between neighbouring columns are minimised [17, 18]. Therefore, as an approximation, the intensity that falls on the HAADF detector ($I(\underline{r}, \underline{r}_p)$) can be described

as a convolution of the intensity in the incident probe ($|\psi_p(\underline{r}, \underline{r}_p)|^2$) with the specimen object function ($V(\underline{r}, \underline{r}_p)$) [10]. $V(\underline{r}, \underline{r}_p)$ is, approximately, the probability for scattering out to the large angles of the HAADF detector and is related to the projected atomic specimen potential. Furthermore, the specimen object function is strongly peaked at atom sites and the spatial resolution is limited only by the probe characteristics [19].

The way in which HAADF signals are affected by the nature of atomic columns is still not fully understood. For instance, longitudinal coherence along the vertical direction of atomic columns may exist [17]. However, it is believed that phonons in the specimen are sufficient to destroy any longitudinal coherence effects. Nevertheless, it is evident that the complicated scattering of the electron probe within the specimen has a direct influence on the character of HAADF images. This scattering is (in general) dependent upon the structure, composition and thickness of the material. Furthermore, several studies have also considered the effect of probe channelling down atomic columns [20]. This effect is due to the presence of strong potentials that are generated by the atomic nuclei along the columns. For instance, the strong potentials attract the imaging electrons and force them to propagate close to the columns. However, after a certain depth of crystal, most of the electrons will have been scattered away from a particular column.

2 computational methods can be employed to calculate the intensity distribution inside specimen crystals. One of these, the multislice approach, is discussed in the computer modelling investigation into the scattering of a 1Å probe in III-V materials. This is presented in Chapter 4. On the other hand, the second method entails the use of Bloch waves which are periodic solutions to the Schrödinger equation. It can be shown that an electron inside a crystal can be described by a sum of Bloch waves [2]. In addition, the 1s Bloch state is the most tightly bound and, therefore, has the broadest distribution in reciprocal space. Furthermore, the large angles of the HAADF detector result in the selection of the HAADF signal from these tightly bound 1s states as they add constructively whereas the less localised states interfere destructively at high angles of scattering [17]. With only one dominant Bloch state, dynamical diffraction effects are almost totally removed leaving only a column channelling effect [19]. Hence, the selection of the 1s Bloch states provides an equivalent explanation of the existence of the channelling condition along atomic columns. In fact diffraction and channelling represent the reciprocal and real space viewpoints of the same process [21].

2.3.4 CTEM / STEM Instrument

A Tecnai F20 microscope was used to collect experimental data. As was stated in Section 2.2.3, this particular instrument is operated at an accelerating voltage of 200kV and is fitted with a Schottky field emission gun. A schematic of the instrument is shown in Figure 2.6. It can be seen that the condenser system (situated after the gun) is composed of C1 and C2 electromagnetic lenses along with their associated apertures. The C1 and C2 lenses control the beam spot size and beam convergence angle, respectively. On the other hand, the purpose of the C1 aperture is to remove any stray electrons from the gun whereas the C2 aperture defines the maximum convergence angle of the beam that is incident on the sample.

The specimen in the Tecnai F20 is immersed in the magnetic field of the objective lens. Therefore, the objective lens produces a pre-specimen and post-specimen field. In addition, a further mini-lens is also located above the pre-specimen lens field. The exploitation of this mini-lens allows the instrument to be operated in either CTEM or STEM imaging modes. For instance, if the mini-lens is switched on, a beam cross-over is created in between the mini-lens and pre-specimen objective lens. The convergence angle of the illumination that is incident on the specimen can then be altered by changing the current through the pre-specimen objective lens. Hence, the instrument acts as a CTEM. In comparison, if the mini-lens is not used, a beam cross-over is produced in the specimen plane. For that reason, a small electron probe is incident on the specimen and the instrument can be operated as a STEM. It should also be noted that the objective lens has a C_3 aberration coefficient equal to 1.2mm and the overall obtainable image point resolution is less than 2Å.

The scattered electrons from the specimen form a diffraction pattern in the back focal plane of the objective lens. A series of lenses below the specimen (see Figure 2.6) can be used to focus the scattered electrons into an image on the viewing screen. In addition, the strength of the diffraction lens can be reduced in order to image the diffraction pattern instead. The projector lenses alter the magnification of the image in CTEM mode. In contrast, the magnification of the image in STEM mode is controlled by changing the area of the specimen that is scanned. This is achieved via the STEM scan coils.

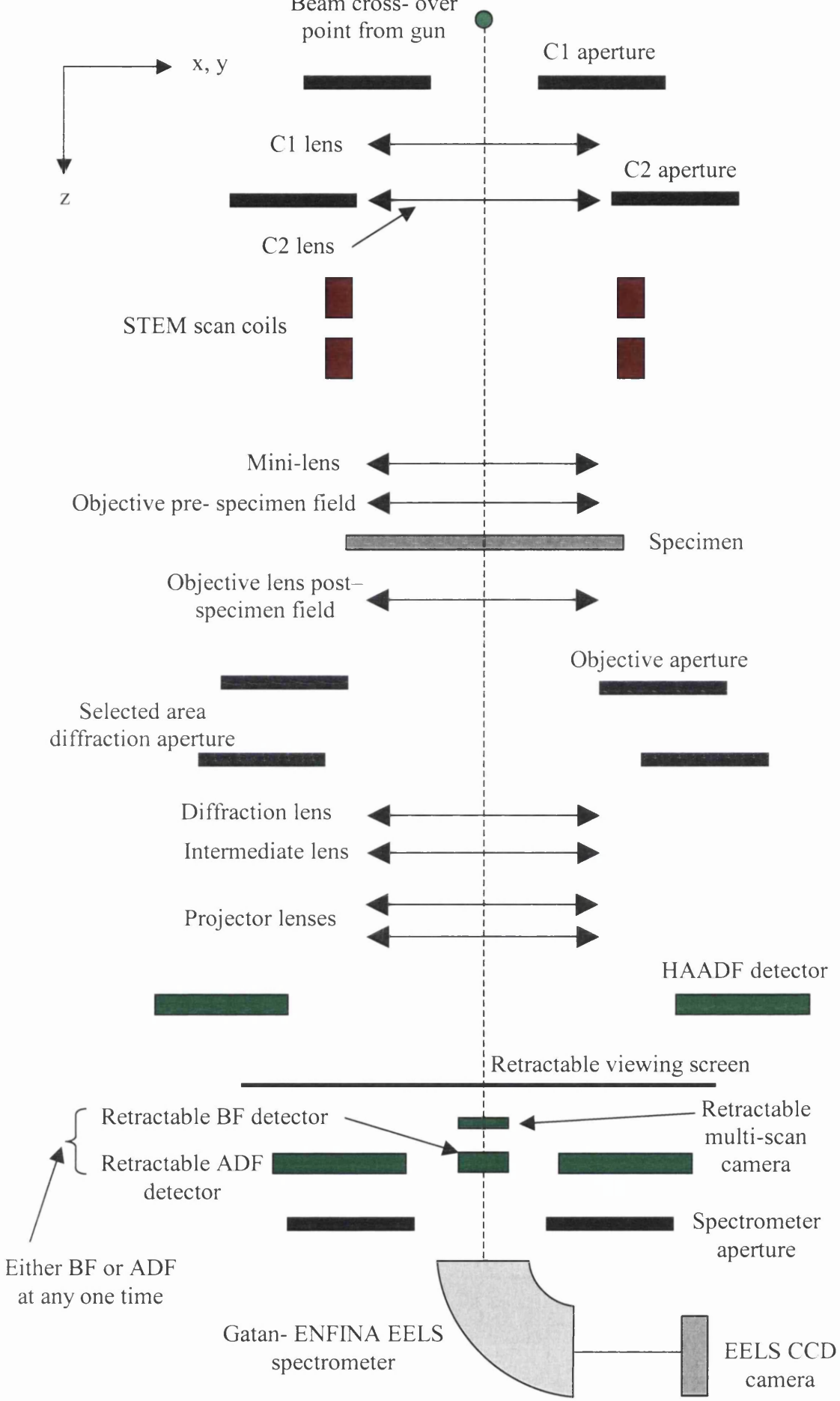

Figure 2.6: Schematic of the Tecnai F20 instrument. Distances are not to scale.

In order to allow CTEM images to be acquired, a retractable Gatan multi-scan camera (a CCD camera) is located below the viewing screen. In CTEM imaging mode, the series of projector lenses can be used project the image onto the CCD instead of the viewing screen. However, in STEM imaging mode, 3 electron detectors can be utilised to capture the CBED pattern produced by the specimen. These include HAADF and either bright field or annular dark field detectors (see Figure 2.6). They are all scintillator– PMT based detectors as described in Section 2.2.5. Moreover, the inner and outer angles of the 2 annular detectors depend upon the specific camera length that is employed. In addition to the image detectors, the instrument is also fitted with a Gatan ENFINA spectrometer. This permits the acquisition of electron energy loss spectra. This technique is described in Section 2.5.

2.4 Aberration-corrected STEM

2.4.1 Background

Many factors can restrict the attainable resolution in an electron microscope. For instance, the electron source always has a finite size that leads to a limit in the degree of spatial coherence of the beam. In addition, mechanical vibration, acoustic noise, earth loops, external AC magnetic fields and instability in the supplies to the alignment coils may also reduce the overall image resolution [22]. Specimen drift also degrades the information that can be obtained over a microscope session. This is sensitive to air and water temperature, airflow patterns and even atmospheric pressure. However, as was expressed in Section 2.2.4, the aberrations that are associated with standard electromagnetic lenses are the fundamental limit to the resolution of traditional electron microscopes.

In 1937, Scherzer showed that spherical and chromatic aberrations are always present in rotationally symmetric electromagnetic lenses. However, in his analysis, he assumed that the optical system was round, produces a real image, does not vary with time and has no charge on the axis [6]. Hence, he also proposed that the aberrations could be corrected through the use of non-round lenses. These are essentially multipole lenses that are capable of generating a negative value of C_3. For that reason, the positive spherical aberration of a round lens can be cancelled through the use of multipole lenses. This has lead to the creation of 2 basic types of aberration correctors that are based on octupole / quadrupole (pioneered by Scherzer, Deltrap and Krivanek) and hexapole (pioneered by Crewe, Rose and Haider) systems [7]. For example, an octupole / quadrupole system was created by

Deltrap over 40 years ago that corrected spherical aberration in a probe forming system but without an actual increase in resolution [8].

An electron beam that travels through a multipole lens will experience a Lorentz force between the individual poles that is directed either towards or away from the optic axis. This creates a focusing, or defocusing, action (on the electron beam) that is determined by the radial dependence of the magnetic field of the particular multipole. For instance, in a quadrupole, the electron beam is focused in a direction that is perpendicular to the optic axis. On the other hand, the deflection of the electron beam that is associated with an octupole increases as the cube of the off-axis distance. The deflection that is associated with a lens with spherical aberration also increases as the cube of the off-axis distance. [6]. However, octupoles are also associated with a four fold symmetry about the optic axis (with an alternating sign on rotation by 45 degrees). Hence, an octupole provides the opposite focus to rays that are rotated by 45 degrees from each other in a round beam.

In an octupole / quadrupole corrector, a series of quadrupoles are needed in order to distort the beam in such a way that it acquires a negative value of C_3 from the octupoles. The quadrupoles are used to focus the beam in certain directions in order for the octupoles to act on the beam appropriately. The quadrupoles also form a round beam in the exit plane of the corrector. In addition, 3 octupoles are necessary in order to correct the spherical aberration in the x, y and 45 degree directions [6, 8].

In order to assess the effect of aberration correction on the probe size in a STEM, the contributions to the probe size must be considered. For instance, a first order approximation of the FWHM diameter of a STEM probe (with a Gaussian intensity profile) can be given as the combination (in quadrature) of the following 3 quantities. These quantities are the diameter of the Gaussian de-magnified image of the finite source (d_g), the spherical aberration disk diameter of the objective lens (d_s) and the Airy disk diameter (d_d) [2]. The Airy disk diameter is associated with the diffraction due to the intrinsic lens aperture [2]. This combination is similar to the estimate of the spatial resolution of a lens (given in Section 2.2.4) except for the fact that the effect of the de-magnified source size is included. It should be noted that d_g is equal to $(2/\alpha\pi)(I/B)^{1/2}$ where α is the divergence semi-angle of the electrons from the de-magnified source, I is the de-magnified source current and B is the brightness of the de-magnified source [2]. In addition, d_s is proportional to $C_3\beta^3$ and d_d is equal to $1.22\lambda/\beta$ [2]. Hence, a spherical aberration-corrected instrument allows the d_d term to be minimised through the use of a large probe semi-convergence angle (β>20mrad). This provides the opportunity to form a

smaller probe size than would be possible in an equivalent uncorrected microscope. However, the contribution of the de-magnified source size then starts to be the main limiting factor to the probe size. d_g can be reduced by increasing the source demagnification but this also reduces the current in the probe. Therefore, the desired probe size and the desired probe current determine the choice of the probe convergence angle and the degree of source demagnification.

2.4.2 SuperSTEM 1 Instrument

The majority of the experimental data was obtained from the use of SuperSTEM 1. This instrument is a VG HB501 100kV STEM that has been retrofitted with a second generation NION aberration corrector. The microscope also contains a cold FEG that is operated with an extraction voltage below 4kV. The energy resolution of the gun is 0.3eV and has a gun brightness of $10^8 Acm^{-2}Sr^{-1}$. Furthermore, a specimen drift rate of about 5-10nm per hour can be achieved. This is considerably better than the drift rate in typical commercial microscopes such as the Tecnai F20 (i.e. about 60nm per hour).

A schematic of the microscope is shown in Figure 2.7. It can be noted that the microscope is equipped with a scintillator-PMT based HAADF detector and a Gatan-ENFINA spectrometer (energy resolution ~0.35eV). The HAADF detector has inner and outer angles of 70mrad and 210mrad, respectively. In addition, another detector (a CCD camera) is positioned after the HAADF detector. This allows far field diffraction images to be taken and is essential to the correction procedure for the measurement of the aberrations.

SuperSTEM 1 also contains a quadrupole coupling module (QCM) along the STEM column (see Figure 2.7). This is a post-specimen lens system that is composed of a series of quadrupoles and octupoles. The presence of this module is necessary because the retrofit of the NION aberration corrector shifted the different microscope components below the specimen from their designed positions. It is also needed due to the larger probe convergence angle that is employed in SuperSTEM 1 (24mrad semi-angle). Hence, the QCM is used to compress the angular distribution of the transmitted electrons from the specimen in order to match the acceptance angle of the Gatan-ENFINA spectrometer that is present in SuperSTEM 1. The reason that an additional lens cannot be used to focus the scattered electrons is that there is not enough room in the column close to the objective lens for its placement. Hence, the QCM gives the best fix for the problem. However, only 1 part of a spectrum that is obtained from the spectrometer of SuperSTEM 1 is exactly in focus. As a result, the collection and analysis of multiple high energy loss energies in a

single spectrum is problematic. The optical column of the next generation instrument, SuperSTEM 2, has been designed to minimise this effect.

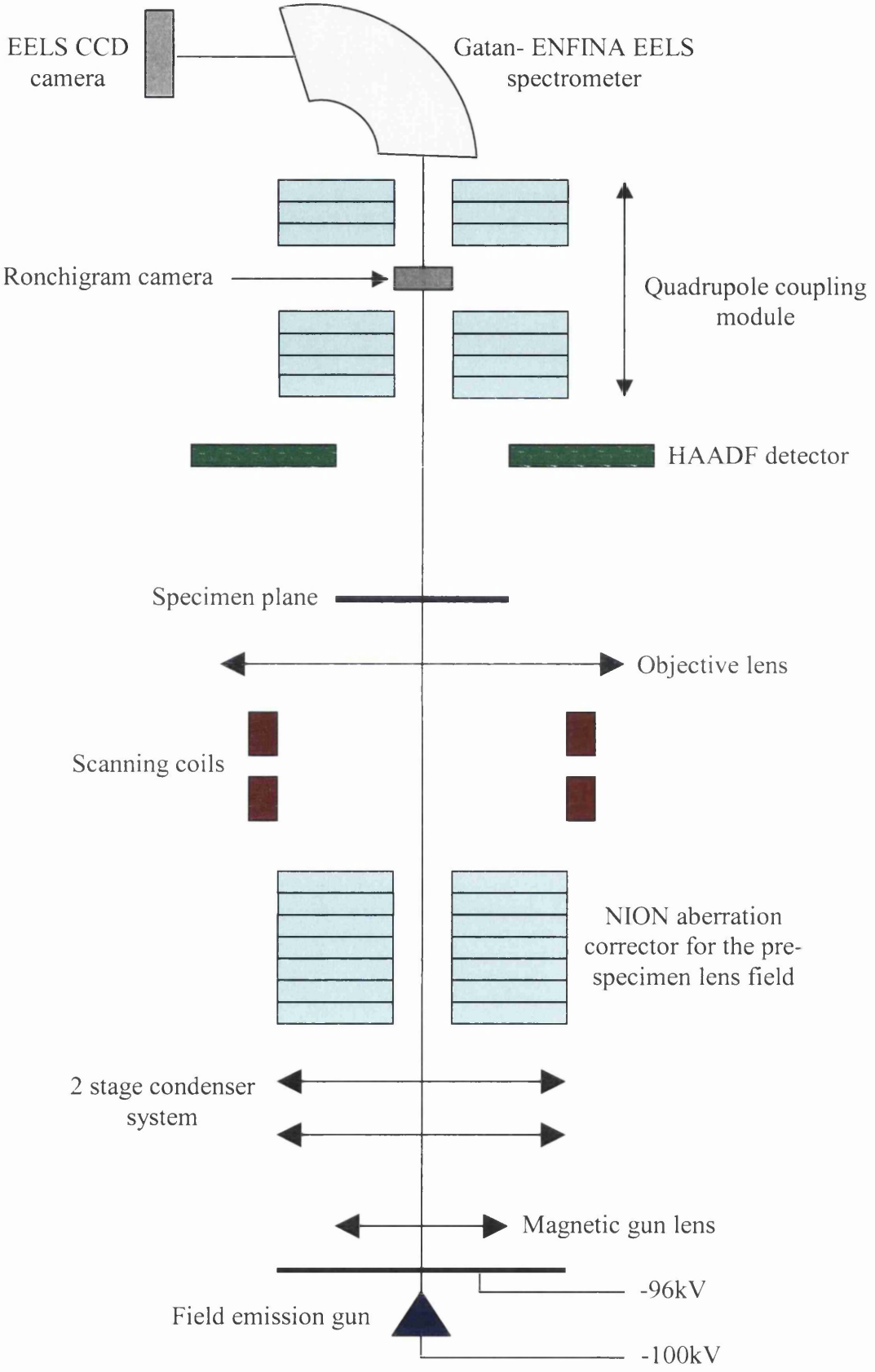

Figure 2.7: Schematic of the SuperSTEM 1 instrument. Distances are not to scale.

2.4.3 Method of Aberration Correction in SuperSTEM 1

If the probe is stationary on the specimen, the transmitted electrons can be collected as a function of angle on the CCD camera. The image that forms on the CCD camera is termed a Ronchigram [23]. Figure 2.8(a) highlights the main features of a typical Ronchigram in a probe forming system in which spherical aberration is present. In this case, the probe has an associated defocus value and is incident on an amorphous specimen. Hence, the low angle rays of the probe form a distorted bright field image of the specimen and can be seen in the centre of the Ronchigram.

On the other hand, due to the presence of spherical aberration, the high angle rays of the probe are perfectly focused on the specimen. As a result, these rays produce a ring of azimuthal infinite magnification in the Ronchigram. It is apparent, therefore, that the Ronchigram can show the presence of spherical aberration in an optical system. In a similar way, the region of radial infinite magnification is due to off-axis rays that cross on the specimen. Moreover, the other aberrations that are associated with a round probe forming lens can also be detected through the use of a Ronchigram. This is due to the fact that the local magnification in a Ronchigram is related to the second differential of the lens aberration function [24].

Figures 2.8(b) and (c) show that that the defocus value of the probe changes the appearance of a Ronchigram. For instance, at a defocus value of 0nm (Figure 2.8(c)) the centre of the Ronchigram has a region of infinite magnification in which all of the rays are focused in the same plane. This region defines the non-aberrated angular range of the probe. Beyond that region, the aberrations of the lens cause the rays to be focused in different places. For that reason, an aperture (of angular size β) is usually implemented in order to remove the aberrated portion of the probe. The size of the aperture determines the angular range of the probe that is incident on the specimen and therefore dictates the size of the STEM probe ($\sim\lambda/\beta$). In SuperSTEM 1, the objective aperture has a semi-angle equal to 24mrad.

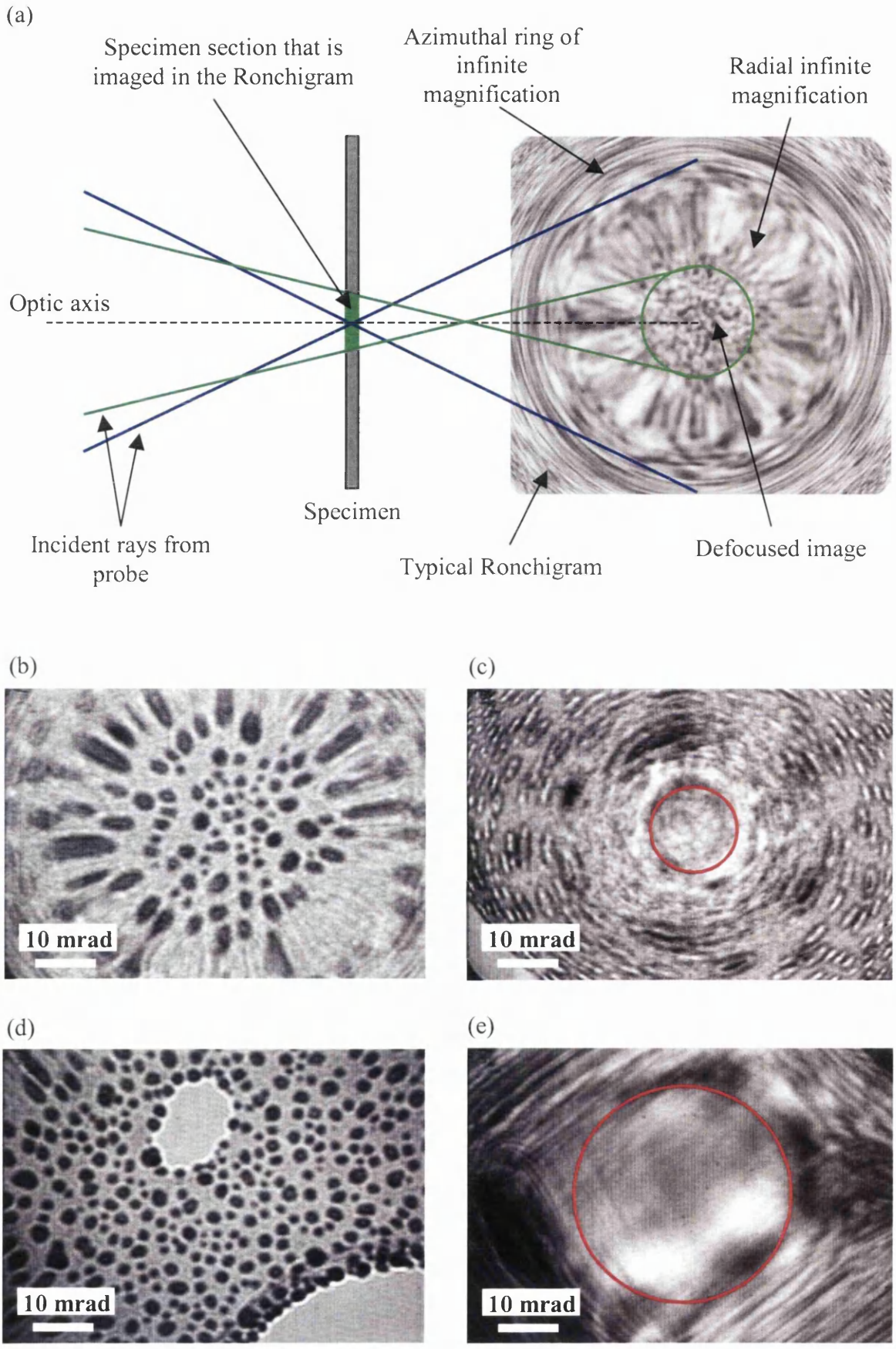

Figure 2.8(a): A description of how a typical Ronchigram image is formed by different probe incident angles **(b)** is a Ronchigram with C_3 = 1.2mm and defocus = -2700nm. **(c)** is a Ronchigram with C_3 = 1.2mm and defocus = 0nm. **(d)** is a SuperSTEM 1 Ronchigram with C_3 = 0mm and defocus = -2700nm. **(e)** is a SuperSTEM 1 Ronchigram with C_3 = 0mm and defocus = 0nm. The rings refer to the size of the objective aperture. Figure is courtesy of the SuperSTEM team.

The SuperSTEM 1 aberration corrector is an example of an octupole / quadrupole corrector. This consists of 4 strong quadrupoles and 3 strong octupoles as well as 24 additional multipoles whose role is to deal with parasitic aberrations [24]. The function of 2 of the quadrupoles is to squeeze the electron beam in a specific direction in order for a corresponding octupole to perform a correction of the aberrations in a particular direction (x or y). The middle quadrupole forms a round beam in order for the corresponding octupole to correct the aberrations along the 45 degree directions. In reality, the electron beam emerges from the corrector with the precise amount of aberration (of opposite sign) to cancel that introduced by the other lenses in the system (primarily that of the objective lens). In consequence, the effect of aberrations up to and including third order can be eliminated in SuperSTEM 1. In actual fact, there is also some compensation of fifth order aberrations in SuperSTEM 1. It is understood that it will be also possible to correct fifth order aberrations in SuperSTEM 2.

This entire correction process is only achievable through the use of computer control that enables accurate measurement of the aberrations and regulates the excitation of the corrector's components. Furthermore, auto-tuning software is also utilised in order to measure the value of the different aberration coefficients (up to fifth order). The aberrations are measured from a Ronchigram image of amorphous material [25]. The software then changes the excitation of the various corrector components in order to reduce the aberrations. This procedure is repeated until the measured aberrations have been reduced to levels that are small enough for the desired probe size [8]. Figure 2.8(e) reveals a SuperSTEM 1 Ronchigram at a defocus of 0nm. It is clear that the angular size of the non-aberrated part of the probe is much greater than in an uncorrected probe at the same defocus value (see Figure 2.8(c)).

In practical operation, third and higher order aberrations remain stable over hours if there are no drastic changes in the operating conditions of the microscope such as a change in specimen height. However, lower order aberrations are less stable and the microscope must be re-tuned every so often. The final outcome of the correction process is a doubling of the achievable image resolution from 2Å to below 1Å and a related increase in the probe current that is available in an atom-sized probe by about ten times. For example, the current in the 1Å scale probe of SuperSTEM is 0.1nA.

An example of a typical HAADF STEM image from SuperSTEM 1 is shown in Figure 2.9(a). GaAs was used as the specimen in this case. The material was orientated in the [110] orientation which generates the dumbbell configuration of the zinc-blende structure.

Figure 2.9(b) shows the FT (Fourier transform) of the image in Figure 2.9(a). This reveals the existence of a strong 004 reflection. Hence, the GaAs dumbbell spacing (1.4Å) is clearly resolved by SuperSTEM 1. In addition, Figure 2.9(b) highlights the presence of reflections that approach the 1Å information limit. It should be noted that the resolution is always better along one direction than it is along the perpendicular direction (i.e. there are missing reflections at the top and bottom of the ring in Figure 2.9(b)). This asymmetry in the resolution is always present and it means that the specimen must be put into the microscope in the correct position in order to get the highest resolution along the direction that is perpendicular to any interfaces that are of interest. In the case of the materials that are presented in later chapters, the highest resolution should always be along the [001] direction.

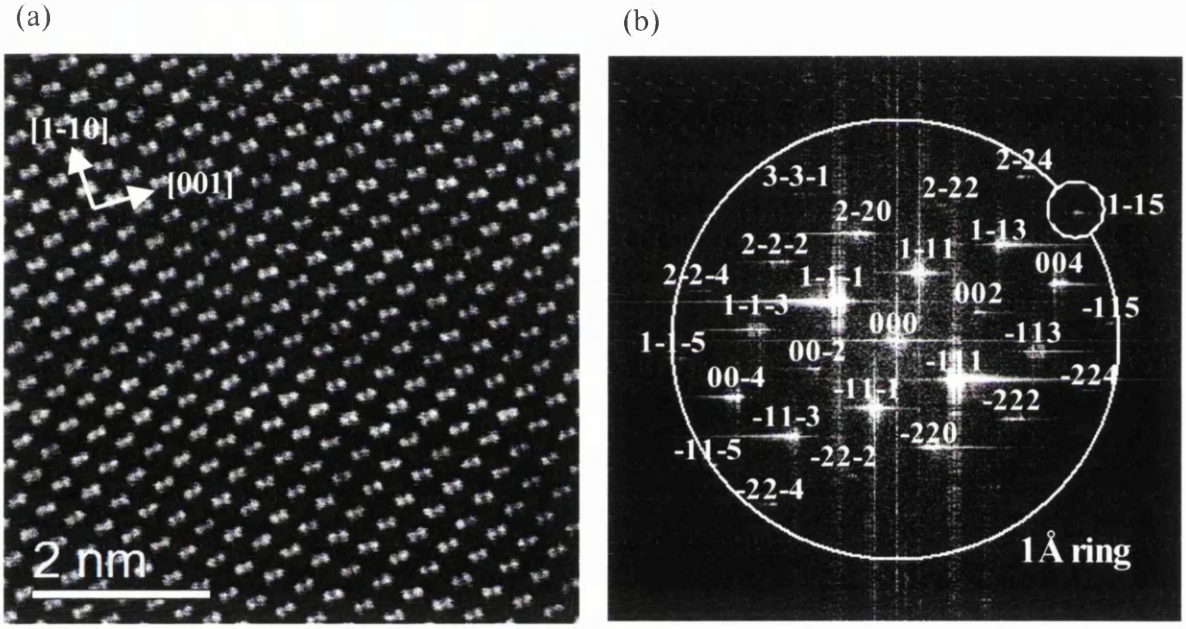

Figure 2.9(a): SuperSTEM 1 HAADF STEM image of several repeats of GaAs [110]. **(b)** is a FT of (a). The reflections extend to the 1Å information limit.

2.5 Electron Energy Loss Spectroscopy

Electron energy loss spectroscopy (EELS) is an analytical technique that allows the composition and chemical properties of a specimen to be ascertained [2]. This technique relies upon the collection and analysis of the energy loss distribution of transmitted electrons that have interacted with the specimen material through inelastic processes (see Section 2.2.2.3). An electron energy loss spectrum (a plot of electron intensity versus energy loss) can be divided into 3 principal regions. If the specimen is thin enough, the dominant feature of a spectrum is the zero loss peak (ZLP). This is formed by electrons

that have preserved the original beam energy and by electrons that have an energy loss that cannot be resolved by the spectrometer (for example from phonon scattering). In addition, the width of the ZLP provides a measure of the energy resolution of the spectrometer.

The second region of a spectrum centres on the low loss region in which electrons have energy losses up to ~50eV. This part of the spectrum is generated through the interaction of the imaging electrons with the weakly bound outer shell electrons of the atomic orbitals in the specimen. In fact, the orbitals are often delocalised due to interatomic bonding and, therefore, extend over several atomic sites. One feature of the low loss region is the presence of interband transitions which involve the excitation of valence electrons to low energy unoccupied electronic states that exist above the Fermi energy. However, the low loss region is dominated by collective, resonant oscillations of the valence electrons that are known as plasmons (see Section 2.2.2). The energy of the plasmon peak is related to the valence electron density of the specimen.

In addition, the probability of plasmon excitation increases with increasing specimen thickness (as does all inelastic scattering processes). In fact, the specimen thickness (t) can be measured through the calculation of the ratio of the total intensity in the spectrum (I_T) to the intensity in the ZLP (I_{ZLP}). For instance, it can be shown that $t = \Lambda \ln(I_T / I_{ZLP})$ where Λ is the mean free path for inelastic scattering for a particular material [9]. In practice, the Digital Micrograph software package is implemented in order to calculate the specimen thickness from any acquired spectra. It should be noted that I_T is extrapolated to higher energy losses in Digital Micrograph in order that the acquisition of a large energy range is not required. The absolute thickness value from this software is based on a calculation of the inelastic mean free path that is derived from the effective atomic number of the material under study. For instance, the following scattering theory equations are used to calculate Λ [26]:

$$\Lambda \approx \frac{106F(E_0/E_m)}{\ln(2\beta E_0/E_m)} \qquad \text{and} \qquad E_m \approx 7.6Z^{0.36}$$

F is a relativistic factor, E_0 is the incident beam energy, β is the collection semi-angle and Z is the effective Z number of the material. These equations are only valid up to a collection semi-angle of about 15mrad at 100kV accelerating voltage [26].

The final part of a spectrum is the high loss region which extends from about 50eV to many thousands of eV. The high loss region is characterised by the presence of increased intensity (edges) that lie on top of a downward sloping background. The electrons that

generate the increased intensity of the edges will have interacted with tightly bound inner-shell electrons of single atoms within the specimen whereas the background arises from other energy loss processes. Background contributions include plasmons, the tails of preceding edges and possibly Bremsstrahlung energy losses [26]. Plural scattering also contributes to the background. For instance, an incident electron may excite more than one valence electron before exiting the specimen. This results in an increased background at some energy loss as spectrum intensity is transferred from lower energies. In addition, plural scattering also causes a redistribution of the spectrum intensity away from the edge onset energy [27]. This is because an incident electron can excite both a core and a valence electron before exiting the specimen.

The probability of multiple scattering is given by Poisson Statistics and is a function of the mean free path of the material and of specimen thickness [27]. It can be shown that plural scattering is not a major problem at low specimen thicknesses [27]. However, the background signal must always be removed in order to analyse the different edge signals. In order to do this, a least-squares fit of the form AE^{-r} (where E is the energy loss) is typically implemented in Digital Micrograph to model the background before the onset of each edge [26].

The intensity of an edge scales with atomic concentration and, therefore, allows a quantitative analysis to be performed. In addition, the value of the energy loss at which a specific edge begins is determined by the binding energy of a particular electron energy subshell within an atom. Since this value is unique for each element, the type of atom can be identified. The quantification of the edge then allows the atomic concentration to be ascertained. This is usually accomplished through the EELS tools that are available in Digital Micrograph.

In order to collect an electron energy loss spectrum, the microscope must be fitted with a suitable spectrometer. Over the years many different types of electron spectrometers have been developed such as the Zeiss Ω filter and Wien filter [9]. However, the Tecnai F20 and SuperSTEM 1 instruments both employ a Gatan-ENFINA spectrometer. The magnetic prism inside this type of spectrometer is exploited in order to deflect the trajectories of the transmitted electrons (through 90 degrees) onto a yttrium aluminium garnet (YAG) scintillator that is connected to a CCD (see Section 2.2.5). Electrons that possess different kinetic energies are deflected by different amounts by the magnetic prism due to the Lorentz force [27]. In this way, an energy loss spectrum is produced on the CCD. Furthermore, at the exit of the prism, a series of quadrupole lenses are used to focus the

spectrum into a line and also to control the energy dispersion of the spectrometer (i.e. the energy loss range for a single pixel on the CCD). On the other hand, quadrupole and sextupole lenses (at the entrance to the magnetic prism) are used to align the shape of the ZLP and, hence, the spectrum as a whole.

The start energy of a spectrum can be altered through the application of a voltage to the electrically isolated drift tube that is present in the spectrometer. Hence, the intense ZLP can be removed from a spectrum in order that the acquisition time can be increased without damage to the YAG scintillator. In addition, through the application of the drift tube voltage and through the control of the dispersion value, particular areas of the spectrum (such as an ionisation edge) can be concentrated upon during the acquisition.

A STEM that is equipped with an electron spectrometer can also be operated to obtain spectrum images. A spectrum image is a one or two dimensional map that is composed of a spectrum at each pixel. In this case, the spectra are acquired over a particular (usually HAADF) image region. Hence, EELS information can be related to imaging.

2.6 Specimen Preparation

All of the results that are presented in later chapters were obtained from crystalline specimens that were prepared using the cross-section technique [33]. This technique is briefly outlined below. It should be noted that cross-section specimens become electron transparent through the process of ion-milling. This was achieved through the use of a Gatan Precision Ion Polishing System (PIPS) for each specimen. However, it is known that ion-milling produces a degree of roughness to the surface of the specimen along with an amorphous surface layer that is composed of damaged specimen material [28]. These are obviously unwanted features of the ion-milling process as their presence limits the information that can be obtained from the specimen. Hence, each specimen also underwent a final polish in a low energy Technoorg Linda GentleMill in order to minimise the damage. This is also described below.

In the first step of the cross-section process, 2 thin strips of sample material are cut from the parent wafer along the <110> crystal direction. It should be noted that all of the specimens were prepared from [001] orientated wafers (i.e. the wafer growth direction is along the [001] direction) and were viewed along the <110> direction in the microscopes. The 2 thin strips of sample material are glued together using an epoxy resin and subsequently placed into a pre-cut molybdenum (Mo) rod. These pieces are then placed

into a hollowed out brass tube which compresses the entire structure slightly. A schematic of this structure is shown in Figure 2.10(a). Once the glue has set, the structure is cut into individual discs using a diamond saw. The discs are then ground down using a hand grinder to a thickness of about 120μm. Both sides are then polished on a rotating wheel with a 3μm diamond paste in order to remove any surface scratches.

In the next stage of the process, a Gatan dimple grinder is used to mechanically thin the discs to the thickness required for ion-milling. This device uses a rotating wheel to dimple each side of a disc. The stainless steel wheel is coated in 3μm diamond paste in order to coarsely grind away the material to within 5μm of the target depth. The remaining material is taken off through the use of a felt wheel that is coated in 0.25μm diamond paste. This produces a disc that is double dimpled with a centre thickness of about 10μm. Each disc is then cleaned to remove any debris that was introduced from the dimpling process.

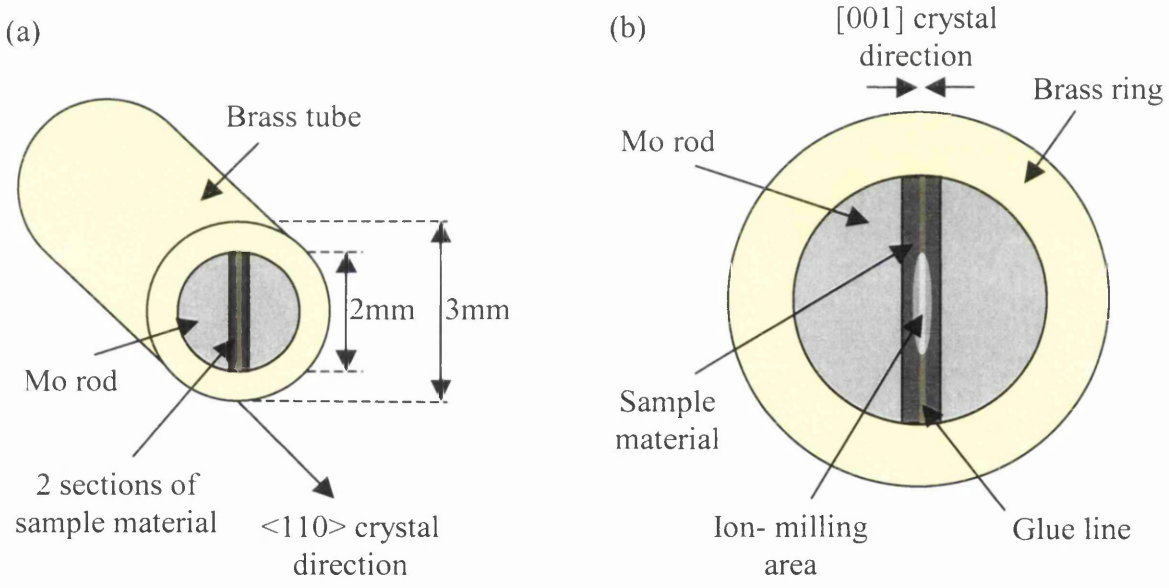

Figure 2.10(a): Schematic of encapsulated sample material before disc cutting **(b)** is a schematic of a finished cross- section specimen viewed along the <110> direction.

A disc is made electron transparent through the application of a Gatan PIPS. This device contains 2 miniature Penning ion guns that each delivers an argon ion beam onto the specimen surface. One beam is directed onto the top surface of the disc and the other is directed onto the bottom surface. An ion beam thins the disc by sputtering sample material away from its surface. However, an ion beam always penetrates the specimen to some depth and can introduce point defects and vacancies in the material [1]. This is the cause of some of the surface damage but this damage is minimised by inclining the incident beam to the specimen surface [2]. In addition, small angles of incidence (less than 5 degrees) also

avoid the preferential thinning of the different materials contained within the specimen [2]. In general, milling rates are higher at larger angles and at larger beam voltages. However, the level of surface damage is also greater [28]. For instance, it has been shown that the thickness of the amorphous surface layer in GaAs decreases from 2.1nm to about 0nm as the ion energy is reduced from 2.1keV to 0.25keV [28]. In addition, the level of surface roughness also decreases as the ion energy is reduced.

The PIPS allows the beam accelerating voltage (up to 6kV) and the incident beam angle (up to a maximum angle of 7 degrees) to be manually controlled. For each specimen that was prepared, an ion beam voltage of 4kV and an incident angle of 4 degrees were employed. In addition, each disc was rotated at 3rpm during the milling process. Furthermore, the milling time under these conditions is roughly about 1-2 hours. Milling is stopped once a small hole is observed (using binoculars) in the sample material. This ensures that the surrounding sample material is electron transparent. A schematic of a finished specimen is shown in Figure 2.10(b). Once a finished specimen is placed into an electron microscope, the electron beam is incident along the <110> crystal direction as shown in Figure 2.10(b). Moreover, Figure 2.10(b) also reveals that the 2 sections of the sample material are orientated along the [001] direction towards the glue line.

As was stated above, the PIPS produces a cross-section specimen with different types of damage such as surface roughness, amorphous surface layers and point defects [29, 30]. These adversely affect the information that can be obtained from a specimen especially in the analysis of interface sharpness (see Chapters 3, 5, 6 and 7). For instance, the amorphous layer should affect the intensity distribution of the probe that is incident on the crystalline material below the amorphous material, thereby changing the channelling of the electrons down the atomic columns. In addition, surface roughness generates patches of different intensity across the area of the specimen that is imaged. This degrades the ability to distinguish different features, such as layer boundaries, in the sample material.

In order to reduce the PIPS damage in cross-section specimens, a Technoorg Linda GentleMill was employed to provide a final polish to the specimens. This machine was specifically designed to minimise the damage that is introduced by high energy ion-millers such as the PIPS. The GentleMill operates a single low energy argon ion beam (100-2000eV) whose incident angle can be adjusted from 0 to 45 degrees. In addition, a 120 degree specimen oscillation is also used during the milling process. However, due to the fact that the GentleMill contains only 1 ion gun, each side of the specimen must be milled independently.

All of the specimens underwent a post-PIPS polish in the GentleMill using a beam energy of 400eV and an incident angle of 6 degrees. A Tecnai F20 CTEM image of a GaAs [110] cross-section that was thinned using the PIPS then GentleMill is shown in Figure 2.11(b). The equivalent specimen that was thinned in the PIPS alone is shown in Figure 2.11(a). It is clear that the level of surface mottling (patchiness) in Figure 2.11(b) is significantly reduced compared to that seen in Figure 2.11(a). Hence, the improvement in specimen quality due to the application of the GentleMill is apparent.

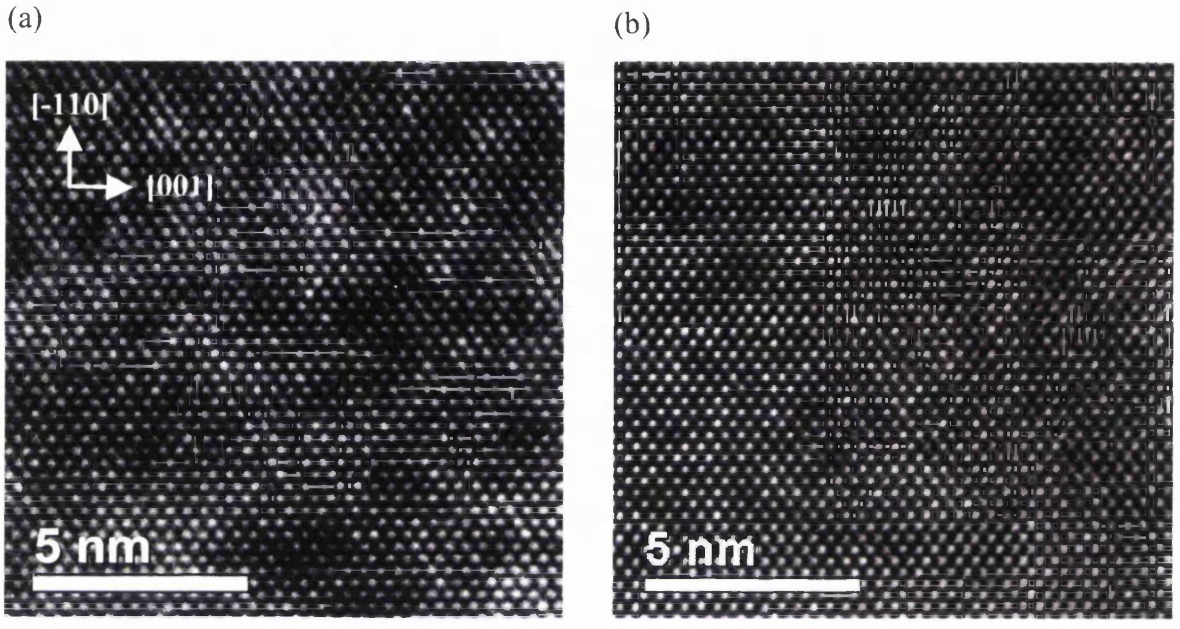

Figure 2.11(a): Tecnai F20 CTEM image of GaAs [110] prepared by the cross- section technique followed by a 4kV ion mill in the PIPS. **(b)** Tecnai F20 CTEM image of GaAs [110] prepared by the cross- section technique followed by a 4kV ion mill in the PIPS and 400V ion mill in the GentleMill.

An investigation into the thickness of the amorphous layer in PIPS and PIPS plus GentleMill specimens was attempted. This involved the use of a Focused Ion Beam (FIB) in order to cut out a section of material from each type of specimen. The FIB allows a smaller specimen to be made from these sections but crucially it also allows these smaller specimens to be orientated in such a way that the thickness of the damage layer can be seen when they are placed in an electron microscope. For instance, the specimen in Figure 2.11(a) is orientated along the [110] direction and the damage layer is present on the top (and bottom) surface of the specimen. The FIB produces a smaller specimen that is orientated along the [001] direction. Hence, the damage layer should appear as a layer on top of the underlying crystalline material. However, to date, the amorphous layer has not been observed in the PIPS or PIPS plus GentleMill specimens. The reason for this is

unclear but the investigation is currently being undertaken by other members of the Glasgow SSP Group.

2.7 Summary

The fundamentals of electron microscopy were presented in this chapter. This included an account of electron sources, a description of the problems that are associated with the use of electromagnetic lenses that control the trajectory of electrons and an overview of the typical devices that are exploited in order to detect scattered electrons. Background information on CTEM and STEM instruments were also provided along with the corresponding imaging techniques. The usefulness of HAADF STEM imaging was also explained. Furthermore, a description was given of the electron microscopes that were used to collect the experimental data that is shown in later chapters. This centred upon the aberration-corrected SuperSTEM 1 instrument that provides information on the structure of specimens down to an information limit of 1Å. In addition, the method of specimen preparation was also discussed.

References

[1] P. J. Goodhew, F. J. Humphreys, Electron microscopy and analysis 2nd edition, Taylor and Francis (1988)

[2] D. B. Williams, C. B. Carter, Transmission electron microscopy, Plenum Press (1996)

[3] M. H. Loretto, Electron beam analysis of materials, Chapman and Hall (1994)

[4] R. D. Heidenreich, Fundamentals of transmission electron microscopy Volume XIII, Interscience monographs and texts in physics and astronomy, John Wiley & Sons, Inc. (1964)

[5] J. A. Belk, Electron microscopy and microanalysis of crystalline materials, Applied Science Publishers LTD (1978)

[6] M. Valera, A. R. Lupini, K. van Benthem, A. Y. Borisevich, M. F. Chisholm, N. Shibata, E. Abe, S. J. Pennycook, Materials characterization in the aberration-corrected scanning transmission electron microscope, Annual Review of Materials Research, Vol. 35, 359-569 (2005)

[7] C. Hetherington, Aberration correction for TEM, Materials today (2004)

[8] O. L. Krivanek, N. Dellby, A. R. Lupini, Towards sub-Å electron beams, Ultramicroscopy 78, 1-11 (1999)

[9] R. Brydson, Electron energy loss spectroscopy, RMS Microscopy Handbooks (2001)

[10] E. J. Kirkland, Advanced Computing in Electron Microscopy, Plenum Press, New York (1998)

[11] S. Horiuchi, L. He, High-resolution transmission electron microscopy, Cambridge University Press

[12] D. L. Misell, Image analysis, enhancement and interpretation: practical methods in electron microscopy, North Holland Publishing Company (1978)

[13] S. J. Pennycook, M. Varela, C. J. D. Hetherington, A. I. Kirkland, Materials advances through aberration-corrected electron microscopy, MRS Bulletin, Volume 31, (2006)

[14] P. D. Nellist, S. J. Pennycook, Probe and object function reconstruction in incoherent scanning imaging transmission electron microscope imaging, Scanning Microscopy Vol. 11, 81-90 (1997)

[15] S. J. Pennycook, D. E. Jesson, High-resolution incoherent imaging of crystals, Physical Review Letters, Volume 64, Number 6 (1990)

[16] P. D. Nellist, Atomic resolution annular dark field imaging: theory and simulation, SuperSTEM summer school (2006)

[17] S. J. Pennycook, D. E. Jesson, High-resolution Z-contrast imaging of crystals, Ultramicroscopy 37, 14 (1991)

[18] B. Rafferty, P. Nellist, J. Pennycook, On the origin of transverse incoherence in Z-contrast STEM, Journal of Electron Microscopy 50, 227-233 (2001)

[19] N. D. Browning, D. J. Wallis, P. D. Nellist, S. J. Pennycook, EELS in the STEM: determination of materials properties on the atomic scale, Micron Vol. 28, No. 5 pp. 313-348 (1997)

[20] C. Dwyer, J. Etheridge, Scattering of Å-scale electron probes in silicon, Ultramicroscopy 96, 343-360 (2003)

[21] S. J. Pennycook, B. Rafferty, P. D. Nellist, Z-contrast imaging in an aberration-corrected scanning transmission electron microscope, Microscopy Microanalysis 6, 343-352 (2000)

[22] A. J. Craven, Perspectives in nanoanalysis, EMAG (2003)

[23] J. M. Rodenburg, E. B. Macak, Optimising the resolution of TEM / STEM with the electron Ronchigram, Microscopy and Analysis (2002)

[24] O. L. Krivanek, P. D. Nellist, N. Dellby, M. F. Murfitt, Z. Szilagyi, Towards sub-0.5Å electron beams, Ultramicroscopy 96, 229-237 (2003)

[25] J. M. Rodenburg, A. R. Lupini, Measuring lens parameters from coherent Ronchigrams in STEM, Institute of Physics Conference Series No. 161, 339-342 EMAG (1999)

[26] R. F. Egerton, Electron energy-loss spectroscopy in the electron microscope, 2nd edition, Plenum Press (1996)

[27] M. M. Disko, Transmission electron energy loss spectrometry in materials science, Publication of the Materials, Metals and Materials Society (1992)

[28] A. Barna, B. Pecz, M. Menyhard, Amorphisation and surface morphology development at low-energy ion milling, Ultramicroscopy 70, 161-171 (1998)

[29] S. D. Walck, J.P. McCaffrey, The small angle technique applied to coatings and thin films, Thin Solid Films 308-309 (1997)

[30] C. B. Boothroyd, R. E. Dunin-Borkowski, W. M. Stobbs, C. J. Humphreys, Quantifying the effects of amorphous layers on image contrast using energy filtered transmission electron microscopy, MRS Symposium Proceedings Vol 354, pp. 495-500 (1995)

[31] P. E. Fischione, Materials specimen preparation for transmission electron microscopy, E.A. Fishione Instruments, Inc. Export, PA USA

[32] S. K. Chapman, Understanding & optimising electron microscope performance, 1. Transmission microscopy, Science Review Limited (1980)

[33] C. P. Scott, A. J. Craven, P. Hatto, C. Davies, TEM cross-section preparation with minimal ion milling time, Journal of Microscopy, Vol. 182, Pt 3 pp. 186-191 (1996)

[34] P. A. Doyle, P. S. Turner, Acta Cryst., A24, 390 (1968)

[35] P. B. Hirsch, A. Howie, R. B. Nicholson, D. W. Pashley, M. J. Whelan, Electron microscopy of thin films, Butterworth, Sevenoaks (1965)

[36] S. J. B Reed, The single-scattering model and spatial resolution in X-ray analysis of thin foils. Ultramicroscopy, 7, 405–410 (1982)

3 The Investigation of a MODFET Heterostructure Using SuperSTEM 1

3.1 Introduction to the MODFET Heterostructure

In this chapter, the results from the first experimental investigation in this project that used SuperSTEM 1 are presented. The focus of the study centred upon a MBE grown III-V semiconductor heterostructure that was designed to form part of a high frequency modulation doped field effect transistor (MODFET). The aim was to investigate the quality and physical nature of the various layers that comprised this structure. A related goal was to ascertain the potential of SuperSTEM 1 to detect the different elements that were present in the heterostructure. This necessitated the creation of new processing techniques to deal with the unprecedented resolution of SuperSTEM 1. Hence, this was considered to be a 'sighting shot' experiment as well.

A STEM sample was prepared using the cross-section technique and was finished with a low energy ion mill at 400eV at an angle of 6 degrees through the use of a GentleMill (see Section 2.6).

Figure 3.1(a) illustrates the overall target structure of the heterostructure. The individual layers were grown epitaxially on top of the GaAs substrate along the [001] crystal direction. This produced a structure with 3 distinct regions. These are a 100nm wide deep superlattice, a 400nm wide $Al_{0.3}Ga_{0.7}As$ buffer region and a surface layer section. The layers were grown with an intended accuracy of the order of 1 monolayer (ML). When viewed along the [110] direction, 1ML of a composite material (such as GaAs) is defined as containing 2 atomic planes each made from a different type of atoms. Hence, 1ML of this sort of material would appear as a single row of dumbbells (along the [1-10] direction) if viewed in the [110] orientation. In the particular case of the heterostructure that is shown in this chapter, the material was viewed along the equivalent [1-10] direction that also generates the dumbbell configuration.

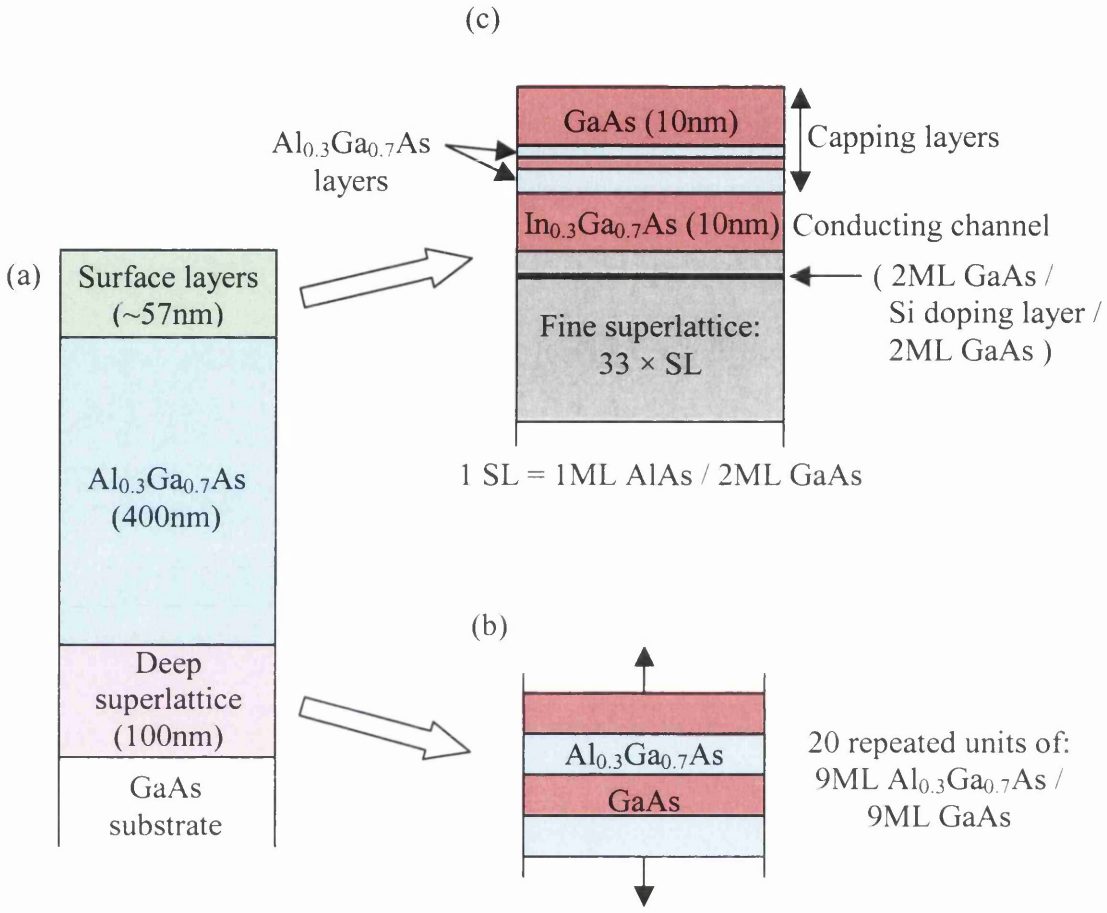

Figure 3.1(a): Schematic of the overall target structure of the III-V pre- MODFET heterostructure. Also shown is a schematic of the structure of the deep superlattice **(b)** and that of the surface layers **(c)**.

3.2 Deep Superlattice

3.2.1 Background

The first area that was examined using SuperSTEM 1 was the deep superlattice. This was grown directly on top of the GaAs substrate. The purpose of the superlattice has nothing to do with its electronic properties. In reality, its numerous interfaces are used to trap many growth defects and impurities so that they do not migrate with the growth process towards the more important surface layers [1]. These impurities are introduced during the manufacture of the epitaxial wafer before the MBE growth process starts.

The superlattice itself was composed of 20 repeated units of: 9ML $Al_{0.3}Ga_{0.7}As$ / 9ML GaAs and was grown at a substrate wafer temperature of 635°C. In addition, the wafer rotation was set to 50rpm (revolutions per minute). During the growth process, the temperature of the Ga oven was fixed at 960°C and the temperature of the Al oven was 1079°C. The As oven was set at a temperature of 141°C and the As and Ga shutters were open continuously during the whole growth process. On the other hand, the Al shutter was only opened in order to grow requisite amount of Al in the $Al_{0.3}Ga_{0.7}As$ layers. In addition, the growth rates for the individual $Al_{0.3}Ga_{0.7}As$ and GaAs layers were 0.98ML / sec and 0.69ML / sec, respectively.

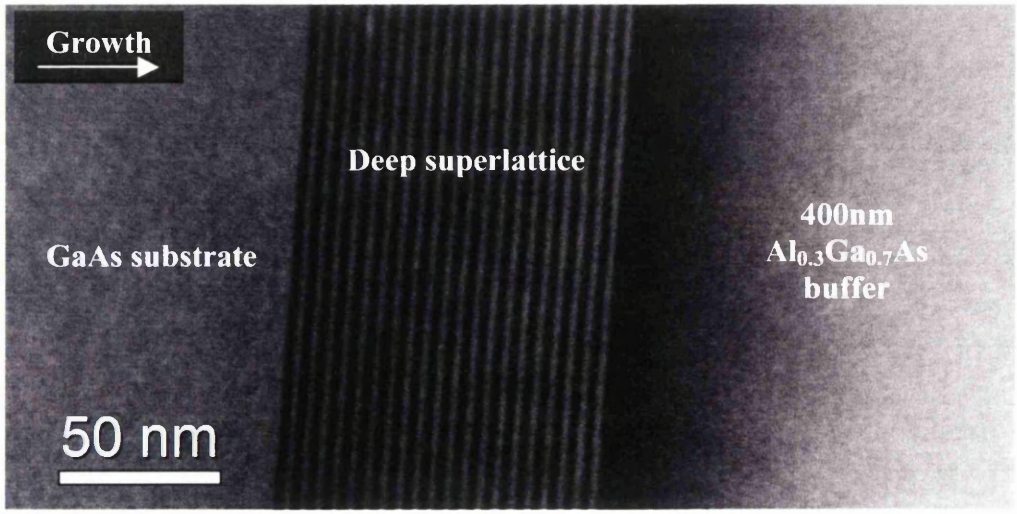

Figure 3.2: Low magnification SuperSTEM 1 HAADF STEM image over the whole deep superlattice.

The entire structure can be seen in the HAADF STEM image of Figure 3.2. In this instance, the GaAs layers appear more intense than the $Al_{0.3}Ga_{0.7}As$ ones due to the atomic number dependence of the imaging process.

3.2.2 Image Background Signal

Figure 3.3(a) is a high magnification SuperSTEM 1 HAADF image taken over several repeat units of the deep superlattice. The characteristic dumbbell configuration of the zinc-blende crystal structure is now apparent. Figure 3.3(b) is a line profile that reveals the intensity variation, taken over the indicated image region, as a function of position. This has the form of high spatial resolution peaks, associated with the dumbbell locations, which sit upon a background with a small modulation. It should be noted that at the start of every session on SuperSTEM 1 the image black levels were set so that a few image counts (~5-10) were recorded in the absence of any specimen material. Typical image counts in the presence of the specimen are of the order of 10,000.

The likely explanation of the background modulation centres upon the effect of probe spreading. The specimen thickness was about 60nm in the region corresponding to Figure 3.3(a). Simple theory asserts that the strong atomic potentials of the dumbbell columns attract the electron probe and forces it to propagate down the columns for distances larger than otherwise would be expected from geometrical arguments [2]. In this channelling condition, subsequent collisions with the atomic nuclei (in a column) scatter some of the electrons out of the potential at high angles where they will be picked up by the HAADF detector (see Section 2.3.3). This is the familiar Rutherford scattering mechanism through which the high spatial resolution peaks (as seen in the line profile) arise. As such, they have an intensity that is approximately proportional to Z^2 [3]. However, this beam confinement is gradually lost with increasing depth in the specimen. At greater depths, the electrons will spread into the adjacent columns (see Chapter 4). Indeed, the recorded value of column intensity / total intensity, in Figure 3.3(b), gives a value of 0.14 (the column intensity is given as peak intensity – background intensity). If the thickness of the specimen at this point is taken to be 60nm, the value of 0.14 suggests that the beam confinement by channelling occurred only in the top 8.4nm of the specimen. It should be noted that other authors have considered this simple qualitative model that describes the origin of the image background signal and the column peaks observed in HAADF images [11]. In addition, after a certain specimen thickness, the column intensity starts to reduce due to multiple scattering (both elastic and inelastic) that scatters electrons outside of the detector (see Chapter 4) [12].

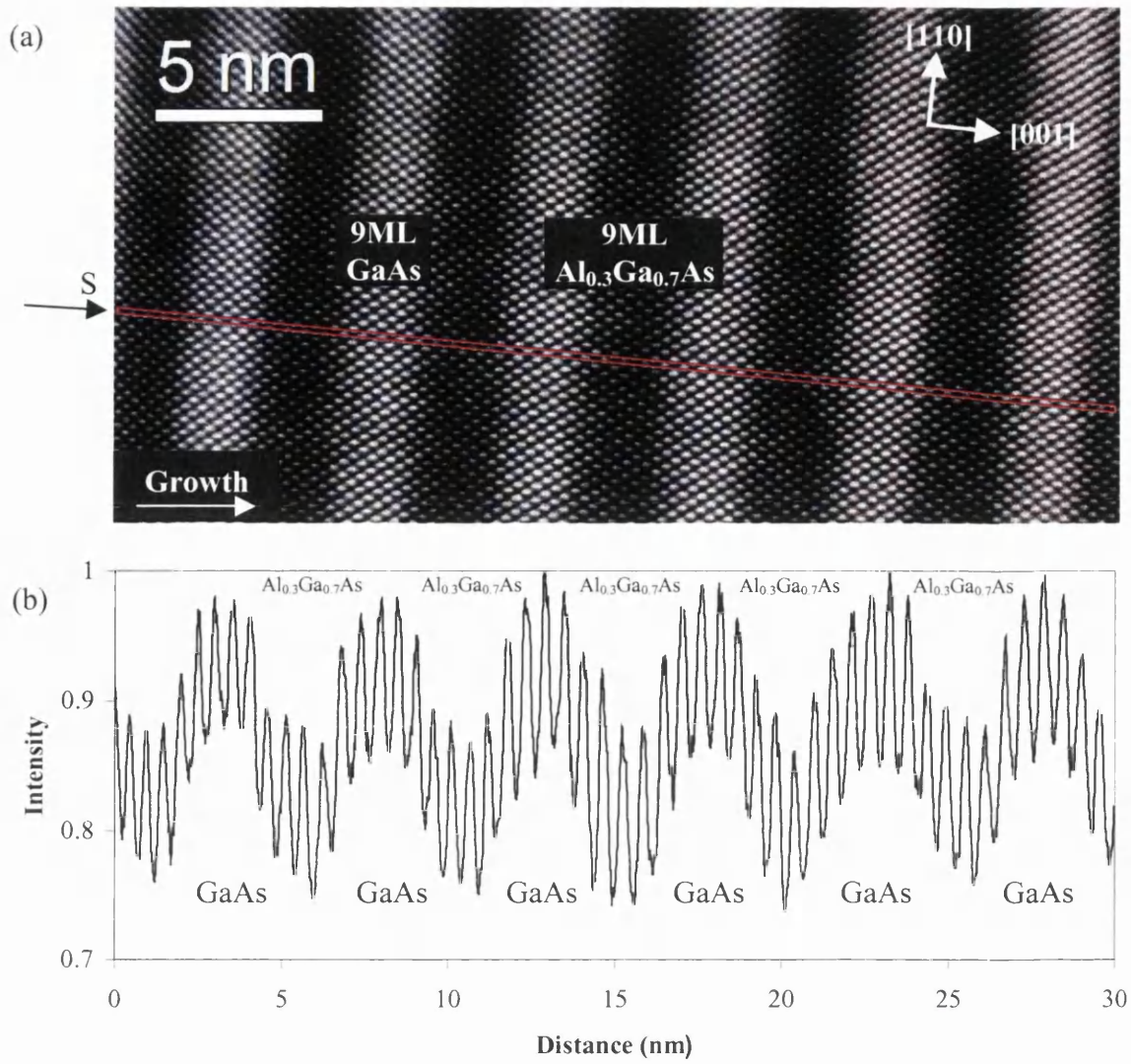

Figure 3.3(a): SuperSTEM 1 HAADF STEM image of 6 repeats of the deep superlattice. **(b)** is an intensity profile taken across the image section S. This section is 10 pixels in width. Therefore, every point of the intensity profile is generated from the average of 10 image pixels summed along the [110] direction.

It has been noted that every image pixel has an intensity related to (the square of) the average atomic number of the material sampled by the beam. Due to the fact that the probe was scanned across alternating layers with different average Z^2 numbers in the deep superlattice, a fluctuating background signal was expected. However, the exact nature of this background will be dependent upon the width of the layers in the sample and also on the specimen thickness as discussed below.

It is informative to consider only the geometrical spread of the beam into the neighbouring columns [4]. This is the spreading that occurs inside a conical region defined by the incident probe angle (24mrad semi-angle for SuperSTEM 1). Given that the specimen has a thickness of about 60nm, the geometrical spreading of the probe will generate a beam 2.9nm wide at the bottom surface of the specimen. This is similar in width to the 9ML

layers of the deep superlattice and, hence, a quasi-sinusoidal background signal should be observed. This is indeed the case (see Figure 3.3(b)).

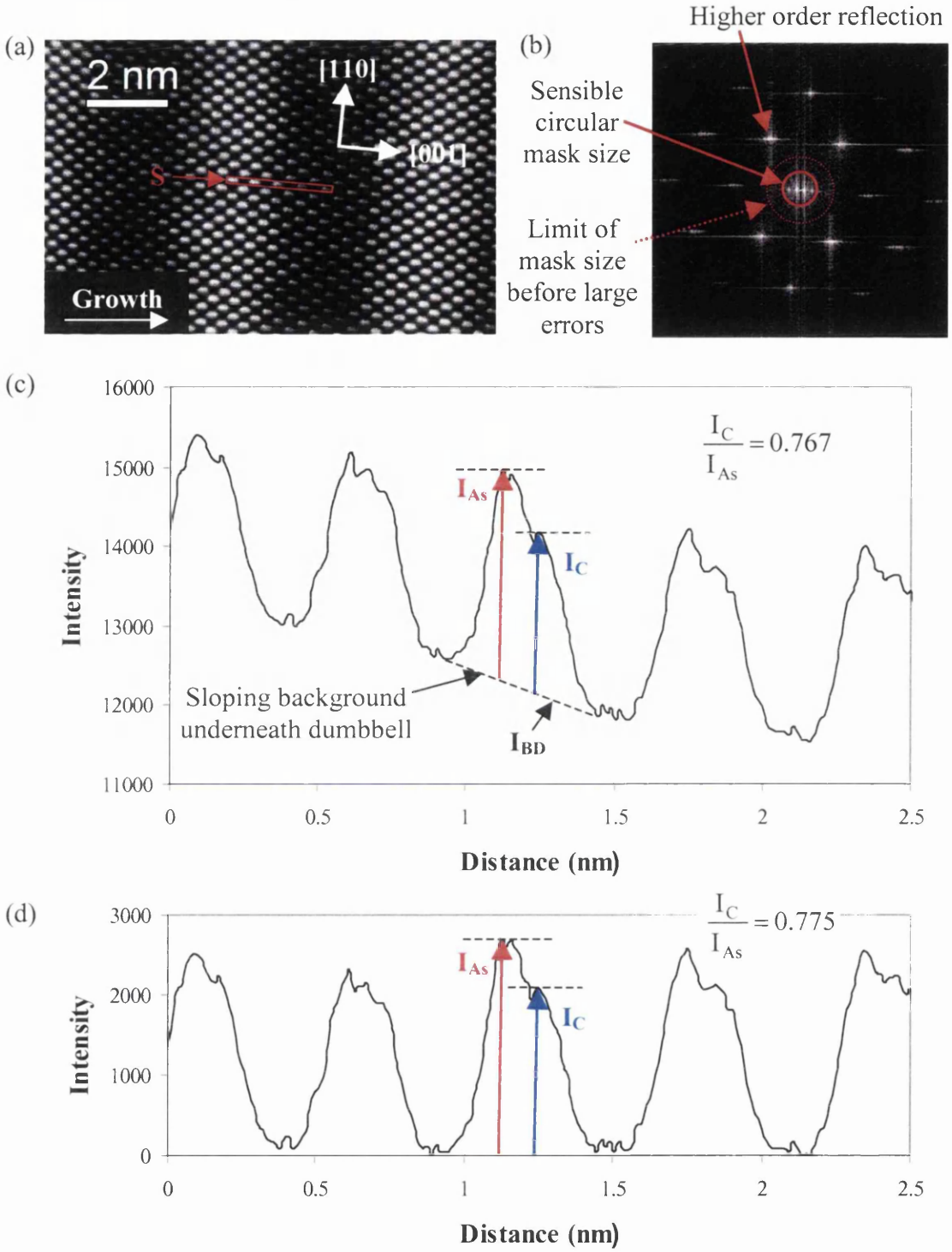

Figure 3.4(a): SuperSTEM 1 HAADF STEM image of 2 repeats of the deep superlattice. **(b)** shows the Fourier transform of the image in (a). The position of the central mask that is applied to the Fourier transform in order to remove the underlying background modulation is also shown. **(c)** is an intensity profile taken across the image section S in (a). Every point of the intensity profile is generated from the average of 10 image pixels summed along the [110] direction. The value of the intensity is as recorded. **(d)** is an intensity profile taken across the image section S in (a) after the background has been removed (see text for explanation).

In order to eliminate the signal that results from the effect of beam spreading, and hence only leave the high spatial resolution column peaks, an image (such as in Figure 3.4(a)) must have the background signal removed. When confronted with an image of a material with uniform composition (and constant thickness) across the image dimensions then it is a simple manner to subtract the background as it manifests itself as a uniform intensity level across the entire image. However, as is shown in Figure 3.3, a modulated background signal is obtained from a superlattice image as the composition changes across the image dimensions. Hence, the background cannot simply be removed and some additional steps are required.

The first step in the background removal process involves the application of a circular mask on the Fourier transform (FT) of the image. The mask removes the low spatial frequencies that give rise to the modulated background (e.g. superlattice reflections). The size of mask that is typically used is shown on the FT of a deep superlattice image in Figure 3.4(b). The size of mask should be large enough in order to eliminate all of the superlattice reflections but not so large that higher order reflections are entirely or partly removed. For instance, if higher order reflections are clipped then some high spatial resolution information is lost and the processing technique creates a processed image that has incorrect dumbbell profiles and intensities. Fortunately, this is never really a serious problem with the materials studied in this project as all of the superlattice reflections are confined in close proximity to the central FT spot. Therefore, it is easy to place the mask around these reflections without ever clipping the higher order reflections. In addition, as long as the superlattice reflections are removed and the high order ones are not clipped, then the circular mask can be of any size and the processing technique will generate the same dumbbell profiles and intensities. For example, the final processed image will not be affected if the size of the mask is increased from the smaller mask to the larger one shown in Figure 3.4(b). The larger mask is the limit after which high order reflections start to be clipped.

It should be noted that the mask also removes the central FT spot. Hence, after an inverse Fourier transform of the masked FT is performed, a processed image is generated with an average intensity equal to zero in conjunction with no background modulation. In actual fact, in such a processed image, the dumbbell columns have a positive intensity value above zero and the positions between dumbbells have a negative intensity value. The next step of the process then involves the addition of a uniform level of intensity (equal in magnitude to the minimum intensity value in the processed image) across the image so that the minimum level in the new processed image is now set to zero (i.e. at the positions

between the dumbbells). Hence, this gives the desired processed image since the dumbbell columns sit upon a zero background level without a background modulation.

Figure 3.4(c) shows an intensity profile taken across the unprocessed image of the deep superlattice (the image is presented in Figure 3.4(a)). In contrast, Figure 3.4(d) shows an intensity profile taken across the background removed image version of Figure 3.4(a). It is clear that not only has the background modulation from the superlattice been removed but also that the intensity between dumbbells is now zero. It can also be seen that the shape of the unprocessed intensity profile in Figure 3.4(c) has been preserved in the processed image intensity profile in Figure 3.4(d). Furthermore, it should be noted that the processing technique results in a ~4% change in the absolute intensity values for the As and right hand column (I_{As} and I_C, respectively) for the dumbbell at the 1nm position in the intensity profile of Figure 3.4(c). However, this small discrepancy is likely due to the fact that the level of background is uncertain in this case as the dumbbell is positioned on a GaAs / $Al_{0.3}Ga_{0.7}As$ interface which generates a sloping background (I_{BD}). Nevertheless, it can be shown that the ratio of I_C / I_{As} is the same in both the unprocessed and processed intensity profiles in Figure 3.4 (equal to 0.767 and 0.775, respectively). Section 3.2.3 will discuss that it is this ratio that is of significance in the determination of composition from HAADF images. Therefore, it is apparent that the process of background removal does not introduce any unwanted artefacts into compositional analysis. In summary, the use of this processing technique generates an image that displays only the high spatial information, which makes it much easier to identify the type of dumbbell present than it was using the unprocessed image alone.

3.2.3 Dumbbell Column Ratio Maps

Figure 3.5 reveals the typical shape of GaAs and $Al_{0.3}Ga_{0.7}As$ dumbbells present in SuperSTEM 1 HAADF images. These dumbbells were located at the centre of their respective layers within the deep superlattice. The left hand side (LHS) of each dumbbell have the higher intensity. This indicates that these were generated from 100% As columns. In contrast, the $Al_{0.3}Ga_{0.7}$ column has a lower average Z^2 number than that of the 100% Ga column (in the case of GaAs). Consequently, the $Al_{0.3}Ga_{0.7}$ column scattered less strongly out to high angles. This therefore resulted in a reduced intensity on the detector. As a result, the $Al_{0.3}Ga_{0.7}As$ dumbbell looks more asymmetric than the GaAs dumbbell.

Hence, the difference between the two types of materials occurs only on the right hand side (RHS) of the dumbbells. This fact can be used to calculate the dumbbell column ratio by simply dividing the RHS column intensity by the LHS column intensity. The column intensity is equal to the full HAADF intensity located at a particular column (I_{Ga} or I_{As}) – the background signal (I_{BD}). Hence, the dumbbell column ratio for GaAs is equal to:

$$\text{Dumbbell Column Ratio} = \frac{\text{Ga column HAADF signal}}{\text{As column HAADF signal}} = \frac{I_{Ga} - I_{BD}}{I_{As} - I_{BD}}$$

The value obtained for the ratio should then be related to the actual composition present in the dumbbell [11]. For instance, the simple Z^2 scattering theory dictates that Ga / As = 0.88 and ($Al_{0.3}Ga_{0.7}$) / As = 0.66. The column ratio of the GaAs dumbbell in Figure 3.5(a) closely matches the value predicted by the simple theory. However, Figure 3.5(b) also demonstrates that the ratio for the $Al_{0.3}Ga_{0.7}As$ dumbbell is less well predicted by the simple theory. Nevertheless, it is clear that the dumbbell column ratio does indeed give an indication of the relative local composition, where a high ratio value suggests the presence of an element with a high Z number. The average column ratio for the different materials present in the MODFET heterostructure is discussed in Section 3.4.2.

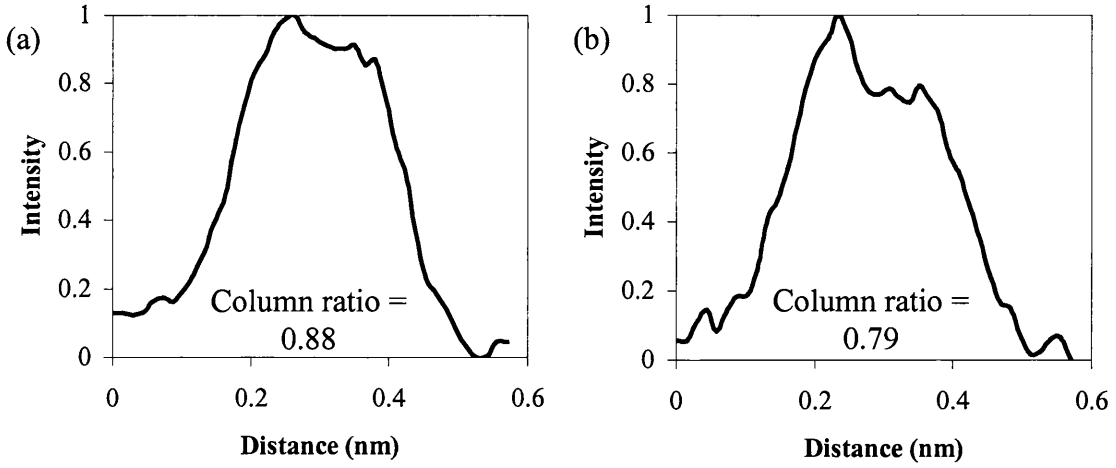

Figure 3.5(a): Typical SuperSTEM 1 HAADF background removed image intensity profile of GaAs from the centre of the 9ML GaAs layer in the deep superlattice. **(b)** is a typical SuperSTEM 1 HAADF background removed image intensity profile of $Al_{0.3}Ga_{0.7}As$ from the centre of the 9ML $Al_{0.3}Ga_{0.7}As$ layer in the deep superlattice. Every point in the intensity profiles is generated from the average of 10 image pixels summed along the [110] direction.

In the sample studied in this chapter, the Group V element is always As. Thus, the column ratio is defined with reference to the intensity of the As column. Hence, the column ratio will be less than 1 for dumbbells that contain a column that is composed of atoms with a average scattering power less than that of As, as is the case with AlAs. However, when the scattering power of the other column is greater than that of As, the column ratio should be greater than 1. For example, the In column in InAs dumbbells (Z number of In is 49) is more intense than the As column in this simple approach.

It is very difficult to determine the precise elemental distribution of a sample by simply looking at a high-resolution image. Hence, the notion of the dumbbell column ratio is extremely useful if applied over an entire image. A general outline of the composition may be obtained via the background signal but, as was shown in Section 3.2.2, this signal does not give high spatial resolution information. The usual method of investigation involves the time consuming process of taking several line profiles across the dumbbells, which must then be analysed individually. Therefore, in order to help with the analysis, a series of Digital Micrograph scripts were created. These help to convert a standard image into a map that displays the dumbbell column ratio for every dumbbell in the original image. This makes it possible to actually see the distribution of the dumbbell shapes, and hence the compositional variation, at a glance.

The process of converting a high-resolution HAADF STEM image into a dumbbell column ratio map is shown in Figure 3.6. To create a column ratio map, firstly the background is removed via the process explained in Section 3.2.2. The positions of the all the dumbbells in the original image (Figure 3.6(a)) are then measured, and recorded, using Digital Micrograph's particle locator tool. This tool outputs the image coordinates of the central position of each dumbbell.

In the second step, a line profile (40 pixels long and averaged over a width of 10 pixels) is drawn across the entirety of every dumbbell in the background subtracted image (along the [001] direction). The line profile is, therefore, 40 points long where each point is generated from the average of an image section 1 pixel by 10 pixels in size. Each line profile is centred on the dumbbell middle (found from the particle locator tool) and is long enough to encompass the point half way between the dumbbell and the next one on either side. The method of image background removal (as outlined in section 3.2.2) can also sometimes result in a small residual background signal with an intensity equal to about 1-2% of the dumbbell intensity. This is likely due to local fluctuations in the in the original image that were not totally removed by the processing technique. The removal of the residual

background is achieved by measuring the minimum residual background signal (from the line profile) on either side of a particular dumbbell. The average of these 2 values is then removed from every point in the line profile.

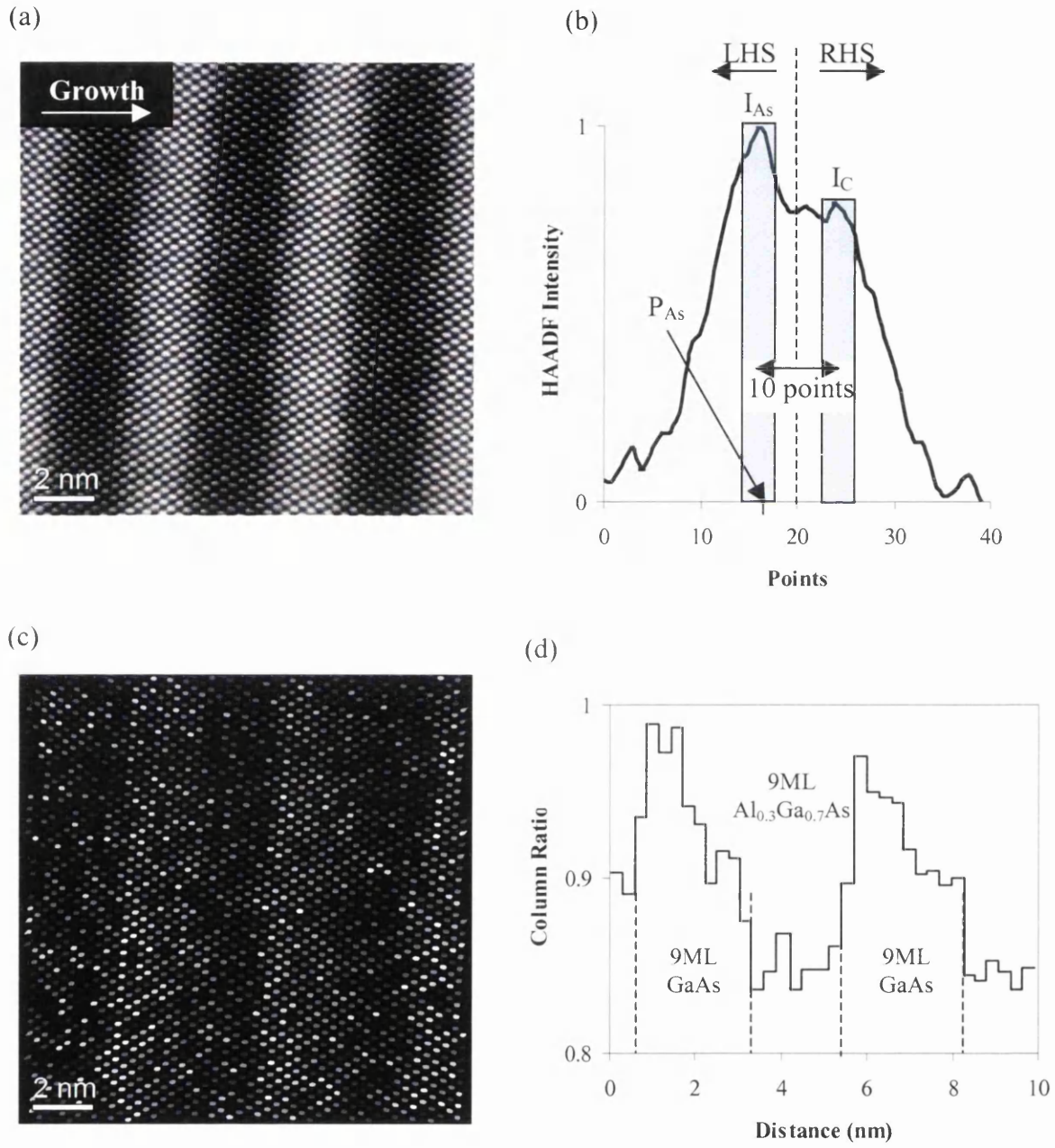

Figure 3.6(a): SuperSTEM 1 HAADF STEM image of the deep superlattice. **(b)** is an example of a background removed dumbbell intensity line profile. Every point of the intensity profile was generated from the average of 10 image pixels summed along the [110] direction. The script finds the position of the maximum intensity on the LHS (P_{As}) and calculates the average intensity over 4 points (I_{As}). The script then calculates the average intensity over 4 points that are displaced from P_{As} by 10 points. This gives I_C, the average intensity in the non- As column. A measure of the dumbbell column ratio is then found by dividing I_C by I_{As}. **(c)** is the image in (a) re-plotted as a dumbbell column ratio map. Bright dumbbells have high column ratios. **(d)** is a average profile taken across (c).

The line profile of every dumbbell then undergoes the following process one at a time. The position of the maximum HAADF intensity on the side of the dumbbell that contains the As column (P_{As}) is firstly located (Figure 3.6(b)). The side of the dumbbell that contains the As column is determined by the direction of the growth in the image. This is because at the start of the MBE process a layer of Group V atoms is required to have already been grown on the substrate in order for As atoms to take up positions in the crystal structure [10]. Therefore, the Ga (or Al) will always be deposited in the plane below the As (along the growth direction, [001]). Hence, if the growth direction is towards the right in the image, the As will always be situated in the RHS of each dumbbell if the structure is viewed along the [110] direction. In the example given in Figure 3.6, the growth direction runs left to right in the image but the structure is viewed along the [1-10] direction. Hence, the As is on the LHS of every dumbbell (see Figure 3.6(b)).

The HAADF intensity, centred on the point P_{As} (in a particular line profile), is then averaged over 4 points. This gives a measure of the intensity of the As column (I_{As}). After that, the average intensity of 4 points, displaced from P_{As} by 10 points (towards the opposite side of the dumbbell), is measured. The displacement of 10 points was chosen as this is equal to a distance of 1.4Å, which is the dumbbell spacing in GaAs (see Figure 3.6(b)). Hence, the average of 4 points that are centred on the position of the other column provides a measure of the intensity of the other column (I_C). It should be noted that the intensity of each atom column is taken to be an average over several points in order to reduce the effect of noise on the eventual calculation of the column ratio. The ratio is finally calculated by dividing I_C by I_{As}.

The process outlined above was used to measure the column ratio for a large number of dumbbells. The values that were obtained from this method were compared with those obtained from the standard manual approach. It was found that both methods gave very similar results. Hence, the intricacies of the automated approach are valid. Nonetheless, if the magnification changes across an image due to (for example) mains interference, the automated approach would produce an incorrect measure of the column ratio at some locations. However, the degree of magnification change across a SuperSTEM 1 image is far too low for it to affect the automated approach.

In addition, the error in a single measurement of the dumbbell column ratio was estimated. The error was calculated from considering the standard error in the measurement of each column in a single dumbbell. For instance, the intensity of one column is generated from the average intensity of an image section that has an area of 4 pixels by 10 pixels (i.e. the

average of 4 points in the individual 40 point line profile). Hence, a standard error in each column measurement can be calculated from the variance in the pixel values. It was found that an individual column ratio measurement had an overall error of 5-6%. This level of error was consistently observed for many individual dumbbells.

Once the value of the column ratio is collected for all the dumbbells in the image, the image is re-plotted as a map containing these values. For instance, every pixel that formed the area of a dumbbell in the original image now possesses the associated column ratio for a particular value. In this way, the brightest looking dumbbells in the map have the highest ratios. A high column ratio suggests the presence of a powerful scatterer and, hence, the presence of high Z atoms in the non-As column. In addition, the values of the pixels between dumbbells in the map are set to zero. One example of the usefulness of calculating a column ratio map can be seen in Figure 3.6(c). This demonstrates that the particular layers aren't as homogeneous as first suggested by the original image (see Figure 3.6(a). In addition, a line profile can also be taken across the map to give an averaged line profile as shown in Figure 3.6(d).

3.2.4 Compositional Variation across the Deep Superlattice

Figure 3.7(a) presents an expanded version of the column ratio map that is shown in Figure 3.6(c). This was calculated across several repeat units of the deep superlattice. From Figure 3.7(a), it is clear that a range of dumbbell shapes is present in both the GaAs and $Al_{0.3}Ga_{0.7}As$ regions. Nevertheless, the overall difference between the 2 types of layers is still visible in the map. There also seems to be an absence of a distinct changeover in the dumbbell column ratios along the layer boundaries. Moreover, there are several places where small groups of GaAs or GaAs-like dumbbells exist within the $Al_{0.3}Ga_{0.7}As$ layers. These observations suggest a high level of non-uniformity of the superlattice than was not anticipated by the growers.

It is unfortunate that the column ratio values in the map could not be compared against standard values for GaAs and $Al_{0.3}Ga_{0.7}As$. This could have been achieved by obtaining the average column ratio over a large section of the 2 materials. This would have given an indication whether the clumping of column ratio values, as seen in the Figure 3.7(a), was a true reflection of the superlattice composition or was exactly what would have been expected from the random scatter of the values. This problem is addressed in Chapter 5 through the measurement of standard values of the dumbbell column ratio for GaAs and AlAs. It is shown in Chapter 5 that the standard column ratio of GaAs remains close to a value of 1 over a wide thickness range.

Figure 3.7(b) is an averaged line profile taken across the column ratio map in Figure 3.7(a). The error bars are equal to 2 times the standard error of the averaged column ratio. More precisely, the standard error was calculated from the collection of column ratios that were averaged together to produce 1 point in the averaged line profile. Figure 3.7(b) highlights the existence of a noticeable trend in the dumbbell shapes across the GaAs layers. More specifically, the dumbbell column ratios are lower than expected (from the results of Chapter 5) along the final edges (RHS) of the GaAs layers. In fact, the GaAs ratio values only reach a level that is consistent with the results from Chapter 5 at the starting edge (LHS). Hence, there may be some Al present within the GaAs layers. This indicates that an Al flux was somehow incident on the wafer despite the fact that the Al oven should have been shuttered. The reason behind this is unclear. However, other defects were also found in the surface region (see later), which suggests there was something wrong with the MBE control program when the wafer was grown.

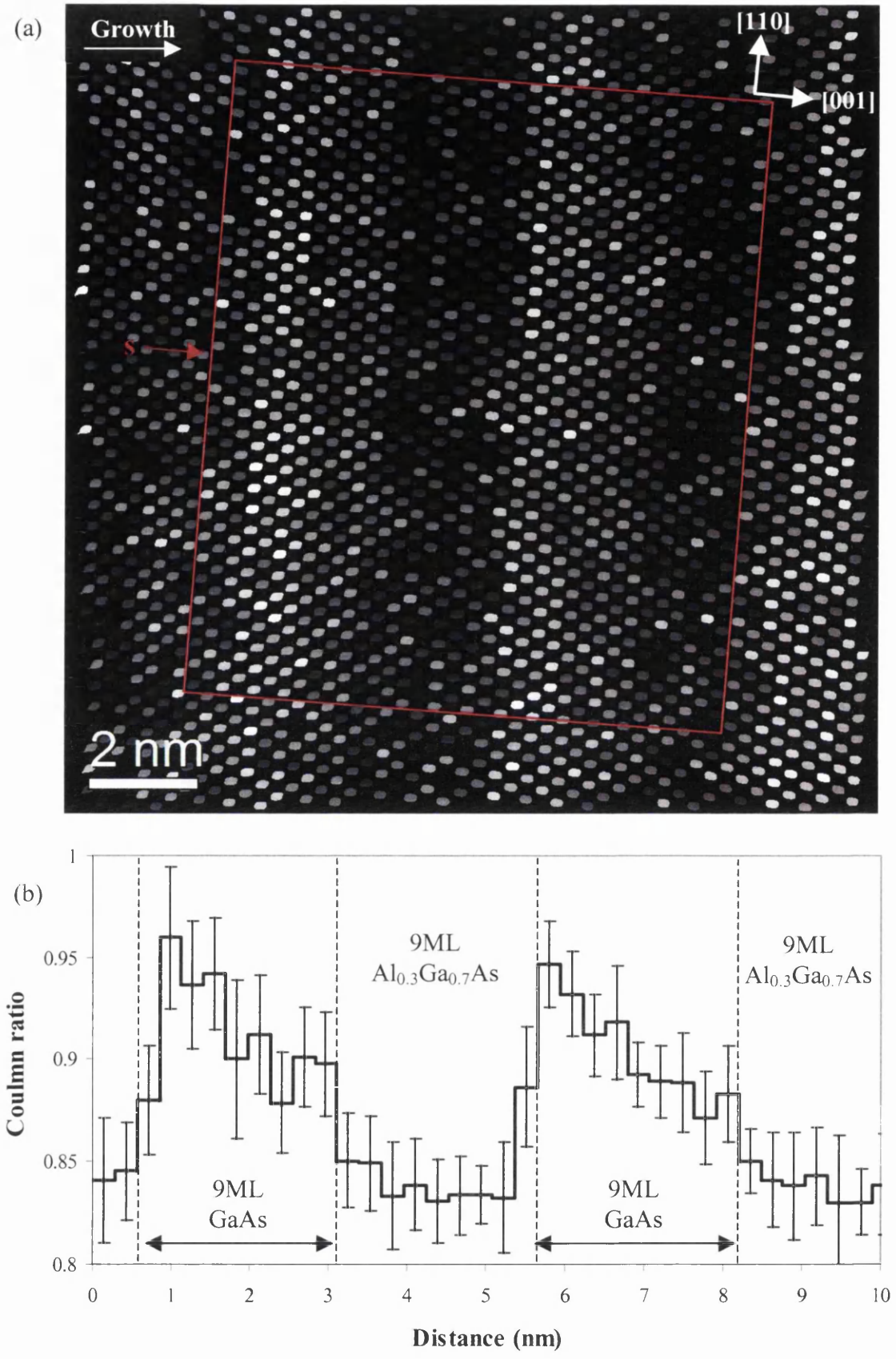

Figure 3.7(a): Dumbbell column ratio map over 3 repeats of the deep superlattice. The brightest dumbbells have the highest ratios. **(b)** is an average line profile taken across the column ratio map section S in (a).

In order to complement the information obtained from the imaging data, EELS data was also acquired from the deep superlattice (see Figure 3.8). The EELS edges that were acquired were the Ga L_3 (1115eV), As L_3 (1323eV) and the Al K (1560eV). The edges were acquired at the same time using 0.7eV per channel, a 19mrad collection angle and an integration time of 1.5sec.

It can be seen that the As signal stays fairly constant across the superlattice as expected. Furthermore, it was found that there was indeed a signal that confirmed the presence of Ga at each of the 9ML GaAs repeats in the structure (see Figure 3.8(c)). In addition, the strength of the Ga signal falls by 20 to 30%, as anticipated, in the 9ML $Al_{0.3}Ga_{0.7}As$ repeats. The reason why the Ga signal drops by this amount is because the percentage of Ga in the RHS of the dumbbells in the 9ML $Al_{0.3}Ga_{0.7}As$ repeats drops to 70%. However, it can be seen that the Ga peaks (in the 9ML GaAs repeats) do not rise to the same level as the signal in the GaAs substrate. This may suggest that the 9ML wide repeats are not fully GaAs and that they contain some Al as well. In fact, the trend in the column ratio map profile (Figure 3.7(b)) that was observed across the 9ML GaAs layers may also have revealed this. On the other hand, it is likely that the probe would have spread into the neighbouring $Al_{0.3}Ga_{0.7}As$ repeats when it was positioned on the GaAs repeats. Hence, there would be an EELS signal component from the $Al_{0.3}Ga_{0.7}As$ layers and, therefore, the Ga EELS signal from the GaAs repeats would be lower than that from the GaAs substrate.

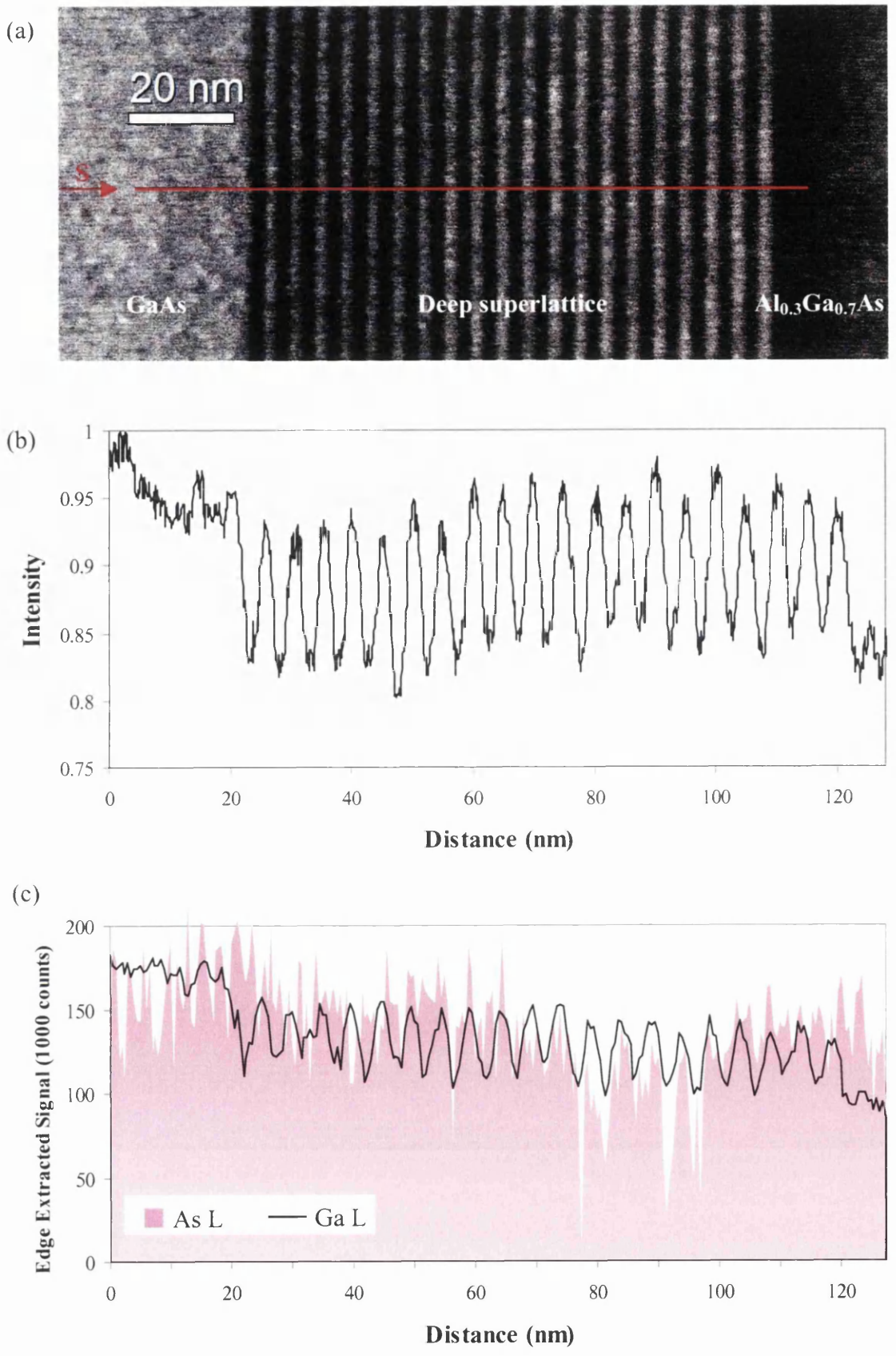

Figure 3.8(a): SuperSTEM 1 HAADF image over the deep superlattice. **(b)** is an intensity profile taken over image section S. Each point of this profile is generated from the average of 20 image pixels. **(c)** is the profile of edge extracted signals taken over image section S.

3.3 Surface Region

3.3.1 Background

The second area of the MODFET heterostructure that was studied using SuperSTEM 1 was the surface region. A schematic of the surface region is shown in Figure 3.9. This region was grown after the 400nm wide $Al_{0.3}Ga_{0.7}As$ buffer section. The surface region is of primary significance to the device's functionality as it contains a 10nm wide $In_{0.3}Ga_{0.7}As$ conducting channel in which the charge carriers travel. The surface region also comprises a fine superlattice (33 repeat units of 1ML AlAs / 2ML GaAs), a 4ML wide GaAs layer and some capping layers.

On one particular gallium plane (within the 4ML wide GaAs layer) about 1% of the atoms had been replaced by silicon atoms to form a silicon δ-doped layer (see Section 1.2.3). In fact, the concentration of the silicon atoms was $6\times10^{12}cm^2$. This layer of silicon functions as a remote provider of carriers to the conducting channel. Such a layer has the effect of improving the carrier mobility, and hence, the overall performance of the parent device, by reducing the scattering of the carriers from ionised donors. In addition, the purpose of the fine superlattice is actually to set up the conditions necessary for the dopant atoms (within the 4ML GaAs layer) to function properly.

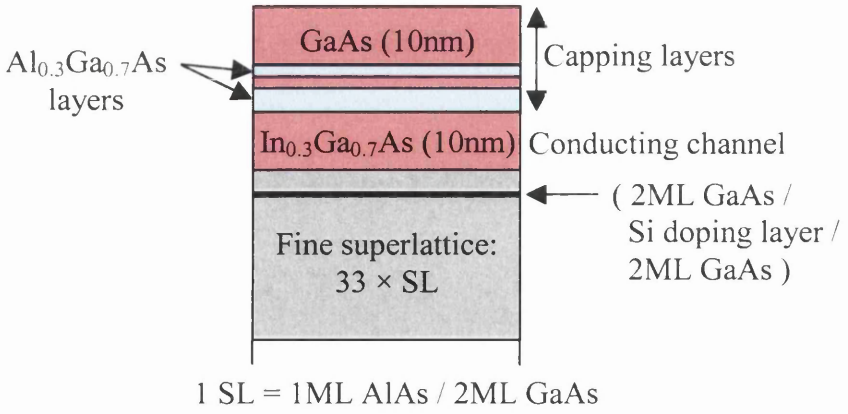

Figure 3.9: Schematic of the structure of the surface region.

There is direct evidence that, above a certain doping concentration, the Si doping efficiency drops off [5]. Indirect evidence also suggests that this may be the result of silicon clustering which involves the spreading of silicon over more than the ideal single Ga plane [6]. Furthermore, this spreading was detected at a lower doping concentration

than was used in this particular heterostructure. Hence, it was expected that the clustering of the silicon was present in this specimen as well. If this was indeed the case, then the silicon replaced both Ga and As atoms thereby giving equal and opposite doping.

The surface region also includes some capping layers. These layers contain a sacrificial $Al_{0.3}Ga_{0.7}As$ layer. This layer acts as an etch stop when the contacts are placed onto the top surface of the heterostructure to create a working device. Al is used because it is a reactive metal and, therefore, reacts vigorously with the etch. This prevents the oxidation of the conducting channel. Furthermore, in a working device, several contacts would also be deposited onto the surface of the capping layers.

The surface region was grown with a substrate temperature of 520°C and a wafer rotation of 50rpm. The temperatures of the Al and Ga ovens were 1079°C and 960°C, respectively. In addition, the As oven temperature was set to 166°C and the In oven temperature was 838°C. The Si oven temperature was 1000°C. The growth rates for the individual AlAs and GaAs layers from the fine superlattice were 0.29ML / sec and 0.69ML / sec, respectively. The growth rate for the $In_{0.3}Ga_{0.7}As$ was 0.49ML / sec. On the other hand, the Si shutter was open for a total of 72sec, which gave a growth rate equal to 0.014ML / sec.

The general purpose of the investigation into the surface layers was to discover how exact the growth technique was at confining the individual layers to their designated locations within the fine superlattice. Furthermore, the identification of the distribution of the silicon atoms and their degree of spreading was of also great interest. An additional objective was to explore the reason behind the doping saturation effect if possible. In fact, the investigation into the Si δ-doped layer provides a difficult challenge even to detect the Si due to the relative small amount present within the surface region. Hence, this investigation was also considered as an assessment of the sensitivity of SuperSTEM 1.

3.3.2 Growth Errors

Figure 3.10 illustrates that the deposition process proceeded contrary to the growth map. For instance, there are several places in which the fine superlattice extends into the 400nm $Al_{0.3}Ga_{0.7}As$ buffer region, giving rise to a distorted interface between the two. In fact, near to those particular defects, the image shows that the superlattice layer structure is totally absent. In reality, this was probably caused by the formation of a depression in the buffer region on top of which the superlattice was grown.

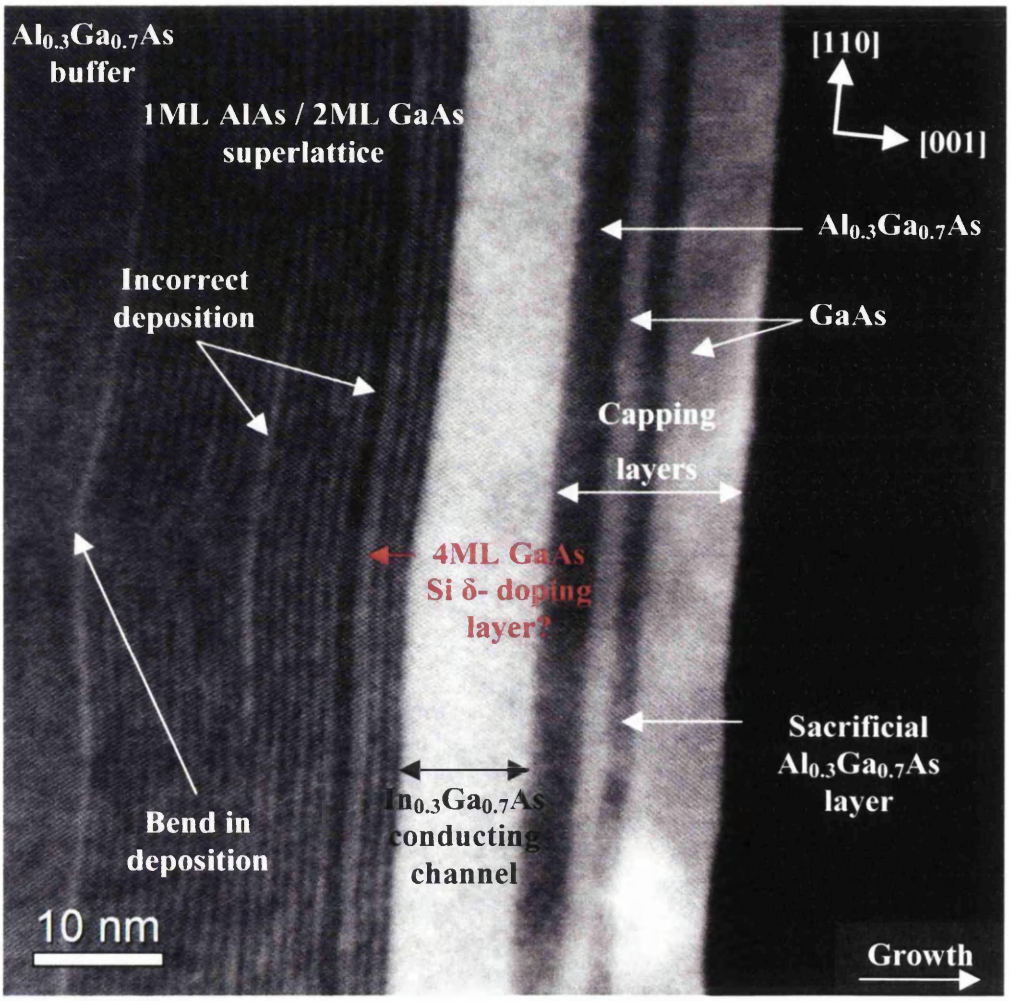

Figure 3.10: SuperSTEM 1 HAADF STEM image of the surface region.

Figure 3.10 also reveals the presence of extra wide layers at 2 locations within the fine superlattice. In addition, the 10nm $In_{0.3}Ga_{0.7}As$ conducting channel also exhibits signs of non-sharpness along one of its boundaries. This distortion is, however, absent on the final edge of the channel. Hence, it is clear that the depression that existed on the top surface of the buffer region has been filled in by the end of the deposition of the $In_{0.3}Ga_{0.7}As$ layer.

Figure 3.11(a) displays a high magnification SuperSTEM 1 HAADF STEM image taken over a section of the surface region far from the deposition distortions. The 1ML AlAs / 2ML GaAs fine superlattice is not well defined but is still visible on the left hand side of the image. The location of the 4ML GaAs layer, which contains the Si δ-doping layer, is also shown. As was the case with the deep superlattice, there seems to be a certain degree of roughness to the interfaces between some of the layers. This is indicative of 1 or 2MLs of elemental intermixing or possibly stepping (see Section 1.4). In addition, some of the GaAs layers in the superlattice seem to be 3ML wide as indicated in Figure 3.11(a). Finally, the actual number of layers present in the fine superlattice does not match the growth map.

Of greater concern though, is the seeming existence of a growth error, which interrupts the periodicity of the superlattice. This has the form of a dark layer, of about 4ML across, and is followed by the expected 4ML GaAs layer. This can be quite clearly in Figure 3.11(a). It is probable that the defect layer is composed of 4MLs of AlAs since the HAADF background signal is much lower in the defect region. Unfortunately, due to the existence of this growth defect, along with an incorrect number of layer repeats, the location of the silicon δ-doping layer was in doubt. Consequently, a detailed study of this layer could not be implemented as its exact location is required if the small changes in composition are to be detected.

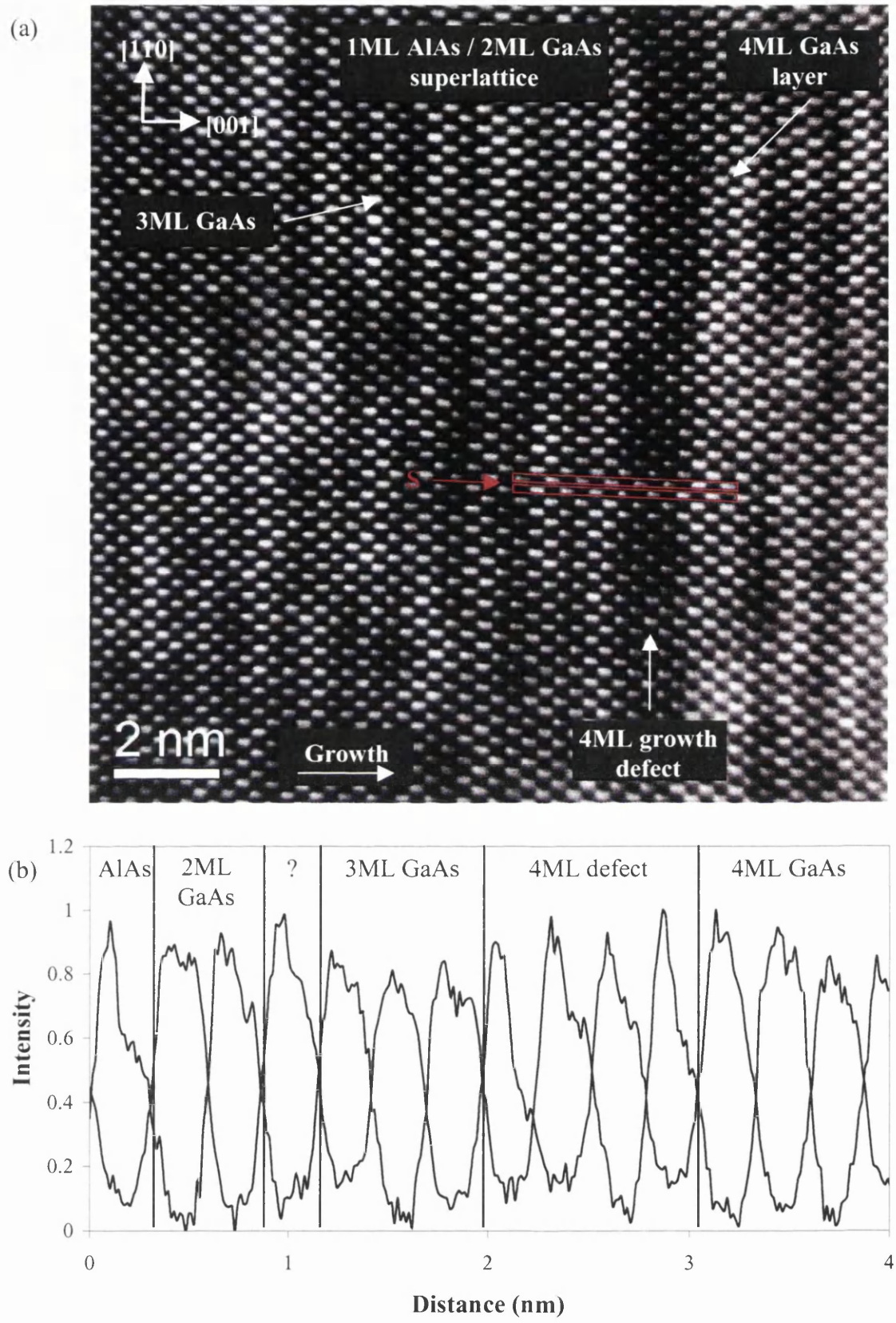

Figure 3.11(a): SuperSTEM 1 HAADF STEM image over several repeats of the fine superlattice and the 4ML growth defect. **(b)** is an intensity profile taken across image section S. 2 interleaving profiles are shown. Every point of the intensity profile is generated from the average of 10 image pixels summed along the [110] direction. The background has also been removed.

3.3.3 Composition of the Surface Region

Figure 3.11(b) provides a selected view of a line profile taken across the fine superlattice. The line profile for the adjacent row of dumbbells is also presented in order to pick out the 1ML wide AlAs layers. The distinction between the different types of dumbbells is now more apparent than in the case of the deep superlattice. This is because the 100% Al columns, in AlAs, have much weaker potentials than those of the $Al_{0.3}Ga_{0.7}$ columns in the 9ML $Al_{0.3}Ga_{0.7}As$ layers within the deep superlattice. Hence, such columns scatter less strongly out to high angles and the reduced intensity on the detector means that there is a greater disparity between the column ratios of GaAs and AlAs. For example, Figure 3.12 demonstrates the typical AlAs dumbbell shape found within the fine superlattice.

The experimental column ratio for AlAs is equal to 0.56 (simple theory predicts Al / As = 0.16). Hence, GaAs and AlAs dumbbells should be readily distinguishable. This can be seen in Figure 3.11(b), which shows that the 2-1 periodicity of the fine superlattice is absent in the image section S. Figure 3.11(b) also points to the fact that the 4ML wide defect is composed of AlAs.

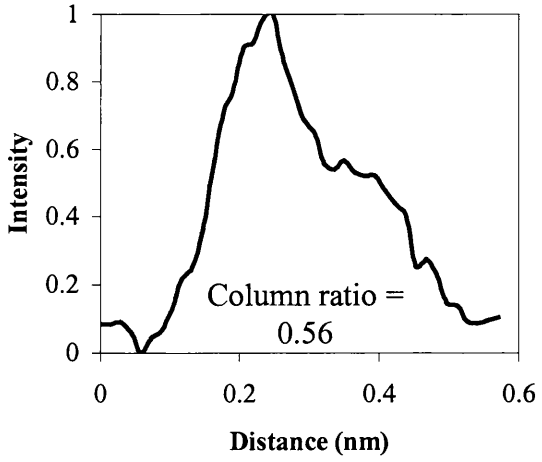

Figure 3.12: Typical SuperSTEM 1 HAADF image intensity profile of AlAs from the centre of the 4ML AlAs layer in the fine superlattice. Every point of the intensity profile is generated from the average of 10 image pixels summed along the [110] direction.

Figure 3.13(a) shows a column ratio map that was calculated from the image in Figure 3.11(a). It is apparent that, as was the case with the deep superlattice, a range of dumbbell shapes is present throughout the fine superlattice. However, a periodicity is still clearly visible across the structure. Figure 3.13(b), which is an averaged line profile taken across the column ratio map in Figure 3.13(a), shows several peaks in the column ratio that indicates the presence of GaAs layers. The peaks are typically separated by a significant reduction in the column ratio. These dips are associated with the 1ML wide AlAs layers. It can be noted that the GaAs peaks seem to be generally 3ML in width. This suggests that the periodicity is in fact mostly 3-1 (i.e. 3ML GaAs / 1ML AlAs), as was implied by the HAADF image. A possible reason behind this may be that the Ga shutters were left open for too long a time during the MBE growth process. This would have resulted in wider GaAs layers.

However, another feasible interpretation of Figure 3.13(b) is also possible. It can be seen that the column ratio does not stay constant over the 3ML wide GaAs layers. In fact, the most GaAs like dumbbells (values closest to 1) only occur in the centre of the layers. It then takes 2MLs for the dumbbell shape to switch to fully AlAs like. Therefore, the layers may not be made of 1ML AlAs / 3ML GaAs at all but may actually be made of 2ML AlAs / 2ML GaAs. Therefore, it may also be difficult to determine the correct periodicity due to the possible presence several monolayers of compositional intermixing (or stepping) across the interfaces. The extent of spread in the dumbbell column ratio across AlAs / GaAs interfaces is considered in Chapter 6.

The 4ML wide growth defect is also discernible in Figure 3.13(b). It is evident that most of the dumbbells in this region can be identified as mostly AlAs due to their low column ratios. Nevertheless, some areas within the defect appear to be more GaAs than AlAs like. Yet again, the interfaces show signs of compositional intermixing or stepping.

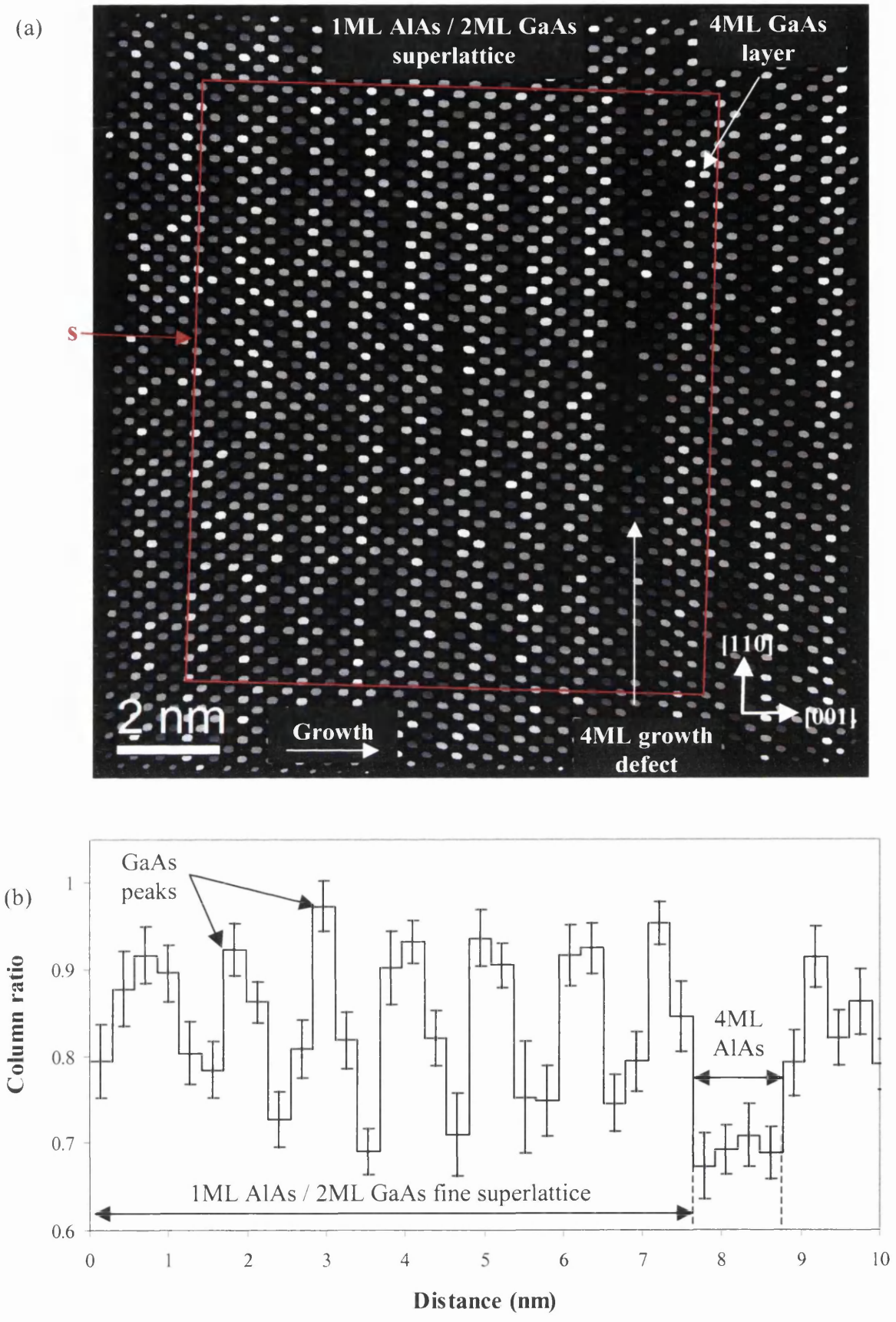

Figure 3.13(a): Dumbbell column ratio map over several repeats of the fine superlattice and the 4ML AlAs growth defect. The brightest dumbbells have the highest column ratios. **(b)** is an average profile taken across section S in (a).

(a)

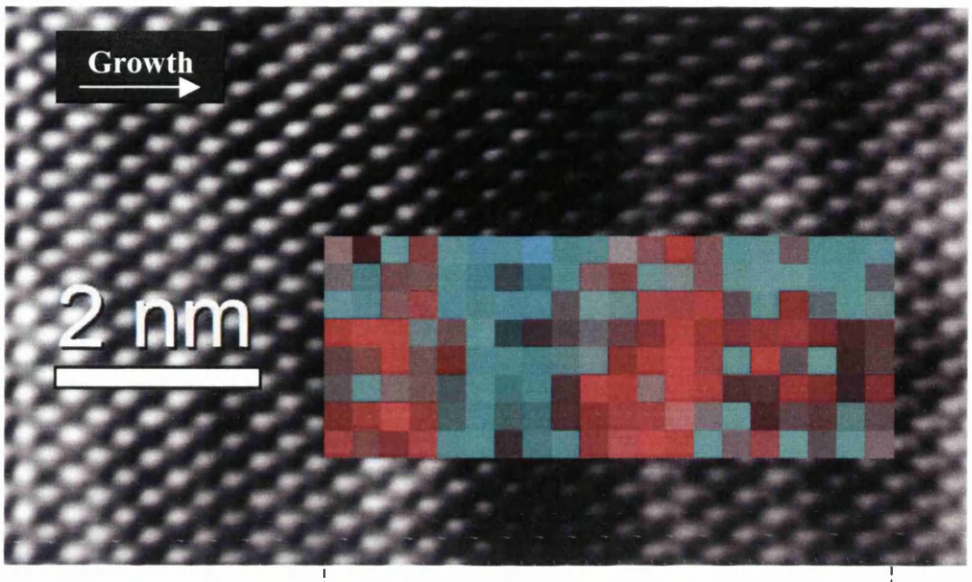

(b)

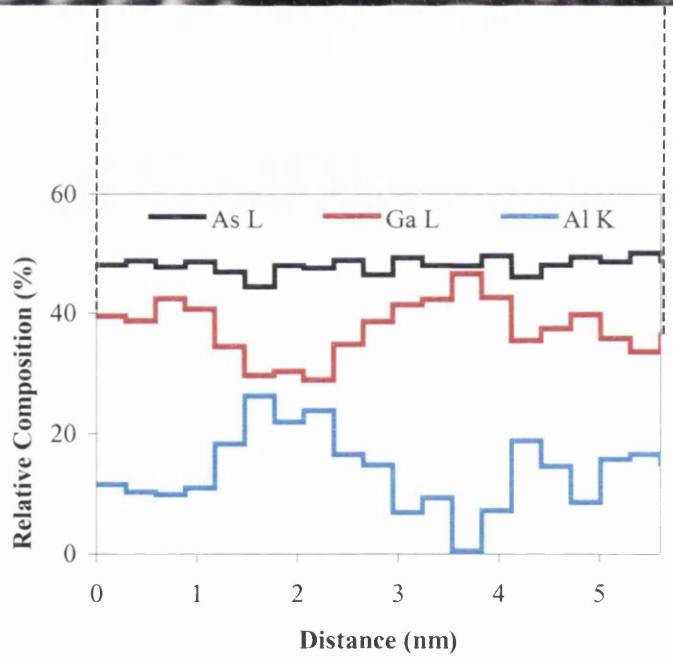

Figure 3.14(a): SuperSTEM 1 FFT filtered HAADF STEM image of a part of the fine superlattice and the growth error. EELS data was obtained from the rectangular area (inset). In this area, the lateral length of each pixel is equal to the lateral size of 1 dumbbell. The intensities of these pixels give Ga and Al concentrations normalised by their cross- sections. Red signifies high Ga concentration whereas Green / Blue signifies high Al. **(b)** is a profile taken across the EELS data in the inset.

Figure 3.14(a) presents a FT (Fourier transform) filtered SuperSTEM 1 HAADF STEM image taken near to the 4ML wide growth error in the surface region. The image was filtered through the application of a mask around each reflection in the FT. This artificially removes noise from the image and sharpens the dumbbell profile. The analysis of the EELS data has been overlaid on top of this image from the area where it was acquired (see the inset of Figure 3.14(a)). Another image was acquired after the EELS map was taken. This showed that specimen drift was not an issue in this case. The EELS analysis map displays the position of high Ga and high Al content over this section. The pixel intensity in this map gives the Ga and Al concentrations normalised by their cross-sections. The values were obtained through the use of the quantification program in Digital Micrograph. Red signifies high Ga concentration whereas Green / Blue signifies high Al.

It can be seen that the dark and light bands, which comprise the growth error and 4ML GaAs layer, correspond to two bands of high Al and high Ga content in the inset of Figure 3.14(a). As a result, it is highly likely that the growth error is composed of 4ML AlAs (or at the least high Al content) followed by the 4ML wide GaAs layer. Moreover, as was seen previously, this deduction is also in agreement with the shapes of the dumbbells that are present across the growth defect.

Figure 3.14(b), which is a line profile taken across the EELS analysis in the inset of Figure 3.14(a), shows that the As L_3 signal remains constant across the data set as expected. In addition, the lack of sharpness to the boundaries of the bands (as seen in Figure 3.14(b)) again supports the view that the growth process had introduced several monolayers of compositional spreading or interfaces with steps. However, the lack of sharpness may also be an effect of beam spreading in a thick part of the specimen. This would result in the Al K and Ga L_3 signals being generated at all positions of the probe within the fine superlattice. In addition, Figure 3.14(b) also reveals that 100% AlAs and 100% GaAs is never reached in the 4ML GaAs layer and 4ML (supposedly) AlAs defect region. This may again be due to compositional spreading, surface stepping or beam spreading. The degree of beam spreading as a function of specimen thickness is calculated in Chapter 4 for various materials and is discussed further in Chapter 6.

3.3.4 Conducting Channel

As was stated previously, the conducting channel is composed of 10nm of $In_{0.3}Ga_{0.7}As$. The charge carriers from the dopant atoms (i.e. Si δ-doping layer) are trapped by the deep potential well of the $In_{0.3}Ga_{0.7}As$. In a working device, the carriers are driven back towards the dopant ions by the electric field of the depletion region. This creates a 2 dimensional electron gas (2DEG) along one of the edges of the $In_{0.3}Ga_{0.7}As$. This edge is the one nearest to the substrate and can be seen in the SuperSTEM 1 HAADF STEM image of Figure 3.15(a). It can be seen that the $In_{0.3}Ga_{0.7}As$ appears much more intense than the neighbouring materials due to the relatively high Z number of In. Furthermore, as was stated previously, the low magnification image in Figure 3.10 reveals that there is distortion along the 2DEG edge of the $In_{0.3}Ga_{0.7}As$ channel. This would lead to an increase in the scattering of the charge carriers thereby resulting in a reduction of carrier mobility.

Figure 3.15(b) is a line profile taken across the end of the fine superlattice and a section of the conducting channel. The simple Z^2 scattering theory states that the column ratio for $In_{0.3}Ga_{0.7}As$ should be equal to 1.28. However, as the line profile reveals, that level of asymmetry was not close to being attained by any $In_{0.3}Ga_{0.7}As$ dumbbell within the channel. This may have been the result of the probe being rapidly de-channelled because of the high scattering power of the In atoms. Another curious effect concerns the degradation in the intensity height of the dumbbell signal across the channel. It can be seen that the dumbbell height reduces in intensity towards the RHS of the line profile. A possible reason for this may be the presence of a slight bend in specimen at this place so the orientation is not exactly along the [1-10] direction.

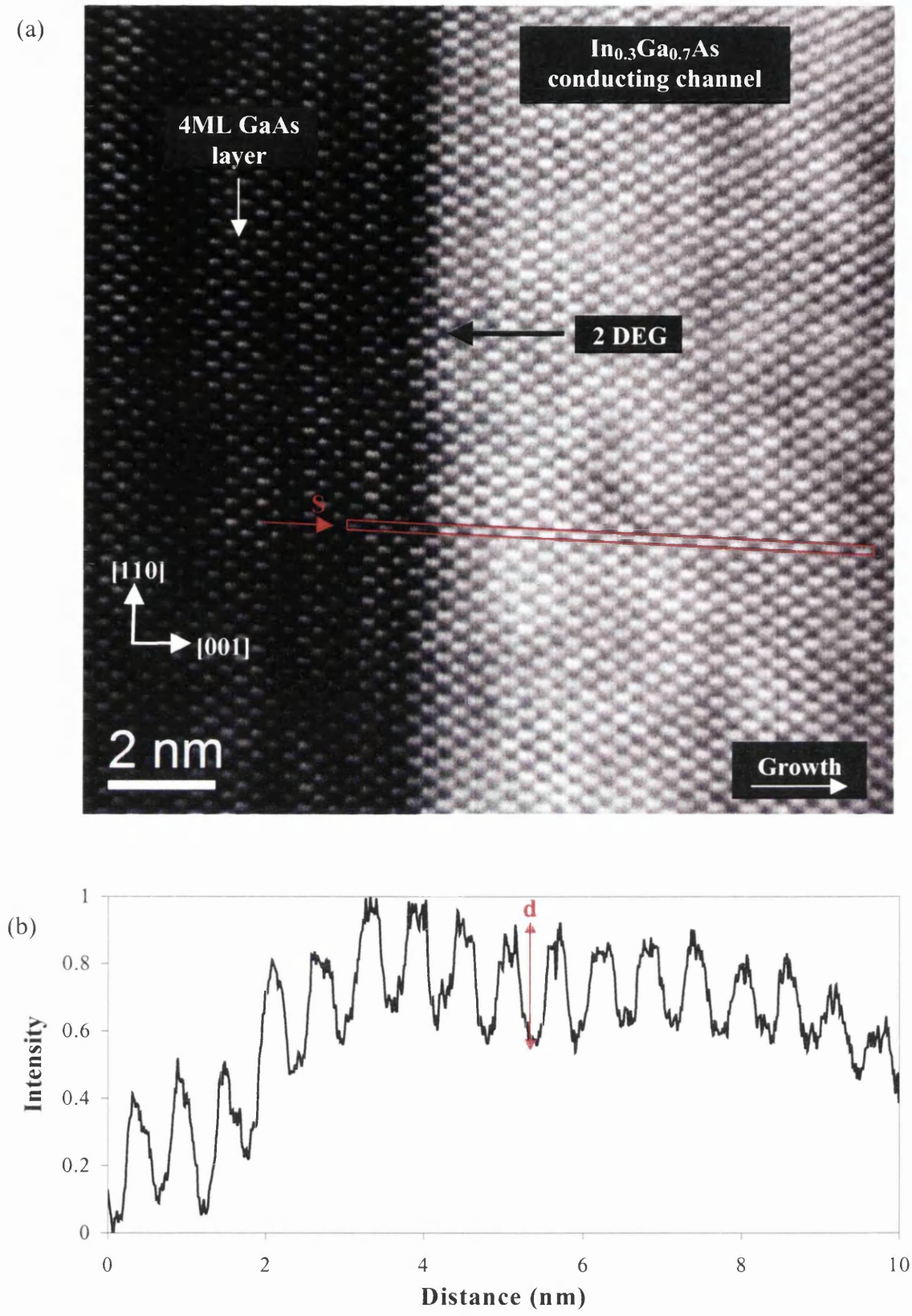

Figure 3.15(a): SuperSTEM 1 HAADF STEM image of part of the fine superlattice and the $In_{0.3}Ga_{0.7}As$ conducting channel. **(b)** is an intensity profile taken across the image section S. Every point of the intensity profile is generated from the average of 10 image pixels summed along the [110] direction. The superlattice background has been removed. The arrow d is the intensity height for the dumbbell signal.

Figure 3.16(a) is a column ratio map that was calculated from the image in Figure 3.15(a). The end of the fine superlattice and the 4ML wide GaAs layer is visible in the map. These features have a similar behaviour to that highlighted in the column ratio map of the superlattice in Figure 3.13. The $In_{0.3}Ga_{0.7}As$ column ratio is distinguishable from the other materials present in the map. Hence, the extent of the channel region is recognisable. In fact, the boundary between the final AlAs layer and the conducting channel is also very well defined. Only a few dumbbells along the interface seem to have an incorrect column ratio. The averaged line profile taken across the column ratio map (see Figure 3.16(b)) also supports this opinion. This draws attention to the fact that there is a distinctive change in the column ratio across the interface.

It should also be noted that the wiggle observed down the image (along the [110] direction) does not affect the line profile because the profile is created by the individual summation of each column of dumbbells independently. It is likely that this wiggle was introduced by the 50Hz mains interference and it does not represent a true reflection of the uneven nature of the interfaces. In addition, the effect of the mains interference on the perpendicular direction across the image (along the [001] direction) was measured to be less severe than the wiggle going down the image.

Figure 3.16(b) also shows that the $In_{0.3}Ga_{0.7}As$ column ratio is in general higher than that of GaAs, as it should be, but is still some way short of that predicted the simple theory. Chapter 4 presents a more rigorous estimate of the dumbbell column ratio of GaAs and the simulated column ratio of InAs is presented in Chapter 7. The column ratio is also shown to be highly variable within the conducting channel as it frequently drops to below 0.9. The reason for this may be that as the wafer was rotated during the MBE process, parts of it periodically became closer and then further away from the Ga and In ovens in turn. Hence, a periodic change in the composition would be expected across the wafer [7]. This ripple effect has been reported in MBE grown uniform ternary films (such as InGaAs) by other authors [7].

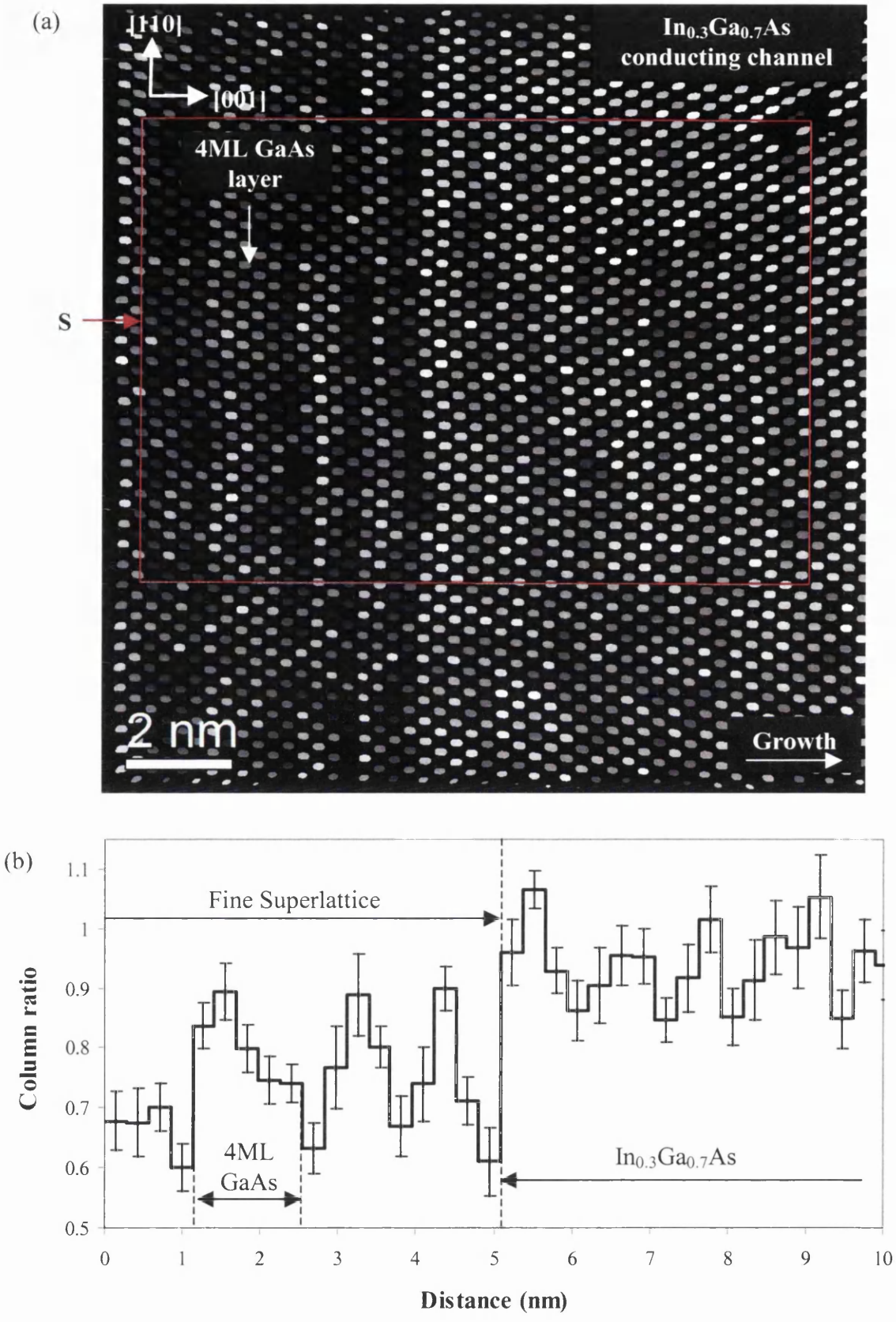

Figure 3.16(a): Dumbbell column ratio map over part of the fine superlattice and $In_{0.3}Ga_{0.7}As$ conducting channel. The brightest dumbbells have the highest column ratios. **(b)** is an average line profile taken across the map section S in (a).

3.4 Discussion

3.4.1 Summary of Results from the MODFET Heterostructure

The various constituent parts of the MODFET heterostructure where studied using both HAADF imaging and EELS. It was unfortunate that the first MBE material that was studied using SuperSTEM 1 turned out to have a faulty deposition. However, subsequent structures that were grown by MBE did match the growth sheet very well (see Chapter 6). Nonetheless, the experiment on the MODFET heterostructure highlighted key areas where a deeper understanding was required.

The investigation of the deep superlattice showed that it was important to perform a new type of image processing when dealing with high-resolution data obtained from SuperSTEM 1. This involved the removal of the background signal and the analysis of the dumbbell shapes using column ratio maps. These techniques allow the most information to be taken from the SuperSTEM 1 data.

The actual results from the deep superlattice revealed that the dumbbell shapes were a mixture of the different materials along layer boundaries. However, it is unclear what the reason behind this non-sharpness actually is. For instance, it could be the case that the layer interfaces are sharp over a few monolayers due to compositional spreading. On the other hand, it could be result of a surface step effect through the vertical direction of the material. To clarify, the interfaces may actually be sharply defined along this stepped structure but because the acquired image is essentially a projection of this structure, an averaged column composition and, hence, an averaged column ratio is obtained. Chapter 6 explores the reason behind the perceived interfacial non-sharpness.

The HAADF images of the surface region highlighted the existence of several growth errors. These included the incorrect deposition of the fine superlattice and the presence of an extra 4ML wide layer that was probably composed of AlAs. The cumulative effect of these defects made it impossible to study the Si δ-doped layer using the heterostructure. Hence, a subsequent investigation of δ-doping was carried out (see Chapter 7).

The ability of SuperSTEM 1 to investigate composition via EELS was shown to be less effective than via HAADF imaging, especially in the detection of Al. This is due to the fact that only one part of the spectrum obtained from SuperSTEM 1 is in focus at any one time, as was discussed in Chapter 2. Hence, it is difficult to acquire edges that have widely

different ionisation energies. In addition, the layers in the MODFET heterostructure range from 9ML (in the case of the deep superlattice) to only 1ML (in the case of the AlAs layers within the fine superlattice). Hence, with the probe situated on one particular layer and assuming geometrical beam spreading with a specimen thickness of ~60nm, EELS signals are also likely to be produced from the elements within the neighbouring layers due to spread of the probe into these surrounding materials.

3.4.2 Averaged Column Ratios

The averaged dumbbell column ratios for each of the materials, which comprised the MODFET heterostructure, are tabulated in Table 3.1. These were derived by the calculation of the mean column ratio value from the sections of the column ratio maps that consisted of only 1 material. However, values were not obtained from the GaAs substrate or from the $Al_{0.3}Ga_{0.7}As$ buffer region because their importance was only realised after the data from the MODFET was acquired. The column ratio values are given as the mean plus or minus 2 times the standard error in each case.

Area	Material	Column ratio: Z^2 theory	Column ratio: experiment
Deep Superlattice	GaAs	0.882	**0.900** ± 0.010 (N = 140)
	$Al_{0.3}Ga_{0.7}As$	0.664	**0.838** ± 0.017 (N = 88)
Fine Superlattice	AlAs	0.155	**0.581** ± 0.019 (N =20)
4ML Defect Region	AlAs	0.155	**0.560** ± 0.017 (N = 20)
Conducting Channel	$In_{0.3}Ga_{0.7}As$	1.279	**0.940** ± 0.010 (N = 667)

Table 3.1: Averaged dumbbell column ratios for each of the materials that comprised the MODFET heterostructure. The experimental column values are given as the mean plus or minus 2 times the standard error. N is the number of dumbbells that were averaged.

It can be seen that the random errors associated with each averaged column ratio are rather small. In addition, Figure 3.17 graphically illustrates the spread in the column ratio values that are associated with $Al_{0.3}Ga_{0.7}As$, GaAs and $In_{0.3}Ga_{0.7}As$ dumbbells. It was found that

all dumbbell values (for the 3 materials) were within 3 standard deviations of the respective mean value.

A comparison with the column ratio that is predicted by the Rutherford scattering model is also presented in Table 3.1. It is apparent that only in the case of GaAs do the experimental and theoretical values coincide. This poor agreement may be mostly due to the relatively unsophisticated nature of the simple Z^2 theory. A better approach (based on multislice simulations) is given in Chapter 4. This approach also takes into account the thickness of the specimen.

Every measured column ratio of a single dumbbell will also be affected by random noise in the original image. However, averaging over several image pixels in order to calculate the intensity of each column in a dumbbell reduces this effect. This process was explained in Section 3.2.3.

Another reason for the poor experimental and theoretical correspondence may be due to the fact that the sections, over which the column ratio was averaged, were rather confined in spatial extent. Hence, other materials closely bounded the sections and the effect of compositional intermixing and stepping on the calculated column ratios cannot be ruled out. This is highlighted by the fact that the column ratio for AlAs, from the fine superlattice, is slightly higher than that of AlAs from the wider defect region. It is therefore clear that a series of standard column ratio values need to be obtained from wide layer materials. These values are presented in Chapter 5. The standard values were useful in the determination of the composition of other specimens (see Chapters 6 and 7).

In summary, the study of the MODFET heterostructure led to a number of subsequent investigations. These included the determination of the dumbbell column ratios for AlAs and GaAs as a function of specimen thickness. Moreover, a theoretical estimate of the dumbbell column ratios was also shown to be necessary. In addition, due to the obvious growth defects associated with the MODFET, a new investigation into Si δ-doping was also required. Furthermore, the typical accuracy of the MBE process at growing the various III-V layers could not be ascertained because of the presence of the growth defects. Hence, another investigation into interfacial sharpness was needed with a specimen that had been grown correctly.

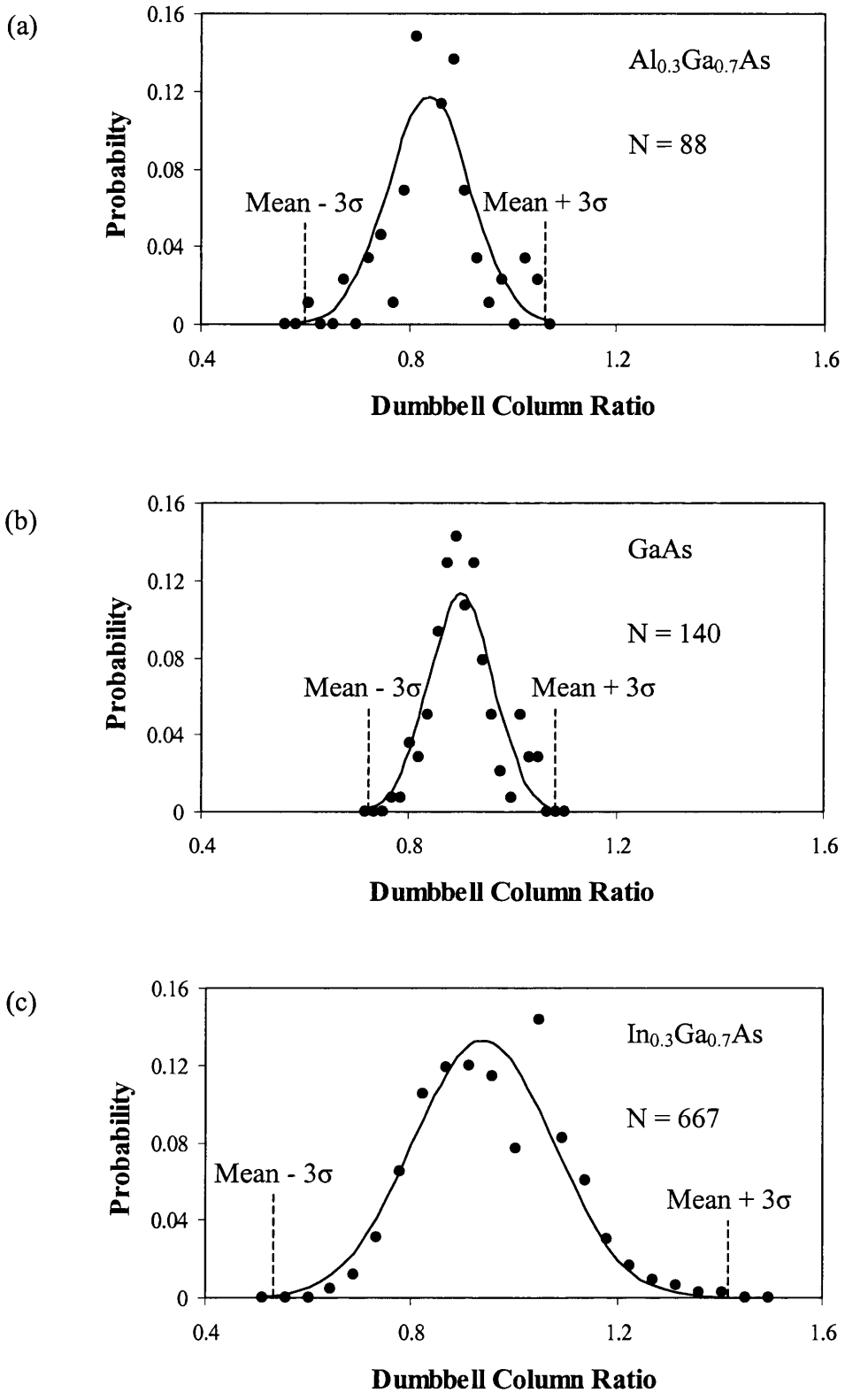

Figure 3.17: Dumbbell column ratio statistics for **(a)** $Al_{0.3}Ga_{0.7}As$ (from the deep superlattice), **(b)** GaAs (from the deep superlattice) and **(c)** $In_{0.3}Ga_{0.7}As$ (from the conducting channel). N refers to the total number of dumbbells that were averaged. The probability is given as the frequency (over a particular range of the column ratio) divided by N. σ is the standard deviation in each case.

References

[1] J. H. Davies, The physics of low-dimensional semiconductors, Cambridge University Press (2005)

[2] S. van Aert, P. Geuens, D. van Dyck, C. Kisielowski, J. R. Jinschek, Electron channelling based crystallography, Ultramicroscopy 107, 551-558 (2007)

[3] M. H. Loretto, Electron beam analysis of materials, Chapman and Hall (1994)

[4] R. F. Egerton, Limits to spatial, energy and momentum resolution of electron energy-loss spectroscopy, Ultramicroscopy, doi: 10.1016/j.ultramic.2006.11.005 (2007)

[5] G. Li, C. Jagadish, Confinement and concentration of electrons in Si δ-doped $Al_xGa_{1-x}As$ (x=0 and 0.35) grown by metalorganic vapour phase epitaxy, Journal of Crystal growth 167, 421-428 (1996)

[6] L Hart, Si δ-doping in GaAs: investigation of the degree of confinement and the effects of post-growth annealing, Semiconductor Science Technology 10, 32-40 (1995)

[7] W. L. Sarney, S.P. Svensson, Characterization of compositional oscillations in InGaAs films induced by MBE cell configuration and substrate rotation, Sensors and Electron Devices Directorate, U.S. Army Research Laboratory, Adelphi, MD 20783 USA (2005)

[8] N. D. Browning, EELS in the STEM: determination of materials properties on the atomic scale, Micron Vol. 28, No. 5. pp. 333-348 (1997)

[9] M. M. Disko, C. C. Ahn, B. Fultz, transmission electron energy loss spectrometry in materials science, A publication of the Minerals, Metals and Materials Society (1992)

[10] K. Y. Cheng, Molecular beam epitaxy technology of III-V compound semiconductors for optoelectronic applications, Proceedings of the IEEE, Vol. 85, No. 11 (1997)

[11] D. O. Klenov, S. Stemmer, Contributions to the contrast in experimental high-angle annular dark- field images, Ultramicroscopy 106, 889-901 (2006)

[12] S. J. Pennycook, Structure determination through Z-contrast Microscopy, Oak Ridge National Laboratory

[13] B. Rafferty, P. D. Nellist, S. J. Pennycook, On the role of transverse incoherence in Z-contrast STEM, Journal of Electron microscopy 50(3), 227-233 (2001)

[14] S. J. Pennycook, B. Rafferty, P. D. Nellist, Z-contrast imaging in an aberration-corrected scanning transmission electron microscope, Microscopy Microanalysis 6, 343-352 (2000)

[15] S. J. Pennycook, M. Varela, C. J. D. Hetherington, A. I. Kirkland, Materials advances through aberration-corrected electron microscopy, MRS Bulletin, Volume 31, (2006)

[16] P. D. Nellist, S. J. Pennycook, Probe and object function reconstruction in incoherent scanning imaging transmission electron microscope imaging, Scanning Microscopy Vol. 11, 81-90 (1997)

4 Computer Modelling: The Scattering of Å-scale Electron Probes in III-V Semiconductor Crystals

4.1 Introduction

This chapter deals with a computer modelling investigation into how Å-scale electron probes are scattered by various semiconductor materials. The majority of the investigation was carried out using an electron STEM probe similar in size to that of SuperSTEM 1. This simulated probe had a FWHM (full width at half maximum) of 1Å and a convergence semi-angle of 24mrad. However, the results obtained from this probe were also compared with those from two other electron probes. These possessed FWHM sizes of 1.6Å and 0.7Å and convergence semi-angles of 12mrad and 50mrad, respectively. The part of the investigation that utilised these two probes was a first attempt and the results indicate that a more detailed study of probe conditions is required in order to determine the optimum conditions for a particular application. The individual probe parameters are catalogued in Table 4.1. Each probe was simulated using an accelerating voltage of 100kV at the optimum defocus (see later). The details of Table 4.1 are also explained later on during the discussion into the characteristics of the individual probes. However, it should be noted that the values of the last 2 measures of the probe size in Table 4.1 overestimate the probe size. This problem is explained in Section 4.3.1.

Due to the fact that the experimental data from Chapter 3 (and later chapters) were mainly obtained through the use of the 1Å-scale, 24mrad probe of SuperSTEM 1, the main focus of the modelling investigation centred on the 1Å-scale, 24mrad simulated probe. Furthermore, the study of the scattering (and the HAADF signal generation) behaviour of the 24mrad simulated probe was undertaken in order to provide a greater understanding of the results obtained from the MODFET structure that was shown in Chapter 3 (and also from later investigations). For example, the experimental results from SuperSTEM 1 (in Chapter 3) showed that although 1Å spatial resolution was achieved, it was difficult to interpret the data correctly due to a lack of detailed understanding of how the HAADF signal is generated. In particular, it was unclear as to the precise effect that the different Z numbers of the materials within the heterostructure (and their positions) had on the observed HAADF intensity. Therefore, the sharpness of the interfaces in the MODFET could not be determined definitively. In addition, due to the effect of electron column channelling, it is important to understand which parts of the atomic columns actually

generates the HAADF signal. Knowledge of the depth over which this channelling occurs becomes critical when attempting to interpret images of doping layers (see Chapter 7). Furthermore, an awareness of the distribution of the electron intensity along individual columns is important in understanding the generation of EELS signals.

	12mrad	24mrad	50mrad
Accelerating voltage (kV)	100	100	100
C_3 (mm)	0.1	0.1	0.03
Defocus (nm)	23.56	23.56	12.91
FWHM (nm)	0.159	0.104	0.071
Diameter of central maximum (nm)	0.361	0.219	0.153
Probe density of central maximum (fraction of total intensity / nm^2)	6.30	9.20	8.22
Beam Diameter that contains 90% of total probe intensity (nm)	0.79	1.24	4.97
% of total beam current contained in central maximum	64.3	34.7	15.2

Table 4.1: A table of the input parameters along with the various measures of probe size of the 3 simulated probes (12mrad, 24mrad and 50mrad).

In contrast to the simulations of the 24mrad probe, which were performed in order to provide a comparison with actual experimental data, the simulation of the 50mrad probe provided a prediction of the likely behaviour of SuperSTEM 2. This dedicated 100kV STEM, which is not yet operational, has been designed specifically to take advantage of aberration correction technology (unlike the column of SuperSTEM 1). Although the ultimate operating performance of SuperSTEM 2 is as yet unknown, its obtainable spatial resolution is expected to be about 0.7Å with a convergence semi-angle of 50mrad. Hence, the simulation of the 0.7Å, 50mrad probe allows a prediction to be made of SuperSTEM 2's scattering behaviour along with the associated generation of HAADF signals.

The simulation of the 50mrad probe also allows a comparison with the current behaviour of the SuperSTEM 1 probe to be made with that expected of SuperSTEM 2. This should

give an indication of the likely benefits or disadvantages to using SuperSTEM 2. For instance, although the improved resolution of SuperSTEM 2 should allow more detail to be obtained from a specimen, its greater convergence angle may result in a shorter channelling depth and a greater degree of beam spreading. This would be disadvantageous as it would require a thinner specimen to achieve the same quality of EELS data. In addition to the 50mrad probe, the simulation of a larger 1.6Å, 12mrad probe was also performed. This probe size cannot resolve the GaAs dumbbell spacing (1.4Å) and is therefore equivalent to that found in uncorrected STEMs. Hence, the simulation of the 12mrad probe permits a comparison to be made between corrected and uncorrected probes.

4.2 Computer Modelling Background

4.2.1 Software Package

E. J. Kirkland's computer modelling software was used to carry out the modelling investigation. The various computer programs that constitute this software package allow the behaviour of an electron microscope to be simulated. In essence, the programs calculate the elastically scattered electron wavefunction at the exit face of the specimen using the common multislice approach [1]. Thermal diffuse scattering of the electron probe can be simulated by performing frozen phonon calculations (see Section 4.2.3). In this way, the scattering behaviour of Å-scale probes in 3 different III-V materials commonly used in semiconductor devices (GaAs, AlAs, and InAs) was examined (InAs was not simulated for the 12mrad and 50mrad probes). For each particular material, the distribution of electron intensity (in real space) was considered as a function of specimen thickness and probe position. Simulations of the HAADF signal were also performed. Precise details of the simulations are given in Section 4.2.4.

4.2.2 Simulation Interpretation

This section gives a brief overview of how E. J. Kirkland's computer software functions. A more in-depth explanation of the underlying theory can be found in Kirkland's book [2]. The actual simulation process can be understood by separating it into different stages. The first stage in a STEM calculation involves the setting up of the required probe wavefunction $\psi_p(\underline{r}, \underline{r}_p)$. The required probe parameters include the accelerating voltage, probe convergence semi-angle and a C_3 aberration coefficient value. The values of these parameters for the 3 different probes are given in Table 4.1. The probe wavefunction is a

complex variable with amplitude and phase components and is also a function of position in 2D real space (variable $\underline{r}$) and of probe position in 2D real space (variable $\underline{r}_p$). Hence, the intensity of the probe can be calculated by taking the modulus squared of $\psi_p(\underline{r}, \underline{r}_p)$. The expression of the probe wavefunction also assumes that the image of the electron source, after demagnification by the condenser system, has a negligible size [2].

The next step of the process centres on the interaction of the probe wavefunction with the specimen. The common multislice approximation is used to simulate the effect of this interaction. A representation of this approach is shown in Figure 4.1. In this method, the specimen crystal is firstly divided into many thin slices along the direction of the beam. Each slice has a thickness of the order of 1 atomic layer (Δz). The crystal potential of each slice is then projected into a single plane to form a weak phase object (WPO). When the electron wavefunction is transmitted through a WPO it experiences only a small phase shift. It should also be noted that there is no absorption of electrons in Kirkland's software but electron intensity can be lost at the edges of the simulated specimen if it is not large enough.

Every plane is separated from its neighbours by a small vacuum layer of thickness Δz. The wavefunction propagates through these vacuum layers to reach the next projected potential plane. Due to the small distances and angles involved, the propagation of the wavefunction is achieved by using Fresnel (near field) diffraction. Finally, to simulate the effect of the whole specimen, the wavefunction is recursively transmitted and propagated through every slice that constitutes the specimen.

The multislice process generates a transmitted electron wavefunction $\psi_t(\underline{r}, \underline{r}_p)$ at the exit face of the specimen. The amplitude component of this type of wavefunction is given in Figure 4.2(b). The next step of the simulation procedure then depends upon the nature of the calculation. For a HAADF STEM calculation, the wavefunction is firstly Fourier transformed onto the diffraction plane (see Figure 4.1) to give a variable that is a function of reciprocal space. The wavefunction is denoted by $\Psi_t(\underline{k}, \underline{r}_p)$. The intensity of this wavefunction is then calculated over the diffraction plane to give a CBED pattern. The HAADF signal (for one probe position only) is found by integrating the CBED intensity over the detector angles. The simulations in this chapter were performed with a HAADF detector with an inner angle of 70mrad and an outer angle of 210mrad, identical to SuperSTEM 1. An example of a simulated CBED pattern, along with the detector dimensions, is shown Figure 4.2(d).

Instead of performing a typical HAADF STEM calculation, the exit surface wavefunction can be used in another way. The intensity of the wavefunction can be calculated to produce a real space intensity map of the electron intensity at some depth within the crystal. An example of this type of map is given in Figure 4.2(c).

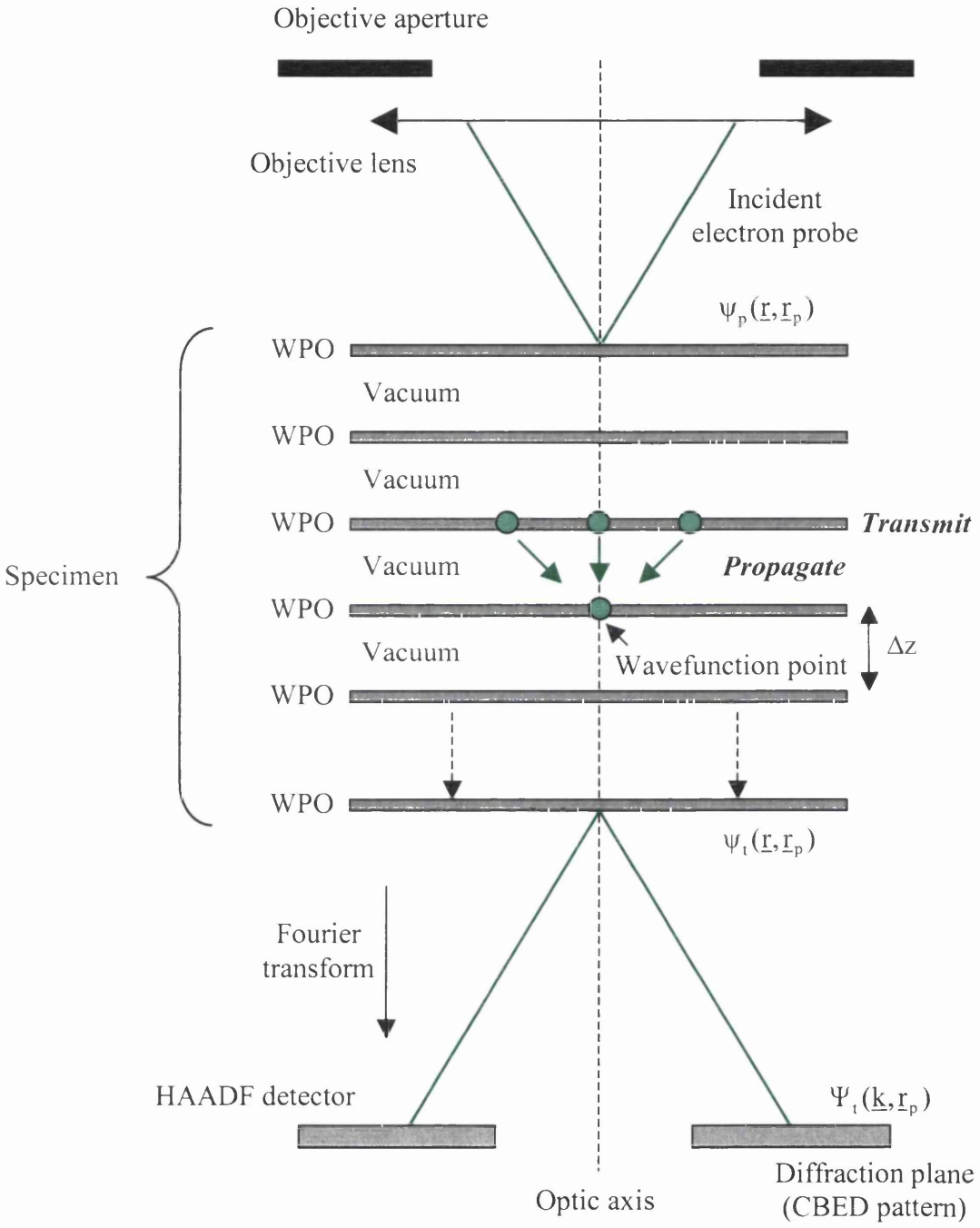

Figure 4.1: Simple schematic of the HAADF STEM simulation process in E. J. Kirkland's computer software. The electron wavefunction at important places are noted. The specimen is modeled using the multislice approach.

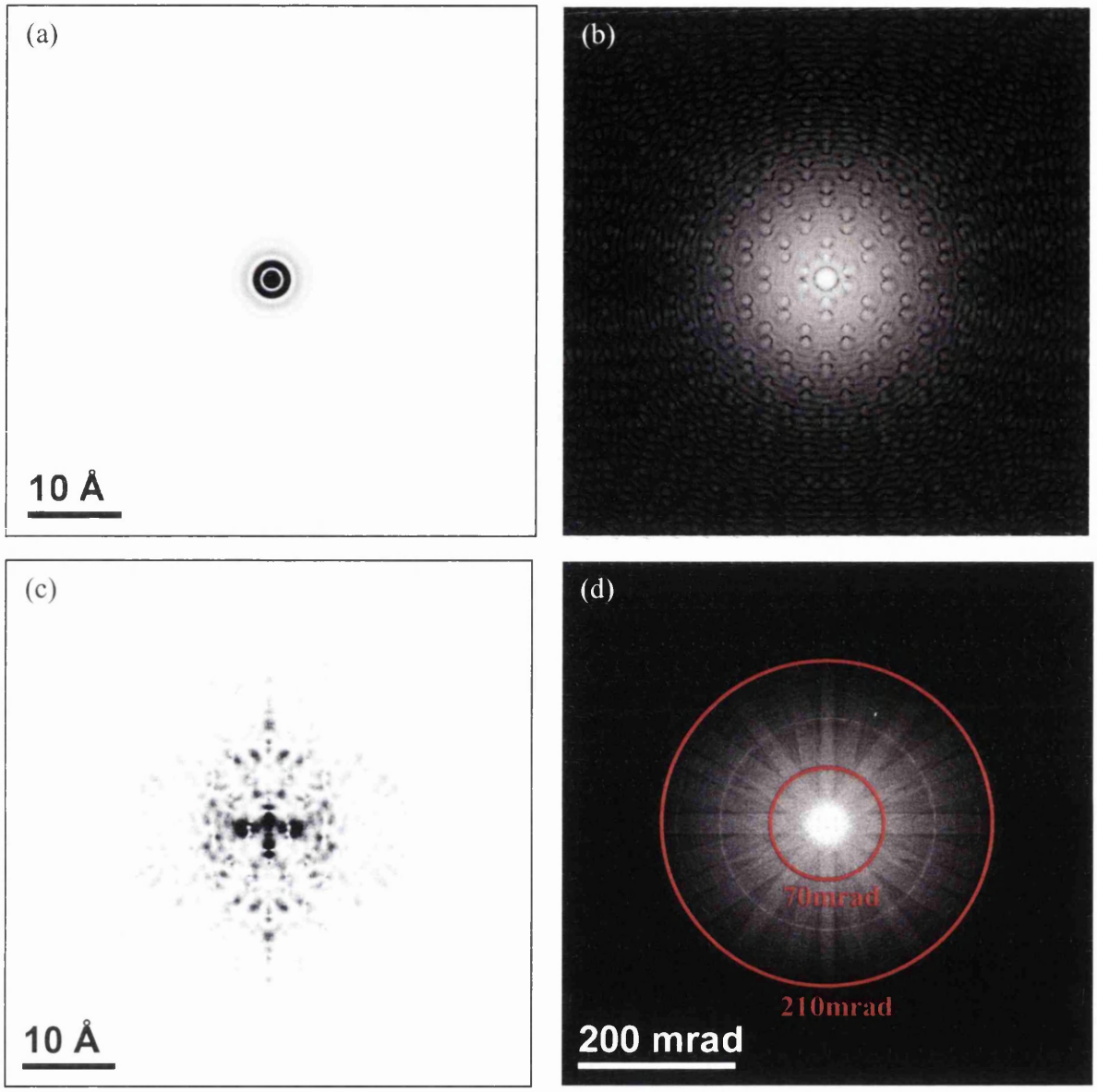

Figure 4.2(a): Simulated 1Å, 24mrad probe intensity map in real space. Black pixels have the highest intensity and the contrast has been enhanced. **(b)** shows the amplitude component of a simulated complex electron wavefunction at the exit face of the specimen. White pixels have the highest amplitude. **(c)** is a real space intensity map of the electron wavefunction shown in (b). Black pixels have the highest intensity and the contrast has been enhanced. **(d)** is a simulated CBED pattern produced in the HAADF detector plane. White pixels have the highest intensity. The rings indicate the inner (70mrad) and outer angles (210mrad) of the HAADF detector used in SuperSTEM 1.

4.2.3 Frozen Phonon Method

The discussion of the multislice approach, in Section 4.2.2, treated the specimen atoms as completely stationary. However, in a real specimen, the atoms vibrate very slightly. Furthermore, the vibrational quantized energy units are called phonons. Hence, to get a closer approximation to reality, phonon scattering must be included. One way of achieving this entails the use of the frozen phonon method. This method relies upon the fact that the time taken for 1 imaging electron to traverse the specimen ($<1\times10^{-15}$sec at 100nm thickness and electron velocity = 1.64×10^{8}m/s) is much less than the period of atomic vibration (the vibration period is $\sim1.4\times10^{-13}$sec for GaAs) [3]. Importantly, this has the effect that, whilst the imaging electron is inside the specimen, the atomic positions do not change their positions significantly. Thus, the electrons interact with an atomic configuration that is stationary but also slightly offset from equilibrium. Furthermore, the electron current is usually small enough in order to ensure that the time between 2 successive imaging electrons is long compared to period of atomic oscillation. Therefore, each imaging electron 'sees' a different atomic configuration whilst inside the specimen.

Since the final image is made up from the average of many different imaging electrons, the frozen phonon method works by taking the average of many different atomic configurations. The averaging process must be performed in the image or diffraction plane and not in the specimen plane. This is in order that the phase of the electron wavefunction is preserved until the detection plane. The actual number of configurations that are necessary has not been established. 8 configurations have previously been averaged to simulate the HAADF signal for Si using Kirkland's software [4]. Furthermore, Kirkland has demonstrated [2] that the number of configurations that are required to form a smooth CBED pattern of Si is somewhere between 4 and 16. Due to the large number of calculations that were required, the time required to implement 16 configurations for every simulation that is shown in this chapter was considered prohibitive. Hence, for every simulation condition presented in this chapter, 8 independent configurations were averaged. In order to check the validity of using this number of configurations, a number of comparisons were made with calculations that used 16 configurations. It was found that 8 configurations overestimated the HAADF signal by about 5% compared to using 16 configurations.

Every atom in a single atomic configuration is given a slight displacement from the normal lattice position (the normal lattice configuration generates a fully elastic calculation). The

random atomic offsets are generated through a random number generator with a Gaussian distribution and a standard deviation equal to the square root of $\langle u^2 \rangle$ in each of the 3 directions. $\langle u^2 \rangle$ is the mean square of the atomic displacement and the Debye-Waller factor is equal to $8\pi^2 \langle u^2 \rangle$ [5]. This method of introducing thermal diffuse scattering is equivalent to the Einstein model of the density of states for phonons [2].

One drawback of the frozen phonon method is the lack of distinction between phonon and elastically scattered electrons. This means that an independent analysis of phonon and elastic electrons cannot be carried out. However, the simulations presented in this chapter are not concerned with distinguishing the different scattering mechanisms.

4.2.4 Simulation Outline

As was stated previously, the 3 materials that were considered were GaAs, AlAs and InAs. These were selected due to their frequent inclusion in III-V semiconductor heterostructures. Moreover, experimental work was also carried out on other semiconductor structures that contained all these materials. The results from these are presented in Chapters 6 and 7. Simulations on these particular materials therefore allowed a useful comparison to be made between theoretical and actual results.

The materials were all simulated in the [110] crystal orientation. Due to the fact that the materials all have the fcc zinc-blende structure, they all exhibit the dumbbell configuration along that particular orientation. This is the orientation of the all the structures that were studied experimentally. For the 3 materials (GaAs, AlAs and InAs) this means that 1 dumbbell column is composed of 100% As atoms and the other column made from 100% of the other type of atoms. Furthermore, Figure 4.3(a) shows a representation of 1 unit cell of an fcc crystal that is viewed along the [001] direction. It can be seen that a perfect crystal of this sort can always be split into 2 repeating slices A and B along the [110] direction. The atomic configurations of these slices are used as inputs to the multislice calculation.

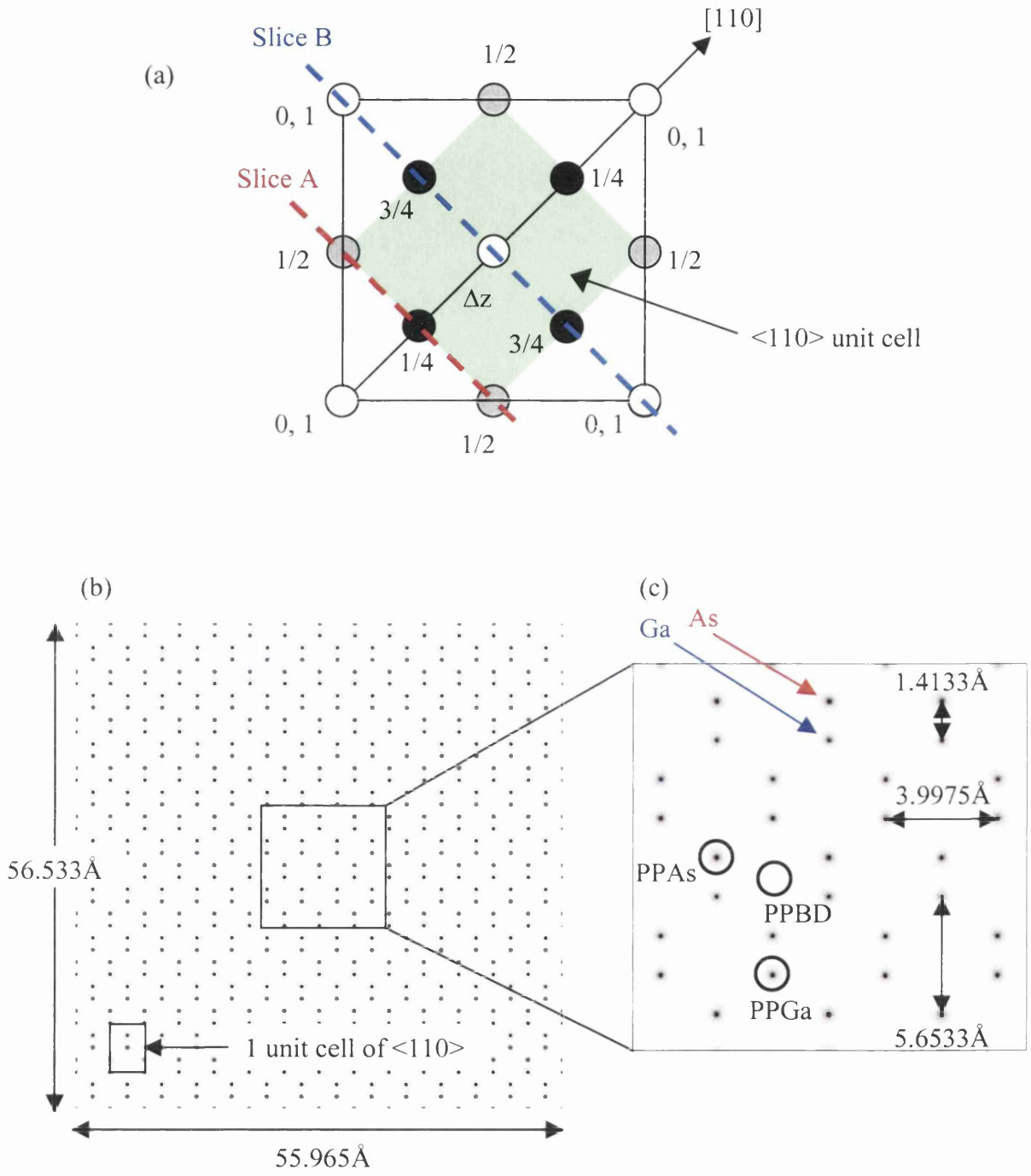

Figure 4.3(a): A schematic diagram of the crystal structure of 1 unit cell of a fcc crystal viewed along the [001] crystal direction. The numbers refer to the fractional vertical height of the atoms in the unit cell. The green area indicates the <110> unit cell which is split into 2 slices A and B for the computer simulations. **(b)** is a pictorial representation of the simulated area of GaAs. **(c)** shows the 3 probe positions considered in the simulations.

The materials all have different lattice constants and, therefore, different dumbbell spacings and Δz values (Δz is the distance between the slices used in the multislice approach as was described in Section 4.2.2). The relevant crystal spacings are displayed in Table 4.2. Table 4.2 also shows the Z_{RMS} values of the different materials. This is the root mean square of the Z numbers of the 2 columns in each material. Z_{RMS}^2 is therefore proportional to the average Rutherford scattering ($\sim Z^2$) from each material. The root mean square of the atomic displacements (found from the corresponding Debye-Waller factor at 300K) is also shown for each atom type in the 3 materials [6]. These values are used to provide the atomic displacements from the equilibrium position that are required in the frozen phonon method. The values were taken from [6] except for those that are associated with AlAs as the Debye-Waller factor is not recorded for this material. Hence, the value of Si at 300K was used for Al atoms since Si has a very similar Z number (Z = 14) to that of Al. The value that was used for As atoms in AlAs was similar to that of As atoms in GaAs.

		AlAs	GaAs	InAs
Z number	Column 1	13	31	49
	Column 2	33	33	33
	Z_{RMS}	35.5	45.3	59.1
Dimensions	Lattice constant (nm)	0.56600	0.56533	0.60583
	Δz (nm)	0.20011	0.19987	0.21419
	Dumbbell Spacing (nm)	0.14150	0.14133	0.15146
Debye-Waller Factor: root mean square displacement (nm)	Column 1	0.00780	0.009056	0.011037
	Column 2	0.00900	0.009392	0.009084

Table 4.2: A table of the important characteristics of the 3 simulated materials. Column 1 and column 2 refer to the constituent columns of a single dumbbell. Z_{RMS} refers to the root mean square of the Z numbers of column 1 and 2.

To examine the dispersion of the probe inside the various materials, frozen phonon simulations of the scattered electron intensity, in real space, as a function of crystal thickness were performed. The intensity was mapped in the x-y plane for crystal thicknesses up to 120nm. Each map is constructed from 14 × 10 unit cells of the <110> fcc orientation. This means that the area of the maps is slightly different for each material. For instance, in the case of GaAs, the area of the intensity map is 5.5965nm × 5.6533nm. This is shown in Figure 4.3(b). For adequate sampling of the wavefunction, each map is constructed from 1024 × 1024 pixels.

3 probe positions were considered at every thickness of crystal that was simulated: PPAs, PPGa (in the case of GaAs) and PPBD. For instance, the probe is incident on an As column for the PPAs condition, incident on an Ga column for the PPGa condition and incident between dumbbells for the PPBD condition. This can be seen in Figure 4.3(c). The same dumbbell was not chosen for conditions PPAs and PPGa because the atoms from the respective columns do not sit at the same height down the crystal. In fact, they are offset by Δz from each other in vertical direction. Hence, in order that conditions PPAs and PPGa were equivalent, the probe was situated on columns with no vertical height offset between them.

The use of the PPAs and PPGa conditions not only allow the degree of probe channelling to be ascertained but also allow the calculation of the HAADF intensity from the respective columns (as was explained in Section 4.2.2). On the other hand, the calculation of the HAADF intensity from the PPBD condition provides a value of the HAADF background image signal (this signal was discussed in Section 3.2.2). Hence, the dumbbell column ratio for HAADF imaging (as a function of thickness) can be determined. This is achieved, in the case of GaAs, by dividing the Ga column HAADF signal by the As column HAADF signal:

$$\text{Dumbbell Column Ratio} = \frac{\text{Ga column HAADF signal}}{\text{As column HAADF signal}} = \frac{I_{PPGa} - I_{PPBD}}{I_{PPAs} - I_{PPBD}}$$

This presents the opportunity to compare experimentally derived column ratios with a much better theoretical estimate than was used in Chapter 3. This analysis is presented in Chapter 5. It should be noted, however, that this measure of the column ratio is calculated from Ga and As signals that are generated from columns from 2 different dumbbells instead of from the same one. This results in a small error since there is a relative height

difference between the same types of atoms in neighbouring dumbbells. For instance, if there is an As atom on the top surface in 1 dumbbell then the As atom in the neighbouring dumbbell (along the [1-10] direction) will be at a depth of 2Å. The reason that the HAADF signal was not calculated from the columns within the same dumbbell was because the relative height difference would have resulted in a different probe starting condition on the Ga column compared to the As column. Hence, the electron intensity distribution down the different columns could not have been compared properly as the starting conditions would not have been equivalent. However, the simulated value of the dumbbell column ratio that was calculated from the columns of a single dumbbell (for GaAs) reveals that the relative height difference only results in about a 5% error in the column ratio for really thin specimens (~2nm thick). The error drops to about 1% for thicker specimens (>40nm).

4.3 24mrad Probe Results

4.3.1 24mrad Probe Characteristics

The parameters that are associated with the 24mrad probe were chosen in order to create a probe similar in size to that of SuperSTEM 1. These include an accelerating voltage of 100kV, a probe convergence semi-angle of 24mrad and a C_3 aberration coefficient value of 0.1mm. These values were given in Table 4.1. However, in order to choose the appropriate defocus value for the probe, certain measures of its size and intensity distribution were calculated as a function of defocus. The amount of defocus is defined as the deviation of the defocused image plane from the ideal Gaussian image plane [2]. Figure 4.4(a) shows how the FWHM width and the diameter of the central maximum of the probe intensity vary as a function of defocus. It is clear that the diameter of the central maximum steadily drops as the defocus value is increased. On the other hand, the value of the FWHM does not drop in the same linear fashion. Figure 4.4(a) also reveals that defocus values of 15nm and 23.56nm both give a 1Å-scale probe at FWHM as desired. However, the diameter of the central maximum is clearly smaller in the case of the 23.56nm defocus probe. This would, therefore, seem to be the best choice of defocus value for the 24mrad probe. In fact, this value is at the Scherzer defocus value as defined by Kirkland (equal to $(1.5C_s\lambda)^{1/2}$) [2]. This provides the optimum defocus value as it is a compromise between the FWHM width and the probe tails beyond the central maximum.

Figure 4.4(b) gives the variation of 2 more measures of the quality of the probe as a function of defocus. The diameter of the probe that contains 90% of the total probe intensity is shown to steadily decrease as the defocus value is increased. Hence, the Scherzer defocus value again provides the better choice of the defocus value compared to a defocus value of 15nm. On the other hand, the percentage of the total probe intensity that is contained within the central maximum reaches its greatest value, of about 40%, at a defocus value of 15nm before dropping off markedly. Consequently, on this measure, the 15nm defocus value provides the best probe. Nevertheless, the Scherzer defocus value was used for all of the 24mrad probe simulations as this defocus value clearly gives the best probe shape in 2 out of the 3 measures. In addition, the input parameters and probe characteristics are catalogued in Table 4.1.

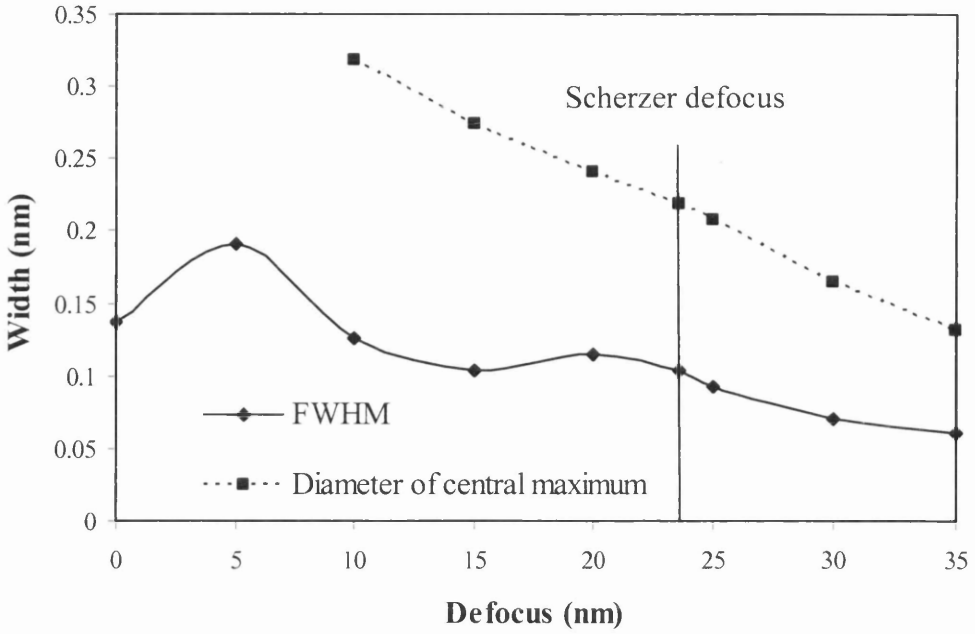

Figure 4.4(a): A graph of 2 measures of the probe width as a function of defocus. The measures of the probe size are the FWHM and the diameter of the central maximum. The constant probe parameters are V = 100kV, convergence angle = 24mrad and C_3 = 0.1mm.

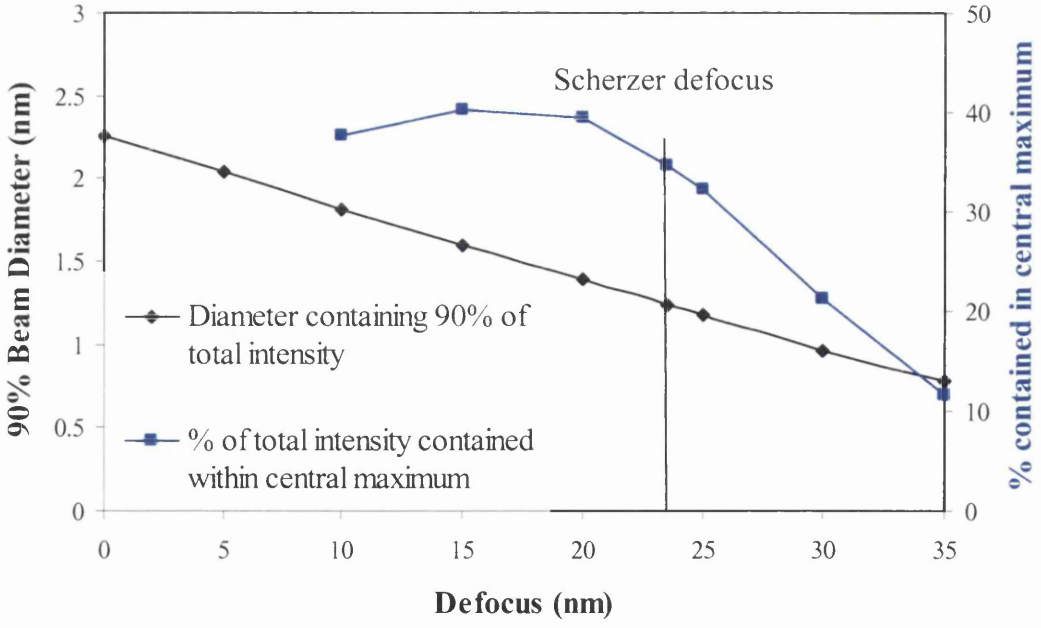

Figure 4.4(b): A graph of 2 measures of the probe size as a function of defocus. The measures of the probe size are the diameter that contains 90% of the total probe intensity and the % of the total intensity that is contained within the central maximum. The constant probe parameters are V = 100kV, convergence angle = 24mrad and C_3 = 0.1mm.

Figure 4.5 shows a line profile taken across the intensity of the 24mrad probe. It is evident that the central maximum of the simulated probe intensity is 1Å in size at FWHM, similar to that of SuperSTEM 1. In addition, the secondary maximum ring reaches 13% of the value of the central maximum. This probe shape is kept constant for all of the following simulations that use the 24mrad probe.

It should also be noted that the intensity of the probe several nanometres distant from the probe centre is very small but not equal to zero. Although this very small background is insignificant compared to the intensity of, for example, the central maximum, it does become important in the measurement of the total probe intensity. This is due to the fact that most of the pixels in the probe map (5.5965nm × 5.6533nm for GaAs) consist solely of this small background. Hence, the small background will form a portion of the total probe intensity. This is the partly the reason for the fact that it requires a diameter of 1.2nm to contain 90%. In fact, this diameter is further increased (~5nm) in the case of the smaller FWHM 50mrad probe (see Table 4.1).

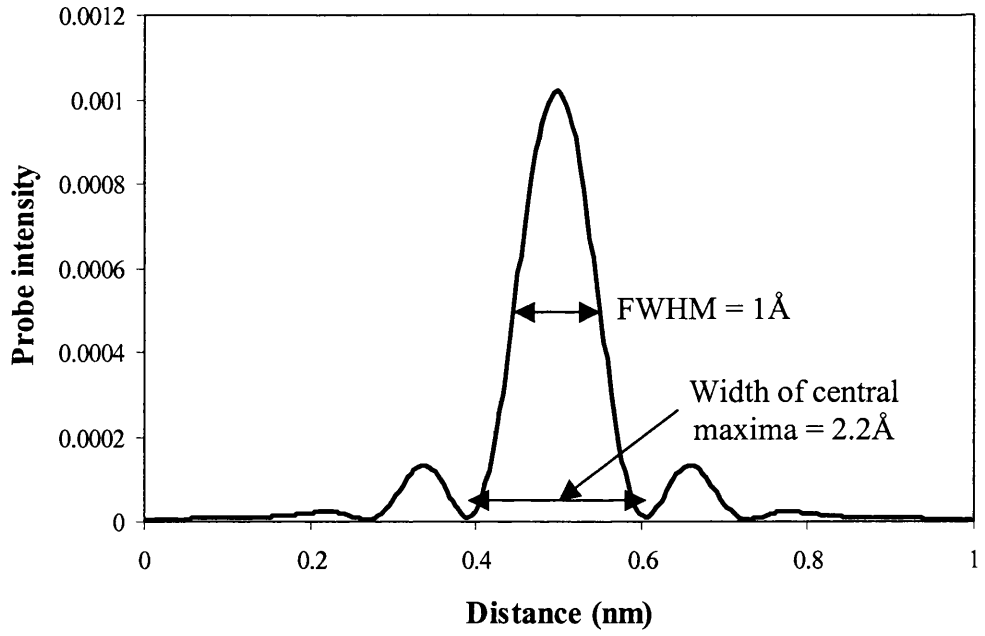

Figure 4.5: Line profile taken across the simulated 24mrad probe intensity map. Hence, Scherzer defocus was used. The FWHM is 1Å at 100kV accelerating voltage. The total electron intensity of the probe = 1.

The small intensity background was removed from the probe intensity maps of the 12mrad, 24mrad and 50mrad probes. The various measures of the probe size were then re-calculated. The results are shown in Table 4.3. It is apparent that the values shown in Table 4.3 are closer to what would be expected for these probes. For instance, the beam diameter

that contains 90% of total probe intensity is significantly reduced in all 3 probes with the removal of the small background. This is especially so for the 50mrad probe i.e. 90% of the total probe intensity is now contained within a diameter of 0.67nm, which is a lot smaller than the value of about 5nm before the background removal. The probe density in the central maximum (given as the fraction of the total intensity contained within the central maximum divided by its area) is also significantly altered by the background removal. For instance, the density of the 50mrad probe is now about double that of the 24mrad probe and the density of the 24mrad probe is now about double that of the 12mrad probe. This seems closer to reality since an increase in probe convergence angle (of a source with a negligible size) results in the intensity being focused into a smaller central maximum.

In addition, Table 4.3 shows that the spatial diameter of the central maximum in each probe does not change. Hence, it is evident that the small background does have a significant effect on the probe measures that involve the measurement of intensity rather than spatial diameters. Unfortunately, the small intensity background could not be subtracted from the results that are shown in the later sections. Consequently, the probes were not optimised for the calculation of, for example, the degree beam spreading as a function of specimen thickness and more care had to be taken to interpret the results correctly.

	12mrad	24mrad	50mrad
FWHM (nm)	0.159	0.104	0.071
Diameter of central maximum (nm)	0.361	0.219	0.153
Probe density of central maximum (fraction of total intensity / nm^2)	6.72	12.18	24.04
Beam Diameter that contains 90% of total probe intensity (nm)	0.56	0.62	0.67
% of total beam current contained in central maximum	68.9	46.0	44.4

Table 4.3: A table of the various measures of probe size of the 3 simulated probes (12mrad, 24mrad and 50mrad) after the removal of the small background intensity.

4.3.2 GaAs Results

4.3.2.1 Real Space Crystal Intensity Maps

The real space intensity maps at 6 depths within a crystal of GaAs [110] are presented in Figure 4.6. These maps have dimensions in the x-y plane and are, therefore, perpendicular to the direction of the incident probe (along the z direction). In Figure 4.6, the probe was situated on an As column on the top surface of the crystal. The intensity maps have been normalised with respect to the total intensity of the incident probe. Thus, a pixel with an intensity of 1 would mean that all of the intensity of the probe is contained within that pixel. In addition, on each map, 'max' refers to the highest intensity value that any pixel possesses. Furthermore, the contrast of each map has also been enhanced in order to improve detail. However, each map also has a companion inset that shows a magnified, 10Å × 10Å view of the map. These insets are centred on the initial probe position and have a contrast setting that range from 0 to the max value that is associated with each individual map. Finally, each map also displays a circle that has a radius equal to the convergence semi-angle (α) multiplied by the specimen thickness (t). Hence, each circle corresponds to the expected size of the beam (at a specific thickness) due to purely geometrical spreading.

The intensity map in Figure 4.6(a) is for a very small crystal depth of 2nm. Each column is composed of only 5 atoms and, therefore, the potential only interacts with the electrons over a short distance. For that reason, the intensity distribution is similar to that of the incident probe itself (compare with Figure 4.2(a)). For example, Figure 4.6(a) reveals the existence of a central maximum of about 1Å at FWHM. Nevertheless, a secondary maximum has, to some extent, formed on the neighbouring Ga column at a thickness of 2nm. The inset at 2nm thickness also shows the presence of an intense peak on the As column.

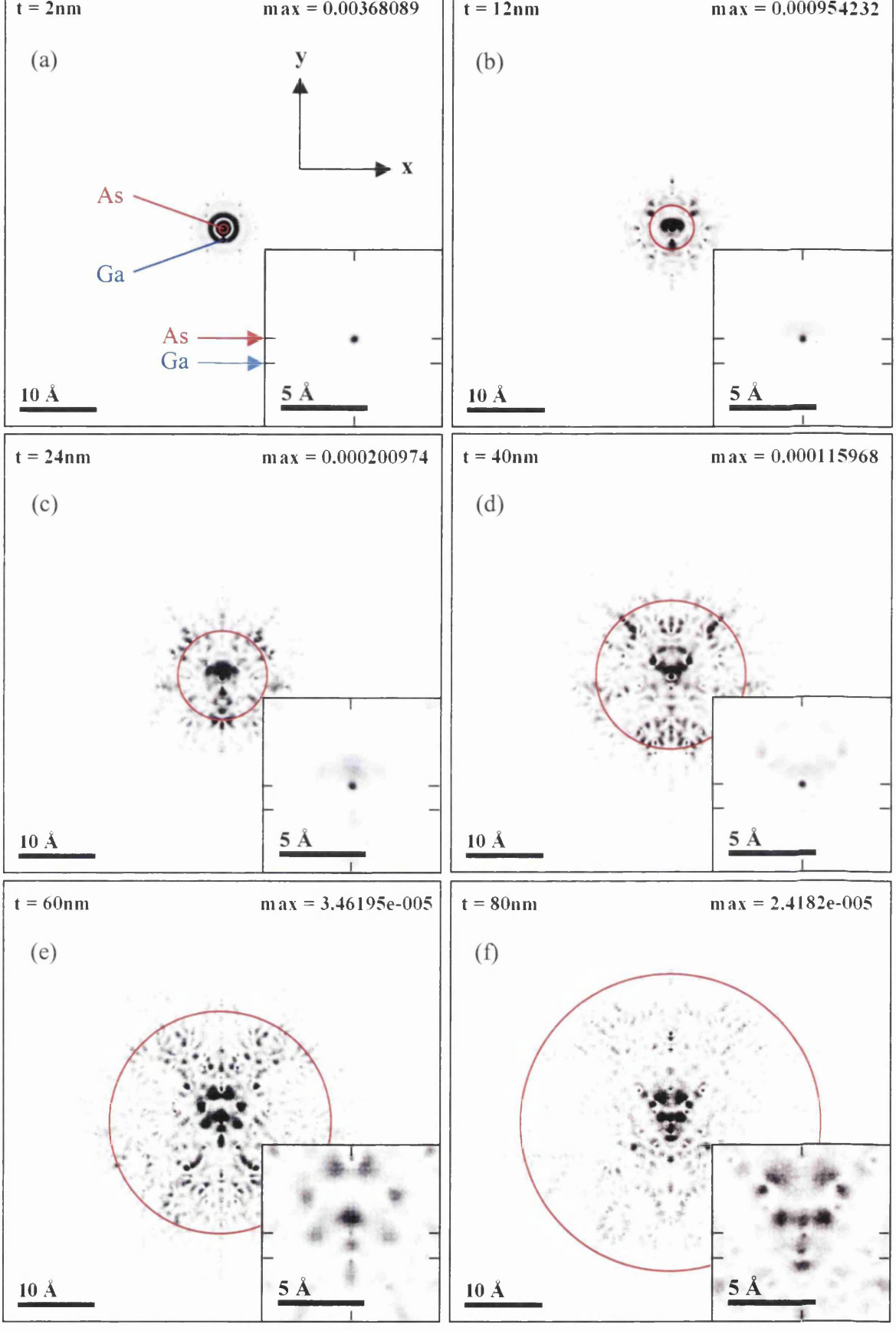

Figure 4.6: Contrast enhanced simulated electron intensity maps at various depths in a crystal of GaAs [110]. The insets show a magnified view of the central region of each map taken over the full intensity range. A 24mrad, 0.1nm probe is incident on an As column. Black pixels are the most intense. The crystal depths are: **(a)** 2nm **(b)** 12nm **(c)** 24nm **(d)** 40nm **(e)** 60nm and **(f)** 80nm. Max refers to the maximum intensity contained within a single pixel. Circle radius = αt. The total electron intensity of the probe = 1.

At a crystal depth of 12nm, where the columns contain 30 atoms (Figure 4.6(b)), the characteristic Airy disc shape of the probe is missing. However, there still is an intense central maximum centred on the As column. Nevertheless, this intensity appears to have begun to spread away from the primary column to some extent. The neighbouring Ga column has also captured some intensity at a depth of 12nm but it too seems to be scattering the intensity away somewhat. Furthermore, in the middle of the dumbbell, the intensity drops virtually to zero. This would suggest that the high Z columns capture electron intensity quite effectively but also scatter it away from the primary dumbbell after the electrons pass through just a small amount of material. The surrounding dumbbells have also picked up a small amount of intensity at this depth of crystal. In addition, the region of the map that contains intensity greater than the small background level (~zero) is slightly larger in extent than expected from the geometrical beam spread at this thickness.

In Figure 4.6(c), at a depth of 24nm (60 atoms), the situation is a lot more complex with significant intensity located between dumbbells. Even so, a strong central peak on the As column is still apparent except that it is now wider in extent. The neighbouring Ga column, in conjunction with the appearance of strong areas of intensity nearby, has retained some intensity by this thickness. At a depth of 40nm (100 atoms), it is clear that the area over which electron intensity exists has expanded radially away from the probe position (Figure 4.6(d)). Much of the intensity inside this area exists between the dumbbells.

The final 2 crystal depths in Figure 4.6, at 60nm and 80nm respectively, are characterised by a further increase in the overall area of intensity. Indeed, the sequence of maps from 2nm up to a thickness of 80nm exhibits an expansion in the area covered by the intensity. This spreading of the beam is measured later in this section using the PPBD condition. The insets of Figure 4.6(e) and Figure 4.6(f) also reveal that the highest intensity is no longer positioned on the primary As column at these depths of crystal. In fact, the distribution of the most intense areas is quite complicated in both cases with intensity located on and off columns. Consequently, in order to gain a greater understanding of the scattering process, the value of the intensity at important map positions are displayed in graphical format (as a function of specimen thickness). This is shown later in Section 4.3.2.2 after the intensity maps from the PPGa and PPBD conditions are presented.

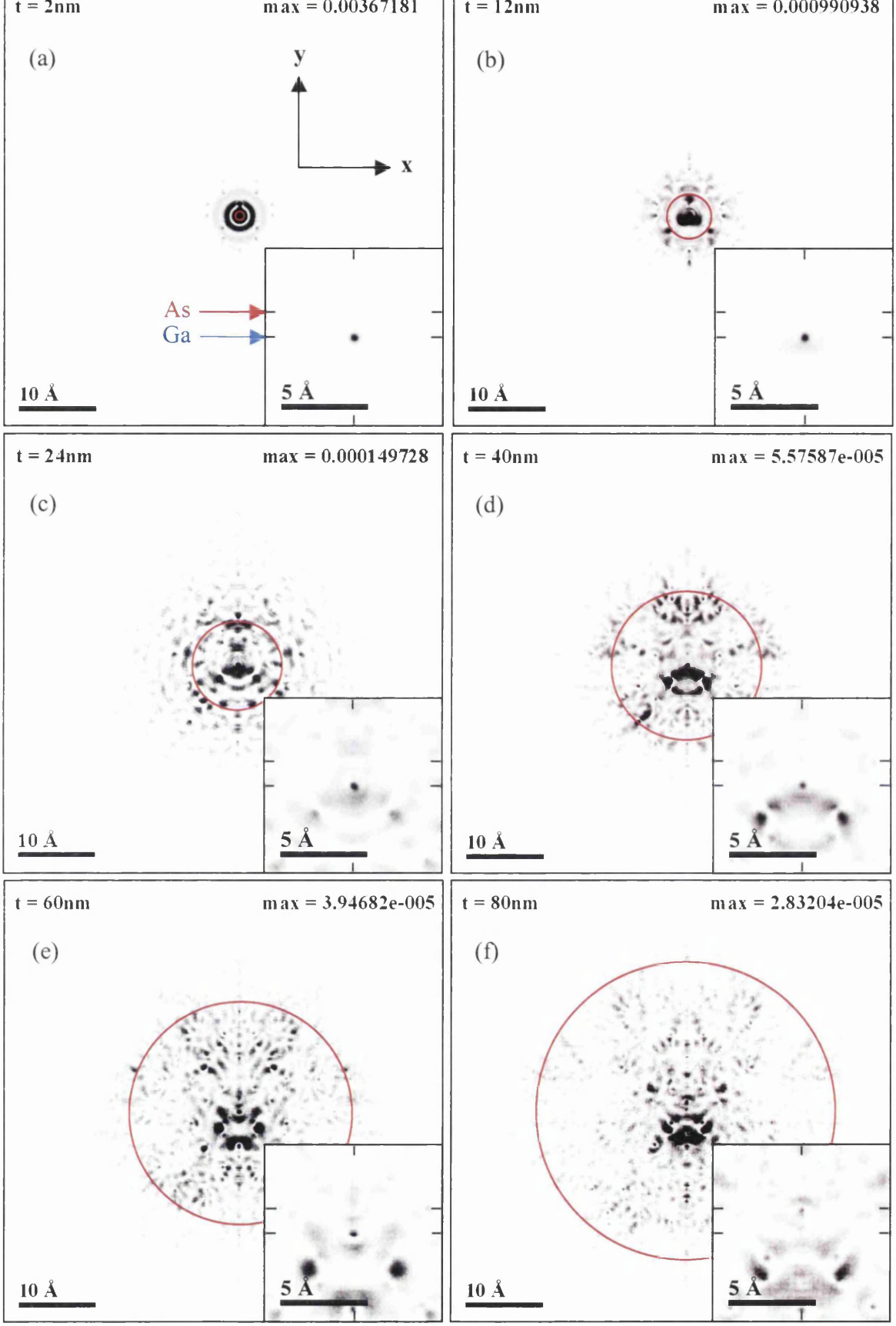

Figure 4.7: Contrast enhanced simulated electron intensity maps at various depths in a crystal of GaAs [110]. The insets show a magnified view of the central region of each map taken over the full intensity range. A 24mrad, 0.1nm probe is incident on a Ga column. Black pixels are the most intense. The crystal depths are: **(a)** 2nm **(b)** 12nm **(c)** 24nm **(d)** 40nm **(e)** 60nm and **(f)** 80nm. Max refers to the maximum intensity contained within a single pixel. Circle radius = αt. The total electron intensity of the probe = 1.

Figure 4.7 shows the real space intensity maps at 6 depths within GaAs with the probe now situated a Ga column (PPGa condition). These maps are very similar to the ones associated with the PPAs condition. For example, the probe distribution is still visible at very low crystal depths before the build up of a central maximum on the primary column. Moreover, the central maximum also decays as the depth increases. This produces significant intensity between dumbbells that are several nanometres distant from the starting probe position. The fact that the PPAs and PPGa conditions should generate very similar intensity maps is not entirely surprising since their Z numbers are also very similar ($Z_{As} = 33$ and $Z_{Ga} = 31$). However, at depths greater than 60nm, the maps for the PPGa condition do become more distinct from those associated with the PPAs condition.

On the other hand, the intensity maps for the PPBD condition (Figure 4.8) are quite unlike the ones for PPAs and PPGa conditions. However, at a crystal depth of 2nm, Figure 4.8(a) shows that the intensity of the probe is still visible. This was the case with the other 2 probe positions as well. At a depth of 4nm (Figure 4.8(b)), the central maximum is clearly visible in free space but it has increased in size to 1.5Å at FWHM. The intensity that is located on the surrounding dumbbells originates from the secondary maximum ring of the probe.

The intensity distribution takes on an interesting character at a thickness of 24nm, as is shown in Figure 4.8(c). The central maximum of the probe has increased in size again but has obviously lost its circular shape. The potentials of the surrounding 4 dumbbells have attracted the electrons towards their positions. This has created a star like distribution with intensity leaking onto the columns of the 6 nearest atomic columns.

The intensity map, at a depth of 40nm, is noticeably different in appearance from previous maps (Figure 4.8(d)). The point at which the probe was incident on the material no longer has any intensity and the central maximum is totally absent. All of the prior intensity that formed the central maximum now lies mostly in the positions between the neighbouring dumbbells and not on the dumbbells themselves. Nevertheless, after another 20nm of crystal (see Figure 4.8(e)), the central intensity maximum has re-established itself. There may be a beating effect that occurs in which the intensity spreads away from the initial probe position only to be re-scattered back by the surrounding dumbbells. Significant intensity can also be found on dumbbells that are not nearest neighbours.

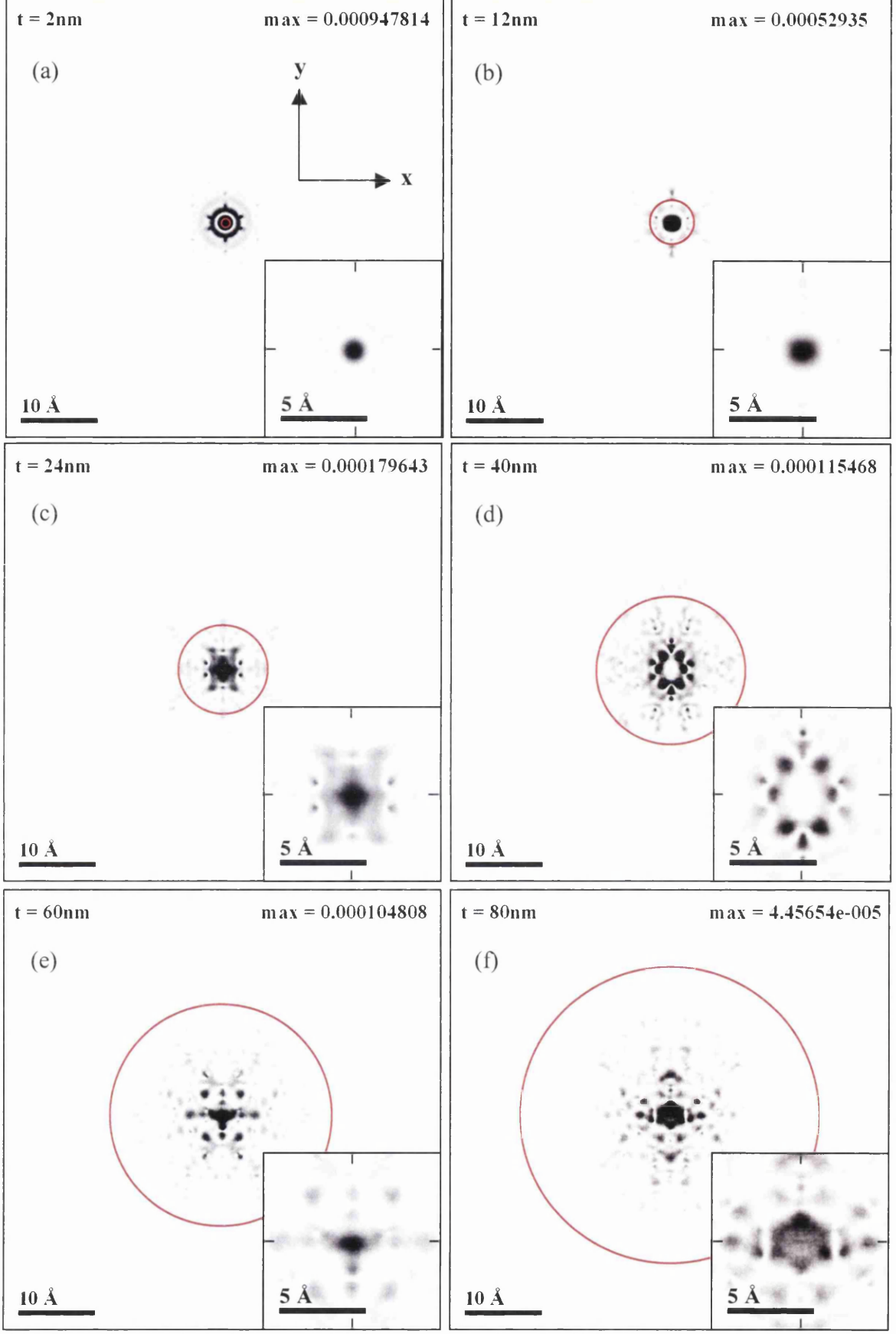

Figure 4.8: Contrast enhanced simulated electron intensity maps at various depths in a crystal of GaAs [110]. The insets show a magnified view of the central region of each map taken over the full intensity range. A 24mrad, 0.1nm probe is incident between dumbbells. Black pixels are the most intense. The crystal depths are: **(a)** 2nm **(b)** 12nm **(c)** 24nm **(d)** 40nm **(e)** 60nm and **(f)** 80nm. Max refers to the maximum intensity contained within a single pixel. Circle radius = αt. The total electron intensity of the probe = 1.

Figure 4.8(e) shows the situation after 80nm. The overall area in which electron intensity can be found is smaller than in the previous 2 cases (PPAs and PPGa). This would, therefore, suggest that the potential of the 4 surrounding dumbbells (in the PPBD case) effectively confines the electrons to the space between them even for large crystal thicknesses. This thereby limits the level of intensity that is scattered far from the initial probe position inside a crystal of GaAs. It is also apparent that the overall area of the intensity in the PPBD case is smaller than expected than geometrical spreading after a depth of 80nm (Figure 4.8(f)).

4.3.2.2 Channelling, EELS and the HAADF STEM Signal

Figure 4.9 reveals the value of the intensity, that exists on the primary As column and neighbouring Ga column, as a function of specimen thickness, for the PPAs condition. In addition, the sum of the intensity on the 6 nearest neighbouring dumbbells (6NNs) is also shown. The values were measured directly from the intensity maps like the ones shown in Figure 4.6. The value that is measured at each depth for each column (As, Ga and the columns that comprise the 6NNs), is the sum of the intensity contained within a 0.25Å radius (9pixels × 9pixels) centred on the respective column position. This radius was chosen because that is the distance at which the atomic potential for a single As atom drops to 10% of its maximum value. Hence, any electrons at this distance from the atomic core should still undergo adequate scattering by the potential. The maximum depth that was simulated was 120nm.

It can be seen that the peak intensity on the primary As column occurs at a depth of 4nm in Figure 4.9. This means that the intensity from the probe has been pulled towards the As column due to its strong potential. Thus, the electrons are said to have undergone channelling. Subsequently, the intensity drops off rapidly during the next 4nm of material. A secondary maximum then occurs at a thickness of 12nm and the intensity remains very low after a depth of 20nm. The oscillations in the column intensity are due to the refocusing of scattered intensity back onto the primary As column [7].

After a depth of 20nm, practically no intensity remains on the As column until the intensity finally drops to zero (<0.5% of maximum intensity) at a depth of 60nm. This implies that the channelling condition lasts up to 20-60nm in the top portion of the crystal. However, it is clear that a strong channelling condition (bounded by the point at which the intensity becomes less than 5% of the maximum intensity on a column) only lasts up to the top 20nm of the specimen only. Figure 4.9 also shows the thickness value that corresponds to

the onset of the maximum As column HAADF signal as found from Figure 4.11 (see later). This is the thickness at which the As column HAADF signal no longer increases. It can be seen from Figure 4.9 that this maximum in the HAADF occurs at a depth of 20nm, which is equal to the limit of strong As column channelling.

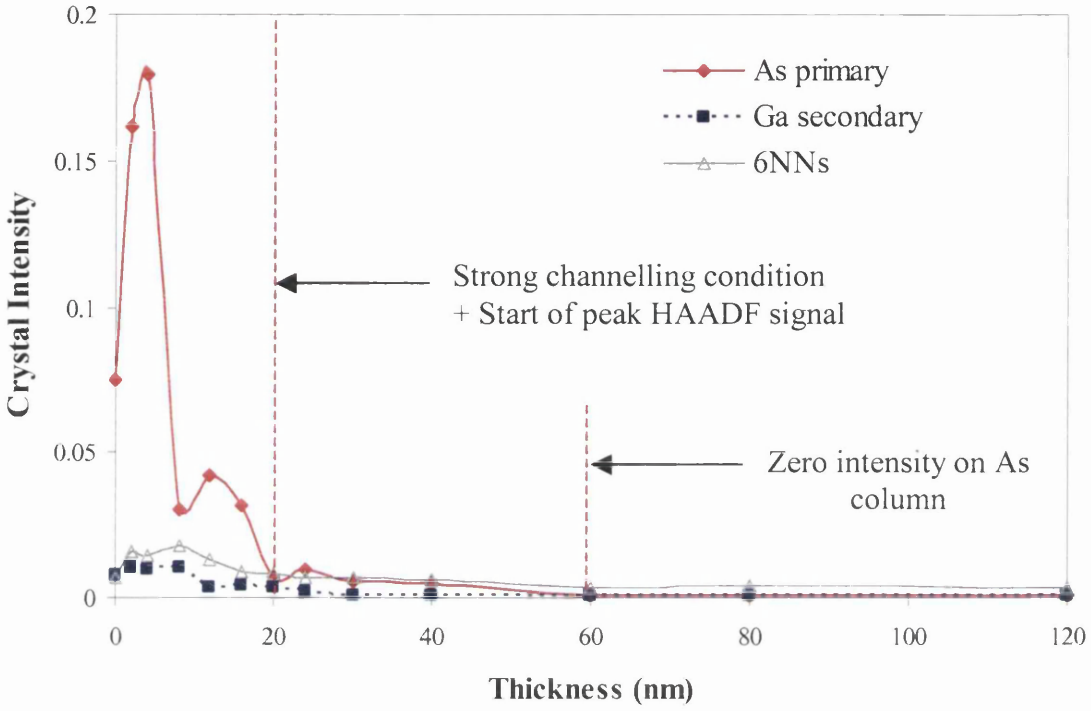

Figure 4.9: A graph of the simulated real space electron intensity along 2 columns in GaAs [110] as a function of specimen thickness. The probe is incident on an As column on the top surface of the specimen. The intensity on the primary As column (red), on the neighbouring Ga column (blue) and the sum of the intensity on the nearest 6 dumbbells (grey) are plotted. The values are the sum of a 9pixel × 9pixel area around each column in the intensity maps. The intensity is normalised with respect to the total intensity in the probe (equal to 1).

In Chapter 3 (Section 3.2.2), the column intensity / total intensity for the As column in the GaAs layers from the deep superlattice was given a value of 0.14. If the thickness of the specimen was 60nm, then a value of 0.14 indicates that the channelling condition lasted for the top 8.4nm of the specimen. This channelling depth is about half of the value found for the limit of the strong channelling condition (20nm) in Figure 4.9. In order that the experimental and simulated channelling depths agree, the thickness of the deep superlattice must be equal to about 140nm, which is a lot thicker than the assumed 60nm.

In addition to the intensity on the primary As column, Figure 4.9 also displays the intensity captured by the neighbouring Ga column. It is clear that this intensity is significantly lower in value than that of the primary column for all crystal thicknesses. It is also evident that the intensity lost by the primary column does not become captured by the neighbouring Ga potential but instead spreads further out. Indeed, Figure 4.9 highlights the fact that the combined intensity on the surrounding 6 dumbbells actually becomes greater than that on the primary and secondary columns. This occurs only after a crystal thickness of 30nm. Furthermore, the intensity on the surrounding columns remains fairly constant at depths greater than 60nm.

The variation of electron intensity on atomic columns has important implications for the interpretation of EELS data. In order to directly relate the measured EELS signal with local atomic structure then it is clear that the EELS signal should derive chiefly from the atoms within the column beneath the probe position. Furthermore, the EELS signal should also be generated with equal strength from each atom within the column. With this in mind, it is evident that simulations of the intensity distribution, as a function of thickness, can be used to estimate which part of the specimen generates the EELS signal [4]. This is because the K-shell atomic ionization is only significant close to atomic nuclei along the columns [4].

The fluctuation in the primary column intensity in Figure 4.9 implies that the As atoms do not influence the EELS signal in equal measure. For example, the atoms in the top 8nm of the specimen contribute far more to the As EELS signal than the atoms at about 20nm which contribute very little. This has important consequences for the ability to detect dopant atoms through the use of EELS. It is apparent that the actual position of the dopants on an atomic column has a significant effect on the generated EELS signal. If a dopant atom were present at a particular column location in which no electron intensity can be found then its presence would go undetected.

Due to the fact that the maps in Figure 4.6 and the graph in Figure 4.9 only provide a snapshot of the intensity at particular depths, the total EELS signal cannot be directly established as a function of thickness. This is because the EELS signal is not only generated at the bottom of the specimen but is in fact dependent upon the crystal intensity distribution at all depths of the specimen. In fact, the EELS signal that is generated from an atomic column is proportional to the total electron intensity that interacts with the column through the entire thickness of the specimen. Hence, in order to estimate the EELS signal that is generated from the primary As column, the area under the As curve shown in Figure 4.9 must be integrated as a function of thickness. This is shown in Figure 4.10(a). It can be

seen that the integrated crystal intensity increases up to about 30-40nm before reaching a constant value at greater depths. Hence, it is only the top 30-40nm of the primary As column that generates the associated As EELS signal. If the specimen is any thicker then no benefit in terms of the signal from the primary As signal is gained.

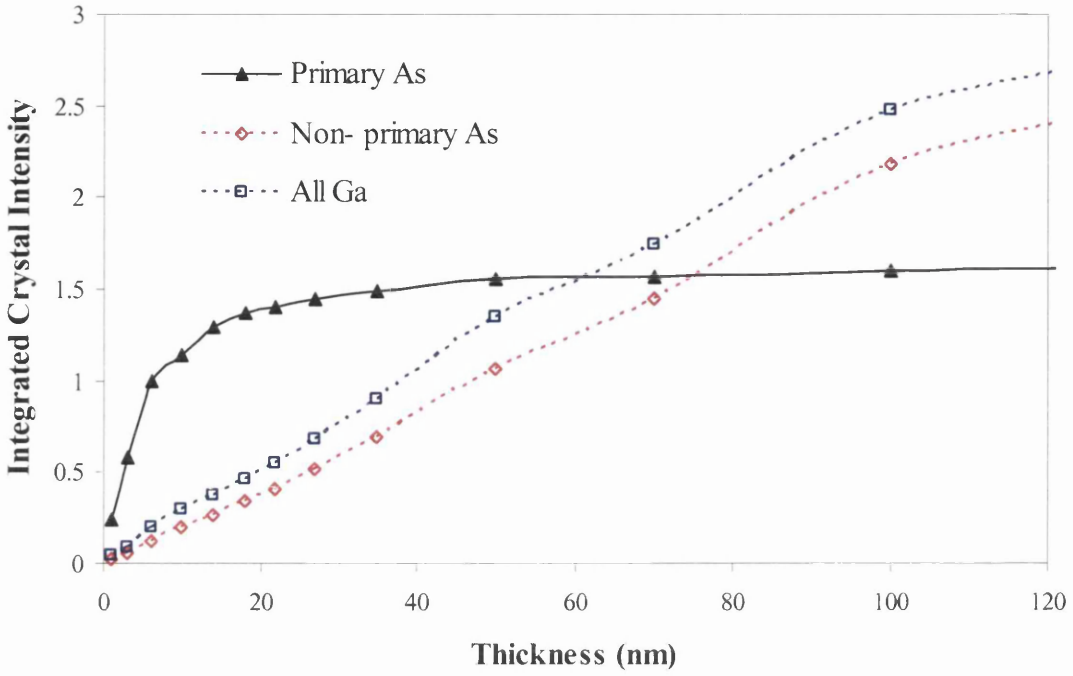

Figure 4.10(a): A graph of the simulated integrated crystal intensity on the primary As column, all non-primary As sites and all Ga sites as a function of thickness.

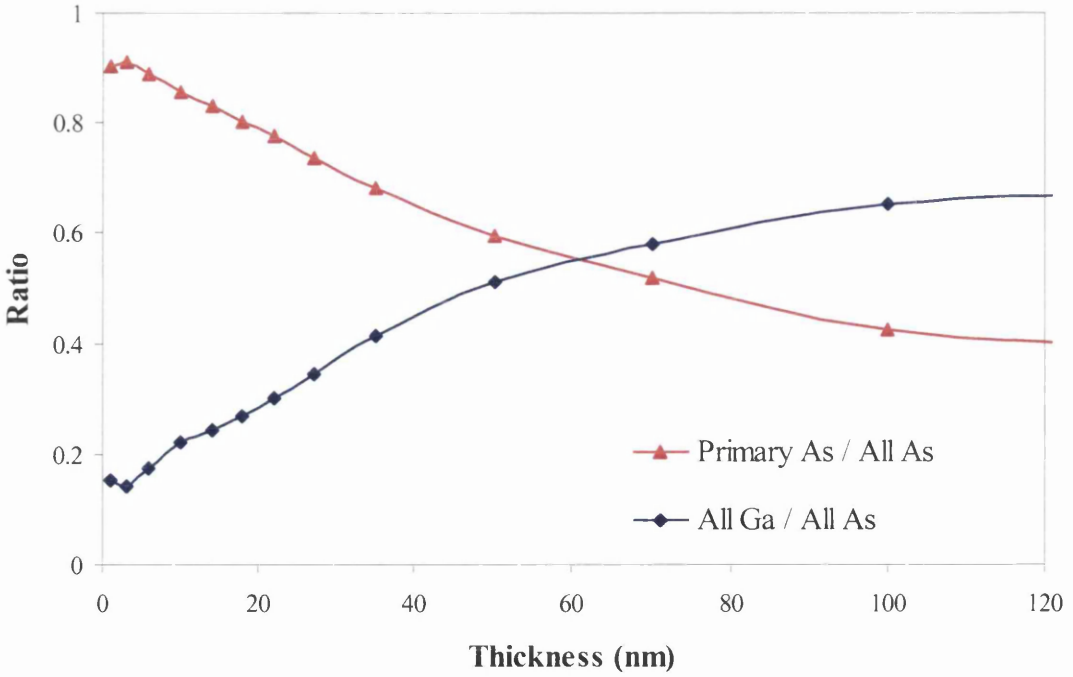

Figure 4.10(b): A graph of the simulated integrated crystal intensity on the primary As column / all As sites as a function of thickness. Also shown is the simulated integrated crystal intensity on all Ga sites / all As sites as a function of thickness.

Although the EELS signal from the primary As column should remain constant after a certain depth of crystal due to de-channelling, it is apparent that the signal from the surrounding dumbbells should increase due to the spread of the beam. For instance, at a depth of 8nm (the first minimum in the As column intensity) in Figure 4.9, the intensity on the 6 nearest dumbbells approaches the value of the intensity present on the primary As column. Hence, the surrounding As columns also provide a contribution to the total As EELS signal.

In order to estimate the influence to the EELS signal by the non-primary columns, the intensity on all of these columns (in the maps) were measured in the same way as was performed for the intensity on the primary As column. The plot of this intensity as a function of thickness was also integrated to give the total electron intensity that interacts with the non-primary As columns. This is plotted in Figure 4.10(a). It is clear that, unlike the primary As signal, the EELS signal from the non-primary As columns steadily increases as the thickness increases. This is likely due to the continuous spread of the intensity away from the centre of the maps. The ratio of the (integrated) intensity on the primary As column / the (integrated) intensity on all As columns is shown in Figure 4.10(b). This indicates that the contribution to the total As EELS signal by the primary As signal will steadily decrease as the thickness goes up.

A Ga EELS signal will also be produced due to the scattering from the neighbouring Ga column as well as from the surrounding dumbbells. The integrated crystal intensity on all Ga columns is shown in Figure 4.10(a). This suggests that the Ga EELS signal will increase in a similar fashion as the signal from the non-primary As columns. Figure 4.10(b) illustrates the variation of the (integrated) crystal intensity on all Ga sites / the (integrated) intensity on all As sites as a function of thickness. It is apparent that this ratio increases as the thickness is increased, which signifies that the ability to differentiate between the As and Ga columns in a dumbbell, though the use EELS, will be reduced at greater depths of the crystal. To clarify, a ratio equal to one signifies that the Ga and As EELS signals were of the same intensity and, therefore, EELS could not be used to distinguish the type of column that the probe was centred upon.

In order to obtain a fuller understanding of the imaging process in SuperSTEM 1, the HAADF STEM intensity was also simulated. The HAADF calculations permit an investigation to be carried out on how the channelling and spreading of the electron intensity (which was witnessed in the intensity maps) affects what is observed in the final image from the microscope. The HAADF simulations were performed as described in

Section 4.2.2. The simulated HAADF signal for the probe incident on an As column in GaAs is presented in Figure 4.11, again as a function of specimen thickness. Also shown is the HAADF background signal. This was calculated with the condition of the probe placed between dumbbells (PPBD).

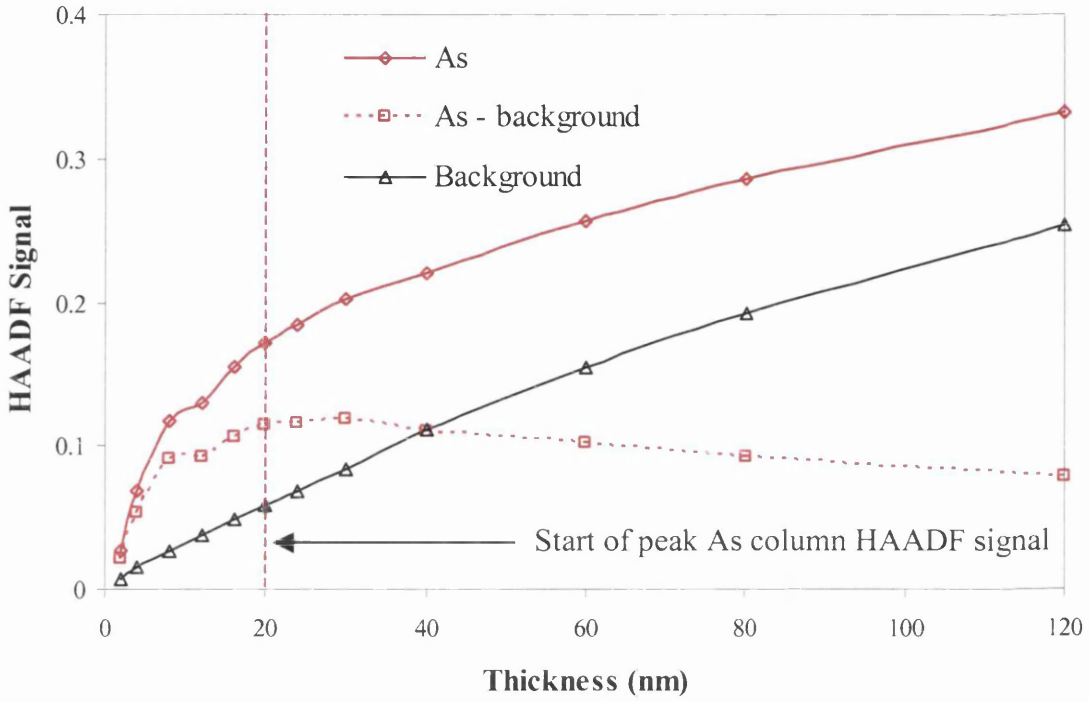

Figure 4.11: Simulated HAADF STEM intensity for GaAs [110] as a function of specimen thickness. The total HAADF signal for an incident probe on an As column (red line) is plotted. Also plotted is the HAADF background signal i.e. for the probe situated between dumbbells (black line). The As – background signal is also shown. The HAADF signal is normalised with respect to the intensity that the probe generates in the detector plane in the absence of a specimen. The HAADF detector has a range of 70mrad to 210mrad.

The total HAADF As signal can be seen to rise steeply for low crystal depths before increasing linearly for larger depths in Figure 4.11. However, in order to measure the actual HAADF signal that is generated by the As column, the background must be removed from the total As signal. The As column HAADF signal is shown as As - background in Figure 4.11. The effect of strong electron intensity channelling on the observed HAADF signal is now apparent. The As column signal only increases for the top 20nm of the specimen which is precisely the depth at which the strong channelling condition terminates on the column (from Figure 4.9). Hence, it is only the very top of an atomic column that generates the column signal in a HAADF image.

Figure 4.11 also demonstrates that, at specimen depths greater than 30nm, the As column HAADF signal starts to decay. A possible reason for this may be due to the fact that the intensity scattered by the top part of the column is re-scattered out to angles that are not picked up by the detector. Finally, as was stated before, the depth at which strong channelling disappears, 20nm, is about 2 times the value estimated in the discussion of the deep superlattice (Section 3.2.2). Indeed, the value of As column intensity / As intensity at a thickness of 60nm, in Figure 4.11, gives a value of 0.4. This is in contrast to the value of 0.14 recorded for the GaAs layers in the deep superlattice (mixture of $Al_{0.3}Ga_{0.7}As$ and GaAs). This may be another symptom of the discrepancy between theoretical image calculations and experimentally derived values. This discrepancy is reflected upon in the investigation of image contrast (see Chapter 5).

The reality that only a limited part of an atomic column has an influence on the HAADF signal has important consequences for the analysis of, for example, dopant structures. For instance, the HAADF signal may look different depending on the position of the dopants in the atomic columns. If they are at a depth of crystal at which relatively little electron intensity exists, then they will have little impact on the HAADF image or EELS measurements. It is clear that the phenomenon of channelling and spreading makes the interpretation of HAADF images more complicated than a simple Z^2 based theory would anticipate.

Equivalent behaviour is also observed for the condition of the probe incident on the Ga column (PPGa). The electron intensity present on the Ga column, as a function specimen thickness, is presented in Figure 4.12. Once again, strong channelling occurs for only the top portion of the column. However, the condition persists on the Ga column for a slightly greater depth (24nm) than was seen on the As column. This is because Ga has a slightly lower Z number than As and, therefore, scatters the electrons less strongly. In addition, zero intensity is also reached at a greater depth of 80nm than in the As column case. Furthermore, an equivalent EELS signal behaviour is also observed for the PPGa condition.

The simulated HAADF signal for the Ga column, in Figure 4.13, peaks at a depth of 20nm (similar to the As column case). The signal then proceeds to slowly reduce in size for the remainder of the specimen. This, again, is an indication of the importance of the column channelling of electron intensity on the HAADF signal. However, the peak Ga column HAADF signal is obtained at a depth slightly before the strong channelling condition terminates.

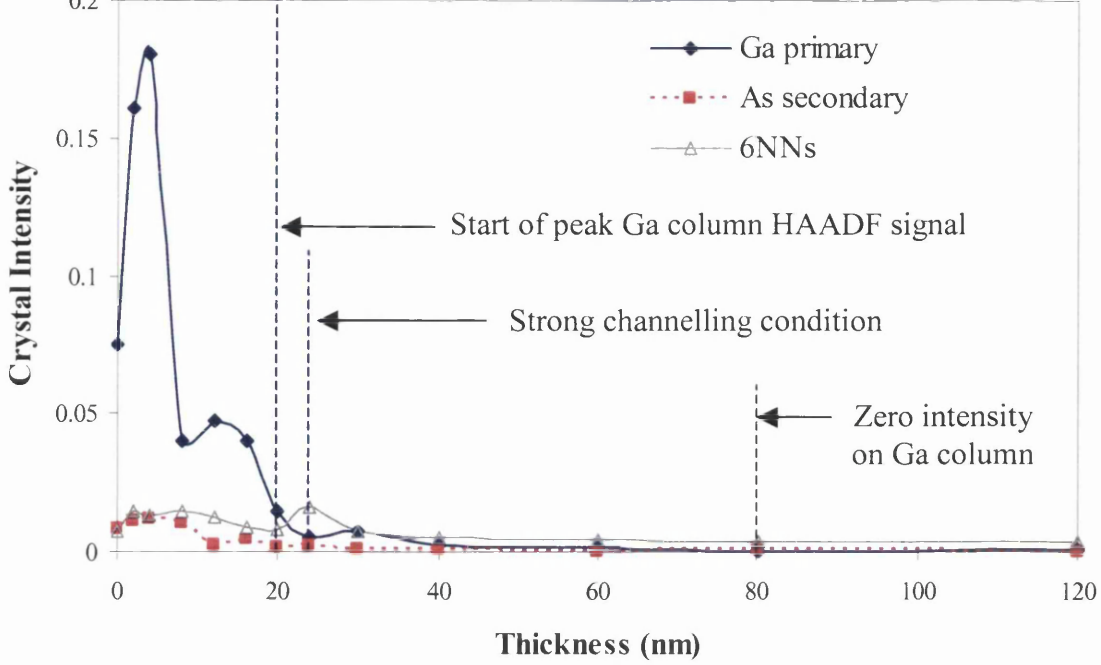

Figure 4.12: A graph of the simulated real space electron intensity along 2 columns in GaAs [110] as a function of specimen thickness. The probe is incident on a Ga column on the top surface of the specimen. The intensity on the primary Ga column (blue), on the neighbouring As column (red) and the sum of the intensity on the nearest 6 dumbbells (grey) are plotted. The values are the sum of a 9pixel × 9pixel area around each column in the intensity maps. The intensity is normalised with respect to the total intensity in the probe (equal to 1).

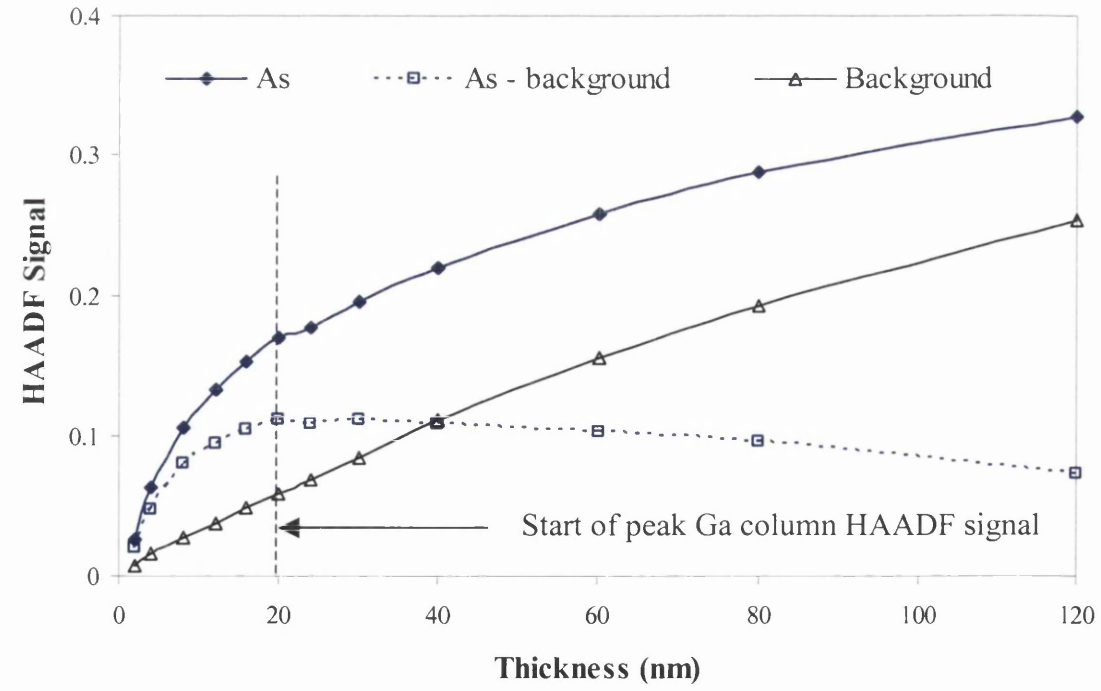

Figure 4.13: Simulated HAADF STEM intensity for GaAs [110] as a function of specimen thickness. The total HAADF signal for an incident probe on a Ga column (blue line) is plotted. Also plotted is the HAADF background signal i.e. for the probe situated between dumbbells (black line). The Ga – background signal is also shown. The HAADF signal is normalised with respect to the intensity that the probe generates in the detector plane in the absence of a specimen. The HAADF detector has a range of 70mrad to 210mrad.

Figure 4.14 gives an indication of what happens to the intensity from the probe when it is centred between dumbbells in GaAs (i.e. the PPBD condition). Figure 4.14 also provides a plot of the intensity located on the 4 dumbbells that surround the starting position of the probe. It is evident that, on the top surface of the specimen, the initial probe intensity that is incident on the surrounding dumbbells is about 5 times less than the intensity that is incident at the probe position. This is due to the shape of the probe and also due to the spacing of the dumbbells in GaAs [110]. For instance, the dumbbells are separated in such a way that the secondary intensity maximum of the probe is only partially incident on the surrounding 4 dumbbells.

Furthermore, Figure 4.14 also reveals that the intensity on the 4 nearest dumbbells rises quickly to reach a maximum value at a depth of 4nm. This is partly because the electron intensity that is incident on the dumbbells is channelled by the column potentials in the same manner as was shown above for As and Ga columns. However, the dumbbells also pick up some intensity scattered from the initial probe position.

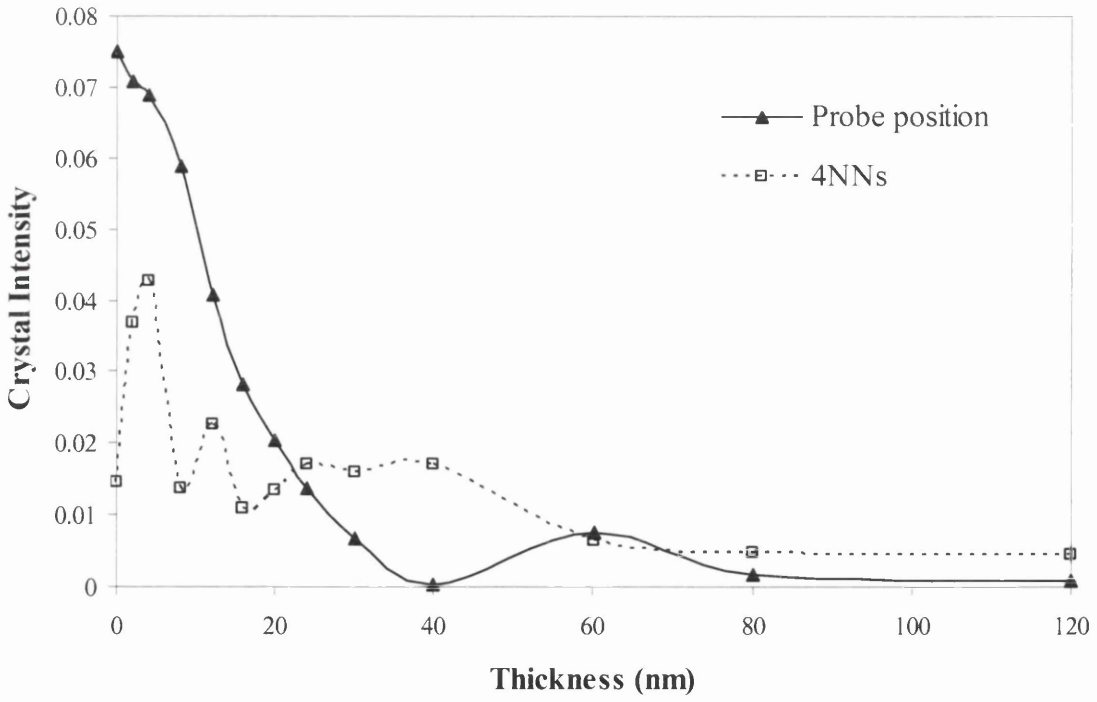

Figure 4.14: A graph of the simulated real space electron intensity in GaAs [110] as a function of specimen thickness. The probe is incident between dumbbells on the top surface of the specimen. The intensity at the probe position (black) and the sum of the intensity on the neighbouring 4 dumbbells (dotted black) is plotted. The values are the sum of a 9pixel × 9pixel area around each column in the intensity maps. The intensity is normalised with respect to the total intensity in the probe (equal to 1).

The intensity at the probe position falls steadily off to reach a zero reading at a depth of 40nm. However, there does not appear to be a direct connection between this reduction in intensity and the value of the intensity on the surrounding dumbbells. In fact, the intensity on the surrounding dumbbells can be seen to fluctuate for the top 24nm of the specimen. This may be due to a combination of the dumbbells scattering and attracting electron intensity in a complicated manner with specimen thickness. Nevertheless, there is an intensity inversion present at a depth of 40nm in which the intensity on the 4 surrounding dumbbells is significantly higher than that at the probe position. The intensity at the probe position then grows for the next 20nm of specimen. This is accompanied by a decline in the intensity on the surrounding dumbbells. Hence, it is likely that the build up of intensity on those 4 dumbbells is scattered back to the probe position. The remainder of the specimen is characterised by a steady decrease in the intensity at the probe position and the continuation of intensity on the surrounding dumbbells.

4.3.2.3 Beam Spreading in GaAs

In Chapter 3, the geometrical spread of the beam seemed to be enough to account for the nature of the small modulation of the background signal observed in the HAADF images of the deep superlattice. The geometrical spread of the beam was stated to occur inside a conical region defined by the incident probe angle (24mrad semi-angle for SuperSTEM 1). Therefore, the extent of the electron intensity (inside the material) should increase linearly with crystal thickness due to geometrical spreading. The calculation of the real space intensity maps permits this hypothesis to be tested against a more rigorous approach.

Figure 4.15 displays the diameter of the electron intensity inside GaAs [110] as a function of crystal depth. The width was measured from the intensity maps in which the probe is incident between dumbbells (the PPBD condition). This probe location was chosen to estimate the beam width because this is the location of the probe that is used to measure the HAADF background signal. In addition, the spreading of the beam in the PPBD condition is due to the scattering produced by the average composition of the material and not by a single column.

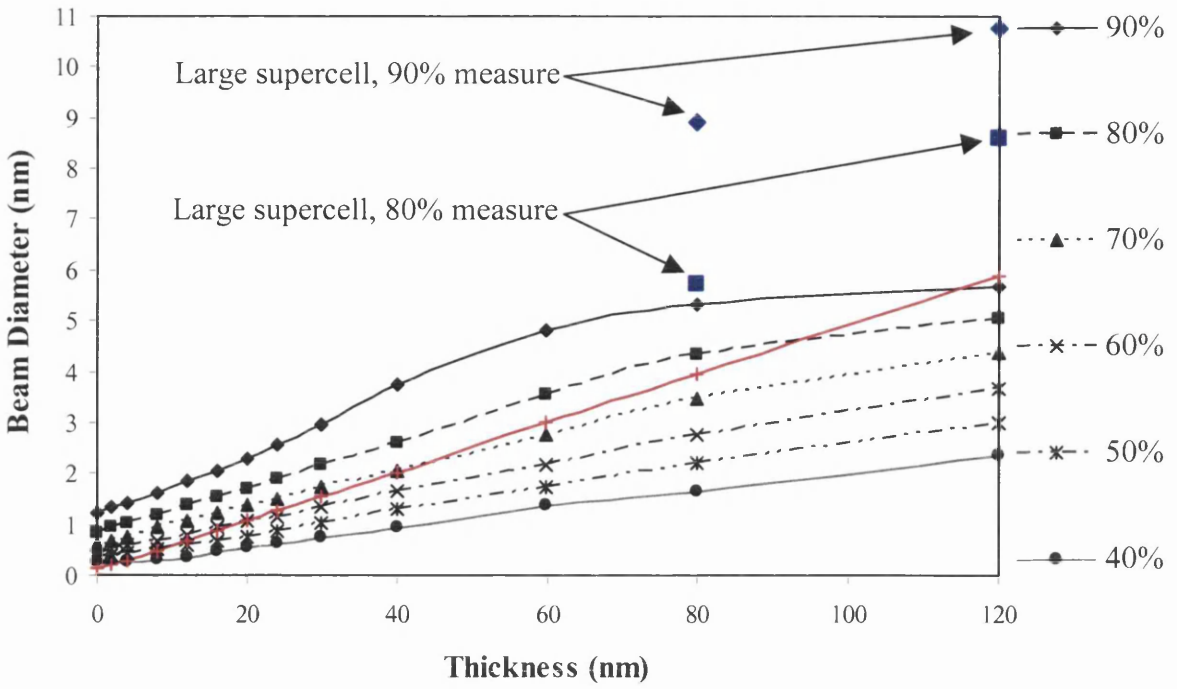

Figure 4.15: A graph of the simulated beam width as a function of specimen thickness in GaAs [110]. The probe was incident between dumbbells (PPBD). The beam width is given as the diameter of circular areas, in the real space intensity maps, in which 90%, 80%, 70%, 60%, 50% and 40% of the total probe intensity is contained. The circular areas are centred on the initial probe position. Also shown is the theoretical geometrical spread of the beam (red line). This has a diameter of 0.1nm at 0nm thickness. Also shown is the 80% and 90% measures of the beam diameter using the larger supercell size at thicknesses of 80nm and 120nm (blue points).

The actual value of the beam width, at a particular thickness, is given by the diameter of a circular region (in the intensity map) that contains a certain percentage of the total probe intensity. In fact, 6 percentages are considered as it is unclear what criteria should be used to measure the width of the intensity spread. It should be noted that the initial probe diameter (at thickness of zero) is finite in size for all percentages. In fact, the diameter is above 1nm for the 90% plot. Hence, a significant portion of the probe will be incident far from the initial probe position i.e. on non-primary columns in the PPGa and PPAs conditions.

Figure 4.15 shows that, for a beam width defined as being 80% to 50% of the total probe intensity, the diameter of the beam increases linearly for small crystal depths up to a thickness of 60-80nm. After that thickness, the rate of beam expansion drops off slightly. On the other hand, the beam diameter that is defined as being 90% of the total probe intensity has a different profile. Its rate of expansion increases up to a depth of about 60nm

before a marked drop off. This reduction is actually a simulation artefact since the value of the beam diameter, at a depth of 80-120nm, is equivalent to the size of the simulated area (5.5965nm × 5.6533nm). Hence, the simulated area is not big enough to contain all of the scattered intensity at that particular thickness of crystal. For that reason, the simulations at the largest 2 thicknesses were repeated using a supercell that was twice as big (i.e. 11.192nm × 11.3066nm). It was found that there was a significant deviation between the beam diameters of the 2 supercell sizes only for the 90% measure at a thickness of 80nm. For instance, at a thickness of 80nm, the 90% beam diameter was measured at 5.3nm for the smaller supercell compared to 8.9nm for the larger supercell. At a thickness of 120nm, large deviations were only found for the 80% and 90% measures. For example, the beam diameter for the 80% measure had a value of 5nm for the small supercell compared to 8.6nm for the large supercell. In addition, the beam diameter for the 90% measure was measured at 5.7nm for the small supercell compared to 10.8nm for the large supercell. Hence, the reduction in the values of the beam diameter using the 80% and 90% measures with the small supercell is due to the fact that the supercell is not large enough to contain all of the beam spread. However, the other percentage measures were not dissimilar when the larger supercell was used (not shown in Figure 4.15 for clarity).

It is clear from Figure 4.15 that the rate of expansion that is predicted by geometrical spreading is greater than that calculated for beam diameters defined as being 80% to 40% of the total probe intensity. This suggests that the degree of beam spreading in GaAs may be overestimated by considering only geometrical spreading. However, the linear shape of the beam diameter, defined as being 90% of the probe intensity, is very similar to that of the geometrical beam spread for crystal depths up to 20nm. The beam diameter (90% of probe intensity) then increases faster than that predicted by the geometrical spread between the thicknesses of 20nm and 60nm.

In summary, the suitability of using the principle of geometrical spreading in order to estimate the width of the beam, at a particular specimen thickness, depends upon how the beam width is measured. If the beam width is chosen to be the diameter of a circular area that contains between 90% and 80% of the total probe intensity then the geometrical beam spread gives a reasonably good estimate of the increase in the width until a thickness of 60-80nm is reached. Hence, all of the following graphs of the beam width in this chapter use the 90% criteria and a maximum thickness of 60nm.

4.3.3.1 Real Space Crystal Intensity Maps

Simulations, analogous to those presented in Section 4.3.2 for GaAs [110], were also performed for AlAs [110]. Figure 4.16 provides the real space intensity maps, at 6 crystal depths within AlAs, for the probe situated on an As column. The maps reveal a similar qualitative behaviour for the intensity distribution on and around the As column as was seen in the maps of GaAs for the PPAs condition (compare with Figure 4.6). For instance, the intensity maximum on the primary column spreads to redistribute the intensity on and off the other dumbbells as before. Moreover, the area that is covered by the scattered electron intensity also appears to be comparable in size to that of the equivalent PPAs condition in GaAs.

However, a major difference is that the intensity that is captured by the neighbouring Al column remains on that column even up to a depth of 80nm. This is in contrast to the situation in GaAs in which the neighbouring Ga column scattered, quite effectively, the intensity it captured from the primary As column. In addition, the most intense feature in the AlAs maps at large crystal thicknesses is not the primary As column. In fact, in AlAs, the most intense feature becomes the neighbouring Al column. This occurs at a thickness of 30nm (map not shown). This indicates that the Al column potential, generated from low Z number atoms (Z = 13), is efficient at both the capture and confinement of the electrons.

Figure 4.17 shows the intensity maps for the probe incident on an Al column in AlAs. These maps are quite different from all the previous ones that were presented above. It is clearly noticeable that much of the intensity is confined to a small central region even at large crystal depths. Furthermore, relatively little intensity has been redistributed onto dumbbells more than 1nm from the primary column. This is in contrast to the AlAs PPAs condition in which significant intensity can be found on many distant dumbbells in the maps. However, the most striking feature of the maps in Figure 4.17 is the continuation of the central intensity maximum on the primary Al column for all crystal depths (see insets). This suggests that although an Al column provides a much weaker attraction to electrons than an As column does (due to Al's lower Z number) it would seem that this is compensated by the fact that the Al atoms scatter electrons much less. As a result, the Al column potential confines the electrons much more strongly than the As column potential.

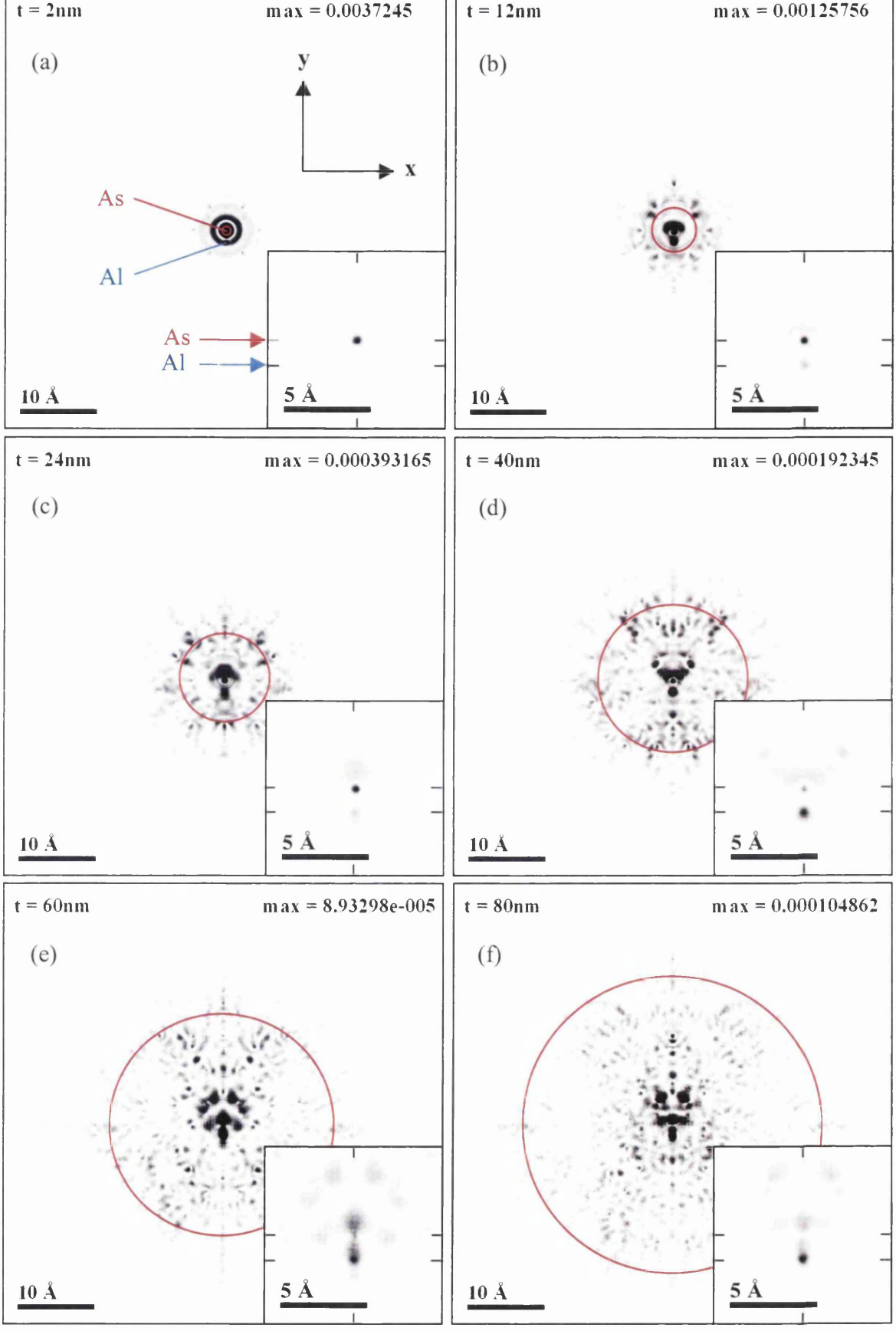

Figure 4.16: Contrast enhanced simulated electron intensity maps at various depths in a crystal of AlAs [110]. The insets show a magnified view of the central region of each map taken over the full intensity range. A 24mrad, 0.1nm probe is incident on an As column. Black pixels are the most intense. The crystal depths are: **(a)** 2nm **(b)** 12nm **(c)** 24nm **(d)** 40nm **(e)** 60nm and **(f)** 80nm. Max refers to the maximum intensity contained within a single pixel. Circle radius = αt. The total electron intensity of the probe = 1.

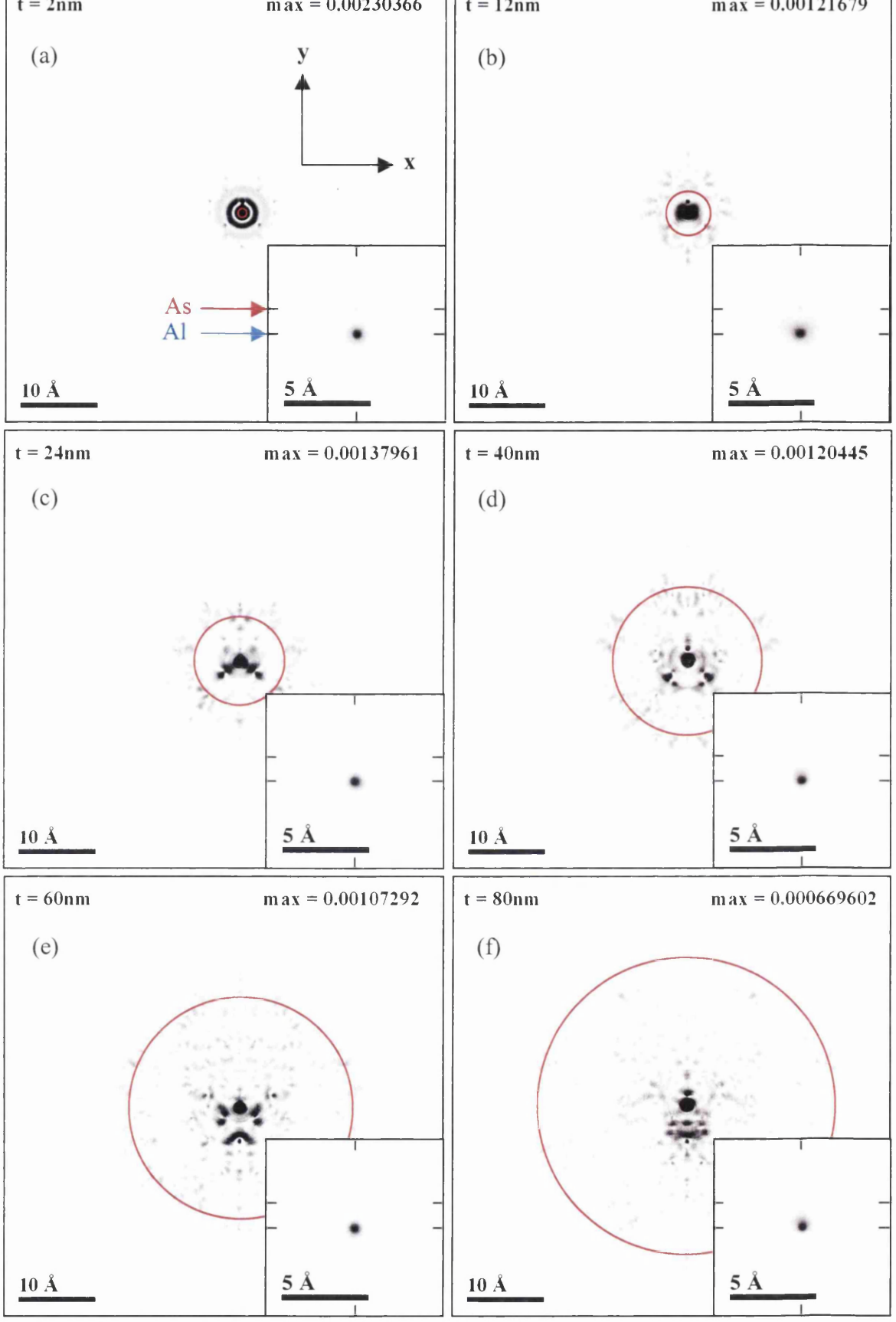

Figure 4.17: Contrast enhanced simulated electron intensity maps at various depths in a crystal of AlAs [110]. The insets show a magnified view of the central region of each map taken over the full intensity range. A 24mrad, 0.1nm probe is incident on an Al column. Black pixels are the most intense. The crystal depths are: **(a)** 2nm **(b)** 12nm **(c)** 24nm **(d)** 40nm **(e)** 60nm and **(f)** 80nm. Max refers to the maximum intensity contained within a single pixel. Circle radius = αt. The total electron intensity of the probe = 1.

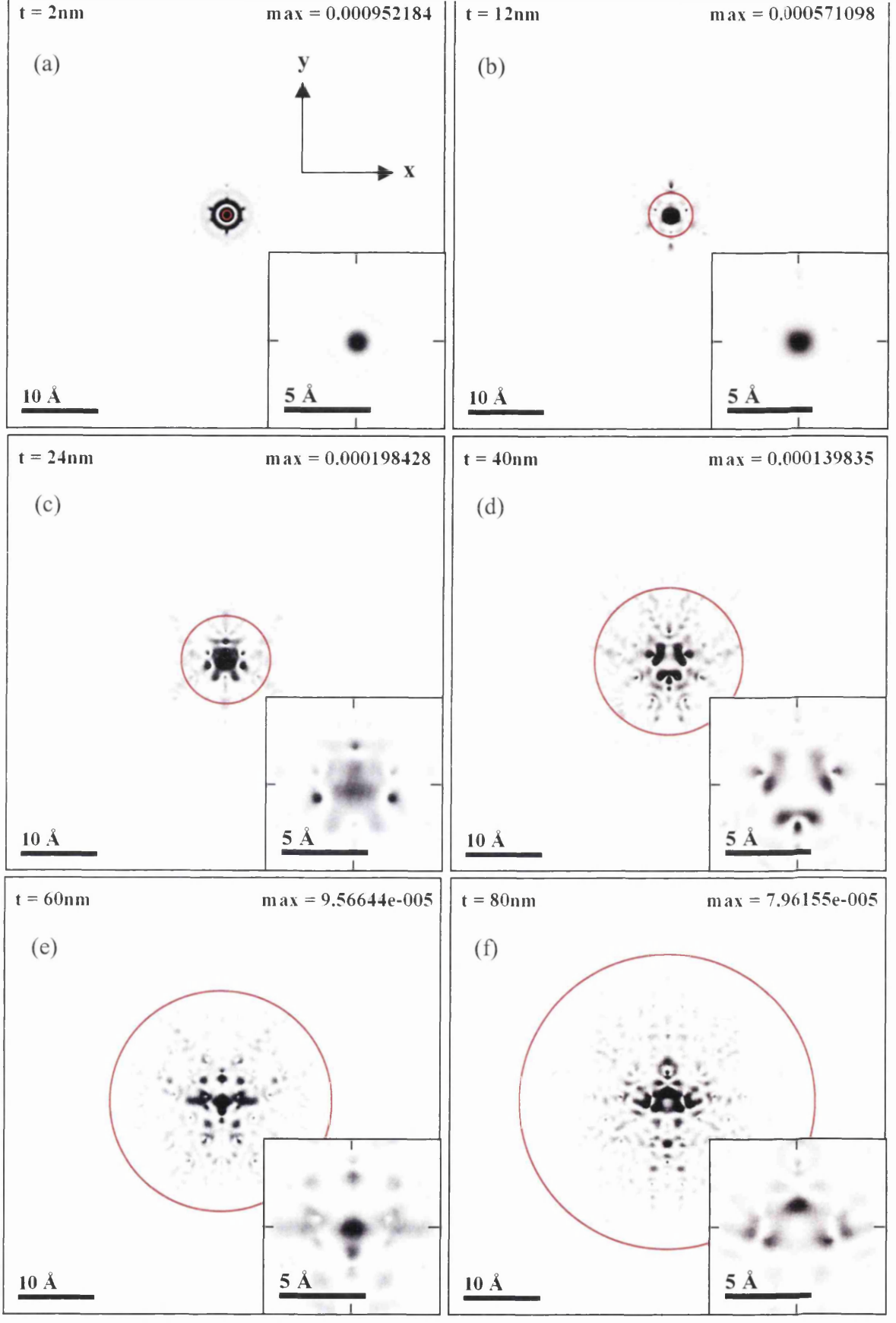

Figure 4.18: Contrast enhanced simulated electron intensity maps at various depths in a crystal of AlAs [110]. The insets show a magnified view of the central region of each map taken over the full intensity range. A 24mrad, 0.1nm probe is incident between dumbbells. Black pixels are the most intense. The crystal depths are: **(a)** 2nm **(b)** 12nm **(c)** 24nm **(d)** 40nm **(e)** 60nm and **(f)** 80nm. Max refers to the maximum intensity contained within a single pixel. Circle radius = αt. The total electron intensity of the probe = 1.

Figure 4.18 provides the intensity maps for the probe situated between dumbbells in AlAs. Much of the intensity is trapped by the potential of the surrounding 4 dumbbells, similar to the maps with the equivalent probe position in GaAs (compare with Figure 4.8). Moreover, at a depth of 40nm, the central maximum has again been displaced onto those nearest dumbbells. However, the nearest 4 Al columns retain a substantial portion of this intensity. It is also uncertain whether the area covered by the scattered intensity is greater or smaller than that of the equivalent case in GaAs. A comparison of the beam width, as a function of thickness, for all the simulated materials is presented in Section 4.3.5.

4.3.3.2 Channelling, EELS and the HAADF STEM Signal in the PPAl Case

Analysis was performed for the AlAs PPAs case in the same way as for the GaAs PPAs case. However, the graphs for the AlAs PPAs case are not presented here for brevity since the results are similar to those shown for the GaAs PPAs case (Section 4.3.2.2). However, the relevant graphs are shown in Appendix A. This section, therefore, deals with the AlAs PPAl case alone.

Figure 4.19 is a graphical display of the value of the electron intensity that exists on the primary Al column (and the neighbouring As column) as a function of specimen thickness. The probe is incident on an Al column in this case (the PPAl condition). The intensity of the 6 nearest dumbbells is also shown. It is clear, from the graph in Figure 4.19, that the intensity on the primary Al column peaks at a low specimen thickness of 4nm before a sharp decline is observed, in a similar fashion to the intensity on both As and Ga columns in GaAs. The intensity then rises to reach a secondary maximum at a depth of 30nm. However, it is apparent that a strong channelling condition exists on the primary Al column for all crystal depths thereafter. This is in stark contrast to the short channelling depths of 20nm for an As column and 24nm for a Ga column as described above. The weak scattering power of the Al column is the reason behind the difference. In addition, the neighbouring As column does not capture any appreciable electron intensity away from the primary Al column. Furthermore, Figure 4.19 also reveals that although the intensity on the 6 dumbbells that surround the primary Al column remains fairly steady after a depth of 60nm, the actual value of this intensity is small compared to that on the primary Al column.

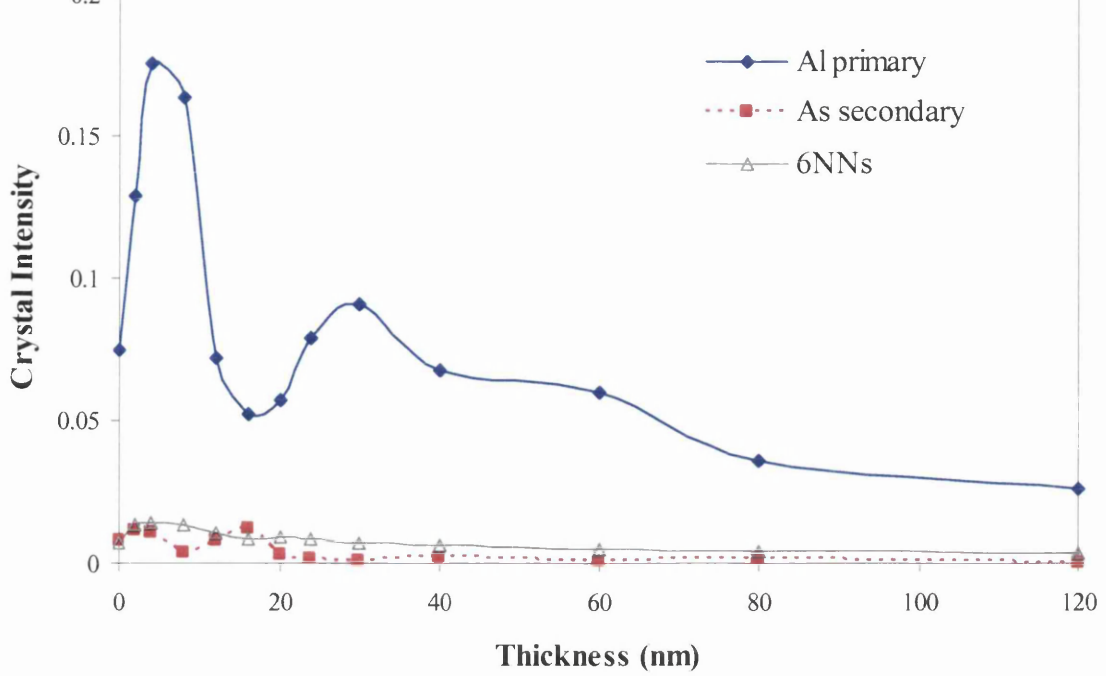

Figure 4.19: A graph of the simulated real space electron intensity along 2 columns in AlAs [110] as a function of specimen thickness. The probe is incident on an Al column on the top surface of the specimen. The intensity on the primary Al column (blue), on the neighbouring As column (red) and the sum of the intensity on the nearest 6 dumbbells (grey) are plotted. The values are the sum of a 9pixel × 9pixel area around each column in the intensity maps. The intensity is normalised with respect to the total intensity in the probe (equal to 1).

Figure 4.20(a) displays the integrated crystal intensity (i.e. the area under graphs of crystal intensity versus thickness) on the primary Al column, non-primary Al sites and all As sites as a function of thickness. It is clear that this graph has some important differences with the equivalent graph in the GaAs PPAs case (Figure 4.10(a)). For example, the primary Al plot increases over all depths of crystal and is always much greater in value than the non-primary Al sites and all As sites. Hence, all crystal depths in the AlAs PPAl case should contribute to the primary Al EELS signal (unlike the behaviour witnessed in the GaAs PPAs case). This is reflected in Figure 4.20(b) which shows the variation of the (integrated) crystal intensity on the primary Al column / the (integrated) intensity on all Al sites as a function of thickness. This plot drops from a maximum value of about 0.9 to a minimum of 0.8 (at a depth of about 100nm). Hence, even at large specimen thickness, the Al EELS signal should be primarily generated from the primary Al column. This is again due to the large channelling depth that is associated with the Al column. Figure 4.20(b) also illustrates the thickness variation of the (integrated) crystal intensity on the all As sites / the (integrated) intensity on all Al sites. Due to the fact that this ratio remains low for all crystal depths, the ability to differentiate between As and Al using EELS should not be adversely affected as the specimen thickness is increased.

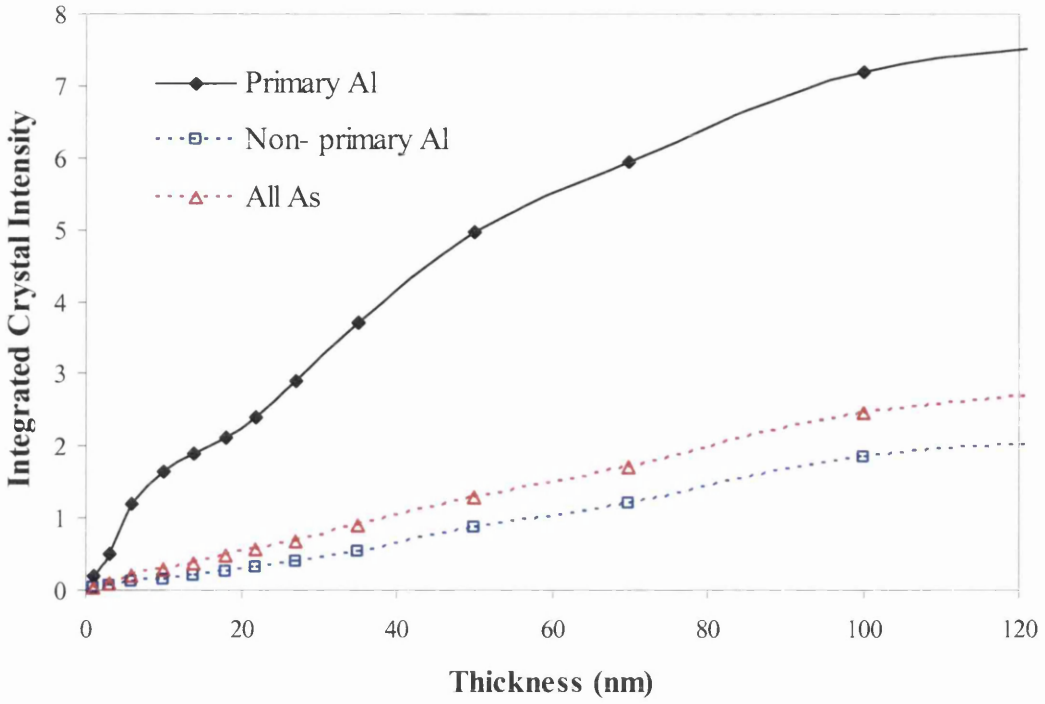

Figure 4.20(a): A graph of the simulated integrated crystal intensity on the primary Al column, all non-primary Al sites and all As sites as a function of thickness.

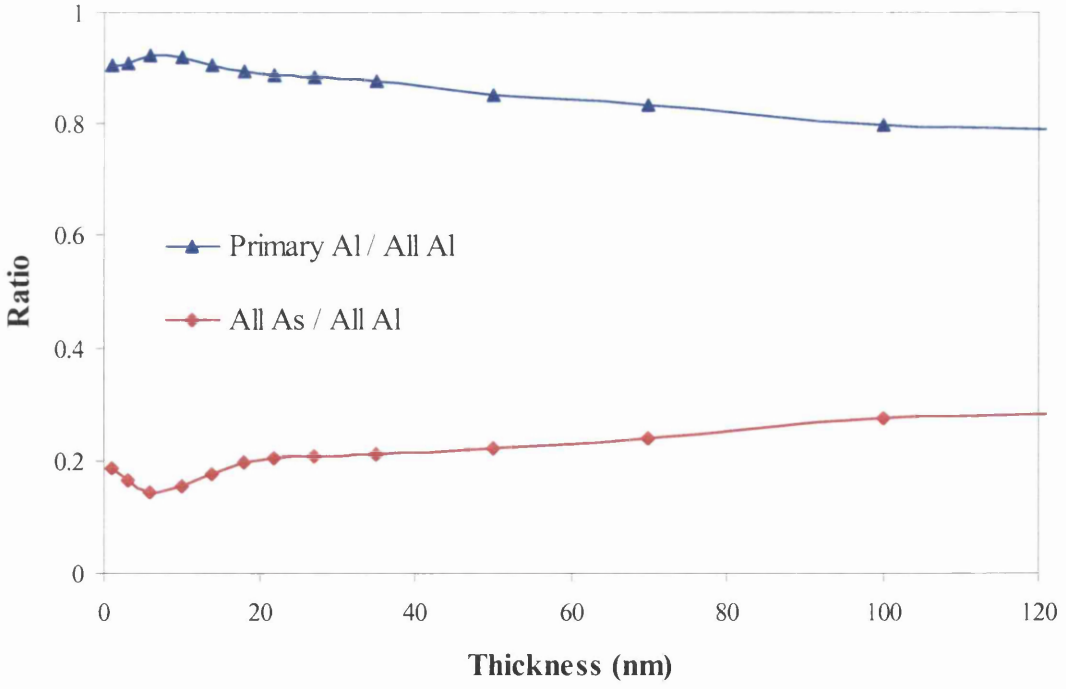

Figure 4.20(b): A graph of the simulated integrated crystal intensity on the primary Al column / all Al sites as a function of thickness. Also shown is the simulated integrated crystal intensity on all As sites / all Al sites as a function of thickness.

The effect of the large channelling depth associated with Al columns can also be observed in Figure 4.21. This reveals the simulated HAADF intensity for the primary Al column and also for the AlAs background signal. The Al column signal can be seen to increase over all depths of crystal due to the existence of the strong channelling condition on the Al column. Furthermore, the HAADF background signal is lower than that observed in GaAs. This is because AlAs (Z_{RMS} = 35.5) has a lower root mean square atomic number than GaAs (Z_{RMS} = 45.3). Hence, there is less electron scattering out to the large angles of the detector. In addition, a comparison of the background signal, as a function of thickness, for all the simulated materials is presented in Section 4.3.5.

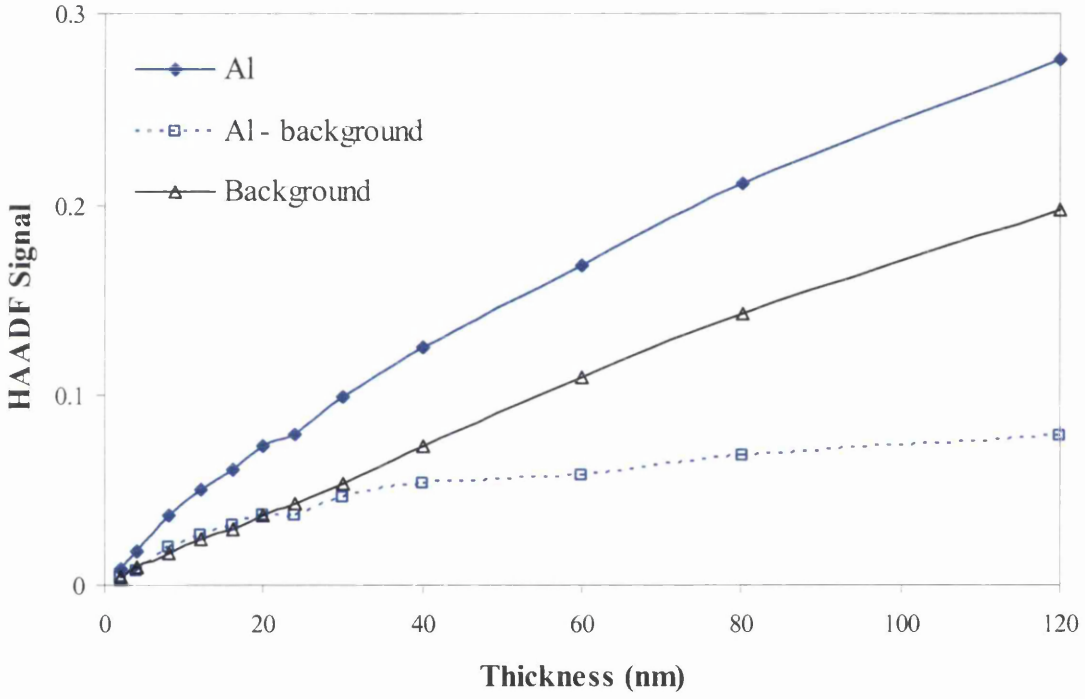

Figure 4.21: Simulated HAADF STEM intensity for AlAs [110] as a function of specimen thickness. The total HAADF signal for an incident probe on an Al column (blue line) is plotted. Also plotted is the HAADF background signal i.e. for the probe situated between dumbbells (black line). The Al – background signal is also shown. The HAADF signal is normalised with respect to the intensity that the probe generates in the detector plane in the absence of a specimen. The HAADF detector has a range of 70mrad to 210mrad.

4.3.4 InAs

4.3.4.1 Real Space Crystal Intensity Maps

Real space intensity maps were also calculated for InAs [110] as a function of specimen thickness. These are presented in Figure 4.22 for the probe incident on an As column. These have a similar character at low crystal depths to the maps for the equivalent probe condition in GaAs. The central intensity maximum on the As column is again scattered effectively by the primary As column. However, extremely little intensity can be found on the neighbouring In column at all depths. The In column has such a high Z number (Z = 49) that practically no electron intensity can remain near to the column for any great depths. This has an effect on the general distribution of the intensity at larger crystal depths. For example, in comparison to GaAs (and AlAs), a higher percentage of the total probe intensity can be found at a considerable distance from the initial probe position. In addition, the area of intensity in Figure 4.22 is clearly larger in extent than the αt circles up to, at least, 40nm.

Figure 4.23 presents the intensity maps for the probe incident on an In column. The map at a thickness of 24nm (see inset) reveals that a lot of the intensity that was incident on the primary In column has already been scattered to a position off the column. Furthermore, the intensity on the As column, next to the primary In column, actually becomes greater than that on the primary column at a depth of only 16nm (map not shown). However, the In column once again becomes more intense than the neighbouring As column at a depth of 24nm (Figure 4.23(c)).

Figure 4.24 presents the intensity maps for the probe incident between dumbbells. It can be seen that the central maximum of the probe remains in the space between the surrounding 4 dumbbells at all depths. However, the value of this intensity is low at depths of 40nm and 60nm, respectively. The intensity from the maximum is quite clearly attracted by the potential of the nearest dumbbells once again. Nevertheless, at a depth of 80nm, the intensity has scattered back to from a significantly more intense area at the initial probe position once again. This therefore exhibits a similar behaviour for the equivalent probe condition in GaAs and AlAs.

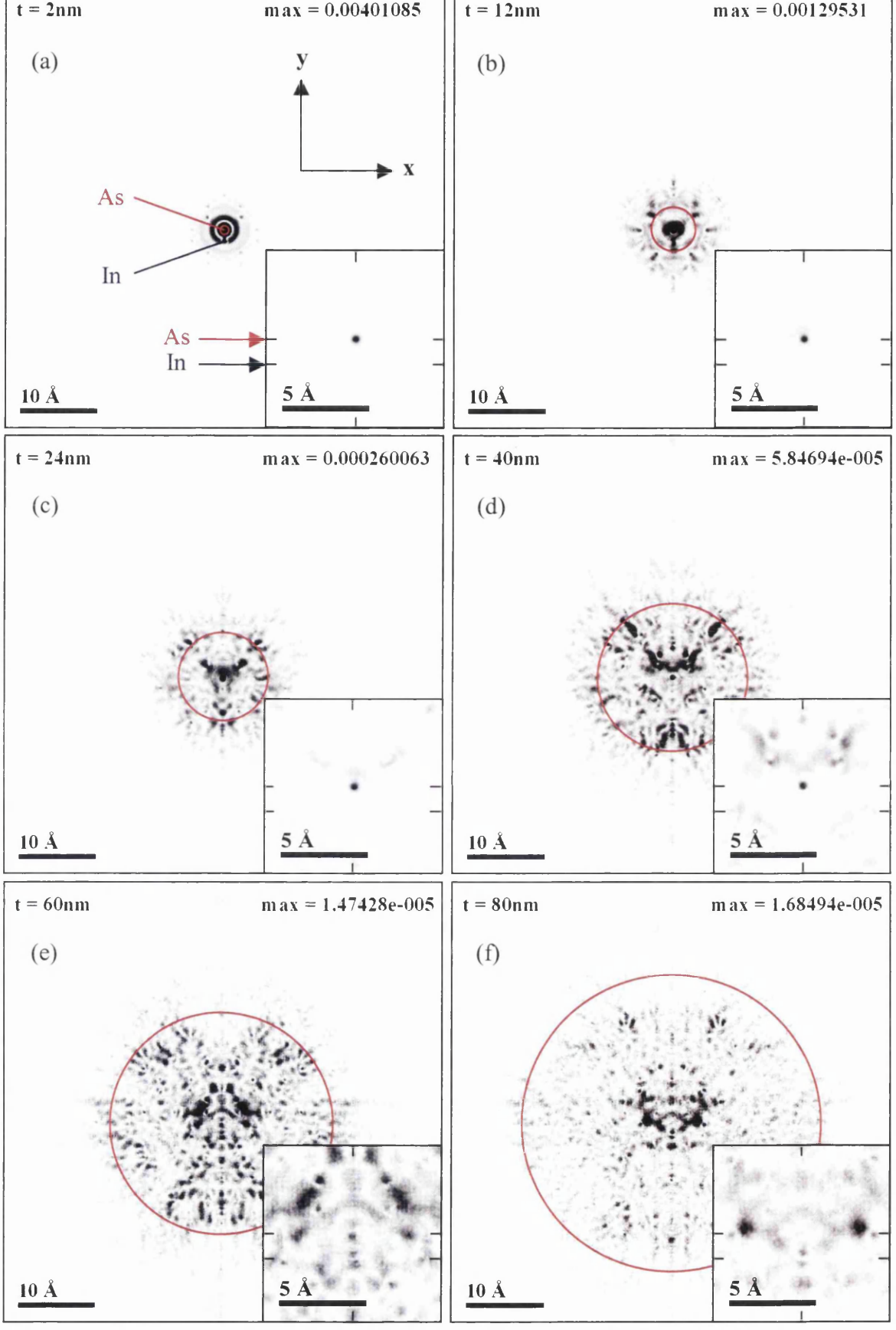

Figure 4.22: Contrast enhanced simulated electron intensity maps at various depths in a crystal of InAs [110]. The insets show a magnified view of the central region of each map taken over the full intensity range. A 24mrad, 0.1nm probe is incident on an As column. Black pixels are the most intense. The crystal depths are: **(a)** 2nm **(b)** 12nm **(c)** 24nm **(d)** 40nm **(e)** 60nm and **(f)** 80nm. Max refers to the maximum intensity contained within a single pixel. Circle radius = αt. The total electron intensity of the probe = 1.

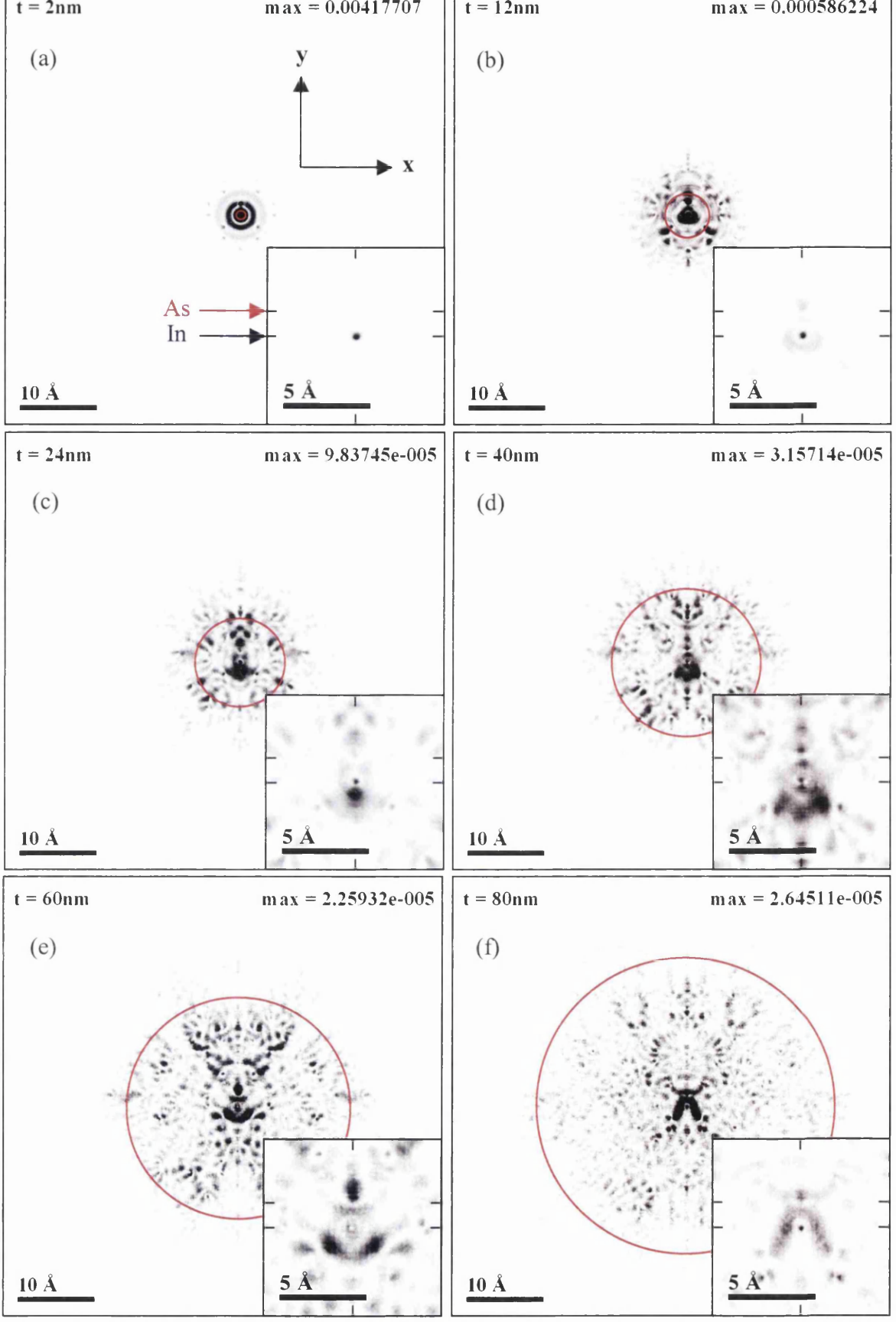

Figure 4.23: Contrast enhanced simulated electron intensity maps at various depths in a crystal of InAs [110]. The insets show a magnified view of the central region of each map taken over the full intensity range. A 24mrad, 0.1nm probe is incident on an In column. Black pixels are the most intense. The crystal depths are: **(a)** 2nm **(b)** 12nm **(c)** 24nm **(d)** 40nm **(e)** 60nm and **(f)** 80nm. Max refers to the maximum intensity contained within a single pixel. Circle radius = αt. The total electron intensity of the probe = 1.

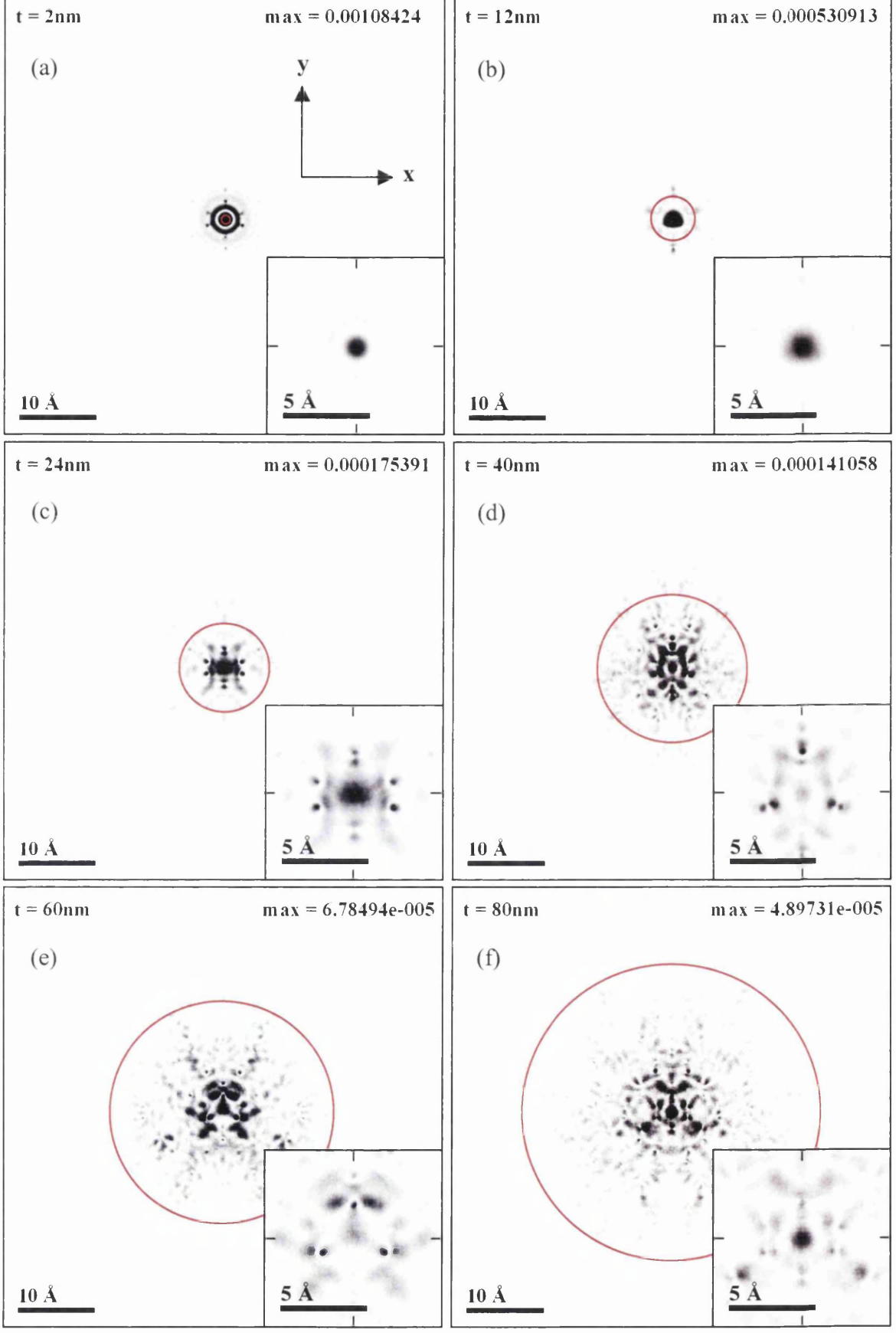

Figure 4.24: Contrast enhanced simulated electron intensity maps at various depths in a crystal of InAs [110]. The insets show a magnified view of the central region of each map taken over the full intensity range. A 24mrad, 0.1nm probe is incident between dumbbells. Black pixels are the most intense. The crystal depths are: **(a)** 2nm **(b)** 12nm **(c)** 24nm **(d)** 40nm **(e)** 60nm and **(f)** 80nm. Max refers to the maximum intensity contained within a single pixel. Circle radius = αt. The total electron intensity of the probe = 1.

4.3.4.2 Channelling, EELS and the HAADF STEM Signal in the PPIn Case

In the same way that the graphs for the AlAs PPAs case was not presented in Section 4.3.3.2 as they were similar to those associated with GaAs PPAs case, the graphs associated with the InAs PPAs case are not presented here. However, the relevant graphs are shown in Appendix A. This section, therefore, deals with the InAs PPIn case alone.

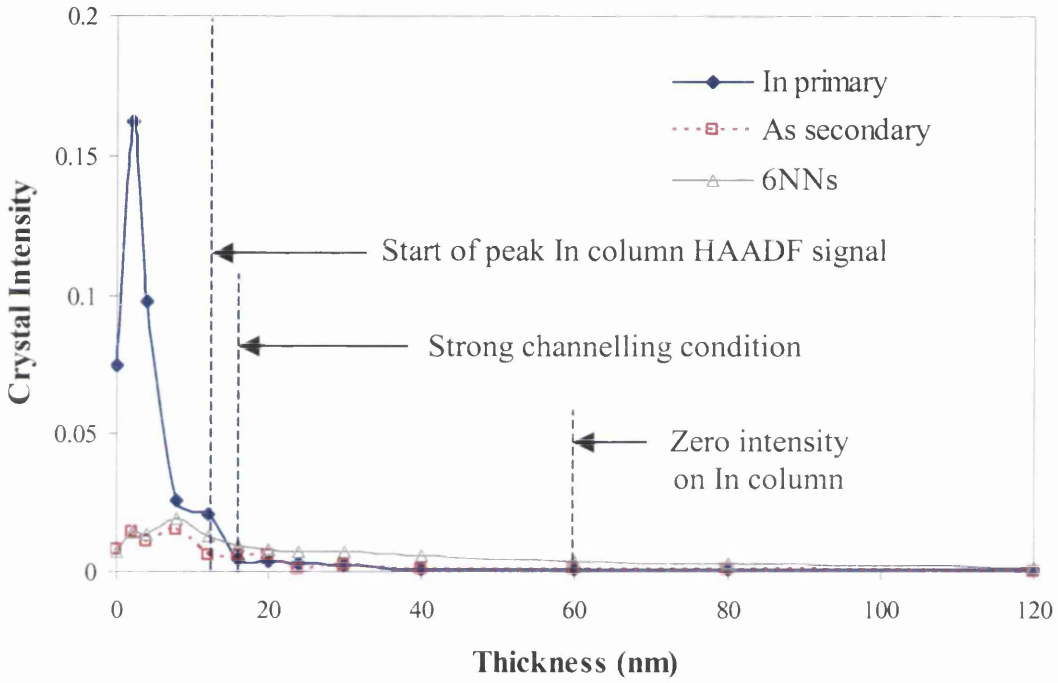

Figure 4.25: A graph of the simulated real space electron intensity along 2 columns in InAs [110] as a function of specimen thickness. The probe is incident on an In column on the top surface of the specimen. The intensity on the primary In column (blue), on the neighbouring As column (red) and the sum of the intensity on the nearest 6 dumbbells (grey) are plotted. The values are the sum of a 9pixel × 9pixel area around each column in the intensity maps. The intensity is normalised with respect to the total intensity in the probe (equal to 1).

Figure 4.25 reveals the value of the intensity that exists on the primary In column and neighbouring As column, as a function of specimen thickness, for the probe centred on an In column. Also shown is the sum of the intensity on the surrounding 6 dumbbells. Unlike the equivalent graphs for GaAs and AlAs, Figure 4.25 shows that the peak intensity on the In column does not take 4nm of crystal to form. In fact, the maximum intensity value develops only after a depth of 2nm on primary column. The electron intensity then rapidly decays away and does not form a small secondary maximum. It can be seen that the strong channelling depth for an In column occurs at a thickness of 16nm, which is shorter than

that of an As, Ga or Al columns. Moreover, it can be seen that the intensity on the neighbouring As column becomes greater than that on the primary column after 16nm as well. On the other hand, the greatest intensity on the surrounding 6 dumbbells occurs after a thickness of 8nm. In addition, the intensity on the In column decays to zero after about 60nm which is the same as that of As columns but less than that of Ga columns in GaAs (Section 4.3.2.2).

Figure 4.26(a) displays the integrated crystal intensity (i.e. the area under graphs of crystal intensity versus thickness) on the primary In column, non-primary In sites and all As sites as a function of thickness. This graph has a similar form to the equivalent one in the case of PPAs GaAs (Figure 4.10(a)). For instance, the plots of the non-primary In and all As sites increase over all thicknesses. The plot for the primary In is also similar except for the fact that it becomes constant at a lower crystal depth. Hence, the contribution to the In EELS signal from the primary In column ceases at a smaller thickness value than in the other types of columns considered before. Moreover, the maximum value of the primary In column plot in Figure 4.26(a) is less than the equivalent plot for the GaAs PPAs case. Therefore, the overall electron intensity that exists on In columns (over the simulated thickness range) is less than that on As (as well as on Ga and Al) columns. This is again due to the high scattering power of In columns.

Figure 4.26(b) shows the variation of the (integrated) crystal intensity on the primary In column / the (integrated) intensity on all In sites as a function of thickness. It can be seen that this in fact drops more sharply than the equivalent plot for the GaAs PPAs case. Consequently, the contribution of the primary In column to the In EELS signal is smaller, at all crystal depths, than the contribution of the primary As column to the As EELS signal in GaAs. Figure 4.26(b) also shows the reduction of the (integrated) crystal intensity on all As sites / the (integrated) intensity on all In sites as a function of thickness. This highlights the reduction of the In EELS signal along with the increase of the As EELS signal in InAs. Hence, the ability to differentiate between As and In using EELS should become worse as the specimen thickness is increased.

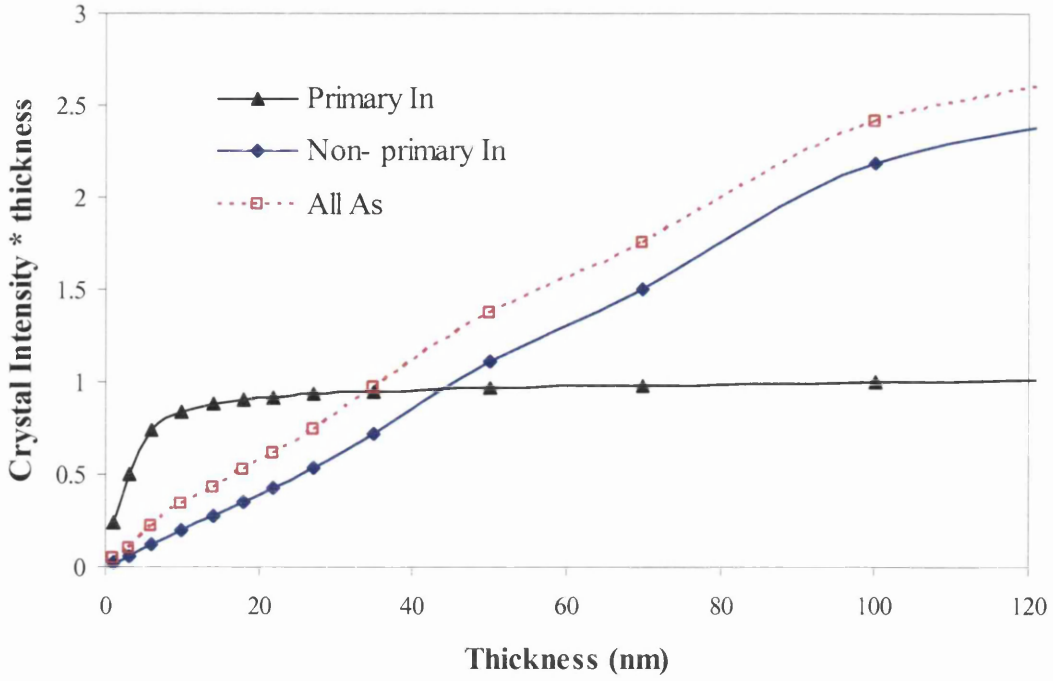

Figure 4.26(a): A graph of the simulated integrated crystal intensity on the primary In column, all non-primary In sites and all As sites as a function of thickness.

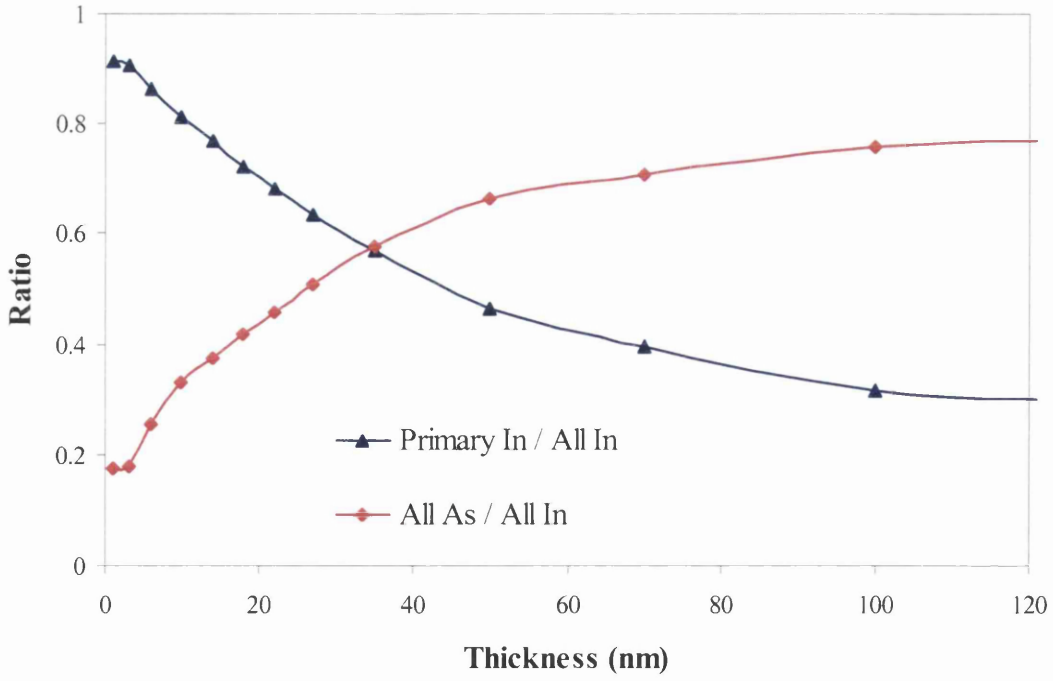

Figure 4.26(b): A graph of the simulated integrated crystal intensity on the primary In column / all In sites as a function of thickness. Also shown is the simulated integrated crystal intensity on all As sites / all In sites as a function of thickness.

The simulated HAADF signal for the probe incident on an In column is presented in Figure 4.27, again as a function of specimen thickness. The background signal shown in Figure 4.27 is greater than that of GaAs and AlAs. This is expected because InAs has a larger value of Z_{RMS} than either of those 2 materials. However, the HAADF signal may again be underestimated due to the expansion of intensity outside the simulated area as was explained in Section 4.3.2.3. This effect is enhanced in simulations of InAs because the intensity reaches the side of the simulated area at a lower specimen thickness than it does in the lower Z materials.

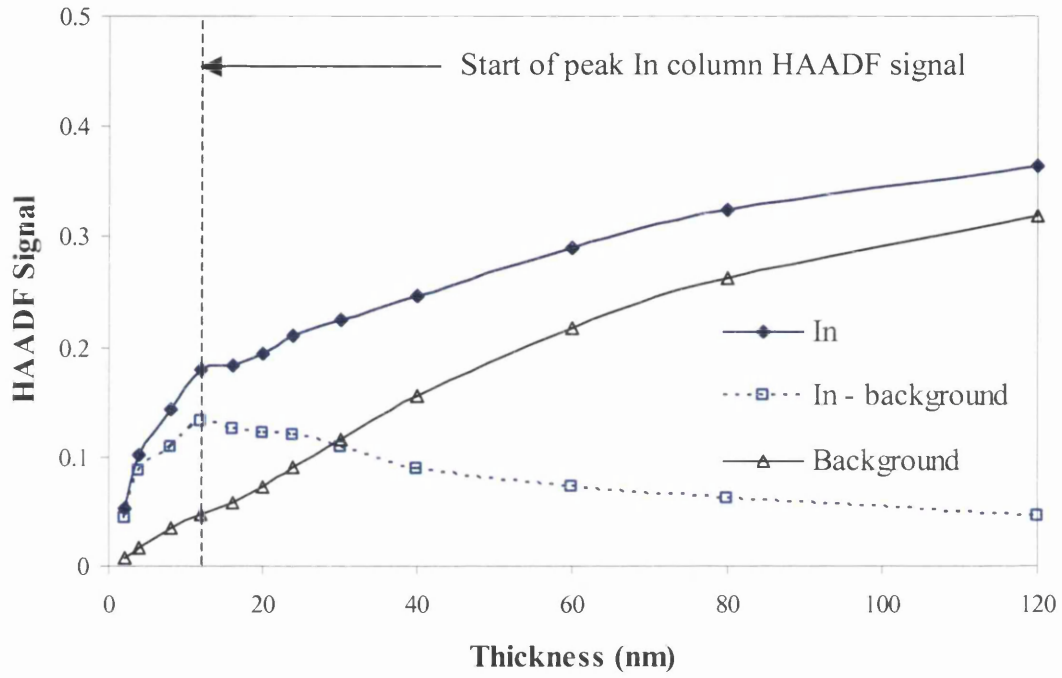

Figure 4.27: Simulated HAADF STEM intensity for InAs [110] as a function of specimen thickness. The total HAADF signal for an incident probe on an In column (blue line) is plotted. Also plotted is the HAADF background signal i.e. for the probe situated between dumbbells (black line). The In – background signal is also shown. The HAADF signal is normalised with respect to the intensity that the probe generates in the detector plane in the absence of a specimen. The HAADF detector has a range of 70mrad to 210mrad.

Figure 4.27 also provides the variation of the In column HAADF signal. This signal reaches a maximum value at a specimen thickness of 12nm, which is close to the limit of strong channelling (16nm). The HAADF signal then drops off steadily, possibly because the electrons that are scattered by the top 12nm of the In column are then re-scattered out to angles that do not hit the HAADF detector. In addition, the value of the HAADF signal for the In column is greater than that of an As column (PPAs condition in InAs) for depths up to 20nm.

4.3.5 24mrad Probe: A Comparison of AlAs, GaAs and InAs

To gain a fuller understanding of the differences between the 3 simulated materials, some of their more interesting attributes are compared in this section. For instance, Figure 4.28 illustrates the difference between the degree of beam spreading observed in AlAs, GaAs and InAs as a function of specimen thickness. The probe was centred between dumbbells in each case. The measure of the beam width is given as the diameter of a circular area, in a real space intensity map, that contains 90% of the total probe intensity. This method of beam width estimation was selected because it provides a reasonable match with the width predicted by the geometrical spread of the beam as was shown in Section 4.3.2.3.

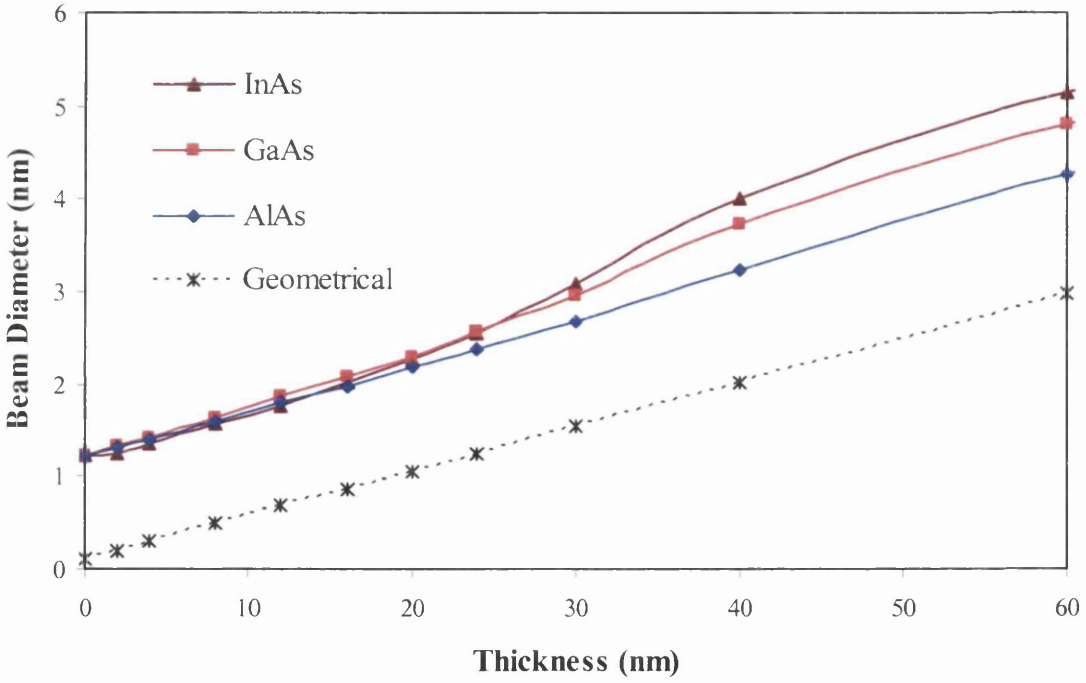

Figure 4.28: A graph of the simulated beam width as a function of specimen thickness in AlAs [110] (blue), GaAs [110] (red) and InAs [110] (brown) as a function of specimen thickness. These were calculated for the probe situated between dumbbells (PPBD condition). The beam width is given as the diameter of circular areas, in the real space intensity maps, in which 90% of the total probe intensity is contained. The circular areas are centred on the initial probe position. Also shown is the theoretical geometrical spread of the beam (red line). This has a diameter of 0.1nm at 0nm thickness.

Figure 4.28 reveals that for the top 20nm of the specimen, the 3 materials generate the same overall beam diameter. This indicates, for the top portion of the specimen, that the spread of the beam is independent of the type of material through which the beam passes.

Furthermore, the rate of beam expansion is similar to that predicted by geometrical spreading. Hence, the beam spread is mainly due to the characteristics of the incident probe and, in particular, to its probe angle (24mrad in this case). However, after a depth of 20nm, the type of material starts to have an effect on the beam width. This is indicated by an increase in the rate of beam expansion in both GaAs and InAs. In addition, the beam width in InAs overcomes that in GaAs at a depth of 30nm and remains so for the rest of specimen. It was also found that the rate of beam expansion reduced significantly between a depth of 80nm and 120nm in InAs (as well as in GaAs). This does not represent a true reflection of the situation as it is a merely a simulation artefact that is introduced by intensity spreading outside of the supercell as was explained in Section 4.3.2.3.

It is also constructive to consider the differences in the HAADF signal for the 3 materials. For example, Figure 4.29 gives a comparison between the simulated HAADF background signals for the 3 simulated materials as a function of specimen thickness. These were calculated with the probe positioned between dumbbells in each material.

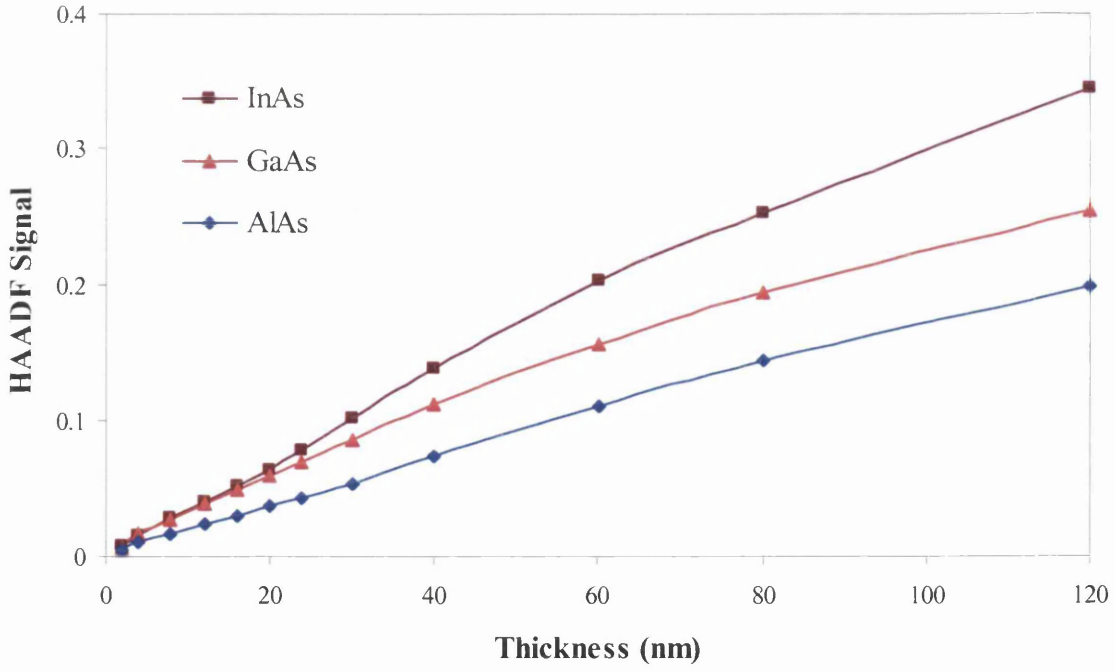

Figure 4.29: Simulated HAADF STEM background signals for AlAs [110] (blue), GaAs [110] (red) and InAs [110] (brown) as a function of specimen thickness. These were calculated for the probe situated between dumbbells. The HAADF signal is normalised with respect to the intensity that the probe generates in the detector plane in the absence of a specimen. The HAADF detector has a range of 70mrad to 210mrad.

Figure 4.29 shows that the HAADF background signal for InAs is always greater than the signals associated with GaAs and AlAs, except for the thinnest crystals (2nm). Moreover, the background of GaAs is intermediate between that of AlAs and InAs. In addition, the background signal does not seem to be significantly modified by the reduction in the beam width (above a thickness of 80nm) that was highlighted in Figure 4.28.

Figure 4.30 is a plot of the thickness variation of the simulated HAADF intensity of Al, Ga, As and In columns. These were calculated for the probe incident on each of the respective columns. The appropriate background signal has also been removed in each case.

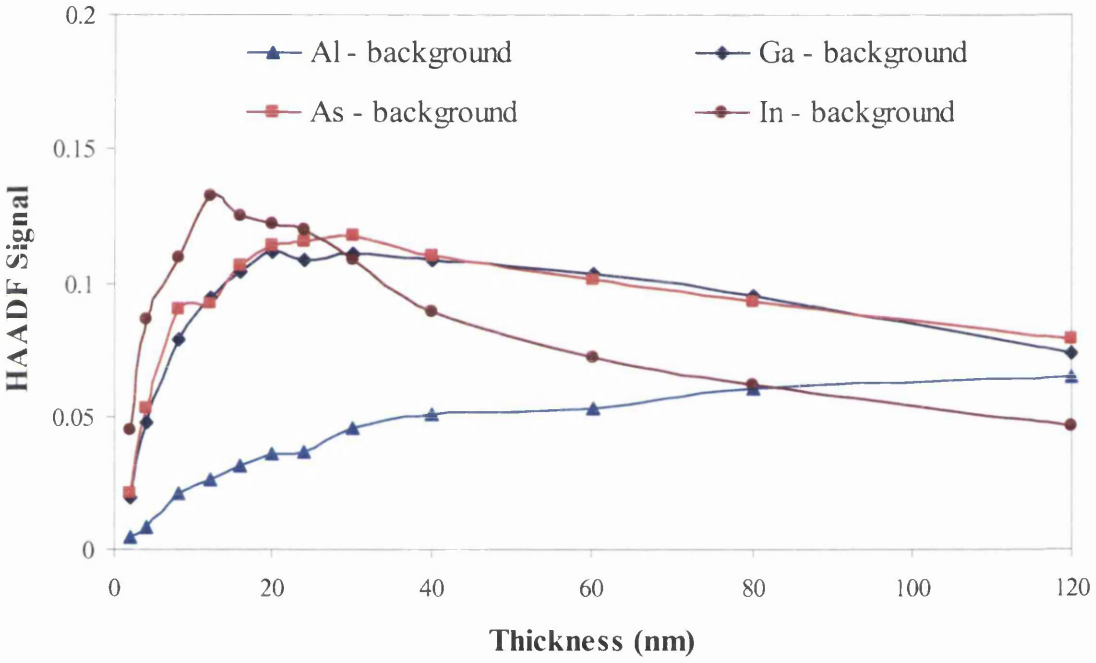

Figure 4.30: Simulated HAADF STEM column intensities as a function of specimen thickness. 4 columns are shown: Al, Ga, As (from GaAs) and In. The intensity values are for the probe incident on each column. The HAADF signal is normalised with respect to the intensity that the probe generates in the detector plane in the absence of a specimen. The HAADF detector has a range of 70mrad to 210mrad.

It is apparent that the Al column signal is far lower in intensity than the other 3 columns up to a depth of 80nm. Furthermore, the Al column signal is the only one that increases over the whole range of specimen thickness that was simulated. The In column, on the other hand, has the greatest signal for the top 24nm of the specimen. It also reaches its peak value at a much lower depth (12nm) than the other columns. However, the In signal also

starts to decay away at this small depth. This is a result of the electrons that were scattered by the top portion of the In column being re-scattered out to angles that do not reach the HAADF detector. This effect is more pronounced in InAs due to it having the highest Z_{RMS} value of the simulated materials. In addition, the Ga and As columns have almost identical HAADF column signals due to their similar Z numbers. The implications of these observations are considered in Chapter 5 in terms of the dumbbell column ratio.

In order to gauge the spatial sensitivity of EELS to a particular type of atomic column, the degree of change in the related EELS signal can be mapped across a single dumbbell in a zinc-blende material. For instance, the EELS spatial sensitivity to an As column in GaAs can be estimated by comparing the total As EELS signal in the PPAs condition to the total As EELS signal in the PPGa condition. If there is not a significant change in the As EELS signal from the PPAs to PPGa conditions then the EELS spatial sensitivity to As columns is poor at that particular specimen thickness.

Figure 4.31 presents an estimate of the EELS spatial sensitivity to Al (in AlAs), Ga (in GaAs), As (in GaAs) and In (in InAs) as a function of specimen thickness. The ratio refers to the integrated crystal intensity down all of the columns of a particular type (e.g. all of the As columns in GaAs) with the probe centred on a column of that particular type (e.g. the PPAs condition in GaAs) divided by the integrated crystal intensity down all of the columns of that particular type with the probe centred on the neighbouring column in the dumbbell (i.e. the PPGa condition in GaAs). The integrated crystal intensity down all of the columns of a particular type was calculated in the same way as that described in Section 4.3.2.2 for Figure 4.10(a). Furthermore, in Figure 4.31, a large ratio value (>1) signifies that a particular EELS signal can differentiate between the columns in a dumbbell. A ratio value of 1 signifies that the sensitivity is poor and the difference in composition between the 2 types of atomic columns in a dumbbell cannot be distinguished using that particular EELS signal.

Figure 4.31 reveals that the Ga and As (from GaAs) ratios are very similar over all thicknesses. In fact, all of the As ratios from AlAs, GaAs and InAs are very similar (not shown). Figure 4.31 demonstrates that the Ga and As ratios peak at a value of 7 at a depth of about 3nm before dropping off to reach a constant value of about 1.5 at a depth of 100nm. Hence, in very thin specimens, the EELS sensitivity to Ga and As is very high and the composition of a dumbbell can be easily distinguished using EELS. However, this sensitivity reduces with increasing thickness and at large crystal depths it is more difficult to see the difference in the dumbbell composition using EELS. In comparison, the In ratio

plot has a similar shape to the Ga and As ratio plots but is smaller in value over all crystal depths. Moreover, above a crystal depth of 50nm, the In ratio remains fairly low (i.e. 1.45-1.28). Therefore, it is only below specimen thicknesses of about 50nm in which there is a large difference in the In EELS signal across an InAs dumbbell. In contrast, the Al ratio stays above a value of 3 for all crystal depths. This indicates that the EELS spatial sensitivity to Al is very good for all specimen thicknesses.

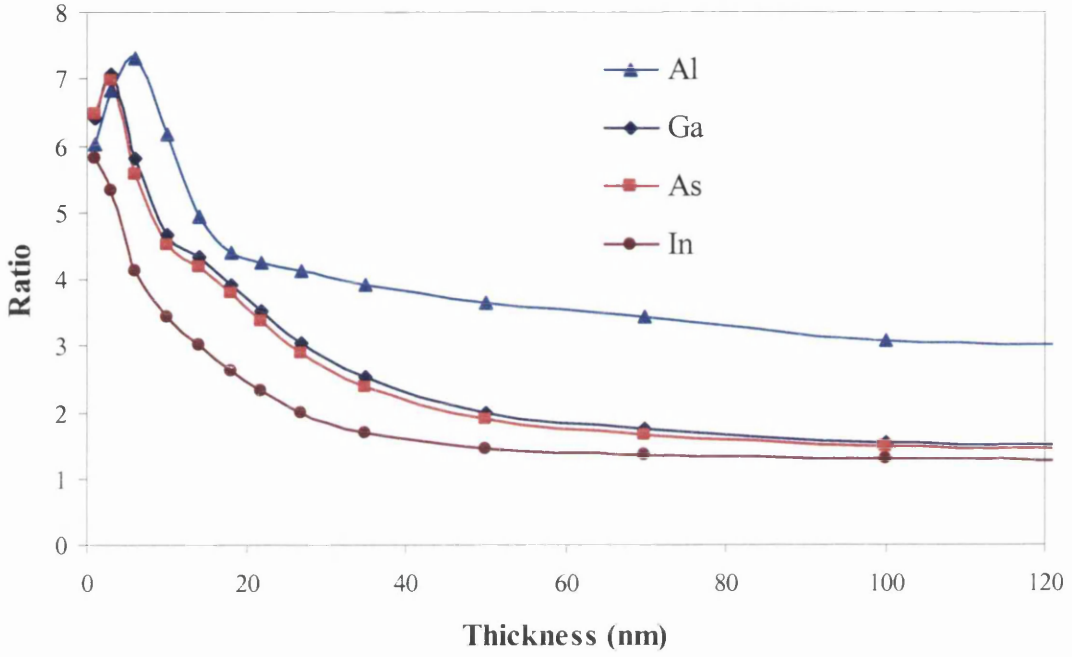

Figure 4.31: A graph of the ratio of the simulated integrated crystal intensity down all of the columns of a particular atom type with the probe centred on a column of the particular atom type divided by the integrated crystal intensity down all of the columns of a particular type with the probe centred on the neighbouring column in the dumbbell as a function of thickness. Al (from AlAs), Ga (from GaAs), As (from GaAs) and In (from InAs) ratios are shown.

4.4 Comparison of the Results from the 3 Probes

4.4.1 Introduction

This section deals with the assessment of the simulations that implemented the 50mrad and 12mrad probes. As was stated previously, the simulations that employed these 2 probes were first attempts and the probe conditions may not be optimum for the investigation. Real space intensity maps for both the 50mrad and 12mrad probes were calculated in the same manner as demonstrated for the 24mrad probe. However, only GaAs [110] and AlAs [110] were simulated for the 50mrad and 12mrad probes. For each material, the PPAs, PPGa (or PPAl) and PPBD probe conditions were simulated. In addition, due to the fact that this chapter is mainly concerned with simulations that are related to SuperSTEM 1, only the most important results from the 12mrad and 50mrad probe simulations are presented. The complete series of real space intensity maps and appropriate graphs are collected in Appendix A. Moreover, the results from the 50mrad and 12mrad simulations are presented in relation to those from the 24mrad probe simulations.

4.4.2 Probe Characteristics

4.4.2.1 50mrad Probe

The parameters that are associated with the 50mrad probe were chosen in order to create a probe similar in size to that expected of SuperSTEM 2. These include an accelerating voltage of 100kV and a probe convergence semi-angle of 50mrad. The version of the Kirkland software that was used does not have the facility to input higher order aberrations. Therefore, a C_3 aberration coefficient value of 0.03mm was used in order to generate a probe with the desired FWHM of 0.7Å. In order to choose the appropriate defocus value for the probe, the 4 measures of the probe size (as outlined in Section 4.3.1) were again considered as a function of defocus. The relevant graphs are shown in Figure 4.32(a) and Figure 4.32(b). However, in this case, there is only 1 defocus value that produces a probe with a FWHM equal to 0.7Å. This is again the Scherzer defocus value as defined by Kirkland and it is this probe defocus that is used in the simulations of the 50mrad probe.

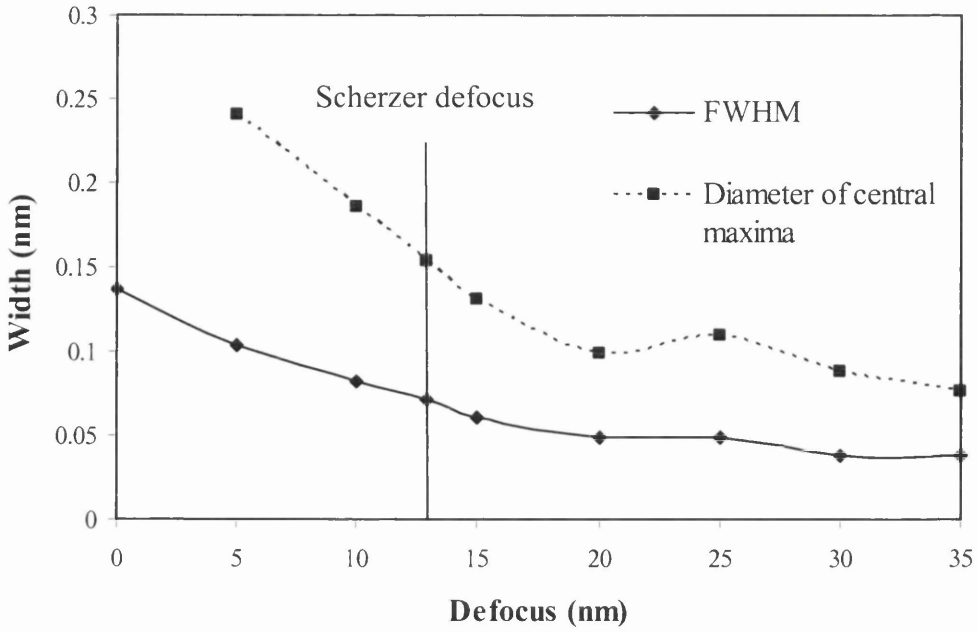

Figure 4.32(a): A graph of 2 measures of the 50mrad probe width as a function of defocus. The measures of the probe size are the FWHM and the diameter of the central maximum. The constant probe parameters are V = 100kV, convergence angle = 50mrad and C_3 = 0.03mm. Note that at a defocus of 0nm there is no central maximum.

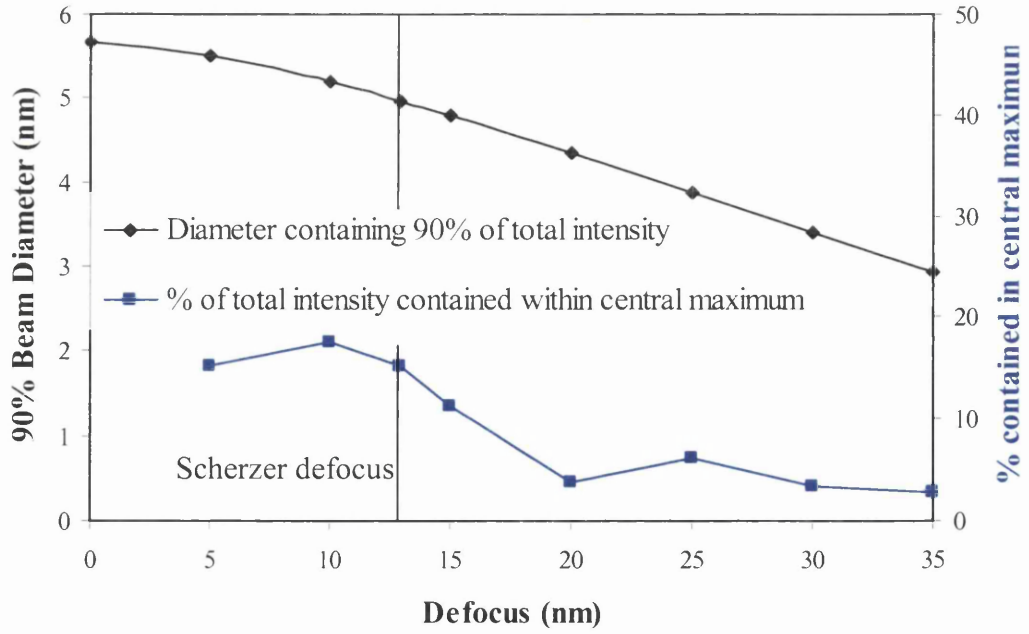

Figure 4.32(b): A graph of 2 measures of the 50mrad probe size as a function of defocus. The measures of the probe size are the diameter that contains 90% of the total probe intensity and the % of the total intensity that is contained within the central maximum. The constant probe parameters are V = 100kV, convergence angle = 50mrad and C_3 = 0.03mm. Note that at a defocus of 0nm there is no central maximum.

Figure 4.32(b) also reveals that it requires almost a diameter of 5nm in order to contain 90% of the total intensity. This is again due to the small background in the probe intensity map as discussed in Section 4.3.1. The values of the measures of the probe size are catalogued in Table 4.1 along with the input parameters. Table 4.3 reveals that if the small background is removed then the 90% of the total probe intensity is contained with a diameter of 0.67nm and 44% of the total probe intensity is contained within the central maximum. Figure 4.33 shows a line profile taken across the intensity of the 50mrad probe.

It should also be noted that the HAADF detector inner and outer angles were again equal to 70mrad and 210mrad, respectively. The inner angle of the detector may not be large enough in order to ensure that no diffraction effects arise. This is due to the fact that the 50mrad probe convergence angle is much larger than in the case of the 24mrad probe. However, the inner angle of the HAADF detector that is used in SuperSTEM 2 (i.e. a 50mrad probe) is unknown at present.

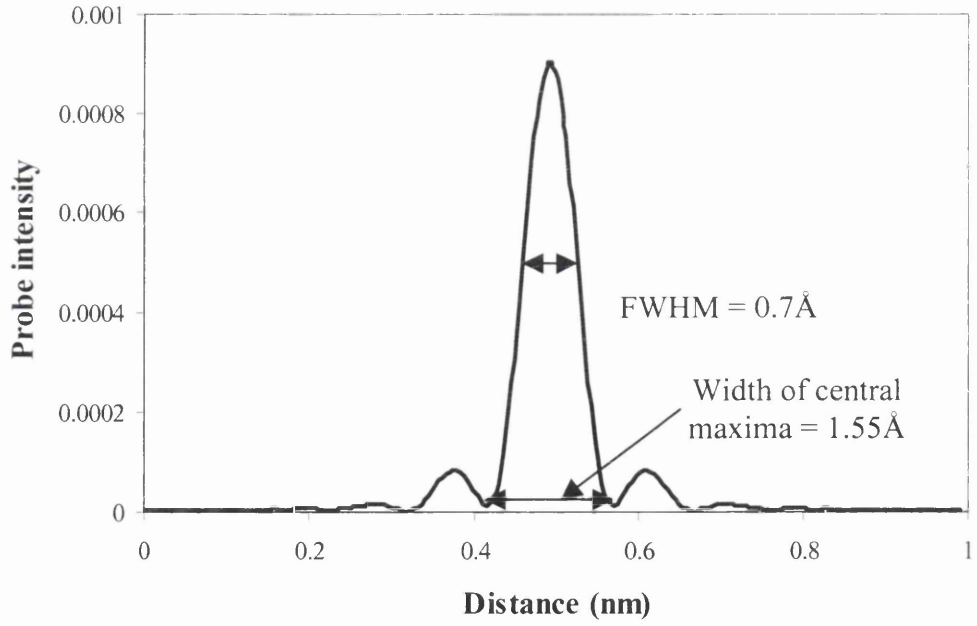

Figure 4.33: Line profile taken across the simulated 50mrad probe intensity map. Hence, Scherzer defocus was used. The FWHM is 0.7Å at 100kV accelerating voltage. The total electron intensity of the probe = 1

4.4.2.2 12mrad Probe

The parameters that are associated with the 12mrad probe were chosen in order to create a probe that could not resolve the dumbbell spacing in GaAs (1.4Å). These include an accelerating voltage of 100kV and a probe convergence semi-angle of 12mrad. The same

C_3 aberration coefficient value that was used for the 24mrad probe (0.1mm) was also used (along with the same HAADF detector angles) for the 12mrad probe. The reason for this choice was that the 12mrad probe simulations would then provide an indication of the probe behaviour in SuperSTEM 1 if a smaller than normal (24mrad) objective aperture was employed.

In order to choose the appropriate defocus value for the 12mrad probe, the 4 measures of the probe size (as outlined in Section 4.3.1) were again considered as a function of defocus. The relevant graphs are shown in Figure 4.34(a) and Figure 4.34(b). In this case, over the entire defocus range, the FWHM width is equal to 1.6Å as desired. In the same fashion, the diameter of the first maximum is almost fairly constant but it does start to reduce after 20nm defocus. Figure 4.34(b) reveals that the best defocus is not at Scherzer defocus unlike the case with the other 2 probes. However, for the 12mrad probe, Scherzer defocus was again employed in order to keep the chosen defocus value consistent with the other 2 probes. Figure 4.35 shows a line profile taken across the intensity of the 12mrad probe. The values of the 4 measures of the probe size are catalogued in Table 4.1 along with the input parameters. Table 4.3 reveals that if the small background is removed then the 90% of the total probe intensity is contained with a diameter of 0.56nm and 69% of the total probe intensity is contained within the central maximum.

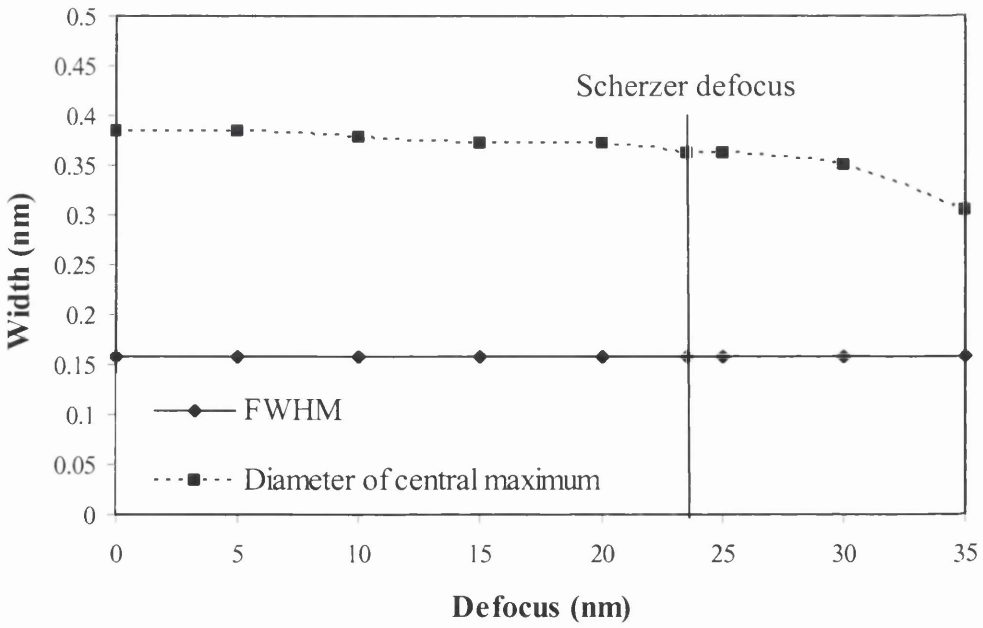

Figure 4.34(a): A graph of 2 measures of the 12mrad probe width as a function of defocus. The measures of the probe size are the FWHM and the diameter of the central maximum. The constant probe parameters are V = 100kV, convergence angle = 12mrad and C_3 = 0.1mm.

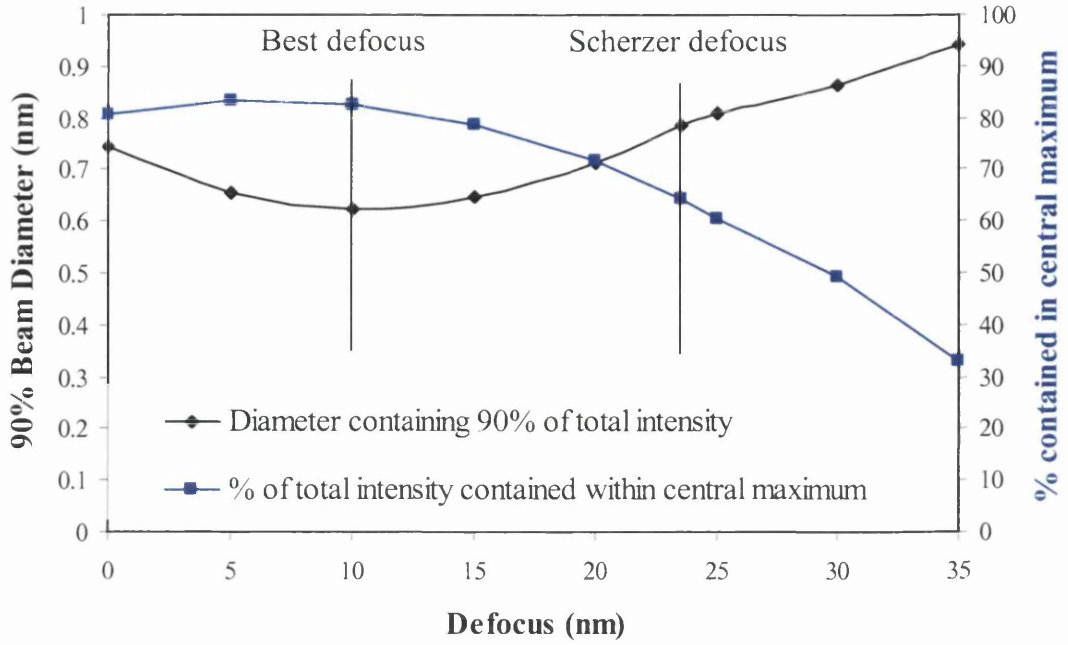

Figure 4.34(b): A graph of 2 measures of the 12mrad probe size as a function of defocus. The measures of the probe size are the diameter that contains 90% of the total probe intensity and the % of the total intensity that is contained within the central maximum. The constant probe parameters are V = 100kV, convergence angle = 12mrad and C_3 = 0.1mm.

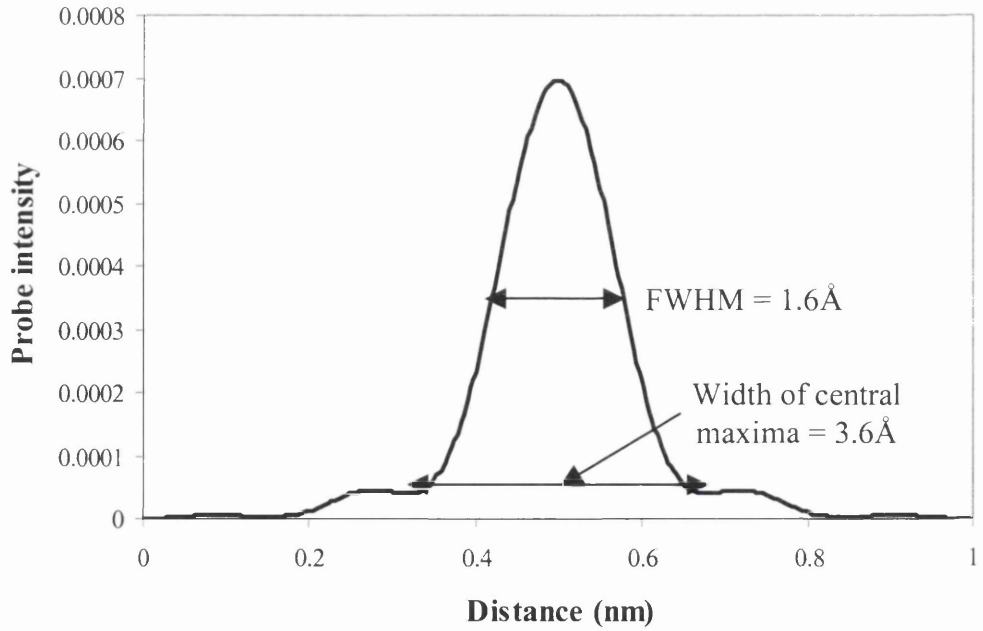

Figure 4.35: Line profile taken across the simulated 12mrad probe intensity map. Hence, Scherzer defocus was used. The FWHM is 1.6Å at 100kV accelerating voltage. The total electron intensity of the probe = 1

4.4.3 Comparison of the Real Space Crystal Intensities

Figure 4.36 shows the value of the real space crystal intensity that exists on the primary As column in GaAs [110] (i.e. the PPAs condition) for the 12mrad, 24mrad and 50mrad probes as a function of specimen thickness. It is evident that the fraction of the incident probe that forms on the As column is greatest in the case of the 12mrad probe and lowest in the case of the 50mrad probe. This is likely due to the different initial intensity distributions of the probes. For instance, although the 50mrad probe has the lowest FWHM width, its central maximum contains only 15% of the total probe intensity in comparison to the 35% and 64% associated with the 24mrad and 12mrad probes (Table 4.1). Hence, a smaller fraction of the intensity is incident on and captured by the primary As column in the case of the 50mrad probe.

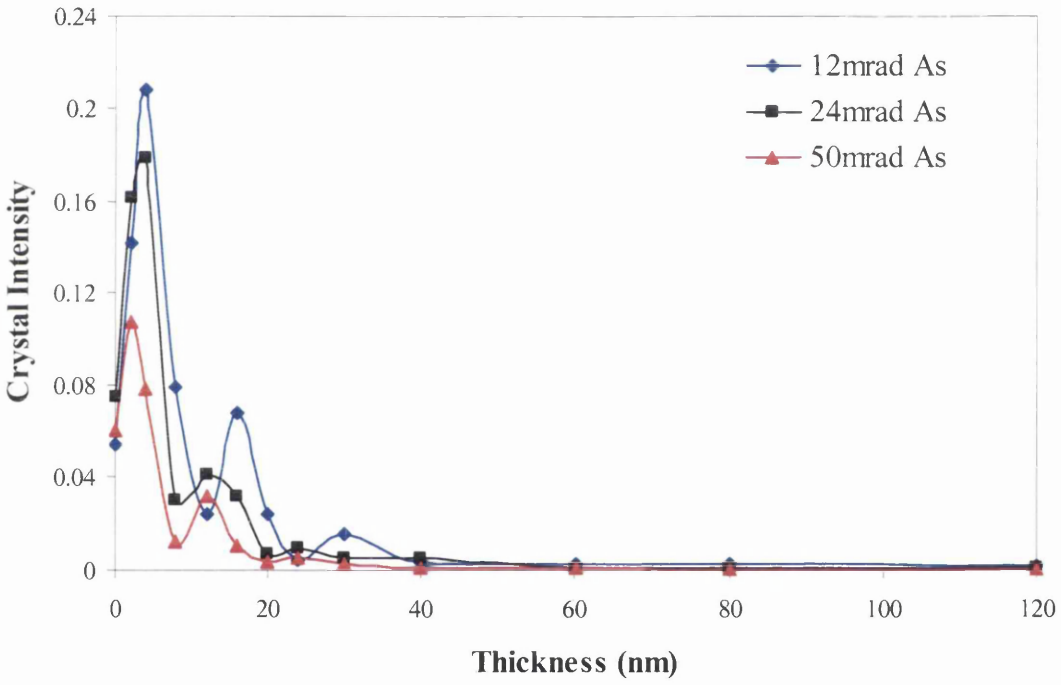

Figure 4.36: A graph of the simulated real space electron intensity along As columns in GaAs [110] for the 12mrad, 24mrad and 50mrad probes as a function of specimen thickness. The probe is incident on an As column on the top surface of the specimen. The values are the sum of a 9pixel × 9pixel area around each column in the intensity maps. The intensity is normalised with respect to the total intensity in the probe (equal to 1).

Figure 4.36 also illustrates that the electron intensity distribution down the As column has a similar appearance for the 24mrad and 50mrad probes. On the other hand, the intensity fluctuations along the column occur at different depths in the 12mrad probe case. In addition, the strong channelling depth (i.e. the depth at which the intensity becomes less than 5% of the maximum intensity on a column) is similar for all probes. For example, it is

equal to 20nm for the 24mrad and 50mrad probes and equal to 24nm in the case of the 12mrad probe.

Figure 4.37 shows the real space crystal intensity that exists on the primary Ga column in GaAs [110] (i.e. the PPGa condition) for the 3 probes as a function of specimen thickness. As expected from the similar Z numbers of Ga and As, the PPGa condition results in similar intensity variations as those associated with the PPAs condition for all 3 probes. For instance, the strong channelling depth on the Ga column is the same as on the As column for all probes. Furthermore, the maximum intensity on the Ga column occurs at a slightly lower thickness of 2nm for the 50mrad compared to 4nm for the other 2 probes. This behaviour is also apparent for the PPAs condition.

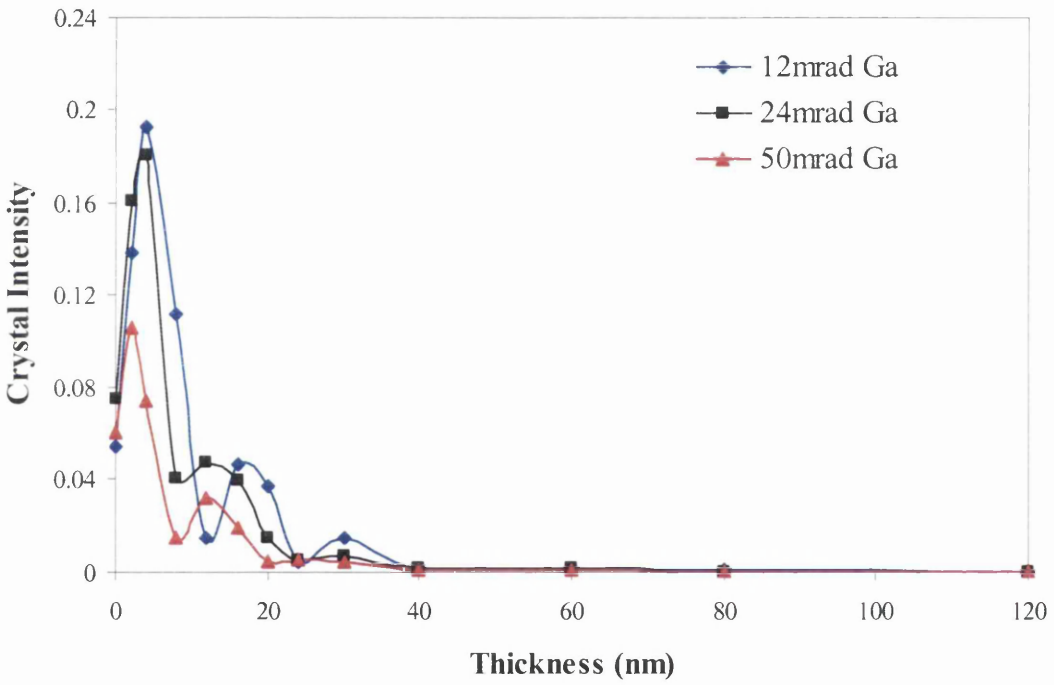

Figure 4.37: A graph of the simulated real space electron intensity along Ga columns in GaAs [110] for the 12mrad, 24mrad and 50mrad probes as a function of specimen thickness. The probe is incident on a Ga column on the top surface of the specimen. The values are the sum of a 9pixel × 9pixel area around each column in the intensity maps. The intensity is normalised with respect to the total intensity in the probe (equal to 1).

Figure 4.38 presents the crystal intensity variation along the primary Al column in AlAs [110] (i.e. the PPAl condition) for the 3 probes as a function of thickness. As was observed with the PPAs and PPGa conditions in GaAs, the Al column captures a higher fraction of the incident intensity in the 12mrad probe case. Figure 4.38 also reveals that the position of

the maximum intensity on the Al column shifts to lower depths as the probe convergence semi-angle is increased from 12mrad to 50mrad. For instance, the maximum intensity occurs at a depth of 8nm, 4nm and 2nm for the 12mrad, 24mrad and 50mrad probes, respectively. In addition, the strong channelling depth is greater than 120nm for all 3 probes.

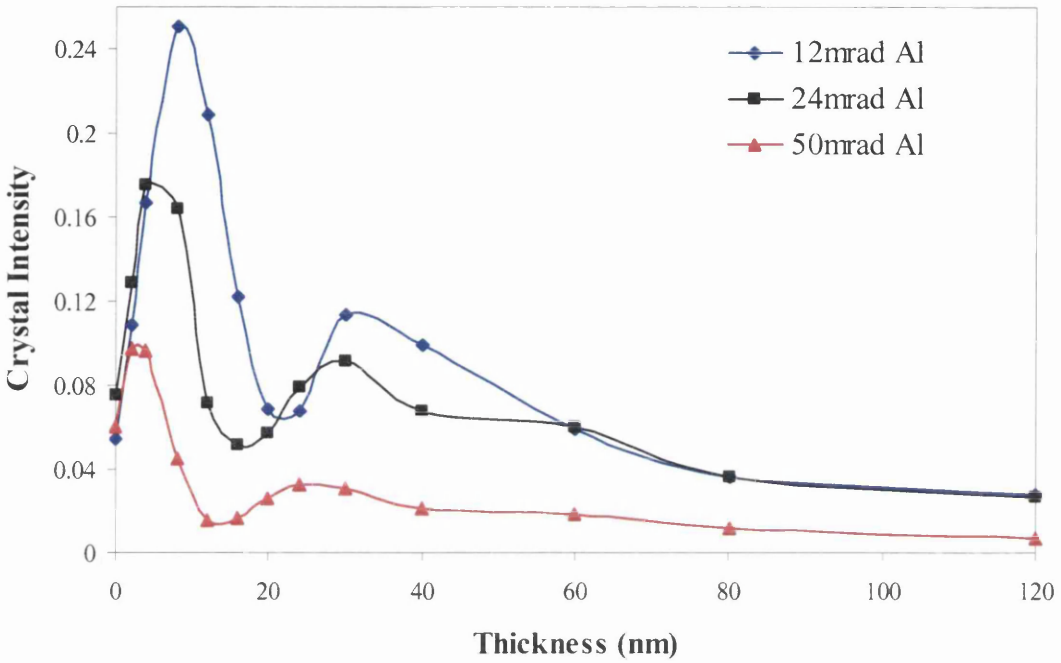

Figure 4.38: A graph of the simulated real space electron intensity along Al columns in AlAs [110] for the 12mrad, 24mrad and 50mrad probes as a function of specimen thickness. The probe is incident on an Al column on the top surface of the specimen. The values are the sum of a 9pixel × 9pixel area around each column in the intensity maps. The intensity is normalised with respect to the total intensity in the probe (equal to 1).

Figure 4.39 shows the thickness variation of the (integrated) crystal intensity on the primary As column / the (integrated) intensity on all As sites in GaAs [110] (PPAs condition) for the 3 different probes. As was discussed in Section 4.3.2.2, these plots provide an estimate of the contribution by the primary As column to the total As EELS signal in GaAs [110] (PPAs condition). Figure 4.39 demonstrates that the contribution of the primary As column is significantly reduced over all thicknesses as the probe convergence semi-angle is increased. This indicates that, despite the greater spatial resolution offered by the 50mrad (and 24mrad) probe(s), the ability to investigate column composition via EELS is proportionally worse in the smaller probes. This is due to the

relatively small portion of the incident probe intensity that is captured by the primary column in the case of the smaller probes.

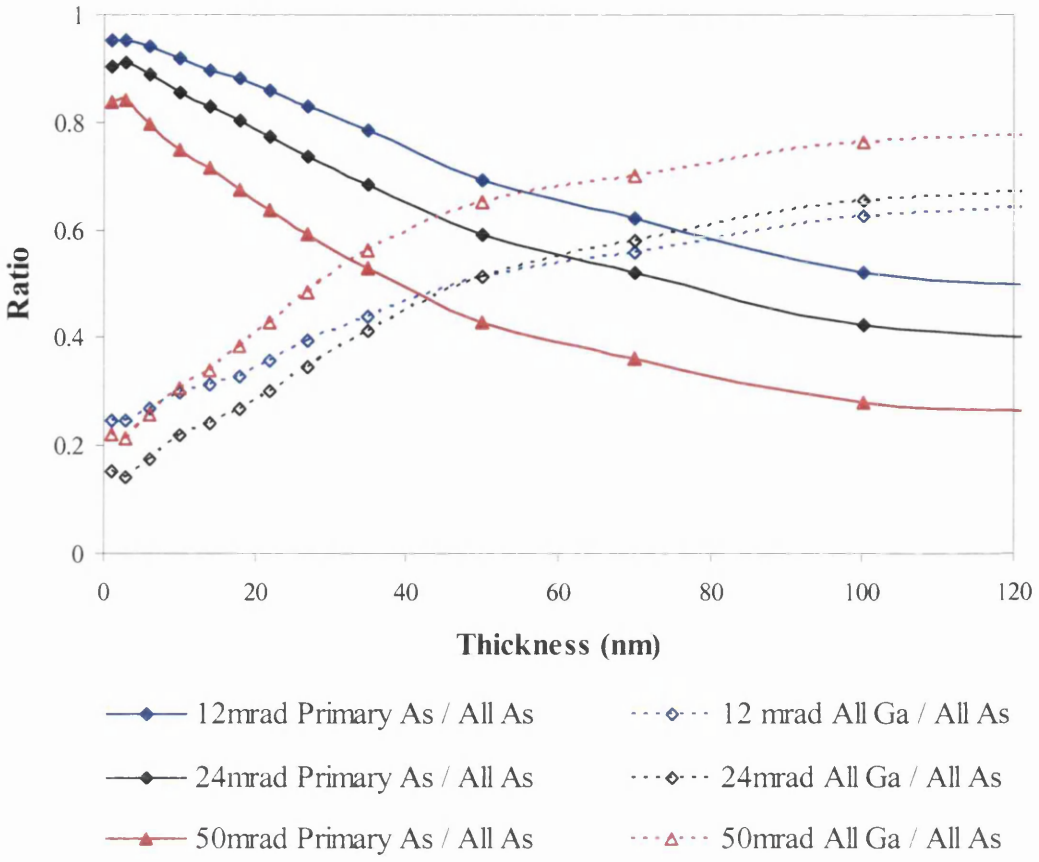

Figure 4.39: A graph of the simulated integrated crystal intensity on the primary As column / all As sites in GaAs [110] for the 12mrad, 24mrad and 50mrad probes as a function of thickness. The probe is incident on an As column on the top surface of the specimen. Also shown is the simulated integrated crystal intensity on all Ga sites / all As sites for the 3 probes as a function of thickness.

Figure 4.39 also shows the (integrated) crystal intensity on all Ga sites / the (integrated) intensity on all As sites in GaAs [110] (PPAs condition) for the 3 different probes. As was discussed in Section 4.3.2.2, these plots give an indication of the strength of the Ga EELS signal in relation to that of the As EELS signal with the probe centred on an As column. Since the plot for the 24mrad is lowest (up to a depth of about 50nm), the ability to discriminate between Ga and As columns using EELS should be the best for this probe (up to 50nm). On the other hand, the 50mrad probe is the worst after a depth of only 10nm.

4.4.4 Comparison of the HAADF STEM Signals and Beam Spread

Figure 4.40 shows the simulated As column HAADF signal in GaAs [110] (PPAs condition) for the 3 probes as a function of thickness. It can be seen that the As column signal for the 12mrad and 24mrad probes are similar in value except between the depths of 8nm and 24nm in which the 12mrad plot has the greatest value. In contrast, the plot for the 50mrad probe is in general much lower than that of the other 2 probes. The maximum HAADF signal for the 12mrad and 24mrad probes also occur at the same depth of 20nm. However, this peak takes place at only 16nm in the case of the 50mrad probe. Equivalent behaviour is also observed for the condition of the probe incident on the Ga column (PPGa) in GaAs [110] (see Figure 4.41).

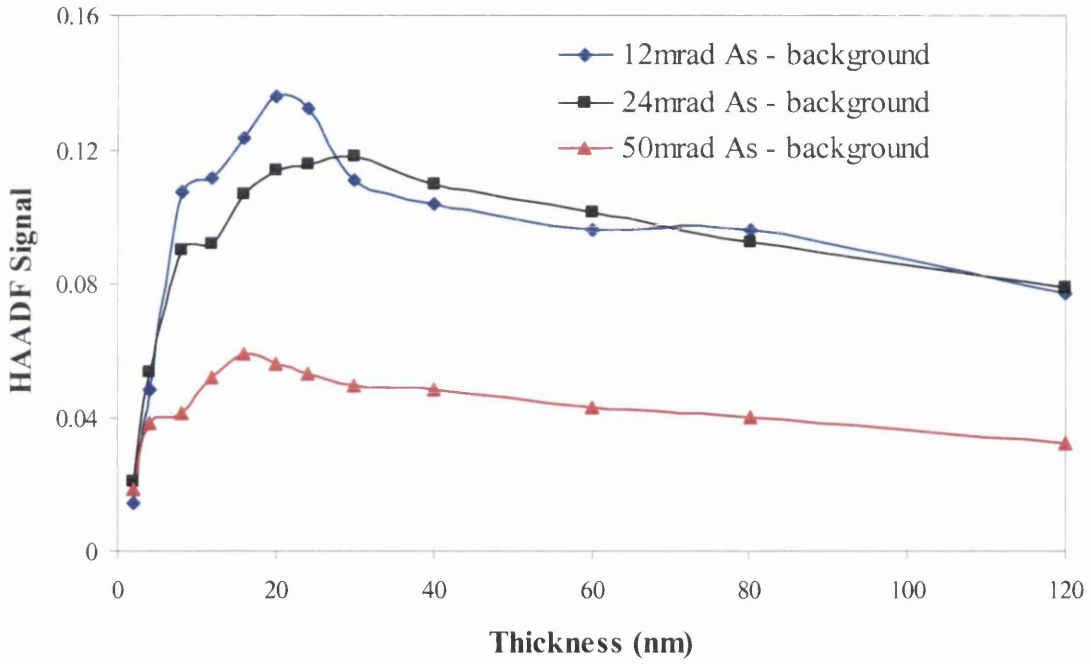

Figure 4.40: Simulated As column HAADF STEM intensities in GaAs [110] for the 12mrad, 24mrad and 50mrad probes as a function of specimen thickness. The probe is incident on an As column on the top surface of the specimen The HAADF signal is normalised with respect to the intensity that the probe generates in the detector plane in the absence of a specimen. The HAADF detector has a range of 70mrad to 210mrad.

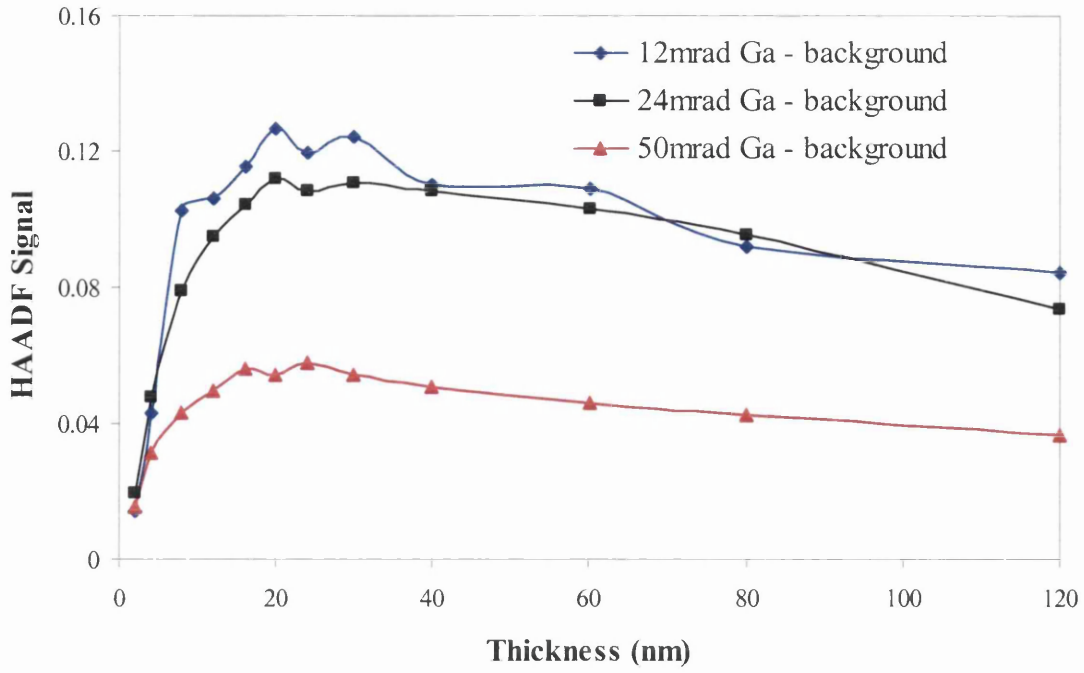

Figure 4.41: Simulated Ga column HAADF STEM intensities in GaAs [110] for the 12mrad, 24mrad and 50mrad probes as a function of specimen thickness. The probe is incident on a Ga column on the top surface of the specimen The HAADF signal is normalised with respect to the intensity that the probe generates in the detector plane in the absence of a specimen. The HAADF detector has a range of 70mrad to 210mrad.

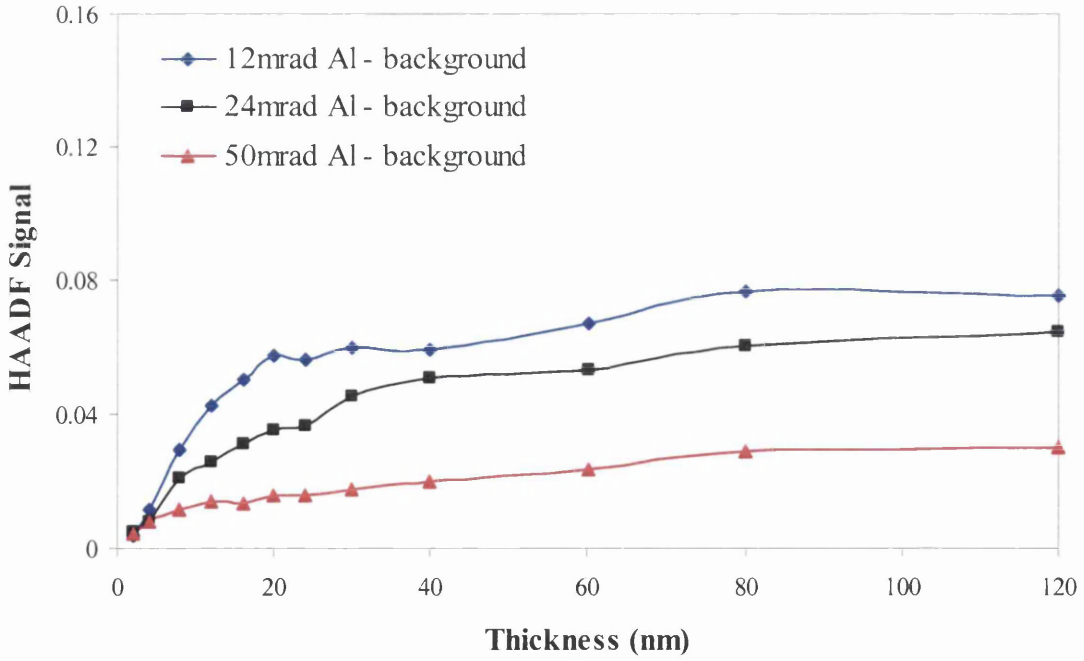

Figure 4.42: Simulated Al column HAADF STEM intensities in AlAs [110] for the 12mrad, 24mrad and 50mrad probes as a function of specimen thickness. The probe is incident on an Al column on the top surface of the specimen The HAADF signal is normalised with respect to the intensity that the probe generates in the detector plane in the absence of a specimen. The HAADF detector has a range of 70mrad to 210mrad.

Figure 4.42 presents the simulated Al column HAADF signal in AlAs [110] (PPAl condition) for the 3 probes as a function of thickness. The Al column signal increases over almost the entire thickness range in all 3 plots due to the large channelling depth that is associated with the probes (see Figure 4.38). However, after 80nm, the plots start to tail off as the crystal intensity on the Al column reduces in value (Figure 4.38). In addition, the 12mrad Al column signal has, once again, the greatest value.

The HAADF background signals for the 3 probes in AlAs [110] (PPBD condition) are shown in Figure 4.43 as a function of thickness. The graph of AlAs is shown instead of GaAs due to the fact that the background signal should be less affected by the limitations in the supercell size (as discussed in Section 4.3.2.3) due to the lower scattering power of AlAs compared to GaAs.

Figure 4.43 reveals that the 12mrad probe generates the largest background signal whereas the 24mrad probe generates the smallest. This is in spite of the fact that the geometrical spread of the 12mrad should be the lowest of the 3 probes due to its smaller convergence semi-angle. Figure 4.44 shows the beam width (defined as the diameter that contains 90% of the total probe intensity) in AlAs [110] (PPBD condition) for the 3 probes as a function of thickness. It is apparent that the beam diameter for the 12mrad is lower than that of the other 2 probes up to a thickness of about 60nm. However, it is also clear that the beam diameter associated with the 12mrad probe does not increase linearly with thickness in the same way as for the 24mrad plot. In fact, the rate of beam expansion increases as the thickness goes up in the 12mrad probe case. The reason for this is unclear. However, Figure 4.43 and Figure 4.44 suggest that the beam diameter (and therefore beam spreading) is not strongly related to the generation of the simulated HAADF background signal. This does not seem physically realistic and could be a result of the fact that the 12mrad and 50mrad probes were not optimised properly.

Figure 4.44 also reveals the thickness variation in the beam diameter of the 50mrad probe. This plot is characterised by a large value of the beam diameter over all depths of crystal. This is due to the initial distribution of the 50mrad probe in which 90% of the total intensity is contained in a diameter of about 5nm (see Table 4.1). Hence, on this measure of the beam diameter, the initial intensity of the probe is almost at the edge of the supercell. Hence, the supercell is not big enough in order to measure the spreading of the 50mrad probe beyond about 30nm, which is the depth at which the 90% circle diameter hits the supercell edge. Therefore, the chosen probe characteristics of the 50mrad probe were clearly not optimum for this type of beam spreading analysis.

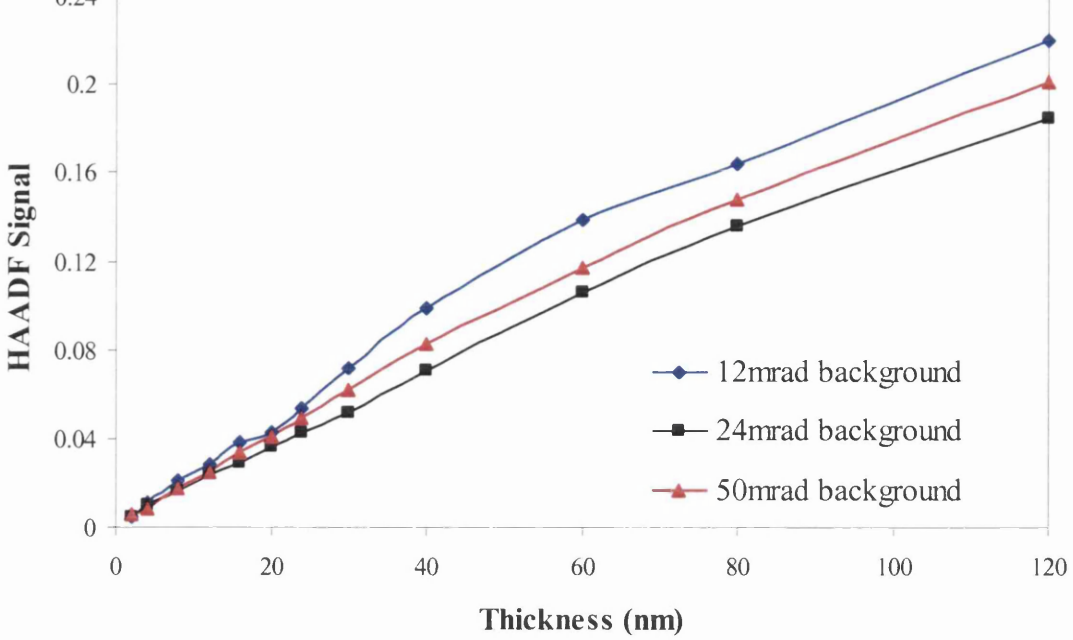

Figure 4.43: Simulated HAADF STEM background intensities in AlAs [110] for the 12mrad, 24mrad and 50mrad probes as a function of specimen thickness. The probe is incident between dumbbells (PPBD condition) on the top surface of the specimen The HAADF signal is normalised with respect to the intensity that the probe generates in the detector plane in the absence of a specimen. The HAADF detector has a range of 70mrad to 210mrad.

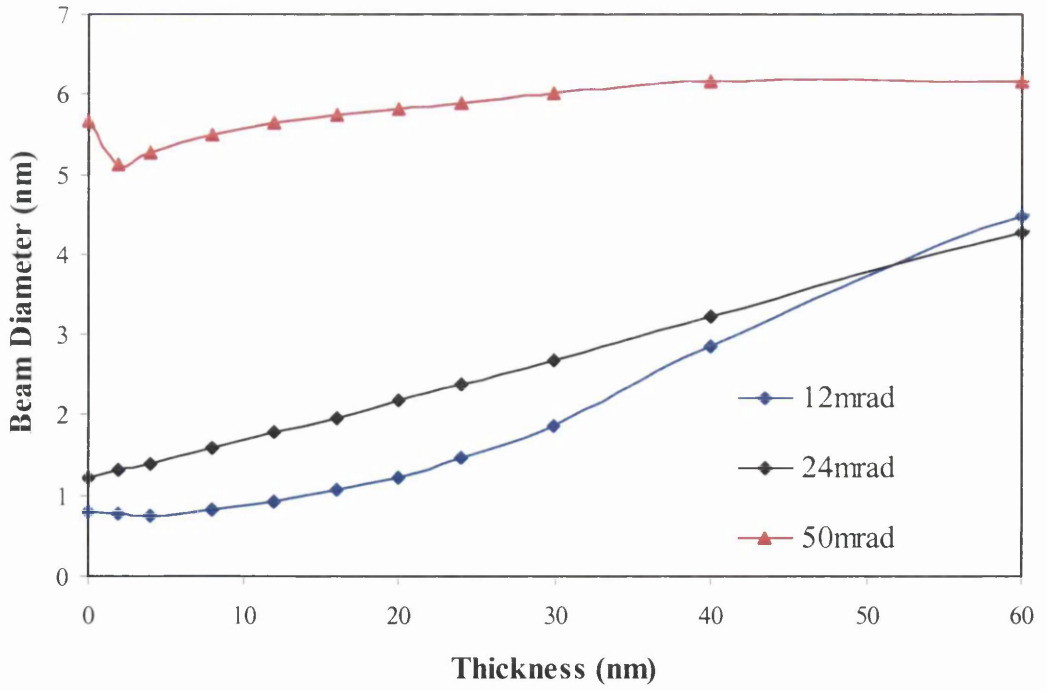

Figure 4.44: A graph of the simulated beam width as a function of specimen thickness in AlAs [110] for the 12mrad, 24mrad and 50mrad probes as a function of specimen thickness. These were calculated for the probe situated between dumbbells (PPBD condition). The beam width is given as the diameter of circular areas, in the real space intensity maps, in which 90% of the total probe intensity is contained. The circular areas are centred on the initial probe position.

4.5 Summary

In this chapter, a computer modelling investigation of the scattering behaviour of Å-scale probes in common III-V semiconductor materials was presented. The majority of chapter focused upon simulations that used a probe with a convergence semi-angle of 24mrad and a FWHM width of 1Å, similar to SuperSTEM 1. A comparison of the results from the 24mrad probe was also made with those from simulations that employed probes with FWHM widths of 0.7Å and 1.6Å and convergence semi-angles of 50mrad and 12mrad, respectively.

The materials were chosen as they are commonly found in high mobility heterostructures and also formed part of structures that were investigated through the use of SuperSTEM 1. The materials comprised the fcc crystals of GaAs, AlAs and InAs. They were studied in the familiar dumbbell configuration of the <110> orientation.

The investigation relied upon the exploitation of E. J. Kirkland's computer software. This allowed multislice calculations to be performed and the simulation of thermal diffuse scattering through the use of the frozen phonon method. For each material, the electron intensity distribution inside the crystal was mapped as a function of specimen thickness for 3 different probe positions. It was found that these intensity maps were complicated and sometimes difficult to interpret correctly. For those reasons, the intensity at important positions within the maps was plotted as a function of thickness. This allowed the degree of column channelling to be ascertained for each material.

For the 24mrad probe in GaAs, it was found that the channelling of the electron intensity down As and Ga columns lasted for 24nm. On the other hand, the shortest channelling depth was found to be just 16nm for an In column (in InAs). However, the channelling was calculated to last over the whole range of specimen thickness (120nm) for an Al column in AlAs. This gives an indication of the importance of the column Z number in the scattering of electron probes.

Furthermore, the intensity distribution down an atomic column was shown to have important consequences for EELS measurements. For instance, it was estimated that it is only the top portion of the atomic column (situated under the incident probe) that contributes to the primary column's EELS signal. Moreover, the fluctuating behaviour of the column intensity as a function of specimen thickness means that a dopant atom is difficult to detect if located at an intensity minimum. In addition, it was also shown that the

ability to differentiate column composition using EELS became worse as the specimen thickness was increased.

HAADF STEM simulations were also performed for the 3 materials using the 24mrad probe. These employed the same detector angles that are used in SuperSTEM 1. The channelling extinction depths were discovered to have important consequences for the HAADF signals generated by atomic columns. For instance, it was shown that the HAADF column signal mainly increased for the thickness range in which electron intensity is channelled along an atomic column.

GaAs and AlAs were also simulated using the 50mrad and 12mrad probes. The most important results from the 3 probes are shown in Table 4.4. It was found that the strong channelling depth along As, Ga and Al columns were not affected by the size and shape of the probe that was incident upon them. However, the actual value of the electron intensity that formed on the columns was significantly reduced in the case of the 50mrad probe. This was due to the relatively small concentration of intensity within the central maximum of the initial 50mrad probe. It is uncertain if this is a realistic starting probe characteristic.

	Column	12mrad	24mrad	50mrad
Strong channelling depth (nm) <5% max	As (GaAs)	24	20	20
	Ga	24	20	20
	Al	>120	>120	>120
Depth of zero intensity (nm) <0.5% max	As (GaAs)	>120	60	80
	Ga	80	80	80
	Al	>120	>120	>120
Depth of maximum HAADF column signal (nm)	As (GaAs)	20	20	16
	Ga	20	24	16
	Al	80	120	120

Table 4.4: A table of the important results for the 12mrad, 24mrad and 50mrad probes in GaAs [110] and AlAs [110].

In addition, it was also established that the capacity to investigate composition via EELS is proportionally worse in the case of the 50mrad and 24mrad probes compared to the wider

12mrad probe. Hence, the improvement in spatial resolution of the latest sub-Å probe of SuperSTEM 2 may be also be accompanied by a deterioration in the quality of the EELS analysis that can be obtained from the instrument.

The HAADF STEM column signals were also calculated in GaAs and AlAs for the 3 probes. There was a slight variation in the thickness at which the maximum HAADF column signal was observed for As and Ga columns for the 3 different probes (see Table 4.4). The HAADF background signals of the 3 probes in AlAs were also compared. It was discovered that the 12mrad probe produced the largest background signal despite the fact that its beam diameter was significantly lower than that of the other 2 probes. This suggests that beam width and beam spreading is not be directly related to the HAADF background signal in these multislice calculations.

It is uncertain how closely the simulated 24mrad probe results match those obtained from experimental methods. For instance, the beam diameter was shown to be incorrect after a depth of 80nm due to intensity spreading outside of the supercell. Hence, Chapter 5 centres on the comparison of simulated and experimental values of image contrast and dumbbell column ratios.

References

[1] K. Ishizuks, A practical approach for STEM imaging based on the FFT multislice method, Ultramicroscopy 90, 71-83 (2002)

[2] E. J. Kirkland, Advanced Computing in Electron Microscopy, Plenum Press, New York (1998)

[3] J. S. Blakemore, Gallium arsenide, Key Papers in Physics, American Institute of Physics (1987)

[4] C. Dwyer, J. Etheridge, Scattering of Å-scale electron probes in silicon, Ultramicroscopy 96, 343-360 (2003)

[5] L. M. Peng, Electron atomic scattering factors and scattering potentials of crystals, Micron 30, 625-648 (1999)

[6] J. S. Reid, Debye-Waller factors of zinc-blende structure materials-a lattice dynamical comparison, Acta Crystallographica Section A, Foundations of Crystallography A39, 1-13 (1983)

[7] S. Van Aert, P. Geuens, D. van Dyck, C. Kisielowski, J. R. Jinschek, Electron channelling based crystallography, Ultramicroscopy 107, 551-558 (2007)

[8] S. J. Pennycook, B. Rafferty, P. D. Nellist, Z-contrast imaging in an aberration-corrected scanning transmission electron microscope, Microscopy Microanalysis 6, 343-352 (2000)

[9] P. D. Nellist, S. J. Pennycook, Subangstrom resolution by underfocused incoherent transmission electron microscopy, Physical Review Letters, Volume 81, Number 19, 9 (1998)

[10] P. D. Nellist, S. J. Pennycook, Incoherent imaging using dynamically scattered coherent electrons, Ultramicroscopy 78, 111-124 (1999)

[11] B. Rafferty, P. Nellist, J. Pennycook, On the origin of transverse incoherence in Z-contrast STEM, Journal of Electron Microscopy 50, 227-233 (2001)

[12] R. F. Egerton, Limits to spatial, energy and momentum resolution of electron energy-loss spectroscopy, Ultramicroscopy, doi: 10.1016/j.ultramic.2006.11.005 (2007)

[13] C. B. Boothroyd, R. E. Dunin-Borkowski, W. M. Stobbs, C. J. Humphreys, Quantifying the effects of amorphous layers on image contrast using energy filtered transmission electron microscopy, MRS Symposium Proceedings Vol 354, pp. 495-500 (1995)

[14] R. F. Egerton, Electron energy-loss spectroscopy in the electron microscope, 2nd edition, Plenum Press (1996)

[15] P. D. Nellist, Atomic resolution annular dark field imaging: theory and simulation, SuperSTEM summer school (2006)

5 Experimentally Derived HAADF STEM Image Contrast and Dumbbell Column Ratios

5.1 Introduction

The computer modelling investigation in Chapter 4 demonstrated the way in which the HAADF signal is affected by the channelling of electrons along atomic columns. This involved the calculation of the HAADF signal at various probe positions as a function of specimen thickness. In order to examine the validity of the results obtained from the calculations, it is apparent that the results need to be compared with those obtained from experiment. However, in SuperSTEM 1, it is not possible to acquire an absolute reading of the electron intensity that falls on the HAADF detector, as there is no facility to directly measure the probe current for each image. The situation is further complicated by the fact that the current from the SuperSTEM 1 FEG varies over time.

Nonetheless, there are two experimental image properties that can be exploited in order to compare with the simulations. The first property is the image contrast. The HAADF image contrast (in a HAADF image of a III-V material orientated in the [110] direction) is defined as the maximum signal (on the dumbbells, I_D) minus the background signal (between the dumbbells, I_{BD}) divided by the background (I_{BD}). Hence:

$$\text{Image Contrast} = \frac{\text{Max dumbbell signal - background signal}}{\text{background signal}} = \frac{I_D - I_{BD}}{I_{BD}}$$

Since the image contrast is a relative quantity, the precise value of the probe current does not have an effect upon it.

The measurement of the HAADF contrast not only provides a greater understanding of the image process but also establishes the specimen thickness range that is necessary in order to obtain an adequate level of image signal above the background in the image. Therefore, this chapter presents an enquiry into the thickness variation of the HAADF image contrast for a variety of materials. Results are shown for the Tecnai F20 as well as for SuperSTEM 1.

The second experimental image property that can be used to explore the validity of the simulations is the dumbbell column ratio. As explained in Chapter 3, the column ratio of GaAs is defined as:

$$\text{Dumbbell Column Ratio} = \frac{\text{Ga column HAADF signal}}{\text{As column HAADF signal}} = \frac{I_{Ga} - I_{BD}}{I_{As} - I_{BD}}$$

where I_{Ga} and I_{As} refer to the full HAADF intensity that is present on the Ga and As sites in a single dumbbell, respectively. The results from the MODFET heterostructure, as shown in Chapter 3, highlighted the poor agreement between the experimentally derived dumbbell column ratios and those predicted by the simple Z^2 theory. In addition, the interpretation of the dumbbell column ratio maps in Chapter 3 (especially the map of the deep superlattice) was made problematic because the actual column ratio values of the different materials were unknown. This chapter, therefore, presents an investigation into thickness variation of the dumbbell column ratio for GaAs and AlAs through the use of SuperSTEM 1.

5.2 Tecnai F20 HAADF Image Contrast

5.2.1 Method

The thickness variation of the HAADF contrast was carried out using 2 different probe conditions in the Tecnai F20. The probe convergence semi-angles were 8.8mrad and 12.6mrad, respectively. Si [110] and GaAs [110] were both investigated using these 2 probe angles. The 2 specimens were prepared using the cross-section technique and were finished with 400eV ions at an angle of 6° through the use of a GentleMill. In addition, the HAADF inner and outer angles for the Tecnai F20 were 50mrad and 227mrad, respectively.

The data for each material, using a particular probe condition, is collected as follows. A small section of the specimen (6nm × 6nm) is chosen in order to acquire a HAADF STEM lattice image. An example of this is shown in Figure 5.1(a). A low loss EELS map is then taken across a region of the image. The EELS collection semi-angle is 1mrad. The spectra from an EELS map allow a measurement to be made of the change in the specimen thickness that is present across the image region. However, due to the small dimensions of the image, the thickness should not change very much across the region. The collection of

the HAADF image and the associated EELS map is then repeated at different specimen positions in order to produce data over a wide thickness range.

In order to measure the image contrast and thickness, several Digital Micrograph scripts were created. These help to analyse the HAADF images and the EELS maps. To begin with, an EELS map is converted into a map of the specimen thickness through the use of the log-ratio method in Digital Micrograph. This software allows the calculation of the absolute specimen thickness (in nm) if the beam energy, STEM convergence semi-angle, EELS collection semi-angle and effective Z number of the material is known (see Section 2.5).

In the next step, the positions of the all the dumbbells in a single HAADF image are measured, and recorded, using Digital Micrograph's particle locator tool. This is the same method as was employed in the scripts that involved the calculation of the dumbbell column ratio maps. These were presented in Chapter 3. Once again, the Digital Micrograph tool outputs the image coordinates of the central position of each dumbbell. In an analogous way, the positions between all of the dumbbells are also recorded.

The position of the pixel within each dumbbell that has the highest image intensity (P_{max}) is then established. In the case of a composite material, such as GaAs, P_{max} should be located on the side of the dumbbell that contains the column with the highest Z number, as was explained in Chapter 3. However, due to the fact that the dumbbell spacing (1.4Å in GaAs) cannot be resolved with the Tecnai F20, no consistent difference in the 2 column intensities can be observed in the dumbbells. This is highlighted by the intensity line profile of 2 GaAs dumbbells in Figure 5.1(b). This clearly shows that the 2 columns cannot be distinguished. Hence, P_{max} can occur anywhere along a dumbbell.

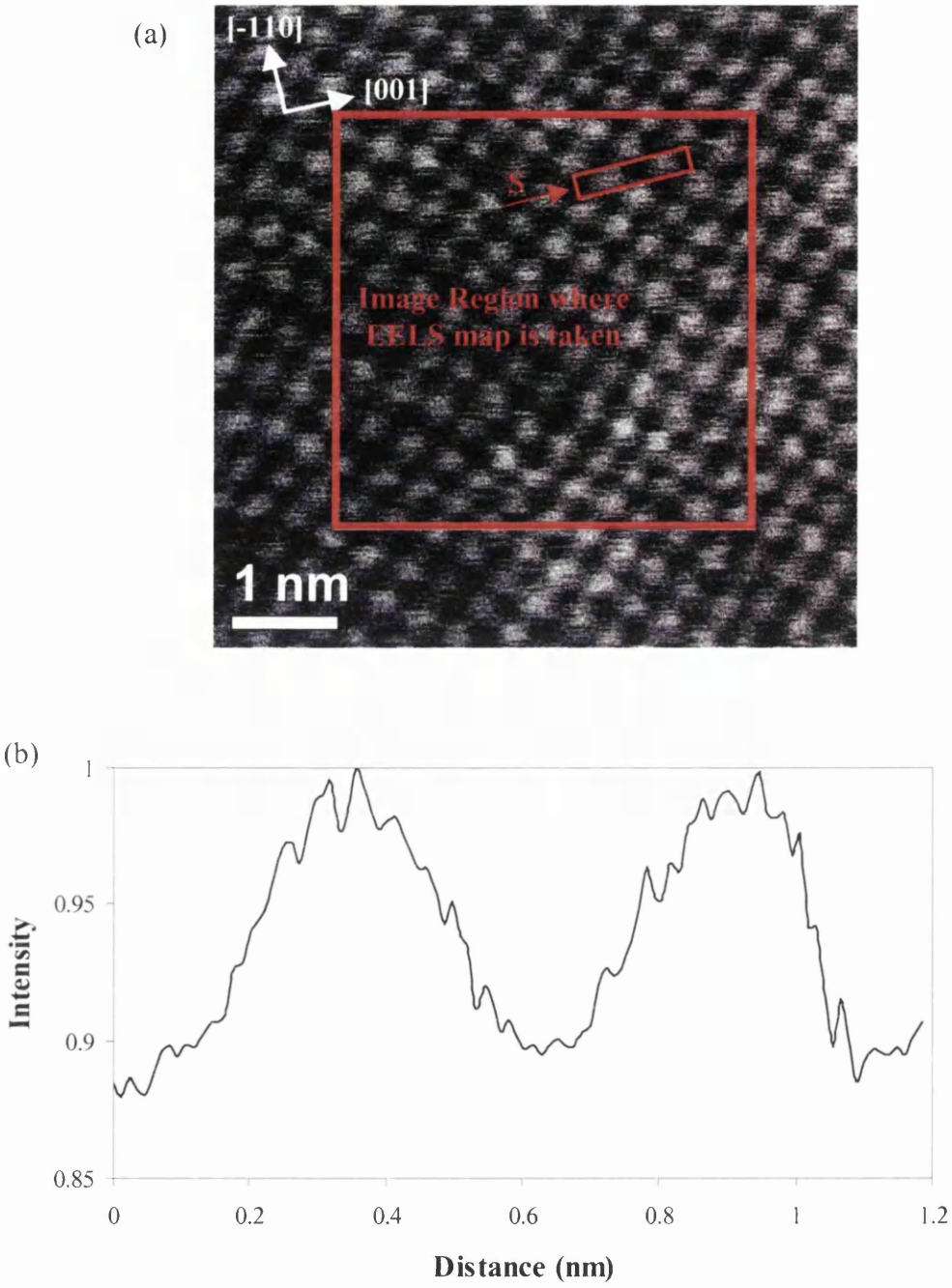

Figure 5.1(a): Tecnai TF20 HAADF STEM image of GaAs [110]. The probe convergence angle was 8.8mrad. The inner angle of the detector was 50mrad. The position of the EELS map is shown. **(b)** is an intensity profile taken across image section S in (a). Every pixel of the profile is generated from the average of 20 image pixels summed along the [-110] direction.

The equivalent position to P_{max} in the associated thickness map is also noted and the particular thickness value is stored for later. Subsequently, the script calculates the average intensity (I_{max}) that is contained within an area of size 6pixels × 6pixels (centred on the position of P_{max}) for every dumbbell. This averaged intensity is defined as the maximum image signal for a particular dumbbell. The script then outputs the I_{max} value for every dumbbell in the image along with their corresponding thickness values. In a similar fashion, the background signal (I_{min}) is output for each position between the dumbbells along with the associated thickness values. The whole process is repeated for every acquired HAADF image and thickness map.

All of the I_{max} and I_{min} values, for a particular image, are then averaged together to generate the image dumbbell signal and image background signal, respectively. The overall image contrast value is then computed by dividing the image dumbbell signal (minus the image background signal) by the image background signal. A contrast value of 1 would mean that the absolute value of the dumbbell signal was double the background signal.

Moreover, the average image thickness is calculated by taking the average of all the individual thickness measurements associated with both on dumbbells (i.e. the dumbbell signal) and between dumbbells (i.e. the background signal). The reason for not simply taking the average value of the thickness map in the first place is that not all of the dumbbells (or positions between the dumbbells) contribute to the calculation of the image dumbbell signal (or the image background signal). For instance, some dumbbells are not included in the averaging process because they are located on the edge of the image region and are not fully contained within the area over which the EELS map is taken. Hence, the thickness map pixels that are associated with those specific image positions should not contribute to the average thickness value. In addition, it is also useful to plot the thickness variation of the intensity of the individual dumbbells (and positions between the dumbbells) from a single image region. The reason behind this is that the build up of contamination often affects the spread of the values. Thus, the areas of the image that are affected by contamination can be removed from the analysis. This type of inspection partly led to a different thickness measurement technique being used for the acquisition of data from SuperSTEM 1 (see Section 5.3.1).

5.2.2 Si [110] Results

The HAADF STEM contrast for Si [110], as a function of thickness, is shown in Figure 5.2 for 2 probe convergence semi-angles in the Tecnai F20. Every point of each plot is the average image contrast measured from 1 HAADF image. The error bars that are associated with the contrast and thickness values have a value of 2 times the standard error in each case. It can be seen that the 2 plots have similar profiles. For example, the contrast is high at low specimen thickness and then drops off markedly as the thickness is increased in both cases. However, it is also apparent that for all specimen thicknesses shown, the 8.8mrad probe gives higher contrast than the 12.6mrad probe. This may be due to the difference in the sizes of the 2 probes. For instance, the radius of the first minimum in the probe intensity can be estimated through the calculation of the square root of $[(0.6\lambda / \beta)^2 + (0.25C_3\beta^3)^2]$ (see Section 2.2.4). The radius is 2.7Å for the 8.8mrad probe angle but is 6.1Å for the 12.6mrad probe angle. Therefore, when the 12.6mrad probe is incident on the specimen, the electron intensity is more widely distributed than in the case of the 8.8mrad probe. In addition, the tails on the 12mrad probe will also contain more intensity. Hence, the tails will increase the scattering from the surrounding dumbbells and the 12.6mrad probe will, therefore, generate a greater background signal than the smaller probe. This will also lead to a reduction in the contrast for the 12.6mrad probe as seen in Figure 5.2.

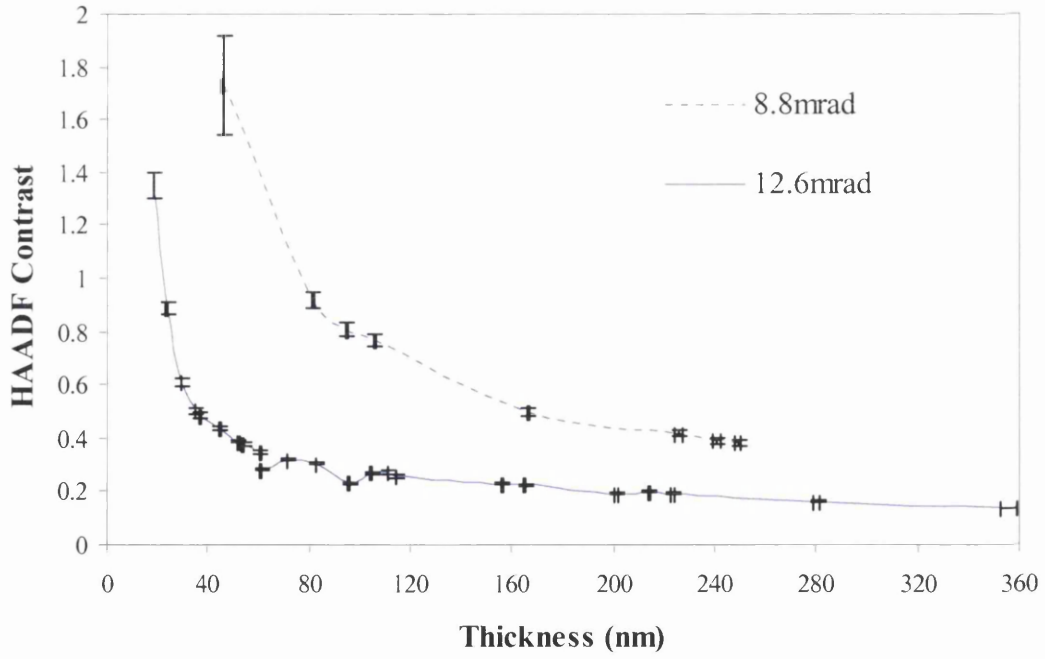

Figure 5.2: A graph of the experimental HAADF STEM contrast of Si [110] using the Tecnai F20 as a function of specimen thickness. 2 probe convergence semi- angles are shown: 8.8mrad and 12.6mrad. Each point in the plots is the average image contrast for 1 image. The error bars have a value of 2 × the standard error. The inner angle of the detector was 50mrad.

5.2.3 GaAs [110] Results

The HAADF STEM contrast for GaAs [110], as a function of thickness, is shown in Figure 5.3 for 2 probe convergence semi-angles in the Tecnai F20. The contrast and thickness values were measured in the same manner as before. As was the case with the Si [110] plots, the smaller probe (8.8mrad angle) generates the highest image contrast over the thickness range. In addition, the plot for the 8.8mrad probe shows similar characteristics as the previous Si [110] plots. For instance, the contrast is high for the lowest specimen thicknesses then decreases rapidly over a small thickness range. In fact, the contrast drops from a value of about 1.4 to below 0.5 in a thickness of just 20nm. On the other hand, the plot for the 12.6mrad is quite different. It is clear that the contrast remains fairly uniform over the experimental thickness range shown. However, the Si [110] plots highlighted the fact that the rapid increase in the image contrast takes place at a lower thickness for the larger probe. Hence, a likely explanation of why the 12.6mrad plot looks dissimilar to the other plots is that the thickness range did not extend low enough in order to sample the rapid increase in the contrast. This is despite the fact that the plot of the 12.6mrad probe extends to lower thicknesses than the plot of the 8.8mrad probe.

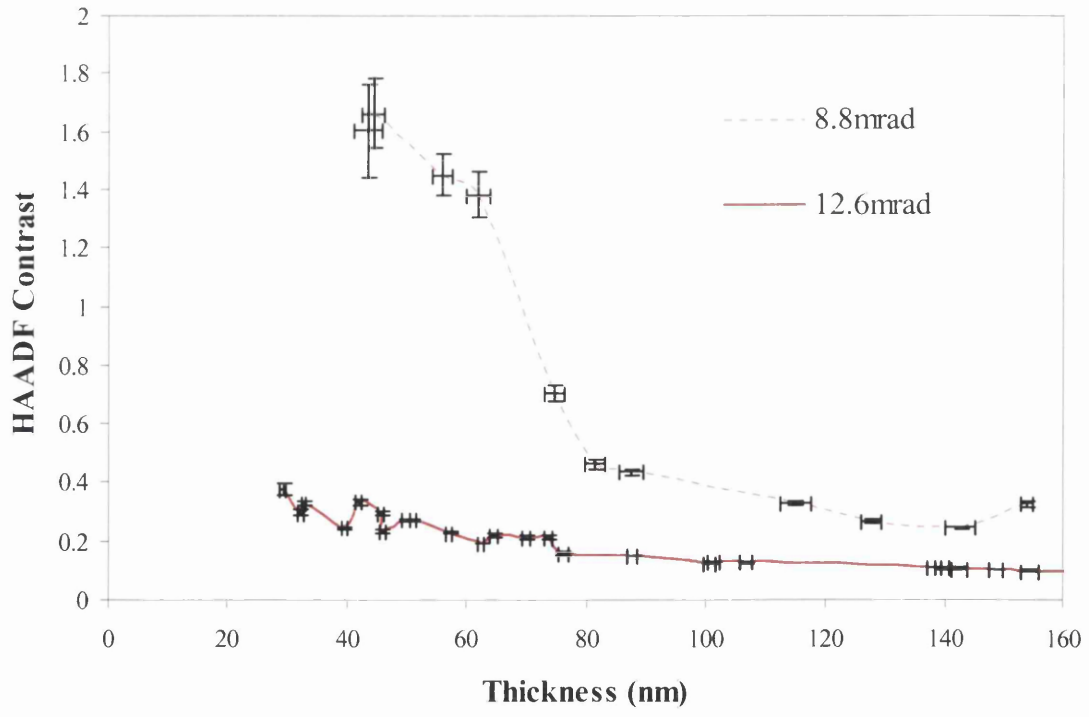

Figure 5.3: A graph of the experimental HAADF STEM contrast of GaAs [110] using the Tecnai F20 as a function of specimen thickness. 2 probe convergence semi- angles are shown: 8.8mrad and 12.6mrad. Each point in the plots is the average image contrast for 1 image. The error bars have a value of 2 × the standard error. The inner angle of the detector was 50mrad.

5.3 SuperSTEM 1 HAADF Image Contrast

5.3.1 Method

The preliminary attempts at the measure of the HAADF image contrast through the use of SuperSTEM 1 highlighted a problem with the measurement technique that was not encountered before. The same procedure as that discussed in Section 5.2.1 was used except for the fact that the image region (over which the EELS map was obtained) was increased to 9.4nm × 9.4nm (Figure 5.4(a)). Nonetheless, the calculation of the thickness maps revealed that, in most cases, there was an area in which the thickness value was considerably higher than in the rest of the map. This was regardless of the small size of the image region, which means that the specimen thickness should not change much over its area and the fact that Figure 5.4(a) reveals that there is no change in the absolute intensity across the HAADF image. However, Figure 5.4(c) reveals that the apparent thickness across a typical thickness map almost doubles from a value of 60nm to 110nm.

In order to investigate this apparent thickness problem, the low loss spectra from the EELS maps were analysed and it was found that carbon was present in the areas that exhibited the highest thickness values. This indicated that the sharp rise in the thickness was likely due to the build up of contamination and not due to a real change in the thickness of the underlying crystalline material. A reason for this not being as severe a problem in the Tecnai F20 experiments is because the time taken to acquire a standard SuperSTEM 1 image is longer than the time taken to acquire a standard Tecnai F20 image. Thus, the probe spends more time in the same location in SuperSTEM 1. Moreover, the probe current is higher in SuperSTEM 1. This means that the SuperSTEM 1 probe can crack more of the long chain hydrocarbons that diffuse across the specimen surface in comparison to the Tecnai F20 probe. It should also be noted that it was possible to reduce the acquisition time for a SuperSTEM 1 image. However, the time was not reduced so that the image conditions for the contrast and dumbbell column ratios (see later) were the same as the conditions used to acquire data of other structures (e.g. the heterostructure in Chapter 3).

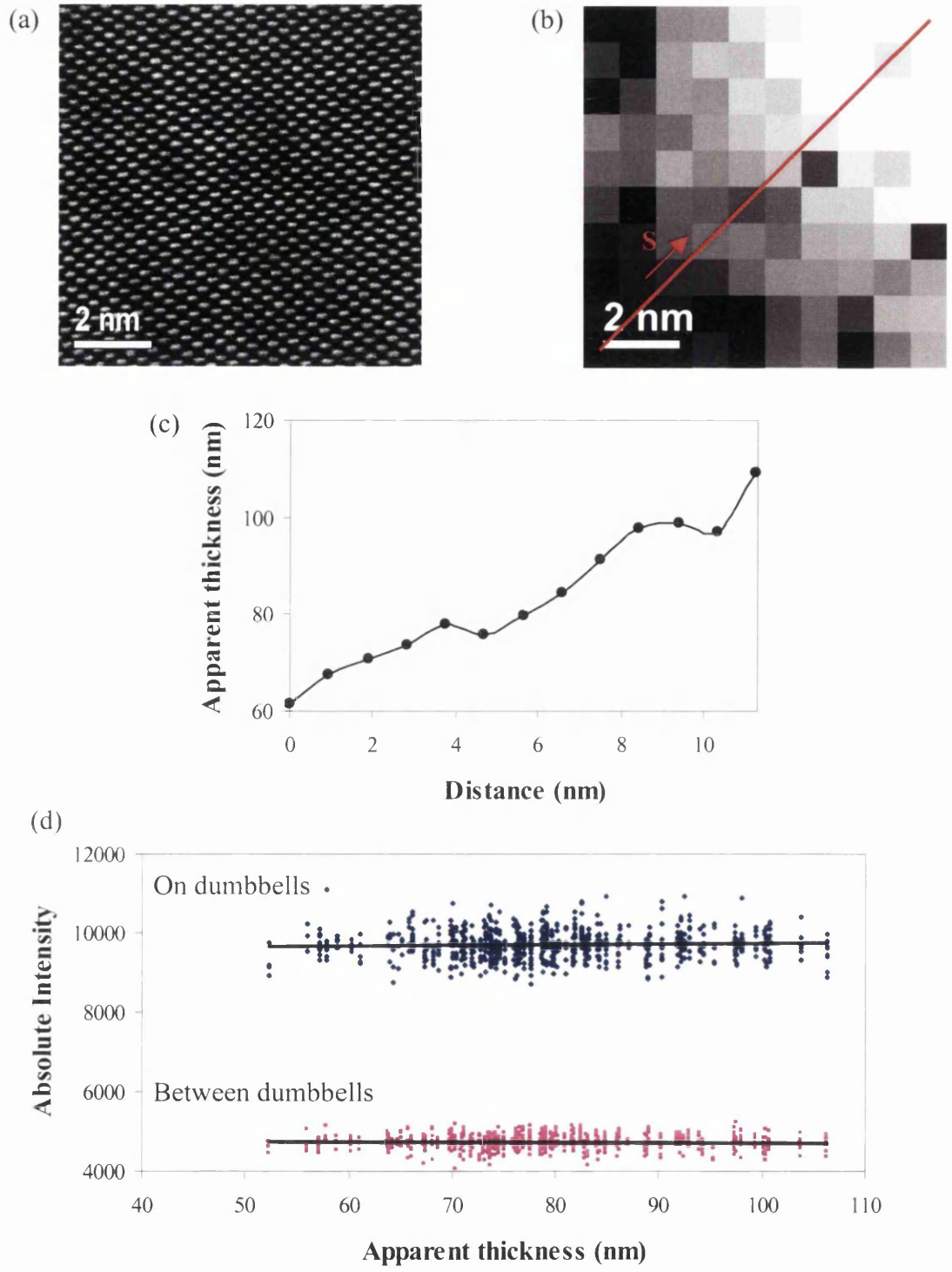

Figure 5.4(a): A SuperSTEM 1 HAADF STEM image of a 9.4nm × 9.4nm region of GaAs [110]. **(b)** is a SuperSTEM 1 thickness map obtained over the image in (a). The brightest pixels have the highest thickness values. **(c)** is a profile taken across the thickness map section S in (b). There is an apparent change in the measured thickness but this does not correspond to an actual change in the thickness of the crystalline material. The thickness change is likely to be related to the build up of contamination after the image in (a) was acquired. **(d)** is a graph of the apparent thickness variation of the intensity of the individual dumbbells from the HAADF image in (a). Also shown is the intensity of the positions between the dumbbells from the same image. The intensity is given as the absolute (as recorded) intensity using a probe angle of 24mrad and HAADF detector angles of 70mrad to 210mrad.

For each HAADF image, graphs of the intensity of individual dumbbells along with the intensity of the positions between the dumbbells were plotted as a function of apparent thickness. An example of such a graph is shown in Figure 5.4(d). It is evident that in this case the points are spread over a wide apparent thickness range (50nm to 110nm). However, the large spread in the apparent thickness value is not accompanied by an observable trend in the intensity value. Hence, the build up of contamination must have taken place primarily after the HAADF image was acquired since the presence of a large amount of contamination should reduce the image contrast but this is not seen in Figure 5.4(a) or Figure 5.4(d). Figure 5.4(d) also shows the existence of a small spread in the intensity values of the dumbbells. This may reflect a degree of surface mottling that was introduced through the ion milling of the material during the preparation of the specimen as discussed in Section 2.6.

Another problem that was associated with the measurement of the thickness using SuperSTEM 1 is illustrated in Figure 5.5. Figure 5.5(a) is a HAADF image taken over a few dumbbells of GaAs [110]. The EELS map from this area is shown in Figure 5.5(b). This map is displayed over the energy range of 28eV to 30eV (i.e. in the middle of the plasmon peak). Hence, the EELS map displays a pseudo dark field image. The difference in the strength of the plasmon signal is clearly visible between positions on the dumbbells and positions between the dumbbells. It should be noted that the reason for the extension of the dumbbells into rows is due to the drift of the specimen. Furthermore, the variation of the plasmon signal has an effect on the calculation of the map of apparent thickness as is shown in Figure 5.5(c). The profile taken across the apparent thickness map, in Figure 5.5(d), reveals that the thickness value apparently changes a great deal between positions on the dumbbells and positions between them. In fact, the apparent thickness value changes from about 80nm to over 100nm over these 2 types of positions. The actual thickness value is not changing across the small area and it is only the measurement of the thickness that is changing.

The problem with the variability in the measured thickness (due the probe being either on or off dumbbells) could result in an erroneous estimation of the average thickness across an image region. For instance, an aliasing situation could occur in which the spectra (from the EELS maps) are inadvertently generated mainly from either dumbbell or between dumbbell positions.

In order to counter the problems that were outlined above, a new measurement technique was used in order to investigate the image contrast using SuperSTEM 1. For instance,

instead of obtaining EELS maps for each image, 50 spectra (per image) were collected. These were acquired whilst the probe was scanned rapidly across the image. This had the effect of reducing the time the probe spent in 1 place, thereby removing the problem of contamination build up. Moreover, the aliasing associated with the on / off dumbbell effect ceased to be a problem because of the continuous movement of the probe across the whole image.

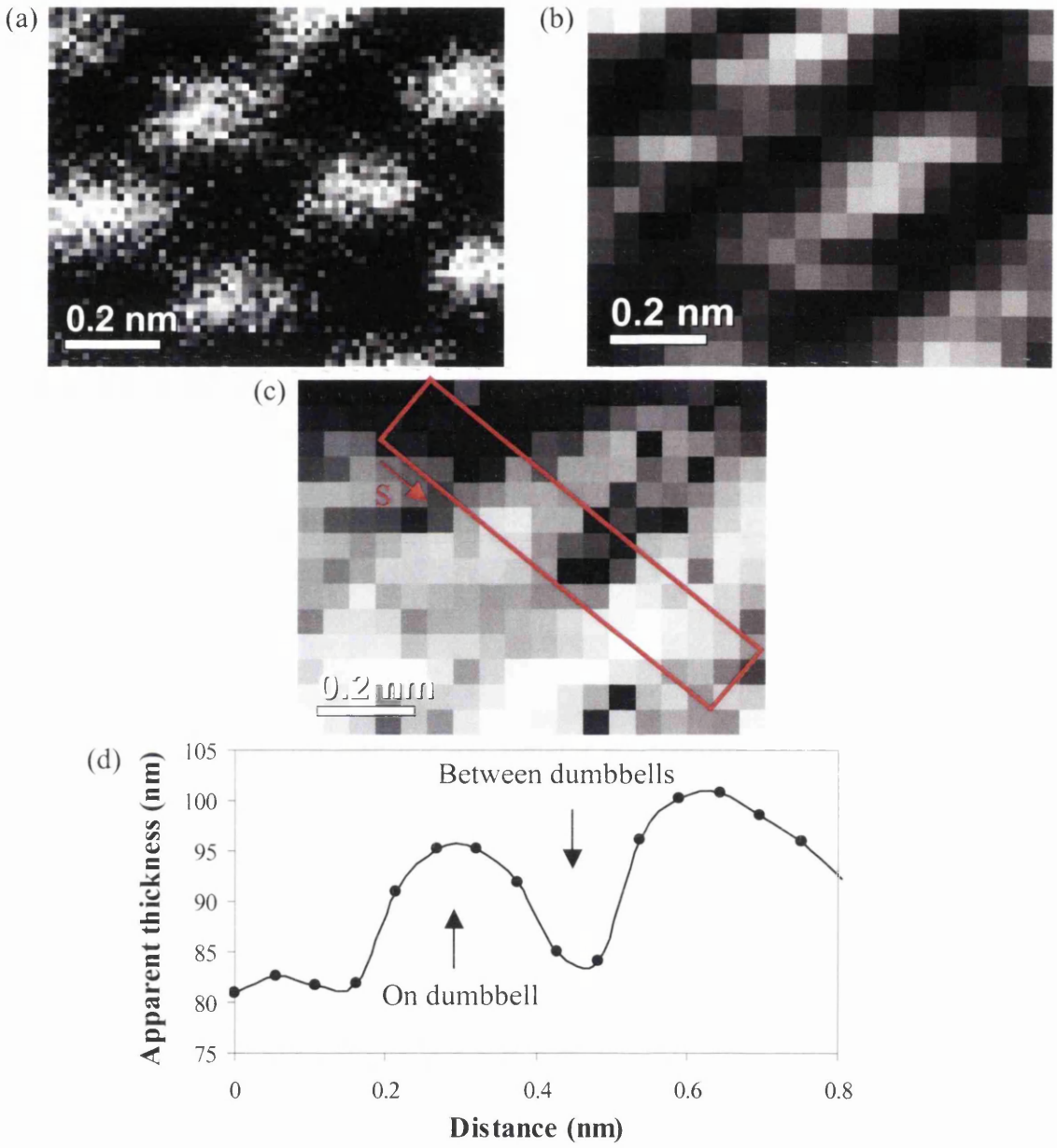

Figure 5.5(a): A SuperSTEM 1 HAADF STEM image over a few dumbbells of GaAs [110]. A probe angle of 24mrad and HAADF detector angles of 70mrad to 210mrad were used. **(b)** is an EELS map taken over (a). The map is viewed over the energy slice of 28eV to 30eV. The brightest pixels have the highest number of counts in that energy range. The map is a pseudo bright field image. **(c)** is the map of apparent thickness calculated from (b). The actual thickness is not changing over the small area- it is only the measurement of the apparent thickness that is altered. **(d)** is a profile taken across the apparent thickness map section S in (c). Every pixel of the profile is generated from the average of 3 pixels.

The contrast (and dumbbell column ratio) data for both GaAs and AlAs were obtained from a single specimen during 1 session on SuperSTEM 1. The specimen was prepared using the cross-section technique and was finished with 400eV ions at an angle of 6^{o} through the use of a GentleMill.

In addition, the wafer that contained the AlAs and GaAs was not rotated during the MBE growth process. This was to ensure that the target composition, which contained numerous other materials, was not affected by the rotation of the wafer. For instance, it has been shown that (depending on the growth rate and the substrate rotation speed) the composition of MBE grown uniform ternary films (such as InGaAs) are not uniform along the growth direction and are not the same across the substrate plane [1]. This effect was possibly observed in the composition of the $In_{0.3}Ga_{0.7}As$ conducting channel of the MODFET heterostructure shown in Chapter 3. Hence, the wafer rotation was not employed during the growth process in order to prevent any possible change to the target composition of the other ternary materials that were present on the same wafer as the AlAs and GaAs. It should be noted that a lack of wafer rotation does not have an adverse effect on the composition of binary layers such as AlAs or GaAs and is, therefore, not a problem in this case.

5.3.2 GaAs [110] Results

The SuperSTEM 1 HAADF STEM contrast for GaAs [110], as a function of thickness, is shown in Figure 5.6 for 2 probe convergence semi-angles. The information limit for the 16mrad probe (calculated from the FT of a lattice image) is 1.6Å. On the other hand, the information limit for the 24mrad probe is 1Å. It can be seen that the smaller probe (24mrad angle) generates higher contrast than the bigger probe (16mrad angle). This was also the case with the Tecnai F20 results where the larger aperture actually gives a larger probe. Nonetheless, the contrast obtained from SuperSTEM 1 is (in general) lower than that from the Tecnai F20. Furthermore, the plot for the 24mrad probe also displays a rapid increase in the contrast at a low specimen thickness. However, the increase in the GaAs occurs at a much lower thickness (~40nm) compared to that seen in 8.8mrad probe plot from the Tecnai F20 (~80nm). In addition, it is apparent that the SuperSTEM 1 plot exhibits significant deviations. These may be a consequence of the presence of amorphous material or mottling on the specimen surface. This would affect the degree of column channelling and also the measurement of the thickness. Deviations are also present in the 16mrad probe plot. Moreover, it is obvious that the thickness range of the 16mrad probe plot is not extensive enough in order to highlight any noticeable trend in the contrast as a function of specimen thickness.

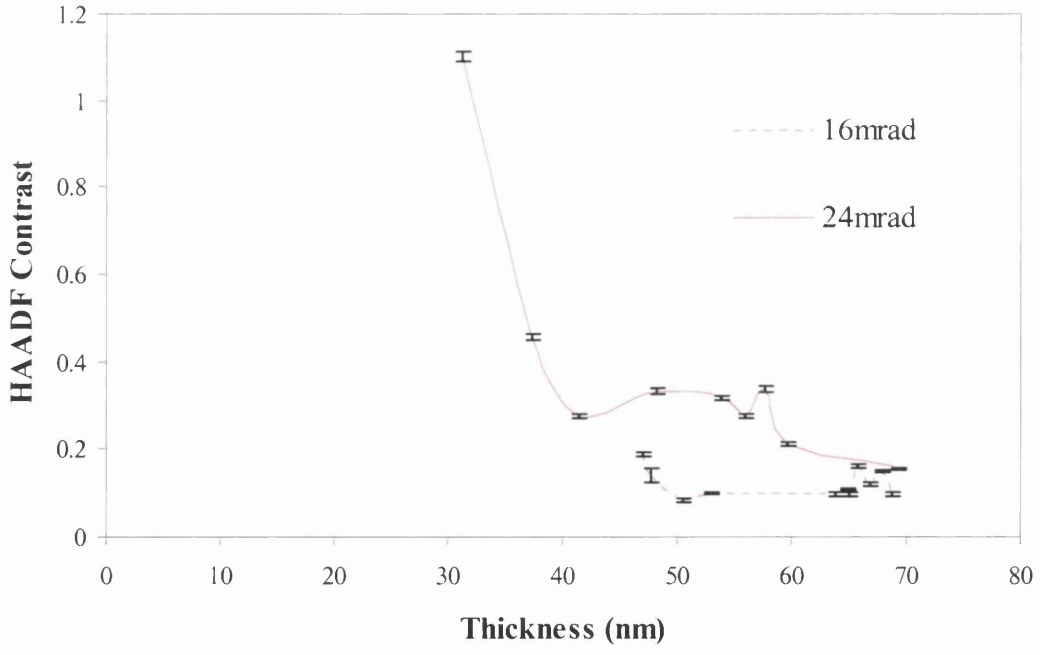

Figure 5.6: A graph of the experimental HAADF STEM contrast of GaAs [110] using SuperSTEM 1 as a function of specimen thickness. 2 probe convergence semi- angles are shown: 16mrad (dotted) and 24mrad (solid). Each point in the plots is the average image contrast for 1 image. The error bars have a value of 2 × the standard error. The HAADF detector angles were 70mrad to 210mrad.

5.3.3 AlAs [110] Results

The SuperSTEM 1 HAADF STEM contrast for AlAs [110], as a function of thickness, is shown in Figure 5.7 for 2 probe convergence semi-angles. The deviations that were noticed in the above GaAs plots are considerably worse in the plots of AlAs. The reason for this may be due to the fact that AlAs is more susceptible to oxidation than GaAs. Hence, the level of surface damage in the AlAs region of the specimen is likely to be greater than the level in the GaAs region. In addition, local changes in the specimen tilts across the AlAs region cannot be ruled out. Furthermore, it was observed that the image contrast was sensitive to the exact focus value of the microscope. Hence, it is possible that the optimum contrast was not recorded at some thickness values due to incorrect focusing. Despite the apparent problems in the plots, the contrast is clearly higher at low specimen thicknesses for the 24mrad angle probe. In addition, the AlAs contrast is higher than the GaAs contrast for all but the thinnest specimens. This is likely due to the reduced HAADF background signal in AlAs because of its lower average Z number (see Section 4.3.5). Once again, the thickness of the 16mrad probe plot does not extend over a large enough range to witness a noticeable trend.

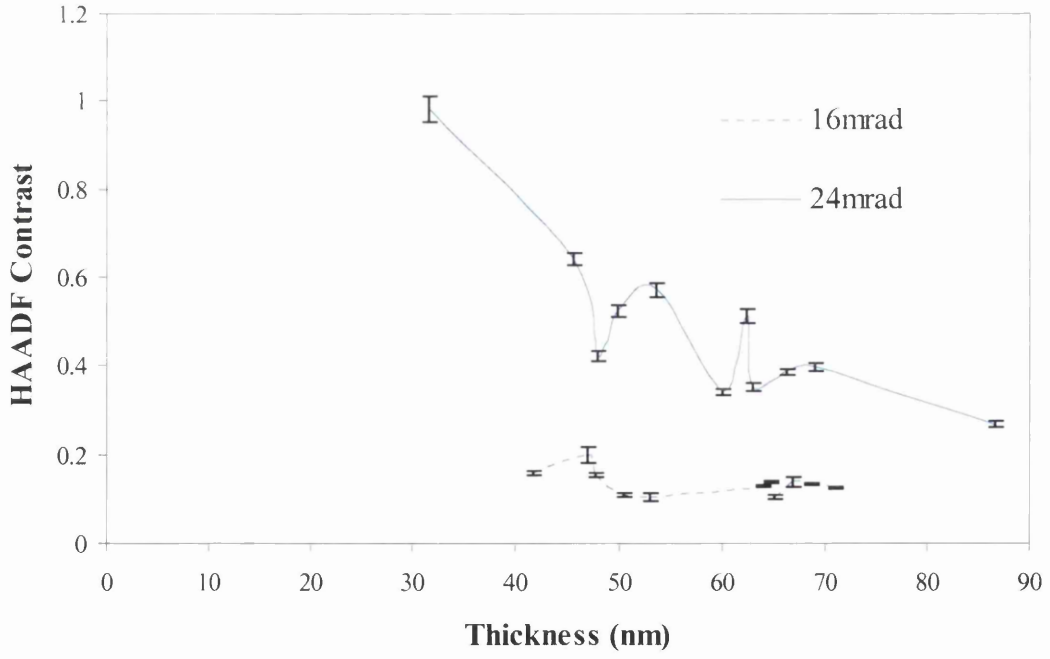

Figure 5.7: A graph of the experimental HAADF STEM contrast of AlAs [110] using SuperSTEM 1 as a function of specimen thickness. 2 probe convergence semi- angles are shown: 16mrad (dotted) and 24mrad (solid). Each point in the plots is the average image contrast for 1 image. The error bars have a value of 2 × the standard error. The HAADF detector angles were 70mrad to 210mrad.

5.3.4 Comparison to Simulations

The 24mrad probe simulations that were presented in Chapter 4 showed how the HAADF signal in GaAs and AlAs varied as a function of specimen thickness. These simulations can also be used to estimate the image contrast (for each material) by dividing the As column signal (i.e. the highest dumbbell signal) by the background in each case. The thickness variation of the simulated image contrast for GaAs is illustrated in Figure 5.8. The simulations were calculated with a probe convergence semi-angle of 24mrad and HAADF detector angles of 70mrad to 210mrad, as described in Chapter 4.

Figure 5.8 reveals that the simulated contrast is highest at low specimen thicknesses and then drops off quickly as the thickness increases. These characteristics are due to the limited existence of channelling along the As column and the continual build up of the background signal as was demonstrated in Chapter 4.

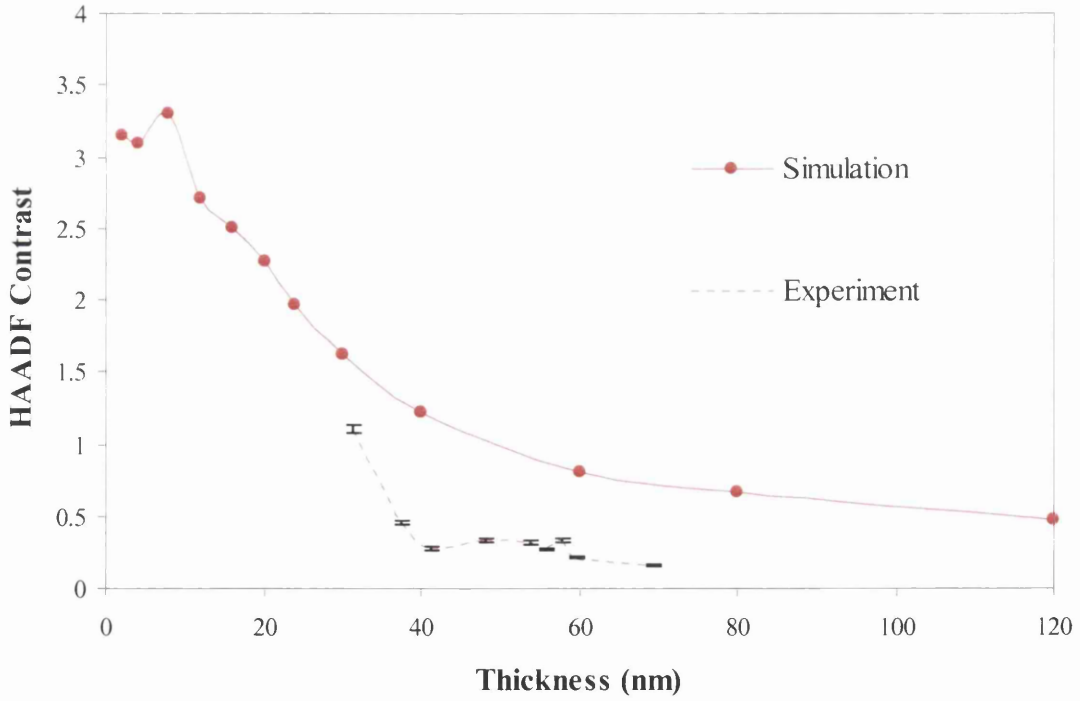

Figure 5.8: A graph of the simulated HAADF STEM contrast of GaAs [110] as a function of specimen thickness (blue). Also shown is the experimental contrast for GaAs from SuperSTEM 1 (black). HAADF detector angles were 70mrad to 210mrad and the probe angle was 24mrad in both cases.

Figure 5.8 also provides a comparison of the GaAs simulated image contrast with the experimentally derived GaAs contrast from SuperSTEM 1. It is evident that the simulations predict a much higher value of contrast than was found experimentally. The ratio of the simulated contrast to the experimental contrast is called the 'Stobbs Factor'. This factor has been discussed by many authors [2-5]. It can be seen from Figure 5.8 that the Stobbs factor has a value of about 3 for most thickness values in this case. This is within the 2-6 range that has been reported for HREM calculations [2-5].

Reference [3] provides a discussion of the possible reasons for the difference between simulation and experiment. One of these includes the presence of an amorphous layer on the surface of the specimen. This is introduced from the ion milling process and from the presence of carbon contamination. The amorphous layer should affect the intensity distribution of the probe that is incident on the crystalline material below the amorphous material, thereby changing the channelling of the electrons down the atomic columns. In addition, the amorphous layer should also increase the measurement of the thickness that is determined via EELS.

It can be shown that the amorphous layer reduces the image contrast through the generation of an additional background signal [6, 12]. This additional background should depend upon the thickness of the amorphous layer. However, as was discussed in Chapter 2, the thickness of the amorphous layer on the surface of specimens that were used in this project could not be determined experimentally. Nevertheless, it is expected that a 400eV polish in the GentleMill should produce an amorphous surface layer in GaAs that is less than 2nm in thickness [13]. This is less than the depth over which the electron flux from a focused electron probe remains parallel to the top surface of a specimen i.e. a simple wave optics calculation gives a value of about 4nm for this depth. Therefore, it is expected that a small shift in the specimen height of less than 2nm (due to the presence of an amorphous surface layer) should not have a large enough effect on the experimental contrast in order to fully account for the Stobbs factor in this case.

Another reason for the reduction in the simulated contrast may involve the use of incorrect atomic scattering factors in the simulations. These factors are used to derive the projected atomic potentials of the columns that make up a specimen. However, it is known that the values of these factors are underestimated at high scattering angles [3]. Hence, the intensity in HAADF simulations is unlikely to match experiment due to a lower level of scattering out to the HAADF detector.

A mismatch between the actual experimental parameters and those that are input into the simulations is also probable. This would, in effect, imply that the simulations were not exactly equivalent to the experiments that they were being compared with. This problem partially arises due to the difficulty in identifying the exact experimental parameters (such as defocus, aberration values, aperture alignment, specimen orientation and specimen vibration) for a particular experimental session. In fact, knowledge of the experimental defocus value is critical as it has been shown that HAADF column intensities are sensitive to the value of defocus [7]. It is apparent, therefore, that a slight change in the defocus value could alter the overall image contrast significantly. In the case of specimen orientation, the channelling of the electrons would again be affected if the specimen was not orientated in the correct fashion. However, it should be noted that care was taken to properly orientate the specimen and large areas of flat material were present on the specimen. On the other hand, the size of the tilt that is required to obtain a significant difference between simulation and experiment is unknown. Furthermore, the precise set up of the probe in SuperSTEM 1 depends on how well the aberration correction procedure was carried out. Hence, the size and shape of the SuperSTEM 1 probe may change from one session to the next. However, all of the data (from both GaAs and AlAs) was acquired over a single session.

In addition, the simulations do not have the facility to replicate the effect of some experimental parameters such as high order aberration coefficients. Hence, the dissimilarity between simulation and experiment, as presented in this chapter, may partly be a result of a difference between the simulated probe shape and the experimental probe shape of SuperSTEM 1. It should also be noted that the simulations do not include inelastic scattering even though the effect of TDS is included via the frozen phonon method. Reference [3] has also considered the effect of inelastic scattering on the Stobbs factor. It was found that although inelastic scattering did affect the image contrast, it was not enough on its own to explain the difference between simulation and experiment [3].

Figure 5.9 presents a comparison between the simulated and experimental image contrast for AlAs as a function of specimen thickness. As was the case with GaAs, the AlAs simulations predict a higher value of contrast than is observed experimentally. It should also be noted that the simulated AlAs contrast is higher than the simulated GaAs contrast for all specimen thicknesses. This was also observed experimentally except for the thinnest specimens.

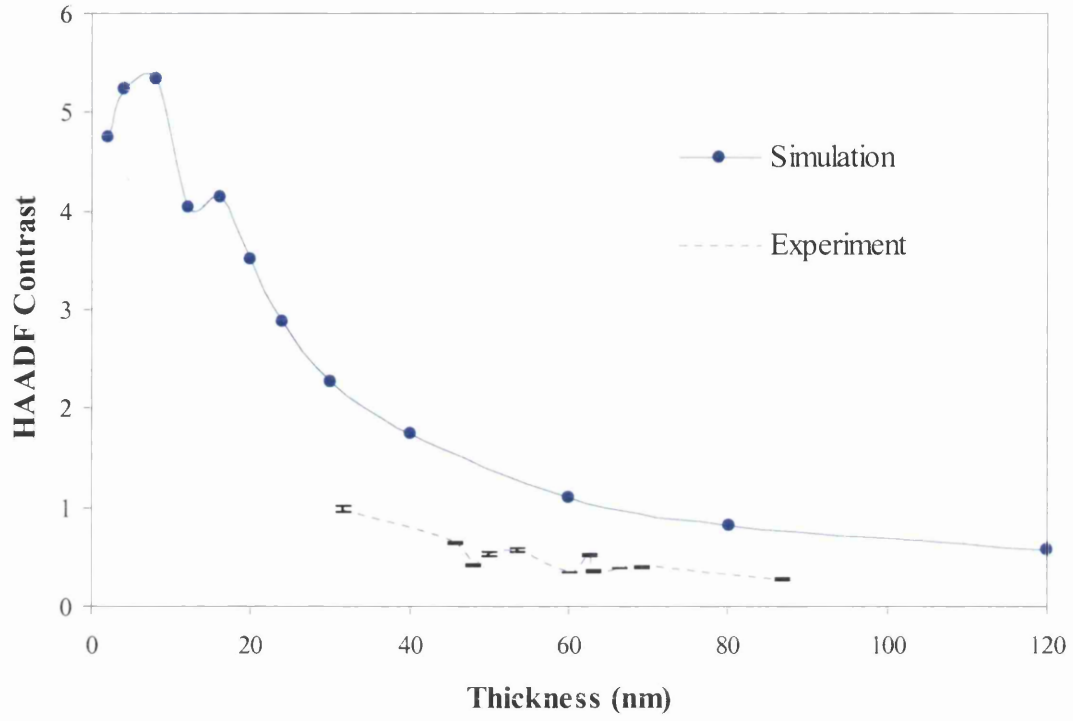

Figure 5.9: A graph of the simulated HAADF STEM contrast of AlAs [110] as a function of specimen thickness (blue). Also shown is the experimental contrast for AlAs from SuperSTEM 1 (black). HAADF detector angles were 70mrad to 210mrad and the probe angle was 24mrad in both cases.

5.4 Dumbbell Column Ratios

The experimental dumbbell column ratio for GaAs [110] is shown in Figure 5.10 as a function of specimen thickness. The same data that was used to measure the image contrast in Section 5.3 was also used to measure the dumbbell column ratios for GaAs and AlAs. The thickness was also measured in the same way as for the SuperSTEM 1 HAADF contrast experiment (Section 5.3.1). Therefore, the value of the column ratio at a particular thickness is the average value of the dumbbells in a particular image. The error bars have a value of 2 times the standard error. In addition, the column ratio was calculated in a similar fashion to that described in Section 3.2.3. Furthermore, the effect of compositional intermixing on the measured column ratio was eliminated by taking measurements from the centre of wide layers of GaAs and AlAs (>50ML).

Figure 5.10 demonstrates that the experimental GaAs column ratio has a value that ranges from 0.9 to about 1.1 over the thickness range shown. However, the ratio does not vary in a distinctive way with specimen thickness. Figure 5.10 also presents the equivalent

simulated column ratio for GaAs. This was calculated by dividing the simulated Ga column HAADF signal by the simulated As column HAADF signal. This procedure was explained in Section 4.2.4. It is noticeable that the simulated column ratio does not vary much and remains close to a value of 1 over the whole thickness range (0-120nm). It, therefore, behaves in a similar way as the experimental column ratio. In fact, the experimental data points are evenly distributed above and below the simulated plot. This is quite unlike the relationship between the simulated and experimental HAADF image contrast plots, which exhibited a poor correspondence.

Figure 5.11 shows the experimental dumbbell column ratio for AlAs [110] as a function of specimen thickness. The column ratio was measured in a similar way as for GaAs. The AlAs column ratio clearly increases as the thickness grows. Indeed, the ratio increases from about 0.4 to 0.6 over the thickness range 30nm to 85nm. Hence, unlike the GaAs column ratio, the specimen thickness has considerable effect on the AlAs column ratio. Figure 5.11 also displays the equivalent simulated AlAs column ratio (Al column HAADF signal divided by the As column HAADF signal). This varies from a value of below 0.2 to 0.7 over the simulated thickness range (0-120nm). Furthermore, there is a good correspondence between the simulated plot and the experimental data points once again. This is an indication that simulations can properly calculate HAADF column intensities and it is only the HAADF background signal that is incorrectly simulated. Other authors have also found this to be the case [7]. In addition, the deviations in the experimental AlAs column ratio plot may be due to the presence of amorphous layers on the specimen surface, incorrect focusing and the difference between the simulated and experimental probes, similar to the situation of the HAADF image contrast plots (see Section 5.3.4).

It can be seen from Figure 5.11 that the value of the AlAs column ratio predicted by the simple Z^2 theory (column ratio value = 0.16) only holds for very thin specimens (~4nm). In comparison, the simulations for GaAs (Figure 5.10) never reach the value predicted by the simple Z^2 theory (column ratio value = 0.88). This simple theory was discussed in Chapter 3 and states that the column ratio is proportional the square of the Z number of Al (or Ga) divided by the square of the Z number of As. In addition, since the AlAs column ratio changes over the thickness range in Figure 5.11, the power that Z is raised to (denoted by n where n is usually taken to be 2 for Rutherford scattering) must also change as the thickness is increased.

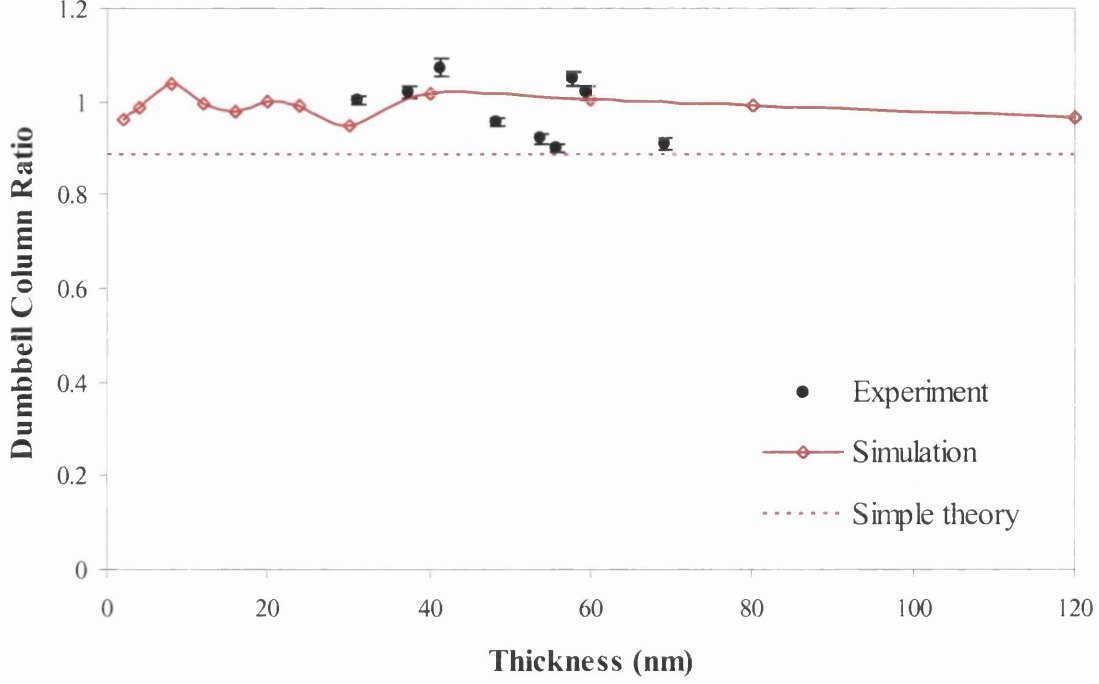

Figure 5.10: A graph of the simulated HAADF dumbbell column ratios of GaAs [110] as a function of specimen thickness (blue). Also shown is the experimental dumbbell column ratio for GaAs from SuperSTEM 1 (black). The error bars have a value of 2 times the standard error. HAADF detector angles were 70mrad to 210mrad and the probe angle was 24mrad in both cases.

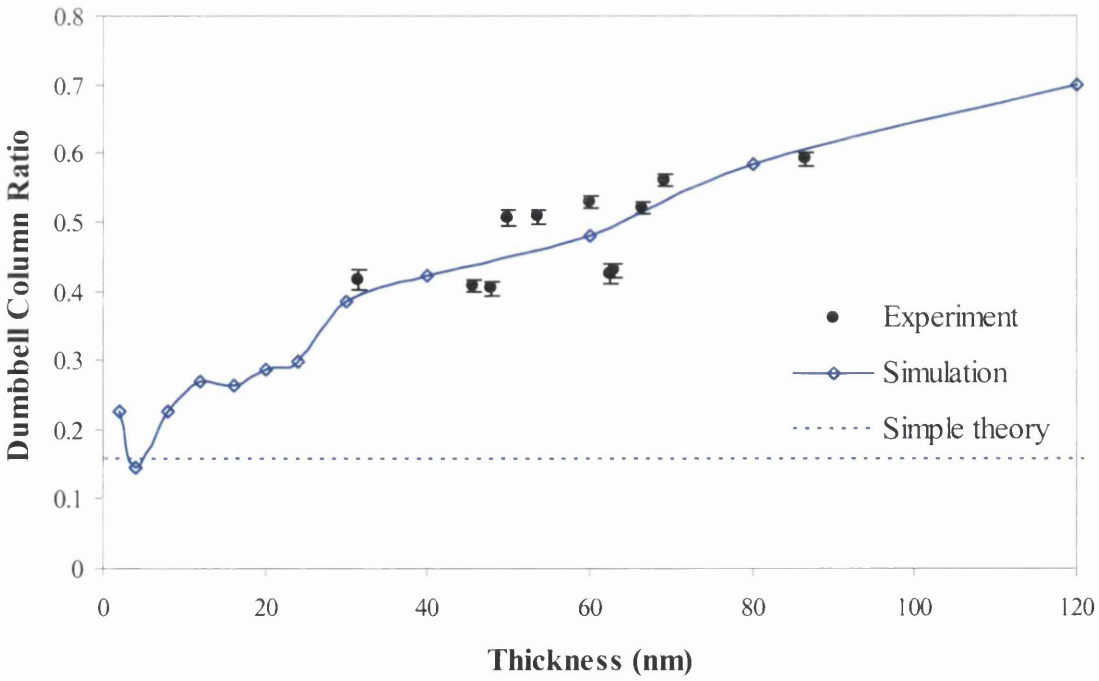

Figure 5.11: A graph of the simulated HAADF dumbbell column ratios of AlAs [110] as a function of specimen thickness (blue). Also shown is the experimental dumbbell column ratio for AlAs from SuperSTEM 1 (black). The error bars have a value of 2 times the standard error. HAADF detector angles were 70mrad to 210mrad and the probe angle was 24mrad in both cases.

In order to investigate Z^n approximation, the graph of the simulated HAADF dumbbell column ratio of AlAs (Figure 5.11) was used to measure the variation of n as a function of thickness. The plot of n against thickness is shown in Figure 5.12. It is clear that n is not equal to 2 and in fact drops off as the thickness is increased. Therefore, the value of n must be a function of specimen thickness and is not equal to some numerical constant. Nevertheless, at a specimen thickness of zero, n does approach the value expected from screened Rutherford scattering (i.e. a value of ~1.77) [14]. In addition, the thickness variation of n that is presented in Figure 5.12 was used to calculate the thickness variation of the GaAs column ratio. It was found that the GaAs column ratio took on a value of 0.9-1.0 over a thickness range of 0-120nm. This change in the column ratio is very similar to that shown in Figure 5.11. This demonstrates that the variation of n that is shown in Figure 5.12 not only holds for AlAs but also for GaAs and possibly other materials. Hence, it is again apparent that the specimen thickness must be known in order to estimate the dumbbell column ratio and the Z^2 (or more exactly $Z^{1.77}$) simple theory is only adequate for ultra thin specimens.

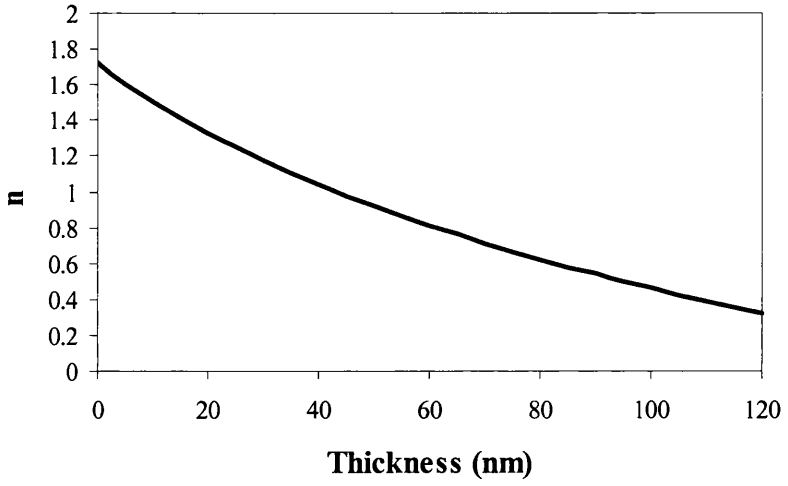

Figure 5.12: A graph of the variation of the simulated n value for AlAs as a function of specimen thickness. This was calculated from the plot in Figure 5.11. n refers to the power that (Z_{Al} / Z_{As}) is raised to obtain the column ratio. The screened Rutherford n value of ~1.77 is approached only at zero specimen thickness.

5.5 Conclusions

In this chapter, an investigation of the HAADF image contrast, as a function of thickness, was presented. Results from the Tecnai F20 were shown for Si [110] and GaAs [110] using 2 different probe sizes. It was found that, for both materials, the image contrast was higher for the smaller probe due to the generation of a smaller background signal. In addition, if the image contrast is required to be greater than a value of 0.5 in order to give a reasonably good dumbbell signal (above the background), then this only occurs for a specimen thickness up to 40nm in Si [110] using the larger probe. However, this value becomes about 160nm for the smaller probe. A similar disparity between the 2 probe sizes is also evident in GaAs [110]. However, the image contrast drops below 0.5 at a thickness of only 80nm in GaAs [110] using the smaller probe. Hence, a specimen of GaAs [110] must be prepared thinner than a specimen of Si [110] in order to give the same level of image signal above the background.

The variation of the HAADF image contrast, obtained from SuperSTEM 1, was also presented for GaAs [110] and AlAs [110]. 2 probe sizes were again shown. However, for both GaAs and AlAs, the thickness range of the bigger probe was too limited to show any noticeable trend. On the other hand, the plots for the smaller probe size exhibited high contrast at low specimen thicknesses. This is despite the fact that the plots contained significant deviations, possibly due to surface mottling and incorrect focusing. Furthermore, the experimental results for both materials (using the smaller probe) were compared against simulations of the image contrast. It was discovered that the contrast values predicted by the simulations were too high over the whole thickness range.

The dumbbell column ratios for GaAs [110] and AlAs [110], as a function of thickness, were also presented. These were obtained from SuperSTEM 1 using a probe convergence angle of 24mrad. It was found that all the values of the individual dumbbells (for both materials) were within 3 standard deviations of the respective mean value.

The column ratio for GaAs was observed to remain about a value of 1 over the whole experimental thickness range. Equivalent behaviour was also seen in the simulated GaAs dumbbell column ratio plot. Furthermore, the experimental and simulated plots for AlAs also agreed well with each other. This is an indication that the simulations predict the HAADF column signals quite well and it is only the background signal that is underestimated (since the HAADF contrast did not match the experiments). Moreover, the AlAs column ratio was found to increase steadily as a function of thickness. This is a sign

that the specimen thickness must be known in order to interpret dumbbell column ratio maps correctly. This requirement is not as important in column ratio maps that contain GaAs since the column ratio does not change as much as it does in AlAs. In addition, the column ratio plots also revealed that the simple Z^n scattering theory is not valid because n is a function of specimen thickness. Hence, it is clear that previous estimates of the dependence of HAADF image intensity on atomic number did not consider the effect of specimen thickness.

References

[1] W. L. Sarney, S.P. Svensson, Characterization of compositional oscillations in InGaAs films induced by MBE cell configuration and substrate rotation, Sensors and Electron Devices Directorate, U.S. Army Research Laboratory, Adelphi, MD 20783 USA (2005)

[2] M. J. Hytch, W. M. Stobbs, Quantitative comparison of high resolution TEM images with image simulations, Ultramicroscopy 53, 191-203 (1994)

[3] C. B. Boothroyd, Why don't high resolution simulations and images match?, Journal of Microscopy 190, 99 (1998)

[4] A. Howie, Hunting the Stobbs factor, Ultramicroscopy 98, 73-79 (2004)

[5] C. B. Boothroyd, R. E. Dunin-Borkowski, The contribution of phonon scattering to high-resolution images measured by off-axis electron holography, Ultramicroscopy 98, 115-133 (2004)

[6] C. B. Boothroyd, R. E. Dunin-Borkowski, W. M. Stobbs, C. J. Humphreys, Quantifying the effects of amorphous layers on image contrast using energy filtered transmission electron microscopy, MRS Symposium Proceedings Vol 354, pp. 495-500 (1995)

[7] D. O. Klenov, S. Stemmer, Contributions to the contrast in experimental high-angle annular dark- field images, Ultramicroscopy 106, 889-901 (2006)

[8] W. Qu, C. Boothroyd, A. Haun, Quantitative measurement of image intensity in transmission electron microscope images, Applied Surface Science 252, 3984-3988 (2006)

[9] K. Ishizuka, A practical approach for STEM image simulation based on the FFT multislice method, Ultramicroscopy 90, 71-83 (2002)

[10] C. Dwyer, J. Etheridge, Scattering of Å-scale electron probes in silicon, Ultramicroscopy 96, 343-360 (2003)

[11] E. J. Kirkland, Advanced Computing in Electron Microscopy, Plenum Press, New York (1998)

[12] T. Yamazaki, Role of surface amorphous film in high-resolution high angle annular dark field STEM imaging, Ultramicroscopy 99, 125-135 (2004)

[13] A. Barna, B. Pecz, M. Menyhard, Amorphisation and surface morphology development at low-energy ion milling, Ultramicroscopy 70, 161-171 (1998)

[14] B. Rafferty, P. D. Nellist, S. J. Pennycook, On the role of transverse incoherence in Z-contrast STEM, Journal of Electron microscopy 50(3), 227-233 (2001)

6 The Characterisation of AlAs and GaAs Based Structures as a Function of Specimen Thickness

6.1 Introduction

In this chapter, an investigation of 3 different types of AlAs and GaAs based nanostructures is presented. These structures were all grown by MBE and were studied through the use of SuperSTEM 1. One of these structures was a single interface between wide layers (50ML) of AlAs and GaAs. Both types of interface were studied i.e. AlAs-on-GaAs and GaAs-on-AlAs (see Section 1.4). The other 2 structures comprised a wide layer 9ML AlAs / 9ML GaAs superlattice and a narrow layer 1ML AlAs / 2ML GaAs superlattice.

The study of these structures allowed an exploration into the reasons behind the non-sharpness that was observed in the MODFET heterostructure (shown in Chapter 3) and in AlAs / GaAs interfaces in general. The improved performance of the aberration corrected SuperSTEM 1 was utilised in order to study these MBE grown interfaces on a scale not previously possible. Furthermore, the analysis of the various structures also took into consideration the results from Chapter 5. For instance, the effect of specimen thickness on the value of the dumbbell column ratio (for GaAs and AlAs) was utilised in order to provide a better estimate of the sharpness of the various interfaces contained within the structures. Hence, the investigation permitted an evaluation of the accuracy of the growth techniques.

All of the structures were grown epitaxially on top of a GaAs substrate along the [001] crystal direction by MBE. Furthermore, STEM samples were prepared using the cross-section technique and were finished with a low energy ion mill at 400eV and at an angle of 6^{o} using the GentleMill (see Section 2.6). All specimens were orientated along the [110] direction.

Table 6.1 reveals that the nanostructures were distributed on 2 separate wafers, called Wafer A and Wafer B. Wafer A contains the single interface and the wide layer superlattice. This wafer also contains InAs / GaAs superlattices and the investigation into these structures is presented in Chapter 7. It should be noted that Wafer A was not rotated during the growth process. This was to ensure that the composition of the wafer, which contained numerous other ternary materials (results are not shown), was not affected by the

rotation as was discussed in Section 5.3.1. For instance, it has been demonstrated that (depending on the growth rate and the substrate rotation speed) the composition of MBE grown uniform ternary films (such as InGaAs) are not uniform along the growth direction and are not the same across the substrate plane [1]. Hence, the wafer rotation was not employed during the growth process in order to prevent any possible change to the target composition of the other ternary materials, which were present on the same wafer as the single interface and the wide layer superlattice. It should be noted that a lack of wafer rotation does not have an adverse effect on the composition of structures that are composed of binary materials such as AlAs or GaAs. Hence, the AlAs and GaAs that formed the single interface and the wide layer superlattice were not affected.

The unusual step of removing the wafer rotation was taken despite the fact that a lack of rotation actually generates a slight thickness gradient in the Group III materials of ternary layers across the wafer (but not along the growth direction). For example, if $In_xGa_{1-x}As$ is grown without a wafer rotation then parts of the wafer will have a higher In percentage than the intended fraction x and other parts will have a lower percentage than x. This is because the ovens, in the MBE machine, are positioned in different places and, therefore, a greater elemental flux will impinge upon the parts of the wafer that are closest to the ovens as opposed to the parts that are further away. However, this is not a problem for the single interface and wide layer superlattice as they composed of layers of binary materials. In addition, the specimen was cut from the middle of the wafer where the elemental fluxes are the same from all of the ovens. Therefore, the ternary layers in the specimen should also contain the target composition.

	Wafer A	Wafer B
Rotation	No	Yes
Single interface: AlAs / GaAs	Yes	No
Wide layer superlattice: 9ML AlAs / 9ML GaAs	Yes	No
Narrow layer superlattice: 1ML AlAs / 2ML GaAs	No	Yes
InAs / GaAs superlattices	Yes	No
Si δ- doping layers	No	Yes

Table 6.1: A description of wafer A and B.

In contrast, the narrow layer superlattice was grown on Wafer B. This wafer also contained Si δ-doped layers which enabled the study of δ-doping (see Chapter 7). This wafer was actually grown primarily for the study of the Si δ-doped layers. Hence, in order to investigate these layers under their usual growth conditions, Wafer B was rotated during the growth process.

At the present, the AlAs / GaAs structure is one of the most studied semiconductor systems. This low dimensional structure is not only important in MODFET heterostructures (like the one investigated in Chapter 3) but also in the development of new optoelectronic devices [2]. It can be noted that in short period superlattices, the reduction in the periodicity is responsible for the creation of the new energy gaps (minigaps) in the electron energy bands of the crystals that form the superlattice [3]. However, it is a challenge to create perfectly abrupt interfaces due to the kinetic and thermodynamic factors that influence the formation of the interfaces in the multilayers.

As was described in Section 1.4, the contribution of surface roughness to the sharpness of interfaces can be separated into the two categories of surface stepping and elemental intermixing [4]. The first category involves the collection of islands of one type of material on the other side of the ideal interface. This can lead to the existence of a stepped boundary between the two materials [4, 5]. The steps are typically associated with a characteristic step length. The second category is associated with the diffusion of the different elements across the boundary. Both categories of roughness are introduced during the growth process. Furthermore, interfacial disorder can ultimately impact the electrical and optical device characteristics by affecting the transport and scattering mechanisms of the carriers in multilayer structures [6].

It has been shown that an AlAs-on-GaAs interface is several MLs sharper than a GaAs-on-AlAs interface at very small specimen thicknesses (see Section 1.4). The reason for the abrupt nature of the AlAs-on-GaAs interface is due to the presence of large steps along the interface. For example, although step lengths have a range of values, the majority of steps along an AlAs-on-GaAs interface are above 55nm in length (along the [110] direction) [5]. In addition, the majority of the steps are below 15nm in length along the [1-10] direction (i.e. perpendicular to the incident electron probe). In comparison, no consistent pattern of stepping has been observed along the equivalent GaAs-on-AlAs interface [5]. The non-sharpness of this interface is likely the result of very small steps and elemental diffusion. Hence, at small specimen thicknesses, it is expected that an AlAs-on-GaAs interface is sharper than a GaAs-on-AlAs interface.

6.2 Single Interfaces

6.2.1 Introduction

In order to test the sharpness of interfaces between AlAs and GaAs, a simple boundary between the 2 materials was investigated. The AlAs and GaAs on either side of boundary stretched for 50MLs. Hence, the degree of compositional intermixing that may exist across the interface was not enhanced by the presence of nearby layers. Consequently, any perceived non-sharpness is solely due to the nature of the MBE process used to grow standalone AlAs and GaAs interfaces. Moreover, the possible reasons for the non-sharpness are also explored in this section. In addition, since an AlAs-on-GaAs interface has a different level of sharpness compared to a GaAs-on-AlAs interface, the two types of AlAs / GaAs interfaces were studied independently.

As was stated in Section 6.1, the simple interfaces were grown on wafer A in which no wafer rotation was employed during the growth process. Furthermore, the 2 materials were grown at a substrate temperature of 730°C. The Ga oven temperature was 1048°C and the Al oven temperature was 1103°C. In addition, the As oven was set at a temperature of 165°C and the elements were deposited under a constant As flux. The growth rates of the GaAs and AlAs regions were 0.74ML / sec and 0.58ML / sec, respectively.

In order to gauge the typical sharpness of AlAs-on-GaAs interfaces, Figure 6.1(a) presents an example of a SuperSTEM 1 HAADF image across an AlAs-on-GaAs boundary. The specimen thickness was measured by low loss EELS to be 45nm. Despite the relatively small thickness of specimen, the difference in the background signal of the 2 layers is apparent in the image. Furthermore, the difference in the intensity of the 2 columns in the AlAs dumbbells is clearly visible. It should also be noted that the As columns are on the RHS of the dumbbells in contrast to the dumbbells in Chapter 3.

Figure 6.1(b) is a pair of intensity profiles that were taken across the boundary in the image shown in Figure 6.1(a). It can be seen that, on either side of interface, the dumbbell column ratios are consistent with the experimentally derived GaAs and AlAs column ratios at a thickness of 45nm. The experimentally derived column ratios were presented in Figure 5.10 and Figure 5.11. For instance, the column ratio on the GaAs side has a value of about 1 (it had a value of 0.96 to 1.07 in Figure 5.10) and the column ratio on the AlAs side has a value about 0.4 (it was equal to 0.41 in Figure 5.11). Nevertheless, Figure 6.1(b) also shows the existence of a 2-3ML wide transition region in which the dumbbells are

intermediate between that of GaAs and AlAs. This demonstrates that AlAs-on-GaAs interfaces may only be sharp over 2-3MLs at this specimen thickness.

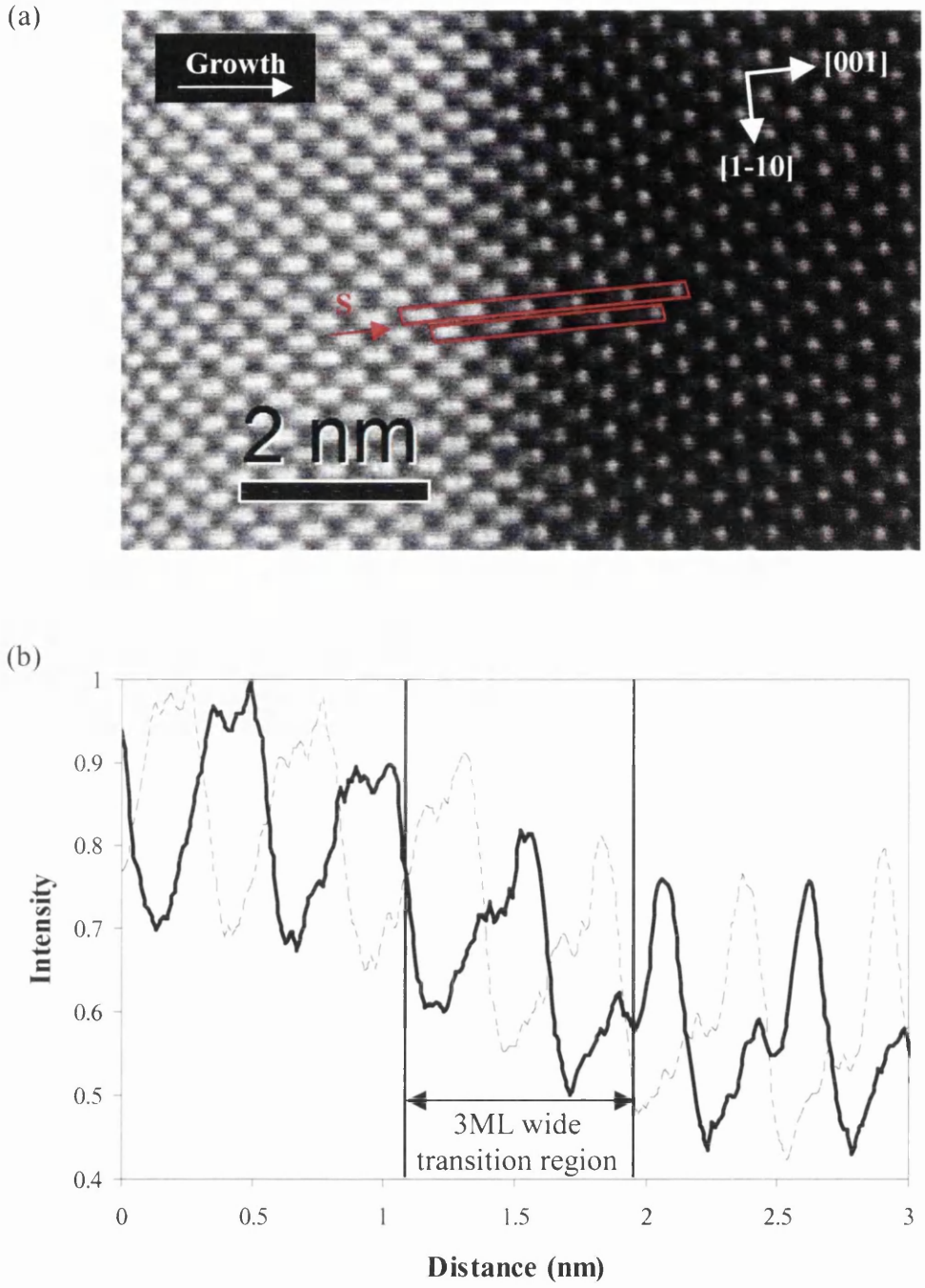

Figure 6.1(a): SuperSTEM 1 HAADF STEM image of an AlAs-on-GaAs boundary. GaAs and AlAs extend for 50nm on either side of the boundary. The specimen thickness was 45nm. **(b)** is an intensity profile taken across the image section S. 2 interleaving profiles are shown. Every point of the intensity profiles is generated from the average of 10 image pixels summed along the [1-10] direction. The intensity is normalised to the maximum intensity.

6.2.2 Beam Spreading Explanation of Non-sharpness

Several explanations are possible for the perceived non-sharpness in the AlAs-on-GaAs interface. First of all, the layers themselves may actually be perfectly defined and the reason that they seem to be rough over 2-3MLs is solely a consequence of the HAADF imaging technique. Chapter 4 demonstrated that a (simulated) electron probe interacts in a complicated manner with atomic columns through the competing effects of channelling and beam spreading. It may therefore be the case that (after a certain depth of crystal) the scattering of a probe, which is positioned close to a boundary between 2 different materials, is influenced by the proximity of the other material. For example, the electrons that are weakly scattered by an Al column (from an AlAs dumbbell) may be re-scattered more strongly by the presence of a nearby region of GaAs since GaAs scatters electrons more effectively than AlAs. This may result in an augmented HAADF signal for the probe positioned on an Al column. Hence, the column ratio that is associated with an interfacial AlAs dumbbell would possess a value that is higher than that expected from bulk AlAs. Such a beam spreading effect may account for the 2-3ML wide transition layer that was observed experimentally.

In order to investigate the exact nature of the effect of the imaging process on the interfacial dumbbells, frozen phonon HAADF STEM simulations were performed across a perfect AlAs / GaAs interface. It should be noted that there is no difference between a GaAs-on-AlAs and an AlAs-on-GaAs interface in the context of the simulations since all of the atoms are in the correct position for a perfectly defined structure. The structure of the simulated area is shown in Figure 6.2. The area is constructed from 4×14 unit cells of AlAs [110] and 5×14 unit cells of GaAs [110]. Due to the slight difference in the lattice parameters of the 2 materials, an average unit cell size (5.65665Å) was implemented along the boundary in order to join the 2 dissimilar materials together. All of the other unit cells have the standard lattice parameters for either GaAs or AlAs. In addition, for adequate sampling of the electron wavefunction to occur, the simulated area was constructed from 1024×1024 pixels.

Figure 6.2 also highlights the specific dumbbells that were simulated across the interface. These comprise 2 GaAs and 3 AlAs dumbbells. For each particular dumbbell, 3 independent probe positions were considered. These consisted of the probe being incident on an As column, an Al (or Ga) column and also incident between dumbbells. The probe

positions are also shown in Figure 6.2. In order to calculate the dumbbell column ratio, the procedure outlined in Section 4.2.4 was used.

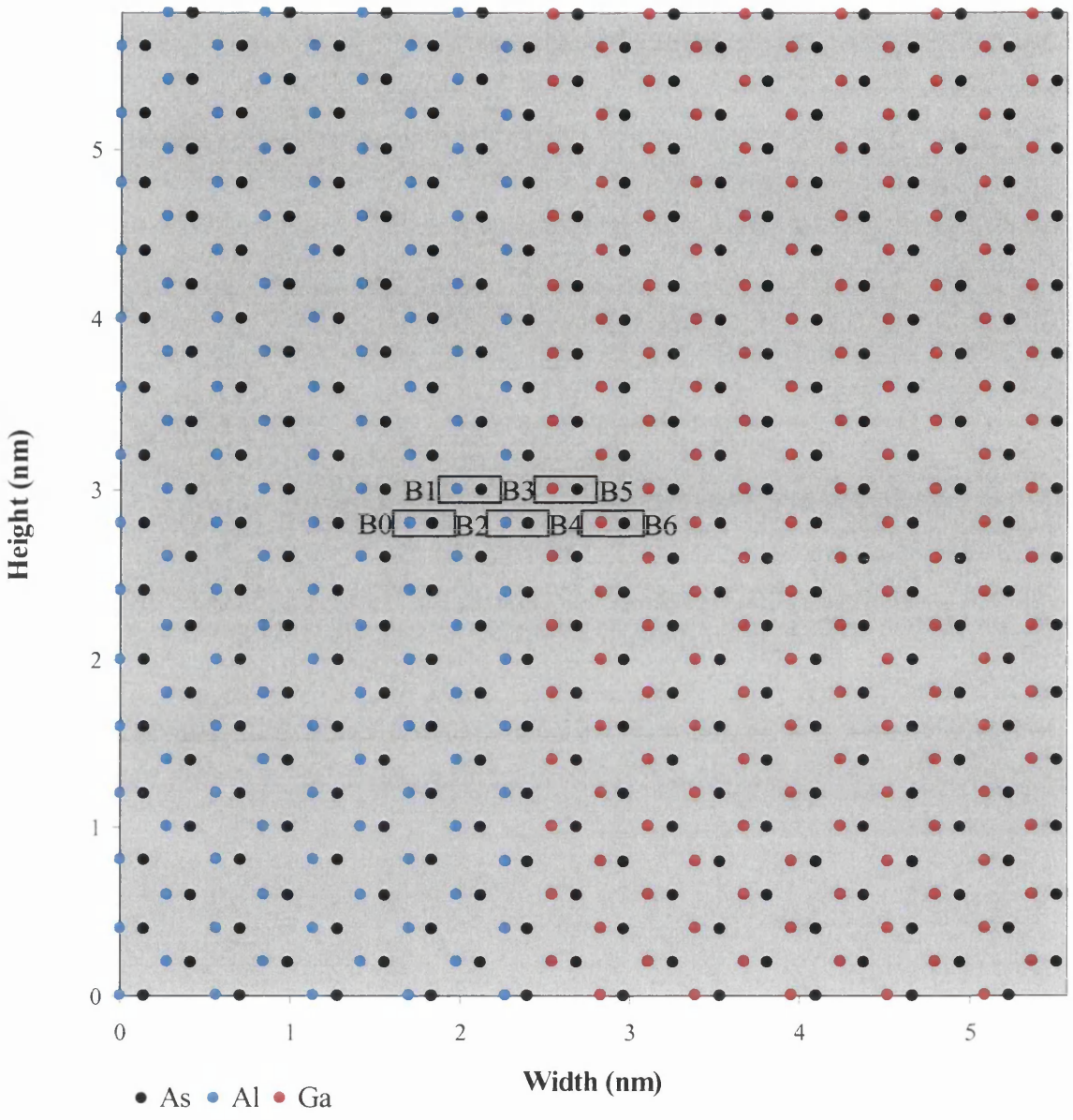

Figure 6.2: The dimensions of the simulated area of a perfect AlAs / GaAs boundary. The rectangles enclose the 5 dumbbells (D1 to D5) from which the dumbbell column ratio was calculated. Calculations were performed for both columns in each dumbbell. B0 to B6 denote the positions of the HAADF background signal calculation.

Due to the fact that the degree of beam spreading (and, hence, any possible effect of the imaging process on the interfacial dumbbells) varies as a function of specimen thickness, the column ratio profile (across the interface) was calculated using a number of different specimen thicknesses. The thicknesses were 40nm, 70nm, 110nm and 160nm. The first 3 values were chosen in order to provide a comparison with experimental data from the 9ML

AlAs / 9ML GaAs superlattice that was obtained at those particular thickness values (see later). In addition, the largest thickness value (160nm) was chosen in order to evaluate the largest possible effect of thickness on the interfacial dumbbells.

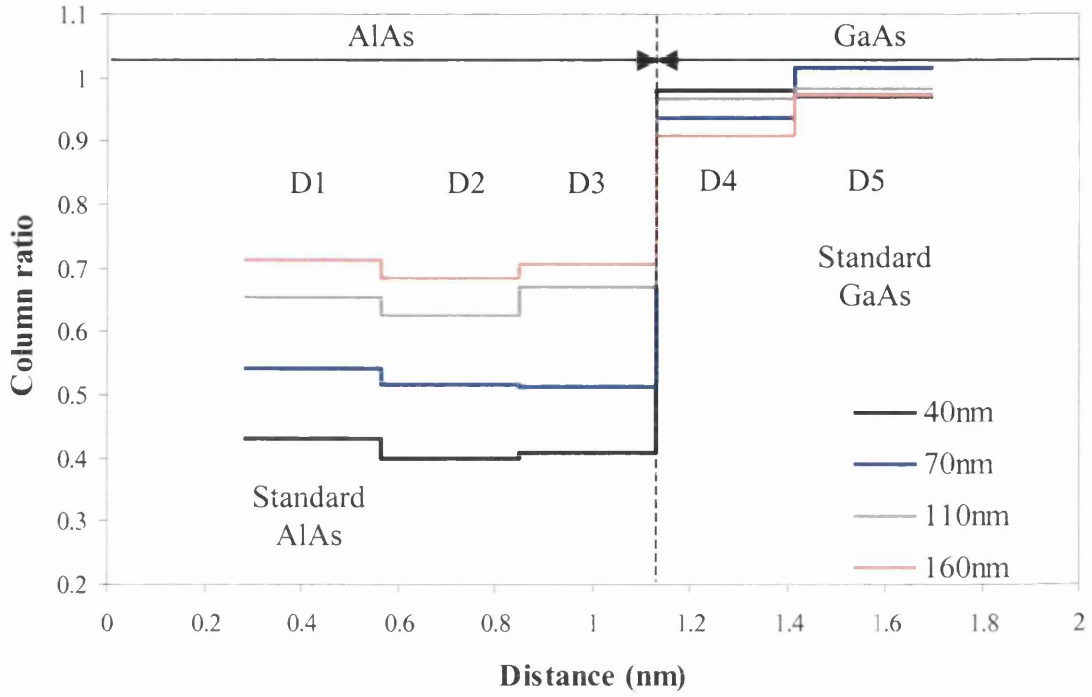

Figure 6.3: Graph of the variation in the simulated HAADF dumbbell column ratio across a perfect AlAs / GaAs boundary. The column ratio for 5 dumbbells is shown for different specimen thicknesses. The HAADF detector has angles from 70mrad to 210mrad. The probe convergence semi- angle was 24mrad.

Figure 6.3 reveals the variation of the simulated column ratio of the 5 dumbbells across the perfect AlAs / GaAs boundary. It can be seen that each of the plots exhibits a different overall column ratio value in the AlAs region (the D1, D2 and D3 dumbbells). This is a result of the thickness dependence of the AlAs dumbbell column ratio, which was discussed in Section 5.4. Furthermore, the actual AlAs values are again consistent with the simulated results shown in Section 5.4.

The small dip in the column ratio for D2 dumbbells is due to the fact that there is a relative height difference between the same types of atoms in neighbouring dumbbells (as explained in Section 4.2.4). For instance, the top most As atom in D2 is on the top surface but the top most As atom in D1 and D3 is 2 Å below the top surface. The relative height difference results in about a 5% change in the column ratio between D2 and D1 (or D3) at the same thickness. In a similar fashion, the column ratio dips in D4 (compared to D5) in

the GaAs region for the same reason. In addition, the actual value of the column ratio also matches the results shown in Section 5.4 for the D5 GaAs dumbbell for all 4 thicknesses.

In conclusion, the simulations of the perfect AlAs / GaAs interface suggest that the dumbbell column ratio is not affected by the nearby presence of different materials. This is evident since there is an abrupt change in the column ratio from pure AlAs to pure GaAs over a wide thickness range. Hence, the explanation for the existence of the 2-3ML wide transition region, which was observed in the experimental AlAs-on-GaAs interface, does not appear to be a result of the imaging process.

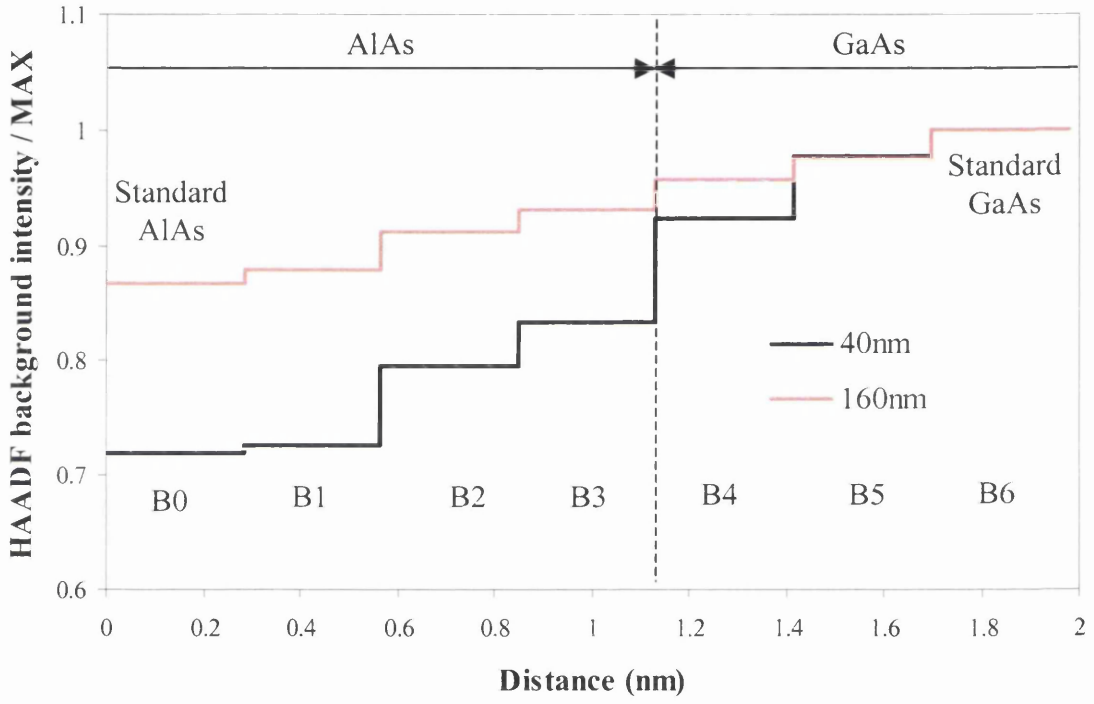

Figure 6.4: Graph of the variation in the simulated HAADF background intensity / maximum intensity across a perfect AlAs / GaAs boundary. 4 specimen thicknesses are shown. The HAADF detector has angles from 70mrad to 210mrad. The probe convergence angle was 24mrad.

Simulations of the HAADF background signal were also performed across the perfect interface. The background signal was simulated at the positions shown in Figure 6.2. However, Figure 6.4 only displays the HAADF background signal variation across the interface at the 2 extreme thicknesses (40nm and 160nm) for clarity. The background signal was normalised with respect to the maximum background signal of each plot. In each case, the maximum occurs in the most RHS position (B6). This is due to the fact that the spread of the beam results in a proportionally greater sampling of the GaAs when the probe is situated at B6. Therefore, since GaAs has a higher Z_{RMS}^2 number (see Section

4.2.4) than AlAs, a greater background signal is generated at B6. For an equivalent reason, the lowest background signal occurs at B0 in the lower Z_{RMS}^2 number material (AlAs). This was also explained in the discussion of the background signal that was observed in the deep superlattice (Section 3.2.2). In addition, the magnitude of the change in the background from the AlAs to the GaAs region is clearly largest in the thinnest (40nm) plot.

The actual value of the background signal at B0 (at a thickness of 40nm and 160nm) reaches the value that was shown in Section 4.3.5 for a wide section of pure AlAs (the value of pure AlAs at 160nm was interpolated from Figure 4.29). In the same way, the value of the background signal at B6 reaches that of pure GaAs at thicknesses of 40nm and 160nm. Hence, the simulated transition region (in terms of the HAADF background signal) is 7ML in width. In addition, Figure 6.4 suggests that the background signal transition width does not change over a wide thickness range (40nm to 160nm). This is clearly unphysical since the geometrical spread of the beam increases with thickness and the width is expected to increase as the thickness is increased. The fact that the background is incorrectly modelled by the simulations was discussed in Section 5.3.4. Furthermore, the experimental investigation into the width of the background signal is presented in Section 6.2.4.2.

6.2.3 Stepping and Diffusion Explanations of Non-sharpness

A second explanation for the observed non-sharpness of the interface, which must be considered, involves the (possible) existence of a surface step profile through the vertical direction of the material. For instance, the interfaces may actually be sharply defined along each of the vertical steps but (due to the fact the acquired image is essentially a projection of this structure) an averaged column composition and, hence, an averaged column ratio would be obtained. A schematic of a simple stepped boundary between AlAs and GaAs is shown in Figure 6.5. Moreover, across the interface, several image dumbbells would exist with shapes that are intermediate between those of the 2 materials on either side of the boundary. The effect of this step profile on an image should diminish if the specimen thickness is reduced. In addition, if the specimen thickness is less than the vertical surface step length, a perfect interface would be observed if only 1 step is projected through.

The diffusion of the various elements (that are present in a particular structure) across the layers (during the growth process), is a third possible explanation for the observed non-sharpness of the AlAs-on-GaAs interface. In this case, the layer boundaries are not well defined and the existence of the 2-3ML wide transition region is a true reflection of the

composition across the interfaces. The effect of this should not disappear at low specimen thicknesses. Therefore, it is clear that the mechanism behind the observed change in the image dumbbell shapes across AlAs / GaAs interfaces can be explored in greater detail by taking into account the thickness of specimen. This endeavour is presented in the Section 6.2.4.

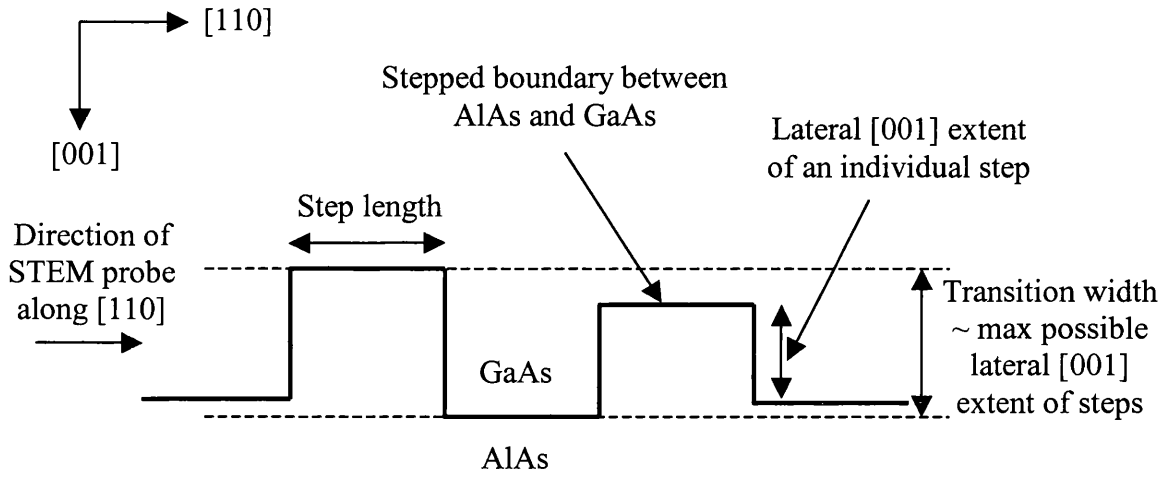

Figure 6.5: A simple schematic of a stepped boundary between AlAs and GaAs. Not to scale. The step length >> transition width.

6.2.4 Level of Sharpness as a Function of Thickness

6.2.4.1 Sharpness of the Interfacial Dumbbell Column Ratio

SuperSTEM 1 was used to acquire HAADF images of AlAs-on-GaAs and GaAs-on-AlAs single interfaces at different thicknesses. Dumbbell column ratio maps were calculated over sections of these images in the same way as was described in Section 3.2.3. For each image, the column ratio map was calculated over the part of the interface that was free from artefacts such as scan noise and surface mottling to ensure that the sharpest part of the interface was examined. Consequently, each column ratio map was different in size. In addition, an averaged line profile was also taken across each column ratio map. The value at each point in a particular profile was calculated from the average value of the dumbbells along the [1-10] direction, perpendicular to the interface.

As an example, Figure 6.6(a) shows a SuperSTEM 1 HAADF STEM image of a GaAs-on-AlAs interface at a specimen thickness of 60nm. As was stated in Section 6.2.1, this type of interface is expected to be not as sharp as an AlAs-on-GaAs interface (see Figure 6.2) at

small thicknesses. However, the way in which the sharpness changes as a function of specimen thickness for both types of interface is unknown.

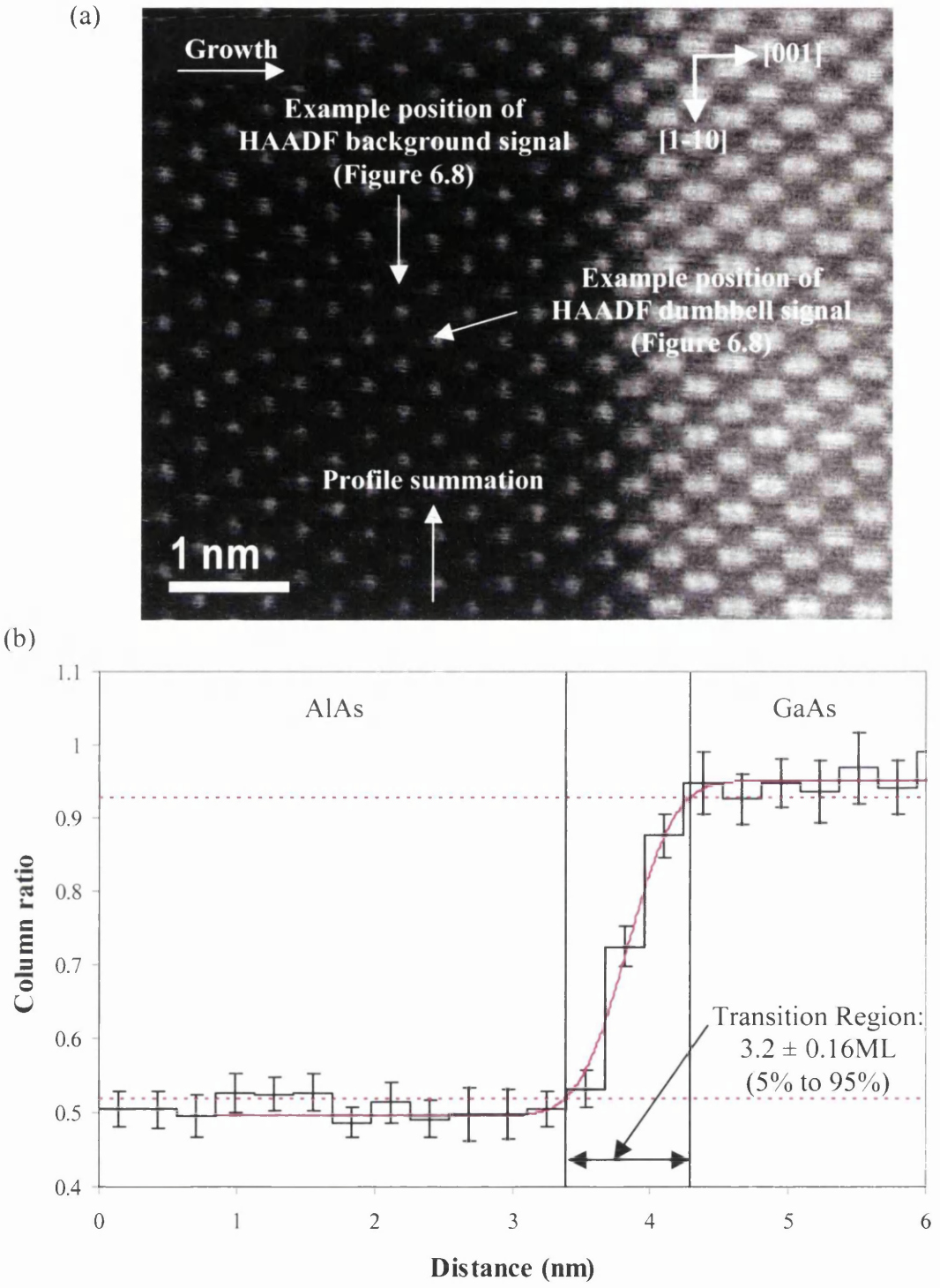

Figure 6.6(a): SuperSTEM 1 HAADF STEM image of a GaAs-on-AlAs boundary. GaAs and AlAs extend for 50nm on either side of the boundary. The specimen thickness was 60nm. **(b)** is an average dumbbell column ratio profile taken across the image in (a). Every point of the column ratio profile was generated from the average column ratio of 25 dumbbells summed along the [1-10] direction. An error function (pink) has been fitted to the column ratio profile. Dotted lines have values of 5% and 95% of the full range of the column ratio values.

Figure 6.6(b) presents an average dumbbell column ratio map profile that was taken across the GaAs-on-AlAs interface in Figure 6.6(a). The AlAs and GaAs column ratios are again consistent with those presented in Section 5.4. Moreover, the profile shows the presence of a 2-3ML wide transition region, which is similar to that observed for the AlAs-on-GaAs interface that was presented in Figure 6.2.

In order to produce a better estimate of the width of the transition region, an error function was manually fitted to the profile of the dumbbell column ratio map. This is shown in Figure 6.6(b) as the pink plot. Since it is unclear what criteria should be used to measure the width of the transition region, a number of measures of the width were compared. For instance, the width that is shown in Figure 6.6(b) was calculated from the distance between the 2 points in the error function that have values of 5% and 95% of the full range of column ratio values. For example, the column ratio value of the error function (in Figure 6.6(b)) extends from 0.495 to 0.95 and has a range equal to 0.455. Therefore, the points that correspond to 5% and 95% have values of 0.51175 and 0.92725, respectively. The points with those values are 3.2 ± 0.16ML apart. The error corresponds to the change in the value of the width that makes no discernable difference to the closeness of the fit to the data. In addition, another measure of the width (25% to 75% of the full range of column ratio values) produces a transition region width equal to 1.32 ± 0.07ML.

A similar analysis was completed for the 2 types of single interface at different thicknesses. It should be noted that at each thickness, the column ratio values for AlAs and GaAs on either side of the interface were again consistent with those presented in Section 5.4. The variation in the width of the transition region as a function of specimen thickness is shown in Figure 6.7 for both types of AlAs / GaAs interfaces. The width was calculated from the 5% to 95% measure as described above. A similar graph is presented in Appendix B that uses the 25% to 75% measure. In addition, only a small number of images were acquired with the necessary level of resolution. However, more results were obtained for the wide layer superlattice (see Section 6.3).

Figure 6.7 reveals that, for the 2 thicknesses shown, the transition region width remains close to 3MLs for the GaAs-on-AlAs interface. On the other hand, there is a large increase in the width of the AlAs-on-GaAs interface after about a thickness of 55nm. For instance, the width is about 3ML at a thickness of 45nm but increases rapidly to become 5-6MLs at 55nm thickness. Figure 6.7 also suggests that the width of the AlAs-on-GaAs interface remains at 5-6MLs up to a thickness of (at least) 90nm.

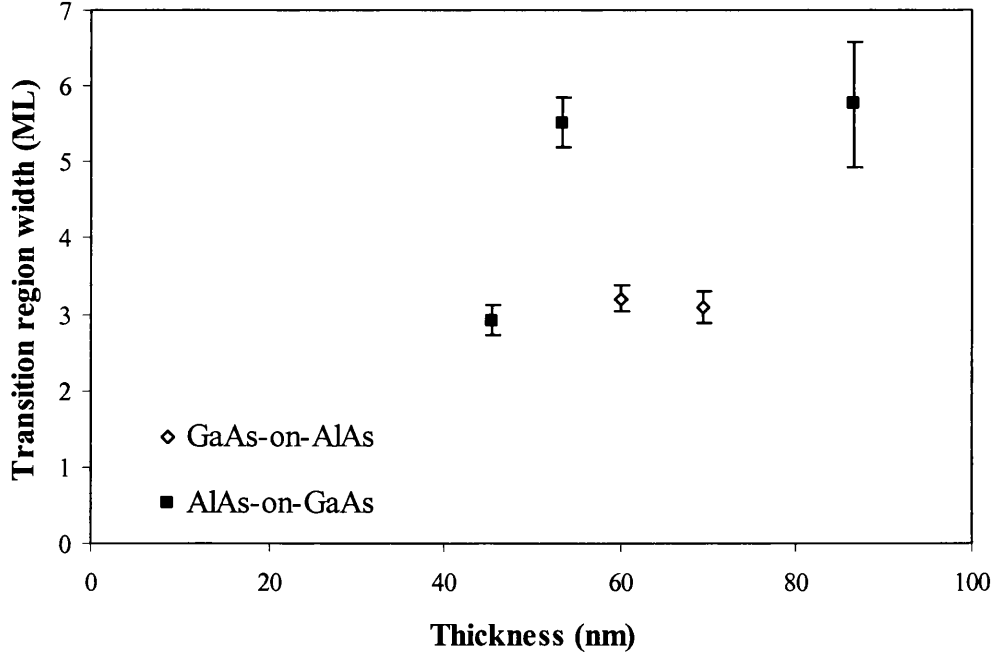

Figure 6.7: A graph of the variation of the column ratio transition region width as a function of thickness for GaAs-on-AlAs and AlAs-on-GaAs single interfaces. Each width was calculated from the fit of the error function using the 5% to 95% measure.

The reduction in the width at the lowest thickness is an indication that AlAs-on-GaAs interfaces are associated with large [110] step lengths. In fact, the transition width decreases rapidly below a thickness of about 55nm. This is the size of the step length that has been reported in previous studies (see Section 1.4). Hence, the transition width decreases as the thickness drops below the average step length as expected from the discussion in Section 6.2.3. Furthermore, the maximum possible lateral [001] extent (see Figure 6.5 for a definition) of these steps is likely to be about 6MLs in size since the maximum value of the transition width stays close to about 6MLs over a wide thickness range (55-90nm). If it is the case that this type of interface has long step lengths and if the width stays constant at a value of 3MLs at lower thicknesses, then the [110] steps may also be characterised by a degree of diffusion (in order to account for the 3ML width). In contrast, the fact that the width does not change (albeit over a small thickness range) for the GaAs-on-AlAs interface suggests that these interfaces are associated with small [110] step lengths (<<60nm) and (or) elemental diffusion. This is further investigated in Section 6.3 in relation to the wide layer superlattice.

6.2.4.2 Sharpness of the Interfacial HAADF Background Signal

The change of the HAADF background signal for the 2 types of interface was also investigated at different thicknesses. As was explained in Section 5.2.1, the HAADF background signal is measured at the positions between dumbbells and is averaged over 6 × 6 image pixels. The HAADF background signal was measured from the same image sections that were used to measure the change in the column ratio in Section 6.2.4.1. Furthermore, an average profile of the background signal was taken across each image section. In this way, each point of a particular profile is formed from the summation of the background signal values along the [1-10] direction, perpendicular to the interface.

Figure 6.8 shows an averaged line profile of the HAADF background signal that was taken across the GaAs-on-AlAs interface shown in Figure 6.6(a). Also shown is the average dumbbell HAADF signal (i.e. the average of 6 × 6 image pixels centred on the As columns) across the interface. The HAADF intensity in Figure 6.8 was normalised with respect to the highest dumbbell HAADF signal that was present in the average line profile.

The change in the HAADF background signal clearly extends for a greater distance across the interface than was observed for the column ratio (Section 6.2.4.1). This was also demonstrated by the simulations in Section 6.2.2. The reason for the larger change of the background signal across the interface (~9ML) is due to the effect of beam spreading in a similar manner that was described in Section 3.2.2 (in relation to the origin of the background signal within the deep superlattice). For instance, a quasi-sinusoidal background signal was observed across the deep superlattice. This was likely the result of the geometrical spread of the beam and the fact that the probe was scanned across alternating layers that possessed different Z_{RMS}^2 numbers. In the case of the background signal change shown in Figure 6.8, a similar situation is evident since the probe is scanned across AlAs and GaAs.

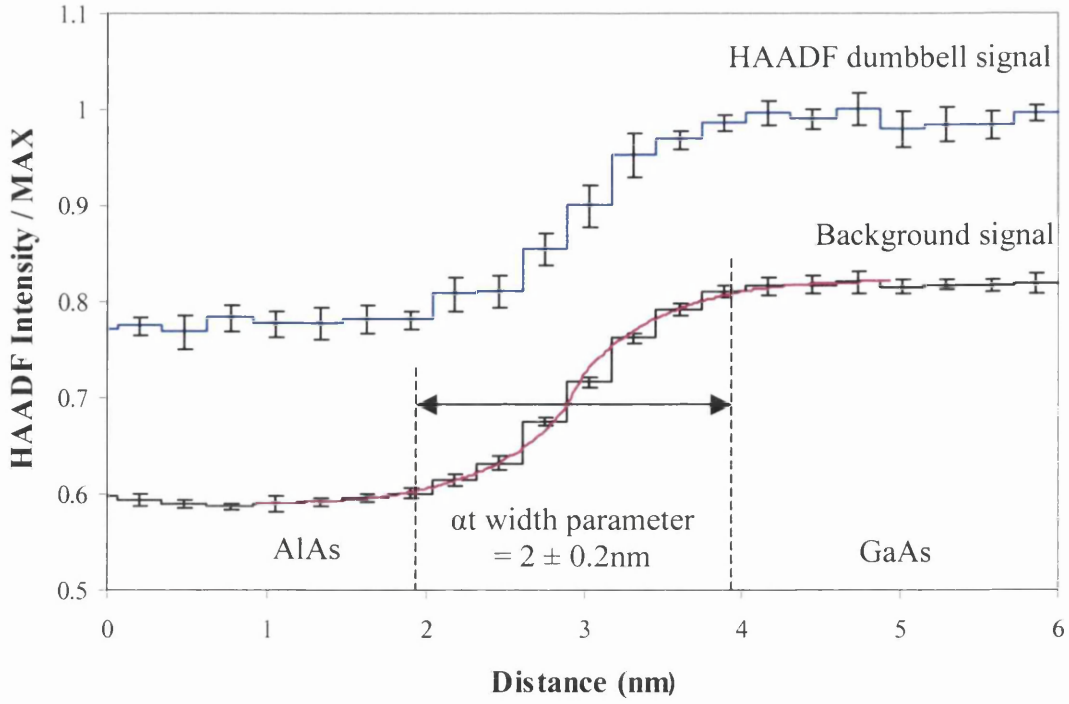

Figure 6.8: An average line profile of the SuperSTEM 1 HAADF background signal (black line) taken across the GaAs-on-AlAs interface shown in Figure 6.6(a). Each point of the profile is generated from the summation of the background signal values along the [1-10] direction. Also shown is an average line profile of the HAADF dumbbell signal (signal on As columns) across the interface (blue line). The HAADF intensity is normalised with respect to the highest dumbbell signal. The fit of the geometrical function is also shown (pink line). The specimen thickness was 60nm.

In order to obtain a measure of the width of the interfacial transition region in terms of the HAADF background signal, a function was fitted to the data. This function was modelled on the geometrical spread of the beam as a function of position across the interface. In this model, the size of the beam at some depth in the specimen (s) is defined by a circle with a radius equal to the convergence semi-angle multiplied by the thickness (αs). At a particular thickness, the area of the circle that lies on one side of the boundary was calculated as a function of position (x). This was done for a range of thickness values.

In order to get the total volume of the beam that lies on one side of the boundary in a specimen of total thickness (t), as a function of position, all of the slices above t were numerically added together. This gave the value of the function at t, as a function of position (x). In order that the function could be fitted to any HAADF background profile, the function was plotted against x / αt. The differential form of this function is shown in Figure 6.9. Figure 6.8 shows the fit of the function (pink plot) to the background signal variation of the GaAs-on-AlAs interface at a thickness of 60nm. A measure of the width of the transition region can then be found from the fit and it is given in terms of the width

parameter αt. In this case, the width is equal to 2 ± 0.2nm. The error corresponds to the change in the width values that make no discernable difference to the closeness of the fit to the data.

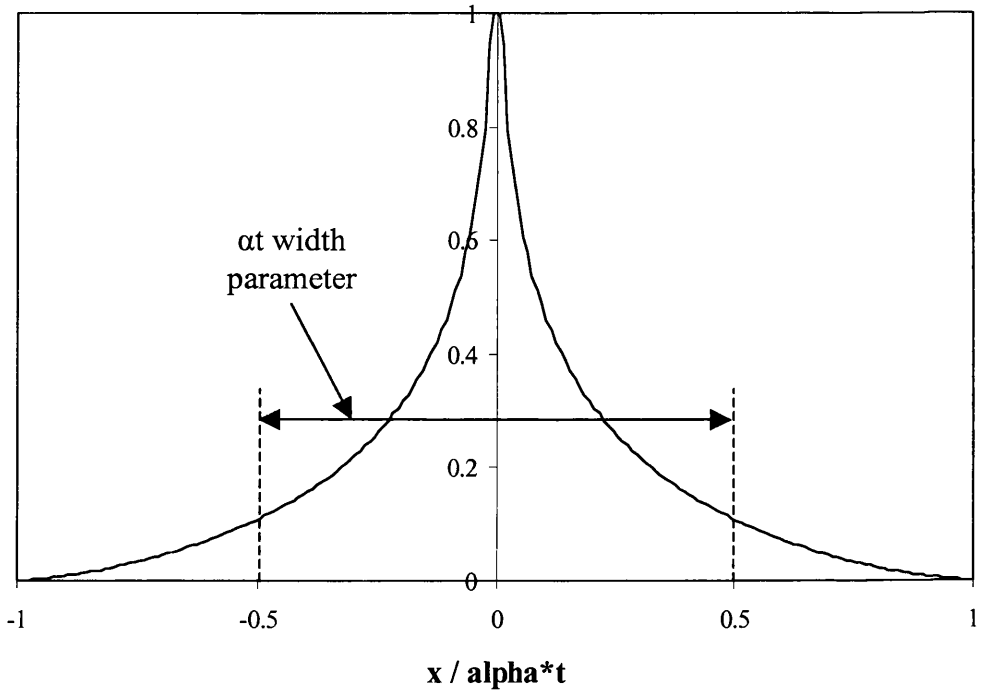

Figure 6.9: Differential form of the geometrical function normalised with respect to highest differential value.

The geometrical function was fitted to the background signal profiles of the interfaces at different specimen thicknesses. The variation of the background signal transition region width (in ML) is shown in Figure 6.10 as a function of thickness. This reveals that the background width for AlAs-on-GaAs interfaces is, in general, higher than that for GaAs-on-AlAs interfaces. This is a consequence of the fact that the projected images of GaAs-on-AlAs interfaces are compositionally sharper than AlAs-on-GaAs interfaces above about a thickness of 45nm (from Figure 6.7). However, Figure 6.10 also shows that even at 45nm thickness, the background width of the AlAs-on-GaAs interfaces is still larger than the width of the GaAs-on-AlAs interface. The reason for this is unclear. In addition, Figure 6.10 also suggests that the background width is greatest at large specimen thicknesses. This is in contrast to the simulations presented in Section 6.2.2.

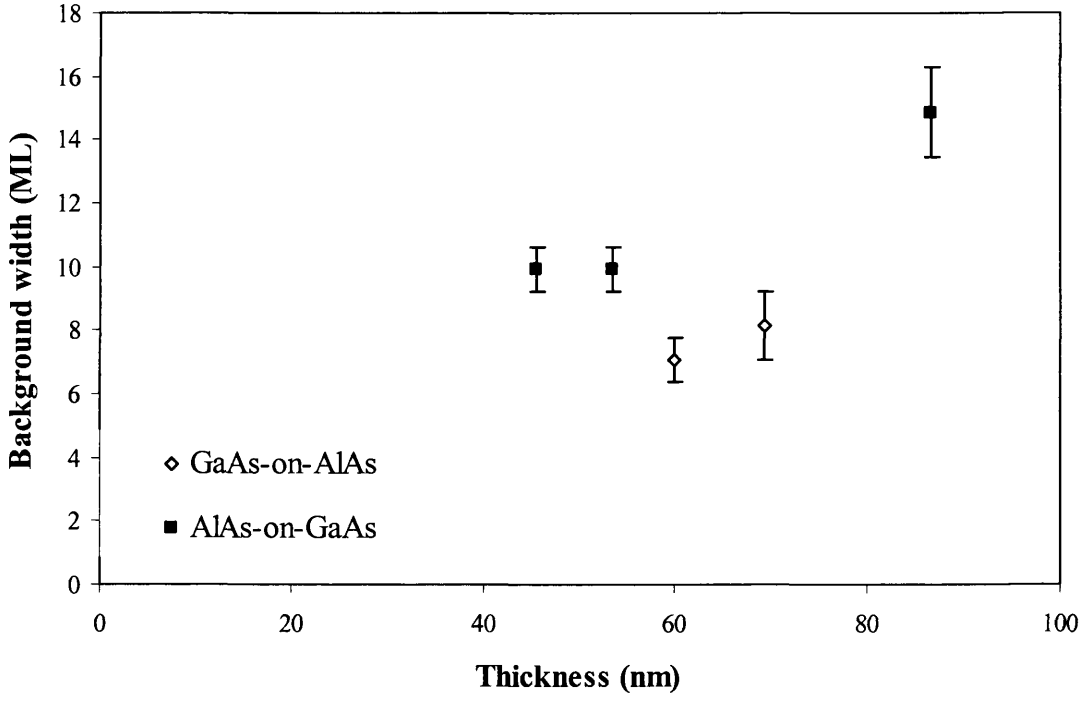

Figure 6.10: A graph of the variation of the background signal transition region width as a function of thickness for GaAs-on-AlAs and AlAs-on-GaAs single interfaces. Each width was calculated from the fit of the geometrical function using the αt measure.

6.3 Wide Layer 9ML AlAs / 9ML GaAs Superlattice

6.3.1 Introduction

Another AlAs and GaAs structure that was examined, through the application of SuperSTEM 1, was a wide layer superlattice that was composed of 10 repeat units of 9ML AlAs / 9ML GaAs. Since the superlattice is constructed from alternating layers, the 2 types of interface (GaAs-on-AlAs and AlAs-on-GaAs) are present in each image taken of it. Hence, the transition region for both interfaces can be determined at the same thickness. However, since the layers repeat after only 9MLs, the maximum possible width of the transition region that can be measured is 9MLs.

As was stated in Section 6.1, the superlattice was grown on wafer A in which no wafer rotation was employed during the growth process. In addition, the structure was grown at a substrate wafer temperature of 730°C. Furthermore, the Ga oven had a temperature of 1048°C and the Al oven had a temperature of 1103°C. On the other hand, the As oven was set at a temperature of 165°C and the As shutter was open continuously during the whole growth process. Moreover, the growth rates for the AlAs and GaAs layers were 0.58ML / sec and 0.74ML / sec, respectively. Hence, these growth conditions are the same as those that were used to grow the single interface that was shown in Section 6.2.

A few repeats of the multilayer structure, in a region 41nm thick, can be seen in the high magnification SuperSTEM 1 HAADF STEM image that is shown in Figure 6.11(a). The difference between the 2 column intensities in the AlAs dumbbells is clearly visible once again. In addition, the value of the image contrast of the AlAs and GaAs layers is consistent with the image contrast in Figure 6.1(a) (similar thickness) and with the results that were presented in Chapter 5 for both AlAs and GaAs. Furthermore, no anomalous regions were observed in the GaAs repeats unlike the case in the deep superlattice in Chapter 3.

Figure 6.11(a) suggests the presence of [1-10] stepping along some of the AlAs-on-GaAs interfaces in the superlattice. The step that is noted in Figure 6.11(a) seems to stretch for 4nm along the [1-10] direction. This length is consistent with the most probable length (about 5nm) that has been reported for [1-10] steps along MBE grown AlAs-on-GaAs interfaces [5].

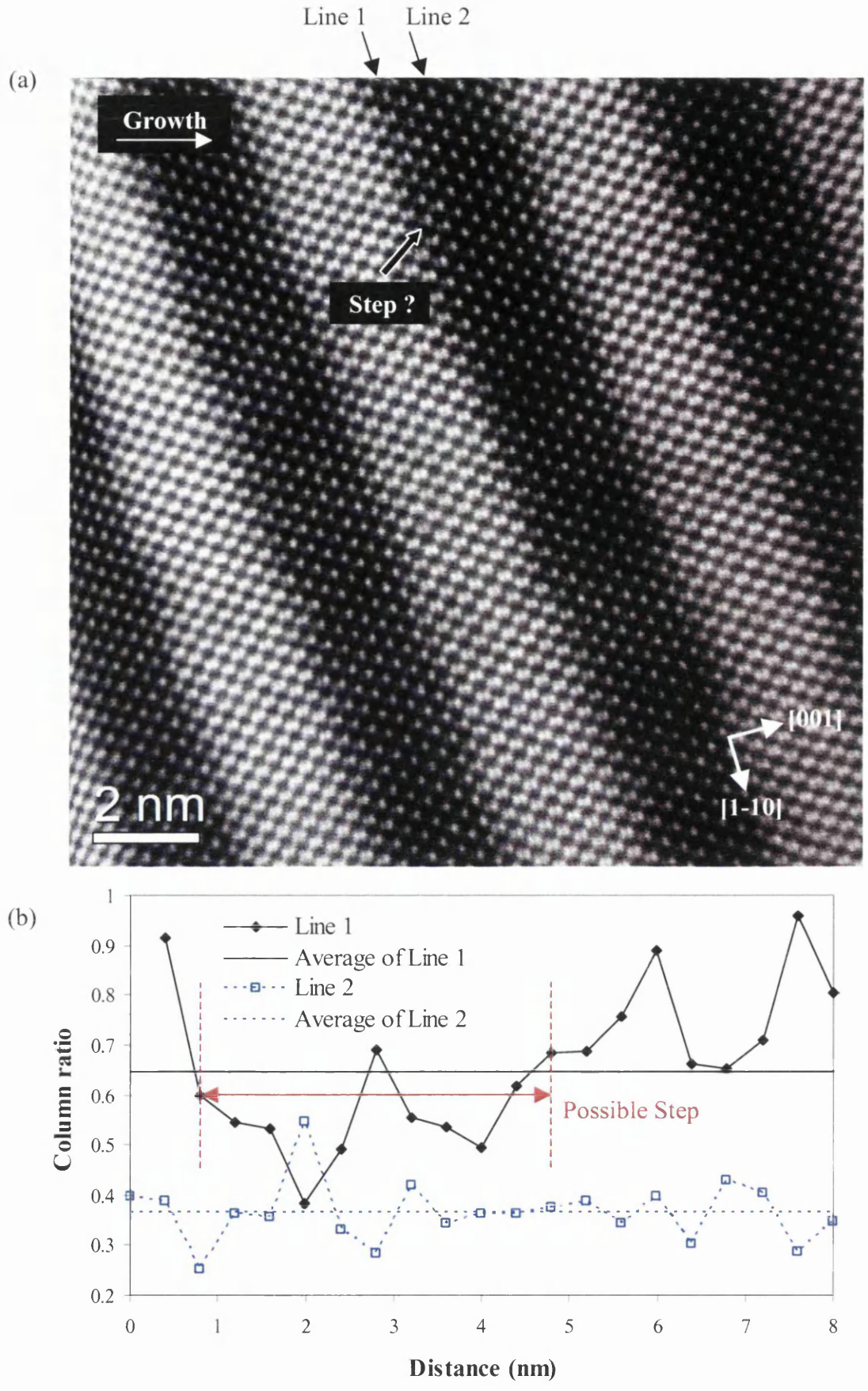

Figure 6.11(a): SuperSTEM 1 HAADF STEM image of several repeats of the 9ML AlAs / 9ML GaAs superlattice. The specimen thickness is 41nm. There may be some evidence of stepping. **(b)** shows 2 column ratio profiles along Line 1 and Line 2. The profiles were taken along the [1-10] direction in each case.

In order to test the existence of the step in Figure 6.11(a), a column ratio line profile was taken along the stepped line of dumbbells, parallel to the interface (Line 1). A similar column ratio line profile was also taken along the central line of an AlAs repeat for comparison (Line 2). The 2 line profiles are presented in Figure 6.11(b). It is clear that the profile of Line 1 is much more variable than that of Line 2. This is an indication that the interface has a degree of roughness along the [1-10] direction.

Figure 6.11(b) reveals that the dumbbells that comprise the possible step have column ratio values that are, in general, lower than the average column ratio value of the entire line. The fact that there is a noticeable difference in the column ratio at the location of the possible step is some evidence in support of the existence of a step with a short step length (~4nm) along the edge of that particular AlAs-on-GaAs interface. Hence, the possible identification of a step in Figure 6.11 adds further support to the view that AlAs-on-GaAs interfaces are associated with stepping along both [110] and [1-10] directions. In addition, no obvious sign of stepping was observed along any of the GaAs-on-AlAs interfaces in Figure 6.11. This is another indication that such interfaces are not associated with large steps.

6.3.2 Sharpness of the Interfacial Transition Region

The 2 types of interface in the wide layer superlattice were studied as a function of thickness in the same manner as was performed for the single interface in Section 6.2.4. For instance, the width of the column ratio transition region was investigated through the calculation of average column ratio map profiles over a range of thickness. The profiles were calculated over image sections that were again chosen from the best part of each image and care was taken not to include any obviously stepped [1-10] interfaces.

Figure 6.12 presents the width of the column ratio transition region of GaAs-on-AlAs and AlAs-on-GaAs interfaces, from the wide layer superlattice, as a function of thickness using the 5% to 95% measure. The values agree closely with those in Figure 6.7. A similar graph is presented in Appendix B that uses the 25% to 75% measure. As was the case in Section 6.2.4.1, the width of the GaAs-on-AlAs interface stays close to 3MLs over the range of thickness (40nm to 100nm). Since the sharpness of the layers does not improve at the lower thickness (40nm), this indicates that compositional spreading of elements during the MBE growth cannot be ruled out as a cause of the transition region. Furthermore, as a result of the fact that the interfaces do not become sharper at the lower thickness, an upper limit on a (possible) [110] surface step length can be set to be much less than 40nm. If the

surface step length was of the order of 40nm, Figure 6.12 should show a narrower transition region at a thickness of 40nm. In fact, as was discussed in Section 6.3.1, the superlattice images do suggest that short order [1-10] steps are not present along the GaAs-on-AlAs interfaces. Hence, it is likely that the diffusion of the elements across the layers was the main reason for the existence of the column ratio transition region in the images of GaAs-on-AlAs interfaces.

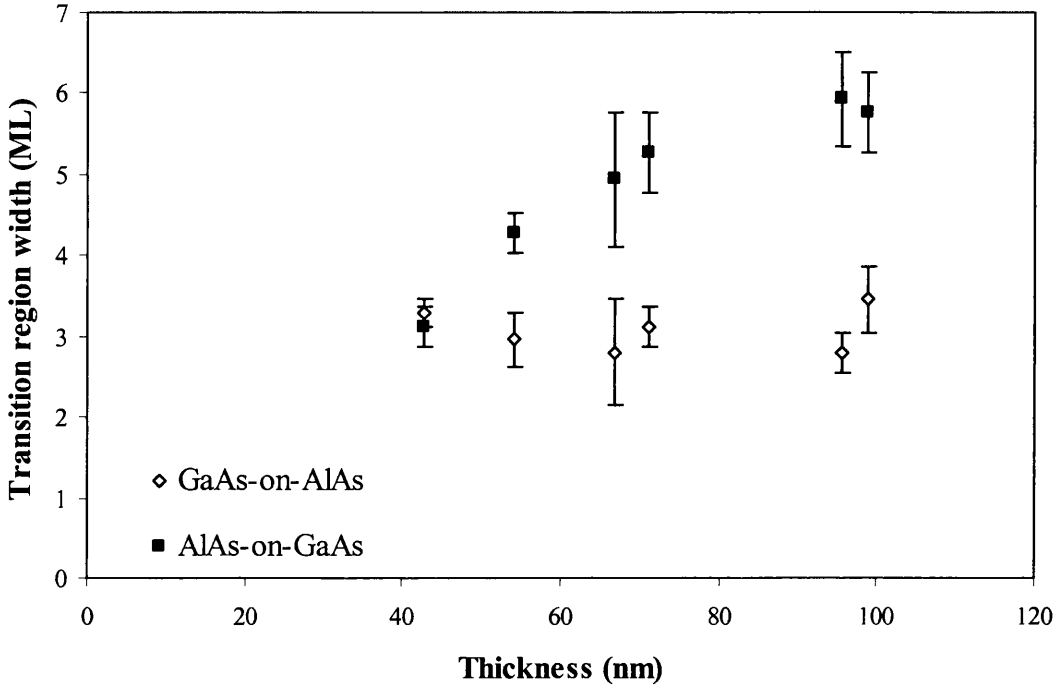

Figure 6.12: A graph of the variation of the column ratio transition region width as a function of thickness for GaAs-on-AlAs and AlAs-on-GaAs single interfaces from the wide layer superlattice. Each width was calculated from the fit of the error function using the 5% to 95% measure.

Figure 6.12 also reveals that the width of the transition region for the AlAs-on-GaAs interface clearly decreases as the specimen thickness is reduced. This again suggests the presence of [110] steps with large step lengths (~40nm). However, due to the fact that the 40nm is the smallest thickness investigated, the existence of elemental diffusion cannot be ruled out. A similar behaviour was also observed for the single AlAs-on-GaAs interface shown in Section 6.2.4.1. In addition, the highest transition region width is again equal to about 6MLs and this occurs at a large specimen thickness (~100nm).

The width of the transition region in terms of the HAADF background signal was also calculated for the 2 types of interface in the wide layer superlattice. This was calculated in a similar fashion as described in Section 6.2.4.2. Figure 6.13 presents the thickness

variation of the background signal width for the 2 interfaces. It is evident that the background width, for both types of interface, remains fairly constant over all thicknesses. The reason that no discernable variation can be observed may be due to the fact that the layer repeats are only 9ML in width. For instance, it was shown in Figure 6.10 that the background width of the AlAs-on-GaAs single interface was always above 10MLs for a thickness range of 45nm to 90nm. Hence, the 9ML repeats are not large enough to encompass the whole background shape. In fact, it was very difficult to fit the geometrical function to the background since the signal never levelled out to a constant value in the AlAs or GaAs regions.

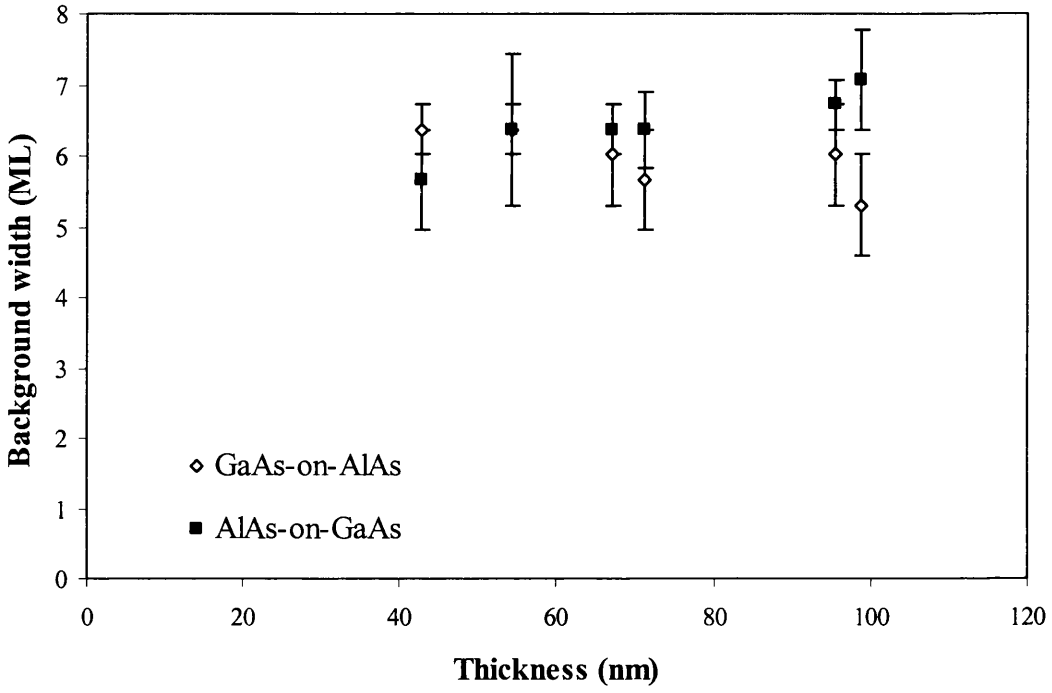

Figure 6.13: A graph of the variation of the background signal transition region width as a function of thickness for GaAs-on-AlAs and AlAs-on-GaAs interfaces from the wide layer superlattice. Each width was calculated from the fit of the geometrical function using the αt measure.

6.4 Narrow Layer Superlattice

The final AlAs and GaAs based structure that was investigated, through the use of SuperSTEM 1, was a short period superlattice. This had the same target structure as the one that formed part of the surface region in the MODFET heterostructure (presented in Chapter 3). However, in this case, the superlattice contained the correct number of repeats.

The superlattice comprised 9 repeat units of 1ML AlAs / 2ML GaAs and was grown on wafer B with a 50rpm substrate rotation. The growth rates of the AlAs and GaAs layers were 0.29ML / sec and 0.69ML / sec, respectively. The substrate wafer was held at a temperature of 615°C throughout the whole growth process. In addition, the Al oven temperature was 1050°C and the Ga oven temperature was 955.5°C. The As oven had a temperature of 165°C and the As shutter was open continuously during the entire growth process. Hence, these growth conditions are significantly different from those that were used to grow the single interface and the wide layer superlattice that were shown in Section 6.2 and Section 6.3, respectively.

A FT (Fourier transform) filtered SuperSTEM 1 HAADF STEM image of the superlattice (at a thickness of 60nm) is given Figure 6.14(a). The image was filtered through the application of a mask around each reflection in the FT. This artificially removes noise from the image and sharpens the dumbbell profile. Figure 6.14(a) shows that, although the layers are less distinct than those in the 9ML AlAs / 9ML GaAs superlattice, the periodicity is clearly visible. Furthermore, the widths of the GaAs layers appear to have the correct widths as opposed to the situation found in the fine superlattice in Chapter 3.

Figure 6.14(b) shows background removed intensity profiles taken across the fine superlattice from the 2 regions marked on Figure 6.14(a). The background was removed from the use of a high pass filter as explained in Section 3.2.2. It is apparent that a range of dumbbells are present across the view of the line profile and that the layer structure is not at all obvious. In fact, some dumbbells clearly demonstrate shapes that are a mixture between AlAs and GaAs dumbbells. This is an expected outcome since the width of the interfacial transition region (with respect to the column ratio), for both types of interface, is over 3MLs at this specimen thickness (see Figure 6.7).

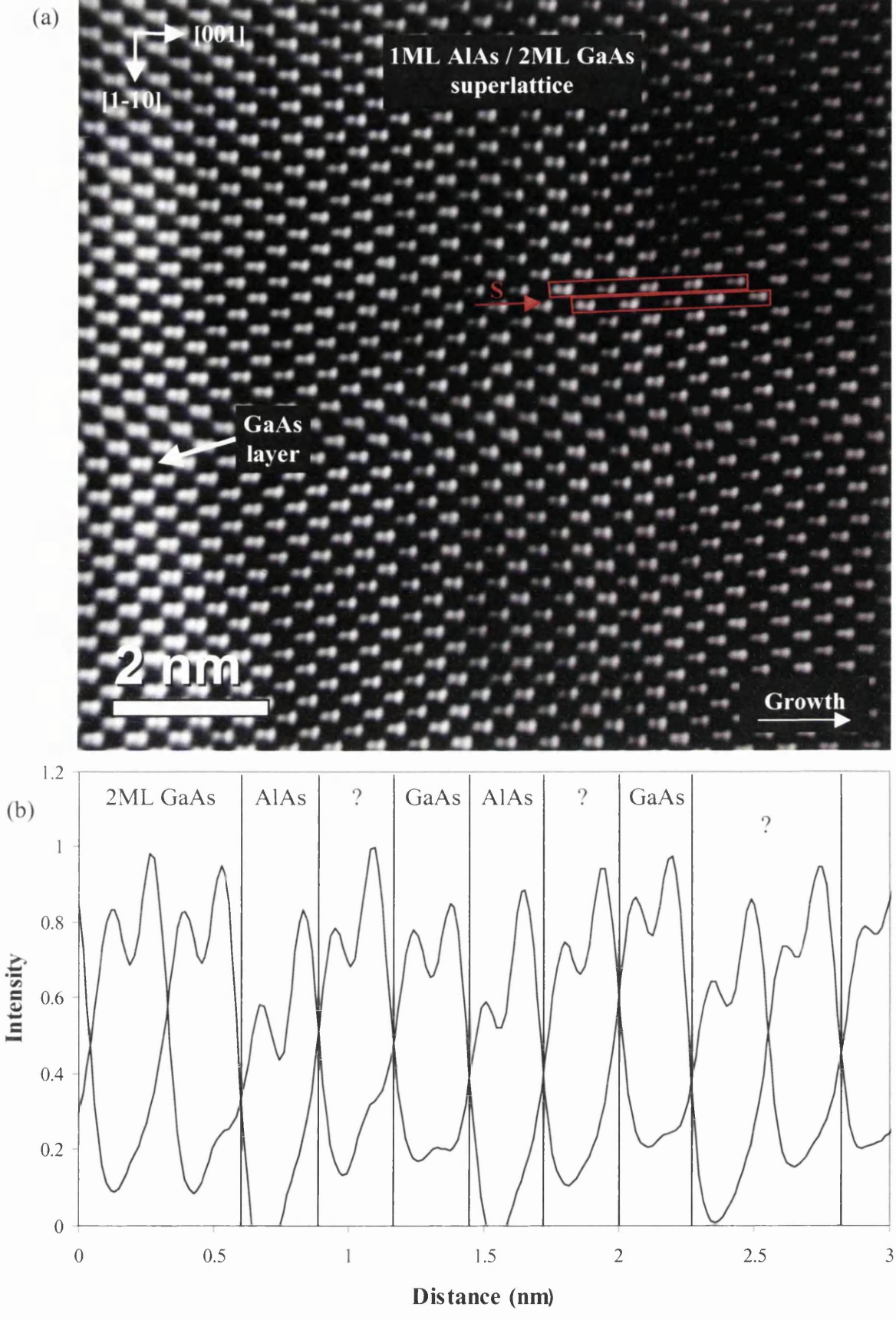

Figure 6.14(a): FT filtered SuperSTEM 1 HAADF STEM image over a 1ML AlAs / 2ML GaAs fine superlattice. A part of a GaAs layer is also visible. **(b)** is an intensity profile taken across image section S. 2 interleaving profiles are shown. Every point of each intensity profile is generated from the average of 10 image pixels summed along the [1-10] direction. The background has also been removed from the profiles from the use of a high pass filter.

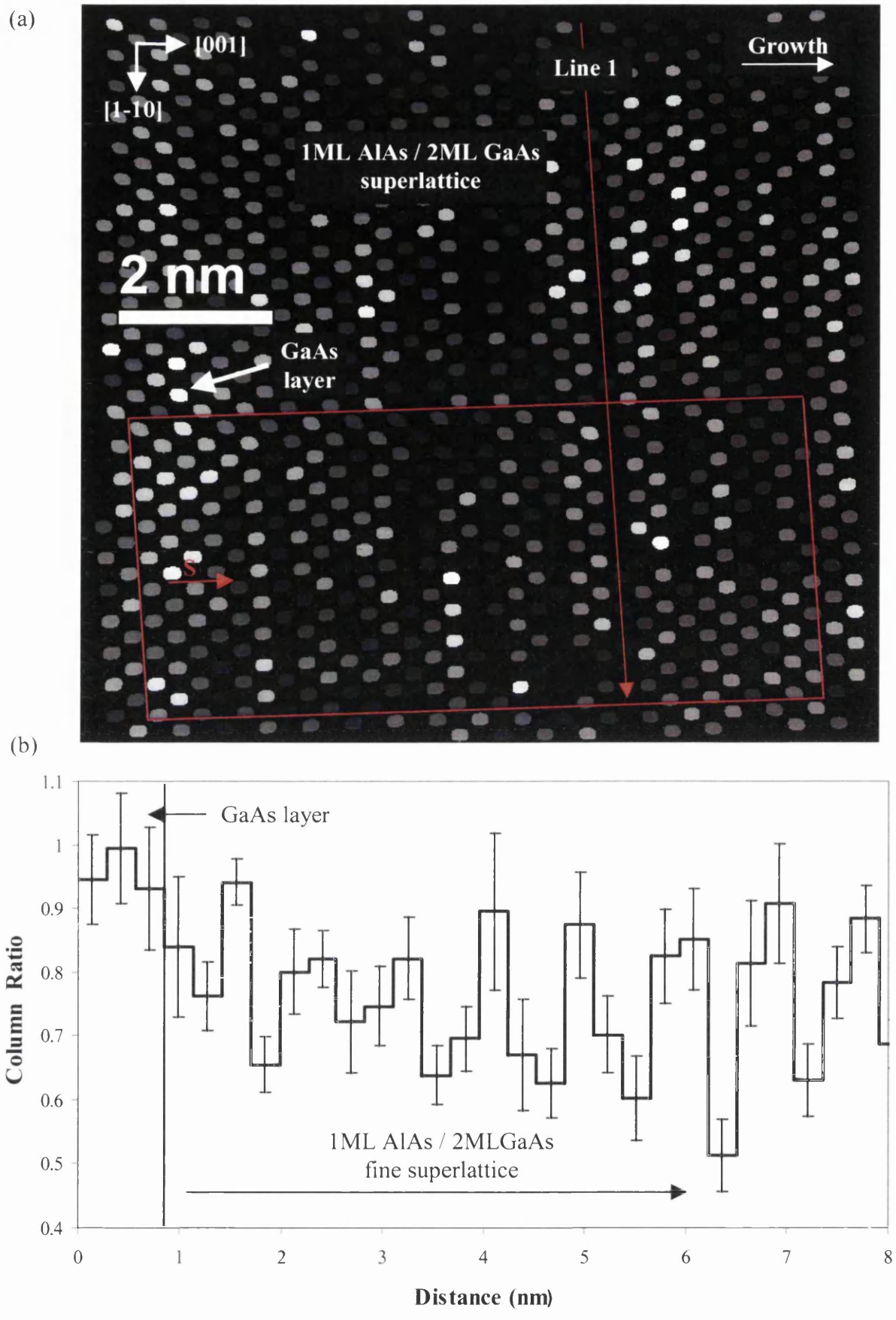

Figure 6.15(a): Dumbbell column ratio map over several repeats of the fine superlattice and part of a GaAs layer. The brightest dumbbells have the highest column ratios i.e. more GaAs like. **(b)** is an average profile taken across section S in (a). Another profile was taken along Line 1 (see Figure 6.15).

Figure 6.15(a) shows a column ratio map that was calculated from the image in Figure 6.14(a). The periodicity of the superlattice is, again, visible across the structure. The start of the GaAs region on the left hand side of the map is also discernible. It should be noted that there is a large variation in the column ratio values (extreme values go from 0.3 to 1.2) in the map. Figure 6.15(b), which is an averaged line profile taken across the column ratio map in Figure 6.15(a), shows several peaks in the column ratio that indicate the location of the GaAs layers. However, the column ratio value of these layers never reaches the value of standard GaAs i.e. a value of about 1 (see Section 5.4). Furthermore, the peaks are separated by a reduction in the column ratio that is associated with the 1ML wide AlAs layers. Nevertheless, the value of the column ratio within most of these dips does not possess the value of standard AlAs at this thickness i.e. a value of about 0.5 (see Section 5.4). Hence, it is evident that the layers in the superlattice are not sharply defined despite the fact that, overall, the superlattice is closer to the target structure than the equivalent MODFET fine superlattice in Chapter 3. This is likely due to diffusion and stepping as explained in earlier sections.

In addition, Figure 6.16 shows a column ratio map profile taken along Line 1 in Figure 6.15(a), parallel to the interface. The average value of this line is 0.65 and is, therefore, considered to be one of the AlAs dips. However, it is clear that there is a large variation of the value along the interface. The fact that the column ratio is, in general, lower than the average value on the LHS of Figure 6.16 and higher on the right may indicate the presence of stepping. Nevertheless, the existence of steps is less apparent than in the case of the wide layer superlattice (Section 6.3.1) due to the shorter periods and the higher level of apparent roughness in the narrow layer superlattice.

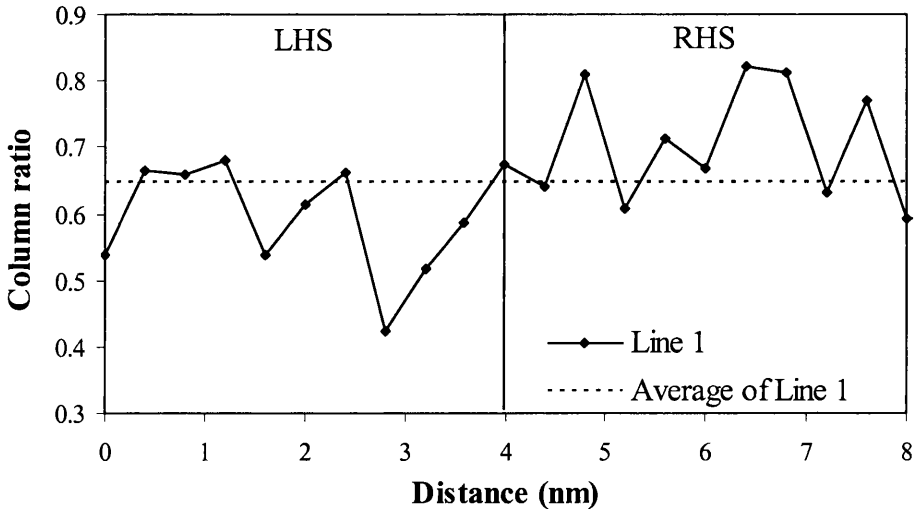

Figure 6.16: Column ratio map profile taken along Line 1 in Figure 6.14(a) i.e. along the [1-10] direction.

6.5 Conclusion

In this chapter, different AlAs and GaAs MBE grown structures were investigated through the use of SuperSTEM 1. The structures included the 2 types of interface between wide layers of AlAs and GaAs. These were studied as a function of thickness and the investigation took into consideration the standard dumbbell column ratios that were derived in Chapter 5. In addition, a wide layer 9ML AlAs / 9ML GaAs superlattice and a narrow layer 1ML AlAs / 2ML GaAs superlattice were also considered.

It was established that a 2-3ML wide transition region was present across a single GaAs-on-AlAs interface over a small thickness range (55nm to 70nm). The dumbbell shapes that comprised this region were intermediate between that of standard AlAs and standard GaAs (found from Chapter 5). Several possible explanations for this observation were proposed. However, it was revealed through frozen phonon multislice calculations across a perfect AlAs / GaAs interface that electron intensity channelling and beam spreading had little effect on the origin of the transition region. Hence, the perceived non-sharpness of the MBE grown interfaces was likely a true reflection of the quality of the layers and not an artefact of the imaging process. In addition, the fact that the width of the transition region did not change with respect to thickness suggested that the GaAs-on-AlAs interface was associated with elemental diffusion that was introduced during the growth process and possibly very short step lengths.

In contrast to the GaAs-on-AlAs single interface, the transition region width of an AlAs-on-GaAs single interface was shown to decrease at the lowest specimen thickness (~45nm). This indicated that such interfaces are associated with large [110] step lengths (>40nm). Furthermore, since the maximum width remained close to 6MLs over a large thickness range (55nm to 90nm), the maximum possible lateral [001] extent of such steps (see Figure 6.5) is likely to be 6MLs.

The width of the transition region, with respect to the HAADF background signal, was also investigated across the 2 types of AlAs / GaAs single interfaces. It was found in both cases that the background width decreased as the thickness was reduced. Moreover, the background width of the GaAs-on-AlAs interface was found to be generally smaller than that of the AlAs-on-GaAs interface. This reflected the sharper nature of GaAs-on-AlAs interfaces at thicknesses above 45nm.

The observed non-sharpness of the 2 types of interface was investigated further through the analysis of several image sections of a 9ML AlAs / 9ML GaAs superlattice at different specimen thicknesses. It was again demonstrated that the width of the transition region of the GaAs-on-AlAs interface did not change as a function of specimen thickness. This established an upper limit of much less than 40nm for the length of any possible [110] steps. However, the specimen thickness was not low enough to rule out the existence of elemental diffusion from the growth process.

The width of the transition region of the AlAs-on-GaAs interface in the wide layer superlattice was found to vary in a similar fashion to that of the AlAs-on-GaAs single interface. For instance, it was shown that the width decreased from about a value of 6MLs at a large thickness (100nm) to a value of 3MLs at 40nm thickness. This is again indicative of [110] steps with a large step length. In addition, the images of the interface also suggested the presence of short length [1-10] steps along the AlAs-on-GaAs interfaces of the superlattice.

The background width of the 2 types of interface in the superlattice was also explored as a function of thickness. However, due to the fact that the layer repeats were only 9MLs in size, the full background profile of either type of interface was never reached. Hence, no variation in the background width was observed.

A narrow layer 1ML AlAs / 2ML GaAs superlattice was also studied. The column ratio map taken over the superlattice showed that a wide range of dumbbell shapes were present. This was due to the fact that the width of the interfacial transition region (with respect to the column ratio), for both types of interface, is over 3MLs at the particular specimen thickness. Furthermore, the column ratio profile taken parallel to an interface in the superlattice again suggested the existence of stepping. Despite this, the multilayer showed a much closer agreement to the target growth than was the case with the corresponding faulty superlattice from the MODFET in Chapter 3.

In summary, the results of this chapter suggest that the sharpness of MBE grown GaAs-on-AlAs interfaces is associated with diffusion and possibly short steps. For that reason, over the thickness range offered by the cross-section specimen preparation technique, the non-sharpness of GaAs-on-AlAs interfaces remains constant at about 3MLs. On the other hand, the sharpness of AlAs-on-GaAs interfaces was shown to vary considerably over the specimen thickness range. This indicated that these types of MBE grown interfaces were associated with large [110] step lengths and possibly diffusion.

References

[1] W. L. Sarney, S.P. Svensson, Characterization of compositional oscillations in InGaAs films induced by MBE cell configuration and substrate rotation, Sensors and Electron Devices Directorate, U.S. Army Research Laboratory, Adelphi, MD 20783 USA (2005)

[2] S. Magalaes, A. Fonsecaa, N. Francoa, N. P. Barradasa, N. Sobolevc, R. Heyd, H. Grahnd and E. Alves, Damage behaviour of GaAs / AlAs multilayer structures, Nuclear Instruments and Methods in Physics Research B 249, 890-893 (2006)

[3] I. Bartos, T. Strasser, W. Schattke, Surfaces and interfaces in short-period GaAs / AlAs superlattices, Progress in Surface Science 74, 293-303 (2003)

[4] B. R. Nag, Interface roughness scattering limited mobility in AlAs / GaAs, $Al_{0.3}Ga_{0.7}As$ / GaAs and $Ga_{0.5}InP$ / GaAs quantum wells, Semiconductor Science Technology 19, 162-166 (2004)

[5] N. Ikarashi, K. Ishida, High-resolution transmission electron microscopy of AlAs-GaAs semiconductor superlattices, Journal of Materials Science: Materials in Electronics 7, 285-295 (1996)

[6] B. Z. Nosho, W. Barvosa-Carter; M. J. Yang, B. R. Bennett, L. J. Whitman, Interpreting interfacial structure in cross-sectional STM images of III-V semiconductor heterostructures, Surface Science 465, 361-371 (2000)

[7] T. Kitada, S. Shimomura, S. Hiyamizu, Surface segregation of indium atoms during molecular beam epitaxy of InGaAs / GaAs superlattices on (n11)A GaAs substrates, Journal of Crystal Growth, doi:10.1016/j.jcrysgro.2006.11.170 (2006)

[8] V. V. Chaldyshev, Two-dimensional organization of As clusters in GaAs, Materials Science and Engineering B88, 195-204 (2002)

[9] M. A. Herman, D. Bimberg, J. Christen, Heterointerfaces in quantum wells and epitaxial growth processes: Evaluation by luminescence techniques, Journal of Applied Physics, Vol. 70, No. 2 (1991)

7 The Characterisation of Various MBE Grown Nanostructures using SuperSTEM 1

7.1 Introduction

In this chapter, an investigation of 2 different categories of MBE grown nanostructures is presented. These structures were studied through the use of SuperSTEM 1 and comprise InAs / GaAs based superlattices and Si δ-doped layers embedded in GaAs. The Si δ-doped layers are commonly found in MODFET heterostructures, similar to the one shown in Chapter 3. On the other hand, this is not normally the case with the InAs / GaAs based superlattices. In fact, it was uncertain whether such superlattices could actually be grown through the use of MBE due to the tendency of the In to diffuse into the surrounding layers. Furthermore, the general aim (in a similar fashion to Chapter 3) was to investigate the quality and physical nature of the structures in order to evaluate the accuracy of the growth techniques.

Table 7.1 reveals that the InAs / GaAs superlattices and the Si δ-doped layers are contained on 2 different wafers, A and B. These are the same wafers as those described in Chapter 6. The InAs / GaAs superlattices were grown on Wafer A without a wafer rotation for the reasons outlined in Section 6.1. On the other hand, in order to overcome the problems that were encountered with the study of the Si δ-doped layer in Chapter 3, a wafer that contained a range of Si δ-doped concentrations was grown specially (Wafer B). This wafer was grown with a 50rpm substrate rotation.

	Wafer A	Wafer B
Rotation	No	Yes
InAs / GaAs superlattices	Yes	No
Si δ- doping layers	No	Yes

Table 7.1: A description of wafer A and B.

All of the structures were grown epitaxially on top of a GaAs substrate along the [001] crystal direction by MBE. Furthermore, STEM samples were prepared using the cross-section technique and were finished with a low energy ion mill at 400eV and at an angle of 6^{o} using a GentleMill (see Section 2.6). All specimens were orientated along the [110] direction as before.

7.2 InAs / GaAs Based Superlattices

7.2.1 Background

The purpose of the investigation of the InAs / GaAs based superlattices was, as before, to determine the level of compositional sharpness of the interfaces that were present within the multilayers. It has been noted that InAs based quantum dots are an important class of materials [1]. They are used in semiconductor devices because their properties can be adjusted through the alteration of their size [1]. InAs is also of interest for use as the conducting channel in III-V MODFETs. In comparison, InAs / GaAs based superlattices are not commonly found in semiconductor devices. The reason for this centres on the fact that the In has a tendency to spread into the surrounding GaAs layers. In fact it is widely known that in InGaAs / AlGaAs systems, surface segregation of the In atoms (during the MBE process) is recognized as a cause of severe degradation of the compositional abruptness of the heterointerfaces. This has been observed by Auger electron spectroscopy, X-ray photoemission spectroscopy and reflection high-energy electron diffraction [2]. Hence, it is evident that such InAs based structures are difficult to grow to the same quality as equivalent AlAs / GaAs based structures.

If a superlattice could be made to a suitable quality from an InAs / GaAs system, then the performance of semiconductor devices could be improved. For instance, in a typical MODFET heterostructure (like the one presented in Chapter 3) a uniform layer of $In_xGa_{1-x}As$ is exploited in order to form an appropriate conducting channel. The mobility, which is associated with the charge carriers in the channel, would be improved if the $In_xGa_{1-x}As$ layer is substituted with a similar composition InAs / GaAs superlattice. The explanation for this is that the charge carriers are scattered less by the more ordered superlattice structure than they are by a regular layer of $In_xGa_{1-x}As$. Hence, it was of great interest whether an InAs / GaAs superlattice could be grown by MBE.

2 different MBE grown InAs / GaAs multilayer structures were investigated. The first one was a superlattice composed of 6 repeat units of 1ML InAs / 6ML GaAs. On the other

hand, the second structure was a superlattice composed of 10 repeat units of 1ML InAs / 3 ML GaAs. Due to the fact that the 1ML InAs / 3 ML GaAs superlattice is a shorter period structure, it was expected that a similar level of interfacial roughness would have a bigger effect than in the 1ML InAs / 6ML GaAs superlattice.

It should be noted that in order to study the InAs / GaAs superlattices, analysis of the dumbbell column ratio was desired in a similar fashion to that shown in earlier chapters. However, unlike the case of AlAs and GaAs, the experimental variation of the InAs column ratio as a function of thickness was not measured. However, Figure 7.1 shows the simulated HAADF dumbbell column ratio for InAs [110] as a function of thickness for a 24mrad probe convergence semi-angle. The simulations were performed in the same way as was discussed in Chapter 4 and Chapter 6. Figure 7.1 shows that the column ratio has a value greater than 1 (i.e. the intensity of the In column is greater than that of the As column) for thicknesses up to 20nm. The column ratio then remains close to 0.85 for greater crystal depths. Thus, the dumbbell column ratio can appear bigger or smaller than that of GaAs (about equal to 1 over a wide thickness range- see Section 5.4) depending on the thickness of the specimen.

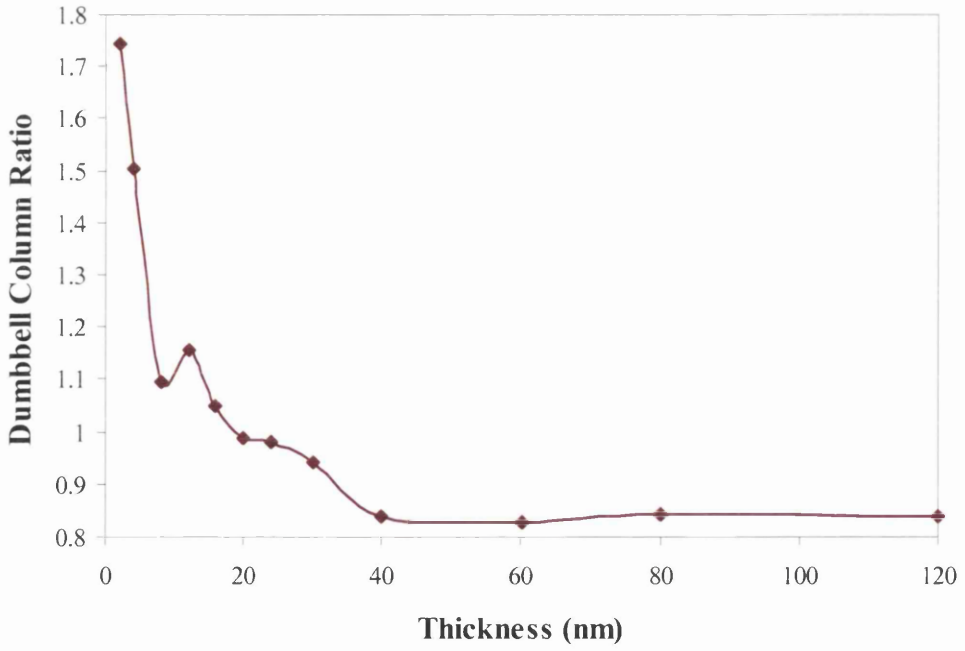

Figure 7.1: A graph of the simulated HAADF STEM contrast of InAs [110] as a function of specimen thickness HAADF detector angles were 70mrad to 210mrad and the probe semi- angle was 24mrad.

7.2.2 1ML InAs / 6ML GaAs Superlattice

The 6 repeat 1ML InAs / 6ML GaAs superlattice was grown with a substrate wafer temperature of 575°C. The substrate temperature for InAs structures is generally lower than equivalent AlAs / GaAs structures in order to suppress re-evaporation and segregation of the In atoms [3]. The superlattice was grown on Wafer A and, therefore, no wafer rotation was employed. In addition, the In and Ga oven temperatures were 882°C and 1048°C, respectively. Also, the As oven had a temperature of 210°C and the multilayer was grown under a constant flux of As. Furthermore, the individual growth rates of the InAs and GaAs layers were 0.25ML / sec and 0.74ML / sec, respectively.

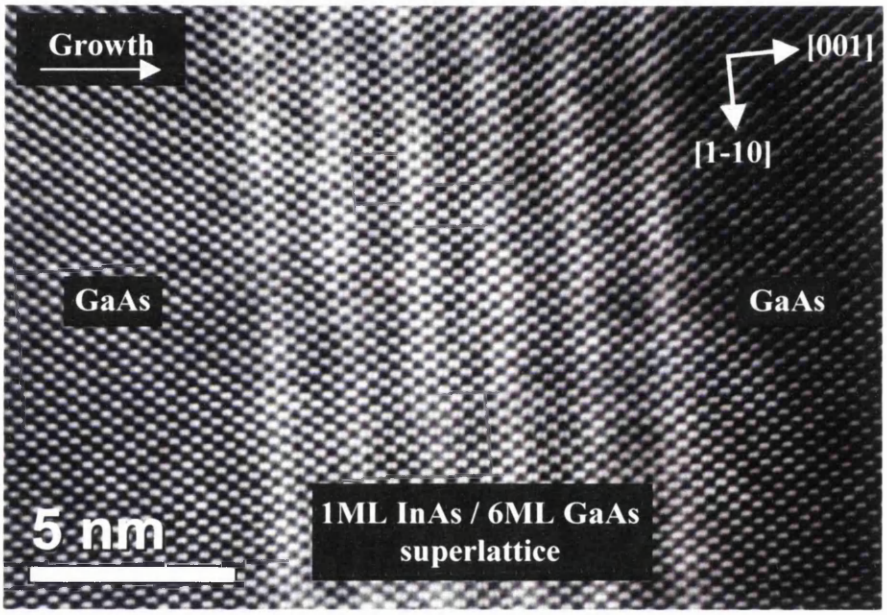

Figure 7.2: FT filtered SuperSTEM 1HAADF STEM image of the 6 repeat 1ML InAs / 6ML GaAs superlattice.

A FT filtered SuperSTEM 1 HAADF STEM image over the 6 repeats of the superlattice is displayed in Figure 7.2. The image was filtered through the application of a mask around each reflection in the FT as described in Section 6.4. The multilayer is shown between 2 GaAs spacer regions in Figure 7.2. The image reveals that the periodicity of the superlattice is, in fact, present in this case. This, therefore, indicates that MBE has the ability to grow such structures. In Figure 7.2, the InAs layers appear as the most intense features due to the atomic number sensitivity of the HAADF imaging process. It can be seen that the bands of high intensity are extended over several monolayers. However, this does not immediately indicate that the individual InAs layers are not confined (as intended)

to 1 monolayer. The apparent extent of the InAs layers may simply be due to the nature of the HAADF background signal alone.

Figure 7.3(a) gives a FT filtered (high magnification) SuperSTEM 1 HAADF STEM image of the 6 repeat of the 1ML InAs / 6ML GaAs superlattice. The specimen thickness was measured to be 41nm by low loss EELS. This value is less than the thickness of the superlattice that was shown in Figure 7.2. Hence, the periodicity of the structure is less apparent due to the overall reduction in the HAADF background signal. In addition, the As columns are on the RHS of the dumbbells.

Figure 7.3(b) provides 2 background removed (via a high pass filter) interleaving intensity profiles that were taken across the middle of the (likely) position of a 1ML InAs layer. These profiles show that some of dumbbells have relative column intensities expected of GaAs at this thickness (see Figure 5.10). In addition, Figure 7.3(b) highlights the fact that 2 neighbouring dumbbells have higher intensity on the non-As side of the dumbbells. For instance, the dumbbell at the 0.8nm position in Figure 7.3(b) clearly has a higher intensity on the LHS column. In fact, the column ratio of the dumbbell at the 0.8nm position has a value of about 1.3, which is higher than that of standard GaAs (Figure 5.10). This column ratio value is representative of the dumbbells across most of the InAs layers in the HAADF image. However, the simulated graph of Figure 7.1 suggests that (at a specimen thickness of 40nm) the InAs column ratio should be equal to about 0.85. Hence, the non-As (i.e. In) column should be less intense than the As column in the HAADF image. Therefore, it seems that the simulated column ratio of InAs is unreliable in this instance since the profile of the 2 dumbbells in Figure 7.3(b) clearly indicates that the experimental column ratio of InAs is actually higher than 1.

The column ratio map in Figure 7.4(a), which was calculated from the image in Figure 7.3(a), also highlights the fact that the experimental InAs column ratio is higher than the simulated value. For example, the maximum column ratio value contained within the map is equal to 2.2. This is a lot higher than any value observed in previous maps of AlAs and GaAs based structures. In addition, the start of a large GaAs region can also be seen on the LHS of Figure 7.3(a). The average column ratio profile in Figure 7.4(b) reveals that this GaAs region has about the value that is expected from the standard GaAs value given in Figure 5.10. Hence, the column ratio peaks in the profile (values above 1) must be associated with the InAs repeats.

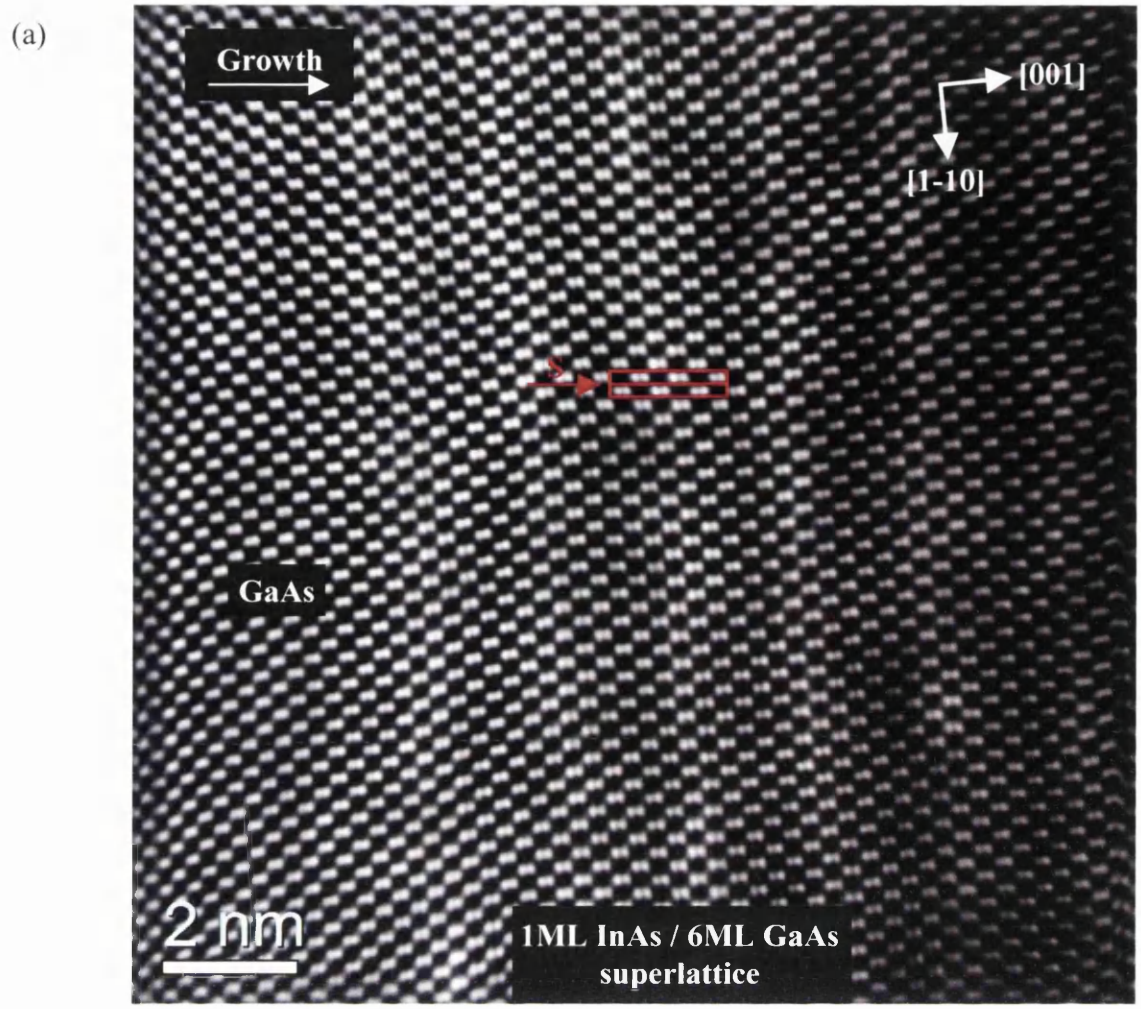

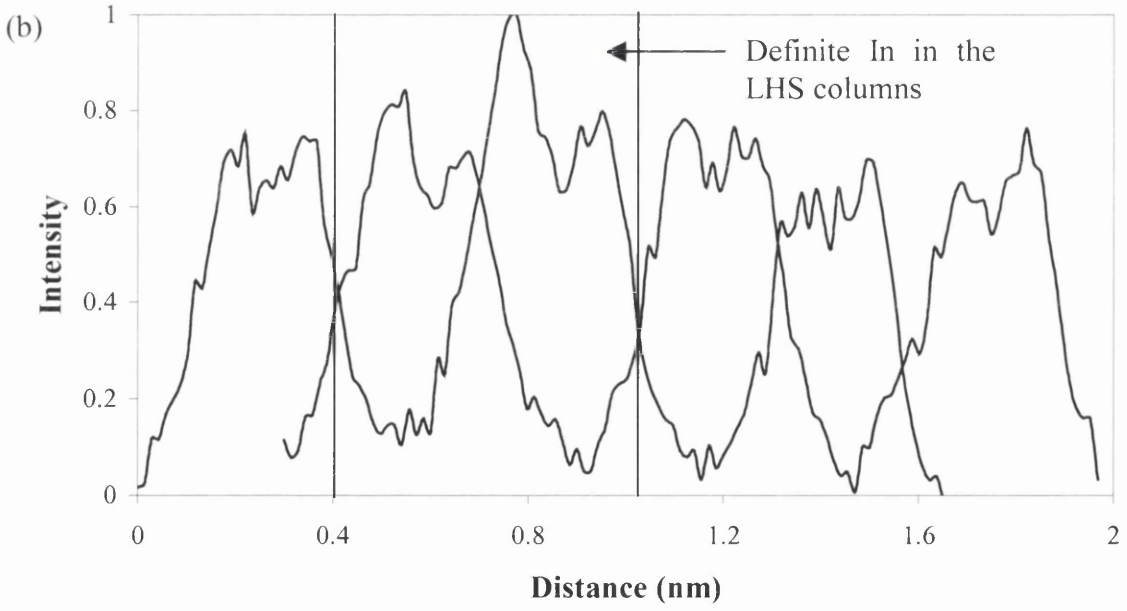

Figure 7.3(a): FT filtered SuperSTEM 1 HAADF STEM image of the 6 repeat 1ML InAs / 6ML GaAs superlattice. The specimen thickness was 41nm. **(b)** is an intensity profile taken across the image section S. 2 interleaving profiles are shown. Every point of each intensity profile is generated from the average of 10 image pixels summed along the [1-10] direction. The background has been removed from each profile from the use of a high pass filter.

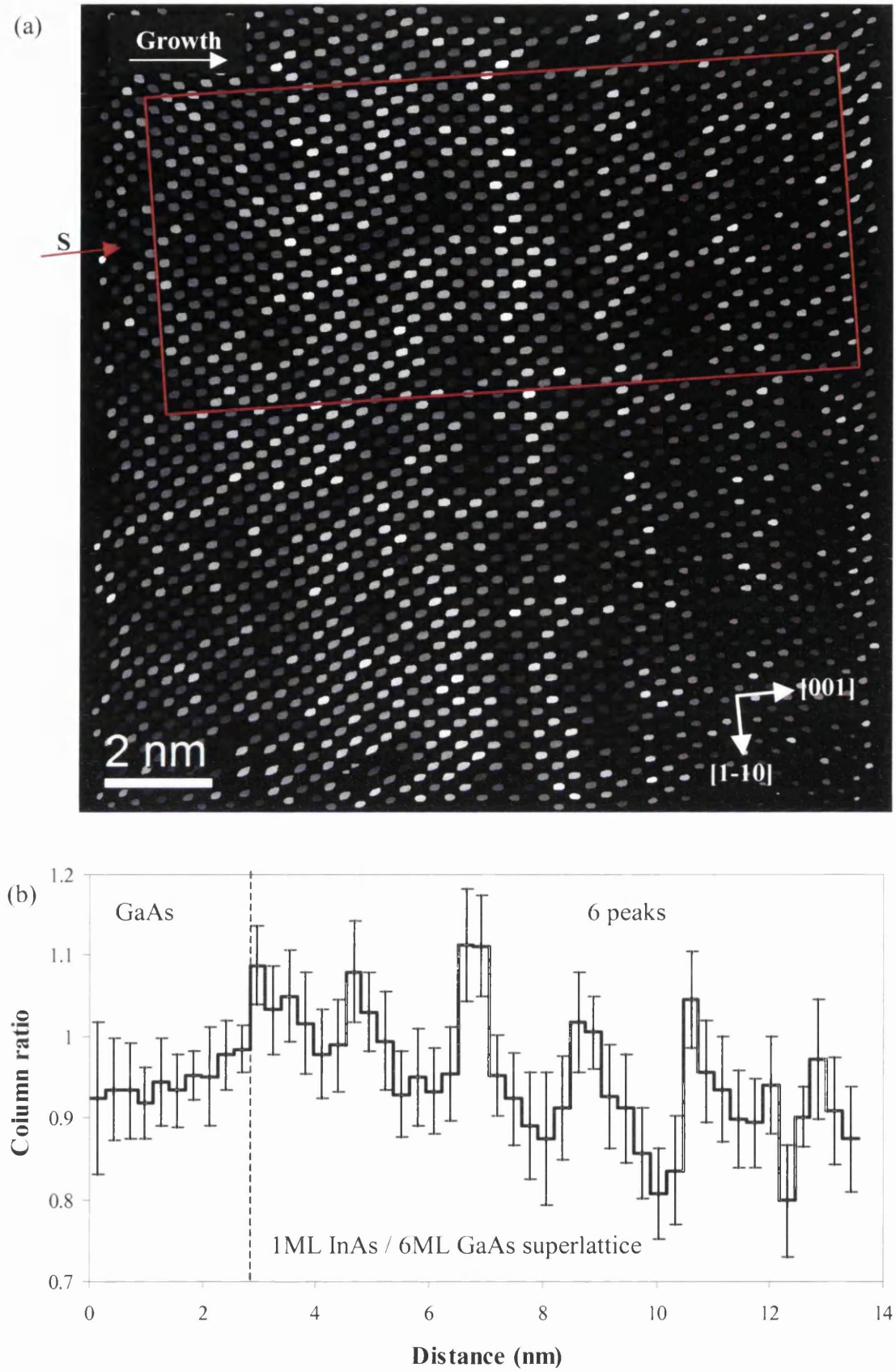

Figure 7.4(a): Dumbbell column ratio map over 6 repeats of the 1ML InAs / 6ML GaAs superlattice. The brightest dumbbells have the highest column ratios. **(b)** is an average column ratio profile taken across the column ratio map section S.

It should also be noted that the column ratio drops to a value of about 0.8 in some of the 6ML GaAs repeats of the superlattice. This is in conjunction with a gradual reduction in the overall column ratio value towards the RHS of the map in Figure 7.4(a). This reduction corresponds to an area of the image in Figure 7.3(a) in which the dumbbells appear to be not as clear as in other parts of the image. This may be due to a bend in the specimen at that point. This may account for the low column ratio values of the GaAs dumbbells from this section.

The fact that the experimental column ratio value of InAs did not match the simulated value is in contrast to the simulations of AlAs and GaAs in which a good correspondence to experiment was found (Section 5.4). The reason for this is unclear since there does not seem to be a problem with the image resolution from the best section of the image in Figure 7.3(a) (i.e. the image FT reflections show 1Å resolution). This suggests that the simulations underestimate the scattering from high Z atoms. Hence, the correct column ratio value of InAs (as a function of thickness) is unknown but it is likely to be above 1 at a thickness of about 40nm. This means that In rich dumbbells should appear to be the brightest ones in column ratio maps.

In addition, it is apparent that a range of dumbbell shapes is present across the entire map in Figure 7.4(a). In fact, it is difficult to recognize the layer structure of the superlattice from the map due to this large variation. This may be an indication of the inherent roughness of InAs / GaAs interfaces. Nevertheless, 6 column ratio peaks are visible in the average column ratio map profile in Figure 7.4(b). This shows that the periodicity of the superlattice is present and that it can be detected through the calculation of the column ratio.

The column ratio map profile in Figure 7.3(b) (from the clearest image areas of Figure 7.3(a)) suggests that the In peaks are 2-4MLs in width. This observation may provide evidence of the segregation of In atoms over several MLs across each interface. Alternatively, the apparent spread of the In may be a consequence of the existence of short surface steps in the vertical direction of the material as was discussed in Chapter 6 for AlAs and GaAs based structures. In summary, the periodicity of the 1ML InAs / 6ML GaAs superlattice is present but there does seem to be a great deal of variation in the composition of the superlattice.

7.2.3 1ML InAs / 3ML GaAs Superlattice

In order to assess the appropriate MBE growth conditions for the finer 10 repeat 1ML InAs / 3ML GaAs superlattice, the structure was grown twice using a different substrate wafer temperature on each occasion. The temperatures considered were 575°C and 525°C, respectively. It was anticipated that the higher temperature would produce the multilayer with the most compositionally abrupt layers since higher temperatures create smoother surfaces. This is despite the fact that, as was stated previously, InAs structures are typically grown at lower substrate temperatures in order to prevent In inter-diffusion. The reason behind the formation of smoother surfaces from the use of higher temperatures centres upon the fact that In atoms tend clump on top of each other when an In flux is incident on a (relatively) cold surface. This produces uneven interfaces. On the other hand, In atoms that impinge upon a (relatively) warm surface tend to reposition themselves evenly along the 2 dimensional surface. This results in much sharper interfaces. Of course, it should also be noted that if the temperature is too high then a greater diffusion of the In atoms will occur across the interfaces [7, 8].

Both 1ML InAs / 3ML GaAs superlattices were grown on Wafer A, without a wafer rotation. In addition, the In and Ga oven temperatures were 882°C and 1048°C, respectively. Also, the As oven had a temperature of 210°C and the both structures were grown under a constant As flux. Furthermore, the growth rates of the InAs and GaAs layers, in both superlattices, were 0.25ML / sec and 0.74ML / sec, respectively.

Figure 7.5 presents a low magnification, SuperSTEM 1 HAADF STEM image of the 2 (10 repeat) 1ML InAs / 3ML GaAs superlattices. The thickness is not known. The presence of a 10.6nm wide $In_{0.25}Ga_{0.75}As$ layer and 2 GaAs spacer regions can also be seen. It is apparent, from the image, that the periodic structure of the 2 superlattices is present. Hence, as was the case with the longer period 1ML InAs / 6ML GaAs superlattice, short period InAs / GaAs multilayers are able to be deposited though the use of MBE. Figure 7.5 also reveals the difference that the substrate temperature had on the quality of the multilayers. The layers of the superlattice, which were grown at the higher temperature, are clearly better defined than the ones from the superlattice that was grown at the lower temperature. Indeed, the superlattice that was grown at 525°C exhibits a significant degradation in the flatness of the interfaces compared to the one grown at 575°C. It is reasonable to assume, therefore, that the quality of InAs / GaAs superlattices can be directly controlled and improved through the fine-tuning of the MBE growth conditions.

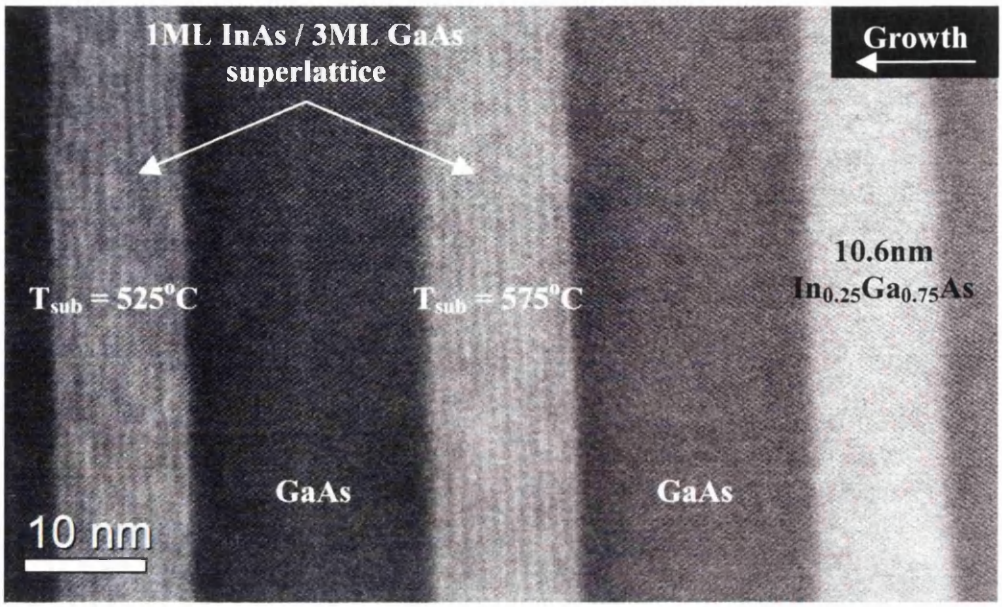

Figure 7.5: Low magnification SuperSTEM 1 HAADF STEM image of 2 superlattices made of 10 repeats of 1ML InAs / 6ML GaAs superlattice. They were grown with different substrate temperatures (T_{sub}).

In order to gain an understanding of the nature of the interfacial roughness that can be introduced by the growth process, the superlattice that was grown at the lower substrate temperature of 525°C was studied in greater detail. A high magnification, FT filtered SuperSTEM 1 HAADF STEM image of the 1ML InAs / 3ML GaAs superlattice is shown in Figure 7.6(a). The thickness is equal to 49nm. The periodicity of the superlattice is again visible. However, it is apparent that the structure demonstrates a great deal of non-uniformity across most of the layers. This is a possible indication of extensive compositional spreading of the elements in the structure.

Furthermore, the background removed 2 interleaving intensity profiles in Figure 7.6(b) highlights the occurrence of strong intensity on the non-As columns of neighbouring dumbbells in a section of the superlattice. The diffusion of the In atoms, across several monolayers, is a likely cause of the enhanced HAADF intensity on the LHS dumbbell columns. Figure 7.6(b) also reveals the effect that the (likely) In inter-diffusion has on the perceived periodicity of the superlattice. It can be seen that the repeat unit appears to be composed of 2ML InAs / 2ML GaAs. Nevertheless, the intensity profile also indicates that the In may exist in the supposed 2ML GaAs layers as well. As was the case with the AlAs and GaAs structures in Chapter 6, the reason behind the observed non– sharpness of the layers may either be due to compositional diffusion or due to the presence of surface steps.

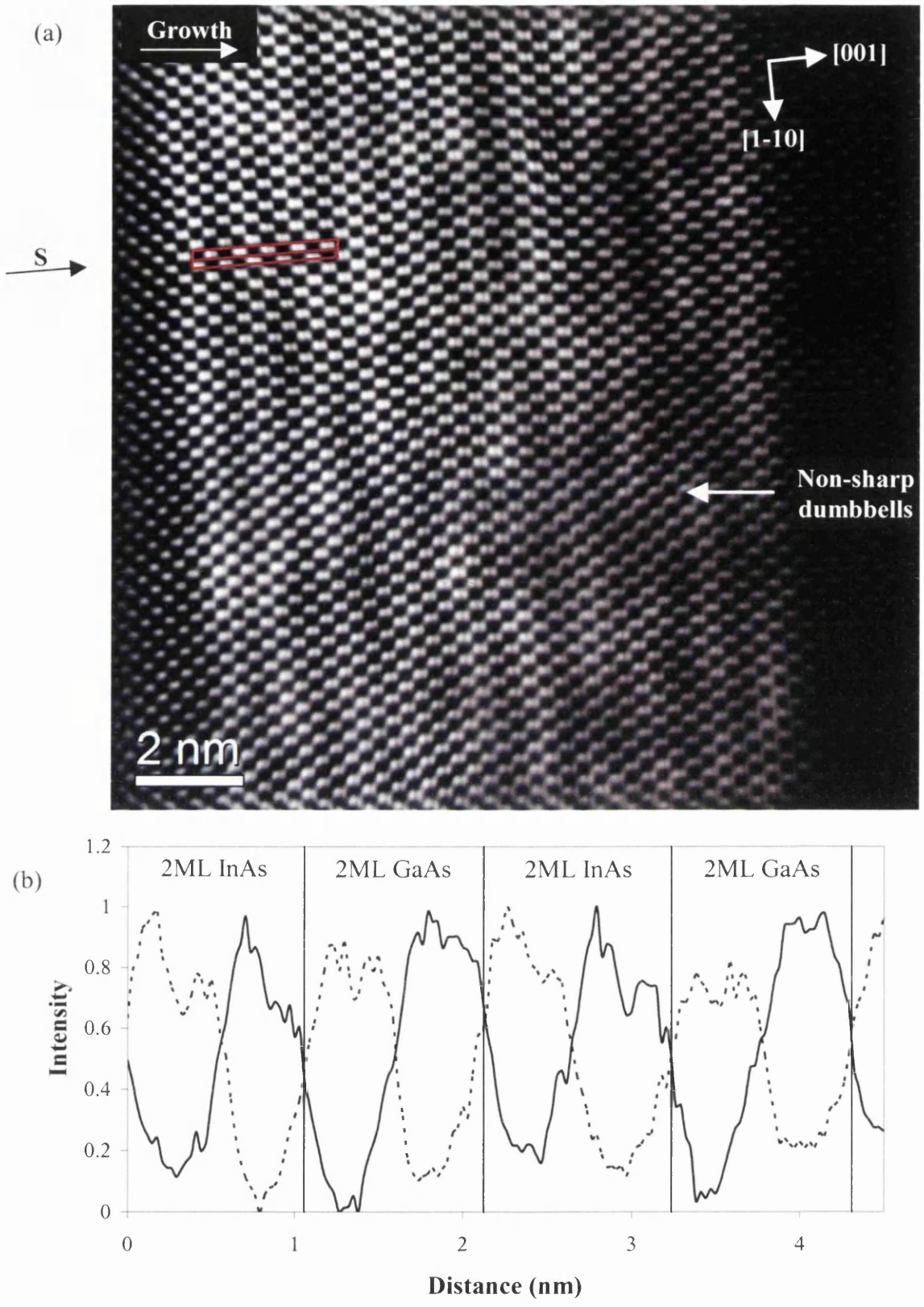

Figure 7.6(a): FT filtered SuperSTEM 1 HAADF STEM image of 10 repeats of the 1ML InAs / 3ML GaAs superlattice. The substrate temperature is 525°C. Thickness is 49nm. **(b)** is an intensity profile taken across the image section S. 2 interleaving profiles are shown. Every point of the profiles is generated from the average of 10 image pixels summed along the [1-10] direction. The background has also been removed from the profiles from the use of a high pass filter.

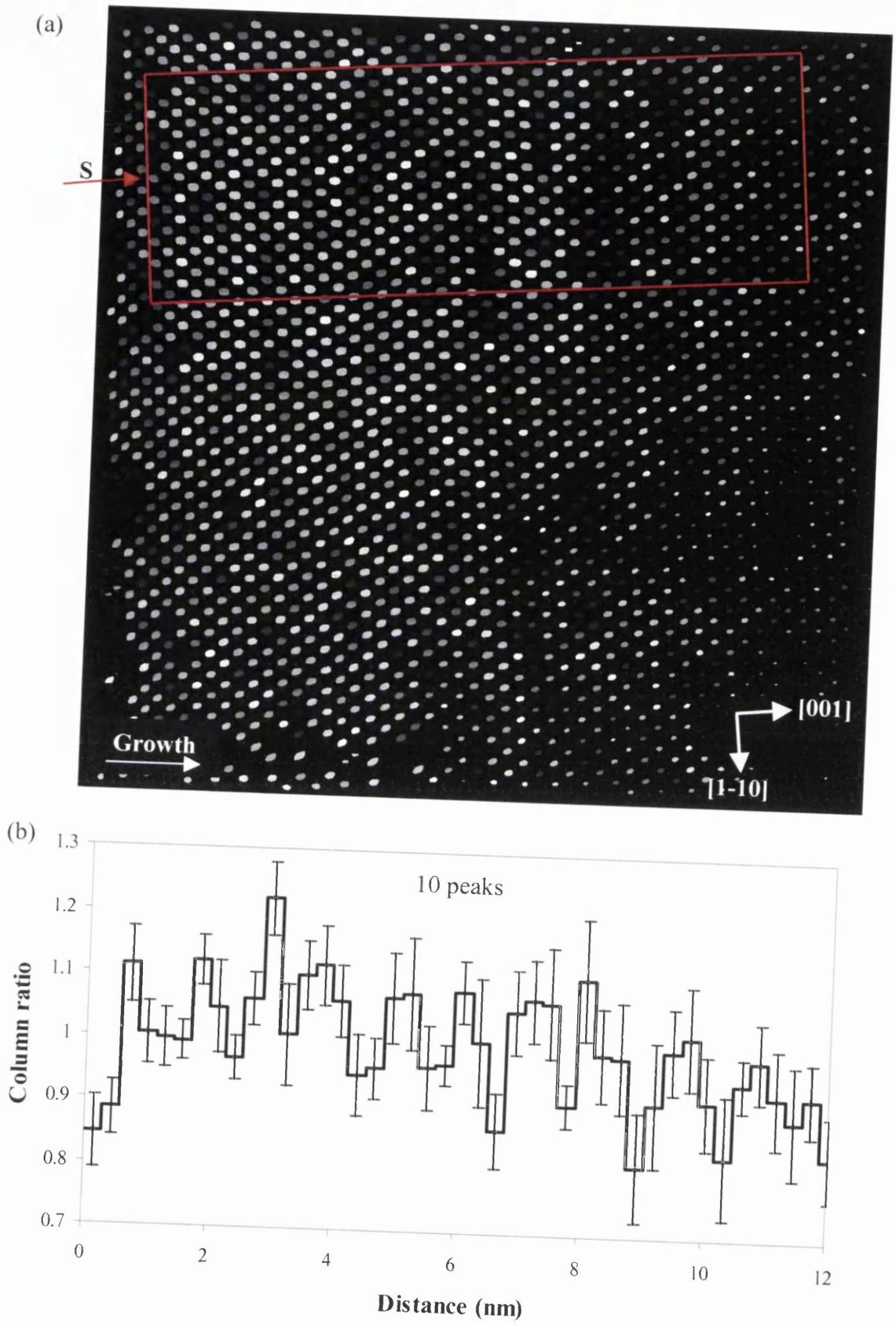

Figure 7.7(a): Dumbbell column ratio map over the 10 repeats of the 1ML InAs / 3ML GaAs superlattice. The substrate temperature is 525°C. The brightest dumbbells have the highest column ratio values. **(b)** is an average asymmetry profile taken across the column ratio map in (a)

Figure 7.7(a) presents a dumbbell column ratio map that was calculated across the image in Figure 7.6(a). This map reveals a significant interruption in the layer repeats throughout a large section of the superlattice. However, as was the case with the image of the 1ML InAs / 6ML GaAs superlattice, the absence of the superlattice structure may be due to the fact that part of the image in Figure 7.6(a) appears to be less well focused than other parts. Nevertheless, the periodicity is not at all visible from the column ratio map.

Figure 7.7(b) is an averaged line profile that was taken across a part of the column ratio map shown in Figure 7.7(a). This was taken over the area of the map that appears to best retain the superlattice structure. The profile highlights the existence of 10 column ratio peaks that are associated with the positions of the InAs layers. This suggests that the periodicity is present. However, it is apparent that the layers are not well defined in this case since some of the peaks are spread over several MLs.

In comparison to the fine layer 1ML AlAs / 2ML GaAs superlattice in Section 6.4, the fine layer InAs / GaAs based superlattice seems to be less well defined. For instance, the periodicity of the AlAs / GaAs based superlattice was clearly present in both the image and in the associated column ratio map. However, it should be noted that only the lower temperature fine InAs / GaAs based superlattice was studied in detail. Hence, the better defined high temperature superlattice may have a similar quality to the fine AlAs / GaAs based superlattice.

7.3 Si δ-doped Layers in GaAs

7.3.1 Background

As stated in Section 1.2.3, δ-doping is a technique that confines dopant atoms within a very narrow region during the epitaxial growth of the host material [5, 6, 9]. This technique allows the construction of the smallest possible semiconductor devices, thereby reducing the necessary power consumption and increasing the device operation speed. Furthermore, in high electron mobility transistors, δ-doping produces advantages such as increased free carrier concentration (in the conducting channel) and increased carrier mobility. The carrier mobility is increased due to the fact that δ-doping keeps the ionised donors away from the channel thereby reducing the scattering of the carriers. δ-doping may also allow a smaller gate to channel distance in devices. In addition, δ-doped superlattices could also have future applications in LEDs and light modulators [4].

The determination of the distribution of donor atoms in III-V semiconductor heterostructures has been an actively studied topic for some time. Moreover, the precise location of dopant atoms is related to the fundamental attributes of interface stepping and elemental diffusion within compound semiconductors. In addition, it has also been established that the free electron density in Si δ-doped GaAs actually saturates at a doping concentration of about $1\times10^{13}cm^{-2}$ [5]. This saturation may be associated with the formation of electrically inactive Si clusters in which Si atoms occupy both the donor and acceptor lattice positions in the doped GaAs [6]. The saturation therefore imposes a limit on the performance of devices that incorporate such Si δ-doped layers.

The investigation into the MODFET heterostructure (in Chapter 3) showed the need to examine Si δ-doped layers in a system in which no growth errors are present. To this end, a test specimen was grown by MBE to contain a range of Si δ-doped concentrations, along with suitable identification superlattice layers. The Si δ-doped layers were grown on Wafer B with a 50rpm rotation. The primary aim of the investigation into this specimen was to uncover the minimum level of Si doping that is required for detection by SuperSTEM 1. It should be noted that it is a challenge to detect such 1ML wide layers through the use of HAADF or EELS, even if the Si remains on a single atomic plane. Furthermore, the test specimen facilitates an investigation into the possible existence of silicon clustering at high doping concentrations.

7.3.2 Test Specimen

The test specimen is composed of 6 independent 4ML wide GaAs layers. In the ideal growth situation, Si atoms are substituted on one particular Ga plane in each of these layers. Such Si_xGa_{1-x} planes constitute the 6 δ-doped layers. The doping concentration of these layers range from zero Si content up to a maximum of $1\times10^{14}cm^{-2}$ Si content (above the saturation value). The identification regions are positioned between the doped layers. These are constructed from 18 and 9 repeat units of the familiar 1ML AlAs / 2ML GaAs superlattice (see Section 6.4). It was found that the specimen had been grown correctly and there were no obvious growth errors present.

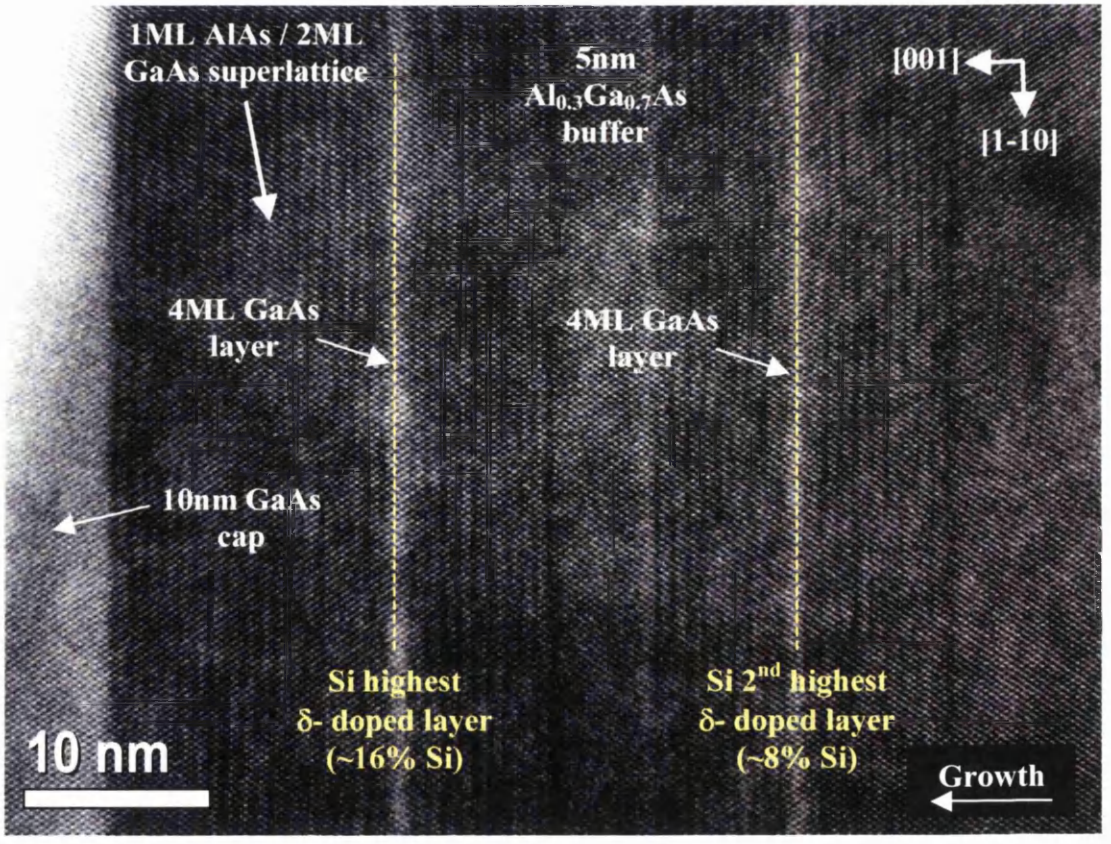

Figure 7.8: Low magnification SuperSTEM 1 HAADF STEM image over the 2 highest concentration Si δ- doped layers. These are bounded by a 1ML AlAs / 2ML GaAs fine superlattice.

Figure 7.8 is a low magnification, SuperSTEM 1 HAADF image of the 2 highest concentration Si δ-doped layers. Ideally, the δ-doped layer is situated in the middle of the 4ML wide GaAs layers. The image also highlights the presence of the 1ML AlAs / 2ML

GaAs superlattices and a 5nm wide $Al_{0.3}Ga_{0.7}As$ buffer region. These regions are used for the identification of the individual Si δ-doped layers during microscopy experiments.

The highest doped layer has an areal concentration of $1\times10^{14}cm^{-2}$ and was grown in 720sec. In contrast, the next highest doped layer has an areal concentration of $5\times10^{13}cm^{-2}$ and was grown in 360sec. The substrate wafer was held at a temperature of 615°C during the growth of both layers. In addition, the Si oven temperature was 1250°C and the layers were grown under a constant As flux.

7.3.3 The Highest δ-doped Si Layer

The highest δ-doped Si layer was studied first of all since it provided the best chance of Si detection. This layer is shown in the high magnification, FT filtered SuperSTEM 1 HAADF STEM image in Figure 7.9(a). The thickness is unknown. An ideal δ-doped layer should only exist in the non-As columns in a single row of dumbbells (within the 4ML GaAs region) as indicated by the dotted line in Figure 7.9(a). However, it is not entirely clear which row of dumbbells actually contains the Si due to the presence of interface diffusion and possible stepping along the edge of the GaAs layer. This makes it difficult to determine the starting point of the 4ML GaAs layer. In addition, identification is made worse by the usual degree of mottling on the specimen surface (see Section 2.6). More exactly, areas of similar composition show non-uniform intensity that was likely introduced by the ion milling process. Nonetheless, the fine superlattice is clearly visible and is of similar quality to that presented in Section 6.4.

The δ-doped layer, with the highest Si concentration, has an ideal non-As dumbbell column composition of $Si_{0.16}Ga_{0.84}$. This type of column should have a scattering power less than that of a Ga column. Hence, $Si_{0.16}Ga_{0.84}As$ dumbbells should have a different column ratio compared to GaAs. However, the value of the dumbbell column ratio (as a function of specimen thickness) of $Si_{0.16}Ga_{0.84}As$ was not investigated as it was for AlAs and GaAs in Chapter 5. Hence, the standard shape of $Si_{0.16}Ga_{0.84}As$ dumbbells is unknown. Nevertheless, a $Si_{0.16}Ga_{0.84}As$ dumbbell should be distinguishable from the surrounding GaAs dumbbells in the HAADF image shown in Figure 7.9(a).

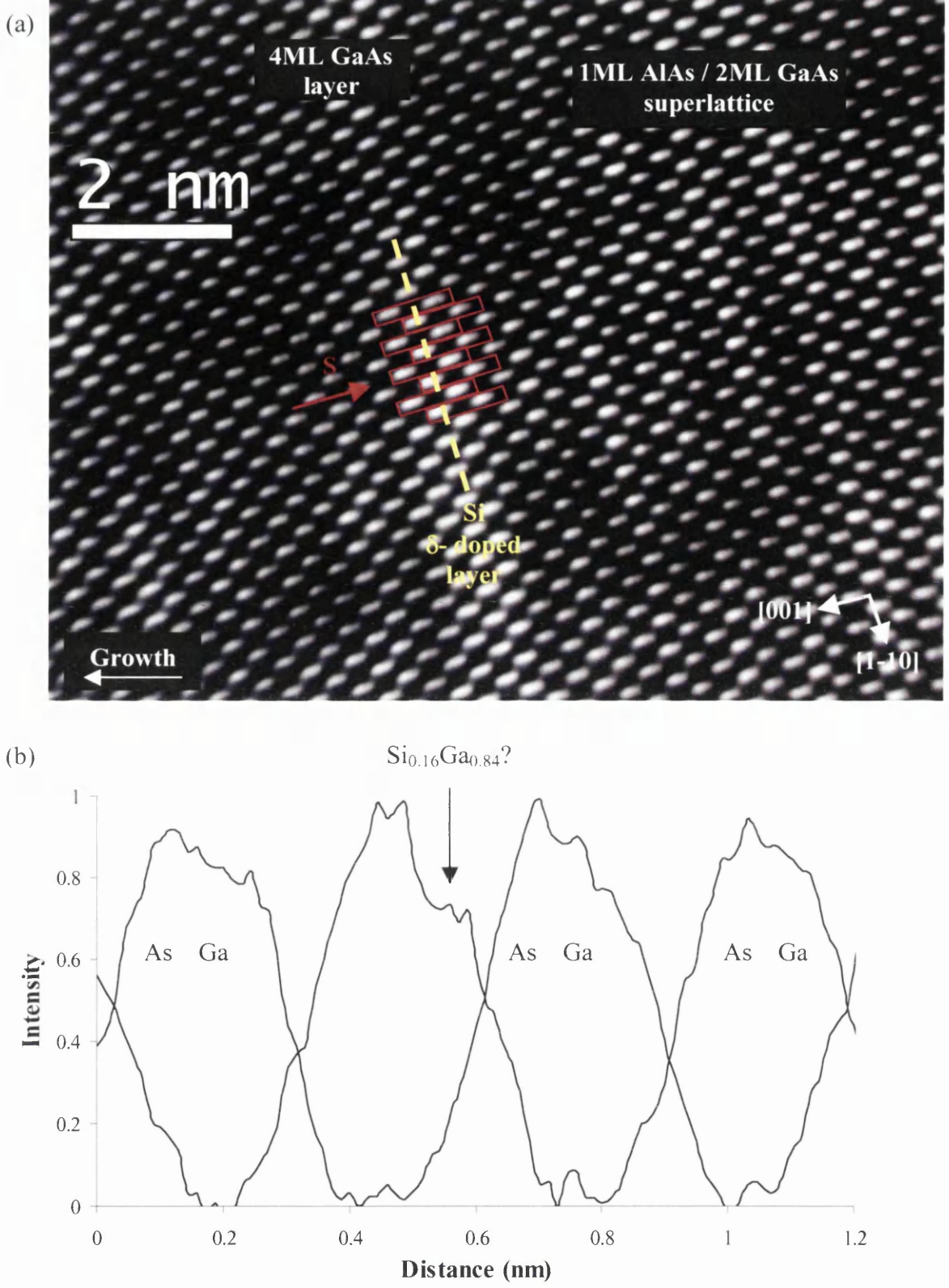

Figure 7.9(a): FT filtered SuperSTEM 1 HAADF STEM image of the highest concentration Si δ- doping layer (~16% Si). The Si is in the middle of a 4ML wide GaAs layer. Also shown is a 1ML AlAs / 1ML GaAs identification superlattice. **(b)** is an intensity profile averaged over the image sections S. 2 interleaving profiles are shown. Each profile is the sum of 4 line traces. Every point of a line trace is generated from the average of 10 image pixels summed along the [1-10] direction. The background has also been removed from the profiles from the use of a high pass filter.

Figure 7.9(b) provides a selected view of 2 background removed interleaved intensity profiles that were taken across 4 dumbbells that comprise the 4ML wide GaAs layer. In order to help with the identification of the dumbbell shapes, the signal to noise ratio was enhanced by the addition of several equivalent line profiles along the [1-10] direction. The location of these line profiles can be seen in Figure 7.9(a).

The simple Z^2 theory asserts that the column ratio of a $Si_{0.16}Ga_{0.84}As$ dumbbell should have a value equal to 0.77. Figure 7.9(b) reveals that there is, in fact, an averaged dumbbell that possesses a column ratio value of 0.77. This dumbbell is also in the expected position of the δ-doped layer. Moreover, this particular dumbbell is distinct from the other dumbbells in the 4ML GaAs layer. However, some of the other dumbbells throughout the image do not seem to exhibit the proper dumbbell asymmetry that is characteristic of AlAs and GaAs dumbbells. This was also the case for the dumbbells in the 1ML AlAs / 2ML GaAs superlattice that was presented in Section 6.4. In addition, most of the dumbbells at the expected Si position in the 4ML GaAs layer did not possess the column ratio value that was expected of $Si_{0.16}Ga_{0.84}As$. Hence, the supposed $Si_{0.16}Ga_{0.84}As$ dumbbell shape in Figure 7.9(b) is not representative of the rest of the image and, therefore, the identification of Si in the dumbbells cannot be confirmed.

Figure 7.10(a) is another high magnification, FT filtered SuperSTEM 1 HAADF STEM image taken over the highest δ-doped Si layer. The thickness was unknown but it is likely that the specimen thickness was less than that in Figure 7.9(a) since the 4ML GaAs layer in Figure 7.10(a) has a smaller background signal and is, therefore, harder to locate. The specimen area covered by the image in Figure 7.10(a) also appears to exhibit less mottling than the specimen area shown in Figure 7.9(a).

Figure 7.10(b) is a dumbbell column ratio map that was calculated over the image section shown in figure 7.10(b). This reveals that a range of dumbbell shapes is present throughout the image section and that the individual layers of the superlattice are not well defined. It should also be noted that the superlattice region is also less distinct than the equivalent fine superlattice that was presented in Section 6.4. Moreover, the averaged line profile in Figure 7.10(c) (which was taken across the column ratio map in Figure 7.10(b)) reveals that the AlAs and GaAs repeats do not possess the standard dumbbell column ratio values shown in Section 5.4. However, unlike the superlattice in Section 6.4, the dumbbell shapes are not a mixture between AlAs and GaAs. For instance, most of the (supposed GaAs) peaks in Figure 7.10(c) have column ratio values that are greater than the standard value. The reason for this may be due to the fact that 1Å resolution was not obtained in the image.

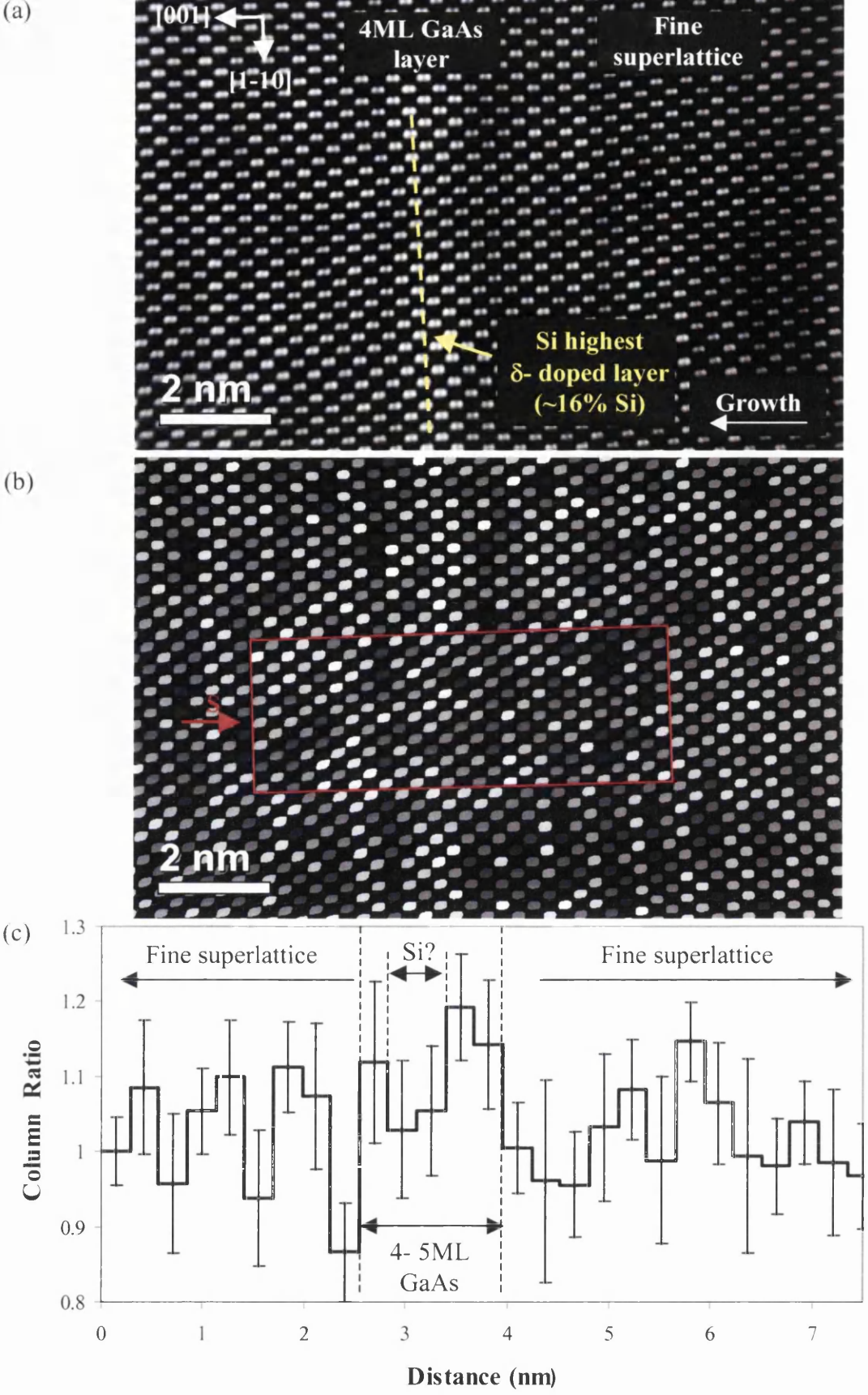

Figure 7.10(a): FT filtered SuperSTEM 1 HAADF STEM image of the highest concentration Si δ- doping layer (~16% Si). The Si is in the middle of a 4ML wide GaAs layer. Also shown is a 2ML GaAs / 1ML AlAs identification superlattice. **(b)** is a dumbbell column ratio map calculated from (a). The brightest dumbbells have the highest column ratios. **(c)** is an average profile taken across section S in (a).

Figure 7.10(c) also demonstrates that there is a reduction in the column ratio over 2MLs within the 4ML GaAs region. This may be another indication of the presence of the Si δ-doped layer. However, single line profiles that were taken across the column ratio map reveal that the dip inside the 4ML GaAs region is not consistently present along the layer. In fact, only a few single line profiles actually show any recognisable reduction of the column ratio inside the 4ML GaAs layer. Furthermore, the size of the 4ML GaAs layer is also variable along the [1-10] direction. This is possibly the result of steps along the interfaces. These observations suggest that the Si δ-doped layer cannot be positively identified from the column ratio map in Figure 7.10(b). However, the fact that the dip in the column ratio only occurs in some parts of the 4ML GaAs layer may actually be a result of Si clustering in those areas. Further investigation of the highest Si δ-doped layer is required in order to ascertain if Si clustering is indeed present.

It is clear that the detection of Si δ-doped layers, even at the highest doping level, is very difficult to achieve through the use of HAADF imaging. For that reason, the lower concentration Si δ-doped layers were not studied in great depth. In addition, the distribution of the Si could not be determined and, thus, the existence of Si clusters could not be confirmed.

In order to complement the HAADF image analysis, EELS data was also obtained across the highest concentration Si δ-doped layer. The area over which the data was acquired is shown in the FT filtered SuperSTEM 1 HAADF STEM image in Figure 7.11(a). 16 individual spectra were taken across the 4ML GaAs layer as indicated. Each spectrum was acquired over 10sec. However, it is apparent from the summed EELS spectrum (given in Figure 7.11(b)) that no Si K signal was obtained. This is also apparent in the background subtracted EELS spectrum signal in Figure 7.11(c). It should be noted that the spectrometer was working correctly on this occasion since the Ga L_3 (1115eV) and As L_3 (1323eV) edges from the GaAs were detectable (not shown).

Furthermore, other attempts at Si identification through the use of EELS were also unsuccessful. This is an indication that, at this particular concentration of Si, the spectrometer of SuperSTEM 1 is insensitive to the presence of Si in GaAs. However, it should also be noted that the ability of the spectrometer to detect the Al K edge (1560eV) from bulk AlAs varied from one session to next. Therefore, it seems that the spectrometer has to be exactly setup in order to generate any useful EELS data at such high energy losses. On the other hand, as was discussed in Chapter 4, the exact position of dopant

atoms along atomic columns can drastically affect the generation of EELS signals. This is due to the uneven distribution of electron intensity that forms along atomic columns. However, it is uncertain whether this is an issue in this case as the Si atoms should be randomly distributed throughout the columns.

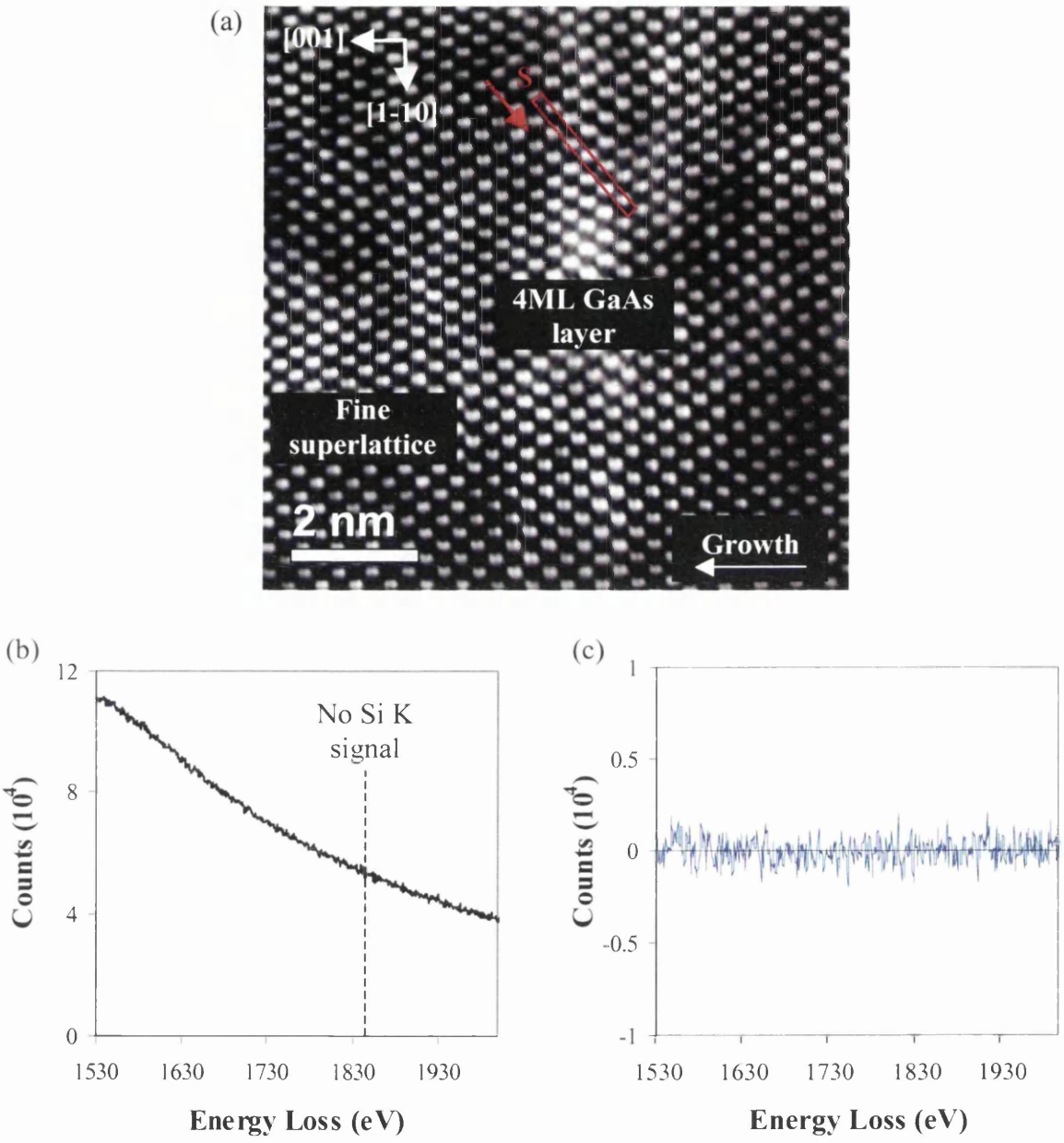

Figure 7.11(a): FT filtered SuperSTEM 1 HAADF STEM image of the highest concentration Si δ- doping layer (~16% Si). The Si is in the middle of a 4ML wide GaAs layer. Also shown is a 2ML GaAs / 1ML AlAs identification superlattice. 16 spectra were acquired across section S. **(b)** is an EELS spectrum calculated from the summation of the 16 spectra from the section S. **(c)** is the background removed signal of (b). A collection angle of 19mrad was used and each spectrum was acquired over 10sec.

7.4 Conclusion

In this chapter, several MBE grown nanostructures were investigated through the use of SuperSTEM 1. The materials that were studied have present and possibly future applications in semiconductor devices. For that reason, the purpose was to characterise the composition and quality of the structures in order to evaluate the accuracy of the growth techniques. However, unlike the case of the AlAs and GaAs based structures in Chapter 6, the overall results on these structures were less conclusive. Part of the problem was the fact that, in most cases, the quality of the images was slightly worse than those presented in Chapter 6. This reduced the usefulness of the column ratio analysis. In addition, the experimental thickness variation of the column ratio that is associated with the constituent materials was not known. This made compositional identification more difficult. Furthermore, in the attempt to compare the experimental InAs column ratio with a simulated value, it was found that the simulations underestimated the column ratio. This is in contrast to the good agreement obtained between the experimental and simulated values associated with AlAs and GaAs in Section 5.4.

The first category of materials that were investigated in this chapter involved InAs / GaAs superlattices. These are an interesting class of materials as they may serve as a replacement to uniform layers of InGaAs in the conducting channel of MODFET heterostructures. This would improve the performance of the parent devices by reducing the scattering of the charge carriers. However, it was unclear whether such multilayers could be grown to a suitable quality by MBE. Nonetheless, it was discovered that the intended periodicity was undeniably present in a MBE grown 6 repeat 1ML InAs / 6ML GaAs superlattice. On the other hand, there did seem to be a wide variation in composition across the layers. For instance, it was shown that In was present in neighbouring dumbbells across many of the layers. It is unclear whether this is the result of the diffusion of In atoms during the growth process or if it is related to surface stepping.

A second InAs based multilayer structure was also studied. This comprised a finer 10 repeat 1ML InAs / 3ML GaAs superlattice. This structure was grown twice under different substrate temperatures. Despite the tendency of the In to diffuse into the surrounding layers, it was found that, in general, the layer system could be observed in both superlattices. Furthermore, a low magnification image demonstrated that the higher substrate temperature multilayer was better defined than the lower temperature one. In

addition, more detailed analysis was also performed on the low temperature superlattice. This revealed that the In was again distributed over a number of MLs.

In summary, it was shown that the expected repeat structure did exist in the wide layer and narrow layer InAs / GaAs superlattices. In addition, the effect of substrate temperature on the quality of the finer superlattice was also demonstrated. Hence, it is apparent that MBE is capable of growing InAs based multilayers. However, it is unclear whether such structures can be grown to a similar quality as equivalent AlAs and GaAs based structures. Moreover, it is uncertain whether the diffusion of the In is any worse than that associated with Al or Ga in equivalent structures. Therefore, in order to fully investigate the suitability of using InAs superlattices in semiconductor devices, the sharpness of the InAs / GaAs interface needs to be studied as a function of thickness in a similar manner to that presented for AlAs / GaAs interfaces in Chapter 6. This would necessitate the determination of the InAs dumbbell column ratio as a function of thickness.

The second category of structures that was assessed using SuperSTEM 1 was Si δ-doped layers embedded in GaAs. The advantages of employing such dopant layers in semiconductor devices include increased free carrier concentration and increased carrier mobility. However, there is existing evidence that the Si spreads over several monolayers thereby reducing their effectiveness in the parent device.

A test specimen, which contained a range of Si δ-doped concentrations, was grown by MBE. The chief aim was to ascertain the doping level that could be detected via SuperSTEM 1. Hence, the highest concentration layer was studied first of all. The dumbbell composition in this particular layer was $Si_{0.16}Ga_{0.84}As$. Even though EELS data could not detect this amount of Si, the analysis of the HAADF images suggested the presence of Si in the designated location. However, the Si was not consistently observed across the centre of the 4ML GaAs layer. Hence, the precise distribution of the dopant atoms could not be determined and the possible existence of Si clusters could not be verified.

One problem that was encountered in the attempt to detect MBE grown Si δ-doped layers involved the interfacial roughness of the surrounding AlAs and GaAs layers. As was the case with the fine superlattice in Section 6.4, the dumbbell shapes throughout the superlattice were a mixture between that of AlAs and GaAs. This made it difficult to distinguish the shape of the (possible) $Si_{0.16}Ga_{0.84}As$ dumbbells with the surrounding GaAs ones. In addition, the spatial extent of the 4ML GaAs layer, in which the Si was deposited,

was uncertain. This was possibly due to stepping along its edge. This added further uncertainty to the position of the δ-doped layer.

In summary, the detection of Si δ-doped layers (even at a concentration higher than that used in real devices) is a challenging problem for SuperSTEM 1. It may be the case that the higher performance (in terms of both HAADF imaging and EELS) of SuperSTEM 2 is required in order to positively detect the Si and to map its distribution.

References

[1] L. Rebohle, F. F. Schreya, S. Hofera, G. Strassera, K. Unterrainera, Energy level engineering in InAs quantum dot stacks embedded in AlAs / GaAs superlattices, Physics E 17, 42-45 (2003)

[2] T. Kitada, S. Shimomura, S. Hiyamizu, Surface segregation of indium atoms during molecular beam epitaxy of InGaAs / GaAs superlattices on (n11)A GaAs substrates, Journal of Crystal Growth, doi:10.1016/j.jcrysgro.2006.11.170 (2006)

[3] T. Noda, N. Sumidab, S. Koshibab, S. Nishiokab, Y. Negib, E. Okunishic, Y. Akiyamaa, H. Sakakia, STEM studies of MBE-grown corrugated structures of GaAs, InGaAs and AlAs on (757)B structures, Journal of Crystal Growth 278, 569-574 (2005)

[4] J. V. Thordson, Two– dimensional limitations when increasing the Si-concentration from δ-doping to thin Si-layers in GaAs, Journal of Crystal Growth 175 / 176, 234-237 (1997)

[5] G. Li, C. Jagadish, Confinement and concentration of electrons in Si δ-doped $Al_xGa_{1-x}As$ (x=0 and 0.35) grown by metalorganic vapour phase epitaxy, Journal of Crystal Growth 167 421-428 (1996)

[6] L. Hart, Si δ-doping in GaAs: investigation of the degree of confinement and the effects of post-growth annealing, Semiconductor Science Technology 10, 32-40 (1995)

[7] K. Eberl, P. M. Petroff, P. Demeester, Low dimensional structures prepared by epitaxial growth or regrowth on patterned substrates, Series E: Applied Sciences Vol. 298, Kluwer Academic Publishers (1995)

[8] K. Y. Cheng, Molecular beam epitaxy technology of III-V compound semiconductors for optoelectronic applications, Proceedings of the IEEE, Vol. 85, No. 11 (1997)

[9] J. H. Davies, The physics of low-dimensional semiconductors, Cambridge University Press (2005)

8 Conclusions and Further Work

8.1 Introduction

In this project, SuperSTEM 1 was used to analyse several MBE grown III-V semiconductor nanostructures. The aim of these investigations was to establish the composition and the quality of the various layers and interfaces that were present in the nanostructures. Consequently, the accuracy of the MBE growth technique could be evaluated by the growth engineers. In addition, the investigations provided a way of exploring the potential of SuperSTEM 1 to detect the different elements contained in the semiconductor materials. This also involved the study of the nature of the HAADF imaging technique as a function of both composition and specimen thickness.

In order to properly interpret data obtained from SuperSTEM 1 (and other aberration-corrected instruments) the results from this project suggest that it is important to have a clear idea of the nature of the imaging process and how the HAADF and EELS signals vary with specimen thickness. The results from this project also highlighted the usefulness of converting high magnification HAADF images into dumbbell column ratio maps that indicate the distribution of dumbbell composition. In addition, the interpretation of such maps (and column ratio values in general) requires standard column ratio values of the constituent materials to be measured as a function of thickness. It was also apparent from this project that investigations that attempt to explore the reasons behind interfacial roughness require the interface sharpness to be studied as a function of specimen thickness. This was exemplified by the investigation into the 2 types of AlAs / GaAs interfaces.

8.2 Conclusions

The first experiment that was undertaken in this project involved the study of a III-V heterostructure that was designed to form part of a high frequency MODFET. Such MBE grown multilayers have not been widely investigated through the use of aberration-corrected microscopy. Hence, the MODFET results from SuperSTEM 1 not only revealed the quality of layers but also gave an indication of the sensitivity of aberration-corrected STEM to Group III and Group V elements that are present in these types of materials.

The study of the heterostructure involved the extensive use of the HAADF imaging technique (as did the other investigations). However, in order to take full advantage of the

Å-scale spatial resolution of SuperSTEM 1, new image processing techniques were employed. For instance, SuperSTEM 1 high-magnification HAADF images were converted into maps of the dumbbell column ratio. Such maps allow the precise elemental distribution of a specimen to be ascertained at a glance. These maps were used instead of the usual time consuming process of analysing dumbbells individually by taking many line profiles across an image. Hence, column ratio maps were used extensively throughout this project to give a quicker and fuller picture of the dumbbell composition from HAADF images. In addition, the concept of the column ratio map could be extended to HAADF images of dumbbell orientated materials that are acquired through the use of other aberration-corrected instruments such as SuperSTEM 2. This would require a slight alteration of the Digital Micrograph scripts that are used to generate the column ratio maps.

The column ratio maps of the 9ML $Al_{0.3}Ga_{0.7}As$ / 9ML GaAs deep superlattice and the 1ML AlAs / 2ML GaAs fine superlattice revealed that the dumbbell shapes were a mixture of the different materials along the layer boundaries. However, it was unclear whether such roughness was a result of elemental diffusion or surface stepping. In addition, the ability of SuperSTEM 1 to investigate composition via EELS was shown to be less effective than via HAADF imaging. This is mainly because only 1 part of a SuperSTEM 1 spectrum is exactly in focus. As a result, the collection and analysis of multiple high energy loss energies in a single spectrum is problematic. Hence, the results that were obtained from the collection of the main edges of interest in the heterostructure (i.e. Ga L_3, As L_3 and Al K) did not provide sufficient sensitivity to study 1ML changes in layer composition unlike HAADF imaging. Consequently, most of the analysis that was conducted in this project centred on the use of HAADF imaging (and the calculation of dumbbell column ratio maps) rather than the use of EELS.

It was also demonstrated, through HAADF STEM imaging, that the MODFET heterostructure contained several growth defects. For example, column ratio analysis showed that the fine superlattice possessed the incorrect number of layer repeats and an extra 4ML wide layer of AlAs was also present within the multilayer. These errors prevented the study of the Si δ-doped layer. However, it should be noted that such errors do not usually occur in MBE grown heterostructures and the overall structure of subsequently studied materials closely matched their respective growth maps.

Despite the obvious problems that were associated with the heterostructure, the study of its layers proved to be invaluable as it revealed a number of key areas where a deeper understanding was required. For example, it was established that there was a poor

correspondence between the experimental column ratios (obtained from the various layers of the heterostructure) and the values that are predicted by the simple Z^2 imaging theory. The reason for this poor agreement was likely due to the unsophisticated nature of the simple Z^2 theory itself and the fact that specimen thickness was not taken into consideration. Moreover, the experimental column ratios were calculated from confined layers in which the effect of compositional spreading and stepping on the column ratio values could not be ruled out. For those reasons, experimentally derived standard dumbbell column ratios were measured for both AlAs and GaAs from wide layers (50ML) at different values of specimen thickness.

It was found that the dumbbell column ratio for GaAs remained close a value of 1 over an experimental thickness range of 30-70nm. In contrast, the AlAs dumbbell column ratio increased steadily from a value of about 0.4 to 0.6 over an experimental thickness range of 30-85nm. The thickness variation of AlAs is an indication that the specimen thickness must be known in order to properly interpret dumbbell column ratio maps in terms of dumbbell composition. However, this requirement is not as important when dealing with GaAs since its column ratio stays close to 1 over the given thickness range. In addition, the column ratio plots also revealed that the simple Z^n scattering theory is not valid because n is a function of specimen thickness. Hence, it is clear that previous estimates of the dependence of HAADF image intensity on atomic number did not consider the effect of specimen thickness.

Thickness dependent values of column ratios in $PbTiO_3$ and $SrTiO_3$ have also been reported by Klenov and Stemmer using an uncorrected 300kV STEM [1]. Nevertheless, the thickness dependence of the dumbbell column ratio in III-V materials using an aberration-corrected STEM has not been reported before this project. Furthermore, the determination of the thickness dependence of the column ratio was extremely useful in the analysis of AlAs / GaAs based structures throughout this project as it allowed the dumbbell composition to be ascertained. Hence, to improve the analysis of future aberration-corrected STEM investigations, it would be a worthwhile exercise to measure the thickness dependence of the column ratio of the constituent materials in a similar way as was performed for AlAs and GaAs in this project.

The experimental column ratios for AlAs and GaAs were also compared against the values obtained from frozen phonon multislice calculations. These simulations were based on the software created by Kirkland [2]. It was found that experimental and simulated values were in good agreement. Klenov and Stemmer also reported that purely elastic multislice

calculations (i.e. without the use of the frozen phonon method) also qualitatively reproduced the behaviour of the column intensities in $PbTiO_3$ and $SrTiO_3$ [1]. However, in this project, there was also an indication that frozen phonon multislice simulations do not properly predict the thickness variation of the InAs column ratio. The reason for this is unclear. Hence, further study of the experimental InAs column ratio is required.

In addition to the dumbbell column ratio, the experimental thickness dependence of the HAADF image contrast was also investigated. This was performed for 2 different probe sizes in both the Tecnai F20 and SuperSTEM 1. The contrast was measured for GaAs [110] and Si [110] in the Tecnai F20 and for AlAs [110] and GaAs [110] in SuperSTEM 1. In each case, the image contrast decayed away from a large value as the specimen thickness was increased. This is a result of the fact that the image background signal steadily increases with specimen thickness. This has been measured by other authors [1, 7]. Furthermore, the smallest probe in each instrument produced a larger value of image contrast compared to the bigger probe. This due to the fact that, in comparison to the smaller probes, the larger ones are more widely distributed and, therefore, a larger background signal is generated from the increased scattering from surrounding atomic columns. It was also established for each instrument that the lower atomic number material (i.e. Si and AlAs) generally gave a higher contrast value than GaAs. The reason for this is that the lower atomic number materials generate a lower background signal compared to GaAs.

The experimental HAADF image contrast from SuperSTEM 1 was also compared with simulations as a function of thickness. In this respect, the experimental and simulated values were not similar. This disagreement is due to the fact that the simulations underestimate the strength of the HAADF background signal at all thickness values. In fact, the difference between the simulated and experimental contrast (termed the Stobbs factor) has been reported by many authors [3-6]. The value of the Stobbs factor in this project was found to lie within the typical range reported by other authors [3-6].

It was also evident from the investigation of the MODFET heterostructure that a more in-depth knowledge of the scattering (and HAADF signal generation) behaviour of the SuperSTEM 1 probe was necessary. In order to achieve this, a computer modelling investigation was conducted into how a 1Å-scale electron probe, similar to that used in SuperSTEM 1, is scattered by various semiconductor materials. The materials (GaAs, AlAs and InAs) were chosen as they are all commonly found in high mobility heterostructures and also formed part of nanostructures that were later investigated through

the use of SuperSTEM 1. A similar modelling investigation has been carried out by Dwyer and Etheridge in which the scattering behaviour of Å-scale probes in Si was examined through multislice calculations [7]. However, they were not concerned with how atomic number affects the scattering of the probes and their results were also not compared against experimentally derived values.

Real space crystal intensity maps were calculated as a function of thickness and at different probe positions for each simulated material. Despite the fact that the intensity maps were complicated, a number of conclusions could be drawn from them. For instance, they revealed that the electron intensity remained strongly channelled down atomic columns over a certain depth of crystal. This type of behaviour has been described by other authors in various materials [7-10].

The strong channelling depth was found to depend on the type of atoms that were present within the column. For example, the strong channelling depth was equal to 20nm for both Ga and As columns. The reason that the channelling depth is identical for Ga and As columns is due to their similar Z numbers giving rise to a similar scattering behaviour. Furthermore, the strong channelling depth was found to be smaller for In columns (a value of 16nm). This is due to the fact that the In atoms (high Z number) result in a strong scatter of intensity away from the columns. In comparison, the strong channelling depth in Al columns was found to be much greater than in the other types of column. In fact, over the entire simulated thickness range of 120nm, a significant portion of the incident of electron intensity remained in close proximity to the Al column. This is a result of the weak scattering power of Al atoms compared to Ga, As and In atoms. Hence, it is clear that the degree of scattering and column channelling of the SuperSTEM 1 probe is sensitive to the Z number of the columns that it is incident upon. Similar behaviour should also be observed for other aberration-corrected probes such as that of SuperSTEM 2.

The value of the strong channelling depth was also shown to have important consequences for the HAADF signal that is generated by an atomic column. For instance, it was demonstrated that the HAADF column signal (for each type of material) principally increased only over the thickness range that corresponded to the strong channelling condition. It was also shown that for depths greater than the strong channelling condition, the HAADF column signal started to decay. A possible reason for this may be that the intensity scattered by the top part of the column is re-scattered out to angles that are not picked up by the HAADF detector.

The calculations of the HAADF column signal were also valuable in understanding the source of the thickness variations of the experimental dumbbell column ratios of AlAs and GaAs. For instance, the reason for the increase in the value of the AlAs column ratio (with respect to specimen thickness) is partly due to the fact that the Al column HAADF signal steadily increases over the experimental thickness range. This is because of the persistence of the strong channelling condition on the Al column for large depths of crystal. In addition, the increase in the Al column HAADF signal is also accompanied by a small reduction in the As column HAADF signal over the experimental thickness range. Hence, the AlAs dumbbell column ratio steadily increases as the thickness is increased. In contrast, the reason that the GaAs dumbbell column ratio remains close to a value of 1 is due to the fact that the Ga and As column HAADF signals are almost identical over the experimental thickness range.

The real space intensity maps and their related graphs also revealed that the intensity distribution down atomic columns had important consequences for EELS measurements. For instance, it was estimated that it is only the top portion of an atomic column (situated under the incident probe) that contributes to the overall EELS signal. It was also found that the ability to investigate composition in Ga, As and In via EELS became worse as the specimen thickness was increased. This is because the contribution to the total EELS signal from columns other than the primary column (i.e. the column that the probe is incident on) rises as the specimen thickness is increased. However, this contribution from non-primary columns is significantly smaller in the case of Al columns. In addition, the fluctuations in the column intensities are also important for the analysis of, for example, dopant materials. In this case, the EELS signal may look different depending on the position of the dopants along the atomic columns. If they are at a depth of crystal at which relatively little electron intensity exists, then they will have little impact on the EELS signal. The modelling investigation by Dwyer and Etheridge also discussed, in a similar fashion, the difficulty of dopant detection due to intensity fluctuations along atomic columns [7]. Hence, the simulations indicate that it is not always easy to directly relate the measured EELS signal with local atomic structure due to the fluctuations in the electron intensity down the atomic columns of a specimen.

Despite the fact that the main focus of the modelling investigation in this project was concerned with the behaviour of a probe similar to that used in SuperSTEM 1, an equivalent group of simulations were also performed using 2 other probes. These 2 other probes had FWHM widths of 0.7Å and 1.6Å, respectively. Whereas the 1.6Å probe allowed the behaviour of uncorrected STEM probes to be estimated, the 0.7Å probe

provided a prediction of the likely behaviour of the next generation probe of SuperSTEM 2. Nevertheless, the part of the investigation that utilised these 2 probes was a first attempt and the results indicated that a more detailed study of probe conditions was required in order to determine the optimum probe input conditions.

It was established that the strong channelling depth along Ga, As and Al columns was not affected by the size and shape of the probe that was incident upon them. However, the actual value of the electron intensity that formed on the columns was significantly reduced in the case of the smallest probe. This was due to the relatively small intensity that was contained within the central maximum of the incident probe. It is uncertain whether this is a realistic starting probe characteristic. Furthermore, it was also revealed that the ability to investigate composition using EELS is proportionally worse in the case of the 0.7Å and 1Å probes compared to the larger, uncorrected 1.6Å probe. Hence, the improvement in spatial resolution of the latest sub-Å probe of SuperSTEM 2 may be also be accompanied by a deficiency in its EELS analysis. This could be a major drawback of such sub-Å scale instruments that employ very large probe convergence angles. Nevertheless, it is clear that further work is required to optimise the probe starting conditions.

It was apparent from the simulations (and from the experimentally derived dumbbell column ratio values) that the specimen thickness must be taken into consideration in order to properly interpret data obtained from SuperSTEM 1. In addition, the specimen thickness is also an important feature in the study of interfacial sharpness of MBE grown semiconductor layers. For example, it is known that the transition region width of a stepped interface will decrease if the specimen thickness is reduced to a value below that of the surface step length [11-13]. In comparison, the transition region width of an interface that is associated with elemental diffusion will not change as the specimen thickness is varied [11-13]. Hence, the study of the transition region width as a function of specimen thickness allowed the reasons behind interfacial roughness (in MBE grown materials) to be investigated.

SuperSTEM 1 was used to study a series of MBE grown AlAs / GaAs based nanostructures as a function of specimen thickness. It was established that the transition region width of GaAs-on-AlAs interfaces was not a function of specimen thickness in either the single interface or 9ML AlAs / 9ML GaAs wide layer superlattice. Therefore, it is likely that such interfaces are associated with elemental diffusion and possibly very short [110] step lengths. In addition, due to the fact that the smallest thickness that was examined was 40nm, an upper limit of much less than 40nm can be established for the

length of any possible [110] steps. This is agreement with the lower resolution CTEM studies of Ikarashi and Ishida in which no discernable [110] steps could be identified along GaAs-on-AlAs interfaces [13]. It should be noted that their studies involved the use of phase contrast CTEM images that could not resolve the individual columns of each dumbbell. Moreover, the interfacial sharpness as a function of thickness was not considered in their case. In fact, an investigation at the atomic scale of the reasons behind the roughness of AlAs / GaAs interfaces has not been previously reported.

In contrast to GaAs-on-AlAs interfaces, the transition region width of AlAs-on-GaAs interfaces was shown to decrease as the specimen thickness was reduced in both the single interface and the wide layer superlattice. This indicates that such interfaces are associated with large [110] step lengths (>40nm). Ikarashi and Ishida also found similar sized steps along AlAs-on-GaAs interfaces [13]. However, due to the fact that the lowest specimen thickness was only 40nm in this project, the presence of elemental diffusion cannot be ruled out as a contribution to the roughness of this type of interface.

The width of the transition region, with respect to the HAADF background signal (i.e. the background-signal-width), was also investigated across the 2 types of AlAs / GaAs interfaces in both the single interface and the wide layer superlattice. It was found that, in the case of the single interface, the background-signal-width of the 2 types of interfaces generally decreased as the thickness was reduced. Moreover, the background-signal-width of the GaAs-on-AlAs interface was found to be generally smaller than that of the AlAs-on-GaAs interface. This reflected the sharper nature of such interfaces at a given thickness (above a thickness of 45nm). This difference in sharpness along the 2 types of MBE grown AlAs / GaAs interfaces has been known for some time. Furthermore, in the case of the wide layer superlattice, the 9ML repeats were not large enough to encompass the whole background shape. Hence, no discernable thickness variation of the background-signal-width was observed.

A narrow layer 1ML AlAs / 2ML GaAs superlattice was also studied. This was grown using conditions that were distinct from the AlAs / GaAs single interface and wide layer superlattice. The column ratio map of the narrow layer superlattice showed that a large range of dumbbell shapes were present throughout the superlattice. This is because the width of the (column ratio related) interfacial transition region (for both types of AlAs / GaAs interface) is over 3MLs at the particular value of specimen thickness. Furthermore, the existence of stepping was again suggested by a column ratio profile that was taken parallel to an interface in the superlattice. Despite this, the multilayer showed a much

closer agreement to the growth map than was the case with the corresponding faulty fine superlattice from the MODFET heterostructure.

The results from the InAs / GaAs based superlattices proved to be less conclusive than those from the AlAs / GaAs based structures. This was partly because the highest possible spatial resolution was not achieved consistently in the SuperSTEM 1 images of these structures. Therefore, the usefulness of the column ratio analysis was reduced in these cases. In addition, the compositional identification was made worse by the fact that the experimental thickness variation of the InAs column ratio was not known. Nevertheless, the investigation into the InAs / GaAs based superlattices did provide some useful results.

Previous studies have showed that InGaAs / GaAs multilayers can be successfully constructed from wide layers of InGaAs and GaAs [14-16]. However, in this project, it was demonstrated that the MBE growth technique is capable of growing InAs based multilayers that incorporate ultra thin layers of InAs and GaAs. This is regardless of the tendency of In to diffuse into surrounding layers that has been previously been reported by other authors [14-16]. The successful growth of the multilayers was confirmed by the fact that the intended repeat structure did exist in both the wide layer (1ML InAs / 6ML GaAs) and narrow layer (1ML InAs / 3ML GaAs) superlattices. Hence, the ability to grow suitable InAs / GaAs multilayers could result in an increase of carrier mobility in semiconductor devices if, for example, the $In_xGa_{1-x}As$ conducting channel in MODFET heterostructures was replaced by InAs / GaAs multilayers.

The effect of substrate temperature on the quality of the narrow layer 1ML InAs / 3ML GaAs superlattice was also illustrated. However, it is still unclear whether such InAs / GaAs based structures can be grown to a similar quality as equivalent AlAs / GaAs based structures. Therefore, in order to fully investigate the suitability of using InAs based superlattices in semiconductor devices, the sharpness of the InAs / GaAs interface needs to be studied as a function of thickness in a similar manner to that presented for AlAs / GaAs interfaces. This would also necessitate the determination of the experimental InAs dumbbell column ratio as a function of thickness.

In comparison to the other nanostructures that have been studied in this project, the detection of Si based δ-doped layers in GaAs was the most challenging problem. For instance, even at Si concentrations far higher than would be used in a real device, the EELS sensitivity of SuperSTEM 1 was not high enough to register any Si K signal. On the other hand, HAADF imaging did suggest the presence of Si in the middle of the 4ML wide

GaAs layer. Nevertheless, the Si was not consistently observed across the whole of this layer. It is unclear whether this is an indication of the existence of Si clusters or whether it is simply a result of the fact that the detection of Si, at such small concentrations, is at the very limit of what can be achieved using SuperSTEM 1. Therefore, the hypothesis that Si clusters form above a certain doping concentration cannot be confirmed.

Part of the problem in the detection of Si δ-doped layers concerned the usual interfacial roughness of the surrounding AlAs and GaAs layers. For example, it was difficult to distinguish the shape of any possible $Si_{0.16}Ga_{0.84}As$ dumbbells from the surrounding GaAs dumbbells. This was due to the fact that most of the dumbbell shapes were a mixture of AlAs and GaAs because of the interfacial roughness. Moreover, it was difficult to locate the precise position of the Si δ-doped layer due to the uncertainty in the spatial extent of the 4ML GaAs layer. Finally, as was the case with the InAs / GaAs based superlattices, the dumbbell column ratio analysis was made worse by the fact that the highest spatial resolution was not achieved in a consistent fashion.

8.3 Improvements and Future Work

It was evident from the results of the simulations that the initial probe conditions were not optimum. For instance, some of the measures of the probe size (e.g. the diameter that contained 90% of total probe intensity) showed that the 0.7Å FWHM probe was distributed over several nanometres. This was probably a result of the small background component that was present in the probe intensity maps as discussed in Chapter 4. Furthermore, it is not at all clear how this small background can be properly removed from the calculations.

It may be the case that the problem of the small background may not arise in the updated version of the Kirkland software. However, the difference between the updated software and the version that was used in this project is unknown. Nevertheless, it is believed that the updated version of the software allows higher order aberrations to be entered into the simulations. This would likely produce more realistic probe intensity profiles. Hence, the simulations (especially the simulations of the 0.7Å FWHM probe) could be improved through the use of the updated version of the software. Moreover, in the case of the simulations that attempted to explore the behaviour of the HAADF signal of the latest SuperSTEM 2 instrument, more realistic results could be obtained by using the actual inner and outer angles of the detector that are to be used in this microscope.

A considerable improvement to the simulations could also be made if a larger supercell size was used. For example, the measurement of the beam spread was shown to be underestimated due to the fact that the spread of intensity reached the edge of the supercell after a depth of only 60nm in the case of the 1Å probe in GaAs. It was demonstrated that this problem was significantly reduced when a supercell of double the length and double the breadth of the original supercell was used as an alternative. However, the increased computational time along with the larger file size (>50MB) that is required to implement each larger supercell calculation may be too prohibitive to run a large set of simulations.

The simulations could also be slightly improved by averaging over more than 8 independent atomic configurations. For instance, the use of 16 atomic configurations results in a 5% change in the calculated HAADF signal. Hence, it is likely that the use of more atomic configurations would give slightly better quantitative results. However, more atomic configurations would probably not have a significant effect on the conclusions that were drawn from the simulations that employed just 8 configurations. For instance, the use of 16 configurations does not generate the level of HAADF background signal that is required to improve the observed Stobbs factor between simulation and experiment.

The experimental plots of the AlAs and GaAs dumbbell column ratios could also be expanded by including a greater range of specimen thicknesses. The deviations in the plots could also be reduced if a specimen with a smaller degree of surface damage was used. However, as was stated in Chapter 5, the data points in the experimental column ratio plots were produced from images taken of a specimen that had undergone a low energy ion mill in the GentleMill. Since the GentleMill minimises the degree of surface damage in cross-section specimens, it is therefore unclear how a significant improvement in surface quality could be made.

It would be of interest to study the sharpness of the 2 types of AlAs / GaAs interfaces over a wider range of thickness values. For instance, if the interfacial sharpness was studied at much lower thicknesses then a better estimate of surface step lengths could be made. In addition, it could also be ascertained whether AlAs-on-GaAs interfaces were associated with elemental diffusion using these smaller thicknesses. However, 30nm is about the lowest possible thickness value that can be obtained from cross-section specimens that do not possess significant surface damage or a bent structure. Hence, a different or improved specimen preparation technique would need to be employed to give much lower specimen thicknesses.

It would also be instructive to repeat the AlAs / GaAs interfacial sharpness experiment using [1-10] oriented specimens. This would allow an investigation to be carried out into the smaller step lengths that are associated with AlAs-on-GaAs interfaces along the [1-10] direction.

The study of the InAs / GaAs superlattices showed the need to determine the experimental InAs dumbbell column ratio as a function of thickness in a similar fashion as was performed for AlAs and GaAs. This would greatly enhance future investigations of structures that contained InAs. For example, the presence of InAs layers could be confirmed by the comparing the standard InAs column ratio value with the values present in column ratio maps. Furthermore, any future study of the InAs / GaAs superlattices would be improved if the sharpness of the InAs / GaAs interface was studied as a function of thickness. This could be done in a similar manner to that presented for AlAs / GaAs interfaces in Chapter 6. However, the feasibility of growing wide layers (~50ML) of InAs alongside GaAs using MBE is not known.

From the investigation of Si δ-doped layers, it seems to be the case that the detection of Si doping is at the very limit of what can be achieved using SuperSTEM 1. This was exemplified by the fact that no Si K EELS signal was identified and the distribution of Si using HAADF imaging could not be ascertained. Consequently, the improved performance (in terms of both HAADF imaging and EELS) of SuperSTEM 2 will probably be required in order to positively detect the Si and to map its distribution. A repeat of the Si δ-doping experiment using SuperSTEM 2 could be performed on the same test specimen as was examined for this project.

References

[1] D. O. Klenov, S. Stemmer, Contributions to the contrast in experimental high-angle annular dark- field images, Ultramicroscopy 106, 889-901 (2006)

[2] E. J. Kirkland, Advanced Computing in Electron Microscopy, Plenum Press, New York (1998)

[3] M. J. Hytch, W. M. Stobbs, Quantitative comparison of high resolution TEM images with image simulations, Ultramicroscopy 53, 191-203 (1994)

[4] C. B. Boothroyd, Why don't high resolution simulations and images match?, Journal of Microscopy 190, 99 (1998)

[5] A. Howie, Hunting the Stobbs factor, Ultramicroscopy 98, 73-79 (2004)

[6] C. B. Boothroyd, R. E. Dunin-Borkowski, W. M. Stobbs, C. J. Humphreys, Quantifying the effects of amorphous layers on image contrast using energy filtered transmission electron microscopy, MRS Symposium Proceedings Vol 354, pp. 495-500 (1995)

[7] C. Dwyer, J. Etheridge, Scattering of Å-scale electron probes in silicon, Ultramicroscopy 96, 343-360 (2003)

[8] S. J. Pennycook, B. Rafferty, P. D. Nellist, Z-contrast imaging in an aberration-corrected scanning transmission electron microscope, Microscopy Microanalysis 6, 343-352 (2000)

[9] S. J. Pennycook, D. E. Jesson, High-resolution imaging of crystals, Physical Review Letters, Volume 64, Number 8, 19 (1990)

[10] Y. Peng, P. D. Nellist, S. J. Pennycook, HAADF-STEM imaging with sub-angstrom probes: a full Bloch wave analysis, Journal of Electron Microscopy 53, 257-266 (2004)

[11] B. R. Nag, Interface roughness scattering limited mobility in AlAs / GaAs, $Al_{0.3}Ga_{0.7}As$ / GaAs and $Ga_{0.5}InP$ / GaAs quantum wells, Semiconductor Science Technology 19, 162-166 (2004)

[12] M. A. Herman, D. Bimberg, J. Christen, Heterointerfaces in quantum wells and epitaxial growth processes: Evaluation by luminescence techniques, Journal of Applied Physics, Vol. 70, No. 2 (1991)

[13] N. Ikarashi, K. Ishida, High-resolution transmission electron microscopy of AlAs-GaAs semiconductor superlattices, Journal of Materials Science: Materials in Electronics 7, 285-295 (1996)

[14] L. Rebohle, F. F. Schreya, S. Hofera, G. Strassera, K. Unterrainera, Energy level engineering in InAs quantum dot stacks embedded in AlAs / GaAs superlattices, Physics E 17, 42-45 (2003)

[15] T. Kitada, S. Shimomura, S. Hiyamizu, Surface segregation of indium atoms during molecular beam epitaxy of InGaAs / GaAs superlattices on (n11)A GaAs substrates, Journal of Crystal Growth, doi:10.1016/j.jcrysgro.2006.11.170 (2006)

[16] T. T. Noda, N. Sumidab, S. Koshibab, S. Nishiokab, Y. Negib, E. Okunishic, Y. Akiyamaa, H. Sakakia, STEM studies of MBE-grown corrugated structures of GaAs, InGaAs and AlAs on (757)B structures, Journal of Crystal Growth 278, 569-574 (2005)

Appendix A: Diagrams from Computer Modelling Investigation

A.1 24mrad Probe Simulations

A.1.1 GaAs PPGa Condition

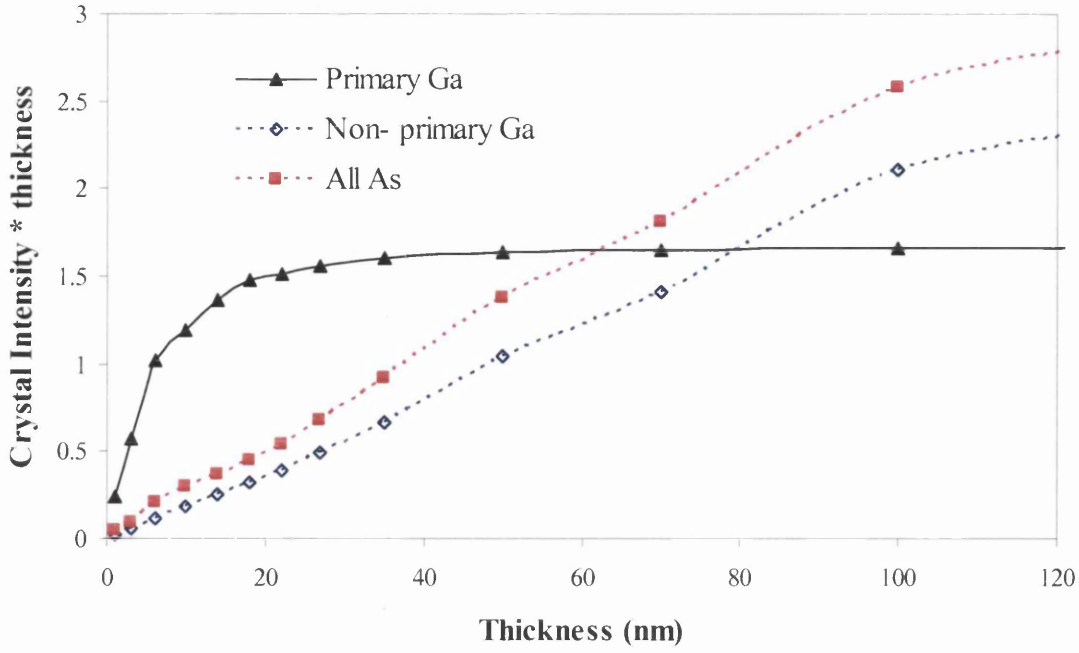

A graph of the simulated integrated crystal intensity on the primary Ga column, all non-primary Ga sites and all As sites as a function of thickness.

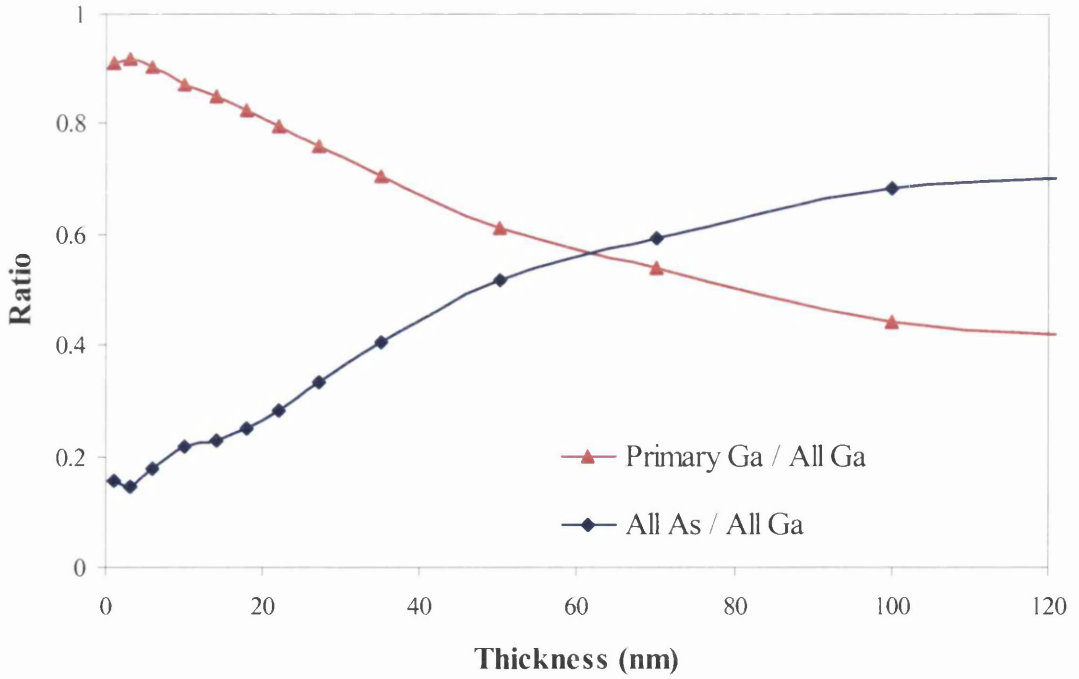

A graph of the simulated integrated crystal intensity on the primary Ga column / all Ga sites as a function of thickness. Also shown is the simulated integrated crystal intensity on all As sites / all Ga sites as a function of thickness.

A.1.2 AlAs PPAs Condition

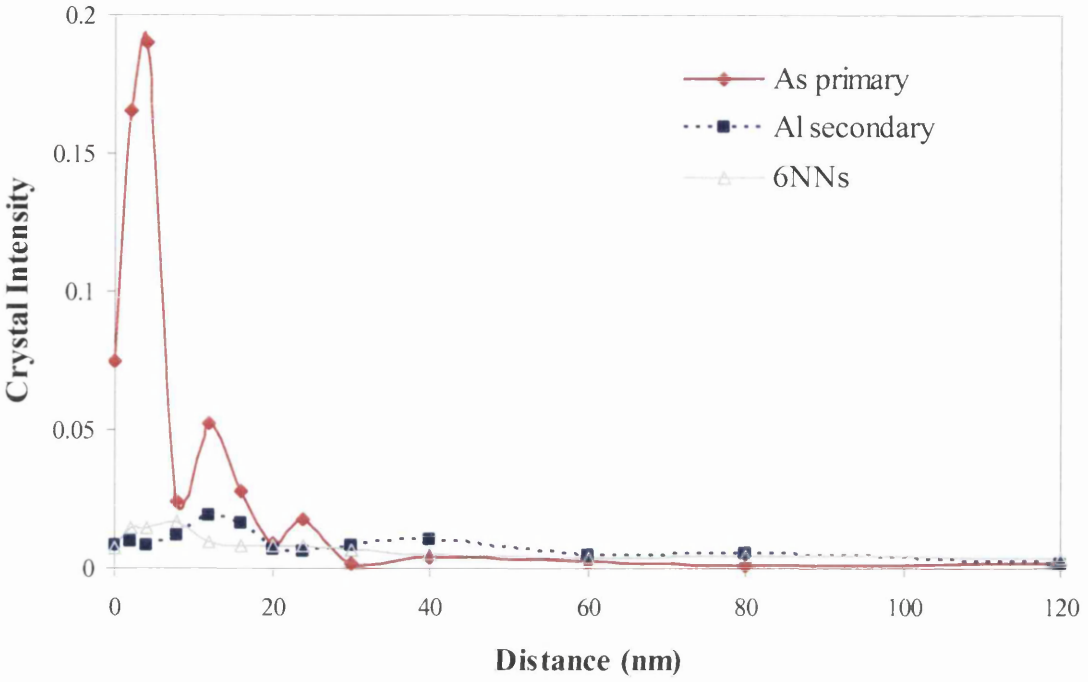

A graph of the simulated real space electron intensity along 2 columns in AlAs [110] as a function of specimen thickness. The probe is incident on an As column on the top surface of the specimen. The intensity on the primary As column (red), on the neighbouring Al column (blue) and the sum of the intensity on the nearest 6 dumbbells (grey) are plotted. The values are the sum of a 9pixel × 9pixel area around each column in the intensity maps. The intensity is normalised with respect to the total intensity in the probe (equal to 1).

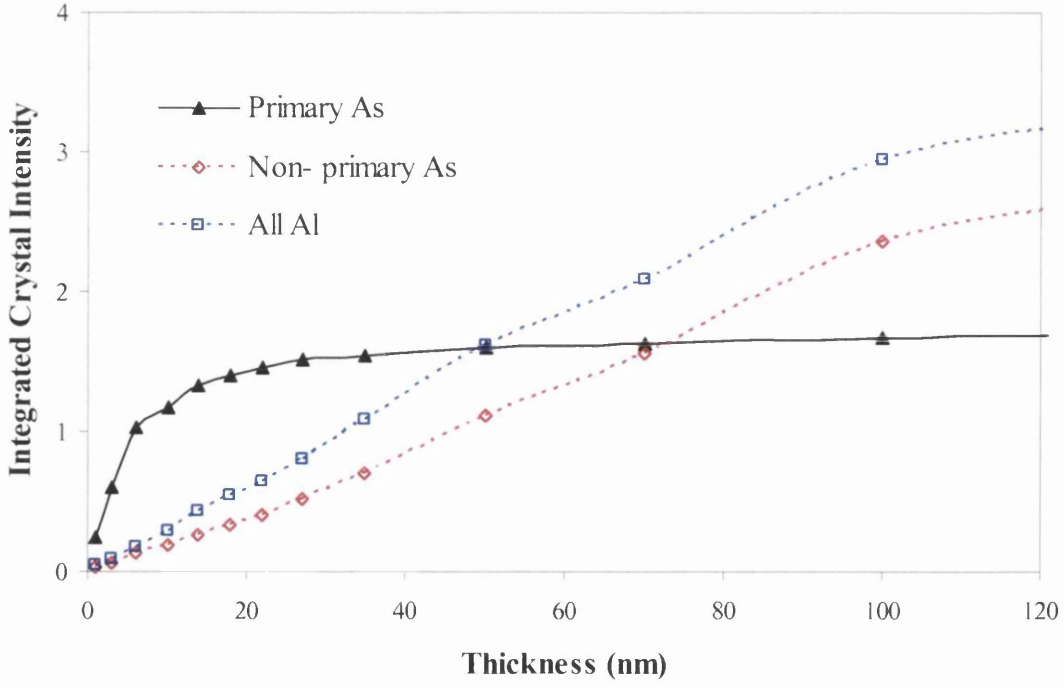

A graph of the simulated integrated crystal intensity on the primary As column, all non-primary As sites and all Al sites as a function of thickness.

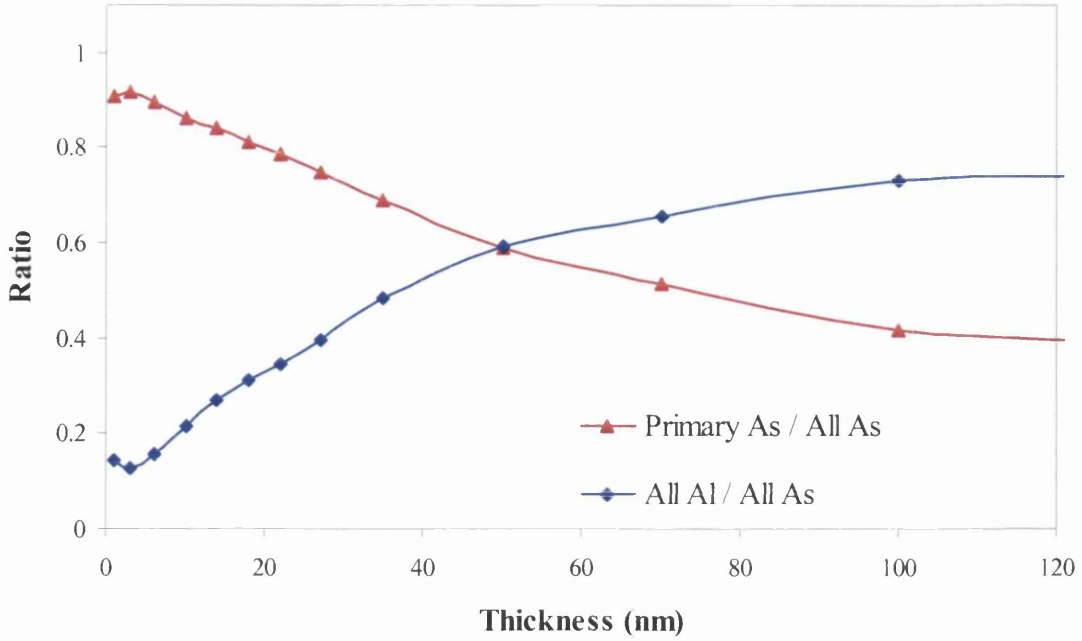

A graph of the simulated integrated crystal intensity on the primary As column / all As sites as a function of thickness. Also shown is the simulated integrated crystal intensity on all Al sites / all As sites as a function of thickness.

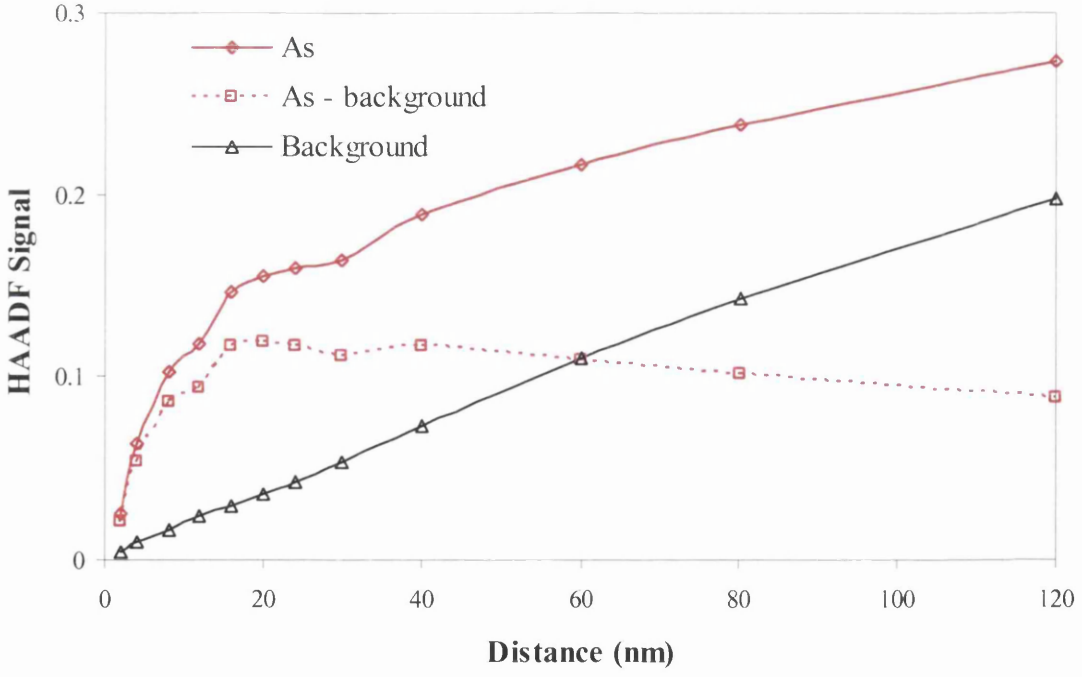

Simulated HAADF STEM intensity for AlAs [110] as a function of specimen thickness. The total HAADF signal for an incident probe on an As column (red line) is plotted. Also plotted is the HAADF background signal i.e. for the probe situated between dumbbells (black line). The As – background signal is also shown. The HAADF signal is normalised with respect to the intensity that the probe generates in the detector plane in the absence of a specimen. The HAADF detector has a range of 70mrad to 210mrad.

A.1.3 AlAs PPBD Condition

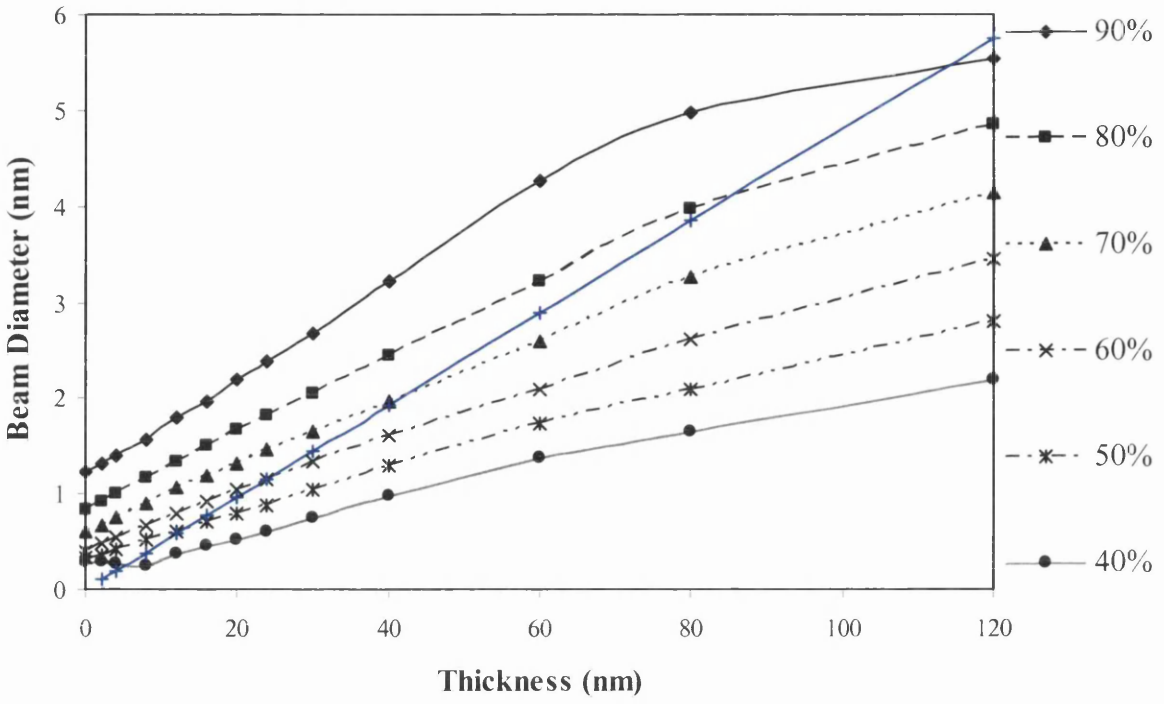

A graph of the simulated beam width as a function of specimen thickness in AlAs [110]. The probe was incident between dumbbells (PPBD). The beam width is given as the diameter of circular areas, in the real space intensity maps, in which 90%, 80%, 70%, 60%, 50% and 40% of the total probe intensity is contained. The circular areas are centred on the initial probe position. Also shown is the theoretical geometrical spread of the beam (red line). This has a diameter of 0.1nm at 0nm thickness.

A.1.4 InAs PPAs Condition

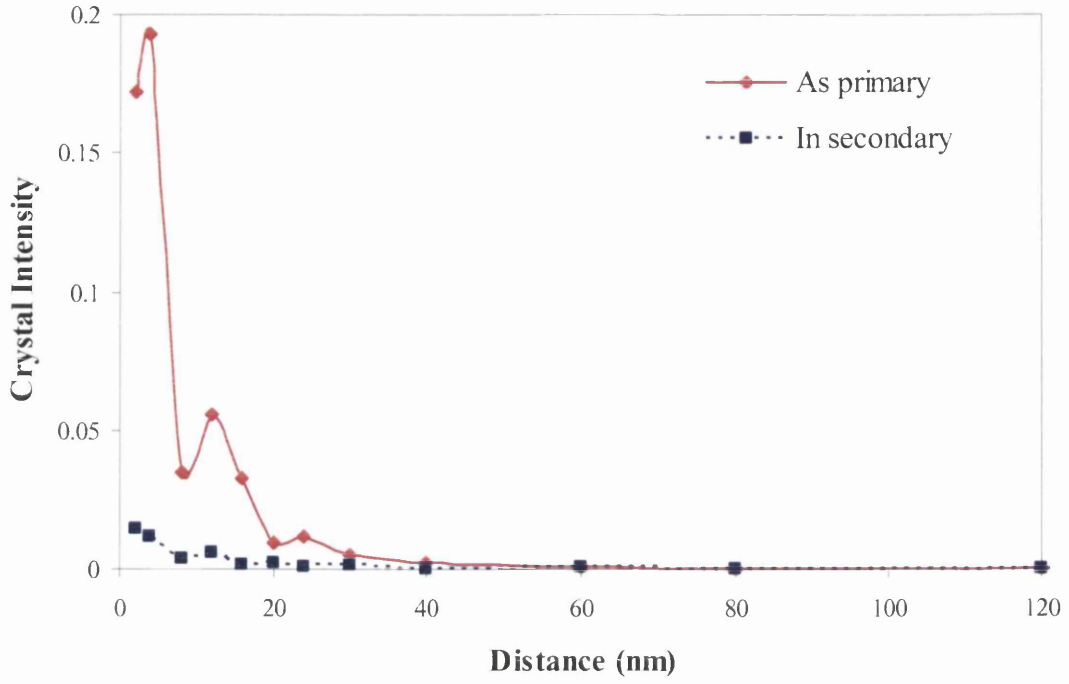

A graph of the simulated real space electron intensity along 2 columns in InAs [110] as a function of specimen thickness. The probe is incident on an As column on the top surface of the specimen. The intensity on the primary As column (red) and on the neighbouring In column (blue) are plotted. The values are the sum of a 9pixel × 9pixel area around each column in the intensity maps. The intensity is normalised with respect to the total intensity in the probe (equal to 1).

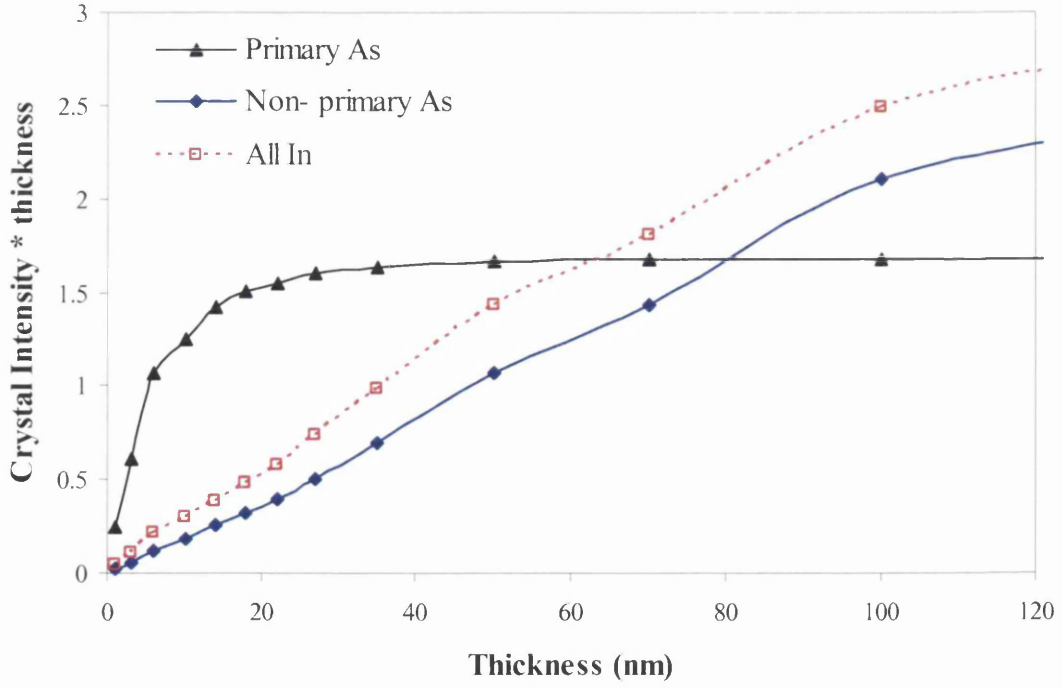

A graph of the simulated integrated crystal intensity on the primary As column, all non-primary As sites and all In sites as a function of thickness.

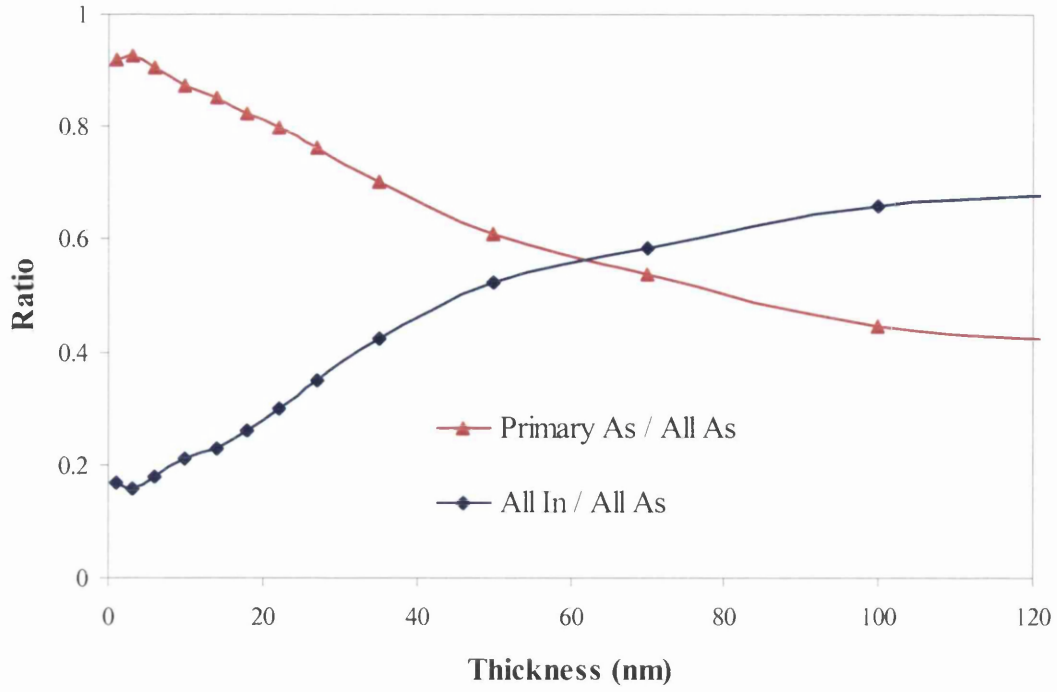

A graph of the simulated integrated crystal intensity on the primary As column / all As sites as a function of thickness. Also shown is the simulated integrated crystal intensity on all In sites / all As sites as a function of thickness.

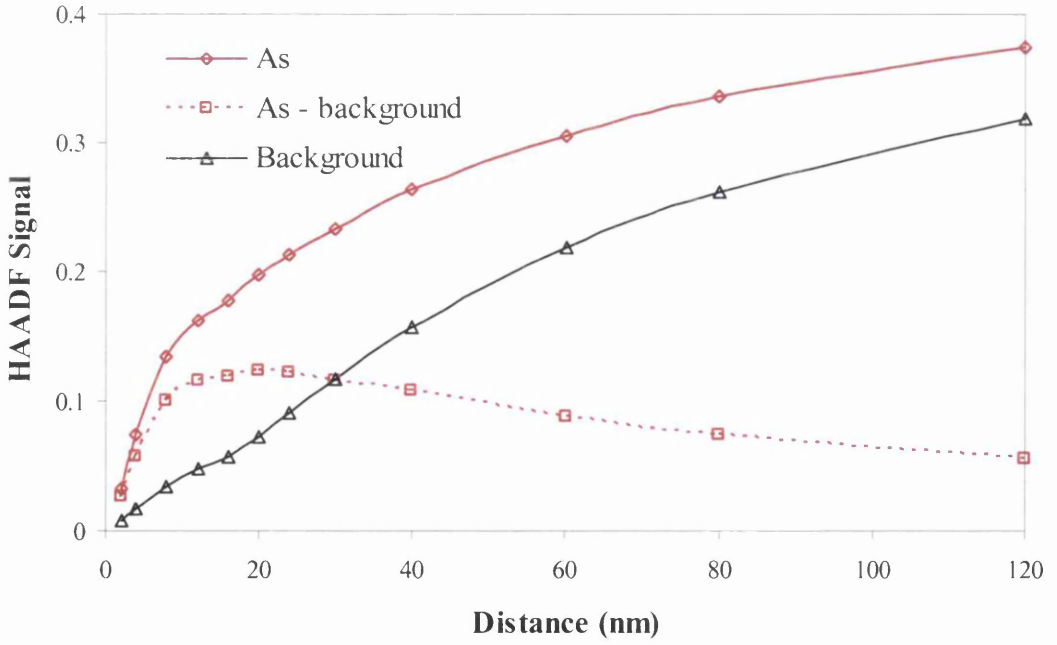

Simulated HAADF STEM intensity for InAs [110] as a function of specimen thickness. The total HAADF signal for an incident probe on an As column (red line) is plotted. Also plotted is the HAADF background signal i.e. for the probe situated between dumbbells (black line). The As – background signal is also shown. The HAADF signal is normalised with respect to the intensity that the probe generates in the detector plane in the absence of a specimen. The HAADF detector has a range of 70mrad to 210mrad.

A.1.5 InAs PPDB Condition

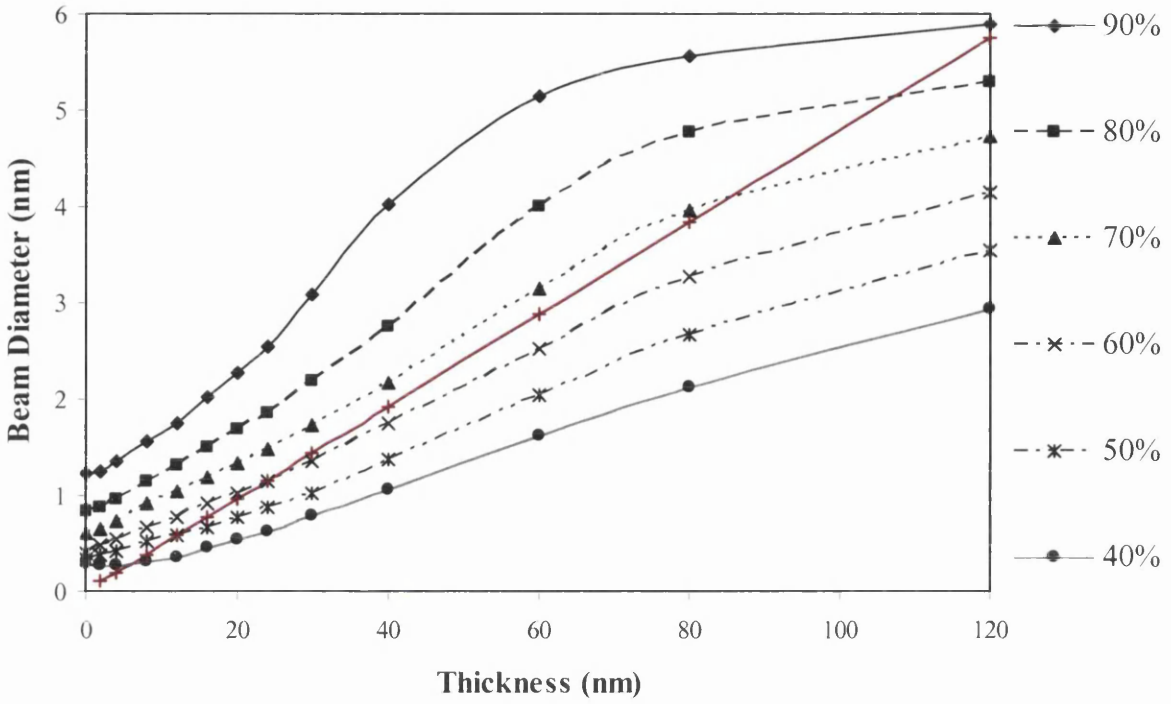

A graph of the simulated beam width as a function of specimen thickness in InAs [110]. The probe was incident between dumbbells (PPBD). The beam width is given as the diameter of circular areas, in the real space intensity maps, in which 90%, 80%, 70%, 60%, 50% and 40% of the total probe intensity is contained. The circular areas are centred on the initial probe position. Also shown is the theoretical geometrical spread of the beam (red line). This has a diameter of 0.1nm at 0nm thickness.

A.2 50mrad Probe Simulations

A.2.1 GaAs Real Space Intensity Maps

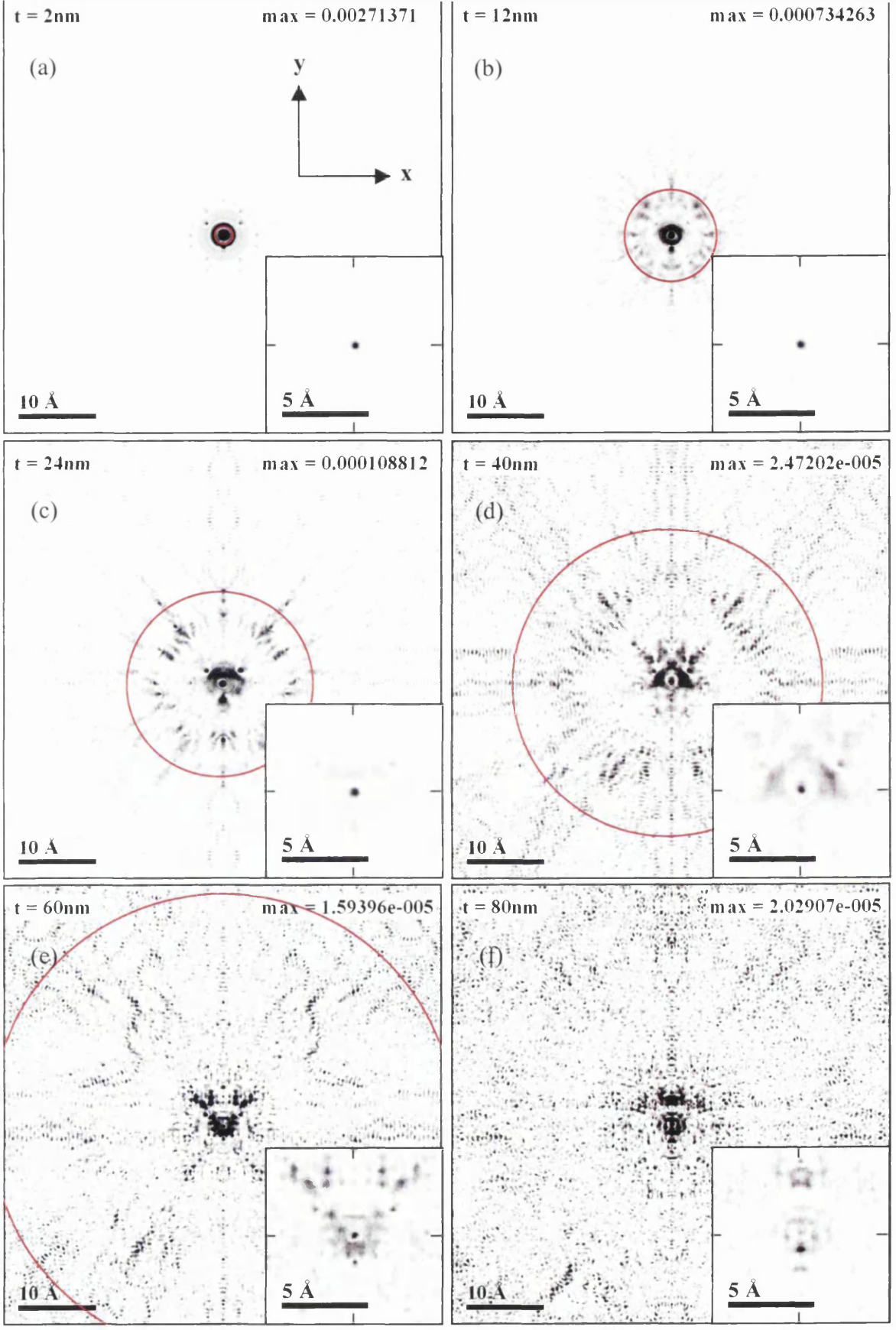

Contrast enhanced simulated electron intensity maps at various depths in a crystal of GaAs [110]. The insets show a magnified view of the central region of each map taken over the full intensity range. A 50mrad, 0.07nm probe is incident on an As column. Black pixels are the most intense. The crystal depths are: **(a)** 2nm **(b)** 12nm **(c)** 24nm **(d)** 40nm **(e)** 60nm and **(f)** 80nm. Max refers to the maximum intensity contained within a single pixel. Circle radius = αt. The total electron intensity of the probe = 1.

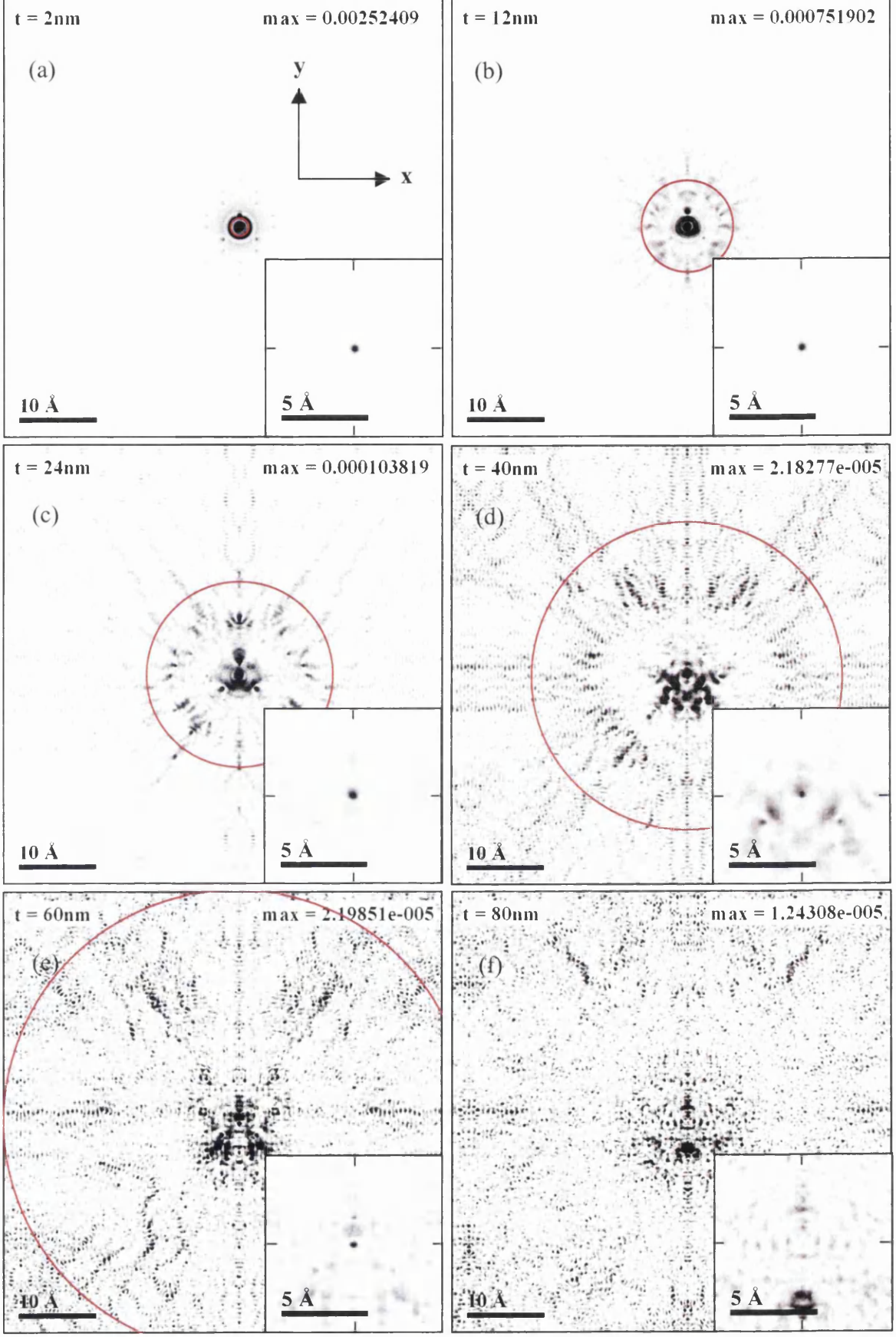

Contrast enhanced simulated electron intensity maps at various depths in a crystal of GaAs [110]. The insets show a magnified view of the central region of each map taken over the full intensity range. A 50mrad, 0.07nm probe is incident on a Ga column. Black pixels are the most intense. The crystal depths are: **(a)** 2nm **(b)** 12nm **(c)** 24nm **(d)** 40nm **(e)** 60nm and **(f)** 80nm. Max refers to the maximum intensity contained within a single pixel. Circle radius = αt. The total electron intensity of the probe = 1.

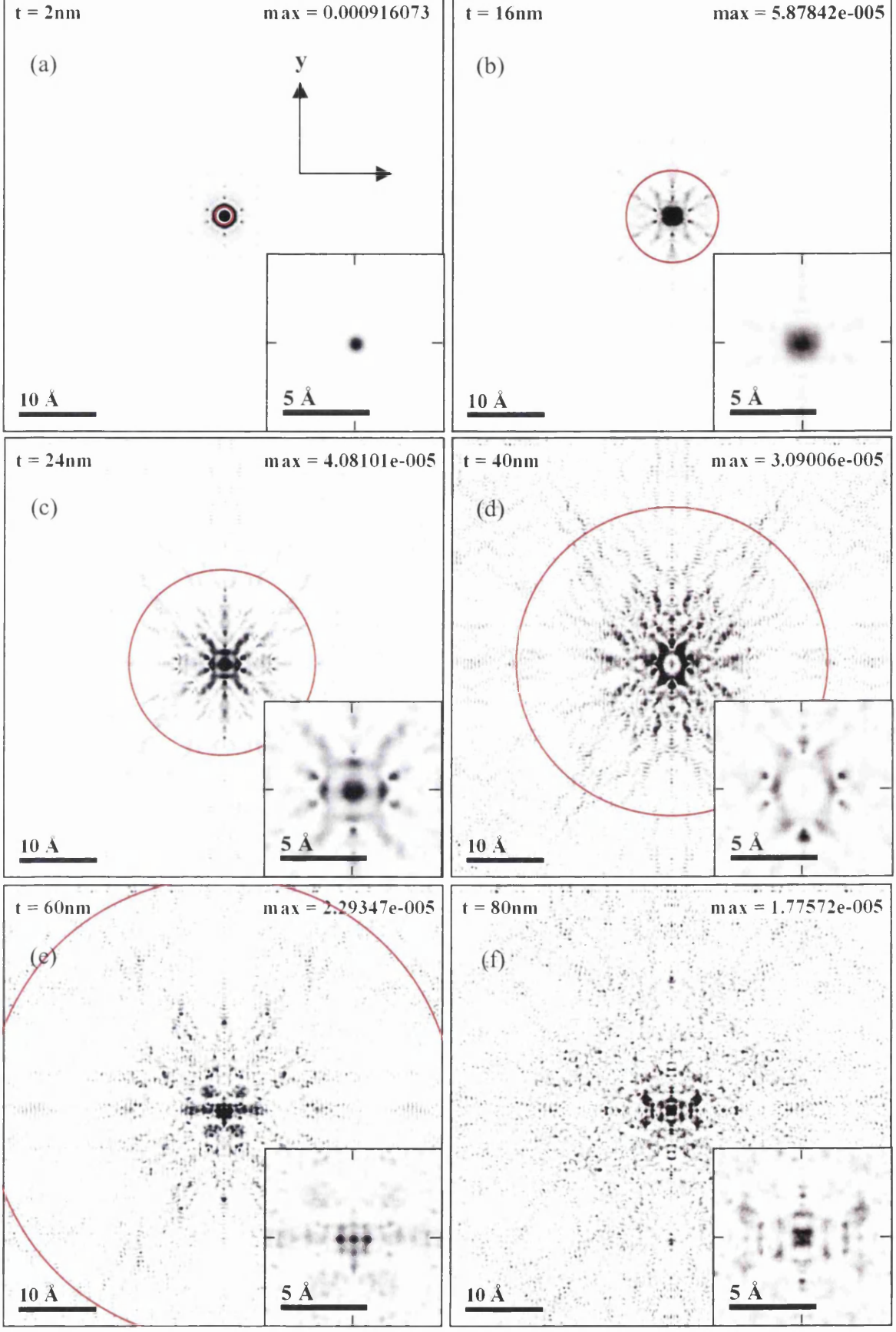

Contrast enhanced simulated electron intensity maps at various depths in a crystal of GaAs [110]. The insets show a magnified view of the central region of each map taken over the full intensity range. A 50mrad, 0.07nm probe is incident between dumbbells. Black pixels are the most intense. The crystal depths are: **(a)** 2nm **(b)** 12nm **(c)** 24nm **(d)** 40nm **(e)** 60nm and **(f)** 80nm. Max refers to the maximum intensity contained within a single pixel. Circle radius = αt. The total electron intensity of the probe = 1.

A.2.2 GaAs PPAs Condition

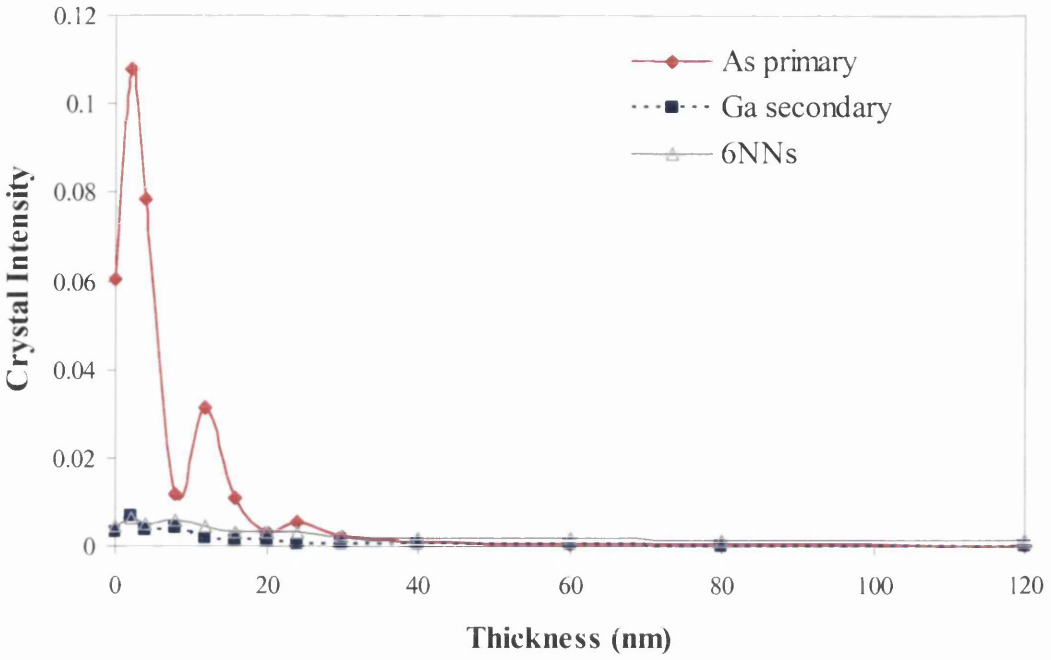

A graph of the simulated real space electron intensity along 2 columns in GaAs [110] as a function of specimen thickness. The probe is incident on an As column on the top surface of the specimen. The intensity on the primary As column (red), on the neighbouring Ga column (blue) and the sum of the intensity on the nearest 6 dumbbells (grey) are plotted. The values are the sum of a 9pixel × 9pixel area around each column in the intensity maps. The intensity is normalised with respect to the total intensity in the probe (equal to 1).

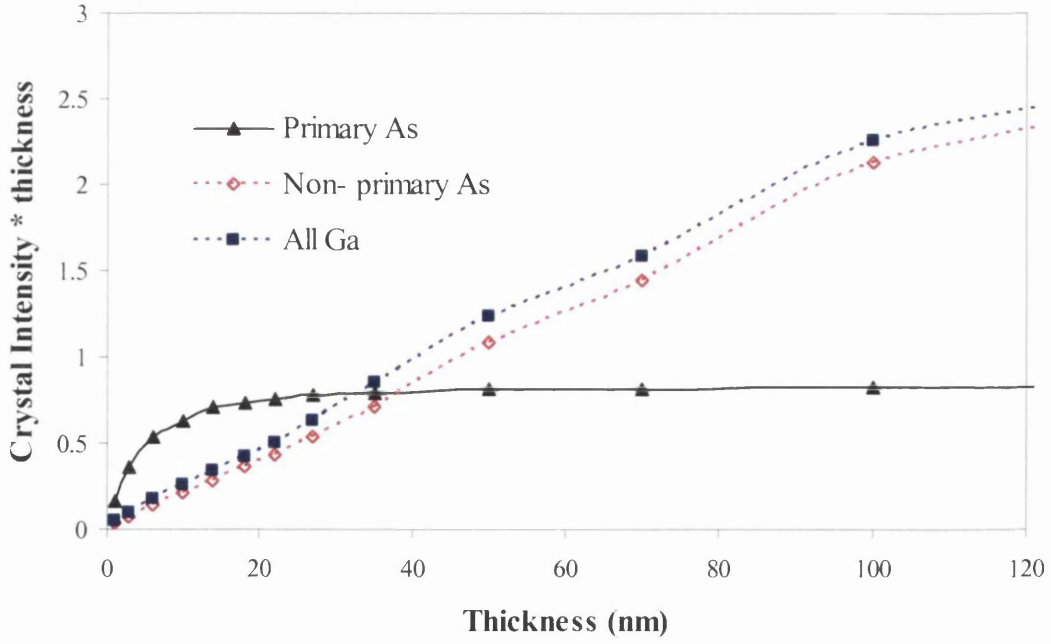

A graph of the simulated integrated crystal intensity on the primary As column, all non-primary As sites and all Ga sites as a function of thickness.

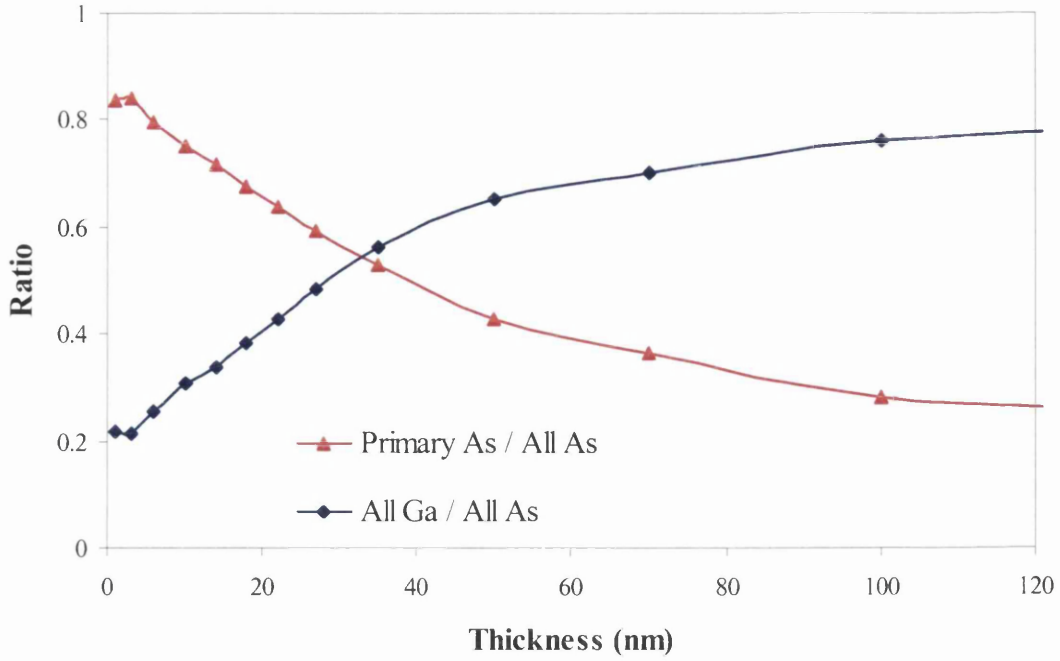

A graph of the simulated integrated crystal intensity on the primary As column / all As sites as a function of thickness. Also shown is the simulated integrated crystal intensity on all Ga sites / all As sites as a function of thickness.

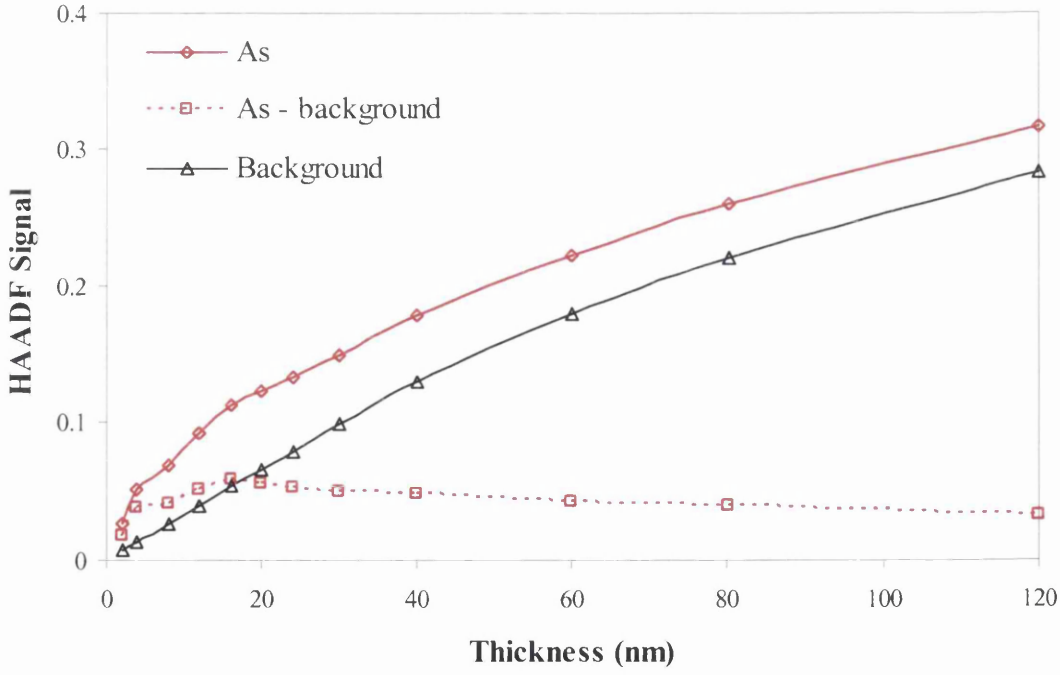

Simulated HAADF STEM intensity for GaAs [110] as a function of specimen thickness. The total HAADF signal for an incident probe on an As column (red line) is plotted. Also plotted is the HAADF background signal i.e. for the probe situated between dumbbells (black line). The As – background signal is also shown. The HAADF signal is normalised with respect to the intensity that the probe generates in the detector plane in the absence of a specimen. The HAADF detector has a range of 70mrad to 210mrad.

A.2.3 GaAs PPGa Condition

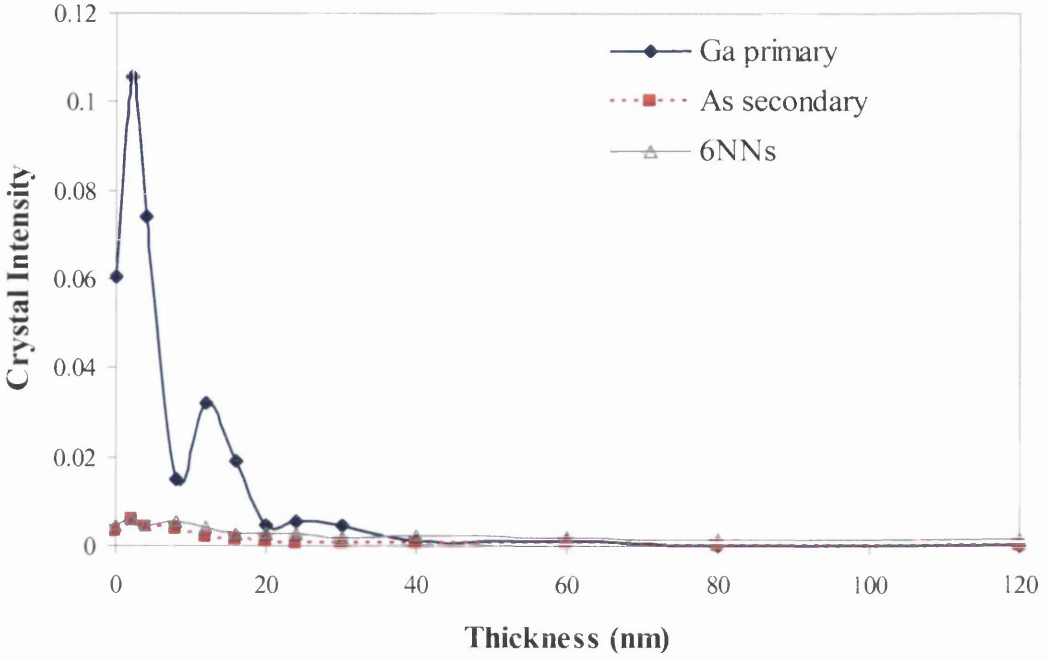

A graph of the simulated real space electron intensity along 2 columns in GaAs [110] as a function of specimen thickness. The probe is incident on a Ga column on the top surface of the specimen. The intensity on the primary Ga column (blue), on the neighbouring As column (red) and the sum of the intensity on the nearest 6 dumbbells (grey) are plotted. The values are the sum of a 9pixel × 9pixel area around each column in the intensity maps. The intensity is normalised with respect to the total intensity in the probe (equal to 1).

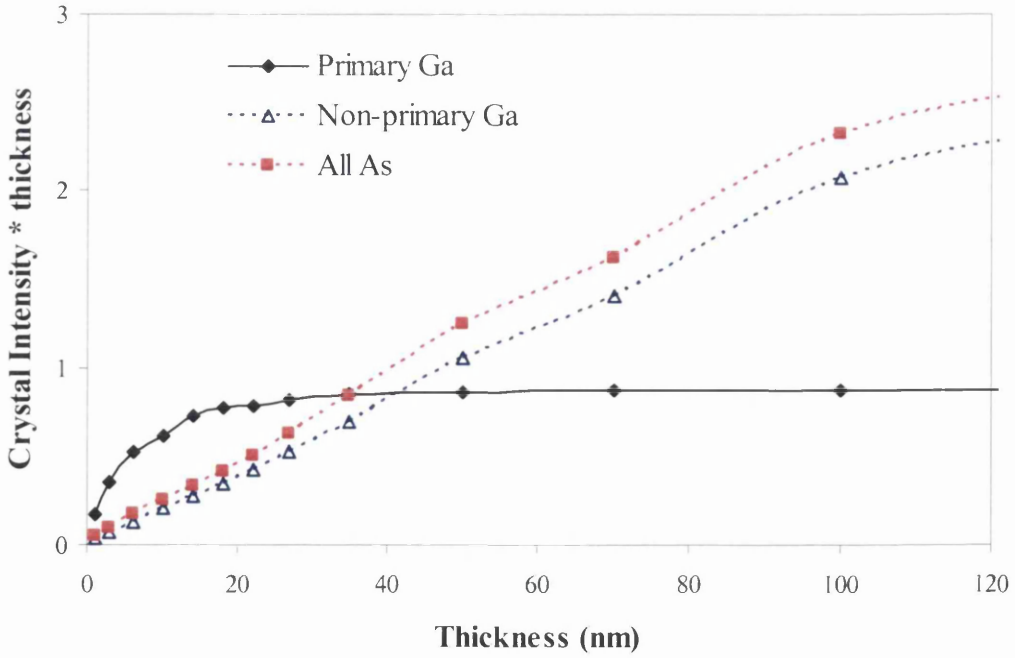

A graph of the simulated integrated crystal intensity on the primary Ga column, all non-primary Ga sites and all As sites as a function of thickness.

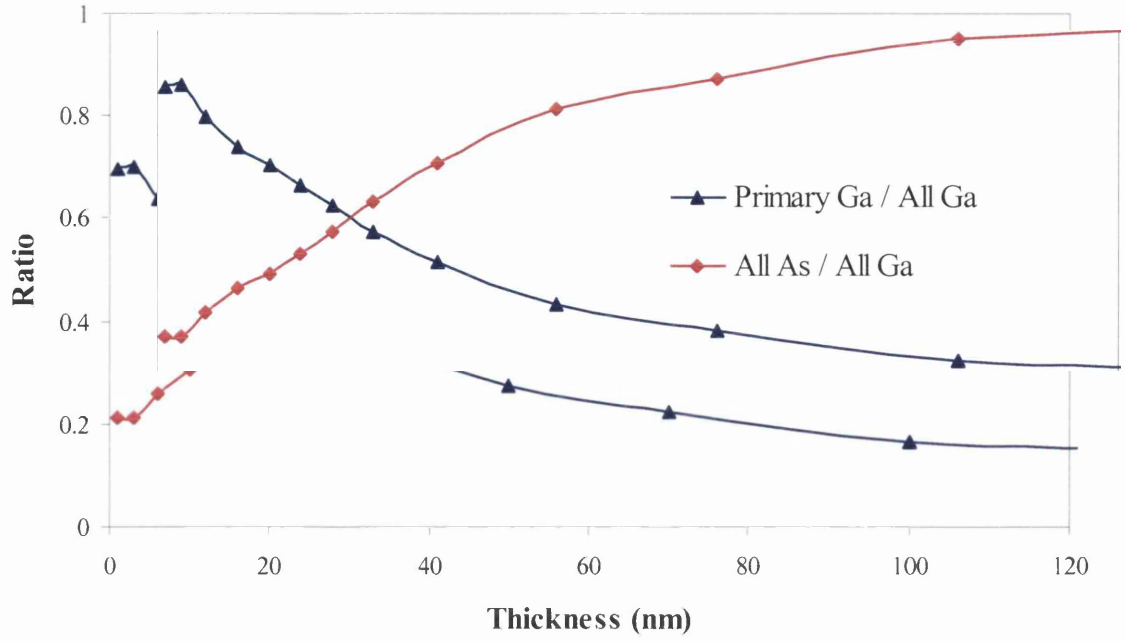

A graph of the simulated integrated crystal intensity on the primary Ga column / all Ga sites as a function of thickness. Also shown is the simulated integrated crystal intensity on all As sites / all Ga sites as a function of thickness.

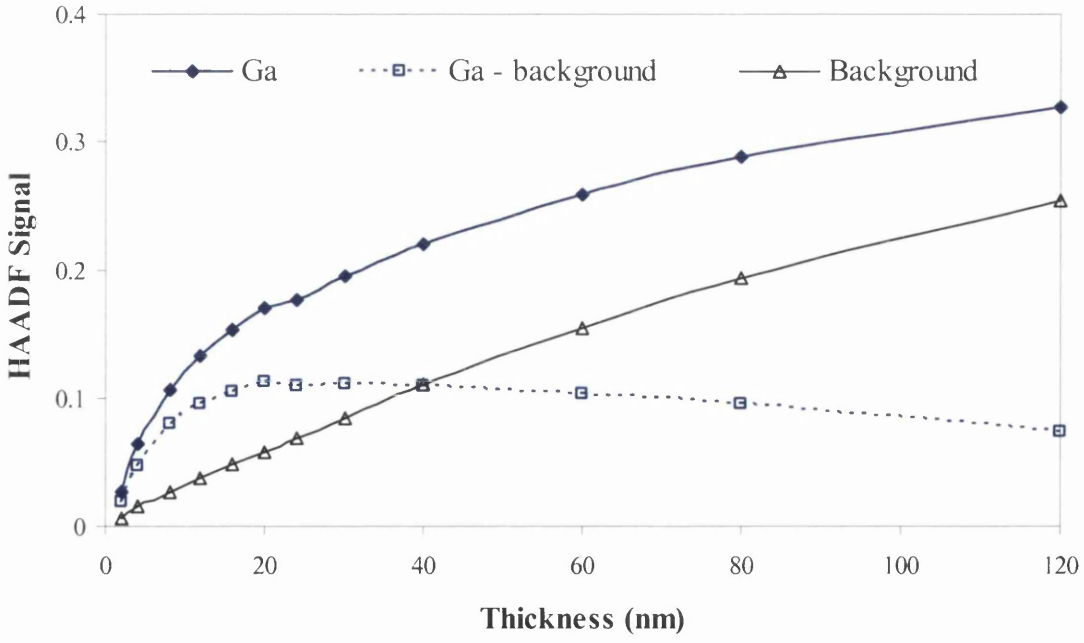

Simulated HAADF STEM intensity for GaAs [110] as a function of specimen thickness. The total HAADF signal for an incident probe on a Ga column (blue line) is plotted. Also plotted is the HAADF background signal i.e. for the probe situated between dumbbells (black line). The As – background signal is also shown. The HAADF signal is normalised with respect to the intensity that the probe generates in the detector plane in the absence of a specimen. The HAADF detector has a range of 70mrad to 210mrad.

A.2.4 GaAs PPBD Condition

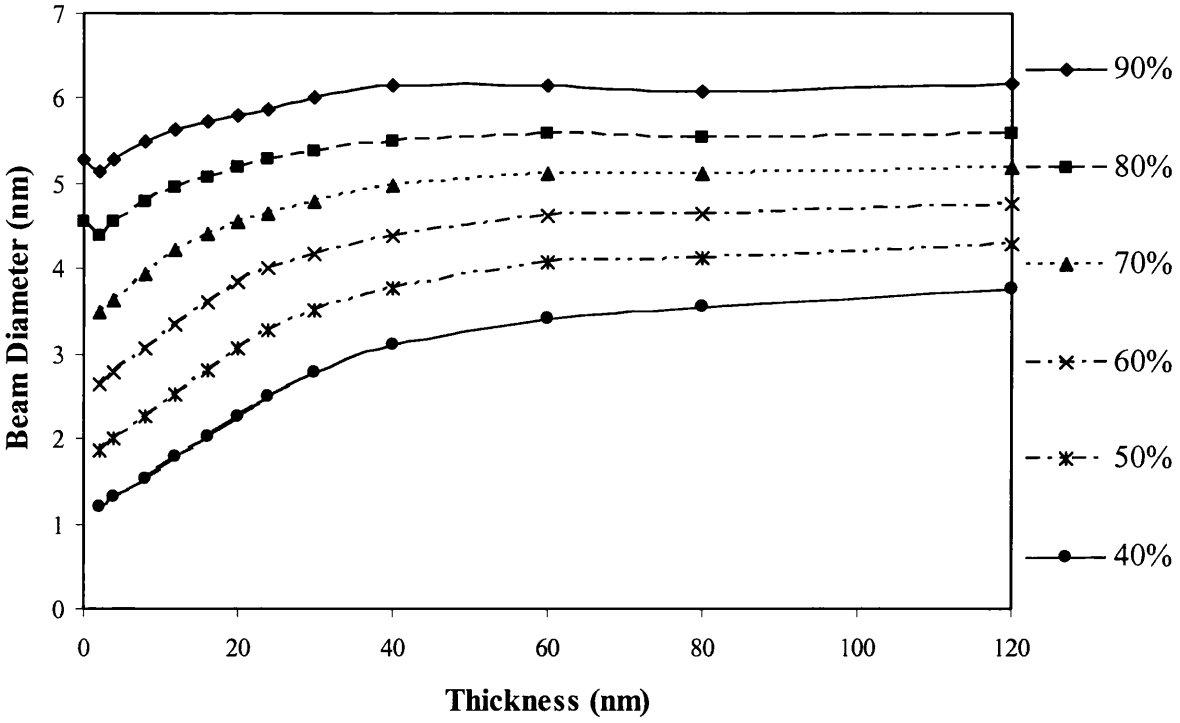

A graph of the simulated beam width as a function of specimen thickness in Gas [110]. The probe was incident between dumbbells (PPBD). The beam width is given as the diameter of circular areas, in the real space intensity maps, in which 90%, 80%, 70%, 60%, 50% and 40% of the total probe intensity is contained. The circular areas are centred on the initial probe position.

A.2.5 AIAs Real Space Intensity Maps

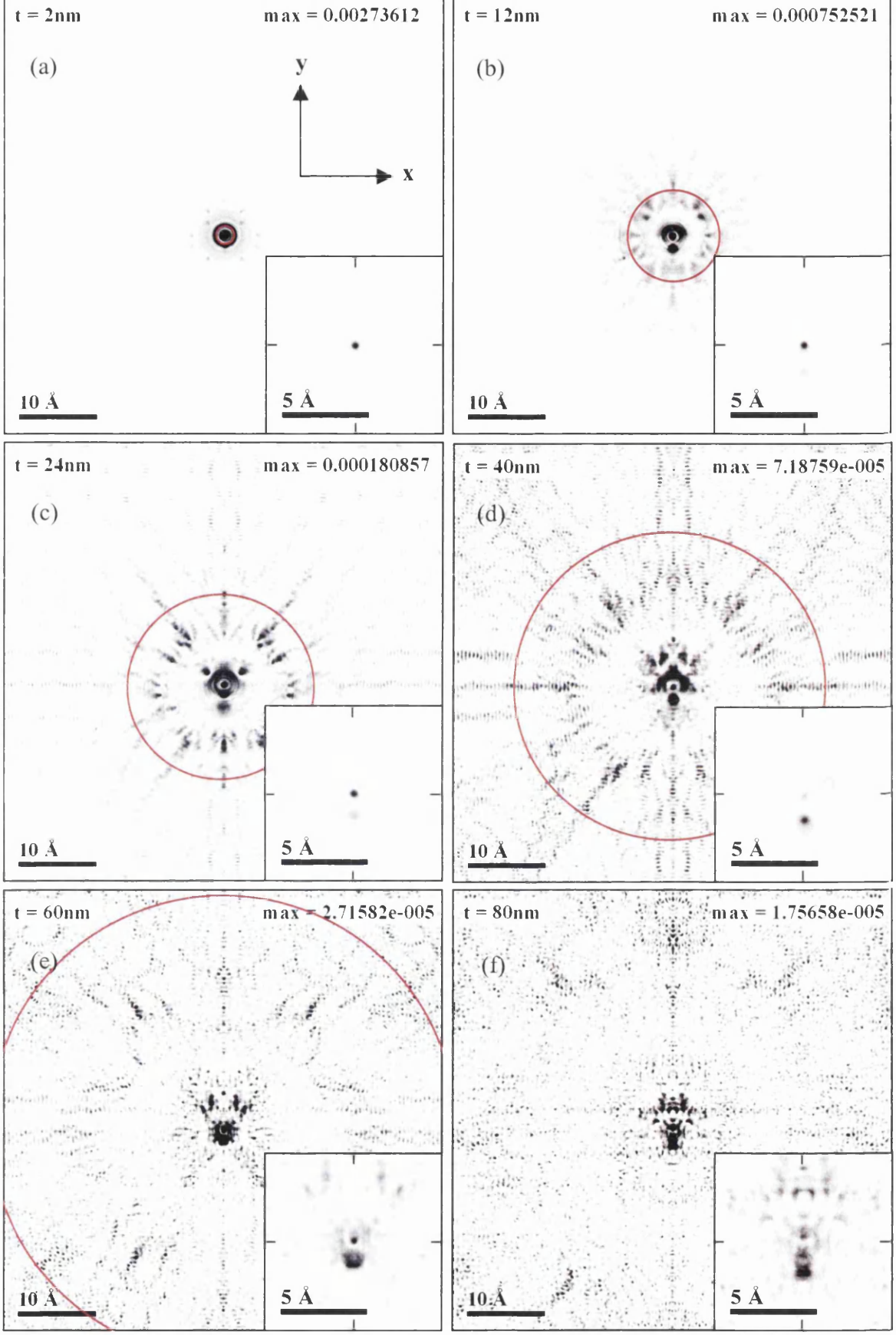

Contrast enhanced simulated electron intensity maps at various depths in a crystal of AlAs [110]. The insets show a magnified view of the central region of each map taken over the full intensity range. A 50mrad, 0.07nm probe is incident on an As column. Black pixels are the most intense. The crystal depths are: **(a)** 2nm **(b)** 12nm **(c)** 24nm **(d)** 40nm **(e)** 60nm and **(f)** 80nm. Max refers to the maximum intensity contained within a single pixel. Circle radius = αt. The total electron intensity of the probe = 1.

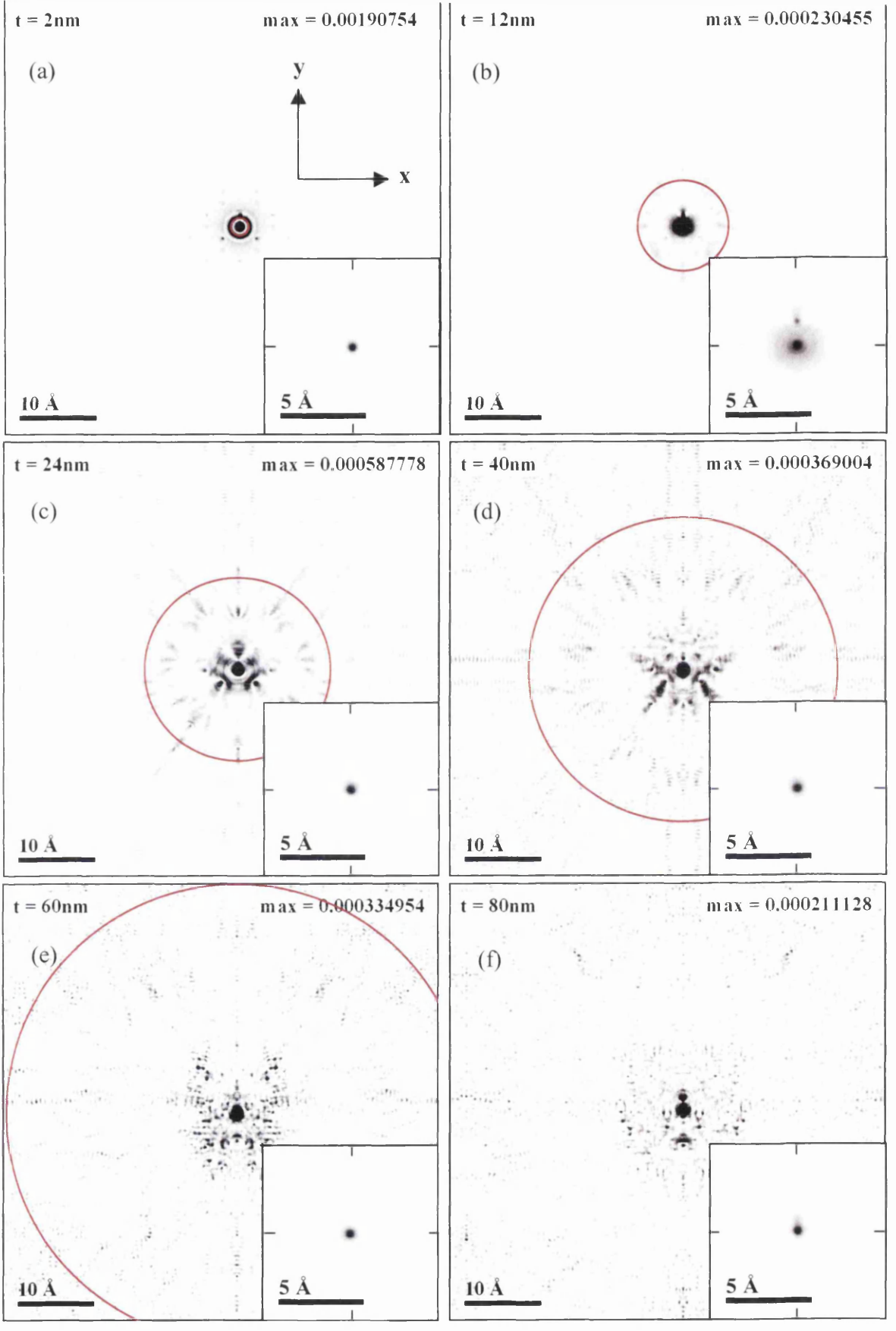

Contrast enhanced simulated electron intensity maps at various depths in a crystal of AlAs [110]. The insets show a magnified view of the central region of each map taken over the full intensity range. A 50mrad, 0.07nm probe is incident on an Al column. Black pixels are the most intense. The crystal depths are: **(a)** 2nm **(b)** 12nm **(c)** 24nm **(d)** 40nm **(e)** 60nm and **(f)** 80nm. Max refers to the maximum intensity contained within a single pixel. Circle radius = αt. The total electron intensity of the probe = 1.

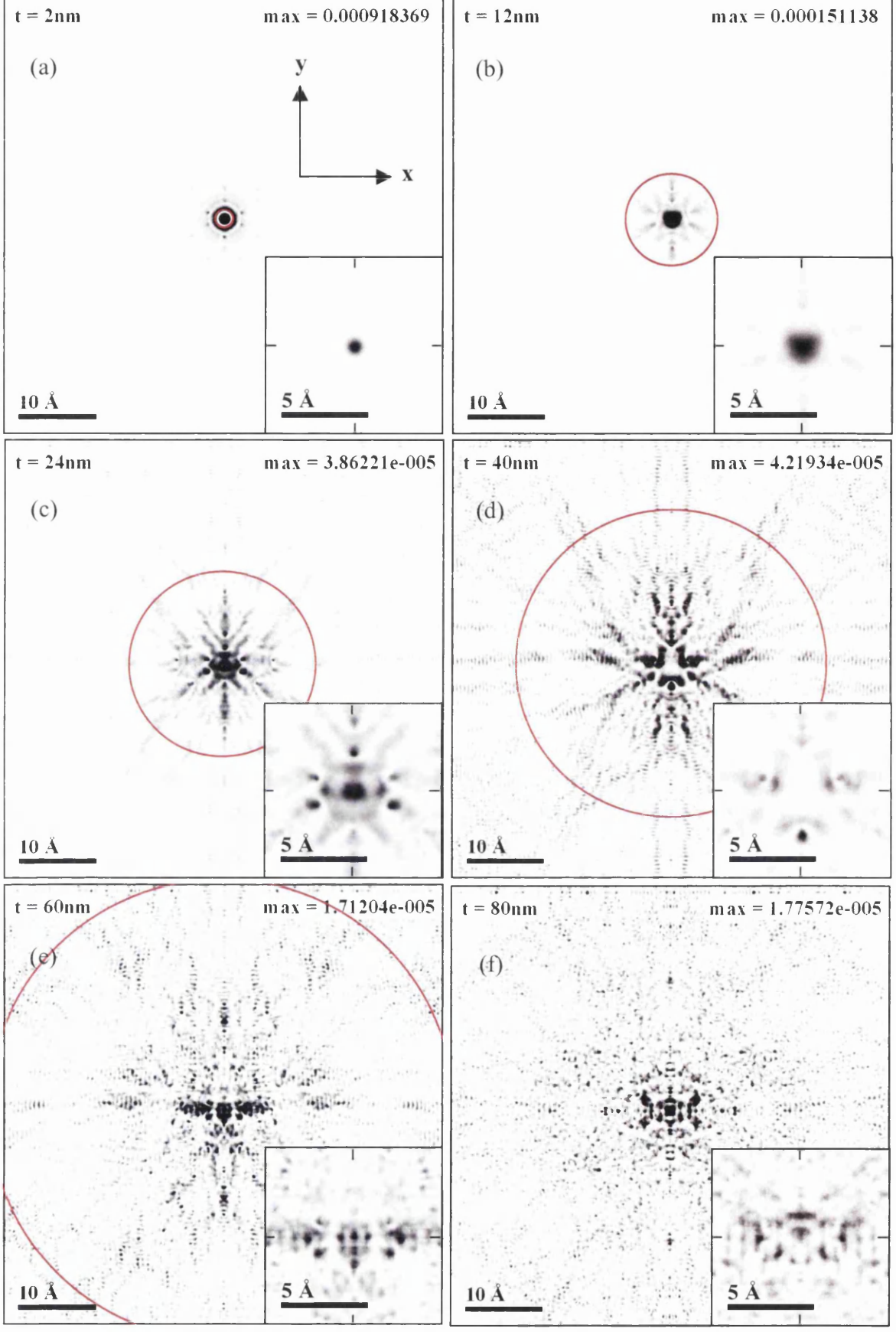

Contrast enhanced simulated electron intensity maps at various depths in a crystal of AlAs [110]. The insets show a magnified view of the central region of each map taken over the full intensity range. A 50mrad, 0.07nm probe is incident between dumbbells. Black pixels are the most intense. The crystal depths are: **(a)** 2nm **(b)** 12nm **(c)** 24nm **(d)** 40nm **(e)** 60nm and **(f)** 80nm. Max refers to the maximum intensity contained within a single pixel. Circle radius = αt. The total electron intensity of the probe = 1.

A.2.6 AlAs PPAs Condition

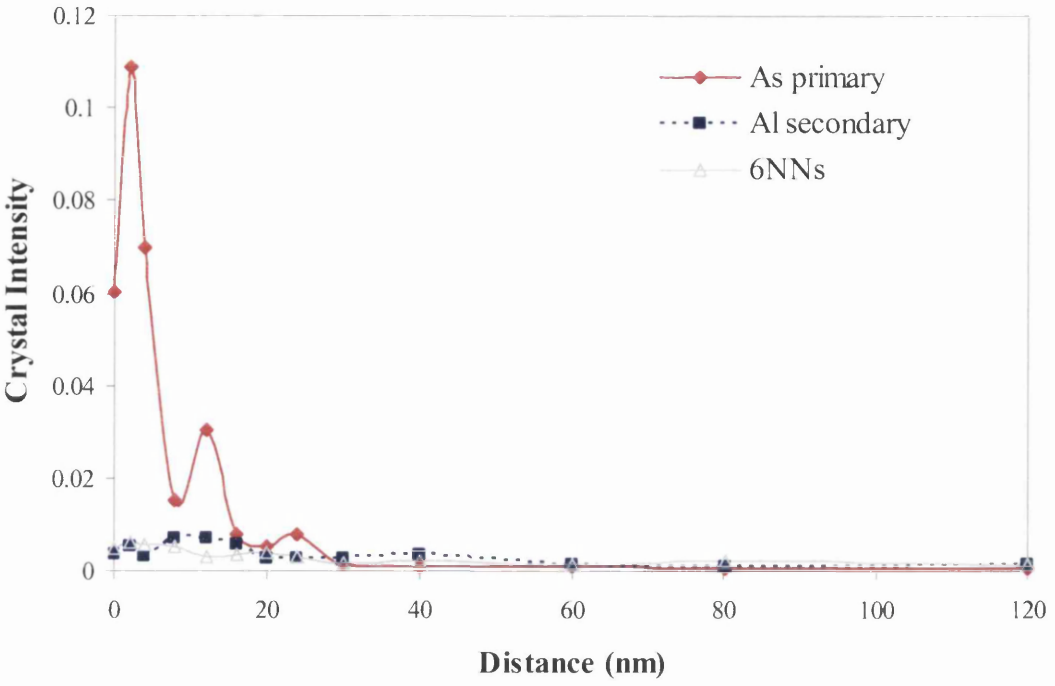

A graph of the simulated real space electron intensity along 2 columns in AlAs [110] as a function of specimen thickness. The probe is incident on an As column on the top surface of the specimen. The intensity on the primary As column (red), on the neighbouring Al column (blue) and the sum of the intensity on the nearest 6 dumbbells (grey) are plotted. The values are the sum of a 9pixel × 9pixel area around each column in the intensity maps. The intensity is normalised with respect to the total intensity in the probe (equal to 1).

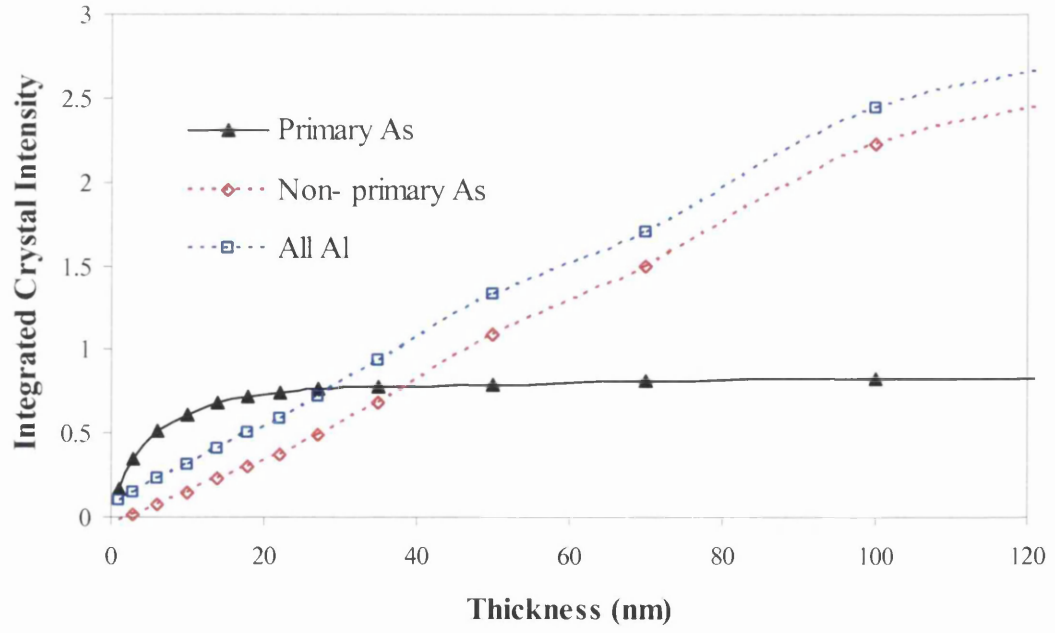

A graph of the simulated integrated crystal intensity on the primary As column, all non-primary As sites and all Al sites as a function of thickness.

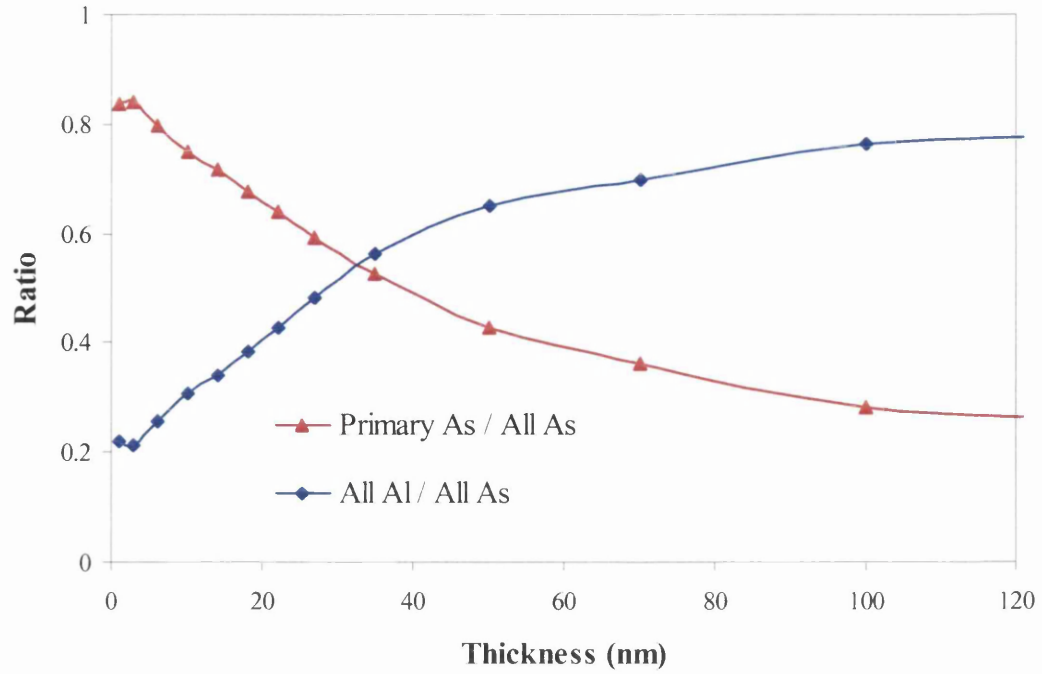

A graph of the simulated integrated crystal intensity on the primary As column / all As sites as a function of thickness. Also shown is the simulated integrated crystal intensity on all Al sites / all As sites as a function of thickness.

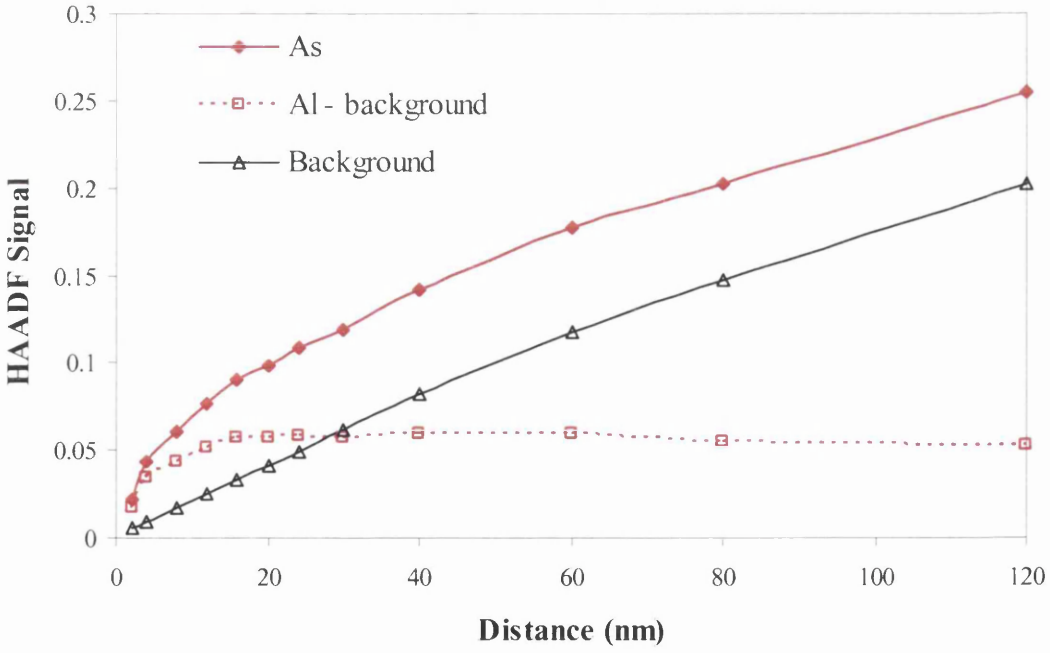

Simulated HAADF STEM intensity for AlAs [110] as a function of specimen thickness. The total HAADF signal for an incident probe on an As column (red line) is plotted. Also plotted is the HAADF background signal i.e. for the probe situated between dumbbells (black line). The As – background signal is also shown. The HAADF signal is normalised with respect to the intensity that the probe generates in the detector plane in the absence of a specimen. The HAADF detector has a range of 70mrad to 210mrad.

A.2.7 AlAs PPAl Condition

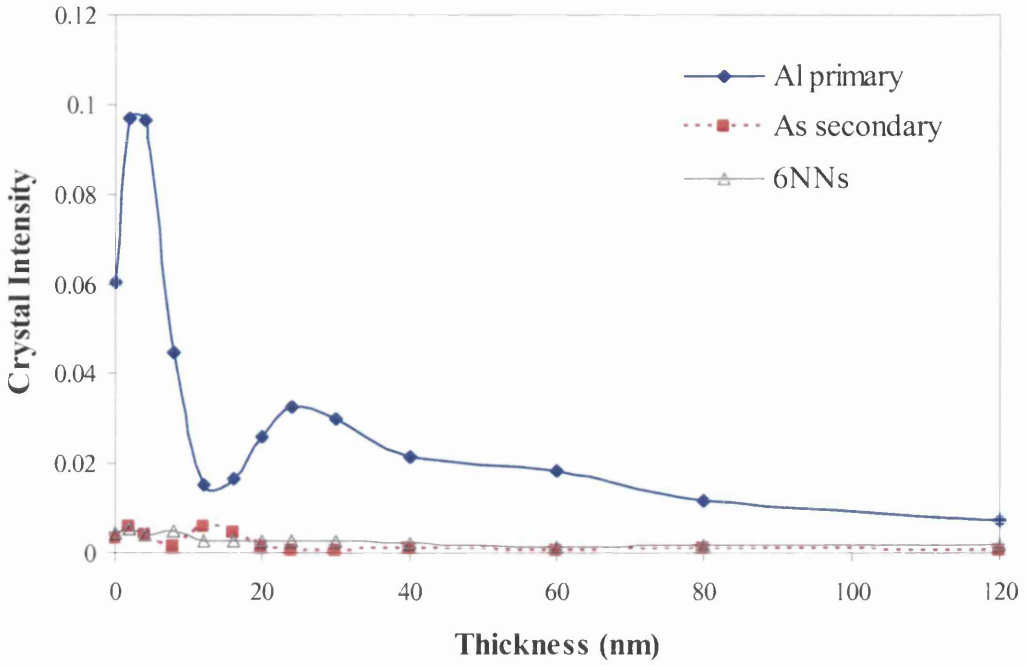

A graph of the simulated real space electron intensity along 2 columns in AlAs [110] as a function of specimen thickness. The probe is incident on an Al column on the top surface of the specimen. The intensity on the primary Al column (blue), on the neighbouring As column (red) and the sum of the intensity on the nearest 6 dumbbells (grey) are plotted. The values are the sum of a 9pixel × 9pixel area around each column in the intensity maps. The intensity is normalised with respect to the total intensity in the probe (equal to 1).

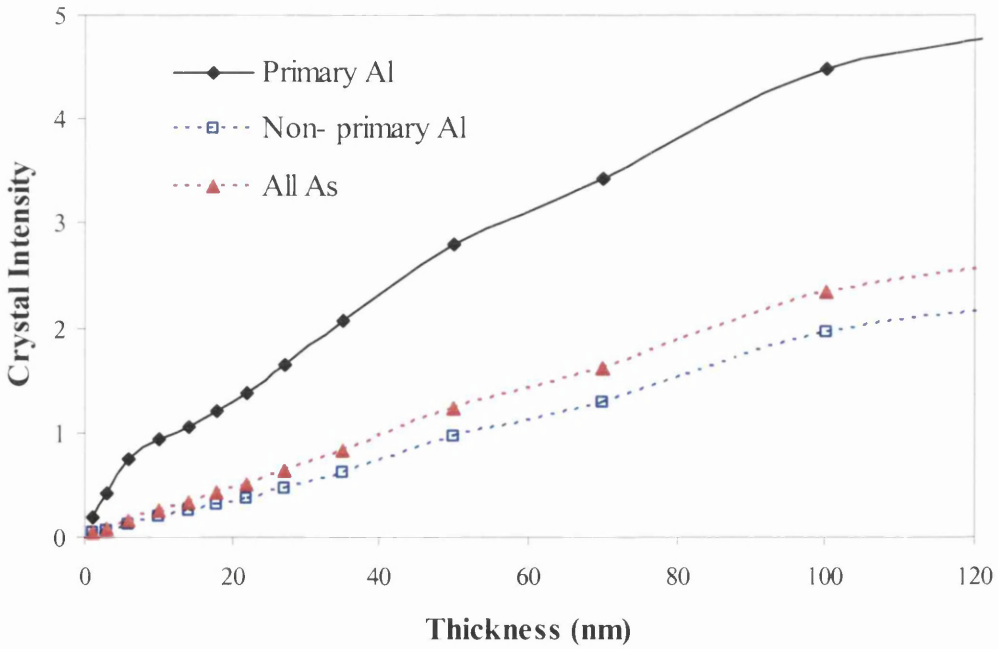

A graph of the simulated integrated crystal intensity on the primary Al column, all non-primary Al sites and all As sites as a function of thickness.

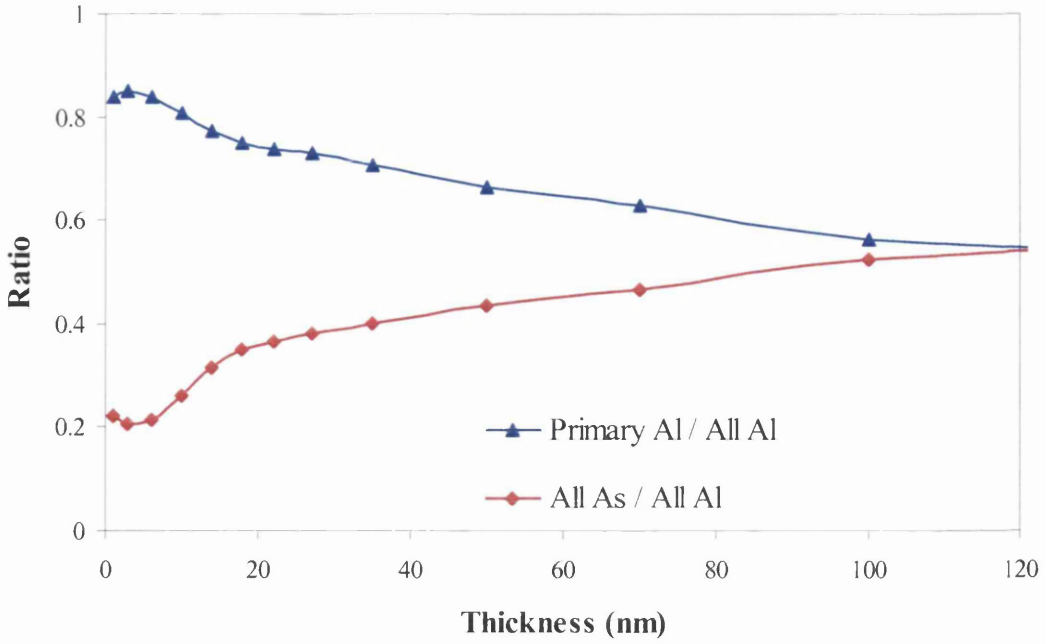

A graph of the simulated integrated crystal intensity on the primary Al column / all Al sites as a function of thickness. Also shown is the simulated integrated crystal intensity on all As sites / all Al sites as a function of thickness.

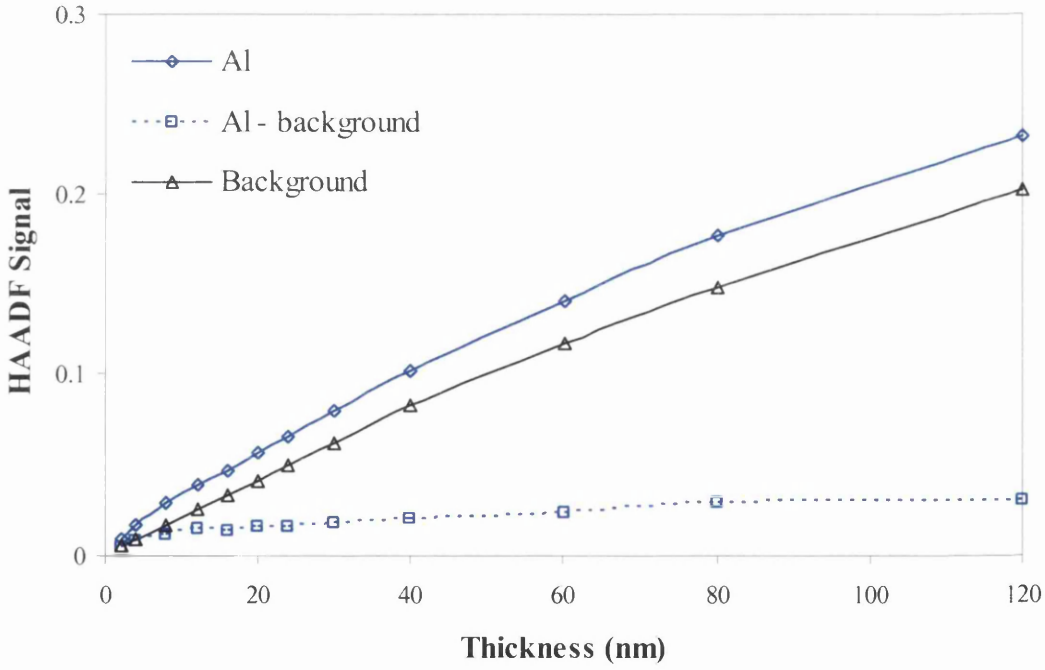

Simulated HAADF STEM intensity for AlAs [110] as a function of specimen thickness. The total HAADF signal for an incident probe on an Al column (blue line) is plotted. Also plotted is the HAADF background signal i.e. for the probe situated between dumbbells (black line). The Al – background signal is also shown. The HAADF signal is normalised with respect to the intensity that the probe generates in the detector plane in the absence of a specimen. The HAADF detector has a range of 70mrad to 210mrad.

A.2.8 AlAs PPBD Condition

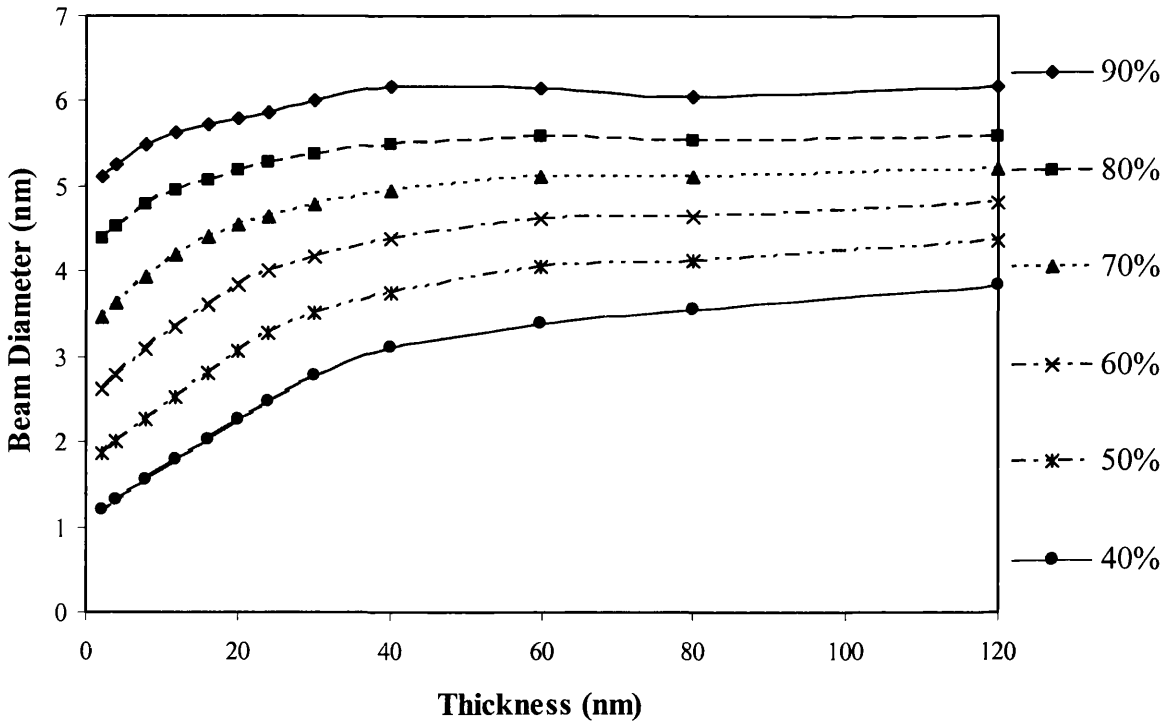

A graph of the simulated beam width as a function of specimen thickness in AlAs [110]. The probe was incident between dumbbells (PPBD). The beam width is given as the diameter of circular areas, in the real space intensity maps, in which 90%, 80%, 70%, 60%, 50% and 40% of the total probe intensity is contained. The circular areas are centred on the initial probe position.

A.3 12mrad Probe Simulations

A.3.1 GaAs Real Space Intensity Maps

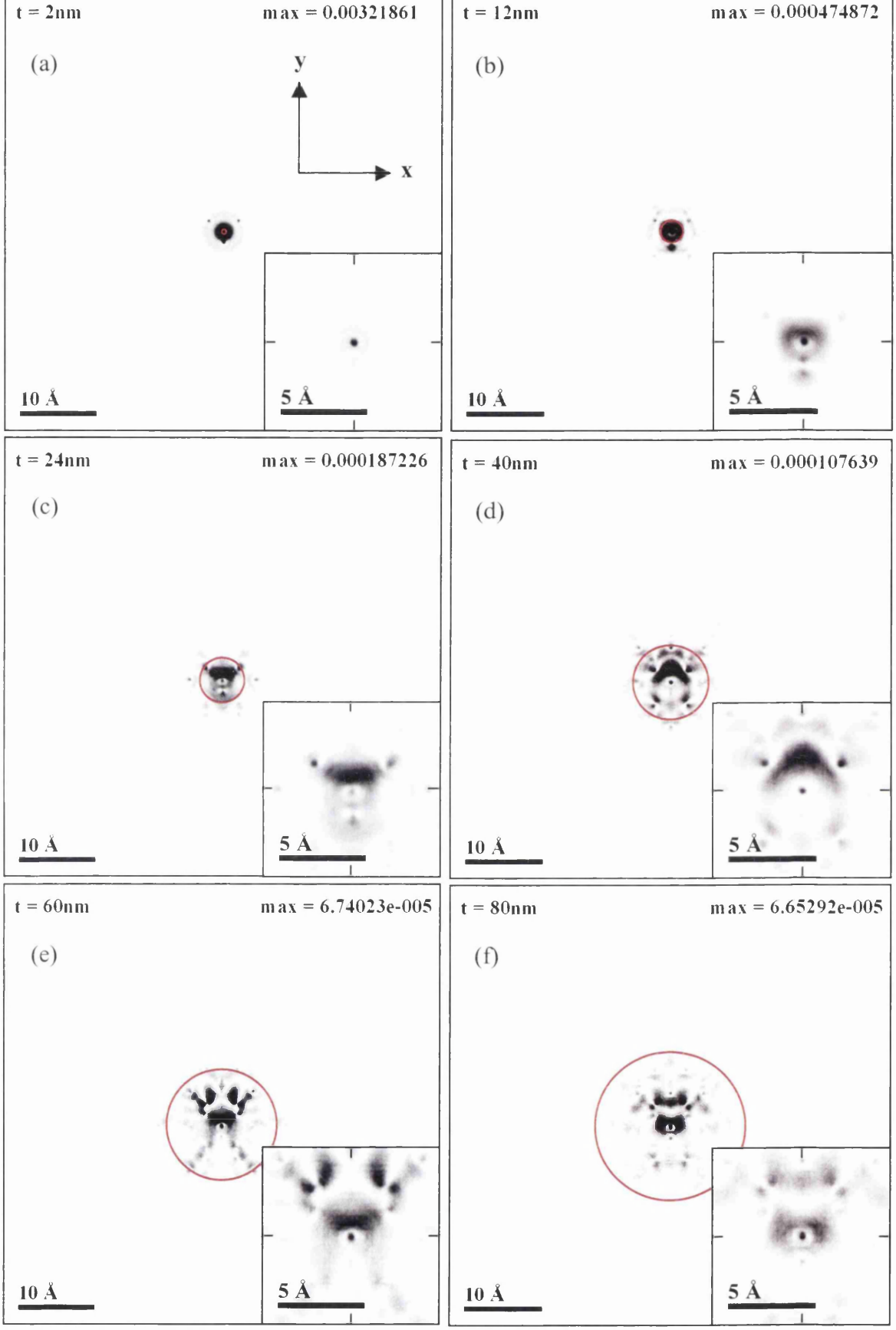

Contrast enhanced simulated electron intensity maps at various depths in a crystal of GaAs [110]. The insets show a magnified view of the central region of each map taken over the full intensity range. A 12mrad, 0.16nm probe is incident on an As column. Black pixels are the most intense. The crystal depths are: **(a)** 2nm **(b)** 12nm **(c)** 24nm **(d)** 40nm **(e)** 60nm and **(f)** 80nm. Max refers to the maximum intensity contained within a single pixel. Circle radius = αt. The total electron intensity of the probe = 1.

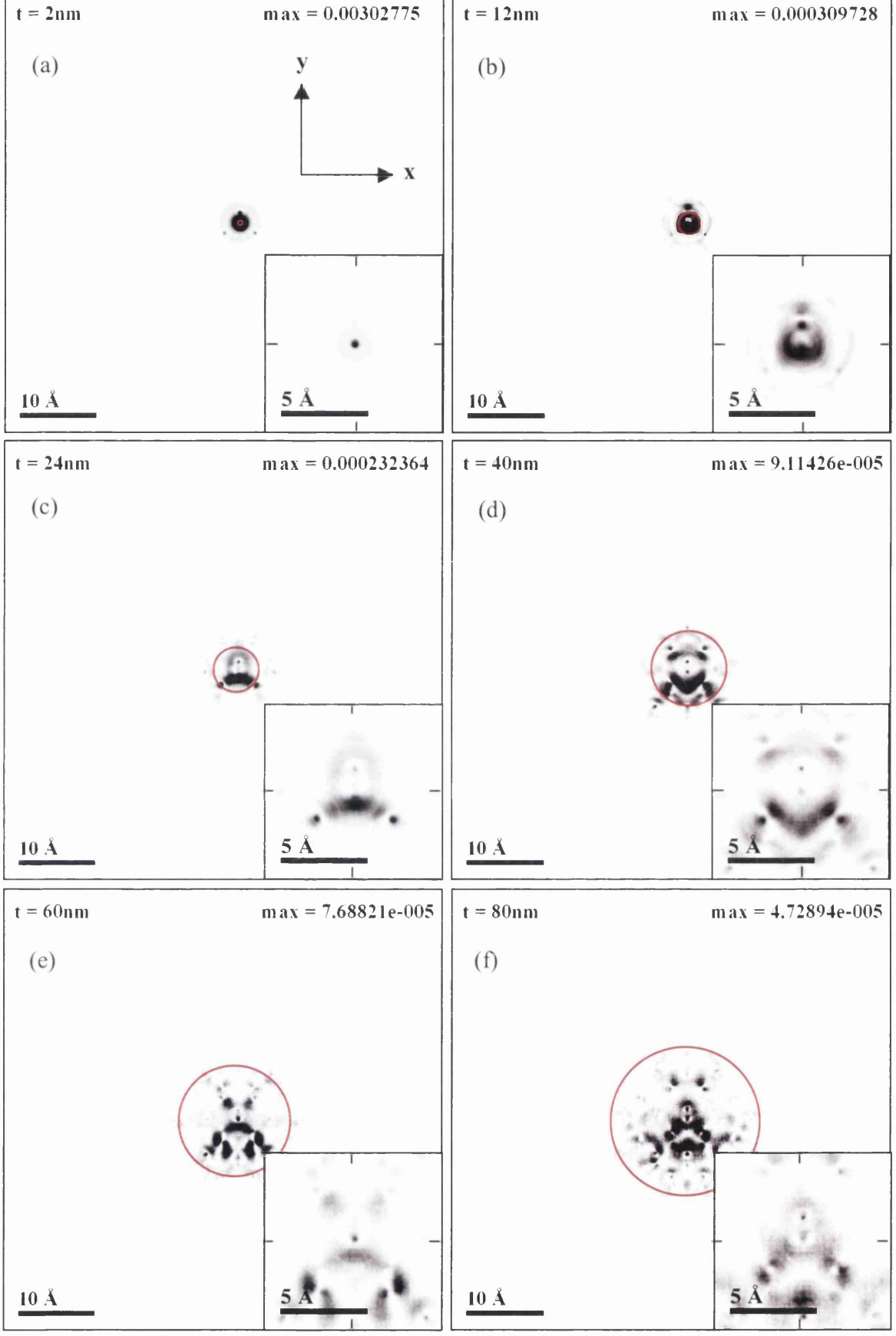

Contrast enhanced simulated electron intensity maps at various depths in a crystal of GaAs [110]. The insets show a magnified view of the central region of each map taken over the full intensity range. A 12mrad, 0.16nm probe is incident on a Ga column. Black pixels are the most intense. The crystal depths are: **(a)** 2nm **(b)** 12nm **(c)** 24nm **(d)** 40nm **(e)** 60nm and **(f)** 80nm. Max refers to the maximum intensity contained within a single pixel. Circle radius = αt. The total electron intensity of the probe = 1.

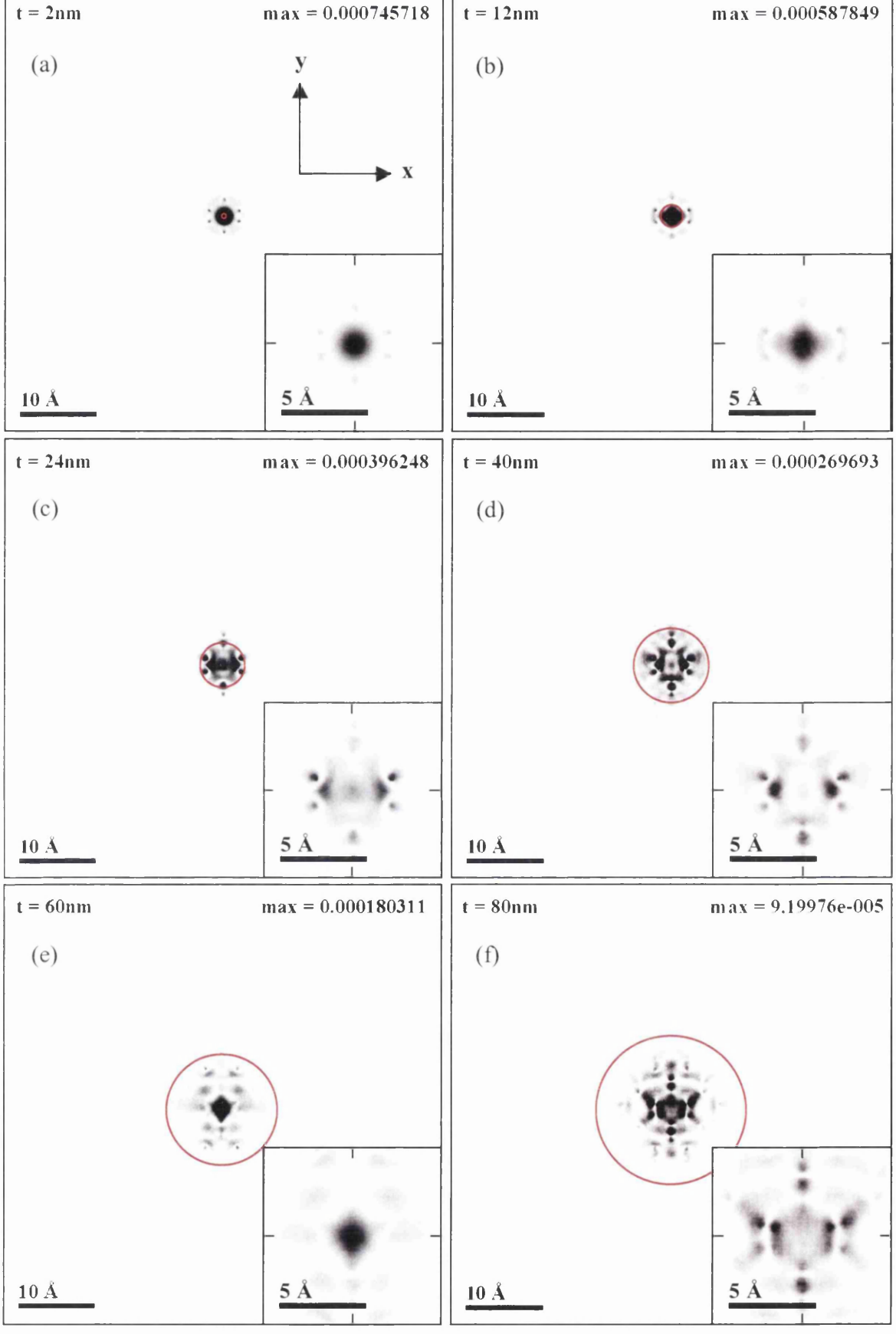

Contrast enhanced simulated electron intensity maps at various depths in a crystal of GaAs [110]. The insets show a magnified view of the central region of each map taken over the full intensity range. A 12mrad, 0.16nm probe is incident between dumbbells. Black pixels are the most intense. The crystal depths are: **(a)** 2nm **(b)** 12nm **(c)** 24nm **(d)** 40nm **(e)** 60nm and **(f)** 80nm. Max refers to the maximum intensity contained within a single pixel. Circle radius = αt. The total electron intensity of the probe = 1.

A.3.2 GaAs PPAs Condition

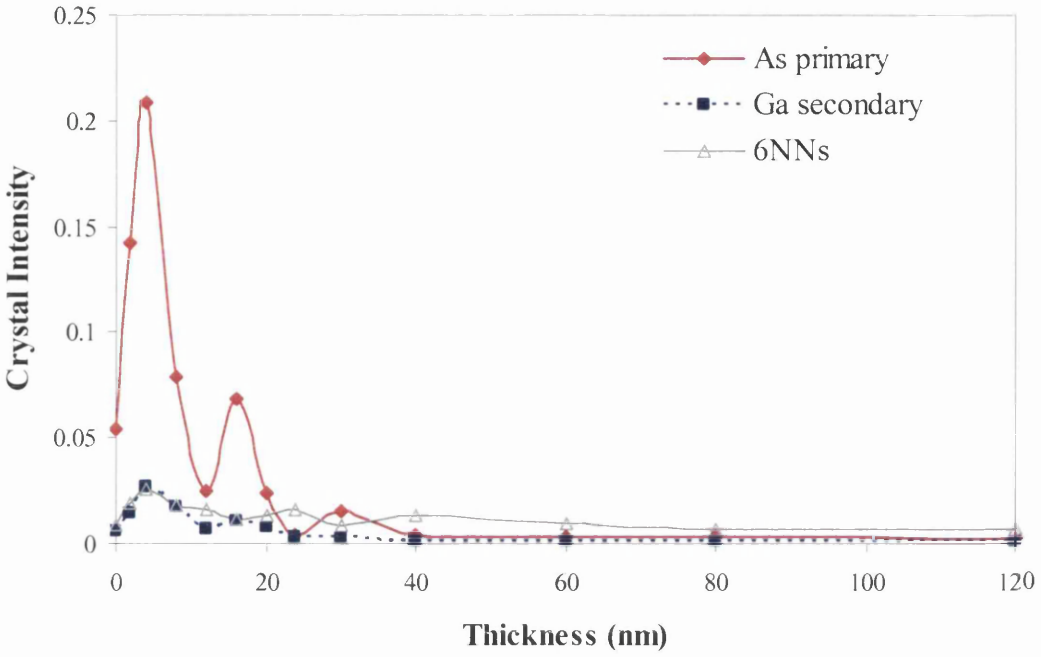

A graph of the simulated real space electron intensity along 2 columns in GaAs [110] as a function of specimen thickness. The probe is incident on an As column on the top surface of the specimen. The intensity on the primary As column (red), on the neighbouring Ga column (blue) and the sum of the intensity on the nearest 6 dumbbells (grey) are plotted. The values are the sum of a 9pixel × 9pixel area around each column in the intensity maps. The intensity is normalised with respect to the total intensity in

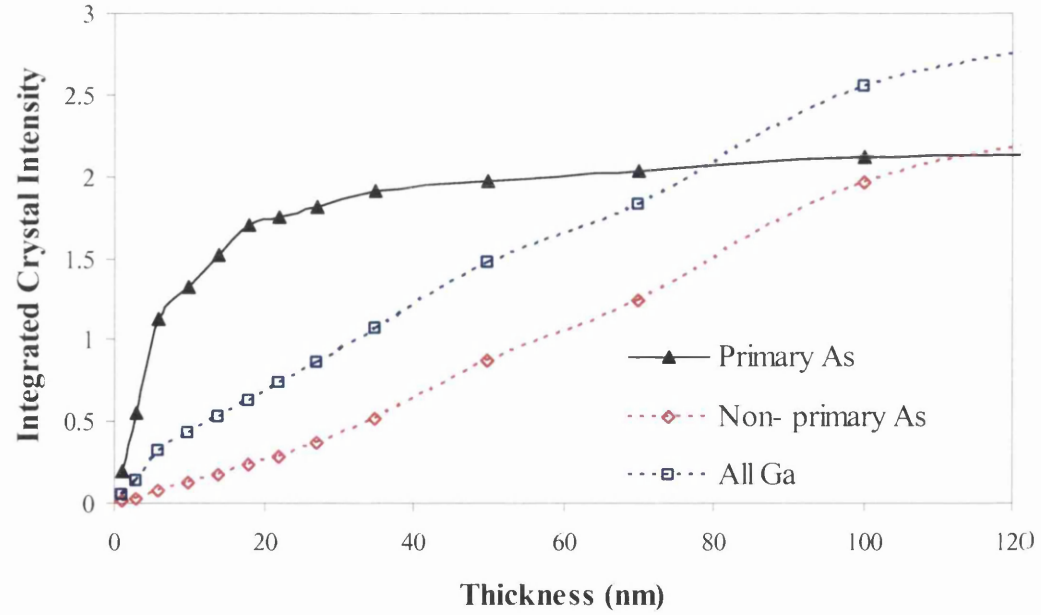

A graph of the simulated integrated crystal intensity on the primary As column, all non-primary As sites and all Ga sites as a function of thickness.

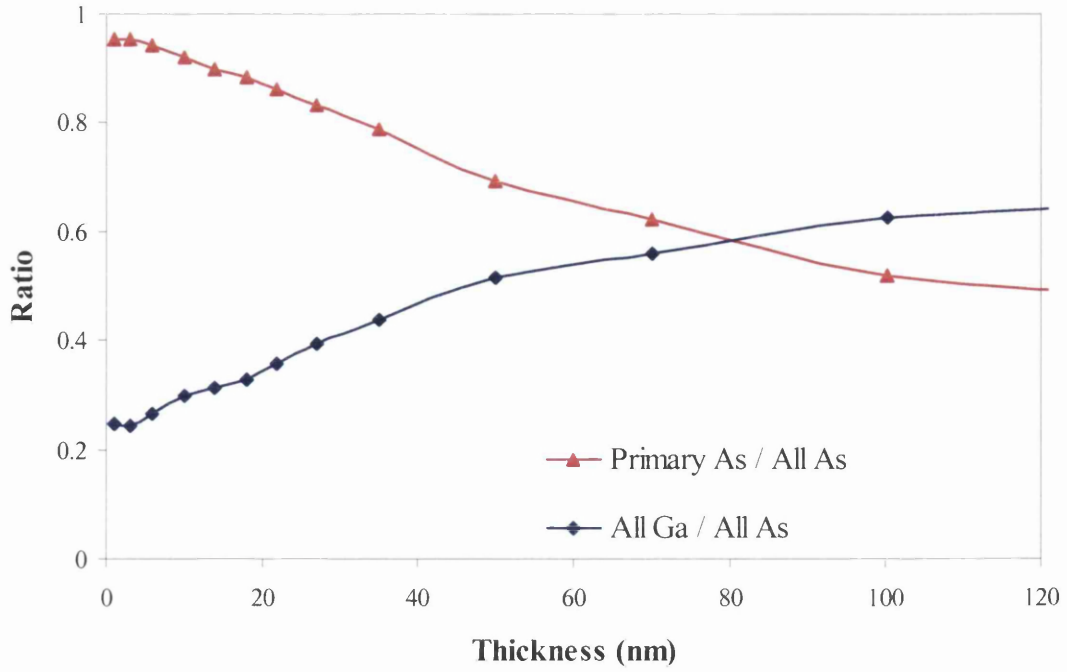

A graph of the simulated integrated crystal intensity on the primary As column / all As sites as a function of thickness. Also shown is the simulated integrated crystal intensity on all Ga sites / all As sites as a function of thickness.

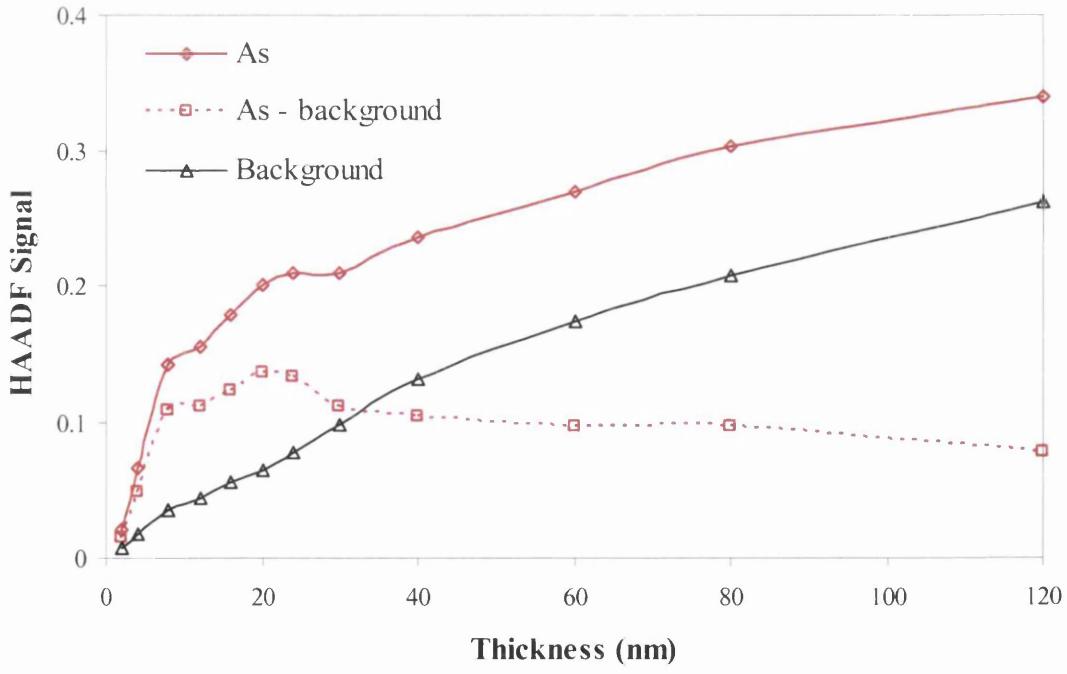

Simulated HAADF STEM intensity for GaAs [110] as a function of specimen thickness. The total HAADF signal for an incident probe on an As column (red line) is plotted. Also plotted is the HAADF background signal i.e. for the probe situated between dumbbells (black line). The As – background signal is also shown. The HAADF signal is normalised with respect to the intensity that the probe generates in the detector plane in the absence of a specimen. The HAADF detector has a range of 70mrad to 210mrad.

A.3.3 GaAs PPGa Condition

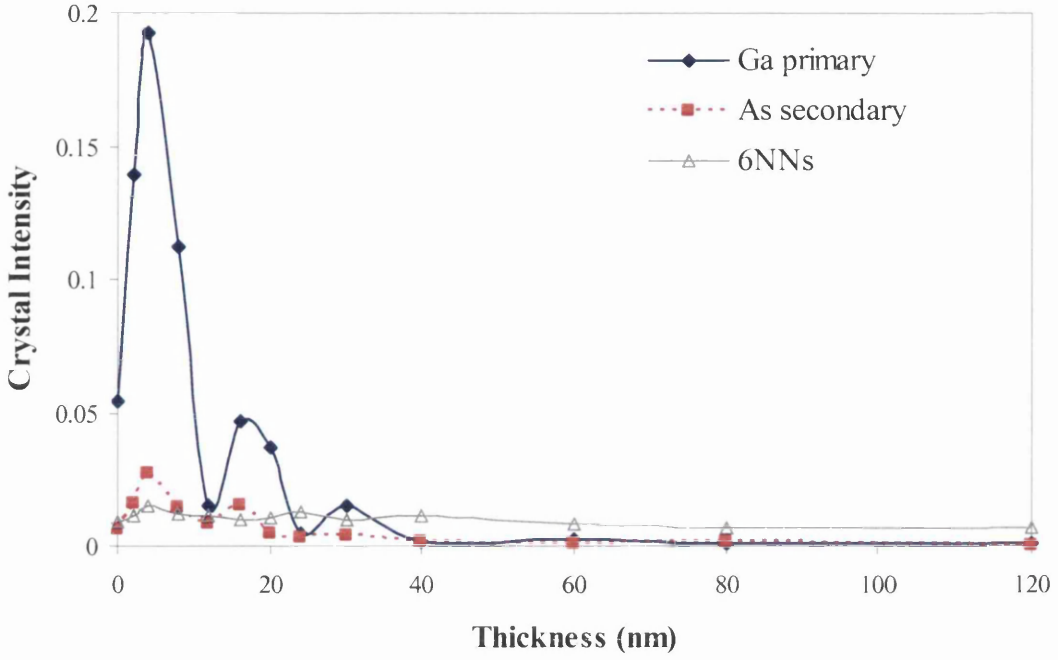

A graph of the simulated real space electron intensity along 2 columns in GaAs [110] as a function of specimen thickness. The probe is incident on a Ga column on the top surface of the specimen. The intensity on the primary Ga column (blue), on the neighbouring As column (red) and the sum of the intensity on the nearest 6 dumbbells (grey) are plotted. The values are the sum of a 9pixel × 9pixel area around each column in the intensity maps. The intensity is normalised with respect to the total intensity in the probe (equal to 1).

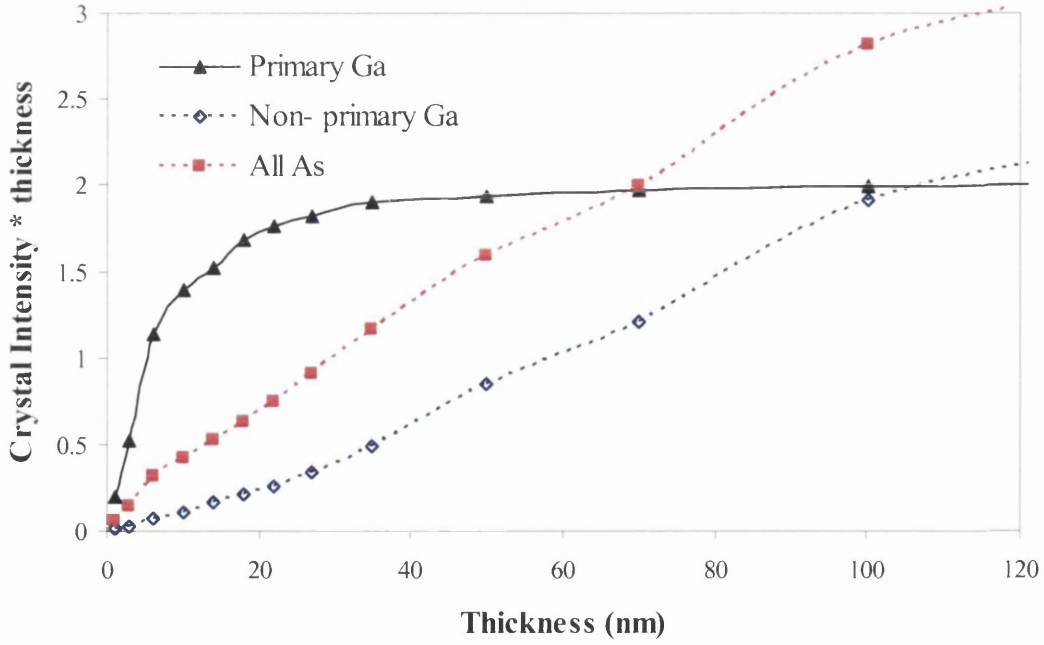

A graph of the simulated integrated crystal intensity on the primary Ga column, all non-primary Ga sites and all As sites as a function of thickness.

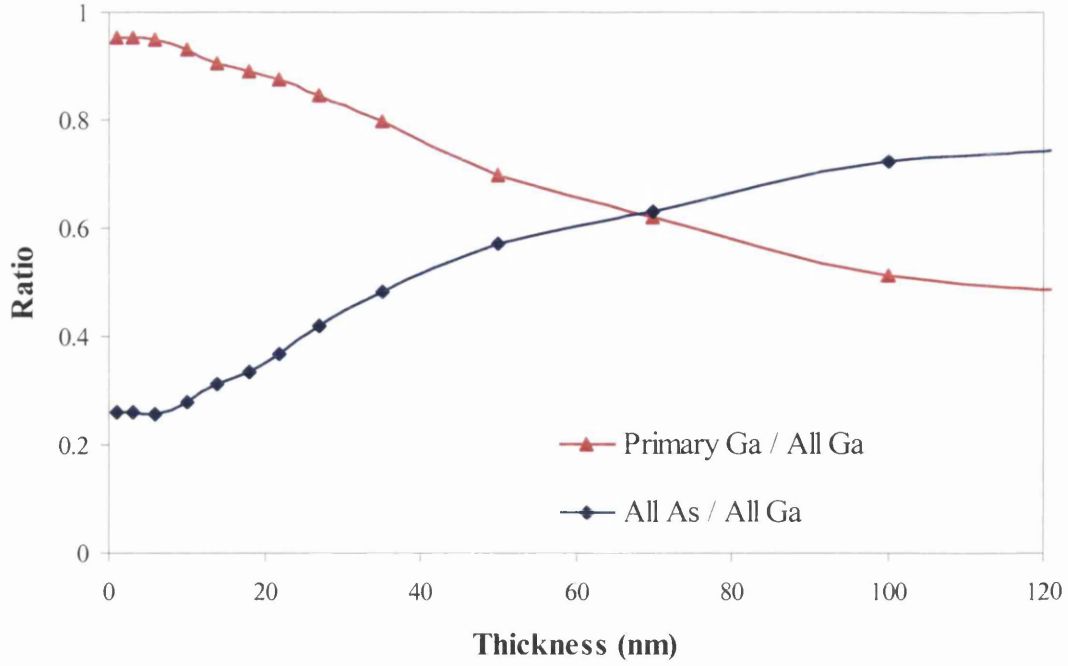

A graph of the simulated integrated crystal intensity on the primary Ga column / all Ga sites as a function of thickness. Also shown is the simulated integrated crystal intensity on all As sites / all Ga sites as a function of thickness.

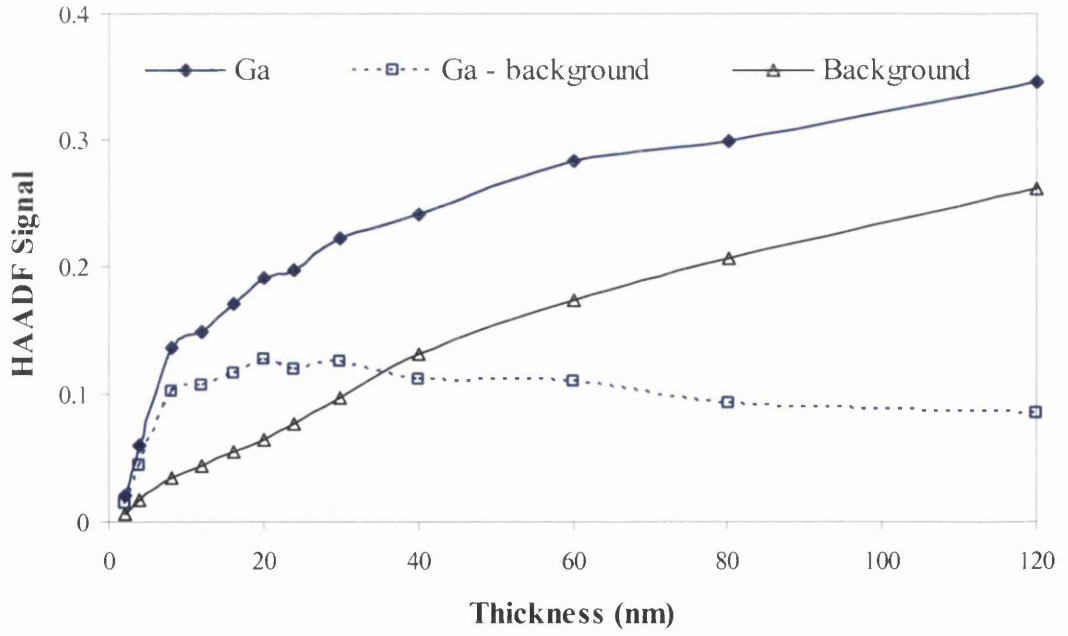

Simulated HAADF STEM intensity for GaAs [110] as a function of specimen thickness. The total HAADF signal for an incident probe on a Ga column (blue line) is plotted. Also plotted is the HAADF background signal i.e. for the probe situated between dumbbells (black line). The As – background signal is also shown. The HAADF signal is normalised with respect to the intensity that the probe generates in the detector plane in the absence of a specimen. The HAADF detector has a range of 70mrad to 210mrad.

A.3.4 GaAs PPBD Condition

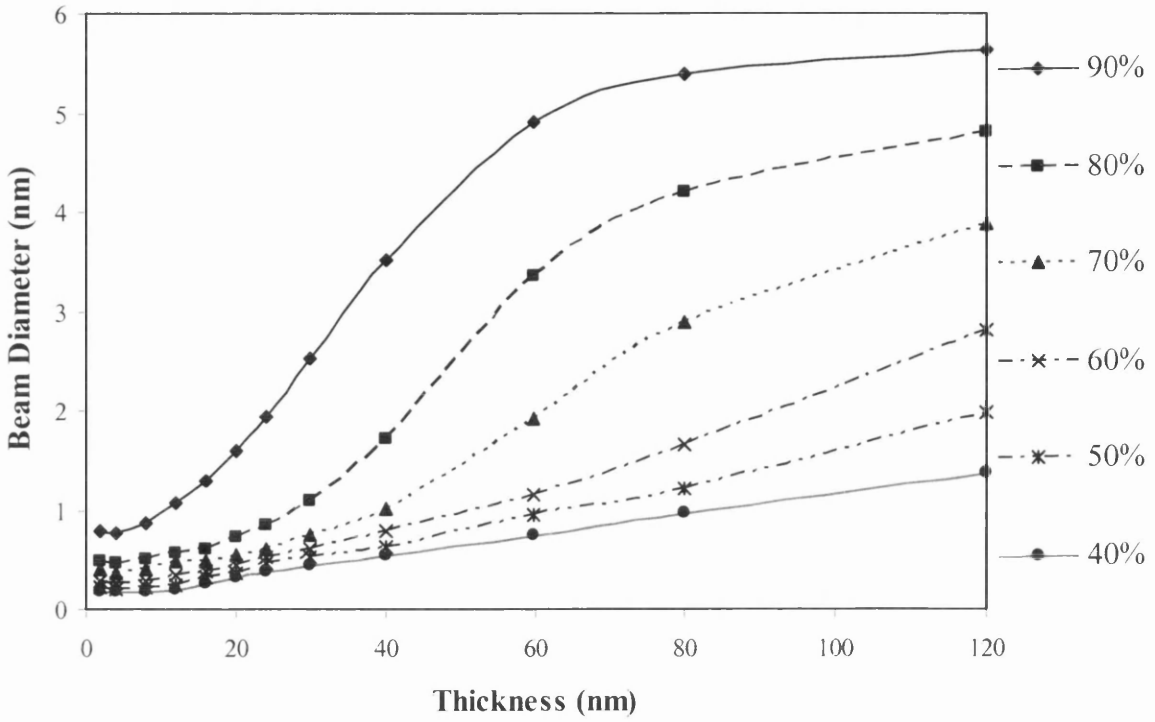

A graph of the simulated beam width as a function of specimen thickness in GaAs [110]. The probe was incident between dumbbells (PPBD). The beam width is given as the diameter of circular areas, in the real space intensity maps, in which 90%, 80%, 70%, 60%, 50% and 40% of the total probe intensity is contained. The circular areas are centred on the initial probe position.

A.3.5 AIAs Real Space Intensity Maps

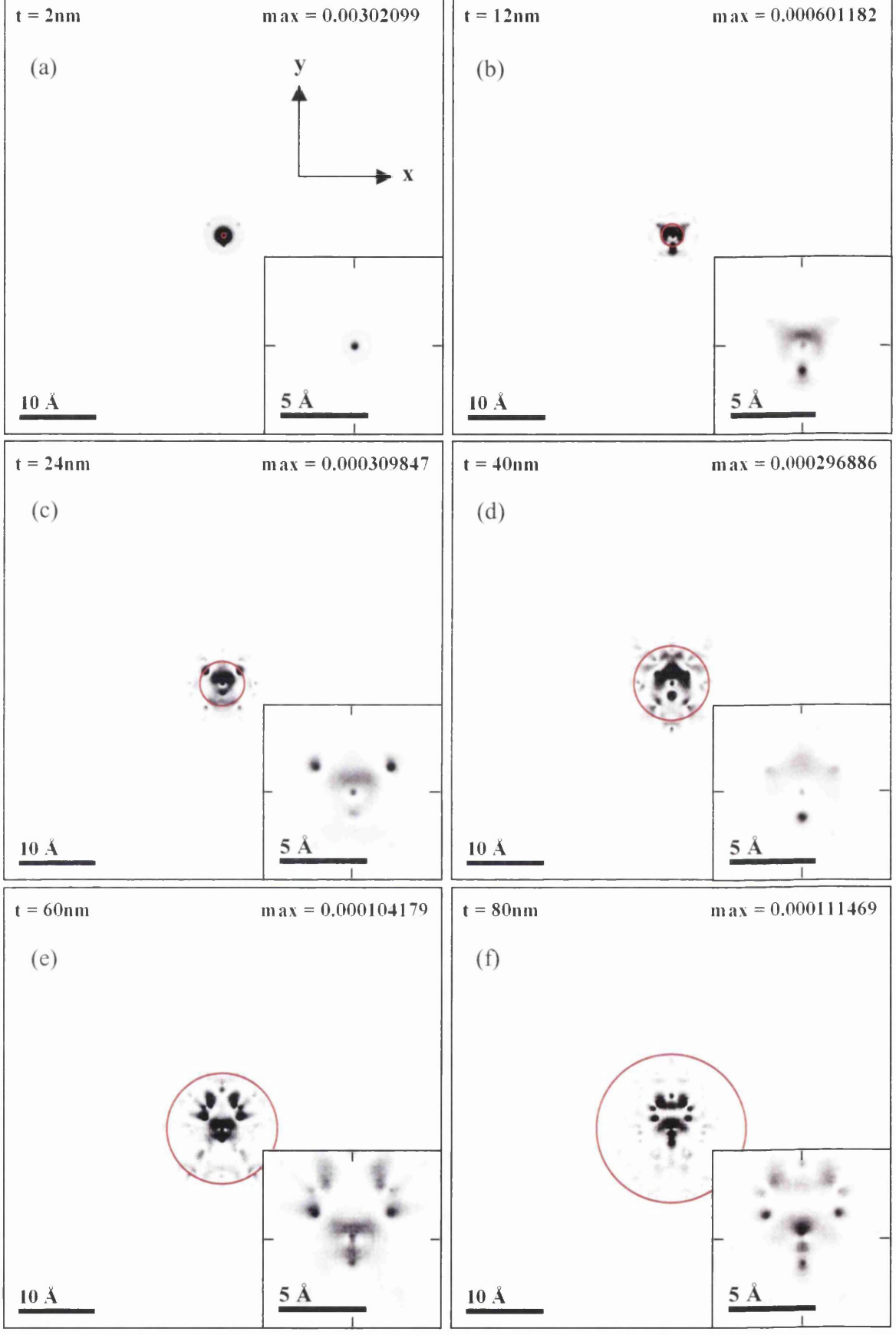

Contrast enhanced simulated electron intensity maps at various depths in a crystal of AlAs [110]. The insets show a magnified view of the central region of each map taken over the full intensity range. A 12mrad, 0.16nm probe is incident on an As column. Black pixels are the most intense. The crystal depths are: **(a)** 2nm **(b)** 12nm **(c)** 24nm **(d)** 40nm **(e)** 60nm and **(f)** 80nm. Max refers to the maximum intensity contained within a single pixel. Circle radius = αt. The total electron intensity of the probe = 1.

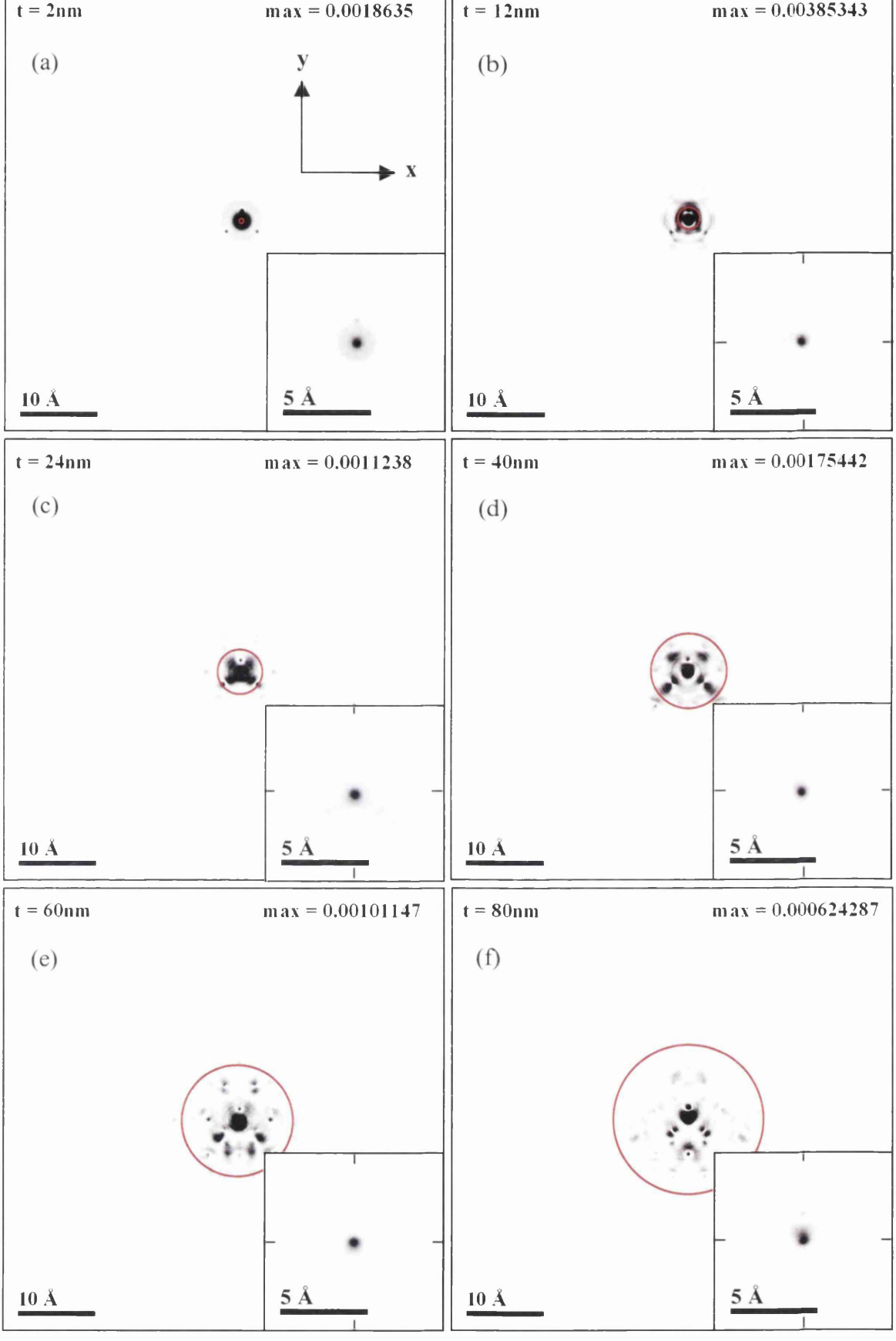

Contrast enhanced simulated electron intensity maps at various depths in a crystal of AlAs [110]. The insets show a magnified view of the central region of each map taken over the full intensity range. A 12mrad, 0.16nm probe is incident on an Al column. Black pixels are the most intense. The crystal depths are: **(a)** 2nm **(b)** 12nm **(c)** 24nm **(d)** 40nm **(e)** 60nm and **(f)** 80nm. Max refers to the maximum intensity contained within a single pixel. Circle radius = αt. The total electron intensity of the probe = 1.

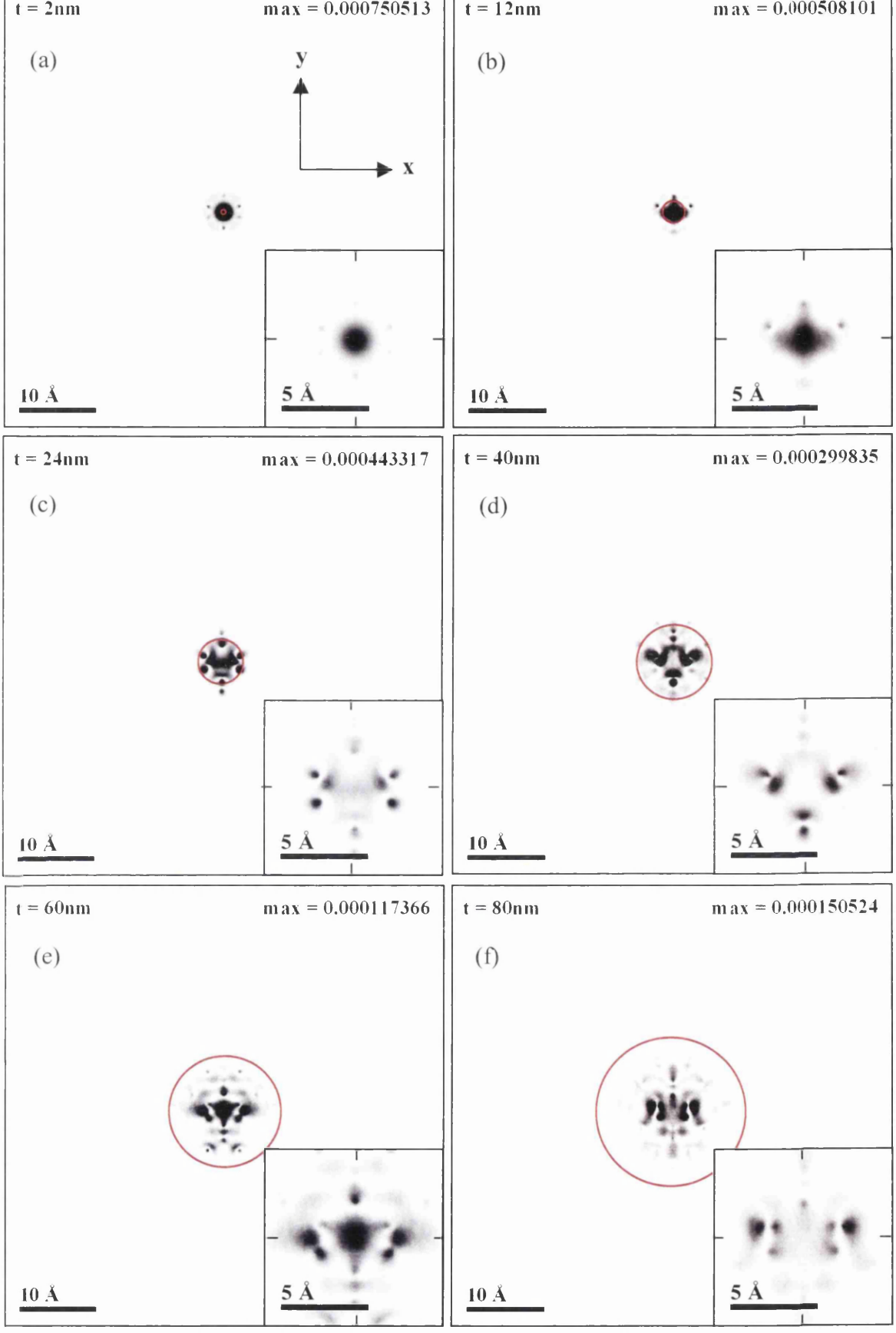

Contrast enhanced simulated electron intensity maps at various depths in a crystal of AlAs [110]. The insets show a magnified view of the central region of each map taken over the full intensity range. A 12mrad, 0.16nm probe is incident between dumbbells. Black pixels are the most intense. The crystal depths are: **(a)** 2nm **(b)** 12nm **(c)** 24nm **(d)** 40nm **(e)** 60nm and **(f)** 80nm. Max refers to the maximum intensity contained within a single pixel. Circle radius = αt. The total electron intensity of the probe = 1.

A.3.6 AlAs PPAs Condition

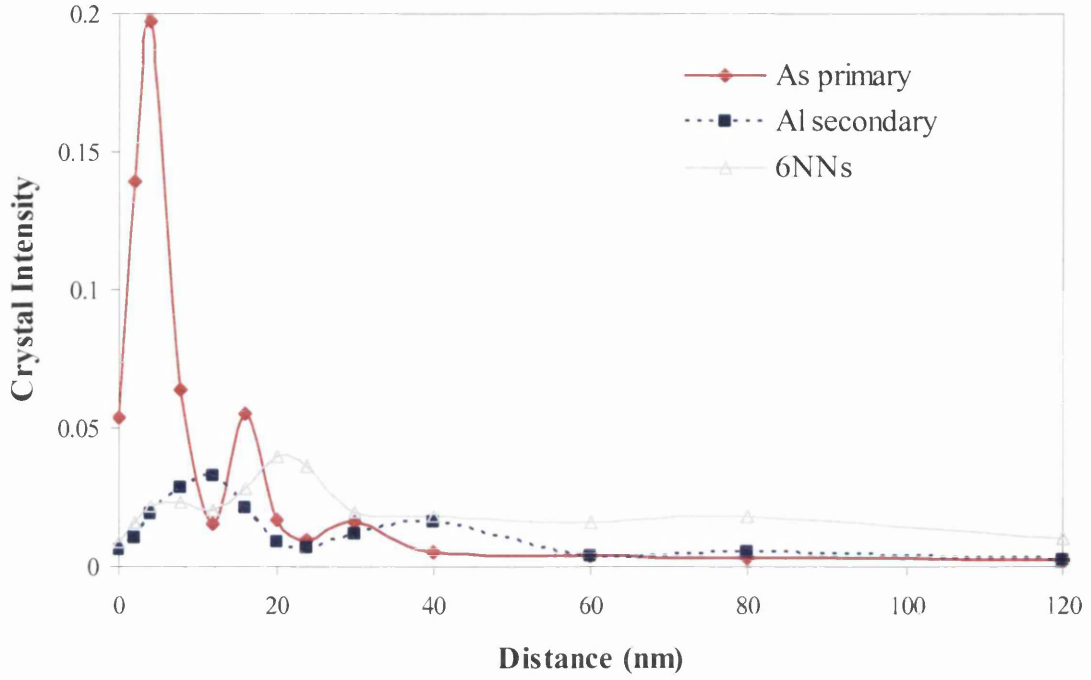

A graph of the simulated real space electron intensity along 2 columns in AlAs [110] as a function of specimen thickness. The probe is incident on an As column on the top surface of the specimen. The intensity on the primary As column (red), on the neighbouring Al column (blue) and the sum of the intensity on the nearest 6 dumbbells (grey) are plotted. The values are the sum of a 9pixel × 9pixel area around each column in the intensity maps. The intensity is normalised with respect to the total intensity in the probe (equal to 1).

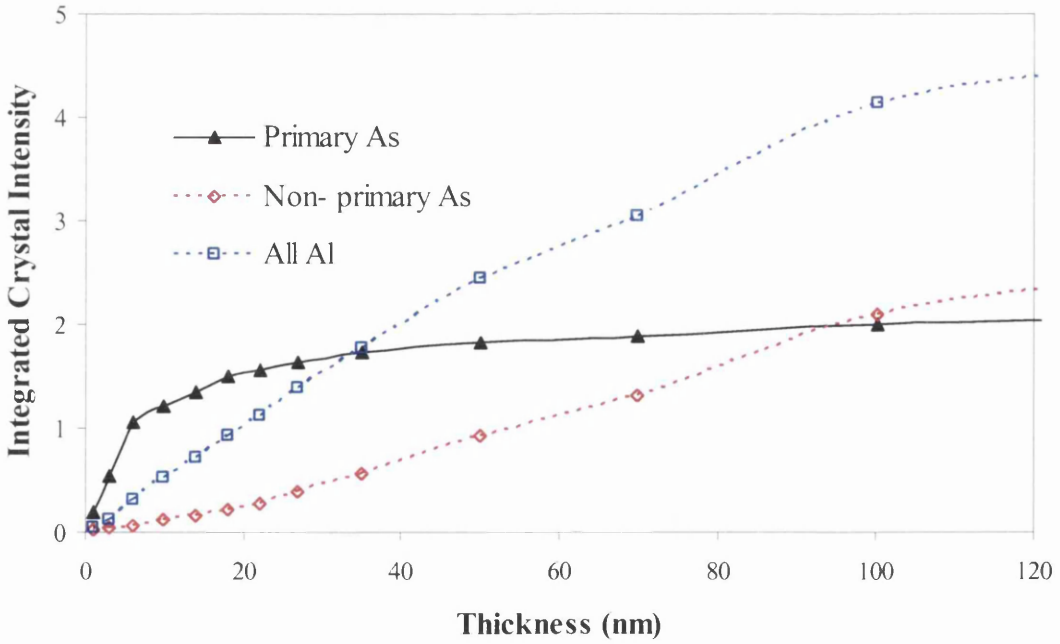

A graph of the simulated integrated crystal intensity on the primary As column, all non-primary As sites and all Al sites as a function of thickness.

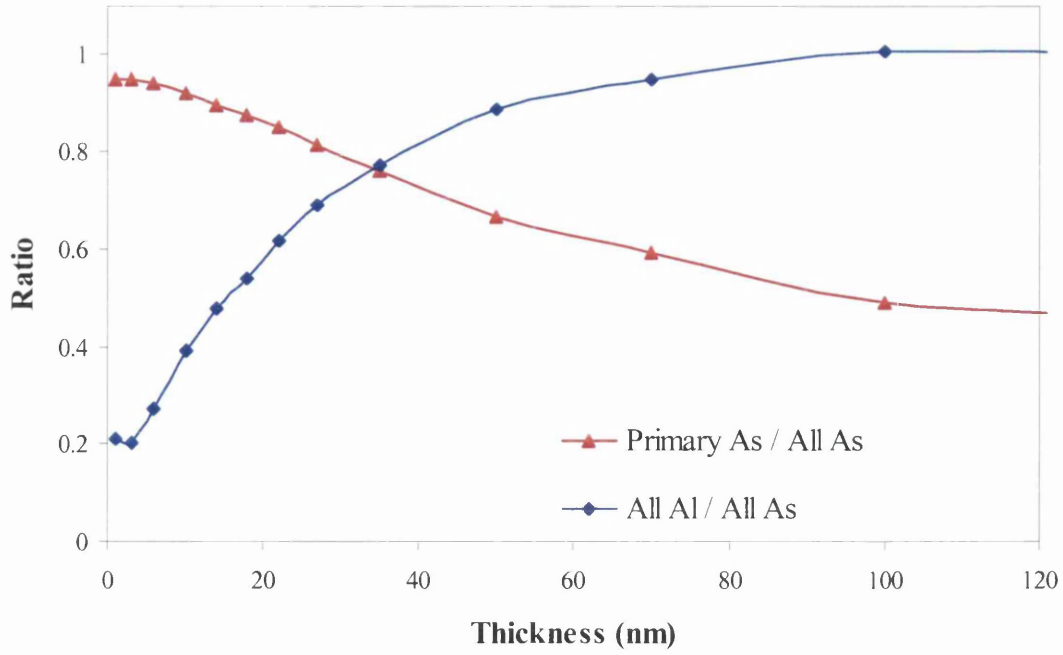

A graph of the simulated integrated crystal intensity on the primary As column / all As sites as a function of thickness. Also shown is the simulated integrated crystal intensity on all Al sites / all As sites as a function of thickness.

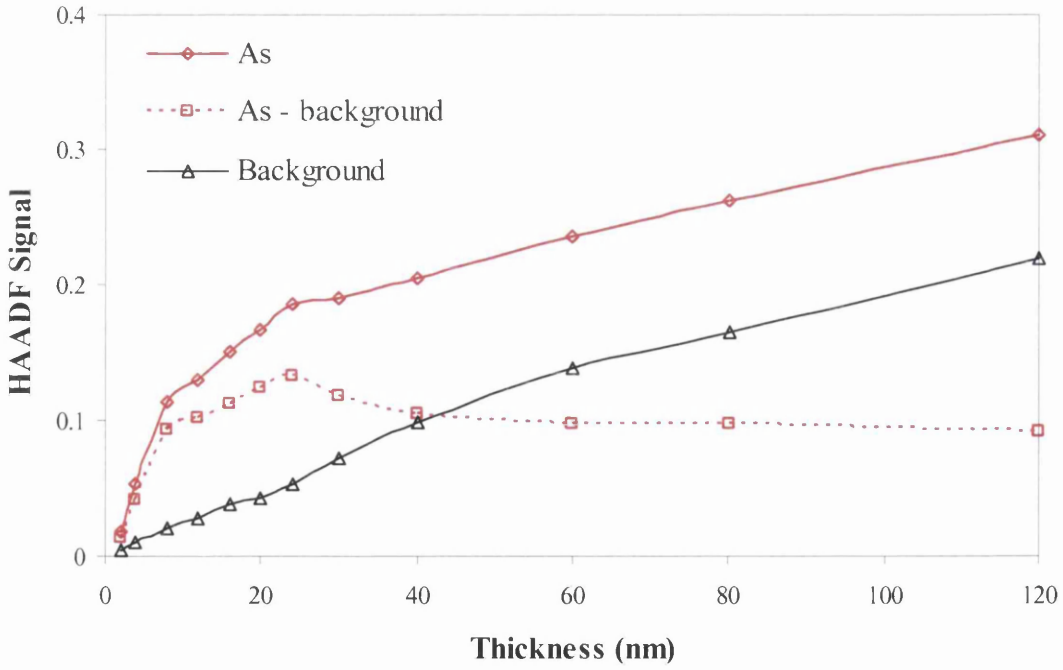

Simulated HAADF STEM intensity for AlAs [110] as a function of specimen thickness. The total HAADF signal for an incident probe on an As column (red line) is plotted. Also plotted is the HAADF background signal i.e. for the probe situated between dumbbells (black line). The As – background signal is also shown. The HAADF signal is normalised with respect to the intensity that the probe generates in the detector plane in the absence of a specimen. The HAADF detector has a range of 70mrad to 210mrad.

A.3.7 AlAs PPAl Condition

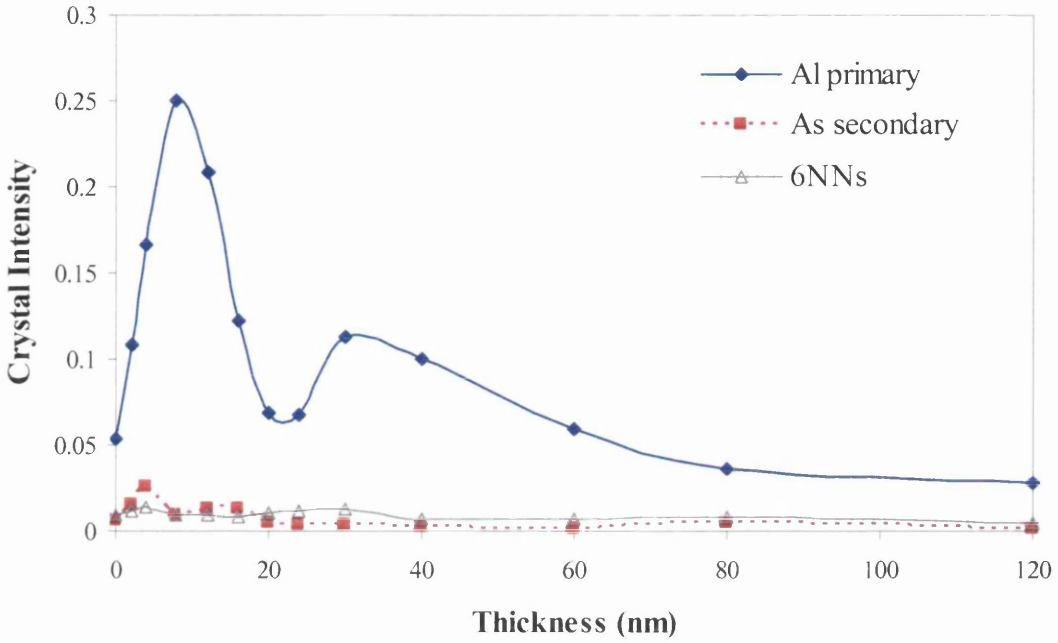

A graph of the simulated real space electron intensity along 2 columns in AlAs [110] as a function of specimen thickness. The probe is incident on an Al column on the top surface of the specimen. The intensity on the primary Al column (blue), on the neighbouring As column (red) and the sum of the intensity on the nearest 6 dumbbells (grey) are plotted. The values are the sum of a 9pixel × 9pixel area around each column in the intensity maps. The intensity is normalised with respect to the total intensity in the probe (equal to 1).

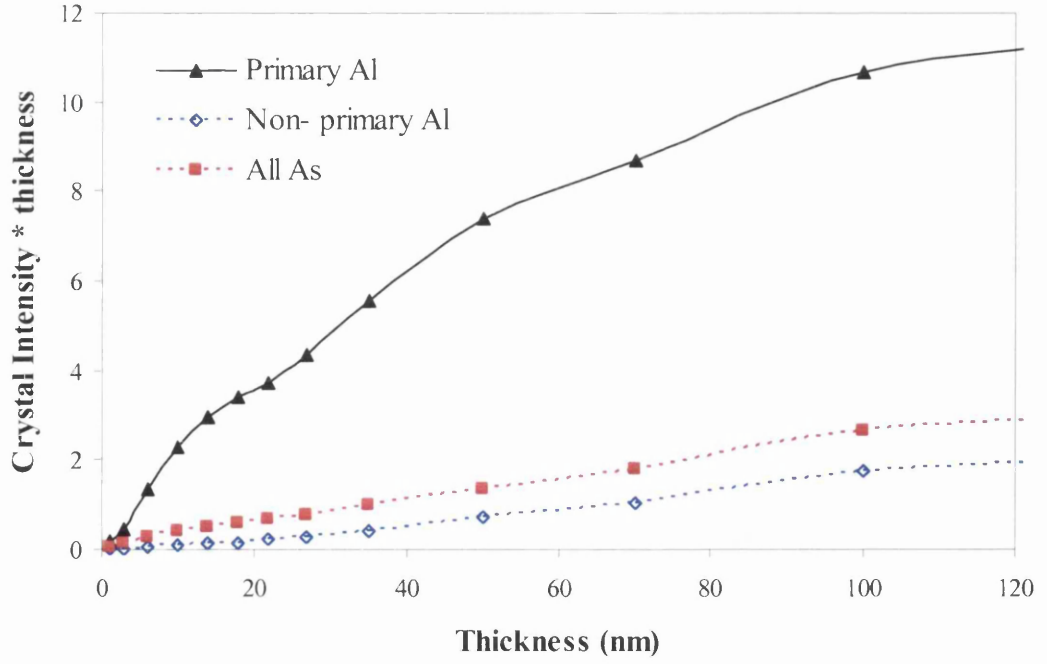

A graph of the simulated integrated crystal intensity on the primary Al column, all non-primary Al sites and all As sites as a function of thickness.

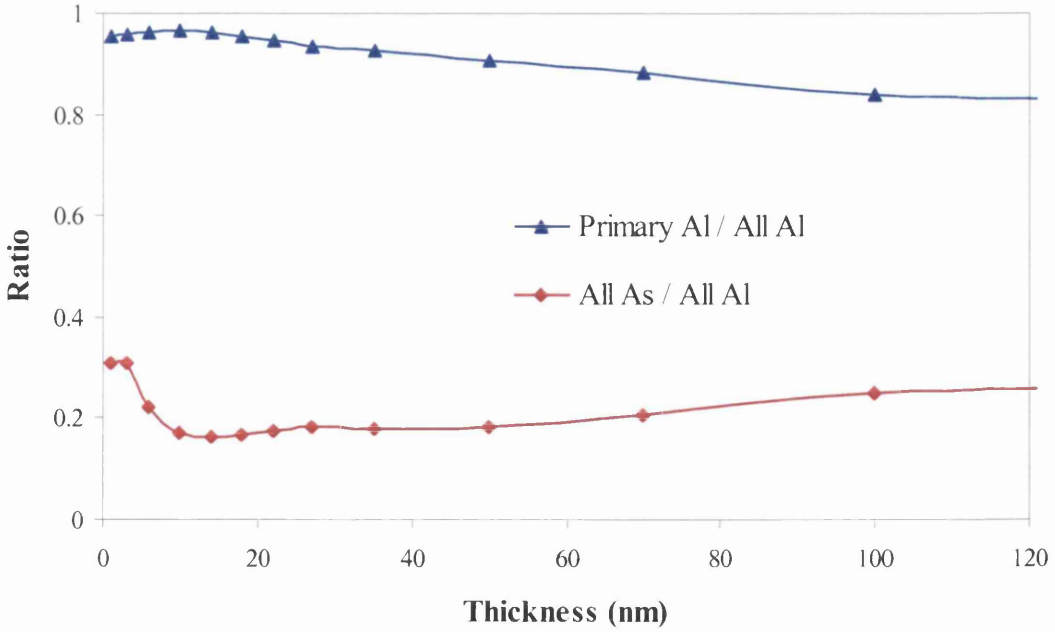

A graph of the simulated integrated crystal intensity on the primary Al column / all Al sites as a function of thickness. Also shown is the simulated integrated crystal intensity on all As sites / all Al sites as a function of thickness.

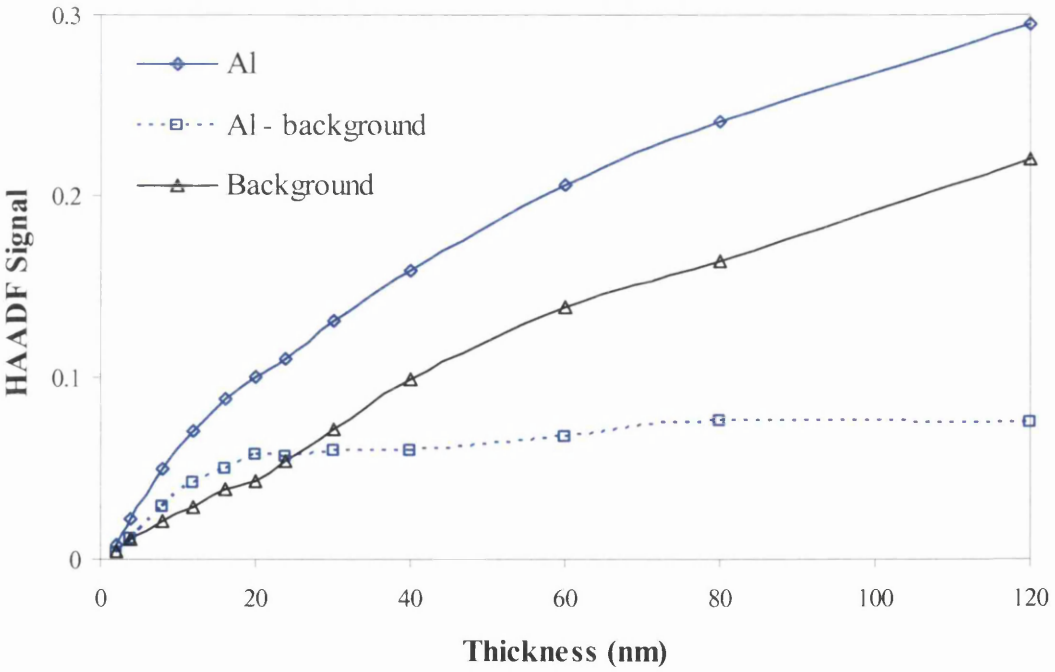

Simulated HAADF STEM intensity for AlAs [110] as a function of specimen thickness. The total HAADF signal for an incident probe on an Al column (blue line) is plotted. Also plotted is the HAADF background signal i.e. for the probe situated between dumbbells (black line). The Al – background signal is also shown. The HAADF signal is normalised with respect to the intensity that the probe generates in the detector plane in the absence of a specimen. The HAADF detector has a range of 70mrad to 210mrad.

A.3.8 AlAs PPAI Condition

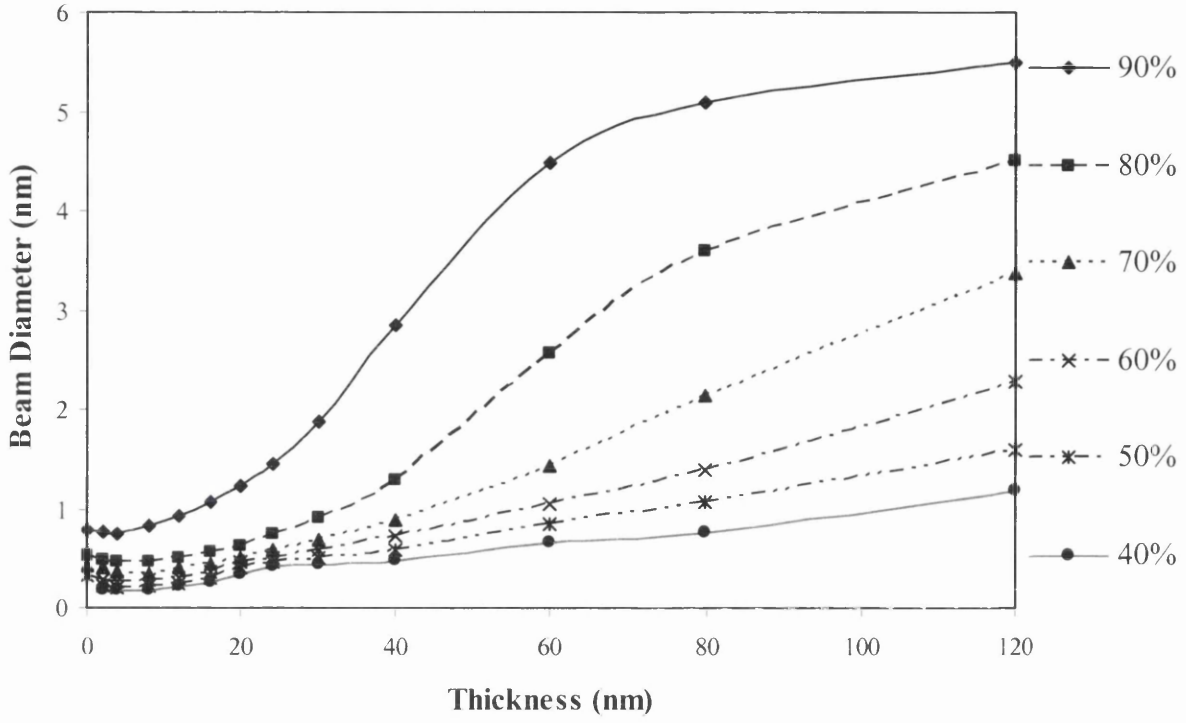

A graph of the simulated beam width as a function of specimen thickness in AlAs [110]. The probe was incident between dumbbells (PPBD). The beam width is given as the diameter of circular areas, in the real space intensity maps, in which 90%, 80%, 70%, 60%, 50% and 40% of the total probe intensity is contained. The circular areas are centred on the initial probe position.

Appendix B: Transition Region Widths of AlAs / GaAs Structures

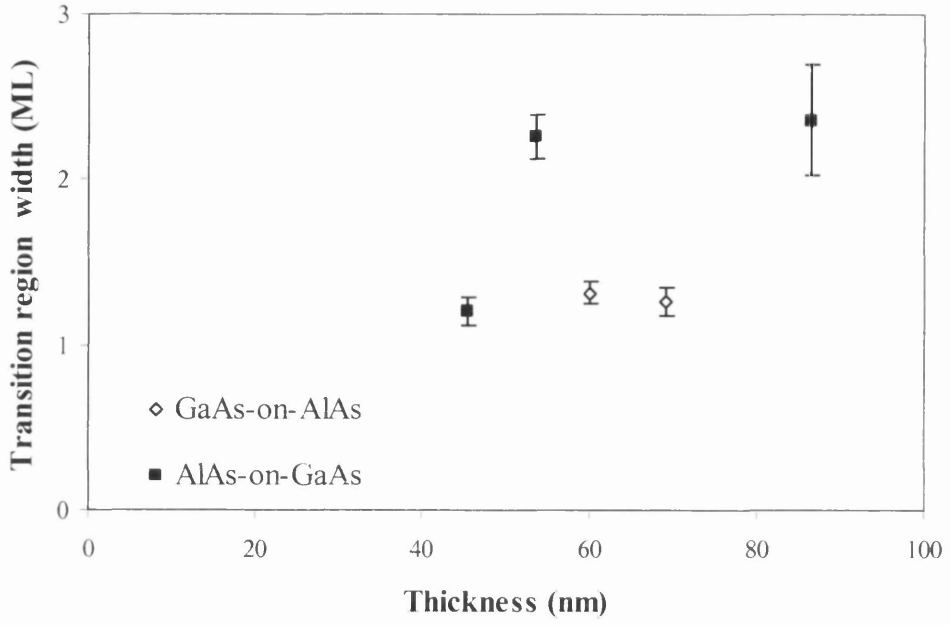

A graph of the variation of the column ratio transition region width as a function of thickness for GaAs-on-AlAs and AlAs-on-GaAs single interfaces. Each width was calculated from the fit of the error function using the 25% and 75% measure.

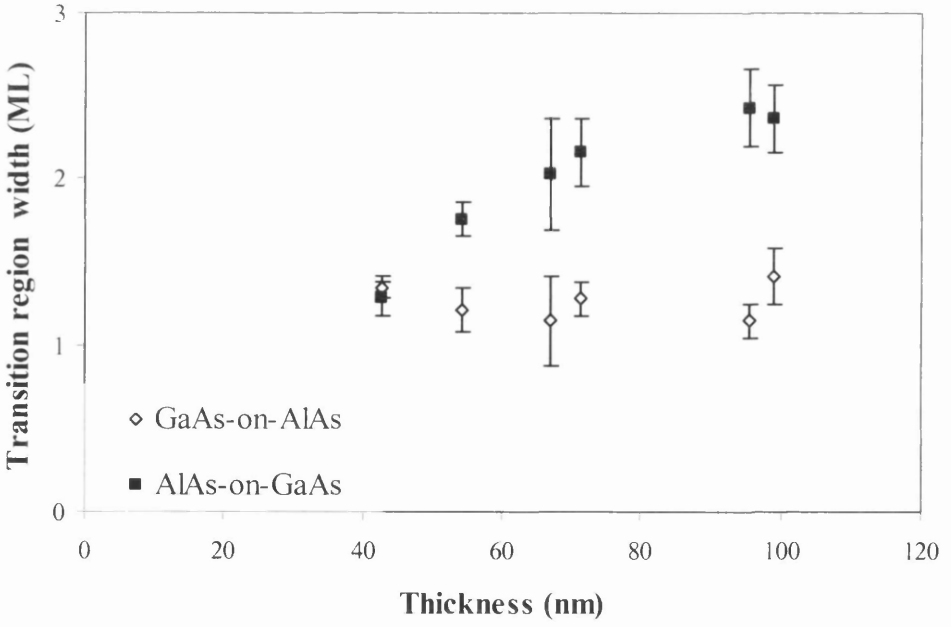

A graph of the variation of the column ratio transition region width as a function of thickness for GaAs-on-AlAs and AlAs-on-GaAs interfaces from the 9ML AlAs / 9ML GaAs superlattice. Each width was calculated from the fit of the error function using the 25% and 75% measure.